Journal of Sensors

AI-Driven Intelligent Sensor Networks: Key Enabling Theories, Architectures, Protocols, and Techniques

Lead Guest Editor: Han Wang
Guest Editors: Khaled Rabie and Wali Ullah Khan

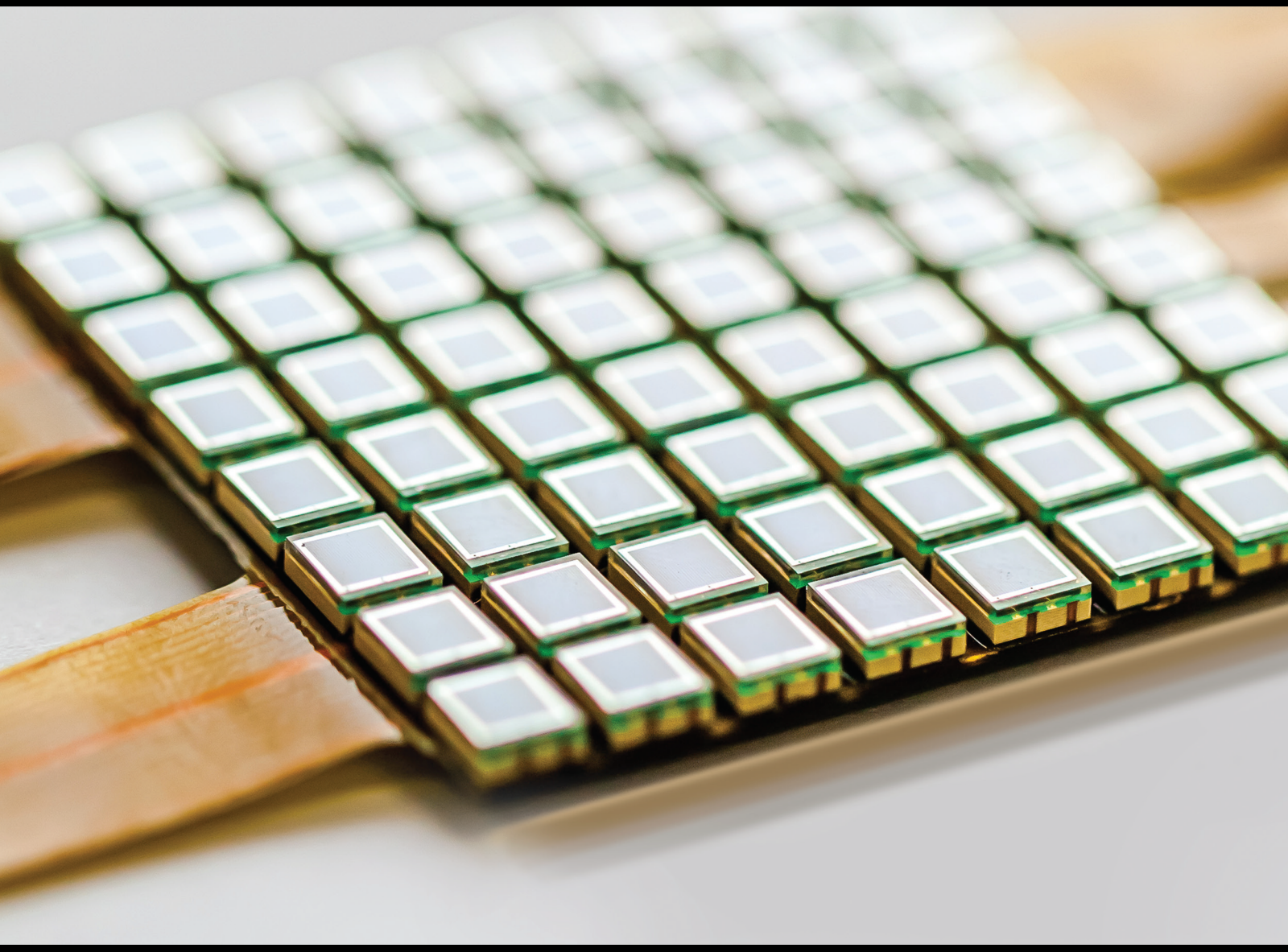

AI-Driven Intelligent Sensor Networks: Key Enabling Theories, Architectures, Protocols, and Techniques

Journal of Sensors

AI-Driven Intelligent Sensor Networks: Key Enabling Theories, Architectures, Protocols, and Techniques

Lead Guest Editor: Han Wang
Guest Editors: Khaled Rabie and Wali Ullah Khan

Contents

Contents

Contents

Hindawi
Journal of Sensors
Volume 2024, Article ID 9858596, 1 page
https://doi.org/10.1155/2024/9858596

Retraction

Retracted: Intelligent Analysis and Application of Preschool Education Language Teaching Quality Based on Deep Neural Network

Journal of Sensors

Received 30 January 2024; Accepted 30 January 2024; Published 31 January 2024

This article has been retracted by Hindawi following an investigation undertaken by the publisher [1]. This investigation has uncovered evidence of one or more of the following indicators of systematic manipulation of the publication process:

(1) Discrepancies in scope
(2) Discrepancies in the description of the research reported
(3) Discrepancies between the availability of data and the research described
(4) Inappropriate citations
(5) Incoherent, meaningless and/or irrelevant content included in the article
(6) Manipulated or compromised peer review

The presence of these indicators undermines our confidence in the integrity of the article's content and we cannot, therefore, vouch for its reliability. Please note that this notice is intended solely to alert readers that the content of this article is unreliable. We have not investigated whether authors were aware of or involved in the systematic manipulation of the publication process.

In addition, our investigation has also shown that one or more of the following human-subject reporting requirements has not been met in this article: ethical approval by an Institutional Review Board (IRB) committee or equivalent, patient/participant consent to participate, and/or agreement to publish patient/participant details (where relevant).

Wiley and Hindawi regrets that the usual quality checks did not identify these issues before publication and have since put additional measures in place to safeguard research integrity.

We wish to credit our own Research Integrity and Research Publishing teams and anonymous and named external researchers and research integrity experts for contributing to this investigation.

The corresponding author, as the representative of all authors, has been given the opportunity to register their agreement or disagreement to this retraction. We have kept a record of any response received.

References

[1] H. Li and C. Niu, "Intelligent Analysis and Application of Preschool Education Language Teaching Quality Based on Deep Neural Network," *Journal of Sensors*, vol. 2022, Article ID 7548686, 11 pages, 2022.

Hindawi
Journal of Sensors
Volume 2024, Article ID 9891450, 1 page
https://doi.org/10.1155/2024/9891450

Retraction

Retracted: A Weighted Cluster Head Selection Algorithm for Energy Efficient Wireless Sensor Networks

Journal of Sensors

Received 23 January 2024; Accepted 23 January 2024; Published 24 January 2024

This article has been retracted by Hindawi following an investigation undertaken by the publisher [1]. This investigation has uncovered evidence of one or more of the following indicators of systematic manipulation of the publication process:

(1) Discrepancies in scope
(2) Discrepancies in the description of the research reported
(3) Discrepancies between the availability of data and the research described
(4) Inappropriate citations
(5) Incoherent, meaningless and/or irrelevant content included in the article
(6) Manipulated or compromised peer review

The presence of these indicators undermines our confidence in the integrity of the article's content and we cannot, therefore, vouch for its reliability. Please note that this notice is intended solely to alert readers that the content of this article is unreliable. We have not investigated whether authors were aware of or involved in the systematic manipulation of the publication process.

Wiley and Hindawi regrets that the usual quality checks did not identify these issues before publication and have since put additional measures in place to safeguard research integrity.

We wish to credit our own Research Integrity and Research Publishing teams and anonymous and named external researchers and research integrity experts for contributing to this investigation.

The corresponding author, as the representative of all authors, has been given the opportunity to register their agreement or disagreement to this retraction. We have kept a record of any response received.

References

[1] S. A. Ali, M. Sarfraz, S. A. Ghauri et al., "A Weighted Cluster Head Selection Algorithm for Energy Efficient Wireless Sensor Networks," *Journal of Sensors*, vol. 2022, Article ID 3055178, 13 pages, 2022.

Hindawi
Journal of Sensors
Volume 2024, Article ID 9860895, 1 page
https://doi.org/10.1155/2024/9860895

Retraction

Retracted: Research on Interior Design and Space Layout Optimization Based on Multi-Intelligent Decision-Making

Journal of Sensors

Received 23 January 2024; Accepted 23 January 2024; Published 24 January 2024

This article has been retracted by Hindawi following an investigation undertaken by the publisher [1]. This investigation has uncovered evidence of one or more of the following indicators of systematic manipulation of the publication process:

(1) Discrepancies in scope
(2) Discrepancies in the description of the research reported
(3) Discrepancies between the availability of data and the research described
(4) Inappropriate citations
(5) Incoherent, meaningless and/or irrelevant content included in the article
(6) Manipulated or compromised peer review

The presence of these indicators undermines our confidence in the integrity of the article's content and we cannot, therefore, vouch for its reliability. Please note that this notice is intended solely to alert readers that the content of this article is unreliable. We have not investigated whether authors were aware of or involved in the systematic manipulation of the publication process.

Wiley and Hindawi regrets that the usual quality checks did not identify these issues before publication and have since put additional measures in place to safeguard research integrity.

We wish to credit our own Research Integrity and Research Publishing teams and anonymous and named external researchers and research integrity experts for contributing to this investigation.

The corresponding author, as the representative of all authors, has been given the opportunity to register their agreement or disagreement to this retraction. We have kept a record of any response received.

References

[1] J. Dong and M. Ran, "Research on Interior Design and Space Layout Optimization Based on Multi-Intelligent Decision-Making," *Journal of Sensors*, vol. 2022, Article ID 7158921, 10 pages, 2022.

Hindawi
Journal of Sensors
Volume 2024, Article ID 9837823, 1 page
https://doi.org/10.1155/2024/9837823

Retraction

Retracted: Embedded Estimation Sequential Bayes Parameter Inference for the Ricker Dynamical System

Journal of Sensors

Received 23 January 2024; Accepted 23 January 2024; Published 24 January 2024

This article has been retracted by Hindawi following an investigation undertaken by the publisher [1]. This investigation has uncovered evidence of one or more of the following indicators of systematic manipulation of the publication process:

(1) Discrepancies in scope
(2) Discrepancies in the description of the research reported
(3) Discrepancies between the availability of data and the research described
(4) Inappropriate citations
(5) Incoherent, meaningless and/or irrelevant content included in the article
(6) Manipulated or compromised peer review

The presence of these indicators undermines our confidence in the integrity of the article's content and we cannot, therefore, vouch for its reliability. Please note that this notice is intended solely to alert readers that the content of this article is unreliable. We have not investigated whether authors were aware of or involved in the systematic manipulation of the publication process.

Wiley and Hindawi regrets that the usual quality checks did not identify these issues before publication and have since put additional measures in place to safeguard research integrity.

We wish to credit our own Research Integrity and Research Publishing teams and anonymous and named external researchers and research integrity experts for contributing to this investigation.

The corresponding author, as the representative of all authors, has been given the opportunity to register their agreement or disagreement to this retraction. We have kept a record of any response received.

References

[1] M. J. U. Rehman, R. Zafar, H. Dilpazir, M. F. Sohail, M. A. Khan, and R. Jahan, "Embedded Estimation Sequential Bayes Parameter Inference for the Ricker Dynamical System," *Journal of Sensors*, vol. 2022, Article ID 4540366, 8 pages, 2022.

Hindawi
Journal of Sensors
Volume 2023, Article ID 9869108, 1 page
https://doi.org/10.1155/2023/9869108

Retraction

Retracted: Design of Virtual Machine Scheduling Algorithm in Cloud Computing Environment

Journal of Sensors

Received 19 December 2023; Accepted 19 December 2023; Published 20 December 2023

This article has been retracted by Hindawi following an investigation undertaken by the publisher [1]. This investigation has uncovered evidence of one or more of the following indicators of systematic manipulation of the publication process:

(1) Discrepancies in scope
(2) Discrepancies in the description of the research reported
(3) Discrepancies between the availability of data and the research described
(4) Inappropriate citations
(5) Incoherent, meaningless and/or irrelevant content included in the article
(6) Manipulated or compromised peer review

The presence of these indicators undermines our confidence in the integrity of the article's content and we cannot, therefore, vouch for its reliability. Please note that this notice is intended solely to alert readers that the content of this article is unreliable. We have not investigated whether authors were aware of or involved in the systematic manipulation of the publication process.

Wiley and Hindawi regrets that the usual quality checks did not identify these issues before publication and have since put additional measures in place to safeguard research integrity.

We wish to credit our own Research Integrity and Research Publishing teams and anonymous and named external researchers and research integrity experts for contributing to this investigation.

The corresponding author, as the representative of all authors, has been given the opportunity to register their agreement or disagreement to this retraction. We have kept a record of any response received.

References

[1] B. Liang, R. Liu, and D. Dai, "Design of Virtual Machine Scheduling Algorithm in Cloud Computing Environment," *Journal of Sensors*, vol. 2022, Article ID 3848165, 8 pages, 2022.

Hindawi
Journal of Sensors
Volume 2023, Article ID 9848312, 1 page
https://doi.org/10.1155/2023/9848312

Retraction

Retracted: Research on Emergency Logistics Vehicle Route Scheduling and Optimization Method Based on Multi-Intelligent Decision System

Journal of Sensors

Received 19 December 2023; Accepted 19 December 2023; Published 20 December 2023

This article has been retracted by Hindawi following an investigation undertaken by the publisher [1]. This investigation has uncovered evidence of one or more of the following indicators of systematic manipulation of the publication process:

(1) Discrepancies in scope
(2) Discrepancies in the description of the research reported
(3) Discrepancies between the availability of data and the research described
(4) Inappropriate citations
(5) Incoherent, meaningless and/or irrelevant content included in the article
(6) Manipulated or compromised peer review

The presence of these indicators undermines our confidence in the integrity of the article's content and we cannot, therefore, vouch for its reliability. Please note that this notice is intended solely to alert readers that the content of this article is unreliable. We have not investigated whether authors were aware of or involved in the systematic manipulation of the publication process.

Wiley and Hindawi regrets that the usual quality checks did not identify these issues before publication and have since put additional measures in place to safeguard research integrity.

We wish to credit our own Research Integrity and Research Publishing teams and anonymous and named external researchers and research integrity experts for contributing to this investigation.

The corresponding author, as the representative of all authors, has been given the opportunity to register their agreement or disagreement to this retraction. We have kept a record of any response received.

References

[1] C. Ji, S. Liang, and Y. Yu, "Research on Emergency Logistics Vehicle Route Scheduling and Optimization Method Based on Multi-Intelligent Decision System," *Journal of Sensors*, vol. 2022, Article ID 2148785, 15 pages, 2022.

Hindawi
Journal of Sensors
Volume 2023, Article ID 9839706, 1 page
https://doi.org/10.1155/2023/9839706

Retraction

Retracted: Research on Learner Modeling and Curriculum Recommendation Based on Emotional Factors

Journal of Sensors

Received 19 December 2023; Accepted 19 December 2023; Published 20 December 2023

This article has been retracted by Hindawi following an investigation undertaken by the publisher [1]. This investigation has uncovered evidence of one or more of the following indicators of systematic manipulation of the publication process:

(1) Discrepancies in scope
(2) Discrepancies in the description of the research reported
(3) Discrepancies between the availability of data and the research described
(4) Inappropriate citations
(5) Incoherent, meaningless and/or irrelevant content included in the article
(6) Manipulated or compromised peer review

The presence of these indicators undermines our confidence in the integrity of the article's content and we cannot, therefore, vouch for its reliability. Please note that this notice is intended solely to alert readers that the content of this article is unreliable. We have not investigated whether authors were aware of or involved in the systematic manipulation of the publication process.

Wiley and Hindawi regrets that the usual quality checks did not identify these issues before publication and have since put additional measures in place to safeguard research integrity.

We wish to credit our own Research Integrity and Research Publishing teams and anonymous and named external researchers and research integrity experts for contributing to this investigation.

The corresponding author, as the representative of all authors, has been given the opportunity to register their agreement or disagreement to this retraction. We have kept a record of any response received.

References

[1] X. Hua, H. Zhang, F. Xie, J. Wei, J. Wei, and H. Li, "Research on Learner Modeling and Curriculum Recommendation Based on Emotional Factors," *Journal of Sensors*, vol. 2022, Article ID 3296713, 9 pages, 2022.

Hindawi
Journal of Sensors
Volume 2023, Article ID 9837069, 1 page
https://doi.org/10.1155/2023/9837069

Retraction

Retracted: Nonlinear Identification of PMSM Rotor Magnetic Linkages Based on an Improved Extended Kalman Filter

Journal of Sensors

Received 19 December 2023; Accepted 19 December 2023; Published 20 December 2023

This article has been retracted by Hindawi following an investigation undertaken by the publisher [1]. This investigation has uncovered evidence of one or more of the following indicators of systematic manipulation of the publication process:

(1) Discrepancies in scope
(2) Discrepancies in the description of the research reported
(3) Discrepancies between the availability of data and the research described
(4) Inappropriate citations
(5) Incoherent, meaningless and/or irrelevant content included in the article
(6) Manipulated or compromised peer review

The presence of these indicators undermines our confidence in the integrity of the article's content and we cannot, therefore, vouch for its reliability. Please note that this notice is intended solely to alert readers that the content of this article is unreliable. We have not investigated whether authors were aware of or involved in the systematic manipulation of the publication process.

Wiley and Hindawi regrets that the usual quality checks did not identify these issues before publication and have since put additional measures in place to safeguard research integrity.

We wish to credit our own Research Integrity and Research Publishing teams and anonymous and named external researchers and research integrity experts for contributing to this investigation.

The corresponding author, as the representative of all authors, has been given the opportunity to register their agreement or disagreement to this retraction. We have kept a record of any response received.

References

[1] T. Chen and B. Chen, "Nonlinear Identification of PMSM Rotor Magnetic Linkages Based on an Improved Extended Kalman Filter," *Journal of Sensors*, vol. 2022, Article ID 9477659, 8 pages, 2022.

Hindawi
Journal of Sensors
Volume 2023, Article ID 9783463, 1 page
https://doi.org/10.1155/2023/9783463

Retraction

Retracted: Performance Evaluation of Spectral Efficiency for Uplink and Downlink Multi-Cell Massive MIMO Systems

Journal of Sensors

Received 19 December 2023; Accepted 19 December 2023; Published 20 December 2023

This article has been retracted by Hindawi following an investigation undertaken by the publisher [1]. This investigation has uncovered evidence of one or more of the following indicators of systematic manipulation of the publication process:

(1) Discrepancies in scope
(2) Discrepancies in the description of the research reported
(3) Discrepancies between the availability of data and the research described
(4) Inappropriate citations
(5) Incoherent, meaningless and/or irrelevant content included in the article
(6) Manipulated or compromised peer review

The presence of these indicators undermines our confidence in the integrity of the article's content and we cannot, therefore, vouch for its reliability. Please note that this notice is intended solely to alert readers that the content of this article is unreliable. We have not investigated whether authors were aware of or involved in the systematic manipulation of the publication process.

Wiley and Hindawi regrets that the usual quality checks did not identify these issues before publication and have since put additional measures in place to safeguard research integrity.

We wish to credit our own Research Integrity and Research Publishing teams and anonymous and named external researchers and research integrity experts for contributing to this investigation.

The corresponding author, as the representative of all authors, has been given the opportunity to register their agreement or disagreement to this retraction. We have kept a record of any response received.

References

[1] R. M. Asif, M. Shakir, A. U. Rehman, M. Shafiq, R. A. Khan, and W. U. Khan, "Performance Evaluation of Spectral Efficiency for Uplink and Downlink Multi-Cell Massive MIMO Systems," *Journal of Sensors*, vol. 2022, Article ID 7205687, 12 pages, 2022.

Hindawi
Journal of Sensors
Volume 2023, Article ID 9850854, 1 page
https://doi.org/10.1155/2023/9850854

Retraction

Retracted: Research on Agricultural Economic Early Warning Based on Genetic Algorithm and SVM

Journal of Sensors

Received 8 August 2023; Accepted 8 August 2023; Published 9 August 2023

This article has been retracted by Hindawi following an investigation undertaken by the publisher [1]. This investigation has uncovered evidence of one or more of the following indicators of systematic manipulation of the publication process:

(1) Discrepancies in scope
(2) Discrepancies in the description of the research reported
(3) Discrepancies between the availability of data and the research described
(4) Inappropriate citations
(5) Incoherent, meaningless and/or irrelevant content included in the article
(6) Peer-review manipulation

The presence of these indicators undermines our confidence in the integrity of the article's content and we cannot, therefore, vouch for its reliability. Please note that this notice is intended solely to alert readers that the content of this article is unreliable. We have not investigated whether authors were aware of or involved in the systematic manipulation of the publication process.

Wiley and Hindawi regrets that the usual quality checks did not identify these issues before publication and have since put additional measures in place to safeguard research integrity.

We wish to credit our own Research Integrity and Research Publishing teams and anonymous and named external researchers and research integrity experts for contributing to this investigation.

The corresponding author, as the representative of all authors, has been given the opportunity to register their agreement or disagreement to this retraction. We have kept a record of any response received.

References

[1] X. Bian, X. Lv, and J. Tian, "Research on Agricultural Economic Early Warning Based on Genetic Algorithm and SVM," *Journal of Sensors*, vol. 2022, Article ID 3109468, 6 pages, 2022.

Hindawi
Journal of Sensors
Volume 2023, Article ID 9850274, 1 page
https://doi.org/10.1155/2023/9850274

Retraction

Retracted: Subdivision of Artistic Objectives of Oil Painting Creation under the Evaluation of Deep Learning Model

Journal of Sensors

Received 8 August 2023; Accepted 8 August 2023; Published 9 August 2023

This article has been retracted by Hindawi following an investigation undertaken by the publisher [1]. This investigation has uncovered evidence of one or more of the following indicators of systematic manipulation of the publication process:

(1) Discrepancies in scope
(2) Discrepancies in the description of the research reported
(3) Discrepancies between the availability of data and the research described
(4) Inappropriate citations
(5) Incoherent, meaningless and/or irrelevant content included in the article
(6) Peer-review manipulation

The presence of these indicators undermines our confidence in the integrity of the article's content and we cannot, therefore, vouch for its reliability. Please note that this notice is intended solely to alert readers that the content of this article is unreliable. We have not investigated whether authors were aware of or involved in the systematic manipulation of the publication process.

Wiley and Hindawi regrets that the usual quality checks did not identify these issues before publication and have since put additional measures in place to safeguard research integrity.

We wish to credit our own Research Integrity and Research Publishing teams and anonymous and named external researchers and research integrity experts for contributing to this investigation.

The corresponding author, as the representative of all authors, has been given the opportunity to register their agreement or disagreement to this retraction. We have kept a record of any response received.

References

[1] M. Wu, "Subdivision of Artistic Objectives of Oil Painting Creation under the Evaluation of Deep Learning Model," *Journal of Sensors*, vol. 2022, Article ID 6825863, 6 pages, 2022.

Hindawi
Journal of Sensors
Volume 2023, Article ID 9837074, 1 page
https://doi.org/10.1155/2023/9837074

Retraction

Retracted: Efficiency Analysis and Utilization of College Sports Equipment Based on Intelligent Computing

Journal of Sensors

Received 8 August 2023; Accepted 8 August 2023; Published 9 August 2023

This article has been retracted by Hindawi following an investigation undertaken by the publisher [1]. This investigation has uncovered evidence of one or more of the following indicators of systematic manipulation of the publication process:

(1) Discrepancies in scope
(2) Discrepancies in the description of the research reported
(3) Discrepancies between the availability of data and the research described
(4) Inappropriate citations
(5) Incoherent, meaningless and/or irrelevant content included in the article
(6) Peer-review manipulation

The presence of these indicators undermines our confidence in the integrity of the article's content and we cannot, therefore, vouch for its reliability. Please note that this notice is intended solely to alert readers that the content of this article is unreliable. We have not investigated whether authors were aware of or involved in the systematic manipulation of the publication process.

Wiley and Hindawi regrets that the usual quality checks did not identify these issues before publication and have since put additional measures in place to safeguard research integrity.

We wish to credit our own Research Integrity and Research Publishing teams and anonymous and named external researchers and research integrity experts for contributing to this investigation.

The corresponding author, as the representative of all authors, has been given the opportunity to register their agreement or disagreement to this retraction. We have kept a record of any response received.

References

[1] C. Li, J. Wang, and Q. Yu, "Efficiency Analysis and Utilization of College Sports Equipment Based on Intelligent Computing," *Journal of Sensors*, vol. 2022, Article ID 7497555, 10 pages, 2022.

Hindawi
Journal of Sensors
Volume 2023, Article ID 9802327, 1 page
https://doi.org/10.1155/2023/9802327

Retraction

Retracted: Integrated Evaluation of Corporate Investment Decision Performance Based on Fuzzy Sets and BP Neural Networks

Journal of Sensors

Received 8 August 2023; Accepted 8 August 2023; Published 9 August 2023

This article has been retracted by Hindawi following an investigation undertaken by the publisher [1]. This investigation has uncovered evidence of one or more of the following indicators of systematic manipulation of the publication process:

(1) Discrepancies in scope
(2) Discrepancies in the description of the research reported
(3) Discrepancies between the availability of data and the research described
(4) Inappropriate citations
(5) Incoherent, meaningless and/or irrelevant content included in the article
(6) Peer-review manipulation

The presence of these indicators undermines our confidence in the integrity of the article's content and we cannot, therefore, vouch for its reliability. Please note that this notice is intended solely to alert readers that the content of this article is unreliable. We have not investigated whether authors were aware of or involved in the systematic manipulation of the publication process.

Wiley and Hindawi regrets that the usual quality checks did not identify these issues before publication and have since put additional measures in place to safeguard research integrity.

We wish to credit our own Research Integrity and Research Publishing teams and anonymous and named external researchers and research integrity experts for contributing to this investigation.

The corresponding author, as the representative of all authors, has been given the opportunity to register their agreement or disagreement to this retraction. We have kept a record of any response received.

References

[1] J. Du, "Integrated Evaluation of Corporate Investment Decision Performance Based on Fuzzy Sets and BP Neural Networks," *Journal of Sensors*, vol. 2022, Article ID 7628124, 7 pages, 2022.

Hindawi
Journal of Sensors
Volume 2023, Article ID 9756492, 1 page
https://doi.org/10.1155/2023/9756492

Retraction

Retracted: Dynamic Evaluation and Prediction for Macroeconomic Based on IGA-LSSVM

Journal of Sensors

Received 8 August 2023; Accepted 8 August 2023; Published 9 August 2023

This article has been retracted by Hindawi following an investigation undertaken by the publisher [1]. This investigation has uncovered evidence of one or more of the following indicators of systematic manipulation of the publication process:

(1) Discrepancies in scope
(2) Discrepancies in the description of the research reported
(3) Discrepancies between the availability of data and the research described
(4) Inappropriate citations
(5) Incoherent, meaningless and/or irrelevant content included in the article
(6) Peer-review manipulation

The presence of these indicators undermines our confidence in the integrity of the article's content and we cannot, therefore, vouch for its reliability. Please note that this notice is intended solely to alert readers that the content of this article is unreliable. We have not investigated whether authors were aware of or involved in the systematic manipulation of the publication process.

Wiley and Hindawi regrets that the usual quality checks did not identify these issues before publication and have since put additional measures in place to safeguard research integrity.

We wish to credit our own Research Integrity and Research Publishing teams and anonymous and named external researchers and research integrity experts for contributing to this investigation.

The corresponding author, as the representative of all authors, has been given the opportunity to register their agreement or disagreement to this retraction. We have kept a record of any response received.

References

[1] X. Bai, "Dynamic Evaluation and Prediction for Macroeconomic Based on IGA-LSSVM," *Journal of Sensors*, vol. 2022, Article ID 6823102, 7 pages, 2022.

Hindawi
Journal of Sensors
Volume 2022, Article ID 4471945, 11 pages
https://doi.org/10.1155/2022/4471945

Research Article

A New Correlation Coefficient for T-Spherical Fuzzy Sets and Its Application in Multicriteria Decision-Making and Pattern Recognition

Wajid Ali,[1] Mehboob Ali,[2] Israr Hussain,[3] Syed Sajid Ullah,[4] Roobaea Alroobaea,[5] Saddam Hussain,[6] Ahmed Binmahfoudh,[7] and Fazlullah Umar[8]

[1]*Department of Mathematical Sciences, Karakorum International University, Gilgit-Baltistan, Pakistan*
[2]*Department of Applied Mathematics, Chung Yuan Christian University, Zhongli, Taiwan*
[3]*Department of Computer Sciences, Karakorum International University, Gilgit-Baltistan, Pakistan*
[4]*Department of Information and Communication Technology, University of Agder (UiA), N-4898 Grimstad, Norway*
[5]*Department of Computer Science, College of Computers and Information Technology, Taif University, P. O. Box 11099, Taif 21944, Saudi Arabia*
[6]*Department of Information Technology, Hazara University Mansehra, 21120 KP, Pakistan*
[7]*Department of Computer Engineering, College of Computers and Information Technology, Taif University, P. O. Box 11099, Taif 21944, Saudi Arabia*
[8]*Department, Khana-e-Noor University, Pol-e-Mahmood Khan, Shashdarak, 1001 Kabul, Afghanistan*

Correspondence should be addressed to Wajid Ali; wajid.ali@kiu.edu.pk, Saddam Hussain; saddamicup1993@outlook.com, and Fazlullah Umar; fazlullahumer@gmail.com

Received 19 April 2022; Revised 5 June 2022; Accepted 8 July 2022; Published 27 July 2022

Academic Editor: Waliullah Khan

The goal of this paper is to design a new correlation coefficient for T-spherical fuzzy sets (TSFSs), which can accurately measure the nature of correlation (i.e., positive and negative) as well as the degree of relationship between TSFS. In order to formulate our proposed idea, we had taken inspiration from the statistical concept of the correlation coefficient. While doing so, we firstly introduce the variance and covariance of two TSFS and then constructed our scheme using these two newly defined notions. The numerical value of our proposed correlation coefficient lies within the interval $[-1,+1]$, as it should be from a statistical point of view, whereas the existing methods cannot measure the negative correlation between TSFS, as their numerical value falls within the interval $[0, 1]$, which is not reasonable both statistically and intuitively. This aspect has also been thoroughly demonstrated using some numerical examples. The comparison results witnessed the dominance and upper hand of our proposed method over the existing definitions, with reliable and better results. In order to demonstrate the feasibility, usefulness, and practical application, we applied our proposed scheme to solve technical and scientific problems of multicriteria decision-making and pattern recognition. The numerical results show that our proposed scheme is practically suitable, technically applicable, and intuitively reasonable.

1. Introduction

The notion of fuzzy sets (FS) was initially proposed by Zadeh [1] to deal with imprecise and vague situations where the membership $M_A(x)$ is assigned to each element [2, 3], and it is a generalization of the crisp set [4]. In crisp set theory, we consider only deterministic and precise situations that could not handle imprecise and vague situations. Alternatively, fuzzy sets provide better solutions for real-life problems. Various researchers have developed certain novel techniques related to fuzzy sets and demonstrated their application in other fields such as [5–14] that are some practical examples. In a fuzzy set, however, only the degree of membership $M_A(x)$ is of relevance to research, and

nonmembership $N_A(x)$ is not an option. In light of this, Atanassov [15] developed the notion of intuitionistic fuzzy sets (IFS), which takes into account both membership and nonmembership functions under a particular condition: $0 \leq M_A(x) + N_A(x) \leq 1$, where $0 \leq M_A(x) \leq 1$ and $0 \leq N_A(x) \leq 1$, and the term $\tau_A(x) = 1 - M_A(x) - N_A(x)$ is called degree of hesitancy. IFS has a wide range of application in many fields, e.g., decision-making [16], logic programming [17], pattern recognition [18–20] medical diagnosis [21], information retrieval [22] and cluster analysis [23], and communication [24–26]. Although the theory of IFS has been successfully applied in different fields, there are some real-life situations where human opinions involve more than two independent statements, like yes, no, abstain, and refusal. Therefore, to deal with these types of situations, Cuong and Kreinovich [27] extended Zadeh FS and Atanassov's IFS into picture fuzzy sets (PFS) with the following condition $(M_A(x) + I_A(x) + N_A(x) \leq 1)$, where $M_A(x)(\in[0, 1])$ is the degree of positive membership, $I_A(x)(\in[0, 1])$ which represents the degree of neutral membership, and $N_A(x)(\in[0, 1])$ is a degree of negative membership. The proposed idea of Cuong and Kreinovich [27] has great importance and application to deal with human opinion efficiently as we have discussed earlier but in some particular scenarios, the sum of membership degrees exceeds 1, i.e., $(M_A(x) + I_A(x) + N_A(x) > 1)$. In these situations, IFS is insufficient to provide a satisfactory result. To address this problem, Mahmood et al. [28] developed the spherical fuzzy set (SFS) by adding new constraints: $(M_A^2(x) + I_A^2(x) + N_A^2(x) \leq 1 \text{ for SFSs})$ and $(M_A^n(x) + I_A^n(x) + N_A^n(x) \leq 1 \text{ for TSFSs})$ which is a generalization of FS, IFS, and PFS, which satisfies the sum of membership degrees is less than or equal to 1. The concept of TSFS is a recent development in fuzzy set theory and successfully applied to medical diagnosis and multiattribute decision-making. In addition, the extensions of IFS method are also found in literature abundantly such as fuzzy multisets [29], type-2 fuzzy sets [30], hesitant fuzzy sets [31], and Pythagorean fuzzy sets, [32].

earson proposed the concept of correlation in 1895, and it has since become one of the most widely used indices in statistics. Correlation is a statistical term that describes how two variables are related in a linear pattern. Murthy et al. [33] introduced the concept of fuzzy set correlation for the first time in 1985. The correlation coefficient for IFS was proposed by Gerstenkorn and Manko [34] who introduced the correlation coefficient for IFS. Later on, Hong and Hwang [35] went on to extend intuitionistic fuzzy sets' association in probability space. Mitchell [36] illustrated new formula for intuitionistic fuzzy sets and interpreted two intuitionistic fuzzy sets as ensembles of ordinary fuzzy sets. Several novel expansions, such as [23, 37–41], have also been proposed in the literature. Ullah et al. [42] recently discovered correlation coefficients for T-spherical fuzzy sets, which they used in clustering and multiattribute decision-making. Guleria and Bajaj [43] also presented a similar idea of the correlation coefficient for TSFSs and illustrated its application in pattern recognition and medical diagnosis. These newly developed ideas are applicable in many areas but their proposed method only measures [0, 1] ranging correlations and is unable to deal with negative correlation. Keeping this drawback in mind, we propose a new correlation coefficient for TSFSs that can easily address the highlighted weaknesses in the existing methods. The numerical value of our proposed correlation coefficient lies within the interval [−1,+1] as it should be from a statistical point of view, whereas the existing methods cannot measure the negative correlation between TSFSs, as their numerical value falls within the interval [0, 1], which is not reasonable both statistically and intuitively.

The organization of this manuscript has been furnished as follows. Section 2 entails basic concepts of IFS, PFS, SFS, and TSFS. It also reviews some existing ideas of the CC of TSFS. Section 3 details our proposed scheme (CC of TSFS), and it also validates and verifies our method with the help of some theorems and propositions. In Section 4, we demonstrate numerical comparisons regarding the performance of our method and the other existing methods to show the strengths and superiority of the proposed idea. Section 5 illustrates the feasibility and usefulness of our idea in the thematic areas of MCDM and PR with the help of some real-world problems. In Section 6, we finalize this manuscript with concluding remarks.

2. Preliminaries

This section has been dedicated to recalling some essential theories, functions, and characteristics of TSFSs as well as the coefficient of correlation to facilitate the understanding of our research study. In the entire paper, we use $M(x)$, $N(x)$, $I(x)$, and $\Lambda(x)$ to represent the degree of membership, nonmembership, abstinence, and refusal in a unit interval [0, 1], respectively.

2.1. Generalizations of Fuzzy Sets

Definition 1. (see [15]). Let F be an intuitionistic fuzzy set (IFS) on a universe of discourse $X = \{x_1, x_2, x_3, \cdots, x_m\}$, and then it can be algebraically defined as $F = \{\langle x, M_F(x), N_F(x)\rangle / x \in X\}$, with a constraint of $0 \leq M_F(x) + N_F(x) \leq 1$, whereas $H = 1 - \{M_F(x) + N_F(x)\}$ is known as the degree of hesitancy for an element $x \in X$ to be belonging to$F$.

Definition 2. (see [44]). A mathematical expression for a PFS P defined over a universe of discourse $X = \{x_1, x_2, x_3, \cdots, x_m\}$ can be presented as $J = \{\langle x, M_J(x), I_J(x), N_J(x)\rangle / x \in X\}$, with a constraint of $0 \leq M_J(x) + I_J(x) + N_J(x) \leq 1$, where the degree of refusal for an element $x \in X$ to be in J is represented as $\Lambda(x) = 1 - \{M_J(x) + I_J(x) + N_J(x)\}$.

Definition 3. (see [45]). The standard negation set of the PFS J can be expressed as $N(J) = \{\langle x, N_J(x), \Lambda_J(x), M_J(x)\rangle / x \in X\}$.

Definition 4. (see [28]). Let S be an SFS on a universe of discourse $X = \{x_1, x_2, x_3, \cdots, x_m\}$, and then it can be mathematically defined as $S = \{\langle x, M_S(x), I_S(x), N_S(x)\rangle / x \in X\}$, with a constraint of $0 \leq M_S^2(x) + I_S^2 + N_S^2(x) \leq 1$, while the degree of refusal for an element $x \in X$ to be belonging to S can be expressed as $\Lambda(x) = \sqrt{1 - \{M_S^2(x) + I_S^2 + N_S^2(x)\}}$.

Definition 5. (see [28]). For a TSFS T on a universe of discourse $X = \{x_1, x_2, x_3, \cdots, x_m\}$, its mathematical representation can be expressed as $T = \{\langle x, M_T(x), I_T(x), N_T(x)\rangle / x \in X\}$, with a constraint of $0 \le M_T^n(x) + I_T^n + N_T^n(x) \le 1$. The degree of refusal for an element $x \in X$ to be in TSFS T is defined as $\Lambda_T(x) = \sqrt[n]{1 - \{M_T^n(x) + I_T^n + N_T^n(x)\}}$.

2.2. Existing Methods (CC of TSFSs)

Definition 6. (see [42]). Let S_1 and S_2 be two TSFSs in a universe of discourse $X = \{x_1, x_2, x_3, \cdots, x_m\}$, and the coefficient of correlation between TSFSs S_1 and S_2 is

$$R(S_1, S_2) = \frac{\sum_{i=1}^{m}\left[M_{S_1}^n(x_i) \times M_{S_2}^n(x_i) + I_{S_1}^n(x_i) \times I_{S_2}^n(x_i) + N_{S_1}^n(x_i) \times N_{S_2}^n(x_i) + \Lambda_{S_1}^n(x_i) \times \Lambda_{S_2}^n(x_i)\right]}{\sqrt{\begin{array}{c}\sum_{i=1}^{m}\left[\left(M_{S_1}^2(x_i)\right)^n + \left(I_{S_1}^2(x_i)\right)^n + \left(N_{S_1}^2(x_i)\right)^n + \left(\Lambda_{S_1}^2(x_i)\right)^n\right] \times \\ \sum_{i=1}^{m}\left[\left(M_{S_2}^2(x_i)\right)^n + \left(I_{S_2}^2(x_i)\right)^n + \left(N_{S_2}^2(x_i)\right)^n + \left(\Lambda_{S_2}^2(x_i)\right)^n\right]\end{array}}}, \tag{1}$$

while the correlation coefficient for weighted TSFSs is

$$R_w(S_1, S_2) = \frac{\sum_{i=1}^{m} w_i\left[M_{S_1}^n(x_i) \times M_{S_2}^n(x_i) + I_{S_1}^n(x_i) \times I_{S_2}^n(x_i) + N_{S_1}^n(x_i) \times N_{S_2}^n(x_i) + \Lambda_{S_1}^n(x_i) \times \Lambda_{S_2}^n(x_i)\right]}{\sqrt{\begin{array}{c}\sum_{i=1}^{m} w_i\left[\left(M_{S_1}^2(x_i)\right)^n + \left(I_{S_1}^2(x_i)\right)^n + \left(N_{S_1}^2(x_i)\right)^n + \left(\Lambda_{S_1}^2(x_i)\right)^n\right] \times \\ \sum_{i=1}^{m} w_i\left[\left(M_{S_2}^2(x_i)\right)^n + \left(I_{S_2}^2(x_i)\right)^n + \left(N_{S_2}^2(x_i)\right)^n + \left(\Lambda_{S_2}^2(x_i)\right)^n\right]\end{array}}}. \tag{2}$$

Both of the above definitions (1) and (2) satisfy the following features:

(a) $R(S_1, S_2) = R(S_2, S_1)$

(b) $0 \le R(S_1, S_2) \le 1$

(c) $R(S_1, S_2) = 1$, iff $S_1 = S_2$

Definition 7. (see [42]). Another form of correlation coefficient between two TSFSs S_1 and S_2 in $X = \{x_1, x_2, x_3, \cdots, x_m\}$ is

$$R^*(S_1, S_2) = \frac{\sum_{i=1}^{m}\left[M_{S_1}^n(x_i) \times M_{S_2}^n(x_i) + I_{S_1}^n(x_i) \times I_{S_2}^n(x_i) + N_{S_1}^n(x_i) \times N_{S_2}^n(x_i) + \Lambda_{S_1}^n(x_i) \times \Lambda_{S_2}^n(x_i)\right]}{\max\left\langle \begin{array}{c}\sum_{i=1}^{m}\left[\left(M_{S_1}^2(x_i)\right)^n + \left(I_{S_1}^2(x_i)\right)^n + \left(N_{S_1}^2(x_i)\right)^n + \left(\Lambda_{S_1}^2(x_i)\right)^n\right], \\ \sum_{i=1}^{m}\left[\left[\left(M_{S_2}^2(x_i)\right)^n + \left(I_{S_2}^2(x_i)\right)^n + \left(N_{S_2}^2(x_i)\right)^n + \left(\Lambda_{S_2}^2(x_i)\right)^n\right]\right]\end{array}\right\rangle}, \tag{3}$$

whereas its weighted form can be defined as

$$R_w^*(S_1, S_2) = \frac{\sum_{i=1}^{m} w_i\left[M_{S_1}^n(x_i) \times M_{S_2}^n(x_i) + I_{S_1}^n(x_i) \times I_{S_2}^n(x_i) + N_{S_1}^n(x_i) \times N_{S_2}^n(x_i) + \Lambda_{S_1}^n(x_i) \times \Lambda_{S_2}^n(x_i)\right]}{\max\left\langle \begin{array}{c}\sum_{i=1}^{m} w_i\left[\left(M_{S_1}^2(x_i)\right)^n + \left(I_{S_1}^2(x_i)\right)^n + \left(N_{S_1}^2(x_i)\right)^n + \left(\Lambda_{S_1}^2(x_i)\right)^n\right], \\ \sum_{i=1}^{m} w_i\left[\left(M_{S_2}^2(x_i)\right)^n + \left(I_{S_2}^2(x_i)\right)^n + \left(N_{S_2}^2(x_i)\right)^n + \left(\Lambda_{S_2}^2(x_i)\right)^n\right]\end{array}\right\rangle}. \tag{4}$$

Equations (3) and (4) also satisfy the following properties:

(a) $R^*(S_1, S_2) = R^*(S_2, S_1)$

(b) $0 \le R^*(S_1, S_2) \le 1$

(c) $R^*(S_1, S_2) = 1$, iff $S_1 = S_2$

Definition 8. (see [43]). Coefficient of correlation between TSFSs S_1 and S_2 in $X = \{x_1, x_2, x_3, \cdots, x_m\}$ is defined as

$$K(S_1, S_2) = \frac{\sum_{i=1}^{m}\left[M_{S_1}^n(x_i) \times M_{S_2}^n(x_i) + I_{S_1}^n(x_i) \times I_{S_2}^n(x_i) + N_{S_1}^n(x_i) \times N_{S_2}^n(x_i) + \Lambda_{S_1}^n(x_i) \times \Lambda_{S_2}^n(x_i)\right]}{\left[\sum_{i=1}^{m}\left(\left(M_{S_1}^n(x_i)\right)^2 + \left(I_{S_1}^n(x_i)\right)^2 + \left(N_{S_1}^n(x_i)\right)^2 + \left(\Lambda_{S_1}^n(x_i)\right)^2\right)\right]^{1/2} \times \left[\sum_{i=1}^{m}\left(\left(M_{S_2}^n(x_i)\right)^2 + \left(I_{S_2}^n(x_i)\right)^2 + \left(N_{S_2}^n(x_i)\right)^2 + \left(\Lambda_{S_2}^n(x_i)\right)^2\right)\right]^{1/2}}, \tag{5}$$

while the correlation coefficient for weighted TSFSs is

$$K_w(S_1, S_2) = \frac{\sum_{i=1}^{m} w_i\left[M_{S_1}^n(x_i) \times M_{S_2}^n(x_i) + I_{S_1}^n(x_i) \times I_{S_2}^n(x_i) + N_{S_1}^n(x_i) \times N_{S_2}^n(x_i) + \Lambda_{S_1}^n(x_i) \times \Lambda_{S_2}^n(x_i)\right]}{\left[\sum_{i=1}^{m} w_i\left(\left(M_{S_1}^n(x_i)\right)^2 + \left(I_{S_1}^n(x_i)\right)^2 + \left(N_{S_1}^n(x_i)\right)^2 + \left(\Lambda_{S_1}^n(x_i)\right)^2\right)\right]^{1/2} \times \left[\sum_{i=1}^{m} w_i\left(\left(M_{S_2}^n(x_i)\right)^2 + \left(I_{S_2}^n(x_i)\right)^2 + \left(N_{S_2}^n(x_i)\right)^2 + \left(\Lambda_{S_2}^n(x_i)\right)^2\right)\right]^{1/2}}. \tag{6}$$

Definition 9. (see [43]). Another definition of the correlation coefficient between two TSFSs S_1 and S_2 is

$$K^*(S_1, S_2) = \frac{\sum_{i=1}^{m}\left[M_{S_1}^n(x_i) \times M_{S_2}^n(x_i) + I_{S_1}^n(x_i) \times I_{S_2}^n(x_i) + N_{S_1}^n(x_i) \times N_{S_2}^n(x_i) + \Lambda_{S_1}^n(x_i) \times \Lambda_{S_2}^n(x_i)\right]}{\max\left\langle \begin{array}{l} \sum_{i=1}^{m}\left[\left(M_{S_1}^2(x_i)\right)^n + \left(I_{S_1}^2(x_i)\right)^n + \left(N_{S_1}^2(x_i)\right)^n + \left(\Lambda_{S_1}^2(x_i)\right)^n\right], \\ \sum_{i=1}^{m}\left[\left[\left(M_{S_2}^2(x_i)\right)^n + \left(I_{S_2}^2(x_i)\right)^n + \left(N_{S_2}^2(x_i)\right)^n + \left(\Lambda_{S_2}^2(x_i)\right)^n\right]\right] \end{array}\right\rangle}, \tag{7}$$

whereas its weighted form can be defined as

$$K_w^*(S_1, S_2) = \frac{\sum_{i=1}^{m} w_i\left[M_{S_1}^n(x_i) \times M_{S_2}^n(x_i) + I_{S_1}^n(x_i) \times I_{S_2}^n(x_i) + N_{S_1}^n(x_i) \times N_{S_2}^n(x_i) + \Lambda_{S_1}^n(x_i) \times \Lambda_{S_2}^n(x_i)\right]}{\max\left\langle \begin{array}{l} \sum_{i=1}^{m} w_i\left[\left(M_{S_1}^2(x_i)\right)^n + \left(I_{S_1}^2(x_i)\right)^n + \left(N_{S_1}^2(x_i)\right)^n + \left(\Lambda_{S_1}^2(x_i)\right)^n\right], \\ \sum_{i=1}^{m} w_i\left[\left(M_{S_2}^2(x_i)\right)^n + \left(I_{S_2}^2(x_i)\right)^n + \left(N_{S_2}^2(x_i)\right)^n + \left(\Lambda_{S_2}^2(x_i)\right)^n\right] \end{array}\right\rangle}. \tag{8}$$

Equations (5)–(8) satisfy the following properties:

(a) $K(S_1, S_2) = K(S_2, S_1)$

(b) $0 \le K(S_1, S_2) \le 1$

(c) $K(S_1, S_2) = 1$, iff $S_1 = S_2$

3. Proposed New Correlation Coefficient of TSFSs

We propose a new correlation coefficient(s) of TSFSs, including both the weighted and unweighted environments, to overcome the drawbacks of the existing definitions [37, 38]. It has been formulated using a statistical theory of correlation coefficient between two phenomena, that is, the mathematical ratio between the covariance of two TSFSs and the geometric mean of their individual variances. Initially, we introduce the variances and covariance of two TSFSs and use those new definitions to construct our proposed correlation coefficient.

Motivated from [46], we designed the structure of our proposed new correlation coefficient of TSFSs, demonstrated as follows.

Let T_1 and T_2 be two TSFSs $X = \{x_1, x_2, x_3, \cdots, x_m\}$, and we describe two new variables based on the deviations of membership grades as

$$\begin{aligned} Q_i(T_1) = \Big\{ &\left\langle M^n_{T_1}(x_i) - \bar{M}^n_{T_1}(x_i) \right\rangle - \left\langle I^n_{T_1}(x_i) - \bar{I}^n_{T_1}(x_i) \right\rangle \\ &- \left\langle N^n_{T_1}(x_i) - \bar{N}^n_{T_1}(x_i) \right\rangle + \left\langle \Lambda^n_{T_1}(x_i) - \bar{\Lambda}^n_{T_1}(x_i) \right\rangle \Big\}, \\ Q_i(T_2) = \Big\{ &\left\langle M^n_{T_2}(x_i) - \bar{M}^n_{T_2}(x_i) \right\rangle - \left\langle I^n_{T_2}(x_i) - \bar{I}^n_{T_2}(x_i) \right\rangle \\ &- \left\langle N^n_{T_2}(x_i) - \bar{N}^n_{T_2}(x_i) \right\rangle + \left\langle \Lambda^n_{T_2}(x_i) - \bar{\Lambda}^n_{T_2}(x_i) \right\rangle \Big\}, \forall x_i \in X, \end{aligned} \tag{9}$$

where

$$\begin{aligned} \bar{M}^n_{T_1}(x_i) &= \frac{1}{m}\sum_{i=1}^{m} M^n_{T_1}(x_i), \bar{I}^n_{T_1}(x_i) = \frac{1}{m}\sum_{i=1}^{m} I^n_{T_1}(x_i), \bar{N}^n_{T_1}(x_i) \\ &= \frac{1}{m}\sum_{i=1}^{m} N^n_{T_1}(x_i), \bar{\Lambda}^n_{T_1}(x_i) = \frac{1}{m}\sum_{i=1}^{m} \Lambda^n_{T_1}(x_i), \\ \bar{M}^n_{T_2}(x_i) &= \frac{1}{m}\sum_{i=1}^{m} M^n_{T_2}(x_i), \bar{I}^n_{T_2}(x_i) = \frac{1}{m}\sum_{i=1}^{m} I^n_{T_2}(x_i), \bar{N}^n_{T_2}(x_i) \\ &= \frac{1}{m}\sum_{i=1}^{m} N^n_{T_2}(x_i), \text{and } \bar{\Lambda}^n_{T_2}(x_i) = \frac{1}{m}\sum_{i=1}^{m} \Lambda^n_{T_2}(x_i). \end{aligned} \tag{10}$$

Definition 10. For two TSFSs $T_1 = \{\langle x, M^n_{T_1}(x), I^n_{T_1}(x), N^n_{T_1}(x)\rangle / x \in X\}$ and $T_2 = \{\langle x, M^n_{T_2}(x), I^n_{T_2}(x), N^n_{T_2}(x)\rangle / x \in X\}$, variances in terms of new variables can be defined as

$$\begin{aligned} \mathrm{Var}(T_1) &= \frac{1}{m-1}\sum_{i=1}^{m} Q_i^2(T_1), \\ \mathrm{Var}(T_2) &= \frac{1}{m-1}\sum_{i=1}^{m} Q_i^2(T_2), \end{aligned} \tag{11}$$

while their covariance is mathematically expressed as

$$\mathrm{Cov}(T_1, T_2) = \frac{1}{m-1}\sum_{i=1}^{m} Q_i(T_1) \times Q_i(T_2). \tag{12}$$

Proposition 11. *For $Cov(T_1, T_2)$ to be the covariance of two TSFSs T_1 and T_2, it should satisfy the following conditions:*

$$\begin{aligned} Cov(T_1, T_2) &= Cov(T_2, T_1) \\ Cov(T_1, T_1) &= Var(T_1), \\ |Cov(T_1, T_1)| &\le \langle Var(T_1)\rangle^{1/2} \times \langle Var(T_2)\rangle^{1/2} \end{aligned} \tag{13}$$

Proof. (i) and (ii) are straight forward

(iii) Using Cauchy-Schwarz inequality, we have

$$\begin{aligned} \left\langle \sum_{i=1}^{n} a_i b_i \right\rangle^2 &\le \left\langle \sum_{i=1}^{n} a_i^2 \right\rangle \times \left\langle \sum_{i=1}^{n} b_i^2 \right\rangle \text{ or } \left| \sum_{i=1}^{n} a_i b_i \right| \\ &\le \left\langle \sum_{i=1}^{n} a_i^2 \right\rangle^{1/2} \times \left\langle \sum_{i=1}^{n} b_i^2 \right\rangle^{1/2}, \\ \text{Hence } \langle \mathrm{Cov}(T_1, T_2)\rangle^2 &= \left\langle \frac{1}{m-1}\sum_{i=1}^{m} Q_i(T_1) \times N_i(T_2) \right\rangle^2 \\ &= \frac{1}{(m-1)^2}\left\langle \sum_{i=1}^{m} Q_i(T_1) \times N_i(T_2) \right\rangle^2, \\ \langle \mathrm{Cov}(T_1, T_2)\rangle^2 &\le \frac{1}{(m-1)^2}\left\langle \sum_{i=1}^{m} Q_i^2(T_1) \times \sum_{i=1}^{m} Q_i^2(T_2) \right\rangle, \\ \langle \mathrm{Cov}(T_1, T_2)\rangle^2 &\le \frac{1}{(m-1)}\left\langle \sum_{i=1}^{m} Q_i^2(T_1) \right\rangle \times \frac{1}{(m-1)}\left\langle \sum_{i=1}^{m} Q_i^2(T_2) \right\rangle, \\ \langle \mathrm{Cov}(T_1, T_2)\rangle^2 &\le \mathrm{Var}(T_1) \times \mathrm{Var}(T_2), \\ |\mathrm{Cov}(T_1, T_2)| &\le \langle \mathrm{Var}(T_1)\rangle^{1/2} \times \langle \mathrm{Var}(T_2)\rangle^{1/2}. \end{aligned} \tag{14}$$

□

Definition 12. Let T_1 and T_2 be two TSFSs on a universe of discourse $X = \{x_1, x_2, x_3, \cdots, x_m\}$. The correlation coefficient between T_1 and T_2 is defined as

$$\begin{aligned} \rho(T_1, T_2) &= \frac{\mathrm{Cov}(T_1, T_2)}{\sqrt{\mathrm{Var}(T_1) \times \mathrm{Var}(T_2)}}, \\ \rho(T_1, T_2) &= \frac{\sum_{i=1}^{m} Q_i(T_1) \times Q_i(T_2)}{\sqrt{\left(\sum_{i=1}^{m} Q_i^2(T_1)\right) \times \left(\sum_{i=1}^{m} Q_i^2(T_2)\right)}}. \end{aligned} \tag{15}$$

Theorem 13. *We have two TSFSs T_1 and T_2, defined over the universe of discourse $X = \{x_1, x_2, x_3, \cdots, x_m\}$, and then the correlation coefficient between them must fulfill the following conditions:*

(a) $\rho(T_1, T_2) = \rho(T_2, T_1)$

(b) $-1 \le \rho(T_1, T_2) \le +1$

(c) $\rho(T_1, T_2) = 1$, *if* $T_1 = cT_2$ *for any constant* $c > 0$, *where* $T_1 = cT_2$ *means,* $M^n_{T_1}(x) = cM^n_{T_2}(x) \in [0, 1]$, $I^n_{T_1}(x) = cI^n_{T_2}(x) \in [0, 1]$, $N^n_{T_1}(x) = cN^n_{T_2}(x) \in [0, 1]$, *and* $\Lambda^n_{T_1}(x) = c\Lambda^n_{T_2}(x) \in [0, 1]$

(d) $\rho(T_1, T_2) = -1$, *if* $T_1 = cT_2$, *for any constant* $c < 0$

Proof.

(a) It is straightforward

(b) From proposition 11 (14), we know that $|\mathrm{Cov}(T_1, T_2)| \le \langle \mathrm{Var}(T_1)\rangle^{1/2} \times \langle \mathrm{Var}(T_2)\rangle^{1/2}$; hence,

$$-\langle \mathrm{Var}(T_1)\rangle^{1/2} \times \langle \mathrm{Var}(T_2)\rangle^{1/2} \le |\mathrm{Cov}(T_1, T_2)|. \tag{16}$$

By using these two inequalities,

$$\begin{aligned} &-\langle \mathrm{Var}(T_1)\rangle^{1/2} \times \langle \mathrm{Var}(T_2)\rangle^{1/2} \\ &\quad \le |\mathrm{Cov}(T_1, T_2)| \\ &\quad \le \langle \mathrm{Var}(T_1)\rangle^{1/2} \times \langle \mathrm{Var}(T_2)\rangle^{1/2}, \end{aligned}$$

$$\begin{aligned} -1 &\le \frac{|\mathrm{Cov}(T_1, T_2)|}{\langle \mathrm{Var}(T_1)\rangle^{1/2} \times \langle \mathrm{Var}(T_2)\rangle^{1/2}} \\ &\le 1 - 1 \le \rho(T_1, T_2) \le +1. \end{aligned} \tag{17}$$

(c) Since for any constant $c > 0$, $M^n_{T_1}(x) = cM^n_{T_2}(x)$, $I^n_{T_1}(x) = cI^n_{T_2}(x)$, $N^n_{T_1}(x) = cN^n_{T_2}(x)$, and $\Lambda^n_{T_1}(x) = c\Lambda^n_{T_2}(x)$, hence

$$\begin{aligned} Q_i(T_1) &= \Big\{\Big\langle M^n_{T_1}(x_i) - \bar{M}^n_{T_1}(x_i)\Big\rangle - \Big\langle I^n_{T_1}(x_i) - \bar{I}^n_{T_1}(x_i)\Big\rangle \\ &\quad - \Big\langle N^n_{T_1}(x_i) - \bar{N}^n_{T_1}(x_i)\Big\rangle + \Big\langle \Lambda^n_{T_1}(x_i) - \bar{\Lambda}^n_{T_1}(x_i)\Big\rangle\Big\}, \\ Q_i(T_1) &= \Big\{\Big\langle cM^n_{T_2}(x_i) - c\bar{M}^n_{T_2}(x_i)\Big\rangle - \Big\langle cI^n_{T_2}(x_i) - c\bar{I}^n_{T_2}(x_i)\Big\rangle \\ &\quad - \Big\langle cN^n_{T_2}(x_i) - c\bar{N}^n_{T_2}(x_i)\Big\rangle + \Big\langle c\Lambda^n_{T_2}(x_i) - c\bar{\Lambda}^n_{T_2}(x_i)\Big\rangle\Big\}, \\ Q_i(T_1) &= c\Big\{\Big\langle M^n_{T_2}(x_i) - \bar{M}^n_{T_2}(x_i)\Big\rangle - \Big\langle I^n_{T_2}(x_i) - \bar{I}^n_{T_2}(x_i)\Big\rangle \\ &\quad - \Big\langle N^n_{T_2}(x_i) - \bar{N}^n_{T_2}(x_i)\Big\rangle + \Big\langle \Lambda^n_{T_2}(x_i) - \bar{\Lambda}^n_{T_2}(x_i)\Big\rangle\Big\}, \\ Q_i(T_1) &= cQ_i(T_2). \end{aligned} \tag{18}$$

Therefore, $\mathrm{Cov}(T_1, T_2) = 1/m - 1\sum_{i=1}^m Q_i(T_1) \times Q_i(T_2) = 1/m - 1\sum_{i=1}^m cQ_i(T_2) \times Q_i(T_2)$.

$$\mathrm{Cov}(T_1, T_2) = \frac{1}{m-1}\sum_{i=1}^m cQ_i^2(T_2), \tag{19}$$

$$\mathrm{Cov}(T_1, T_2) = c\mathrm{Var}(T_2),$$

$$\begin{aligned} \mathrm{Var}(T_1) &= \frac{1}{m-1}\sum_{i=1}^m Q_i^2(T_1) = \frac{1}{m-1}\sum_{i=1}^m c^2 Q_i^2(T_2), \\ \mathrm{Var}(T_1) &= c^2\mathrm{Var}(T_2). \end{aligned} \tag{20}$$

Hence, for any constant $c > 0$,

$$\begin{aligned} \rho(T_1, T_2) &= \frac{\mathrm{Cov}(T_1, T_2)}{\sqrt{\langle \mathrm{Var}(T_1)\rangle \times \langle \mathrm{Var}(T_2)\rangle}} \\ &= \frac{k\mathrm{Var}(T_2)}{\sqrt{\langle k^2\mathrm{Var}(T_2)\rangle \times \langle \mathrm{Var}(T_2)\rangle}}, \\ \rho(T_1, T_2) &= \frac{k\mathrm{Var}(T_2)}{\sqrt{\langle k\mathrm{Var}(T_2)\rangle^2}} = \frac{k\mathrm{Var}(T_2)}{k\mathrm{Var}(T_2)}, \\ \rho(T_1, T_2) &= 1. \end{aligned} \tag{21}$$

(d) Since $A = kB$, so for any constant $c < 0$, $M^n_{T_1}(x) = -cM^n_{T_2}(x)$, $I^n_{T_1}(x) = -cI^n_{T_2}(x)$, $N^n_{T_1}(x) = -cN^n_{T_2}(x)$, and $\Lambda^n_{T_1}(x) = -c\Lambda^n_{T_2}(x)$, therefore,

$$\begin{aligned} Q_i(T_1) &= \Big\{\Big\langle M^n_{T_1}(x_i) - \bar{M}^n_{T_1}(x_i)\Big\rangle - \Big\langle I^n_{T_1}(x_i) - \bar{I}^n_{T_1}(x_i)\Big\rangle \\ &\quad - \Big\langle N^n_{T_1}(x_i) - \bar{N}^n_{T_1}(x_i)\Big\rangle + \Big\langle \Lambda^n_{T_1}(x_i) - \bar{\Lambda}^n_{T_1}(x_i)\Big\rangle\Big\}, \end{aligned}$$

$$\begin{aligned} Q_i(T_1) &= \Big\{\Big\langle -cM^n_{T_2}(x_i) + c\bar{M}^n_{T_2}(x_i)\Big\rangle - \Big\langle -cI^n_{T_2}(x_i) + c\bar{I}^n_{T_2}(x_i)\Big\rangle \\ &\quad - \Big\langle -cN^n_{T_2}(x_i) + \bar{N}^n_{T_2}(x_i)\Big\rangle \\ &\quad + \Big\langle -c\Lambda^n_{T_2}(x_i) + c\bar{\Lambda}^n_{T_2}(x_i)\Big\rangle\Big\}, Q_i(T_1) \\ &= \Big\{-c\Big\langle M^n_{T_2}(x_i) - \bar{M}^n_{T_2}(x_i)\Big\rangle + c\Big\langle I^n_{T_2}(x_i) - \bar{I}^n_{T_2}(x_i)\Big\rangle \\ &\quad + c\Big\langle N^n_{T_2}(x_i) - \bar{N}^n_{T_2}(x_i)\Big\rangle - c\Big\langle \Lambda^n_{T_2}(x_i) - \bar{\Lambda}^n_{T_2}(x_i)\Big\rangle\Big\}, Q_i(T_1) \\ &= -c\Big\{\Big\langle M^n_{T_2}(x_i) - \bar{M}^n_{T_2}(x_i)\Big\rangle - \Big\langle I^n_{T_2}(x_i) - \bar{I}^n_{T_2}(x_i)\Big\rangle \\ &\quad - \Big\langle N^n_{T_2}(x_i) - \bar{N}^n_{T_2}(x_i)\Big\rangle + \Big\langle \Lambda^n_{T_2}(x_i) - \bar{\Lambda}^n_{T_2}(x_i)\Big\rangle\Big\}, Q_i(T_1) \\ &= -cQ_i(T_2). \end{aligned} \tag{22}$$

Hence,

$$\begin{aligned}\mathrm{Cov}(T_1, T_2) &= \frac{1}{m-1}\sum_{i=1}^{m} Q_i(T_1) \times Q_i(T_2) \\ &= \frac{1}{m-1}\sum_{i=1}^{m} -cQ_i(T_2) \times Q_i(T_2), \\ \mathrm{Cov}(T_1, T_2) &= \frac{1}{m-1}\sum_{i=1}^{m} -cQ_i^2(T_2),\end{aligned} \tag{23}$$

$\mathrm{Cov}(T_1, T_2) = -c\mathrm{Var}(T_2)$, and

$$\begin{aligned}\mathrm{Var}(T_1) = \frac{1}{m-1}\sum_{i=1}^{m} Q_i^2(T_1) = \frac{1}{m-1}\sum_{i=1}^{m} c^2 Q_i^2(T_2), \\ \mathrm{Var}(T_1) = c^2\mathrm{Var}(T_2).\end{aligned} \tag{24}$$

So, for $c < 0$,

$$\begin{aligned}\rho(T_1, T_2) &= \frac{\mathrm{Cov}(T_1, T_2)}{\sqrt{\langle \mathrm{Var}(T_1)\rangle \times \langle \mathrm{Var}(T_2)\rangle}} = \frac{-c\mathrm{Var}(T_2)}{\sqrt{\langle c^2\mathrm{Var}(T_2)\rangle \times \langle \mathrm{Var}(T_2)\rangle}}, \\ \rho(T_1, T_2) &= \frac{-c\mathrm{Var}(T_2)}{\sqrt{\langle c\mathrm{Var}(T_2)\rangle^2}} = \frac{-c\mathrm{Var}(T_2)}{c\mathrm{Var}(T_2)}, \\ \rho(T_1, T_2) &= -1.\end{aligned} \tag{25}$$

□

3.1. Special Cases

(a) When $n = 2$, equation (15) reduces to the correlation coefficient of SFSs

(b) When $n = 1$, equation (15) reduces to the correlation coefficient of PFSs

(c) When $n = q$ and $I_A(x_i) = I_B(x_i) = 0$, equation (15) reduces to the correlation coefficient of Q-ROFSs

(d) When $n = 2$ and $\Lambda_{T_1}(x_i) = \Lambda_{T_2}(x_i) = 0$, equation (15) reduces to the correlation coefficient of PyFSs

(e) When $n = 1$ and $\Lambda_{T_1}(x_i) = \Lambda_{T_2}(x_i) = 0$, equation (15) reduces to the correlation coefficient of IFSs

We also propose a weighted correlation coefficient between two TSFSs in the following, to deal with the practical problems and situations, with different objects having unequal importance, in which we consider their weights $-\sqrt{Var_w(A)} \times \sqrt{Var_w(B)} \le |Cov_w(A, B)| \le \sqrt{Var_w(A)} \times \sqrt{Var_w(B)}$ keeping in view their relative importance.

Definition 14. Suppose we have two TSFSs T_1 and T_2 defined over a universe of discourse $X = \{x_1, x_2, x_3, \cdots, x_m\}$, having a weight vector $w = \{w_1, w_2, w_3, \cdots, w_m\}$ for its elements $x_i \in X$, where $w_i \ge 0$ and $\sum_{i=1}^{m} w_i = 1$, then their weighted correlation coefficient can be defined as

$$\begin{aligned}\rho_w(T_1, T_2) &= \frac{\mathrm{Cov}_w(T_1, T_2)}{\sqrt{\mathrm{Var}_w(T_1) \times \mathrm{Var}_w(T_2)}}, \\ \rho_w(T_1, T_2) &= \frac{\sum_{i=1}^{m} w_i Q_i(T_1) \times Q_i(T_2)}{\sqrt{\left(\sum_{i=1}^{m} w_i Q_i^2(T_1)\right) \times \left(\sum_{i=1}^{m} w_i Q_i^2(T_2)\right)}}.\end{aligned} \tag{26}$$

If all of the elements $x_i \in X$ have equal weights ($i.e. w = \{(1/m), (1/m), (1/m), \cdots, (1/m)\}$), then equation (26) can be reduced to equation (15).

From the above definitions, we derive the following proposition and theorem.

Proposition 15. *If we have two SFSs $\rho_w(A, B) = Cov_w(A, B) / \sqrt{Var(A)Var_w(B)} = aVar_w(B)/\sqrt{a^2 Var_w(B)Var_w(B)}$ and $\rho_w(A, B) = aVar_w(B)/\sqrt{a^2 Var_w(B)^2} = aVar_w(B)/aVar_w(B)$ in a universe of discourse $\rho_w(A, B) = 1$, then their weighted covariance satisfies the following conditions:*

(i) $Cov_w(A, B) = Cov_w(B, A)$

(ii) $Cov_w(A, A) = Var_w(A)$

(iii) $|Cov_w(A, B)| \le \langle Var_w(A)\rangle^{1/2} \times \langle Var_w(B)\rangle^{1/2}$

Proof. It can be proved like Proposition 11. □

Theorem 16. *For two TSFSs T_1 and T_2 defined over $X = \{x_1, x_2, x_3, \cdots, x_m\}$, then the weighted correlation coefficient between them must satisfy the following properties:*

(a) $\rho_w(T_1, T_2) = \rho_w(T_2, T_1)$

(b) $-1 \le \rho_w(T_1, T_2) \le +1$

(c) $\rho_w(T_1, T_2) = 1$, *if* $T_1 = cT_2$ *for any constant* $c > 0$

(d) $\rho_w(T_1, T_2) = -1$, *if* $T_1 = cT_2$, *for any constant* $c < 0$

Proof. Theorem 16 can also be proved like Theorem 13. □

Definition 17. Let T be a TSFS defined over a universe of discourse $X = \{x_1, x_2, x_3, \cdots, x_m\}$, and then standard negation set for it be characterized as $M_{N(T)}(x_i) = N_T(x_i)$, $I_{N(T)}(x_i) = \Lambda_T(x_i)$ and $N_{N(T)}(x_i) = M_T(x_i)$ for all $\delta F_{\min} = \min_i |F_A(x_i) - F(x_i)|$ and can be mathematically expressed as $N(T) = \{\langle x, N_T(x), \Lambda_T(x), M_T(x)\rangle / x \in X\}$, where $0 \le M_T^n(x) + I_T^n(x) + N_B^n(x) \le 1$ and where $\Lambda_T(x) = \sqrt{1 - \{M_T^n(x) + I_T^n(x) + N_T^n(x)\}}$ is the degree of refusal for an element $x \in X$ to be in SFSs T.

4. Comparison with Existing Methods

This section has been dedicated to establishing a full comparative study of the results acquired from our suggested scheme and other current approaches [42, 43] using numerical examples to demonstrate the advantage and novelty of

our concept. Using these examples and numerical results, we also intuitively showed the advantages of our proposed method to address the shortcomings of the existing methods. From a statistical as well as intuitive point of view, if two phenomena or datasets are moving in the same direction, then they have a positive relationship, while if their movement is in the opposite direction, then their relationship would be inverse. The correlation coefficient is an important instrument in statistical theory for determining the degree and nature of a link between two processes or variables.

So, our definitions of correlation coefficient should accurately measure both the degree and the nature of relationship between two TSFSs.

We present some numerical examples in the following to show those characteristics of our proposed scheme and its comparison with existing methods.

Example 18. Let T_1 and T_2 be two TSFSs in a universe of discourse $X = \{x_1, x_2, x_3\}$, characterized as

$$T_1 = \{\langle x_1, 0.9, 0.5, 0.7\rangle, \langle x_2, 0.7, 0.6, 0.8\rangle, \langle x_3, 0.5, 0.8, 0.9\rangle\},$$
$$T_2 = \{\langle x_1, 0.7, 0.6, 0.9\rangle, \langle x_2, 0.8, 0.5, 0.7\rangle, \langle x_3, 0.9, 0.4, 0.6\rangle\}. \quad (27)$$

By using our new definition, the standard negation set of a TSFS T_1 is $SN(T_1) = \{\langle x_1, 0.7, 0.,0.9\rangle, \langle x_2, 0.8, 0.,0.7\rangle, \langle x_3, 0.9, 0.,0.5\rangle\}$.

The following Table 1 represents the comparative results of our proposed method and the existing definitions [37, 38] of the correlation coefficient when applied to the above TSFSs.

It is intuitively justifiable that the relationship between a TSFS and its negation set should have an inverse relation, with a negative correlation coefficient. It can be observed from the above Table 1 that none of the definitions [42, 43] can accurately measure the negative relationship between TSFS T_1 and its standard negation set $SN(T)_1$, rather reflecting a positive relation (0.3798, 0.3505) which cannot be possible, while our proposed correlation coefficient shows that there is a negatively strong correlation (-0.9865) between TSFS T_1 and its standard negation set $SN(T)_1$. Similarly, it can be seen that the corresponding membership grades of TSFSs T_1 and T_2 are moving in an opposite direction over the various point of the universe of discourse $X = \{x_1, x_2, x_3\}$. So, they should have an inverse relationship between them, with a negative correlation coefficient. It can be clearly seen from the above Table 1 that the value of our proposed correlation coefficient (-0.9859) portrays that there exists a strongly negative correlation between TSFSs T_1 and T_2, as it should be statistically as well as intuitively. On the other and the existing methods show a positive correlation (0.4304., 0.4051) between them and overlook their inverse relationship. Hence, it shows the superiority and upper hand of our proposed method over the existing definitions of correlation coefficient for TSFSs.

Example 19. Let $w = \{0.22, 0.33, 0.45\}$ be the weight vector for the elements of TSFSs in Example 18. After applying our proposed weighted correlation coefficient and the existing methods for weighted TSFSs [42, 43], we present the comparative performance results in the following Table 2.

Table 1: Coefficient of correlation.

$\rho(T_i, T_j)$	Existing definitions [37, 38]	[37, 38]	Our proposed idea
$\rho(T_1, SN(T_1))$	0.3798	0.3505	-0.9865
$\rho(T_1, T_2)$	0.4304	0.4051	-0.9859

Table 2: Weighted correlation coefficient.

$\rho_w(T_i, T_j)$	Existing definitions [42, 43]	[42, 43]	Our proposed definition
$\rho_w(T_1, SN(T_1))$	0.3153	0.2850	-0.9862
$\rho_w(T_1, T_2)$	0.3774	0.3473	-0.9859

Table 3: T-spherical fuzzy information of alternatives $A_j (j = 1, 2, 3)$.

Alternatives	F_1	F_2	F_3
A_1	<0.8, 0.5, 0.4>	<0.7, 0.4, 0.4>	<0.3, 0.5, 0.4>
A_2	<0.9, 0.2, 0.4>	<0.6, 0.3, 0.2>	<0.4, 0.1, 0.7>
A_3	<0.5, 0.5, 0.5>	<0.8, 0.2, 0.3>	<0.6, 0.4, 0.3>

Table 4: Association between A^* and $A_j (j = 1, 2, 3)$.

$\rho_w(A^*, A_i)$	A_1	A_2	A_3
$\rho_w(A^*, A_i)$	0.9703	0.8307	-0.2530

It can also be clearly seen from Table 2 that our proposed method accurately measures the negative relationship between TSFSs T_1 and its standard negation set $SN(T_1)$ having a weighted correlation coefficient -0.9862, rationally endorsing the strongly negative correlation between them. Contrarily, the existing definitions [42, 43] show a positive correlation (0.3153, 0.2850) between TSFSs T_1 and its standard negation set $SN(T_1)$, which cannot be logically possible. Moreover, there should be a negative correlation between TSFSs T_1 and T_1 (as explained in example 18). Table 2 shows that our method demonstrates a negative correlation (-0.9859) between T_1 and T_1 while the existing methods cannot measure it accurately, as they show a positive correlation coefficient (0.3774, 0.3473), which cannot be intuitively possible, and these shortcomings reduce the reliability and accuracy of the existing definitions. Furthermore, the competency of our proposed method to address these drawbacks shows its effectiveness and advantages.

5. Application in Multicriteria Decision-Making and Pattern Recognition

This section has been designated to illustrate the application of our proposed idea of the correlation coefficient for TSFSs in

Table 5: T-spherical fuzzy pattern information matrix (TSFIM).

Patterns	x_1	x_2	x_3
T_1	<0.42, 0.42, 0.42>	<0.42, 0.42, 0.62>	<0.63, 0.63, 0.72>
T_2	<0.42, 0.42, 0.62>	<0.52, 0.63, 0.82>	<0.72, 0.72, 0.82>
T_3	<0.42, 0.52, 0.63>	<0.52, 0.63, 0.72>	<0.63, 0.72, 0.82>
T	<0.42, 0.42, 0.42>	<0.42, 0.42, 0.52>	<0.63, 0.63, 0.72>

the practical domain of MCDM and pattern recognition to show its suitability and usefulness. Pattern recognition and machine learning are versatile practices that have widely discussed in different disciplines such as [19, 20, 24–26, 47, 48]: these are some examples.

5.1. Application in MCDM. This subsection has been planned to show the application of our proposed scheme in the field of multicriteria decision-making by using a real MCDM problem, taken from [28]. To do so, we present here the implementation procedure of our proposed scheme for dealing with an MCDM problem. Suppose there is a set of "k" alternatives defined as TSFSs $A = \{A_1, A_2, \cdots, A_k\}$ and a set of "m" evaluation features $F = \{F_1, F_2, \cdots, F_m\}$, having weight vector $w = \{w_1, w_2, \cdots, w_m\}^T$, $0 \le w \le 1$, and $\sum_{i=1}^{m} w_i = 1$, we define the ideal alternative A^* as a TSFS by taking maximum membership value, minimum nonmembership, and minimum indeterminacy value for each evaluation criteria across all of the given alternatives, like an ideal positive solution in TOPSIS. $A^* = \{(F_i, \max_{1\le j\le k}\langle M_{A_j}(F_i)\rangle, \min_{1\le j\le k}\langle I_{A_j}(F_i)\rangle, \min_{1\le j\le k}\langle N_{A_j}(F_i)\rangle) / F_i \in F\}$. By applying our proposed correlation coefficient, we calculate the relationship between ideal choice A^* and the given alternatives. Furthermore, by using the principle of the maximum correlation coefficient, we select an alternative as the best option, which has the highest correlation coefficient with an ideal alternative A^*.

Example 20. In order to strengthen the sales and purchase department, a firm had advertised the position of manager and selected 3 candidates after conducting an initial screening of the prospective candidates, who had applied. For the selection of the best candidate, the top management of the firm had considered the following three features to evaluate the aforementioned initially short-listed candidates. (i) F_1: communication skills, (ii) F_2: sense of responsibility, and (iii) F_3: creativity. The candidates, evaluation criteria, and their weights have been presented in the form of sets as a set of alternatives, set of evaluation criteria, and weights vector, respectively, as follows.

$A = \{A_1, A_2, A_3\}$, $F = \{F_1, F_2, F_3\}$, and $w = \{0.20, 0.35, 0.45\}^T$. After a comprehensive evaluation of the candidates, their decision information has been presented in the following Table 3 as a T-spherical fuzzy decision matrix (TSFDM).

It can be clearly seen that the decision information in the above Table 3 is TSFI $n = 3$. So, we apply our proposed scheme to find a correlation coefficient between the ideal candidate $A^* = \{\langle 0.9, 0.2, 0.4\rangle, \langle 0.8, 0.2, 0.2\rangle, \langle 0.6, 0.1, 0.3\rangle\}$ and the initially short-listed three candidates. The results have been furnished in the following Table 4.

Table 6: Relationship between T and $T_j (j = 1, 2, 3)$.

$\rho_w(T, T_j)$	T_1	T_2	T_3
$\rho_w(T, T_j)$	0.9566	0.5185	0.9548

It can be clearly seen that the candidate A_1 has the highest degree of relationship with the ideal choice A^* as compared to that of the other alternatives. Hence, using the principle of maximum correlation, we can say that the candidate A_1 is the most suitable choice for the position of manager. This is in complete agreement with the decision, from where this example has been taken.

5.2. Application in Pattern Recognition. In this section, we show how we used our proposed theory to solve a pattern recognition problem and recognize an unknown pattern while taking into account the properties of several well-known patterns. We develop a relationship between the unknown sample pattern P^* and the set of known patterns $P = \{P_1, P_2, \cdots, P_k\}$ using our proposed correlation coefficient on the basis of a set of evaluation criteria. Taking motivation from the idea of the recognition principle [49], we developed an analogy as a degree of belongingness of the unknown pattern to any one of the known patterns to recognize its actual class as $j^* = \arg\max_j \{\rho(P^*, P_j)\}$, where $\rho(P^*, P_j)$ is the degree of relationship between P^* and P_j that can be calculated using our proposed correlation coefficient. More will be the value of j^*, and more will be the closeness P^* to the jth known pattern. A synthetic/fictitious numerical example has been given in the following to demonstrate the application of our method in pattern recognition problems.

Example 21. Let T_1, T_2, and T_3 be three patterns which are known, and T be an unknown sample pattern, defined as follows in the form of TSFSs. These TSFSs have been defined over a space of points $X = \{x_1, x_2, x_3\}$, and weights have been expressed in the form of a weight vector as $w = \{0.31, 0.36, 0.33\}^T$. The characteristic values of the above-mentioned patterns have been furnished in the following Table 5.

By applying our proposed scheme $n = 5$, we measure the relationship between the unknown sample pattern T and the other three known patterns (T_1, T_2, T_3) to identify its

belongingness. The obtained results have been presented in the following Table 4.

Table 6 clearly shows that the unknown sample pattern T has the highest correlation coefficient with the known pattern T_1 as compared to the other known patterns T_2 and T_3. Hence, using the principle of maximum belongingness $j^* = \arg \max_j \{\rho(P^*, P_j)\}$, we can conclude that the unknown sample pattern T belongs to the known pattern T_1.

6. Conclusions

The TSFS is a useful tool for displaying the degree of positive, neutral, and negative membership, as well as the information's dependability owing to rejection membership. Major correlation coefficient approaches based on the unit interval [0, 1] have been defined in the literature. In accordance with the conventional correlation coefficient in statistics, our newly proposed technique correlation coefficient for T-spherical fuzzy sets is the best choice for dealing with positive, negative, and no correlation [-1, 1]. The mathematical derivations for the upper and lower bound of correlation have been given. To show the novelty, we compare our method with existing methods, and the results demonstrate the good aspect of the proposed idea. Furthermore, to demonstrate the feasibility, usefulness, and practical application, we applied our proposed scheme to solve technical and scientific problems of multicriteria decision-making and pattern recognition.

Data Availability

The data used in this research can be obtained from the corresponding authors.

Conflicts of Interest

The authors declare that they have no conflicts of interest to disclose.

Authors' Contributions

Conceptualization was contributed by WA, MA, SH, SSU, and IH. Methodology was contributed by WA, MA, AB, and RA. Validation was contributed by WA, MA, SH, SSU, AB, RA, and IH. Investigation and funding were contributed by RA and AB. Writing the original draft preparation was contributed by WA, MA, SH, SSU, AB, RA, and IH. Writing-review and editing was contributed by FU, MA, IH, SSU, and SH. Visualization was contributed by WA, AB, RA, SSU, and FU. Project administration was contributed by WA, SH, IH, SSU, FU, AB, and RA.

Acknowledgments

The authors are grateful to the Taif University Researchers Supporting Project number (TURSP-2020/36), Taif University, Taif, Saudi Arabia.

References

[1] L. A. Zadeh, "Fuzzy sets," *Information and Control*, vol. 8, no. 3, pp. 338–353, 1965.

[2] F. Smarandache, "Neutrosophic set-a generalization of the intuitionistic fuzzy set," *International Journal of Pure and Applied Mathematics*, vol. 24, no. 3, pp. 287–297, 2005.

[3] H. Zimmermann, "Fuzzy set theory," *Wiley Interdisciplinary Reviews: Computational Statistics*, vol. 2, no. 3, pp. 317–332, 2010.

[4] B. B. Chaudhuri and A. Bhattacharya, "On correlation between two fuzzy sets," *Fuzzy Sets and Systems*, vol. 118, no. 3, pp. 447–456, 2001.

[5] A. R. Roy and P. K. Maji, "A fuzzy soft set theoretic approach to decision making problems," *Journal of Computational and Applied Mathematics*, vol. 203, no. 2, pp. 412–418, 2007.

[6] B. Tripathy and S. Borgohain, "Some classes of difference sequence spaces of fuzzy real numbers defined by orlicz function," *Advances in Fuzzy Systems*, vol. 2011, Article ID 216414, 6 pages, 2011.

[7] A. J. Dutta and B. C. Tripathy, "On i-acceleration convergence of sequences of fuzzy real numbers," *Mathematical Modelling and Analysis*, vol. 17, no. 4, pp. 549–577, 2012.

[8] S. Sebastian, T. V. Ramakrishnan, and T. V. Ramakrishnan, "Multi-fuzzy sets: an extension of fuzzy sets," *Fuzzy Information and Engineering*, vol. 3, no. 1, pp. 35–43, 2011.

[9] H. T. Nguyen, "A note on the extension principle for fuzzy sets," *Journal of Mathematical Analysis and Applications*, vol. 64, no. 2, pp. 369–380, 1978.

[10] B. Ashtiani, F. Haghighirad, A. Makui, and G. A. Montazer, "Extension of fuzzy TOPSIS method based on interval-valued fuzzy sets," *Applied Soft Computing*, vol. 9, no. 2, pp. 457–461, 2009.

[11] E. Annette Hernandez, V. Uddameri, E. A. Hernandez, and V. Uddameri, "Selecting agricultural best management practices for water conservation and quality improvements using Atanassov's intuitionistic fuzzy sets," *Water Resources Management*, vol. 24, no. 15, pp. 4589–4612, 2010.

[12] M. Fedrizzi, M. Fedrizzi, and W. Ostasiewicz, "Towards fuzzy modelling in economics," *Fuzzy Sets and Systems*, vol. 54, no. 3, pp. 259–268, 1993.

[13] T. Y. Chen, C. H. Chang, and J. F. Rachel Lu, "The extended QUALIFLEX method for multiple criteria decision analysis based on interval type-2 fuzzy sets and applications to medical decision making," *European Journal of Operational Research*, vol. 226, no. 3, pp. 615–625, 2013.

[14] E. Hüllermeier, "Fuzzy sets in machine learning and data mining," *Applied Soft Computing*, vol. 11, no. 2, pp. 1493–1505, 2011.

[15] K. T. Atanassov, "Intuitionistic fuzzy sets," *Fuzzy Sets and Systems*, vol. 20, no. 1, pp. 87–96, 1986.

[16] J. Li and W. Zeng, "A new dissimilarity measure between intuitionistic fuzzy sets and its application in multiple attribute decision making1," *Journal of Intelligent & Fuzzy Systems*, vol. 29, no. 4, pp. 1311–1320, 2015.

[17] K. Atanassov and C. Georgiev, "Intuitionistic fuzzy prolog," *Fuzzy Sets and Systems*, vol. 53, no. 2, pp. 121–128, 1993.

[18] I. K. Vlachos and G. D. Sergiadis, "Intuitionistic fuzzy information - applications to pattern recognition," *Pattern Recognition Letters*, vol. 28, no. 2, pp. 197–206, 2007.

[19] C. Park, C. C. Took, and J. K. Seong, "Machine learning in biomedical engineering," *Biomedical Engineering Letters 8*, vol. 8, no. 1, pp. 1–3, 2018.

[20] T. Hasan, J. Malik, I. Bibi et al., "Securing industrial Internet of Things against botnet attacks using hybrid deep learning approach," *IEEE Transactions on Network Science and Engineering*, vol. 9, 2022.

[21] S. K. De, R. Biswas, and A. R. Roy, "An application of intuitionistic fuzzy sets in medical diagnosis," *Fuzzy Sets and Systems*, vol. 117, no. 2, pp. 209–213, 2001.

[22] Y. Xue, Y. Deng, and H. Garg, "Uncertain database retrieval with measure - Based belief function attribute values under intuitionistic fuzzy set," *Information Sciences*, vol. 546, pp. 436–447, 2021.

[23] Z. Xu, J. Chen, and J. Wu, "Clustering algorithm for intuitionistic fuzzy sets," *Information Sciences*, vol. 178, no. 19, pp. 3775–3790, 2008.

[24] M.-S. Yangy and J.-H. Yangy, "A fuzzy-soft learning vector quantization for control chart pattern recognition," *International Journal of Production Research*, vol. 40, no. 12, pp. 2721–2731, 2002.

[25] A. Orriols-Puig, J. Casillas, and E. Bernadó-Mansilla, "Genetic-based machine learning systems are competitive for pattern recognition," *Evolutionary Intelligence*, vol. 1, no. 3, pp. 209–232, 2008.

[26] W. U. Khan, A. Ihsan, T. N. Nguyen, Z. Ali, and M. A. Javed, "NOMA-enabled backscatter communications for green transportation in automotive-industry 5.0," *IEEE Transactions on Industrial Informatics*, p. 1, 2022.

[27] B. Cuong and V. Kreinovich, "Picture fuzzy sets-a new concept for computational intelligence problems," in *2013 third world congress on information and communication technologies*, pp. 1–6, Hanoi, Vietnam, 2013.

[28] T. Mahmood, K. Ullah, Q. Khan, and N. Jan, "An approach toward decision-making and medical diagnosis problems using the concept of spherical fuzzy sets," *Neural Computing and Applications*, vol. 31, no. 11, pp. 7041–7053, 2019.

[29] S. Miyamoto, "Remarks on basics of fuzzy sets and fuzzy multisets," *Fuzzy Sets and Systems*, vol. 156, no. 3, pp. 427–431, 2005.

[30] J. Mendel and R. I. B. John, "Type-2 fuzzy sets made simple," *IEEE Transactions on Fuzzy Systems*, vol. 10, no. 2, pp. 117–127, 2002.

[31] V. Torra, "Hesitant fuzzy sets," *International Journal of Intelligent Systems*, vol. 25, no. 6, pp. n/a–539, 2010.

[32] R. Yager and A. M. Abbasov, "Pythagorean membership grades, complex numbers, and decision making," *International Journal of Intelligent Systems*, vol. 28, no. 5, pp. 436–452, 2013.

[33] C. A. Murthy, S. K. Pal, and D. Dutta Majumder, "Correlation between two fuzzy membership functions," *Fuzzy Sets and Systems*, vol. 17, no. 1, pp. 23–38, 1985.

[34] T. Gerstenkorn and J. Mańko, "Correlation of intuitionistic fuzzy sets," *Fuzzy Sets and Systems*, vol. 44, no. 1, pp. 39–43, 1991.

[35] D. H. Hong and S. Y. Hwang, "Correlation of intuitionistic fuzzy sets in probability spaces," *Fuzzy Sets and Systems*, vol. 75, no. 1, pp. 77–81, 1995.

[36] H. B. Mitchell, "A correlation coefficient for intuitionistic fuzzy sets," *International Journal of Intelligent Systems*, vol. 19, no. 5, pp. 483–490, 2004.

[37] W. L. Hung and J. W. Wu, "Correlation of intuitionistic fuzzy sets by centroid method," *Information Sciences*, vol. 144, no. 1–4, pp. 219–225, 2002.

[38] D. H. Hong, "A note on correlation of interval-valued intuitionistic fuzzy sets," *Fuzzy Sets and Systems*, vol. 95, no. 1, pp. 113–117, 1998.

[39] H. Bustince and P. Burillo, "Correlation of interval-valued intuitionistic fuzzy sets," *Fuzzy Sets and Systems*, vol. 74, no. 2, pp. 237–244, 1995.

[40] J. H. Park, K. M. Lim, J. S. Park, and Y. C. Kwun, "Correlation coefficient between intuitionistic fuzzy sets," *Fuzzy Information and Engineering*, vol. 2, pp. 601–610, 2009.

[41] E. Szmidt and J. Kacprzyk, "Correlation of intuitionistic fuzzy sets," *Lecture Notes in Computer Science*, vol. 6178, pp. 169–177, 2010.

[42] K. Ullah, H. Garg, T. Mahmood, N. Jan, and Z. Ali, "Correlation coefficients for T-spherical fuzzy sets and their applications in clustering and multi-attribute decision making," *Soft Computing*, vol. 24, no. 3, pp. 1647–1659, 2020.

[43] A. Guleria and R. K. Bajaj, "On some new statistical correlation measures for T-spherical fuzzy sets and applications in soft computing," *Journal of Information Science and Engineering*, vol. 37, no. 2, pp. 323–336, 2021.

[44] B. C. Cường, "Picture fuzzy sets," *Journal of Computer Science and Cybernetics*, vol. 30, no. 4, pp. 409–420, 2015.

[45] B. C. Cuong, V. Kreinovitch, and R. T. Ngan, "A classification of representable t-norm operators for picture fuzzy sets," in *Proceedings -2016 8th International Conference on Knowledge and Systems Engineering, KSE 2016*, pp. 19–24, Hanoi, Vietnam, 2016.

[46] N. X. Thao, "A new correlation coefficient of the Pythagorean fuzzy sets and its applications," *Soft Computing*, vol. 24, no. 13, pp. 9467–9478, 2020.

[47] W.-L. Hung and M.-S. Yang, "On the _J-divergence of intuitionistic fuzzy sets with its application to pattern recognition," *Information Sciences*, vol. 178, no. 6, pp. 1641–1650, 2008.

[48] C. M. Bishop, Nasrabadi, and M. Nasser, *Pattern Recognition and Machine Learning*, Springer, New York, NY, USA, 2006.

[49] L. Dengfeng and C. Chuntian, "New similarity measures of intuitionistic fuzzy sets and application to pattern recognitions," *Pattern Recognition Letters*, vol. 23, no. 1–3, pp. 221–225, 2002.

Hindawi
Journal of Sensors
Volume 2022, Article ID 6888809, 5 pages
https://doi.org/10.1155/2022/6888809

Research Article

A Full-Duplex MIMO System Based on CP-Free OFDM in Sensor Network

Hao Jiang [1,2] **and Hongming Chen** [3,4]

[1]*The Shanghai Taolink Technologies Corporation, Shanghai 201899, China*
[2]*The School of Information Engineering, Zhejiang Ocean University, Zhoushan 316022, China*
[3]*The Key Laboratory of Oceanographic Big Data Mining Application of Zhejiang Province, Zhejiang Ocean University, Zhoushan 316022, China*
[4]*The College of Electronics Information and Optical Engineering, Nankai University, Tianjin 300350, China*

Correspondence should be addressed to Hongming Chen; buildgates@zjou.edu.cn

Received 21 April 2022; Revised 1 June 2022; Accepted 13 June 2022; Published 11 July 2022

Academic Editor: Han Wang

Recently, results have shown that full-duplex (FD) system based on orthogonal frequency division multiplexing (OFDM) is potential for wireless sensor networks. However, extending FD to further improve spectral efficiency by removing cyclic prefix (CP) with optimal canceling self-interference (SI) remains a challenge. In this paper, we analytically study the conventional FD OFDM system and proposed a CP-free system on this basis. The key point of the proposed scheme is the symbols transmitted in a unit of two identical symbols without CP. To eliminate the intersymbol interference, the disturbed part are replaced by the repeated signal at the receiver, which has the same effect as CP. Finally, an SI cancellation is down to restore the transmitted symbols. As a key of analysis, a multiple-input multiple-output (MIMO) FD simulation model is carried to show that our proposed scheme is effectiveness in terms of the bit error ratio (BER).

1. Introduction

As the artificial intelligence (AI) advanced, AI techniques are further combined with Internet of Things (IoT), which emerges a technology, namely, AI IoT (AIoT). During the technology, the ability to continuously collect, elaborate data, and integrate with participatory sensing is needed [1]. Seasonably, the interactive and shareable wireless sensor network (WSN) system that can meet the above requirements has been the one of the basic factors of the technology [2].

The basic function of WSN is to sense data in small to large networks through sensor nodes and collect information to process any application. It also has a wide range of different platforms, which corresponds to the application of IoT, with the result that WSN will be the best sensor interfacing device in the IoT environment [2]. However, the current sensor equipment and wireless communication technology are not complete [3], which make traditional WSN difficult to achieve the delay and minimize power consumption requirement of the next generation's communication system. The full duplex (FD) makes this possible by improved uplink/downlink delay at WSN without an additional energy price. FD is capable of simultaneously transmitting and receiving signals at the same carrier frequency, and it can have twice as high spectral efficiency (SE) in theory in comparison to the traditional communications, which has the advantage of facing the shortage of wide continuous spectrum below 6 GHz [4]. Nevertheless, in widely FD orthogonal frequency division multiplexing (OFDM) systems, cyclic prefix (CP), the one in charge of eliminating the interference, decreases the SE [5]. Through the literature, several attempts have been made to enhance the SE, and [5–7] aim to reduce the CP without distortion. However, due to imposition of the local transmitter signal on the local receiver, the strong self-interference (SI) also blocks the SE [8], and none of the designs [5–7] managed to remove CP in FD systems. Therefore, our focus in this paper is to design CP-free FD system while limit the effect of SI.

In this paper, we propose a CP-free OFDM FD multiple-input multiple-output (MIMO) system. Comparing with the conventional system, the scheme can further improve the spectral efficiency while digital SI can be optimally canceled, which makes WSN more in line with the requirements of next-generation communication. Additionally, the effect of multipath channel on the signal is also eased.

2. Conventional Full-Duplex OFDM Model

In this section, a full-duplex MIMO communication system based on OFDM is shown in Figure 1, where discrete Fourier transform (DFT), radiofrequency (RF), and SI elimination modules compose the system. Without loss of generality, we consider a signal RF chain to illustrate the process. The baseband signal with inserted CP at the local transmitter of the base station (BS) can be written as

$$X[k] = \frac{1}{\sqrt{M}} \sum_{m=0}^{M-1} x_m e^{j2\pi mk/M}, k = -N_{cp}, \cdots, M-1, \quad (1)$$

where x_m is the transmitted symbol at the mth subcarrier with M being the total number of subcarriers and N_{cp} is the length of CP.

After transforms the digital symbols $X[k]$ into the time domain signal $x(t)$. Then, $x(t)$ can be upconverted into the local RF transmit signal by mixing with the transmitter oscillator, and the RF signal $\tilde{x}(t)$ is obtained as

$$\tilde{X}^1(t) = x(t) e^{j2\pi f_c t}, \quad (2)$$

where f_c denotes the carrier frequency.

Before providing the model for the received signal, it should be noted that the RF signal $\tilde{X}^1(t)$ is transmitted to the users while the antenna of the base station also receives the local RF signal, which is a strong SI signal for the receiver signal. Consequently, the received RF signal at BS consists of the imposing SI signal from local transmitter and the signal-of-interest (SoI) from the users. Then, it can be given as

$$\tilde{y}_m(t) = \sum_{s=1}^{N_s} \left(h_{s,r}^1(t) * \tilde{X}^1(t) + h_{s,r}^{21}(t) * \tilde{X}^{21}(t) \right) + n(t), \quad (3)$$

where N_s is the number of antennas, $h_{s,r}^1(t)$ is the SI channel between the sth transmit antenna and rth receive antenna, $*$ denotes the convolution, $h_{s,r}^{21}(t)$ is the multipath SoI channels, $\tilde{X}^{21}(t)$ is the time domain signal form users, and $n(t)$ is the receiver circular symmetric complex Gaussian (CSCG) noise with zero mean and variance σ^2.

In the sequel, $\tilde{y}_m(t)$ downconverted to the baseband, and it is defined as

$$y_m(t) = \tilde{y}_m(t) e^{-j2\pi f_c t}. \quad (4)$$

Following downconversion, in order to restore the signal, CP is removed and DFT is performed on the signal $y_m(t)$, from which we can get the equation as

$$Y_m[k] = \frac{1}{\sqrt{M}} \sum_{s=1}^{N_s} \left(H_{s,r}^1[k] X^1[k] + \sqrt{M} H_{s,r}^{21} x_m^{21} \right) + N(k), \quad (5)$$

where $\{H_{s,r}^1\}_{k=0}^{M-1}$ are the SI channel frequency response, $\{X^1[k]\}_{k=0}^{M-1}$ are digital symbols of the transmitter from the local BS, and x_m^{21} are the symbols from the user. Correspondingly, $H_{s,r}^{21}$ is the frequency domain SoI channel. Then, equation (5) can be rewritten as

$$Y_m[k] = Y_m^{\text{SI}} + H_{s,r}^{21} x_m + N(k), \quad (6)$$

where Y_m^{SI} is the SI signal. Naturally, the SoI signal can be recovered as

$$Y_m^{\text{SoI}} = Y_m - Y_m^{\text{SI}}, \quad (7)$$

where Y_m^{SoI} is the digital frequency domain SoI symbol.

3. CP-Free Scheme

3.1. System Model. In this section, as is shown in Figure 2, a CP-free scheme is introduced, which consists of several identical symbols. Without loss of generality, two identical symbols that are treated as a unit in this figure, we assumed, transmit at the same index of subcarrier, i.e., symbols at the mth subcarrier repeat transmission twice. It is obvious that CP is removed, which leads to the enhanced spectral efficiency.

At the transmitter, the baseband transmitted signal of a unit can be written as

$$s[k] = \frac{1}{\sqrt{M}} \sum_{m=0}^{M-1} x_m e^{j2\pi mk/M}, k = 0, \cdots, 2M-1. \quad (8)$$

Obviously, $s[k]$ is transmit without CP.

Then, the transmitted signal is transformed into the time domain signal $s(t)$ by digital-analog converter and upconverted into the local RF signal by means of the oscillator, which is the same as the conventional scheme, and the RF signal can be given as

$$\tilde{S}^1(t) = s(t) e^{j2\pi f_c t}. \quad (9)$$

At the receiver, the received signal also consists of the SI signal that is obtained by $\tilde{S}^1(t)$ passing through the multipath channel directly and the SoI signal form the users. Then, the received time domain signal goes downconverted

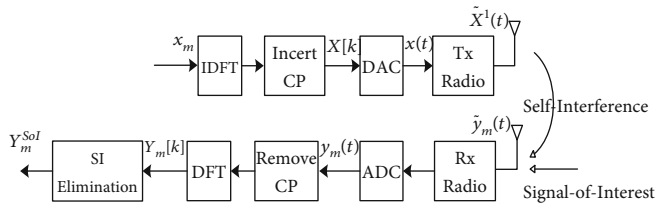

Figure 1: A system model of full-duplex OFDM transceiver.

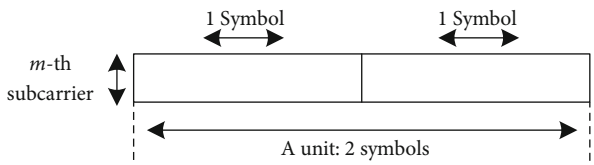

Figure 2: Structure of the proposed unit with two identical symbols.

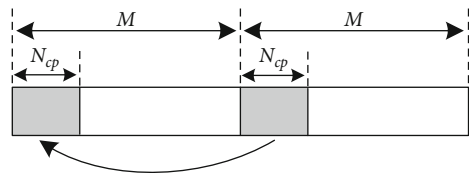

Figure 3: Illustration of signal replacement to construct the circular convolution structure.

from the carrier frequency and it becomes

$$\tilde{r}(t) = \sum_{s=1}^{N_s}\left(h_{s,r}^1(t) * \tilde{S}^1(t) + h_{s,r}^{21}(t) * \tilde{S}^{21}(t)\right)e^{-j2\pi f_c t} + n(t), \tag{10}$$

where $\tilde{S}^{21}(t)$ is the SoI signal. Then, with analog-to-digital converter, the analog signal $\tilde{r}(t)$ is transformed into digital signal $\tilde{r}[k]$.

As we know, CP is aimed at removing the interference which is caused by the multipath channel, without which a great increase of bit error ratio (BER) may happen. Therefore, to eliminate the effect of multi-path channel, in the proposed scheme, as shown in Figure 3, the signal $\tilde{r}[k]$, $k = 0, 1, \cdots, N_{cp} - 1$ is replaced by the signal $\tilde{r}[k]$, $k = M, 1, \cdots, M + N_{cp} - 1$. Then, the signal can be obtained as

$$r[k] = \begin{cases} \tilde{r}[k+M], & \text{if } k = 0, 1, \cdots, N_{\text{cp}} - 1, \\ \tilde{r}[k], & \text{if } k = N_{\text{cp}}, N_{\text{cp}} + 1, \cdots, 2M - 1. \end{cases} \tag{11}$$

We turn the SoI channel into the circular convolution structure which has the same effect as adding CP by (11). Later, carry out a $2M$-point DFT on $r[k]$, and it is thus given as

$$Y_{m_0}[k] = \frac{1}{\sqrt{2M}}\sum_{s=1}^{N_s}\left(\tilde{H}_{s,r}^1[k]X_{m_0}^1[k] + 2\sqrt{M}\tilde{H}_{s,r}^{21}x_{m_0}^{21}\right) + \tilde{N}(k), \tag{12}$$

where $\{\tilde{H}_{s,r}^1(k)\}_{k=0}^{2M-1}$ is the $2M$-point DFT of the discrete SI channel, $\{X_{m_0}^1\}_{k=0}^{2M-1}$ is the SI digital symbols from the Node 1 with $m_0 = 2m$, $\tilde{H}_{s,r}^{21} = \sum_{k=0}^{2M-1} h_{s,r}^{21} e^{-j2\pi lk/2M}$ is the $2M$-point of the lth tap SoI channel, and $x_{m_0}^{21}$ is the SoI symbol with $m_0 = 2m$. It is obvious that $2M$-point DFT change the subcarrier index of the symbols.

Subsequently, the SoI signal can be restored after canceling the SI signal and is given as

$$\tilde{Y}_{m_0}^{SoI} = \tilde{Y}_{m_0} - \tilde{Y}_{m_0}^{SI} = \tilde{H}_{s,r}^{21}x_{m_0}^{21} + \tilde{N}(k). \tag{13}$$

It should note that the received signal $\tilde{Y}_{m_0}^{SoI}$ contains the transmitted symbol at $m_0 = 0, 2, \cdots, 2M - 1$th subcarrier. Therefore, the symbols can be restored by performing a 2-point downsampling on $\tilde{Y}_{m_0}^{SoI}$, and it is given by

$$\varphi_m = \tilde{Y}_{2m}^{SoI}, m = 0, 1, \cdots, M - 1. \tag{14}$$

Finally, the SoI symbol can be restored by channel equation when channel is available at the receiver. The proposed CP-free scheme model is shown at the top this page.

In the following content, we focus on the SI estimation. According (12), the matrix from of the received signal is given as

$$\mathbf{y}_{m_0} = \sum_{s=1}^{N_s}\mathbf{XFh}_{s,r}^1 + \mathbf{y}_{m_0}^{\text{SoI}} + \mathbf{n}, \tag{15}$$

where $\mathbf{X} = \text{diag}\{X[0], X[1], \cdots, [2M-1]\}$ is symbol matrix of the SI digital signal from Node 1, $\mathbf{h}_{s,r}^1 = [h_{s,r}^1(0), h_{s,r}^1(1), \cdots, h_{s,r}^1(2L-1)]^T$ is the SI channel impulse vector, $\mathbf{y}_{m_0}^{\text{SoI}} = [\tilde{Y}_{2m}^{\text{SoI}}[0], \tilde{Y}_{2m}^{\text{SoI}}[1], \cdots, \tilde{Y}_{2m}^{\text{SoI}}[2M-1]]^T$ is the SoI vector, $\mathbf{n} = [\tilde{N}(0), \tilde{N}(1), \cdots, \tilde{N}(2M-1)]^T$ is the additive CSCG noise vector, and $[\mathbf{F}]_{m,k} = e^{-j2\pi mk/2M}$ is a discrete fourier transform matrix. Note that $(\cdot)^T$ is transpose.

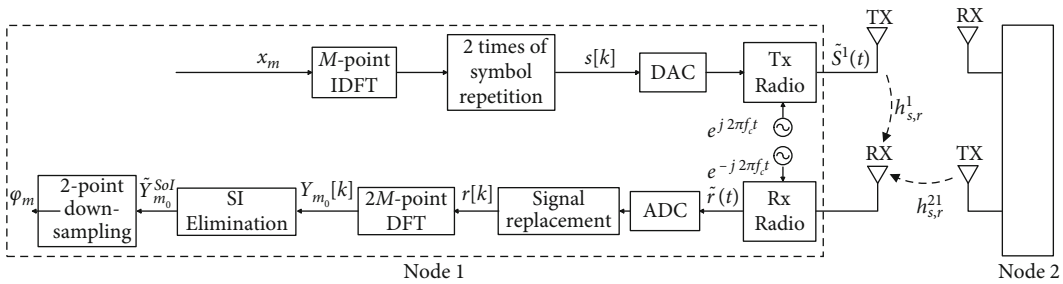

Figure 4: Block diagram of full-duplex CP-free scheme.

According to [9], a weighted linear SI channel estimator can be given as

$$\widehat{\mathbf{h}}^1_{s,r} = \mathbf{WXFh}^1_{s,r} + \mathbf{Wy}^{SoI}_{m_0} + \mathbf{Wn}, \tag{16}$$

where $\mathbf{W}$ is the weight matrix which is used for minimized the residual SI power. Then, the recovered SoI is obtained as

$$\widehat{\mathbf{y}}^{\mathrm{SoI}}_{m_0} = \mathbf{y}_{m_0} - \mathbf{XF}\widehat{\mathbf{h}}^1_{s,r}. \tag{17}$$

When the optimal $\widehat{\mathbf{h}}^1_{s,r}$ is obtained, the residual SI power can be further reduced. The system flow of the proposed scheme is shown in Figure 4.

3.2. Noise Power. Since $\tilde{N}(k)$ has a effect on BER, the correlation processing for the noise is addressed in detail.

In (13), $\widehat{\mathbf{h}}^1_{s,r}$ is channel noise which is Gaussian vector with zero mean and variance σ^2 after DFT. The noise can be expressed as

$$\tilde{N} = \frac{1}{\sqrt{2M}} \sum_{k=0}^{2M-1} n[k] e^{-2j\pi mk/2M}. \tag{18}$$

The mean of $\tilde{N}$ is given as

$$\mathbb{E}\{\tilde{N}\} = \mathbb{E}\left\{\frac{1}{\sqrt{2M}} \sum_{k=0}^{2M-1} n[k] e^{-2j\pi mk/2M}\right\} = 0, \tag{19}$$

where $\mathbb{E}\{\cdot\}$ stands for the expectation operation.

Then, the variance of $\tilde{N}$ is given by

$$\begin{aligned}\mathrm{Var}\{\tilde{N}\} &= \mathbb{E}\left\{\left|\tilde{N}\right|^2\right\} - \left|\mathbb{E}\{\tilde{N}\}\right|^2 \\ &= \mathbb{E}\left\{\left|\frac{1}{\sqrt{2M}} \sum_{k=0}^{2M-1} n[k] e^{-2j\pi nk/2M}\right|^2\right\} \\ &= \frac{1}{2M}\mathbb{E}\left\{\left|\left(\sum_{k=0}^{N_{cp}-1} n[k+M] + \sum_{k=N_{cp}}^{2M-1} n[k]\right) e^{-2j\pi nk/2M}\right|^2\right\}.\end{aligned} \tag{20}$$

Since channel noise $n[k]$ follows Gaussian distribution, the following equation can be rewritten according to that $\mathbb{E}\{n[k]n^*[m]\} = 0$ when $k \neq m$ [5], i.e.,

$$\begin{aligned}\mathrm{Var}\{\tilde{N}\} &= \sigma^2 + \frac{1}{2M}\mathbb{E}\left\{\sum_{k=0}^{N_{cp}-1} |\eta[k+M]|^2 \left(e^{j2\pi m/2} + e^{-j2\pi m/2}\right)\right\} \\ &= \sigma^2 + \frac{2N_{cp}\sigma^2}{2M} \cos(\pi m).\end{aligned} \tag{21}$$

Finally, profiting from the above attributes, we can draw a conclusion that $\tilde{N}$ satisfies the complex Gaussian distribution with mean zero and variance $\sigma^2 + (N_{cp}\sigma^2/M)\cos(\pi m)$.

4. Simulation Results

In this section, simulations result under i.i.d complex normal noise are carried out to analyze the CP-free scheme, in terms of BER. An OFDM-modulated FD communication system is simulated with $M = 64$ subcarriers in each OFDM symbols to carry binary phase shift keying (BPSK) data, and the carrier frequency Δf is set to 15 kHz. Therefore, the sample time is $1/(\Delta f \cdot M) = 1 \times 10^{-6}$. Other parameters are set as follows: the OFDM CP $N_{cp} = M/4 = 16$ and the total transmit antennas $N_s = 64$. To adapt to the typical attenuation value provided by the simulated cancellation [10], the SI channel's Rician factors are set to 30 dB and the Rayleigh channel is considered with a power-delay profile of 0, -5, -10, -15, and -20 dB for delays of 0th, 1st, 2nd, 3rd, and 4-th taps.

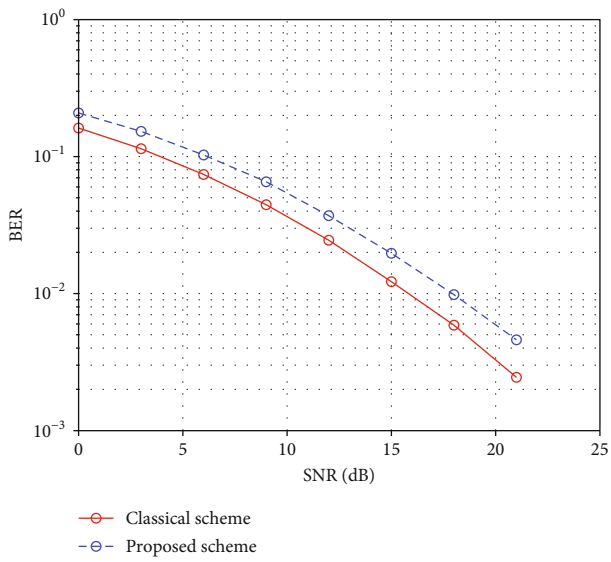

Figure 5: BER of the proposed CP-free scheme and the classical scheme.

The BER is depicted in Figure 5 under complex normal noise and the signal-to-noise ratio (SNR) is defined as SNR= $1/N_0$, where N_0 is the power of noise. The observations above have shown that the proposed CP-free OFDM suffer from some degradation compared to the conventional scheme. The reasons are summarized in the following. From (21), the power of noise increases due to the signal replacement. More precisely, the noise becomes correlated from i.i.d, which leads to the increase of noise variance.

In summary, the proposed scheme eliminate the intersymbol interference and improved the spectrum efficient while it sacrifices BER.

5. Conclusion

In this paper, we concentrated on the CP elimination in a FD MIMO communication system based on OFDM. A novel CP-free scheme was designed in a way that the spectral efficiency is improved. By utilizing duplication and replacement symbol to construct the circular convolution structure of the transmitted signal and channels without interference at the receivers, the system could eliminate the effect of multipath channel as CP. All the CP are removed, which led to an increase in spectral efficiency. Monte Carlo simulation has been carried out to show the comparison with classical work in BER and verify the effectiveness of our proposed scheme.

Data Availability

The data used to support the findings of this study are available from the corresponding author upon request.

Conflicts of Interest

The authors declare that there are no conflicts of interest regarding the publication of this paper.

Acknowledgments

This work was financially supported in part by the Scientific Research Fund of Wuhan Textile University with Grant number 20220321.

References

[1] J. Zhang and D. Tao, "Empowering things with intelligence: a survey of the progress, challenges, and opportunities in artificial intelligence of things," *IEEE Internet of Things Journal*, vol. 8, no. 10, pp. 7789–7817, 2020.

[2] T. M. Behera, S. K. Mohapatra, P. Mukjerjee, and H. K. Sahoo, "Workin-progress: DEEC-VD: a hybrid energy utilization cluster-based routing protocol for WSN for application in IoT," in *In 2017 International Conference on Information Technology (ICIT)*, pp. 97–100, Amman, Jordan, 2017.

[3] H. Wang, L. Xu, Z. Yan, and T. A. Gulliver, "Low-complexity MIMOFBMC sparse channel parameter estimation for industrial big data communications," *IEEE Transactions on Industrial Informatics*, vol. 17, no. 5, pp. 3422–3430, 2020.

[4] H. Wang, P. Xiao, and X. Li, "Channel parameter estimation of mmwave mimo system in urban traffic scene: a training channel-based method," *IEEE Transactions on Intelligent Transportation Systems*, pp. 1–9, 2022.

[5] T. Xiang, D. Qu, F. Zhang, and D. Kong, "Reducing cyclic prefix overhead based on symbol repetition in NB-IoT-based maritime communication," *To Appear China Communications*, 2022.

[6] D. Kong, Y. Xu, G. Song, J. Li, and T. Jiang, "A CP reduction scheme based on symbol repetition for narrow-band IoT systems," *IEEE Internet of Things Journal*, vol. 8, no. 16, pp. 12880–12891, 2021.

[7] J. M. Hamamreh, Z. E. Ankarali, and H. Arslan, "CP-less OFDM with alignment signals for enhancing spectral efficiency, reducing latency, and improving PHY security of 5G services," *IEEE Access*, vol. 6, pp. 63649–63663, 2018.

[8] E. Ahmed and A. M. Eltawil, "On phase noise suppression in full-duplex systems," *IEEE Transactions on Wireless Communications*, vol. 14, no. 3, pp. 1237–1251, 2014.

[9] M. He and C. Huang, "Self-interference cancellation for full-duplex massive MIMO OFDM with single RF chain," *IEEE Wireless Communications Letters*, vol. 9, no. 1, pp. 26–29, 2020.

[10] V. Syrjala, M. Valkama, L. Anttila, T. Riihonen, and D. Korpi, "Analysis of oscillator phase-noise effects on self-interference cancellation in full-duplex OFDM radio transceivers," *IEEE Transactions on Wireless Communications*, vol. 13, no. 6, pp. 2977–2990, 2014.

Hindawi
Journal of Sensors
Volume 2022, Article ID 3962014, 14 pages
https://doi.org/10.1155/2022/3962014

Research Article

An Approach to Improve the Indoor Positioning Performance of Pseudolite/UWB System with Ambiguity Resolution

Xingli Gan,[1] Zhihui Huo,[1] Lu Sun,[2] Shan Yang,[3] and Kaihui Liu[4]

[1]*School of Information and Electronic Engineering, Zhejiang University of Science and Technology, Hangzhou 310023, China*
[2]*Department of Communication Engineering, Institute of Information Science Technology, Dalian Maritime University, Dalian 116026, China*
[3]*China Unicom Smart City Research Institute, Beijing 100048, China*
[4]*Dongguan University of Technology and the Great Bay University, Dongguan 523000, China*

Correspondence should be addressed to Zhihui Huo; 222008855010@zust.edu.cn

Received 20 April 2022; Accepted 7 June 2022; Published 1 July 2022

Academic Editor: Han Wang

Indoor localization is still an open challenge, and some pseudolites have been developed to achieve seamless positioning service based on some commercialized GNSS chips. However, most of these indoor localization technologies often fail in a reasonable solution to the key problems such as low cost and highly accurate and efficient for users. In this paper, we propose an indoor location method based on integrated pseudolite and UWB; the virtual pseudo-range measurements of UWB are used to replace the pseudo-range measurements of pseudolite to solve the indoor multipath problem, which is tightly coupled with the corrected carrier phase measurements of pseudolite. Then, the channel-difference observation equation and UWB-aided ambiguity resolution are proposed for precise positioning. In order to test the proposed method, several experiments are conducted. The results show that the virtual pseudo-range errors from UWB are smaller than that of GNSS, and such a small bias will be better for the fast fixing of ambiguity. In addition, the positioning accuracy of the proposed indoor location method is improved from cm-level for the float solution to mm-level for the fixed solution; these performances would be more convincing to users than that given in the most pseudolite and UWB.

1. Introduction

Global Satellite Navigation System (GNSS) is unable to provide the indoor location service because their signals can be blocked by buildings, and indoor localization is still an open problem. Some indoor localization approaches based on different techniques, such as ultra-wideband (UWB) [1, 2], pseudolite [3], bluetooth [4, 5], Wi-Fi [6], and vision-based on cameras [7, 8], have been developed for location-based services (LBS). The most difficult challenge for indoor positioning is to find an accurate location system, which can use the same receiver from outdoor to indoor. Therefore, many researchers are developing an indoor pseudolite to achieve indoor and outdoor seamless positioning services, such as Indoor Messaging System (IMES) and Locata [9, 10], the in-band GNSS-like signals of which can be received by some commercialized GNSS chips and output pseudo-range and carrier phase measurements.

Some pseudolites for indoor high-precision positioning have also been developed. The multichannel pseudolite with array antenna at a spacing of half a wavelength is proposed [11], which does not require the time synchronization and indoor multipath problems and the positioning accuracy varies from centimeter- to meter-level according to the geometric relation between the antenna array and the receiver. However, the multichannel pseudolite is difficult to support dynamic positioning and has only a 4 m × 4 m positioning coverage area. A combined approach of Doppler and carrier-based hyperbolic positioning with a multichannel Global Positioning System- (GPS-) pseudolite for indoor localization has also been proposed [12], a state equation with three-dimensional (3D) position and orientation, and

ambiguity is established, a nonlinear observation equation for carrier phase difference between pseudolite is used to estimate ambiguity, but it is difficult to overcome such problem as ambiguity resolution. A new indoor multichannel pseudolite system is introduced [13], which overcomes the problem of time synchronization, base stations, and ambiguity resolution of the traditional indoor pseudolite; the multichannel transmitters have an identical clock source and the clock drift of those can also be the same. The high-precision Doppler velocity measurement and positioning method is developed without ambiguity resolution in this work, and the dynamic positioning accuracy is better than 0.3 m. Locata pseudolite consists of a network (LocataNet) of time-synchronized transceivers, which has the potential to allow point positioning with sub-centimeter (cm) precision (using carrier phase and ambiguity resolution) for a mobile unit [14]. To achieve synchronization among all the pseudolite's clock, TimeLoc technology can provide an autonomously synchronized network, which requires the additional ranging signals and the visibility to each other. Therefore, LocataNet is very expensive and difficult to apply in the indoor environment.

Due to the influence of indoor multipath on the pseudo-range measurement for above-mentioned pseudolite, the maximum measurement error of tens of meters may be generated and in different statistics in different indoor scenarios [15], which cannot be used to solve and fix the integer ambiguity based on Least-square Ambiguity Decorrelation Adjustment (LAMBDA) method. Therefore, the Known Point Initialization (KPI) method [16, 17] has been generally adopted to solve ambiguities, but it has three disadvantages which is unacceptable or unusable for most users [18]: One is to survey a large number of known points with precise coordinates; the other is to start positioning at a known point; to make it worse, once the positioning error is more than 2 m, the positioning results using the KPI algorithm will continue to diverge, which needs to start from a new known point, and the positioning process is not continuous; in addition, even if the points of KPI are centimeter-level precision, the ambiguity validation still cannot be passed.

Recently, the ultrawide bandwidth technology has attracted great interest in outdoor/indoor position application. Many UWB systems are now available at commercial level and a set with four anchors and one tag costs only a few hundred dollars. Recent studies have discussed the great potential of tightly coupling UWB with GPS [19]. The effectiveness of tightly coupling GPS and UWB range measurements is used to demonstrate to yield an improved ability to fix integer ambiguity during both kinematic and static applications [20, 21], the accuracy improvement of the float solution was noticeable when UWB measurements were included, and the LAMBDA method was employed to fix solution. UWB is integrated into the Real-time Kinematic (RTK) algorithm to achieve a highly precise positioning with two GPS receivers and reduce the ambiguity resolution search space of LAMBDA method [22]. The positioning strategy is proposed with UWB, low-cost GPS and MEMS onboard sensors, and an unscented Kalman filter is used for the measurement model without any linearization [23]. These researches proposed that the additional measurements of UWB can be directly used to assist ambiguity resolution of phase measurements; as such, the indoor pseudolite system can also be tightly coupled with UWB. Considering that the pseudo-range measurement error of pseudolite is much larger than that of GNSS due to multipath effect; then, the pseudo-range measurements of UWB need to be converted into that of pseudolite.

An indoor precision positioning algorithm is proposed in this paper, which use the carrier phase measurements of pseudolite and the pseudo-range measurements of UWB. The contribution is summarized as follows:

(1) An indoor location system of pseudolite/UWB is proposed, which uses UWB tag and GNSS chip as the receiver to realize precise point positioning. Thus, the proposed system is highly efficient, low cost, and highly accurate for users

(2) With the fusion of carrier phase of pseudolite and virtual pseudo-ranges of UWB, the channel-difference observation equation is proposed, which can effectively reduce the clock offset, and hardware phase delay

(3) To improve the traditional KPI method of indoor pseudolite, the UWB-aided ambiguity resolution is proposed in order to use carrier phase of pseudolite for centimeter-level positioning, and which does not need a known point initialization

The paper is organized as follows: Section 2 provides discussion on the basic terms including the composition of pseudolite/UWB indoor location system and positioning strategy. Section 3 describes the pseudolite integrated navigation model to show the system observation equation, virtual pseudo-range model, phase measurement model, and integer ambiguity resolution. Section 4 provides discussion on the experimental results of the proposed algorithm. Section 5 describes the results and concludes the paper.

2. Indoor Location System Based on Pseudolite and UWB

2.1. Indoor Location System of Pseudolite/UWB. The pseudolite/UWB indoor location system consists of three parts: the indoor synchronous pseudolite, the low-cost UWB system, and the pseudolite/UWB receiver, as shown in Figure 1.

(1) The indoor synchronous pseudolite integrates a multichannel signal transmitter and multiple antennas, the time synchronization of indoor pseudolite is different from that of the outdoor pseudolite, Locata, or GNSS, which uses the same 1 Pulse Per Second (1PPS) to generate the multichannel signals, and the clock offset of each channel can be equal, but the hardware delay is different and must be corrected

(2) The low-cost UWB system uses the DecaWave DW1000 chip with IEEE802.15.4-2011 compliant,

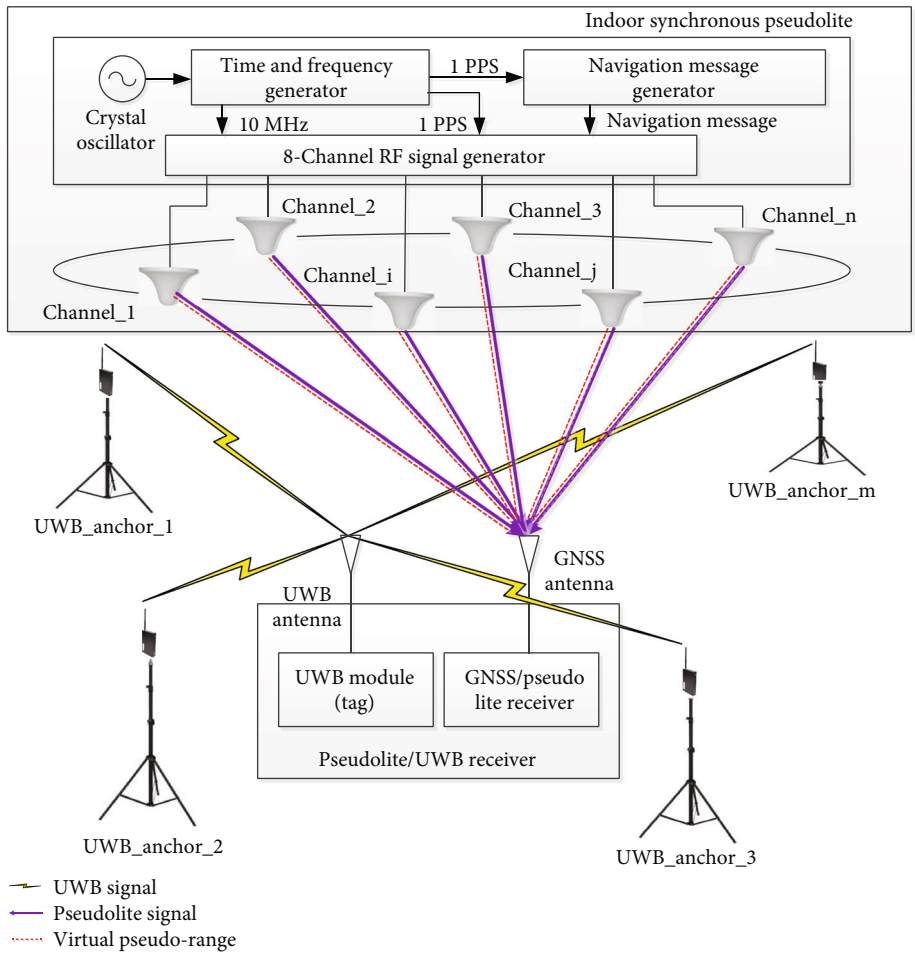

Figure 1: Composition of pseudolite/UWB indoor location system.

which is based on the time of flight ranging measurement to obtain an accurate position, and 95% of the 3D positions have an error equal to or smaller than 50 cm [24–27].

(3) The pseudolite/UWB receiver includes a UWB tag, a GNSS receiver chip (such as ublox M8T/F9P), and their respective antennas. The GNSS chip tracks signals of the indoor pseudolite and provides the carrier phase observation in each epoch, and the UWB tag provides the ranges and the estimated position. The data from each was collected separately for postprocessing and analysis by a laptop, which is synchronized to GPS time

2.2. Pseudolite and UWB-Aided Location Strategies. Based on the composition of pseudolite/UWB indoor location system, the improved indoor positioning strategy is discussed; the use of UWB-aided ambiguity resolution for pseudolite needs to overcome the following problems:

(1) Carrier phase ambiguity resolution is the key problem, and the indoor multipath on pseudo-range measurement error is much greater than that of outdoor, which may be tens of meters; therefore, the pseudo-range measurement of pseudolite cannot be used to the ambiguity resolution. Now, UWB is not only cheap but also can provide centimeter-level ranging accuracy, which can be used to solve the ambiguity for pseudolite and generate a virtual pseudo-range measurement from the pseudolite/UWB receiver to the pseudolite

(2) Hardware delay of receiver and transmitter is also an important influence factor for GNSS or pseudolite positioning [28–30]; the method to measure and calibrate the phase delay is using a reference receiver, and phase measurement models of pseudolite-based positioning need to be modified by inter-channel hardware delay biases

The proposed strategy includes the following steps, as shown in Figure 2: Firstly, we need to estimate the unknown position of the user receiver by UWB, then the virtual pseudo-range measurements are computed from the user receiver to the pseudolite. Secondly, the hardware phase delay of the pseudolite can also be obtained based on the carrier phase measurements of a reference receiver, which is used to correct the carrier phase measurements from the user receiver. Thirdly, the observation equation for indoor

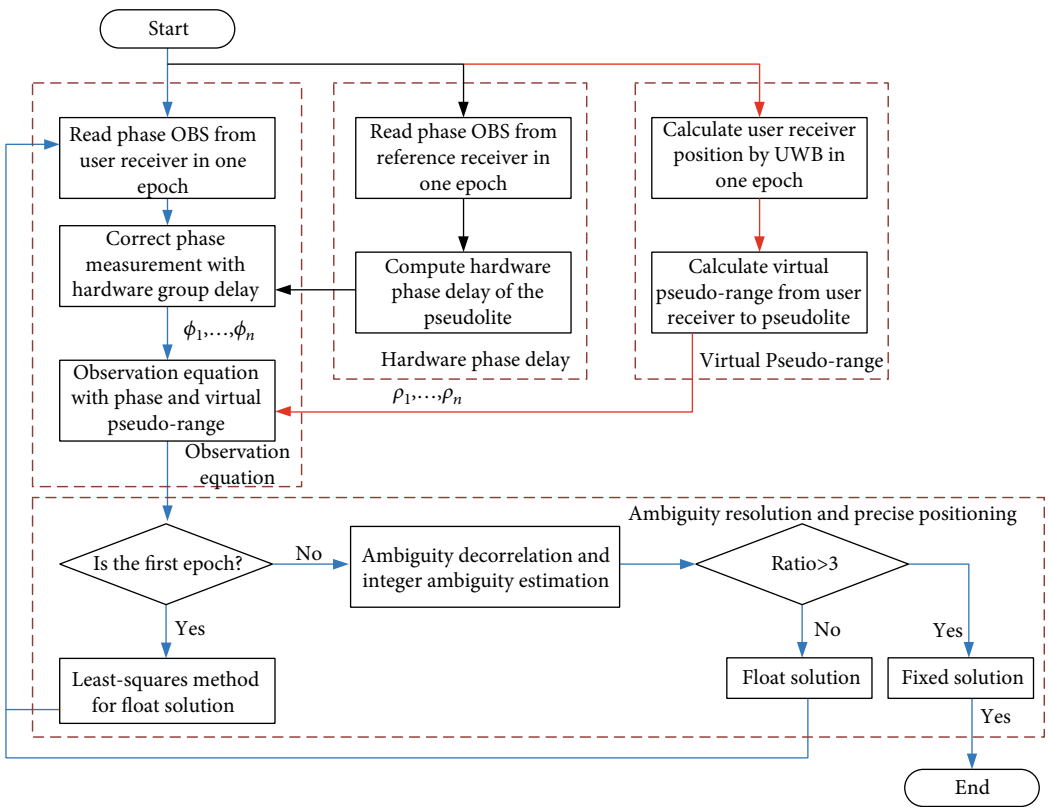

Figure 2: Flowchart for indoor high-precision positioning using pseudolite and UWB.

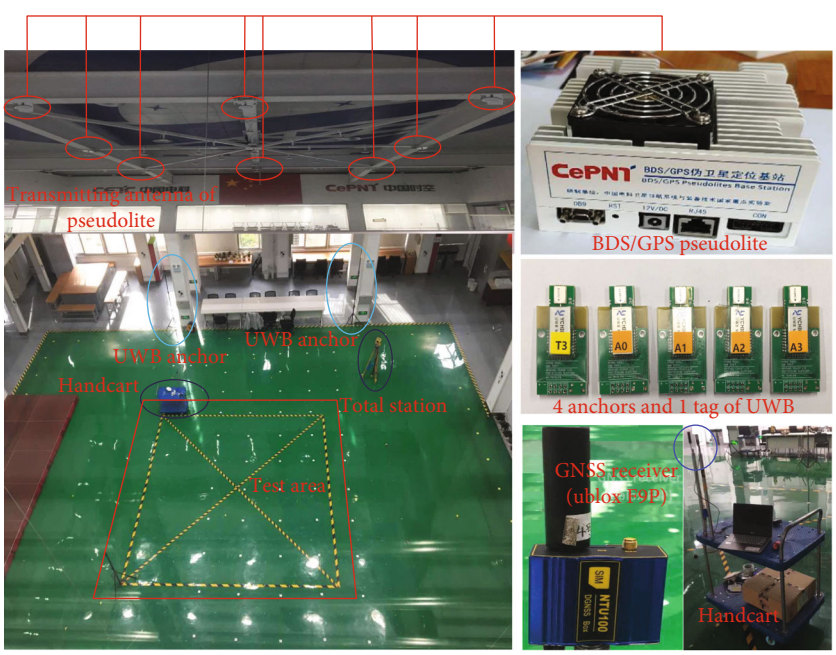

Figure 3: Experimental environment of indoor location system based on pseudolite and UWB.

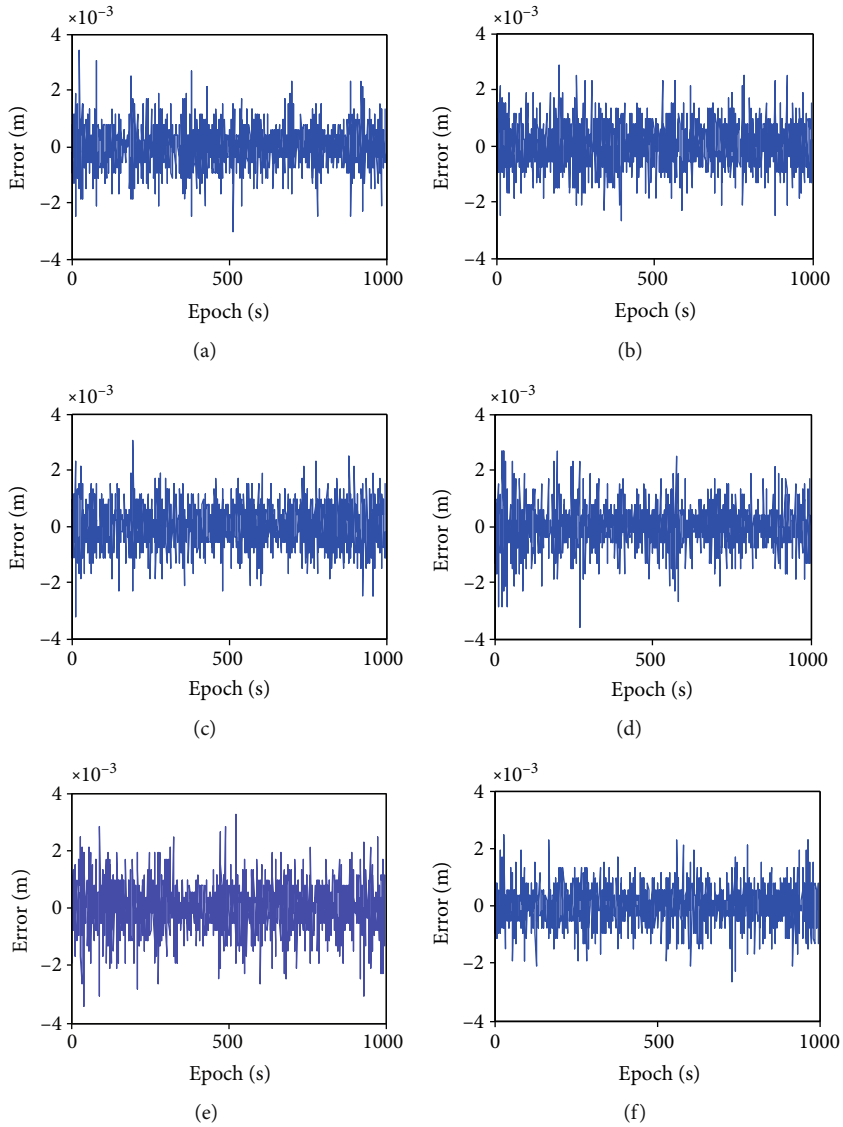

Figure 4: Data quality of the carrier phase measurements using CCD-EED method: (a) C2-C1; (b) C3-C1; (c) C4-C1; (d) C5-C1; (e) C6-C1; (f) C7-C1.

Table 1: Statistical results of CCD-EED method.

	C2-C1	C3-C1	C4-C1	C5-C1	C6-C1	C7-C1
Max (m)	0.0034	0.0029	0.003	0.0027	0.0032	0.0025
Min (m)	-0.003	-0.0027	-0.0032	-0.0036	-0.0034	-0.0027
Mean (m)	1.14×10^{-6}	1.33×10^{-6}	3.8×10^{-7}	1.52×10^{-6}	1.90×10^{-6}	5.71×10^{-7}
STD (m)	8.01×10^{-4}	8.54×10^{-4}	8.24×10^{-4}	8.41×10^{-4}	9.39×10^{-4}	7.32×10^{-4}

high-precision positioning will be established; the corrected carrier phase measurements of pseudolite are tightly coupled with the virtual pseudo-range measurements of UWB. Finally, the carrier phase precise positioning is performed on the user receiver in each epoch, which is based on integrity ambiguity resolution and validation.

3. Methods

3.1. Virtual Pseudo-Range Measurement Model with UWB. The user receiver consists of a UWB module and a GNSS/pseudolite receiver module, once the position of the receiver is calculated by the UWB system, which can be used to

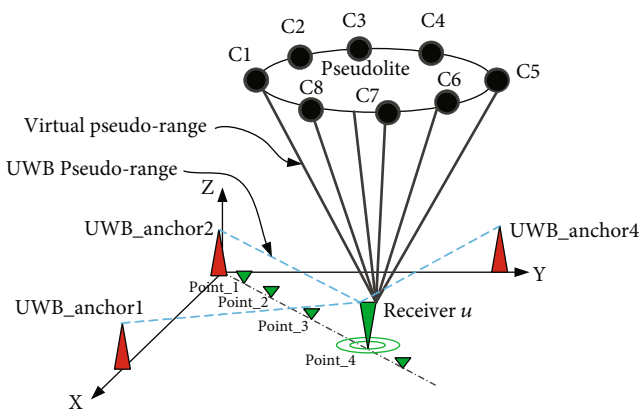

Figure 5: UWB virtual pseudo-range testing.

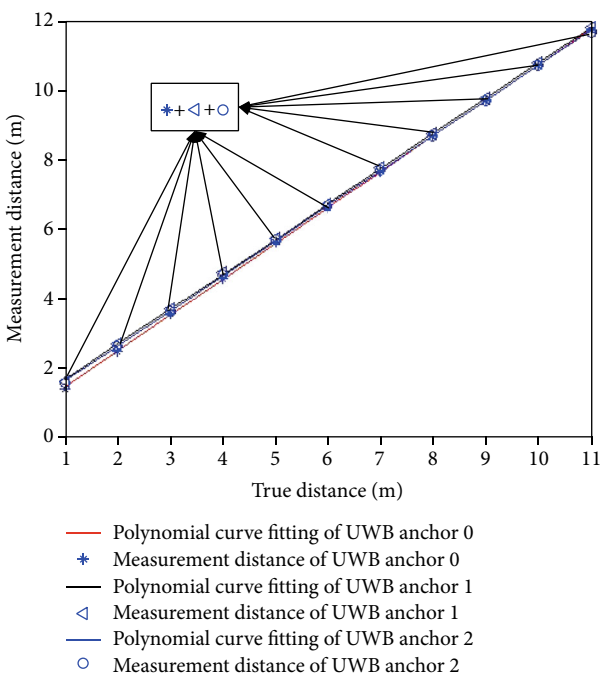

Figure 6: UWB range bias and calibration.

calculate the geometric distance between the receiver and the pseudolite. At the same time, this distance is used to replace the pseudo-range measurement of pseudolite system. The positioning error equation of UWB can be written as:

$$\begin{cases} x_U = x_u + \varepsilon_{Ux} \\ y_U = y_u + \varepsilon_{Uy} \\ z_U = z_u + \varepsilon_{Uz} \end{cases}, \tag{1}$$

where x_U, y_U, and z_U are the coordinates of the user receiver, which is calculated by UWB system; x_u, y_u, and z_u are the true coordinates of the user receiver u; ε_{Ux}, ε_{Uy}, and ε_{Uz} are the virtual measurement errors.

The virtual pseudo-range measurement is built as:

$$\begin{aligned} \rho_u^{PL,i} &= \sqrt{(x_U - x^{PL,i})^2 + (y_U - y^{PL,i})^2 + (z_U - y^{PL,i})^2} \\ &= \sqrt{(x_u - x^{PL,i})^2 + (y_u - y^{PL,i})^2 + (z_\mathrm{u} - y^{PL,i})^2} + \varepsilon_U^{PL,i} \\ &= R_u^{PL,i} + \varepsilon_U^{PL,i}, \end{aligned} \tag{2}$$

where $\rho_r^{PL,i}$ is the virtual pseudo-range measurement between receiver u and pseudolite i; $R_r^{PL,i}$ is the geometric range between receiver u and channel i of the pseudolite; $x^{PL,i}$, $y^{PL,i}$, and $z^{PL,i}$ are the transmitting antenna coordinates of the pseudolite, i for channel number; $\varepsilon_U^{PL,i}$ is the noise of virtual pseudo-range measurement.

3.2. Phase Measurement Model of BDS/GPS Pseudolite

3.2.1. Phase Measurement Model. We consider the carrier phase measurements from pseudolite to receiver; the carrier phase measurement models are described as:

$$\begin{cases} \phi_u^{PL,i} = R_u^{PL,i} + c\left(t_u - t^{PL}\right) + \lambda N_u^{PL,i} + \tau_u^{PL,i} + \varepsilon_u^{PL,i} \\ \phi_u^{PL,j} = R_u^{PL,j} + c\left(t_u - t^{PL}\right) + \lambda N_u^{PL,j} + \tau_u^{PL,j} + \varepsilon_u^{PL,j} \end{cases}, \tag{3}$$

where $\phi_u^{PL,i}$ and $\phi_u^{PL,j}$ are the carrier phase measurements in meters for channel i and j of the pseudolite, respectively; $R_u^{PL,j}$ is the geometric range between receiver u and channel j of the pseudolite; t_u is the receiver clock offset, t^{PL} is the pseudolite clock offset, and c is the speed of light; $N_u^{PL,i}$ and $N_u^{PL,j}$ are the phase ambiguity, and λ is the carrier wavelength; $\tau_u^{PL,i}$ is the phase delay for receiver u and channel i of pseudolite, and $\tau_u^{PL,j}$ is the phase delay for receiver u and channel j of pseudolite; $\varepsilon_u^{PL,i}$ and $\varepsilon_u^{PL,j}$ are the noises of the carrier phase measurement.

Consider that the clock offset of the receiver and the pseudolite is the same, a single difference between channel i and j of pseudolite that cancels the clock offset is built as:

$$\Delta\phi_u^{PL,ij} = \Delta R_u^{PL,ij} + \lambda\Delta N_u^{PL,ij} + \Delta\tau^{PL,ij} + \Delta\varepsilon_u^{PL,ij}, \tag{4}$$

where $\Delta\phi_u^{PL,ij}$ is the difference of phase measurement; $\Delta R_u^{PL,ij}$ is the geometric range difference, and $\Delta N_u^{PL,ij}$ is the ambiguity difference; $\Delta\tau^{PL,ij}$ is the hardware phase delay difference; by forming Equation (4), the phase delay due to the user receiver can be eliminated.

The geometric distance can be calculated by:

$$\begin{aligned} R_u^{PL,i} &= \frac{\left(x_u - x^{PL,i}\right) \times x_u + \left(y_u - y^{PL,i}\right) \times y_u + \left(z_u - z^{PL,i}\right) \times z_u}{\sqrt{\left(x_u - x^{PL,i}\right)^2 + \left(y_u - x^{PL,i}\right)^2 + \left(z_u - x^{PL,i}\right)^2}} \\ &= \left[e_x^i \; e_y^i \; e_z^i\right] \times \begin{bmatrix} x_u \\ y_u \\ z_u \end{bmatrix}, \end{aligned} \tag{5}$$

where $\left[\, e_x^i \quad e_y^i \quad e_z^i \,\right]$ is the geometry matrix.

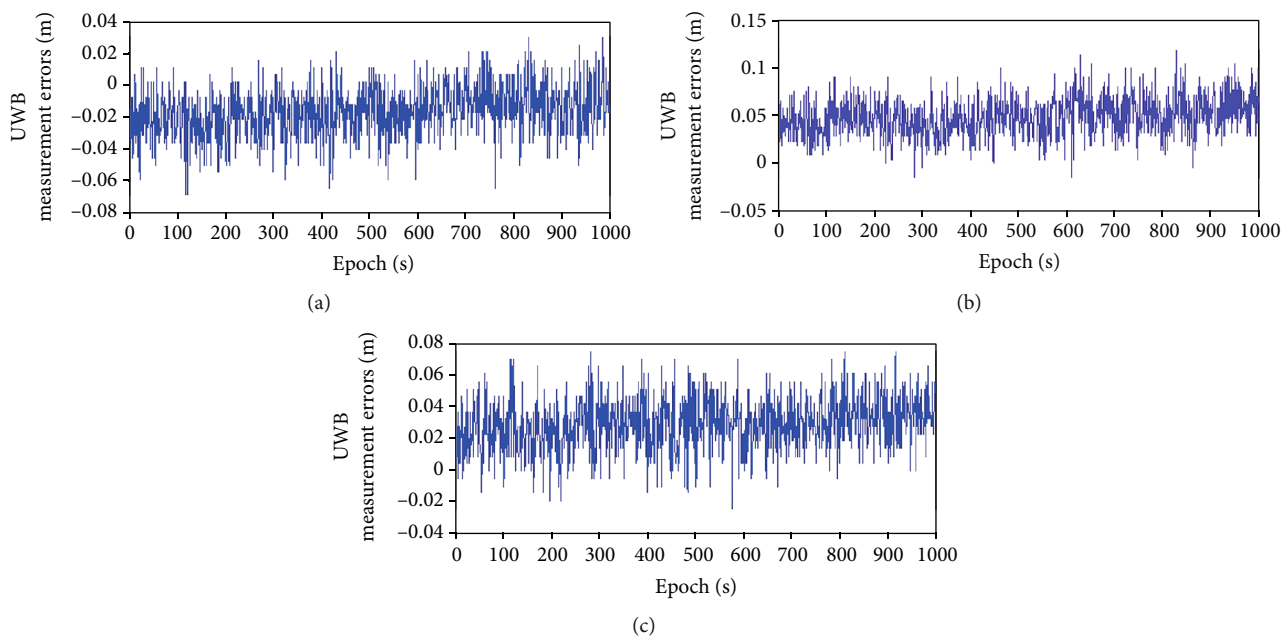

Figure 7: UWB range error vs. epoch: (a) UWB anchor 0; (b) UWB anchor 1; (c) UWB anchor 2.

Then, the geometric range difference equation is denoted by:

$$\begin{aligned}\Delta R_u^{PL,ij} &= \begin{bmatrix} e_x^j - e_x^i & e_y^j - e_y^i & e_z^j - e_z^i \end{bmatrix} \times \begin{bmatrix} x_u \\ y_u \\ z_u \end{bmatrix} \\ &= \begin{bmatrix} \Delta e_x^{ij} & \Delta e_y^{ij} & \Delta e_z^{ij} \end{bmatrix} \times \begin{bmatrix} x_u \\ y_u \\ z_u \end{bmatrix},\end{aligned} \tag{6}$$

where $\begin{bmatrix} \Delta e_x^{ij} & \Delta e_y^{ij} & \Delta e_z^{ij} \end{bmatrix}$ is the difference geometry matrix.

3.2.2. Hardware Phase Delay. The hardware phase delay can be calculated in real time by a reference receiver [31]. When the antenna of the reference receiver and the transmitting antenna of the pseudolite are accurately surveyed by the total station, the distance between the receiver and the pseudolite is considered to be a known parameter; then, the difference equation of phase delay can be represented as:

$$\Delta\widehat{\tau}^{PL,ij} = \Delta\phi_r^{PL,ij} - \left(\Delta\widehat{R}_r^{PL,ij} + \lambda\Delta\widehat{N}_r^{PL,ij}\right) - \Delta\varepsilon_r^{PL,ij}, \tag{7}$$

where $\Delta\widehat{R}_r^{PL,ij}$ is the true geometric distance difference; $\Delta\widehat{N}_r^{PL,ij}$ is the true ambiguity difference, which is the integral part of $\Delta\widehat{R}_r^{PL,ij}$. We can obtain the equations as follows:

$$\begin{cases} \Delta\widehat{\phi}_r^{PL,ij} = \Delta\widehat{R}_r^{PL,ij} + \lambda\Delta\widehat{N}_r^{PL,ij} \\ -\Delta\widehat{N}_r^{PL,ij} = \text{Round}\left(\dfrac{\Delta\widehat{R}_r^{PL,ij}}{\lambda}\right) \end{cases}, \tag{8}$$

where $\Delta\widehat{\phi}_r^{PL,ij}$ is the fractional part of $\Delta\widehat{R}_r^{PL,ij}$; Round$(x)$ is use to separate the integral part and fractional part of a real number.

The true geometric distance difference can be written as:

$$\begin{aligned}\Delta\widehat{R}_r^{PL,ij} = &\sqrt{(\widehat{x}_r - x^{PL,i})^2 + (\widehat{y}_r - y^{PL,i})^2 + (\widehat{z}_r - y^{PL,i})^2} \\ &- \sqrt{(\widehat{x}_r - x^{PL,j})^2 + (\widehat{y}_r - y^{PL,j})^2 + (\widehat{z}_r - y^{PL,j})^2},\end{aligned} \tag{9}$$

where $\widehat{x}_r$, $\widehat{y}_r$, and $\widehat{z}_r$ are the true coordinates of the reference receiver r.

3.3. Pseudolite/UWB Observation Equation. The observation equations for the user receiver can be expressed as follows:

$$\begin{cases} \rho_u^{PL,1} = \sqrt{(x_u - x^{PL,1})^2 + (y_u - y^{PL,1})^2 + (z_u - y^{PL,1})^2} + \varepsilon_U^{PL,1} \\ \vdots \\ \rho_u^{PL,n} = \sqrt{(x_u - x^{PL,n})^2 + (y_u - y^{PL,n})^2 + (z_u - y^{PL,n})^2} + \varepsilon_U^{PL,n} \\ \Delta\widehat{\phi}_u^{PL,21} = \Delta\phi_u^{PL,21} - \Delta\widehat{\tau}^{PL,21} = \Delta R_u^{PL,21} + \lambda\Delta N_u^{PL,21} + \Delta\varepsilon_u^{PL,21} \\ \vdots \\ \Delta\widehat{\phi}_u^{PL,n1} = \Delta\phi_u^{PL,n1} - \Delta\widehat{\tau}^{PL,n1} = \Delta R_u^{PL,n1} + \lambda\Delta N_u^{PL,n1} + \Delta\varepsilon_u^{PL,n1} \end{cases}, \tag{10}$$

where $\Delta\widehat{\phi}_u^{PL,21}, \cdots, \Delta\widehat{\phi}_u^{PL,n1}$ are the differenced term of phase

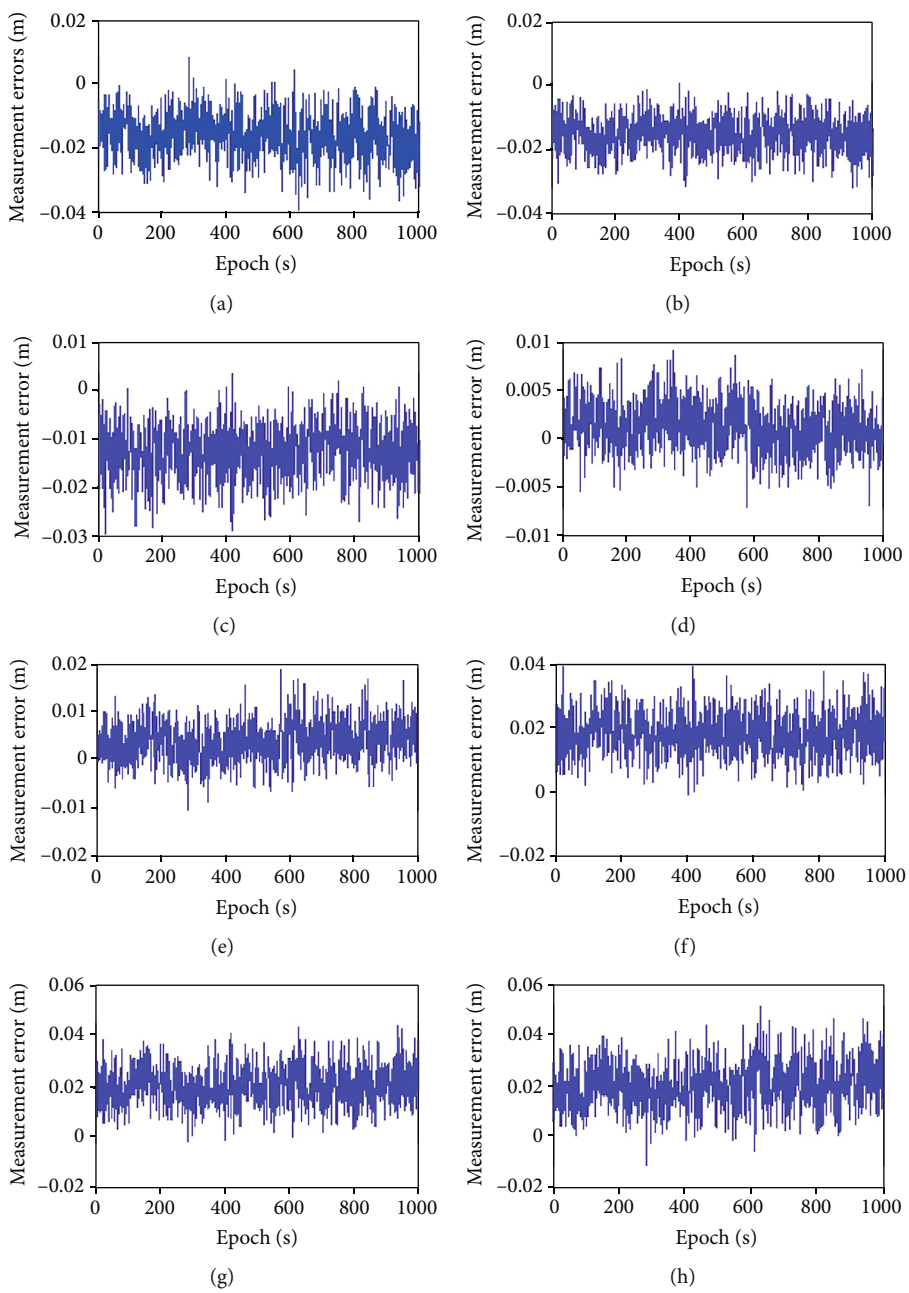

Figure 8: UWB virtual pseudo-range errors: (a) C1_u; (b) C2_u; (c) C3_u; (d) C4_u; (e) C5_u; (f) C6_u; (g) C7_u; (h) C8_u.

Table 2: Statistical results of UWB virtual pseudo-range errors.

	C1_u	C2_u	C3_u	C4_u	C5_u	C6_u	C7_u	C8_u
Max (m)	0.039	0.031	0.030	0.009	0.019	0.040	0.044	0.051
Min (m)	0.008	0.001	0.004	0.007	0.011	0.001	0.002	0.011
Mean(m)	0.016	0.015	0.013	0.001	0.004	0.018	0.020	0.020
STD (m)	0.007	0.006	0.005	0.002	0.004	0.007	0.008	0.009

measurement with the hardware phase delay correction; n is the number of transmission channel.

The observation equation can be written as follows:

$$\begin{bmatrix} \rho_u^{PL,1} \\ \vdots \\ \rho_u^{PL,n} \\ \Delta\widehat{\phi}_u^{PL,21} \\ \vdots \\ \Delta\widehat{\phi}_u^{PL,n1} \end{bmatrix} = \begin{bmatrix} e_x^1 & e_y^1 & e_z^1 & 0 & 0 & 0 \\ \vdots & \ddots & \vdots & \vdots & \ddots & \vdots \\ e_x^n & e_y^n & e_z^n & 0 & 0 & 0 \\ \Delta e_x^{21} & \Delta e_y^{21} & \Delta e_z^{21} & \lambda & 0 & 0 \\ \vdots & \ddots & \vdots & \vdots & \ddots & \vdots \\ \Delta e_x^{n1} & \Delta e_y^{n1} & \Delta e_z^{n1} & 0 & \cdots & \lambda \end{bmatrix} \begin{bmatrix} x_u \\ y_u \\ z_u \\ \Delta N_u^{PL,21} \\ \vdots \\ \Delta N_u^{PL,n1} \end{bmatrix} + \begin{bmatrix} \varepsilon_U^{PL,1} \\ \vdots \\ \varepsilon_U^{PL,n} \\ \Delta\varepsilon_u^{PL,21} \\ \vdots \\ \Delta\varepsilon_u^{PL,n1} \end{bmatrix}. \tag{11}$$

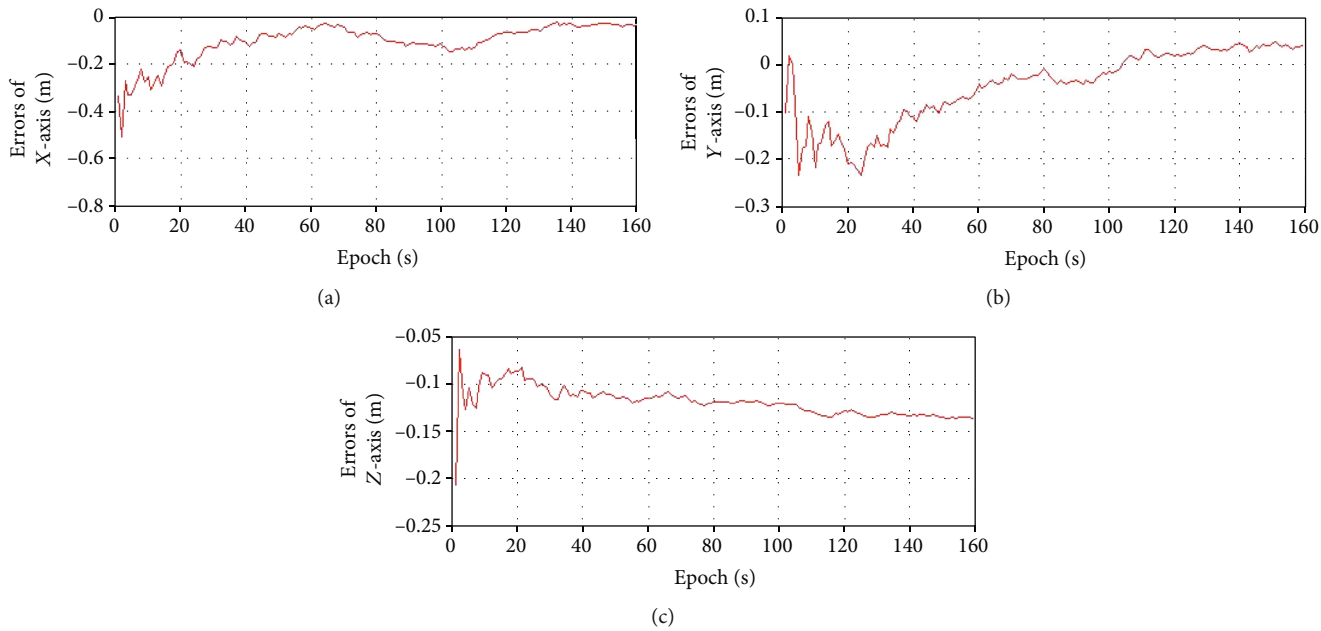

Figure 9: Float solution in the static test: (a) errors of X-axis; (b) errors of Y-axis; (c) errors of Z-axis.

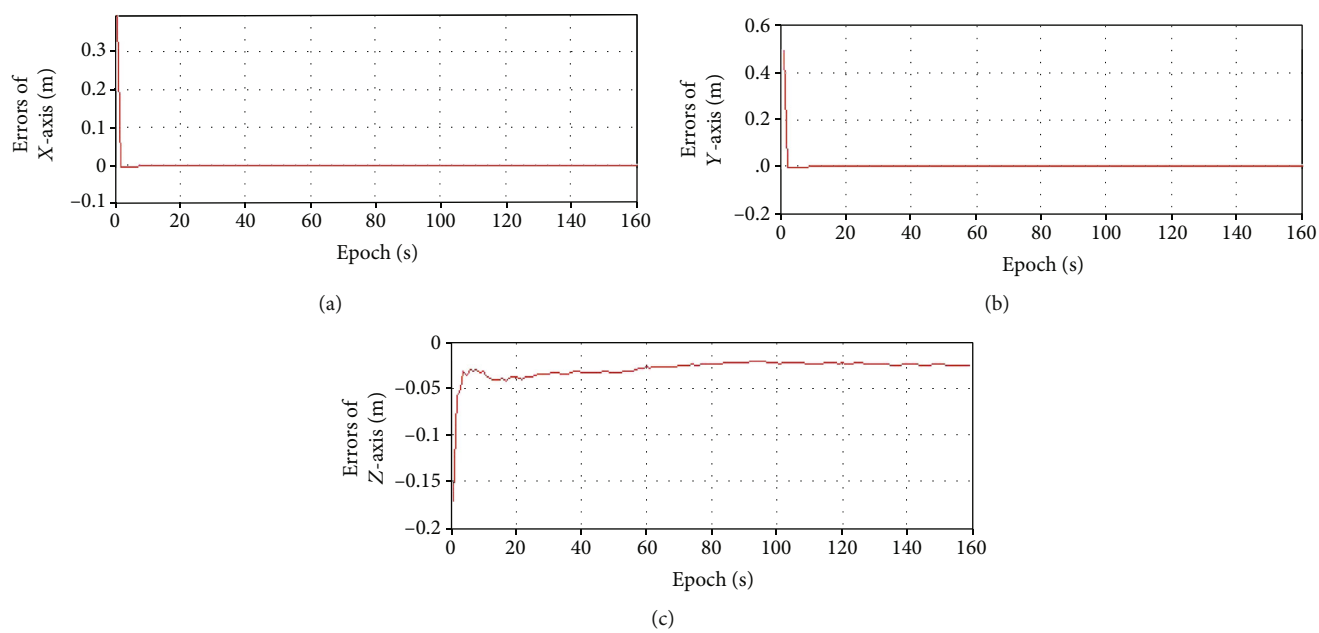

Figure 10: Fixed solution in the static test: (a) errors of X-axis; (b) errors of Y-axis; (c) errors of Z-axis.

Table 3: Statistical results of float solution and fixed solution in the static test.

	Float solution			Fixed solution		
	X-axis	Y-axis	Z-axis	X-axis	Y-axis	Z-axis
Max (mm)	211	231	137	4	3	42
Min (mm)	23	2	83	1	0. 1	22
Mean (mm)	84	34	121	1	0. 5	28
STD (mm)	42	70	12	0.5	0. 4	5.4

3.4. Integer Ambiguity Resolution. The LAMBDA method is adopted for rapid ambiguity resolution [32–34], then Equation (10) can be described by the following form:

$$\boldsymbol{y} = [\boldsymbol{a} \quad \boldsymbol{b}] \begin{bmatrix} \boldsymbol{x} \\ \boldsymbol{n} \end{bmatrix} + \boldsymbol{\varepsilon} = \boldsymbol{ax} + \boldsymbol{bn} + \boldsymbol{\varepsilon}, \tag{12}$$

where $\boldsymbol{y}$ are the differenced observations; and $\boldsymbol{a}$ and $\boldsymbol{b}$ are the corresponding coefficients; $\boldsymbol{x}$ is the vector of the unknown

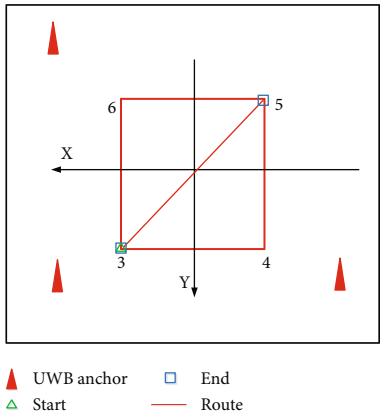

Figure 11: Dynamic positioning with the rectangular route.

coordinate; $\boldsymbol{n}$ is the integer-valued unknown ambiguities; $\boldsymbol{\varepsilon}$ is the measurement noise.

The LAMBDA method has the minimization criterium for solving Equation (12):

$$\min_{\boldsymbol{x},\boldsymbol{n}} \|\mathbf{y} - \mathbf{ax} + \mathbf{bn}\|^2_{Q_y^{-1}}, \text{ with } \begin{cases} x \in R \\ n \in Z \end{cases}, \tag{13}$$

where $\|\cdot\|^2_{Q_y} = (\cdot)^T Q_y^{-1}(\cdot)$ and Q_y^{-1} is the covariance matrix of observables.

The procedure can be divided into three steps: the first step for float solution, by means of a common least-squares method, which takes as starting point for $\hat{\boldsymbol{x}}$ and $\hat{\boldsymbol{n}}$ as real values.

The second step for integer solution with the minimization problem:

$$\min_{\boldsymbol{n}} \|\hat{\mathbf{n}} - \mathbf{n}\|^2_{Q_{\hat{n}}^{-1}}, \text{ with n} \in Zn \in Z, \tag{14}$$

where $Q_{\boldsymbol{n}}^{-1}$ is covariance matrix of integer-valued ambiguities; the LAMBDA method with ambiguity decorrelation (Z-transform) and the actual integer ambiguity estimation are utilized.

In the third step, the fixed ambiguities $\check{\boldsymbol{n}}$ to correct the float parameters $\hat{\boldsymbol{x}}$ and the corresponding variance-covariance matrix:

$$\begin{aligned} \check{\boldsymbol{x}} &= \hat{\boldsymbol{x}} - Q_{\hat{x}\hat{n}} Q_{\hat{n}}^{-1}(\hat{\boldsymbol{n}} - \check{\boldsymbol{n}}), \\ Q_{\check{x}} &= Q_{\hat{x}} - Q_{\hat{x}\hat{n}} Q_{\hat{n}}^{-1} Q_{\hat{n}\hat{x}}. \end{aligned} \tag{15}$$

The least-squares estimates $\check{\boldsymbol{x}}$ and $\check{\boldsymbol{n}}$ are the solution to Equation (13).

4. Implementations and Evaluation

In this section, several experiments are designed to verify the pseudolite and UWB-aided location algorithm. One is a static test to analyze the characterization of pseudolite's carrier phase measurements, UWB's virtual pseudo-ranges, and static positioning results. The other is a dynamic testing for Only-UWB, Only-pseudolite, and pseudolite/UWB.

4.1. Experiment Setup. To evaluate our methods, we conduct field experiments in Figure 3. In order to obtain high-precision carrier phase positioning of pseudolite/UWB, it is necessary in a line-of-sight (LOS) environment. Our field test system included four UWB anchors, one indoor synchronous pseudolite, one receiver with UWB tag and GNSS chip. The indoor synchronous pseudolite has eight signal transmission channels, each of which is connected with a right-handed polarized transmission antenna. At the same time, four UWB anchors are installed in the square test area; it can provide three-dimensional location. A GNSS chip (ublox F9P) with four-arm spiral antennas is used to receive pseudolite's signals and outputs pseudo-range and carrier phase measurements according to UBX protocol through serial port. At the beginning of the test, all antenna coordinates of pseudolite and UWB need to be known. GNSS receiver and UWB tag run at 1 Hz; the frequency of our ambiguity resolutions and position solutions is in accordance with that of GNSS receiver as 1 Hz.

4.2. Static Testing and Analysis

4.2.1. Carrier Phase Characterization of Pseudolite. In the static test situations, the data quality of the carrier phase measurements is analyzed by the epoch-by-epoch difference of Equation (4), which is called CCD-EED method and can be written as:

$$\Delta\phi_u^{PL,ij}(k+1) - \Delta\phi_u^{PL,ij}(k) = \Delta\varepsilon_u^{PL,ij}(k+1) - \Delta\varepsilon_u^{PL,ij}(k), \tag{16}$$

where k is the epoch count.

Figure 4 is the data quality of the carrier phase measurements using CCD-EED method, Cm represents the channel m of pseudolite, C1 is the reference channel. First, using the carrier phase measurement data, the difference between each channel and channel 1 is calculated. Table 1 shows the statistical results obtained by CCD-EED method are more stable, the max error is 0.0034 m (0.018 cycles), the minimum error is -0.0036 m (-0.019 cycles), the mean error is in the range of 5.71 × 10-7 m to 1.90 × 10-6 m, the standard error is in the range of 7.32 × 10-4 m to 9.39 × 10-4 m, and these represent an acceptable in phase measurement error of pseudolite for precise point positioning.

4.2.2. Virtual Pseudo-Range Characterization of UWB. According to Equation (2), the virtual measurement errors can be written as

$$\varepsilon_U^{PL,i} = \rho_u^{PL,i} - R_u^{PL,i}. \tag{17}$$

Figure 5 is the UWB virtual pseudo-range testing. There were few if any sources of signal reflection other than the equipment and the ground. The coordinates of the eleven points were established every 1 m to 11 m starting at UWB anchor; each point was occupied for ten minutes or more and a few thousand UWB range measurements were collected.

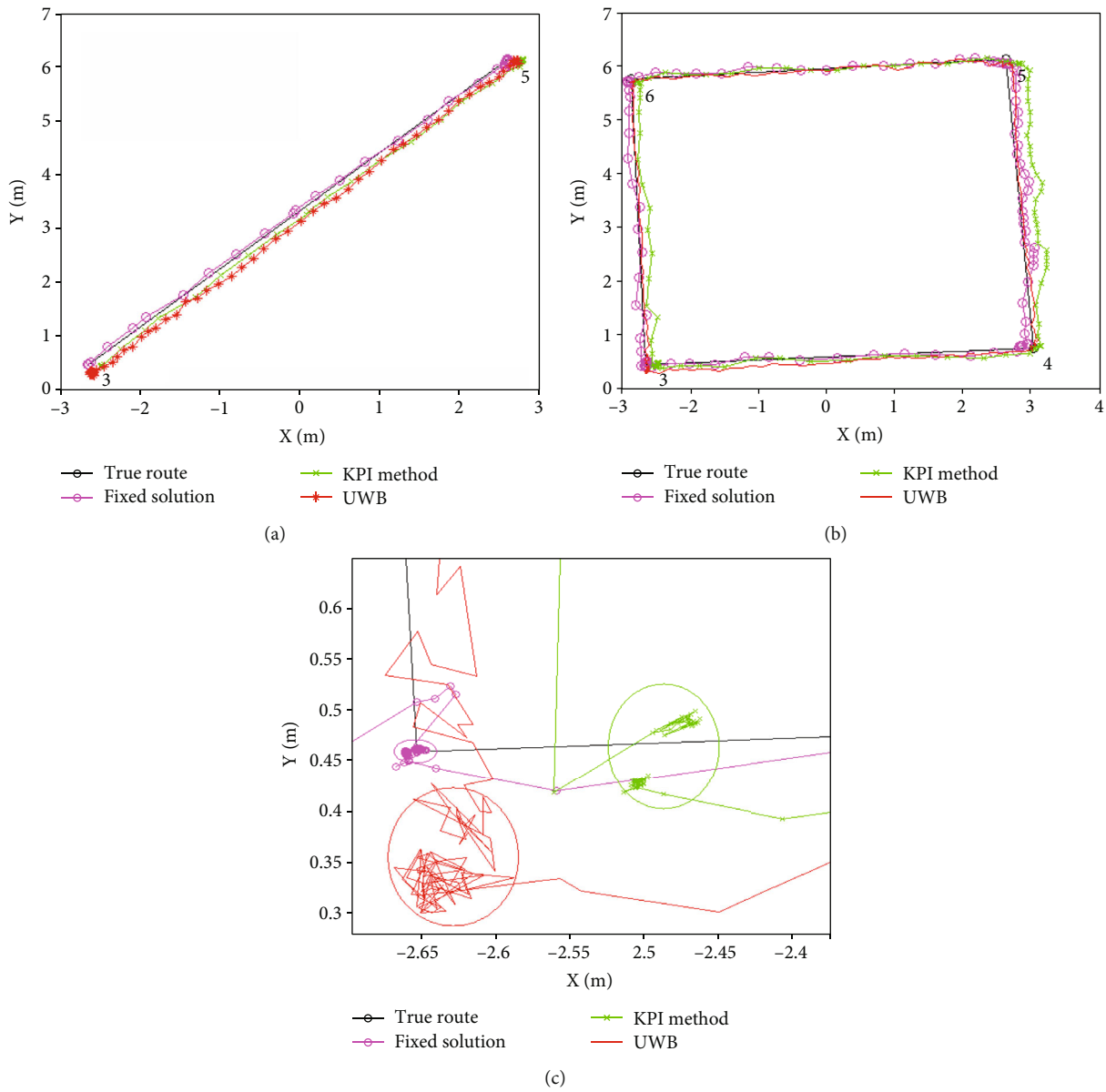

Figure 12: Dynamic positioning results: (a) linear route; (b) rectangular route; (c) closed-loop of the rectangular route.

The UWB ranging bias is well calibrated by a polynomial curve fitting method, as shown in Figure 6. The mean ranging errors based on independent tests from the UWB anchor to the UWB tag are shown in Figure 7 as a function of true distance. It can be seen that the UWB range bias may be 0.6 m before initiating a calibration, but which is less than 0.02 m after the calibration is finished.

After positioning with UWB measurement data, we can obtain the virtual pseudo-ranges from the user receiver to the pseudolite. Figure 8 is the UWB virtual pseudo-range errors, to evaluate the characteristics of the UWB virtual pseudo-range errors; statistical results are performed in Table 2. Results show that the max error of virtual pseudo-range is about 0.051 m, the minimum error is from 0.001 m to 0.011 m, the mean error is from 0.001 m to 0.020 m, and the standard deviation is from 0.002 m to 0.009 m, which means that the UWB virtual pseudo-range may have a deviation of smaller than 1 cycle (GPS L1). Compared to the GNSS pseudo-range, the data quality is much improved; therefore, such a small bias will not affect the ambiguity fixing, but be better for the fast fixing of ambiguity.

4.2.3. Static Positioning Results. Pseudolite and UWB range data were collected at a static point, and the float solution positioning errors are shown in Figure 9. The fixed solution positioning errors are shown in Figure 10, and the statistical results are shown in Table 3. The average three-dimensional positioning error for the float solution is 84 mm, 34 mm, and 121 mm, respectively; and the max three-dimensional positioning error is 211 mm, 231 mm, and 137 mm, respectively. The average positioning error for integer-fixed solutions is 1 mm in the X-axis, 0.5 mm in the Y-axis, and 28 mm in the Z-axis. In summary, with these experimental results,

Table 4: Statistical results at the start/end point in the dynamic test.

	Fixed solution		KPI method		UWB	
	X-axis	**Y-axis**	**X-axis**	**Y-axis**	**X-axis**	**Y-axis**
Max (mm)	7.5	10.1	167.9	26.7	66.2	185.4
Min (mm)	0.3	0.4	154.4	13.2	20.1	119
Mean (mm)	5.4	6.2	160.1	20.8	38.5	155.8
STD (mm)	2.2	2.4	3	4.3	12	19

we conclude that the static positioning accuracy of the indoor location system based on pseudolite and UWB is improved from cm-level for the float solution to mm-level for the fixed solution; these performance specifications would be more convincing to users than the specifications given in the most pseudolite systems [11–14].

4.3. Dynamic Testing and Analysis. A testbed is set up in the indoor open space, as shown in Figure 11, UWB anchors are placed on four corners of the rectangular area, and the test size of the test area is about 6 m long and 5 m wide. The experiment set two routes, one is a linear route from point 3 to point 5, and the other is a rectangular route composed of point 3, point 4, point 5, and point 6. Due to the lack of a reference instrument for millimeter (mm)-level positioning accuracy, we can only evaluate the positioning accuracy at the start point and the end point, the consistency between the estimated trajectory and the true route, and whether it can be closed-loop in the rectangular trajectory.

Figure 12 shows the dynamic positioning results of the two routes, the black line is the true trajectory, the pink line is the estimated trajectory of the fixed solution using pseudolite and UWB-aided location method, the green line is the estimated trajectory using the KPI method of Only-pseudolite [18, 35], and the red line is the estimated trajectory of Only-UWB. Table 4 shows the statistical results at the start/end point in the dynamic test. For the integer-fixed solution, the average position error is 5.4 mm in the X-axis, and 6.2 mm in the Y-axis; the max position error is 7.5 mm in the X-axis, and 10.1 mm in the Y-axis; the minimal position error is 0.3 mm in the X-axis, and 0.4 mm in the Y-axis; the standard deviation in the X-axis is 2.2 mm, and that in Y-axis is 2.4 mm, respectively. For the KPI method, the average position error is 160.1 mm in the X-axis, and 20.8 mm in the Y-axis; the max position error is 167.9 mm in the X-axis, and 26.7 mm in the Y-axis; the minimal position error is 154.4 mm in the X-axis, and 13.2 mm in the Y-axis; the standard deviation in the X-axis is 3 mm, and that in Y-axis is 4.3 mm, respectively. For the UWB method, the average position error is 38.5 mm in the X-axis, and 155.8 mm in the Y-axis; the max position error is 66.2 mm in the X-axis, and 185.4 mm in the Y-axis; the minimal position error is 20.1 mm in the X-axis, and 119 mm in the Y-axis; the standard deviation in the X-axis is 12 mm, and that in Y-axis is 19 mm, respectively. It can be seen that the proposed fixed solution method compared with the KPI method of Only-pseudolite and Only-UWB, the average position accuracy is increased from decimeter-level or cm-level to millimeter-level.

Figure 12(c) shows the closed-loop of the rectangular route, the pink ellipse is the closed-loop of the proposed fixed solution method, the green ellipse is the closed-loop with the KPI method of Only-pseudolite, and the red ellipse is the closed-loop of UWB. Both the KPI method of Only-pseudolite and Only-UWB has a closed-loop deviation, but the proposed fixed solution method can almost be closed-loop.

5. Conclusions

In this paper, a pseudolite/UWB integrated method is proposed to improve the indoor position accuracy, which is based on the fusion of carrier phase measurements of pseudolite and the virtual pseudo-ranges of UWB. The performance of the proposed method has been verified, the data quality of the carrier phase measurements is analyzed by CCD-EED method, and the mean error is in the range of $5.71 \times 10\text{-}7$ m to $1.90 \times 10\text{-}6$ m, which is acceptable for high-precision indoor positioning. The virtual pseudo-range errors of UWB are from 0.001 m to 0.020 m, which means that the UWB virtual pseudo-range may have a deviation of smaller than 1 cycle (GPS L1), and such a small bias will be better for the fast fixing of ambiguity. According to the static and kinematic test, the results show that the positioning accuracy of the indoor location system based on pseudolite and UWB is improved from cm-level for the float solution to mm-level for the fixed solution, and compared with the KPI method of Only-pseudolite and Only-UWB, the average position accuracy of the proposed method is increased from decimeter-level or centimeter-level to millimeter-level.

In the future, the study of pseudolite/UWB integrated method will be focused on the MIMO pseudolite system [36, 37], pseudolite/UWB integrated navigation, and deep learning-aided cycle slip detection and repair [38, 39]. It is foreseen that the precise positioning results will be benefit to the high accuracy, low-cost indoor localization.

Data Availability

The processed data required to reproduce these findings cannot be shared at this time as the data also forms part of an ongoing study.

Conflicts of Interest

The authors declare no conflict of interest.

Authors' Contributions

X.G. conceived and designed the research; X.G. and Z. H provided computational support; L.S. and S.Y. analyzed the data and interpreted the result.

Acknowledgments

This work is supported by the National Natural Science Foundation of China (62101088) and Guangdong Basic and Applied Basic Research Foundation under Grant 2019A1515111193.

References

[1] J. Liang, C. C. Chiau, X. Chen, and C. G. Parini, "Study of a printed circular disc monopole antenna for UWB systems," *IEEE Transactions on Antennas and Propagation*, vol. 53, no. 11, pp. 3500–3504, 2005.

[2] B. Alavi and K. Pahlavan, "Modeling of the TOA-based distance measurement error using UWB indoor radio measurements," *IEEE Communications Letters*, vol. 10, no. 4, pp. 275–277, 2006.

[3] L. Huang, X. Gan, B. Yu et al., "An innovative fingerprint location algorithm for indoor positioning based on array pseudolite," *Sensors*, vol. 19, no. 20, p. 4420, 2019.

[4] X. Gan, C. Sheng, H. Zhang, and L. Huang, "Combination of asynchronous array pseudolites and GNSS for outdoor localization," *IEEE Access*, vol. 7, pp. 38550–38557, 2019.

[5] C. Yang and H. Shao, "WiFi-based indoor positioning," *IEEE Communications Magazine*, vol. 53, no. 3, pp. 150–157, 2015.

[6] W. Xue, W. Qiu, X. Hua, and K. Yu, "Improved Wi-Fi RSSI measurement for indoor localization," *IEEE Sensors Journal*, vol. 17, no. 7, pp. 2224–2230, 2017.

[7] J. Kim and H. Jun, "Vision-based location positioning using augmented reality for indoor navigation," *IEEE Transactions on Consumer Electronics*, vol. 54, no. 3, pp. 954–962, 2008.

[8] D. Manandhar, S. Kawaguchi, and H. Torimoto, "Results of IMES (indoor messaging system) implementation for seamless indoor navigation and social infrastructure platform," in *Proceedings of the 23rd International Technical Meeting of the Satellite Division of The Institute of Navigation (ION GNSS 2010)*, pp. 1184–1191, Portland, OR, 2010.

[9] D. Khan, S. Ullah, and S. Nabi, "A generic approach toward indoor navigation and pathfinding with robust marker tracking," *Remote Sensing*, vol. 11, no. 24, p. 3052, 2019.

[10] N. Kohtake, S. Morimoto, S. Kogure, and D. Manandhar, "Indoor and outdoor seamless positioning using indoor messaging system and GPS," in *Proceedings of the International Conference on Indoor Positioning and Indoor Navigation (IPIN2011)*, pp. 21–23, Guimarães, Portugal, 2011.

[11] K. Fujii, Y. Sakamoto, W. Wang, H. Arie, A. Schmitz, and S. Sugano, "Hyperbolic positioning with antenna arrays and multi-channel pseudolite for indoor localization," *Sensors (Basel)*, vol. 15, no. 10, pp. 25157–25175, 2015.

[12] X. Gan, B. Yu, L. Huang et al., "Doppler differential positioning technology using the BDS/GPS indoor array pseudolite system," *Sensors (Basel)*, vol. 19, no. 20, p. 4580, 2019.

[13] K. Fujii, R. Yonezawa, Y. Sakamoto, A. Schmitz, and S. Sugano, "A combined approach of Doppler and carrier-based hyperbolic positioning with a multi-channel GPS-pseudolite for indoor localization of robots," in *2016 International Conference on Indoor Positioning and Indoor Navigation, IPIN*, pp. 1–7, Alcala de Henares, Spain, 2016.

[14] E. Essa, B. A. Abdullah, and A. Wahba, "Improve Performance of Indoor Positioning System using BLE," in *2019 14th International Conference on Computer Engineering and Systems (ICCES)*, Cairo, Egypt, 2019.

[15] M. O. Kanli, "Limitations of pseudolite systems using off-the-shelf GPS receivers," *Positioning*, vol. 1, no. 8, 2004.

[16] X. Gan, B. Yu, X. Wang et al., "A new array pseudolites technology for high precision indoor positioning," *IEEE Access*, vol. 7, pp. 153269–153277, 2019.

[17] J. P. Montillet, L. K. Bonenberg, C. M. Hancock, and G. W. Roberts, "On the improvements of the single point positioning accuracy with Locata technology," *GPS Solutions*, vol. 18, no. 2, pp. 273–282, 2014.

[18] Y. Zhao, P. Zhang, J. Guo et al., "A new method of high-precision positioning for an indoor pseudolite without using the known point initialization," *Sensors (Basel)*, vol. 18, no. 6, p. 1977, 2018.

[19] Z. Li, R. Wang, J. Gao, and J. Wang, "An approach to improve the positioning performance of GPS/INS/UWB integrated system with two-step filter," *Remote Sensing*, vol. 10, no. 2, p. 19, 2018.

[20] G. Macgougan, K. O'Keefe, and R. Klukas, "Tightly-coupled GPS/UWB integration," *Journal of Navigation*, vol. 63, no. 1, pp. 1–22, 2010.

[21] G. MacGougan, K. O'Keefe, and R. Klukas, "Accuracy and reliability of tightly coupled GPS/ultra-wideband positioning for surveying in urban environments," *GPS Solutions*, vol. 14, no. 4, pp. 351–364, 2010.

[22] E. Broshears, *Ultra-Wideband Radio Aided Carrier Phase Ambiguity Resolution in Real-Time Kinematic GPS Relative Positioning, Master Thesis*, the Auburn University, Auburn, Alabama, 2013.

[23] H. Gao and X. Li, "Tightly-coupled vehicle positioning method at intersections aided by UWB," *Sensors (Basel)*, vol. 19, no. 13, p. 2867, 2019.

[24] A. R. Jiménez Ruiz and F. Seco Granja, "Comparing Ubisense, BeSpoon, and DecaWave UWB location systems: indoor performance analysis," *IEEE Transactions on Instrumentation and Measurement*, vol. 66, no. 8, pp. 2106–2117, 2017.

[25] M. R. Mahfouz, C. Zhang, B. C. Merkl, M. J. Kuhn, and A. E. Fathy, "Investigation of high-accuracy indoor 3-D positioning using UWB technology," *IEEE Transactions on Microwave Theory and Techniques*, vol. 56, no. 6, pp. 1316–1330, 2008.

[26] M. Ridolfi, S. Vandermeeren, J. Defraye et al., "Experimental evaluation of UWB indoor positioning for sport postures," *Sensors*, vol. 18, no. 2, p. 168, 2018.

[27] P. Dabove, V. Di Pietra, M. Piras, A. A. Jabbar, and S. A. Kazim, "Indoor positioning using Ultra-wide band (UWB) technologies: positioning accuracies and sensors' performances," *2018 IEEE/ION Position, Location and Navigation Symposium (PLANS)*, pp. 175–184, 2018.

[28] R. Berry, P. G. Mattos, and I. Kale, "Group delay and phase delay in GNSS systems," *Geo-spatial Information Science*, vol. 16, no. 3, pp. 210–219, 2013.

[29] M. Håkansson, A. B. O. Jensen, M. Horemuz, and G. Hedling, "Review of code and phase biases in multi-GNSS positioning," *GPS Solut*, vol. 21, no. 3, pp. 849–860, 2017.

[30] X. Li, X. Li, Y. Yuan, K. Zhang, X. Zhang, and J. Wickert, "Multi-GNSS phase delay estimation and PPP ambiguity resolution: GPS, BDS, GLONASS, Galileo," *Journal of geodesy*, vol. 92, no. 6, pp. 579–608, 2018.

[31] C. Deng, Q. Liu, X. Zou et al., "Investigation of tightly combined single-frequency and single-epoch precise positioning

using multi-GNSS data," *Remote Sensing.*, vol. 12, no. 2, p. 285, 2020.

[32] P. J. Teunissen, "A new method for fast carrier phase ambiguity estimation," in *In Proceedings of 1994 IEEE Position, Location and Navigation Symposium-PLANS'94*, pp. 562–573, IEEE, 1994, April.

[33] P. J. G. Teunissen, "The least-squares ambiguity decorrelation adjustment: a method for fast GPS integer ambiguity estimation," *Journal of Geodesy*, vol. 70, no. 1-2, pp. 65–82, 1995.

[34] P. J. G. Teunissen, "The probability distribution of the GPS baseline for a class of integer ambiguity estimators," *Journal of Geodesy*, vol. 73, pp. 275–284, 1999.

[35] X. Li, P. Zhang, J. Guo, J. Wang, and W. Qiu, "A new method for single-epoch ambiguity resolution with indoor pseudolite positioning," *Sensors*, vol. 17, no. 4, p. 921, 2017.

[36] H. Wang, P. Xiao, and X. Li, "Channel parameter estimation of mmWave MIMO system in urban traffic scene: a training channel based method," *IEEE Transations on Intelligent Transportation Systems*, pp. 1–9, 2022.

[37] H. Wang, X. Lingwei, T. Zhengqiang Yan, and A. Gulliver, "Low-complexity MIMO-FBMC sparse channel parameter estimation for industrial big data communications," *IEEE Transactions on Industrial Informatics*, vol. 17, no. 5, pp. 3422–3430, 2021.

[38] L. Wan, R. Liu, L. Sun, H. Nie, and X. Wang, "UAV swarm based radar signal sorting via multi-source data fusion: a deep transfer learning framework," *Information Fusion*, vol. 78, pp. 90–101, 2022.

[39] L. Wan, K. Liu, and W. Zhang, "Deep learning-aided off-grid channel estimation for millimeter wave cellular systems," *IEEE Transactions on Wireless Communications*, vol. 21, no. 5, pp. 3333–3348, 2022.

Hindawi
Journal of Sensors
Volume 2023, Article ID 9783463, 1 page
https://doi.org/10.1155/2023/9783463

Retraction

Retracted: Performance Evaluation of Spectral Efficiency for Uplink and Downlink Multi-Cell Massive MIMO Systems

Journal of Sensors

Received 19 December 2023; Accepted 19 December 2023; Published 20 December 2023

This article has been retracted by Hindawi following an investigation undertaken by the publisher [1]. This investigation has uncovered evidence of one or more of the following indicators of systematic manipulation of the publication process:

(1) Discrepancies in scope
(2) Discrepancies in the description of the research reported
(3) Discrepancies between the availability of data and the research described
(4) Inappropriate citations
(5) Incoherent, meaningless and/or irrelevant content included in the article
(6) Manipulated or compromised peer review

The presence of these indicators undermines our confidence in the integrity of the article's content and we cannot, therefore, vouch for its reliability. Please note that this notice is intended solely to alert readers that the content of this article is unreliable. We have not investigated whether authors were aware of or involved in the systematic manipulation of the publication process.

Wiley and Hindawi regrets that the usual quality checks did not identify these issues before publication and have since put additional measures in place to safeguard research integrity.

We wish to credit our own Research Integrity and Research Publishing teams and anonymous and named external researchers and research integrity experts for contributing to this investigation.

The corresponding author, as the representative of all authors, has been given the opportunity to register their agreement or disagreement to this retraction. We have kept a record of any response received.

References

[1] R. M. Asif, M. Shakir, A. U. Rehman, M. Shafiq, R. A. Khan, and W. U. Khan, "Performance Evaluation of Spectral Efficiency for Uplink and Downlink Multi-Cell Massive MIMO Systems," *Journal of Sensors*, vol. 2022, Article ID 7205687, 12 pages, 2022.

Hindawi
Journal of Sensors
Volume 2022, Article ID 7205687, 12 pages
https://doi.org/10.1155/2022/7205687

Research Article

Performance Evaluation of Spectral Efficiency for Uplink and Downlink Multi-Cell Massive MIMO Systems

Rao Muhammad Asif,[1] Mustafa Shakir,[1] Ateeq Ur Rehman,[2] Muhammad Shafiq,[3] Rehan Ali Khan,[4] and Wali Ullah Khan[5]

[1]*Department of Electrical Engineering, The Superior College Lahore, Pakistan*
[2]*Department of Electrical Engineering, Government College University, Lahore 54000, Pakistan*
[3]*Department of Information and Communication Engineering, Yeungnam University, Gyeongsan 38541, Republic of Korea*
[4]*Department of Electrical Engineering, University of Science and Technology, Bannu 28100, Pakistan*
[5]*Interdisciplinary Centre for Security, Reliability and Trust (SnT)/SigCom, University of Luxembourg, 1855 Luxembourg City, Luxembourg*

Correspondence should be addressed to Ateeq Ur Rehman; ateeq.rehman@gcu.edu.pk and Muhammad Shafiq; shafiq@ynu.ac.kr

Received 22 February 2022; Revised 4 June 2022; Accepted 18 June 2022; Published 30 June 2022

Academic Editor: Carlos Marques

Massive multiple-input and multiple-output (MIMO) systems have become the most persuasive technology for 5G as it increased the energy efficiency gigantically as compared to other wireless communication systems. Being the most vibrant research technology in the communication sector, this research work is based on the optimal model development of energy-efficient massive MIMO systems. The proposed model is a realistic model that augmented the spectral efficiency (SE) of massive MIMO systems where a multi-cell model scenario is considered. Channel estimation is carried out at the base stations (BSs) based on uplink (UL) transmission while the minimum mean-squared error (MMSE), Element-wise MMSE, and Least-square (LS) estimators are used for the estimation. We analyze the achievable SE of the UL based on the MMSE channel estimator with different receive combining schemes. Moreover, the downlink (DL) transmission model is also modelled with different precoding schemes by taking the same vectors used in combining schemes. The simulation results show a significant improvement in spectral efficiency by developing UL and DL transmission models and also realized that the average sum of SE per cell can be improved by optimized MMSE channel estimation, installing multiple BS antennas, and serving multiple UEs per cell. The findings of this work specify that the massive MIMO system can be developed by optimizing the channel estimation for the augmentation of SE in UL and DL transmissions. Conclusively, it can be summarized that some complex computations of MMSE channel estimators can enhance the average sum of SE per cell as per the results verified in this model.

1. Introduction

Advancement in Massive MIMO systems is a key factor in encouraging the 5G network as it has high spectral and energy efficiencies having multiple transmitters and receiver antennas [1–3]. Recently many researchers have been enthusiastic about the study of massive MIMO networks whereas channel estimation, uplink (UL) and downlink (DL) transmission, spectral efficiency, energy augmentation models are evaluated in the last decade. On the other hand, the uplink signal assumption becomes inefficient and complex due to the large number of antennas in the massive MIMO system. Meanwhile, the proposed algorithm in [4] is efficient and achieves optimal bit error rate (BER) which depends on the least-square (LS) channel estimator compared to the traditional uplink detection algorithm. Thus, 5G is designed to adjust the high reliability, data traffic, and to improve spectral and energy efficiency with low latency while the Richardson and Neumann series expansion (NSE) method has been used to avoid matrix inversion [5]. Meanwhile, a method in [6] provides a good arrangement between bit error rate and complexity with hundreds or thousands of antennas are used in a system for tens of users to

provide services simultaneously and the channel is also estimated according to the pilot signals which are sent by the user to the base stations (BS) while the massive MIMO system provides the advantage of high reliability, high spectral and energy efficiency. Maximum likelihood, minimum mean square (MMS) method, M-MMSE, S-MMSE, Regular Zero-Forcing (RZF), Zero-Forcing (ZF), maximal ratio combining (MRC), and zero-forcing deduction for channel estimation are used in the [7–10] while MMSE is preferred as it has the ability of better spectral efficiency other than complexity [11]. Although circuit power preference algorithms have been proposed to maximize energy efficiency (EE) in a multi-cell environment but the precoding techniques are developing for increasing spectral efficiency in the MIMO system has a better impact. An antenna selection scheme is used to expand the energy efficiency of the UL transmissions while it has more power consumption of the mobile antennas [9, 12]. Therefore, pilot reuse techniques are proposed for reducing co-channel interference without increasing the bandwidth and cell density is also analyzed. Meanwhile, a low complexity in channel estimation is becoming a big concern, minimum mean-squared error (MMSE), Element-wise MMSE, and Least-square (LS) estimators are used for computing the complexity with the trade-off of SE. Moreover, power consumption and energy efficiency (EE) of the base stations can be improved by using an effective strategy and an efficient downlink MIMO system consisting of zero-forcing, beamforming, and perfect channel in the base station is discussed here. Although, unimodal and user data rate increase together for the point of maximum energy efficiency whereas, unimodal is an average energy efficiency per base station. The linear precoding of channels is an efficient way with downlink and uplink pre-coders to reduce the effect of inter-user and improper noise. Furthermore, large array and multiplexing gain are used for large spectral and energy efficiency where a base station is equipped with a large antenna array to develop the orthogonal channel pairwise among users and base station by the use of small-scale fading [13]. Besides that, a massive MIMO system reduces the transmitted power of the base station and terminal, the research carries some Full-duplex (FD) models that are more suitable for short-range of communication like that WiFi and small-cell network more than arrangements with realistic parameters proposed by zero-forcing (ZF) design [14]. Hence, 5G antennas' spectral efficiency (SE) and energy efficiency (EE) are major factors in the designing of 5G antennas. Furthermore, the latest idea of the massive MIMO networks and distributed antennas system is known to improve inter-cell interference and a balanced quality of experience. Therefore, massive MIMO technology gives an impressive spectral efficiency compared to the conventional co-located MIMO [15]. The achievable spectral efficiency of several precoding and combining structures are getting more attention in analogue-digital implementation and 5G should be supportive of low power consumption [16]. For sustainable development in 5G, it has to improve energy and cost efficiency comparatively by Integrating the massive MIMO with examining the impact of pilot contamination on this new communication scenario. However, existing literature claims that it is probable to attain SE by performance evaluation of UL ad DL transmission models with their channel estimation as some details are in Table 1. The purpose of this article is the mathematical modelling of the UL and DL signals transmission and different channel estimation schemes for the UL transmission are also computed for the SE. We have also compared the complexity and SE of the above-mentioned channel estimators. The second objective is to provide an accurate MR precoding model for DL transmission for enhancing the SE as presented in [17, 18]. A survey of related work has been undergone by considering the key features of the previous work as summarized in Table 1. Furthermore, the latest trends and approximation methods used for the augmentation of EE are particularized while combing and precoding schemes with power consumption models already used by researchers are also considered. The SE enhancement schemes are deeply analyzed, and key factors are elaborated as well.

Table 1: Comparison of Related Work of Se In Massive MIMO.

Work	Cell	UL/DL	Combining/precoding scheme
[7]	Multicell	UL&dl	MMSE precoding and combining
[8]	Multicell	UL&dl	MMSE, RZF, ZF, MR precoding
[9]	Multicell	UL	MMSE precoding
[10]	Single	UL&dl	ZF precoding
[16]	Single	UL&dl	—

Given objectives are well accomplished and summarized as:

(1) A multi-cell scenario is considered where the UL and DL transmission models are taken into account with inter-cell interference and noises

(2) MMSE, EW-MMSE, and LS channel estimator schemes are modelled to carry the max. SE in UL transmission. However, MMSE is better as compared with EW-MMSE, and LS because of high SE and better interference mitigation practice

(3) MR precoding model for DL transmission for enhancing the SE is evaluated in the last section

The computed results of our proposed models are appropriate to indorse the massive MIMO systems that can able to enhance SE in a 5G cellular network. This paper is structured as follows. Section 1 is an illustration of a massive MIMO system model for both uplink and downlink communication. In section 2 the UL Spectral Efficiency with the MMSE estimator is compared with EW-MMSE and LS. Section 4 the MR precoding scheme is modelled for augmentation of DL Spectral Efficiency. Finally, key insinuation conclusions are drawn in Section 5. The Table 2 and Table 3 show the symbolic and acronyms representations used in our paper.

2. System Model for Uplink & Downlink Massive MIMO

This section includes the specifications of a multicell massive MIMO system covering the UL and DL transmission

Table 2: Symbolic Representations.

Symbols	Description
$\mathbb{E}(.)$	*Expectation*
$\lvert . \rvert$ and $\lVert . \rVert$	*Absolute values and Euclidean norm*
$\boldsymbol{I}_K$	$K \times K$ *identity matrix*
Ψ	*Pilot signal sequence*
n_j^{dl}	*Additive receiver noise*
B	*Bandwidth*
T_{coh} & B_{coh}	*Coherence Time & Coherence Bandwidth*
$w_{lr} \in C^{M_l}$	Assigned as transmit precoding vector
$y_j^{UL} \epsilon \mathbb{C}$ and $y_j^{DL} \epsilon \mathbb{C}$	*Transmission symbols (uplink & downlink)*
τ_{UL}/τ_{coh}& τ_{DL}/τ_{coh}	*Uplink transmission & downlink transmission pre log factor*

Table 3: Acronyms Representations.

Symbols	Description
MMSE	Minimum mean-squared error
ZF	Zero-forcing
RZF	Regular zero-forcing
MRC	Maximal ratio combining
LS	Least-Square
SE	Spectral efficiency
MIMO	Massive multiple-input and multiple-output
BSs	Base stations
UL	Uplink
DL	Uplink
BER	Optimal bit error rate
NSE	Neumann series expansion
ML	Maximum likelihood
EE	Energy efficiency
FD	Full-duplex
EW	Element wise

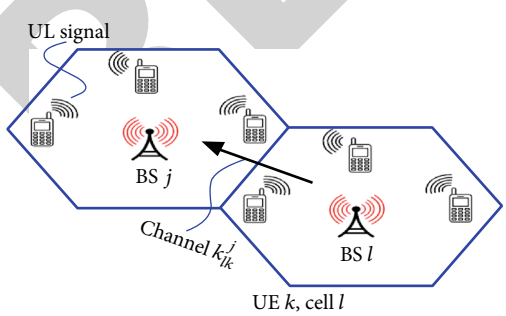

Figure 1: Illustration of the UL Massive MIMO transmission in cell j and cell l.

models, linear processing schemes, and channel models. The systems describe the UL and DL MIMO transmission in cell j and cell l as illustrated in Figure 1. Channel vectors h_{lk}^j and h_{jk}^l are considered in UL and DL, respectively, between the BS j and UE k. The UL data transmission signal has considered the desired signal, inter-cell interference, and noise. On the other hand, DL data transmission signal has added part of the intra-cell signal.

On the above-mentioned consideration, the following segments are modelled.

2.1. Uplink. In this stage, user K transmits the data to one of the correspondence BSs. Let the users K have the transmitted symbol vector in the l cell is $s_l = [s_{l,1} s_{l,2} \cdots s_{l,k}]$ and the received UL signal $y_j^{UL} \epsilon \mathbb{C}^M$ from the users K at BSj can be written as:

$$y_j^{UL} = \sqrt{\rho ul} \sum_{l=1}^{L} \sum_{K=1}^{K_i} h_{lk}^j S_{lk}^{UL} + n_j^{UL} \tag{1}$$

Where $n_j^{UL}$is an additive receiver noise denotes $n_j^{UL} \sim C\mathcal{N}(O_{M_j}, \sigma_{UL}^2 I_{M_j})$ while O_{M_j} is zero mean and σ_{UL}^2 is variance. Then the UL signal in cell l denote $s_{lk}^{UL} \epsilon \mathbb{C}$ has power $p_{UL,lk} = \mathbb{E}\{|s_{lk}^{UL}|^2\}$ and $\rho_{UL} > 0$ means the uplink SNR and UL signal $y_j^{UL} \epsilon \mathbb{C}^M$ is given as:

$$y_j^{UL} = \sqrt{\rho_{UL}} \sum_{K=1}^{K_j} h_{jk}^j S_{jk}^{UL} + \sqrt{\rho_{UL}} \sum_{\substack{l=1 \\ i \neq j}}^{L} \sum_{K=1}^{K_i} h_{li}^j S_{li}^{UL} + n_j^{UL} \tag{2}$$

Whereas, $\sqrt{\rho_{UL}} \sum_{K=1}^{K_j} h_{jk}^j S_{jk}^{UL}$ is desired signal and $\sqrt{\rho_{UL}} \sum_{\substack{l=1 \\ i \neq j}}^{L} \sum_{K=1}^{K_i} h_{li}^j S_{li}^{UL}$ is inter-cell interference. The BS as dedicated in cell j selects the receive combining vector $y_j^{UL} \epsilon \mathbb{C}^M$ at the time of data transmitting for separating the desired

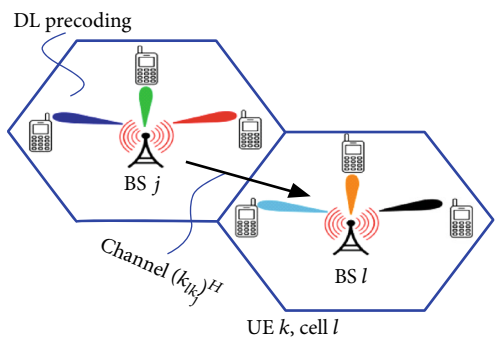

Figure 2: Illustration of the DL Massive MIMO transmission in cell j and cell l.

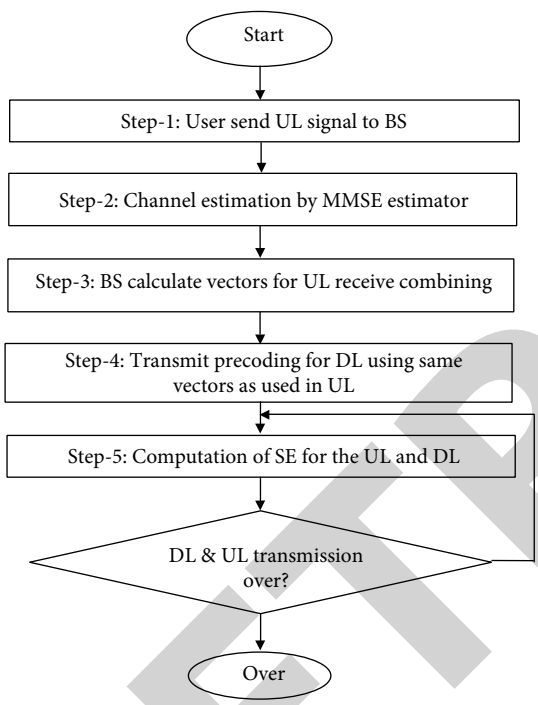

Figure 3: Computational Flow.

UE signal from the interferences and can be written as:

$$V_{jk}^{UL} y_j^{UL} = \sqrt{\rho_{UL}}\, V_{jk}^{UL} h_{jk}^{j} s_{ji}^{UL} + \sqrt{\rho_{UL}} \sum_{\substack{i=1 \\ i \neq k}}^{K_j} V_{jk}^{UL} h_{jk}^{j} s_{ji}^{UL} + \sqrt{\rho_{UL}} \sum_{\substack{i=1 \\ i \neq j}}^{L} \sum_{i=1}^{K_i} V_{jk}^{UL} h_{jk}^{j} s_{ji}^{UL} + n_j^{UL} \tag{3}$$

Then the desired signal becomes $\sqrt{\rho_{UL}}\, V_{jk}^{UL} h_{jk}^{j} s_{ji}^{UL}$ with intra-cell signals and inter-cell interference. The selection of combing vector modelling in terms of spectral efficiency is analyzed with the different combining schemes in the next section.

2.2. Downlink. As per the Massive MIMO illustration in Figure 2 for *dl* transmission, BS *j* transmits the signal in cell *l* that is written as:

$$x_l = \sum_{i=l}^{k_l} W_{lir_{li}} \tag{4}$$

Where $w_{lr} \in C^{M_l}$ is assigned as transmit precoding vector. Then the received signal $y_j^{DL} \epsilon \mathbb{C}$ is modelled as:

$$y_j^{DL} = \sqrt{\rho_{DL}} \sum_{l=1}^{L} \left(h_j^{DL}\right)^H xl + n_j^{DL} \tag{5}$$

The symbol vector is denoted as $x_l = [x_{l,1} x_{l,2} \cdots x_{l,k}]$ and n_j^{DL} is an additive receiver noise. The term $\sqrt{\rho_{DL}} > 0$ means the SNR of *DL*. Then y_j^{DL} can be written as:

$$y_j^{DL} = \sqrt{\rho_{DL}} \sum_{l=1}^{L} \sum_{i=1}^{K_l} \left(h_{jk}^{DL}\right)^H W_{lirli} + n_j^{DL} \tag{6}$$

$$y_j^{dl} = \sqrt{\rho_{DL}} \left(h_{jk}^{j}\right)^H w_{jkr_{jk}} + \sqrt{\rho_{DL}} \sum_{\substack{i=1 \\ i \neq k}}^{K_j} \left(h_{jk}^{j}\right)^H W_{jir_{ji}} + \sqrt{\rho_{DL}} \sum_{\substack{l=1 \\ l \neq j}}^{L} \sum_{i=1}^{K_l} \left(h_{jk}^{DL}\right)^H W_{lir_{li}} + n_j^{DL} \tag{7}$$

Then the desired signal becomes $\sqrt{\rho_{DL}} (h_{jk}^{j})^H w_{jkr_{jk}}$ for the *dl* with intra-cell signals and inter-cell interference. The selection of transmit precoding vectors in terms of spectral efficiency is analyzed with the different precoding schemes in the next section.

3. Methodology and Calculations

M-MMSE, S-MMSE, RZF, ZF, and MR combiner and precoder are used in our model for SE of UL and DL, respectively. The enhancement in ES for the given system and optimized modeling are the main aims of this article. We explored the methodology for the SE in MIMO systems in which, the SE is optimized by proposed estimators. The first comparison of different estimators is done by estimating the channel of MMSE, EW-MMSE, and LS. Although the LS and EW-MMSE are less complex in computing but the loss in SE incurred by these estimators is not ignorable as discussed in the section 4 whereas MMSE is preferred as it has the ability of better spectral efficiency other than complexity [11]. Different combing and precoding schemes are tested by proposed numerical equations for SE of UL and DL transmissions after the selection of MMSE channel estimation. The computational flow of our model is shown in Figure 3. The UL data and channel estimation are calculated in the first two steps. Step 3 and step 4 are the computation stage of

Table 4: Computational complexity per coherence block of different combining schemes.

Scheme	Reception multiplication	Computing combining vectors multiplication
Multicell MMSE	$\tau_{UL}M_jK_j$	$\sum_{l=1}^{L}\frac{\left(3M_j^2+M_j\right)K_l}{2}+\frac{M_j^3-M_j}{3}+M_j\tau_p\left(\tau_p-K_j\right)$
Single-cell MMSE	$\tau_{UL}M_jK_j$	$\frac{3M_j^2K_j}{2}+\frac{M_jK_j}{2}+\frac{M_j^3-M_j}{3}$
RZF	$\tau_{UL}M_jK_j$	$\frac{3K_j^2M_j}{2}+\frac{3K_jM_j}{2}+\frac{K_j^3-K_j}{3}$
ZF	$\tau_{UL}M_jK_j$	$\frac{3K_j^2M_j}{2}+\frac{K_jM_j}{2}+\frac{K_j^3-K_j}{3}$
MR	$\tau_{UL}M_jK_j$	—

Table 5: Simulation parameters.

Parameters	**M = 500**
$\mathbf{CP_1}[\boldsymbol{Watt}]$	15
$\boldsymbol{ETP}\,[\boldsymbol{Watt}]$	2
$\boldsymbol{\sigma^2}$	-3 dBm
$\overline{\boldsymbol{\beta_0^0}}$	
$\boldsymbol{\mu}$	0.5

Table 6: Simulation Parameters.

Simulation parameter	Values.
Required bandwidth (B)	20 MHz
Coherence time (T_{Coh})	10 msec
Maximum distance/cell radius(r)	(200) Meters
Maximum antennas (M)	500
Channel attenuation (ω)	$10^{-3.5}$
UEs (K)	18
The effective SNR	−10 dB to 20 dB
Network layout	Square pattern
Receiver noise power	−94 dBm
Samples per coherence block	$\tau_{coh}=200$

different combing and precoding schemes with the same vectors. In further, the average sum of SE per cell is optimized for UL and DL in step 5 while the data is still not over, then the computation is again computed. In this way the average sum of SE per cell is expended as per the following stages:

3.1. Channel Estimation. In dedicated UL, each cell transmits a pilot sequence for allowing the BSs to compute H_{jj} of their local channel H_{jj} while the sequence is mutually orthogonal. The channel estimation is based on random variables and the statistical distribution of variable are taken into account. The received signal correlates with the pilot sequence and MMSE estimate the channel vector $\widehat{h}_{li}^{j}$, given as:

$$y_{jk}^{tr}=\widehat{h}_{UL}^{j}+\sum_{l\neq j}\widehat{h}_{ULi}^{j}+\frac{1}{\sqrt{\rho tr}}n_{jk} \tag{8}$$

$$\widehat{h}_{ULi}^{j}=\sqrt{p_{ULi}}R_{ULi}^{j}\Psi_{ULi}^{j}Y_{jULi}^{p} \tag{9}$$

Where Y_{jUL}^{p} is the uplink pilot transmission and pilot sequence become:

$$\Psi_{ULi}^{j}=\left(\sum_{(v,i')\in p_{UL}}pvi'\tau_rR_{ULl'i'}^{j}+\sigma_{ULi}^{2}I_{M_j}\right)^{-1} \tag{10}$$

Where the Estimation error is $\widehat{h}_{ULi}^{j}=h_{ULi}^{j}-\widehat{h}_{ULi}^{j}$ has correlation matrix $C_{ULi}^{j}=\mathbb{E}\{\widehat{h}_{ULi}^{j}(\widehat{h}_{ULi}^{j})^{H}\}$ given as:

$$C_{ULi}^{j}=R_{ULi}^{j}-p_{ULi}R_{ULi}^{j}\Psi_{ULi}^{j}R_{ULi}^{j} \tag{11}$$

The MMSE is estimated by invoking the orthogonal property and the estimated error is statistical independent of $\widehat{h}_{UL}^{j}$. As per the pilot communication phenomenon, UEs that have the same pilot sequence for the transmission can mutually pollute the channel estimation. Although channels are statistically independent but the interference reduces the estimation quality by increasing MSE and make the channel estimation statistically dependent. Above channel estimation can mitigate the interference of UEs that practice the same pilot. The massive MIMO systems have a huge influence rather than conventional networks due to large numbers of UEs having pilot sequences that can easily suppress the interference. Besides, the MMSE estimator minimizes the MSE of the channel estimate, given as:

$$\mathbb{E}\left\{\left\|h_{ULi}^{j}-\widehat{h}_{ULi}^{j}\right\|^2\right\}=\mathbb{E}\left\{\left\|\widehat{h}_{ULi}^{j}\right\|^2\right\}=\mathbb{E}\left\{\mathrm{tr}\left(\widehat{h}_{ULi}^{j}\left(\widehat{h}_{ULi}^{j}\right)^{u}\right)\right\}=\mathrm{tr}\left(C_{ULi}^{j}\right) \tag{12}$$

We are considered the cell j and cell l for the $UE\,k$ and ULi the interference, respectively, and the correlation matrix

at BS j is:

$$\mathbb{E}\left\{\widehat{h}_{jk}^{j}\left(\widehat{h}_{ULi}^{j}\right)^{u}\right\}=\begin{cases}\sqrt{p_{ULi}P_{jk}}R_{jk}^{j}\Psi_{ULi}^{j}R_{ULi}^{j} & (UL,i)\in\mathscr{P}_{jk}\\ O_{M_j\times M_j} & (UL,i)\notin\mathscr{P}_{jk}\end{cases} \tag{13}$$

And the antenna correlation coefficient is written as:

$$\frac{\mathbb{E}\left\{\left(h_{ULi}^{j}\right)^{u}h_{ULi}^{j}\right\}}{\sqrt{\mathbb{E}\left\{\left\|h_{jk}^{j}\right\|^{2}\right\}\mathbb{E}\left\{\left\|h_{ULi}^{j}\right\|^{2}\right\}}}=\begin{cases}\dfrac{\mathrm{tr}\left(R_{ULi}^{j}R_{jk}^{j}\Psi_{ULi}^{j}\right)}{\sqrt{\mathrm{tr}\left(R_{jk}^{j}R_{jk}^{j}\Psi_{ULi}^{j}\right)\mathrm{tr}\left(R_{ULi}^{j}R_{ULi}^{j}\Psi_{ULi}^{j}\right)}} & (UL,i)\in\mathscr{P}_{jk}\\ 0 & (UL,i)\notin\mathscr{P}_{jk}\end{cases} \tag{14}$$

Whereas, $\mathbb{E}\{(h_{li}^{j})^{u}h_{li}^{j}\}=0$ for all UEs with $(UL,i)\neq(j,k)$. The expression of non-zero expectation is carried out from the UL transmission section and taking into account all the considerations with $(UL,i)\in\mathscr{P}_{jk}$ while channel vector is $y_{jk}^{p}=y_{jULi}^{p}$, written as $\mathbb{E}\{y_{jULi}^{p}(y_{jULi}^{p})^{u}\}=\tau_p(\psi_{ULi}^{j})^{-1}$ and the normalized MSE (NMSE) is written as:

$$\mathrm{NMSE}_{UL}^{j}=\frac{\mathrm{tr}\left(C_{UL}^{j}\right)}{\mathrm{tr}\left(R_{UL}^{j}\right)} \tag{15}$$

This expression is used for the comparison of the estimation quality using different estimation schemes in different scenarios. The MMSE estimation provides enough statistical information for the UL data transmission that can help in decoding. This computation has required an inverse matrix of Ψ_{ULi}^{j} and makes the method very complex as attached large antennas with huge numbers of users [19]. This provokes us to solve for the simpler calculations and the estimation that is EW-MMSE. Lemma 1 is an EW-MMSE estimation with the statistics of the estimates. The assumption is made on the correlation matrix R_{ULIi}^{j} that depends on $A_{ULi}^{j}|_{mm}$ diagonal.

Lemma 1. *If base l uses an EW-MMSE estimation where the channel is estimated between users k in cell l. Although each element can be estimated by MMSE but the EW-MMSE estimates the vectors with error and vectors without error.*

$$A_{ULi}^{j}\Big|_{mm}=\frac{\sqrt{p_{ULi}}\left|R_{ULIi}^{j}\right|_{mm}}{\sum_{(l',i')\epsilon p_{li}}p_{UL'i'}\tau_p\left|R_{l'i'}^{j}\right|_{mm}+\sigma_{UL}^{2}}\quad m=1,\cdots..M \tag{16}$$

This is quite simpler in computational as compared to MMSE, except in the case of diagonal spatial correlation matrices where each channel element estimates it separately. It is notable that A_{ULi}^{j} reduces the complexity. The EW-MMSE is obtained as:

$$\mathrm{MSE}=\mathrm{tr}\left(R_{ULi}^{j}\right)-\frac{\rho_{ULi\tau_p}\left(\left|R_{ULi}^{j}\right|_{mm}\right)^{2}}{\sum_{(UL',i')\epsilon p_{ULi}}p_{UL'i'}\tau_p\left|R_{UL'i'}^{j}\right|_{mm}+\sigma_{UL}^{2}} \tag{17}$$

In the case of noise-free calculation then the LS channel estimator is considered [20] as it is very simple and low complexity. The LS channel estimator is estimated in Lemma 2.

Lemma 2. *In our model y_{jULi}^{pi} having the desired channel $\sqrt{p_{ULi}}\tau_{pi}\widehat{h}_{ULi}^{j}$ in cell l and $\widehat{h}_{ULi}^{j}$ is an LS estimator of h_{ULi}^{j}. MSE deviation is obtained as $\|y_{jULi}^{pi}-\sqrt{p_{ULi}}\tau_{pi}\widehat{h}_{ULi}^{j}\|^{2}$, $\widehat{h}_{ULi}^{j}$ is written as:*

$$\widehat{h}_{li}^{j}=\frac{1}{\sqrt{p_{ULi}}\tau_{pi}}y_{jULi}^{pi} \tag{18}$$

The LS estimators become simple as discussed $\mathbf{A}_{ULi}^{j}=1/\sqrt{p_{ULi}}\tau_{pi}\mathbf{I}_{M_j}$ and the complexity of the LS estimator is proportional to the Mj. As per equations called in Lemma 1 the MSE is written as:

$$\mathrm{MSE}=\mathrm{tr}\left(\sum_{\left(UL^{\textcircled{i}},i^{\textcircled{i}}\right)\epsilon\mathscr{P}i_{ULi}/UL,i}\frac{p_{UL^{\textcircled{i}}i^{\textcircled{i}}}}{p_{ULi}}\boldsymbol{R}_{UL^{\textcircled{i}}i^{\textcircled{i}}}^{j}+\frac{\sigma_{UL}^{2}}{p_{ULi}\tau_{pi}}\mathbf{I}_{M_j}\right) \tag{19}$$

3.2. Uplink Spectral Efficiency with the Combing Schemes of MMSE Estimator. In this part, we analyze the achievable SE of the UL based on the MMSE estimator with different receive combining schemes. As earlier discussed, a signal $y_j^{ul}\epsilon\mathbb{C}^M$ is received at BSj and the UL signal in cell l from UE k is S_{jk}^{ul}s having the power of $p_{ul,lk}=\mathbb{E}\{|s_{lk}^{ul}|^{2}\}$ and $\rho ul>0$, then the total UL capacity of UE k in cell j is written as:

$$\begin{aligned}\mathrm{V}_{jk}^{\mathrm{UL}}\mathrm{y}_j&=\mathrm{V}_{jk}^{\mathrm{UL}}\widehat{h}_{jk}^{j}\mathrm{s}_k+\mathrm{V}_{jk}^{\mathrm{H}}\tilde{\mathrm{h}}_{jk}^{j}\mathrm{s}_{jk}\\&+\sum_{\substack{i=1\\i\neq k}}^{K_j}\mathrm{V}_{jk}^{\mathrm{H}}\mathrm{h}_{ji}^{j}\mathrm{s}_{jk}\sum_{\substack{l=1\\i\neq j}}^{L}\sum_{i=1}^{K_1}\mathrm{V}_{jk}^{\mathrm{UL}}\mathrm{h}_{Uli}^{j}\mathrm{s}_{li}+\mathrm{V}_{jk}^{\mathrm{UL}}\mathrm{n}_j\end{aligned} \tag{20}$$

$$\mathrm{SE}_{jk}^{UL}=\frac{\tau_{ul}}{\tau_{coh}}\mathbb{E}\left\{\log_2\left(1+\mathrm{SINR}_{jk}^{\mathrm{L}}\right)\right\} \tag{21}$$

Where τ_{ul}/τ_{coh} is a pre-log factor is the ratio of UL data samples per coherence block.

Proposed algorithm
Step 1: According to Table 5, adjust the simulation parameters.
Step 2: Randomly drop UEs in each cell and compute UL sequence
Step 3: Generate random estimated channel vectors $\widehat{h}^{j}_{jk}(\widehat{h}^{j}_{ULi})^{u}$
Step 4: Compute receive combining vectors $\mathbf{V}^{ULM-MMSE}_{jk} = [v_{j1} \cdots v_j k_j]$
Step 5: Compute DL sequence for precoding
Step 6: Compute precoding vectors $\mathbf{V}^{DLM-MMSE}_{jk} = [v_{j1} \cdots v_j k_j]$
Step 7: If MMSE algorithm = true
And resulting SINRUL as eq.(22) and eq. (27)
End
Step 8: Compute SE for
$SE^{UL}_{jk} = (\tau_{ul}/\tau_{coh})\mathbb{E}\{\log_2(1 + SINR^{L}_{jk})\}$ &
$\underline{SE}^{DL}_{jk} = (\tau_{DL}/\tau_{coh}) \log_2(1 + \underline{SINR}^{DL}_{jk})$ bit/Hz
Step 9: Plot of figures
SE for multi-cell combining & precoding schemes; M-MMSE, S-MMSE, RZF, ZF, MR

Algorithm 1: Sequence of Simulation.

Where the effective SNR becomes:

$$SINR^{UL}_{jk} = \frac{p_{jk}\left|v^{H}_{jk}\widehat{h}^{j}_{jk}\right|^{2}}{\sum_{l=1}^{L}\sum_{\substack{i=1\\(Ul,i)\neq(j,k)}}^{K_1} p_{Uli}\left|v^{H}_{jk}\widehat{h}^{j}_{jk}\right|^{2} + v^{H}_{jk}\left(\sum_{l=1}^{L}\sum_{ULi=1}^{K_1} p_{Uli}\mathbf{C}^{j}_{Uli} + \sigma^{2}_{UL}\mathbf{I}_{M_j}\right)v_{jk}} \tag{22}$$

As per $SINR^{UL}_{jk}$ used in (21) for UE k in cell j is optimized through multicell MMSE (M-MMSE) and M-MMSE combining vector for $k = 1, \cdots, K_j$ and $\mathbf{V}^{ULM-MMSE}_{jk} = [v_{j1} \cdots v_j k_j]$ is given as:

$$\mathbf{V}^{ULM-MMSE}_{jk} = \mathrm{tr} * p_{jk}\left[\sum_{l=1}^{L}\sum_{i=1}^{K_1} p_{Uli}\left(\widehat{h}^{j}_{Uli}\left(\widehat{h}^{j}_{Uli}\right)^{u} + \mathbf{C}^{j}_{Uli}\right) + \sigma^{2}_{UL}\mathbf{I}_{M_j}\right]^{-1}\widehat{h}^{j}_{jk} \tag{23}$$

Which further leads to

$$SINR^{ULM-MMSE}_{jk} = \mathrm{tr} * p_{jk}\left(\widehat{h}^{j}_{Uli}\right)^{u}\left[\sum_{l=1}^{L}\sum_{\substack{i=1\\(l,i)\neq(j,k)}}^{K_1} p_{Uli}\widehat{h}^{j}_{Uli}\left(\widehat{h}^{j}_{Uli}\right)^{u} + \sum_{l=1}^{L}\sum_{i=1}^{K_1} p_{Uli}\mathbf{C}^{j}_{Uli} + \sigma^{2}_{UL}\mathbf{I}_{M_j}\right]^{-1}\widehat{h}^{j}_{jk} \tag{24}$$

This is the case when estimated channels are known then it not only optimizes the SINR and also minimizes the MSE. The expression in (24) provides exact and optimize SINR for the massive MIMO systems. As discussed in the previous section, the reduction in complexity has to pay a reduction in SE and MMSE has superior SE. In this regard, the different combining schemes of the MMSE channel estimator proposed in the previous section are shown in Table 4 with Computing combining vectors Multiplication. SE analysis is discussed in section 4.

3.3. Downlink Spectral Efficiency. As related in (7), the DL signal received y^{DL}_{jk} in cell l is:

$$\begin{aligned} y^{DL}_{jk} = {} & \underbrace{E\left\{\sqrt{\rho_{DL}}\left(h^{DL}_{jk}\right)^{H} W^{DL}_{jk}\right\} r^{DL}_{jk}} \\ & + \underbrace{\sqrt{\rho_{DL}}\left(\left(h^{DL}_{jk}\right)^{H} W^{DL}_{jk} - E\left\{\left(h^{DL}_{jk}\right)^{H} W^{DL}_{jk}\right\} r^{DL}_{jk}\right)} \\ & + \underbrace{\sqrt{\rho_{DL}}\sum_{\substack{i=1\\i\neq k}}^{K_j}\left(h^{DL}_{jk}\right)^{H} W^{DL}_{ji} r^{DL}_{ji}} \\ & + \underbrace{\sqrt{\rho_{DL}}\sum_{\substack{l=1\\l\neq j}}^{L}\sum_{i=1}^{K_l}\left(h^{l}_{jk}\right)^{H} W_{DLi} r_{DLi}} + \underbrace{n_{jk}} \end{aligned} \tag{25}$$

Then the desired signal becomes $E\{\sqrt{\rho_{DL}}(h^{DL}_{jk})^{H} W^{DL}_{jk}\}$ r^{DL}_{jk} with average pre-coded channel $E\{(h^{DL}_{jk})^{H} W^{DL}_{jk}\}$ having the third and fourth term as intra-cell interference and inter-cell interference, respectively. The second term is also desired for the unknown channel. The Selection of transmit precoding vectors in terms of spectral efficiency is based on hardening bounding which can take any type of pro coding vector and channel estimation as well. The DL channel capacity in terms of the spectral efficiency of UE k in cell j as a lower bound is:

$$\underline{SE}^{DL}_{jk} = \frac{(\tau_{DL}/\tau_{coh}) \log_2\left(1 + \underline{SINR}^{DL}_{jk}\right)\mathrm{bit}}{\mathrm{Hz}} \tag{26}$$

Where τ_{DL}/τ_{coh} is a pre log factor ratio of samples of DL

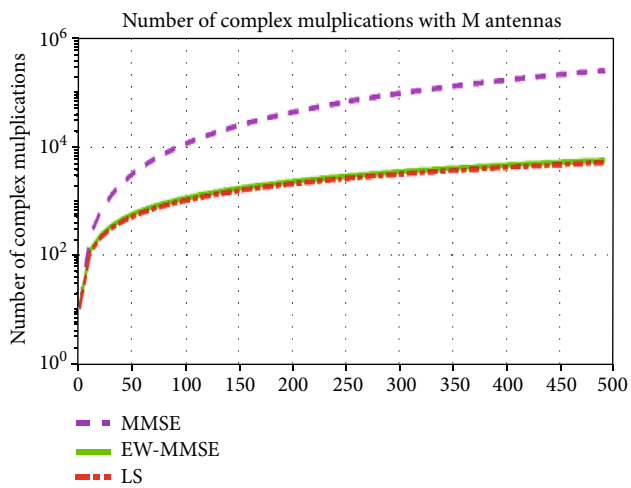

Figure 4: Results of number of complex multiplication vs number of antennas.

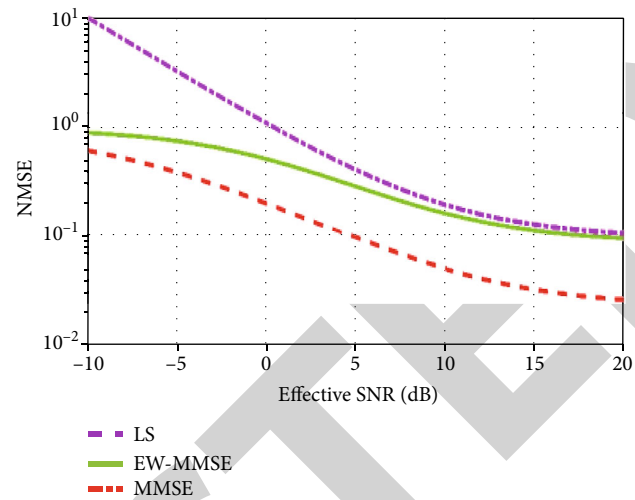

Figure 5: Results of MMSE vs number of antennas.

data and samples per coherent block and then $\underline{SINR}_{jk}^{DL}$ is:

$$\underline{SINR}_{jk}^{DL} = \frac{\rho_{jk}\left|E\left\{W_{jk}^{H}h_{jk}^{DL}\right\}\right|^{2}}{\sum_{l=1}^{L}\sum_{i=1}^{K_l}\rho_{DLi}E\left\{\left|W_{DLi}^{H}h_{jk}^{l}\right|^{2}\right\} - \rho_{jk}\left|E\left\{W_{jk}^{H}h_{jk}^{DL}\right\}\right|^{2} + \sigma_{DL}^{2}} \tag{27}$$

In (26), $\underline{SE}_{jk}^{DL}$ refers $\underline{SINR}_{jk}^{DL}$ as effective SINR of fading channel related to UE k in cell j. $\rho_{jk}|E\{W_{jk}^{H}h_{jk}^{DL}\}|^{2}$ is the gain of the desired signal by the average precoded channel. ρ_{DLi} $E\{|W_{DLi}^{H}h_{jk}^{l}|^{2}\}$ is donated as the total power of all signals and $\rho_{jk}|E\{W_{jk}^{H}h_{jk}^{DL}\}|^{2}$ is the power of the desired signal.

In previous work as done in [20, 21] the energy consumption models include only the radiated power whereas the power consumption of the radio frequency circuit was not included. These models revealed some improved results on Massive MIMO but all are based on theoretical analysis. For example, power allocation and time framing have been analyzed to optimize the EE in [21], and the tradeoff of SE-EE is studied in [20]. There is a need for system design in cellular systems of massive MIMO where EE performance should be reviewed using practical measurements. For an instant, in [22], the authors presented the practical power consumption model by considering the number of antennas, UE_s and power consumption models for optimizing the EE where uplink and downlink of multiuser massive MIMO networks are considered. In our work, we considered some systems parameters including the numbers of antenna estimation, assessment of maximum users, and modelled the practical effective transmit power and circuit power as shown in Table 5.

The SE expression in (26) is computed for precoding based on the MMSE channel estimation computed in the previous section. If $W_{jk} = \hat{h}_{jk}^{DL}/\sqrt{E\{t||\hat{h}_{jk}^{DL}||^{2}\}}$ then $\underline{SINR}_{jk}^{DL}$ for MR precoding based on MMSE channel estimation is:

$$\underline{SINR}_{jk}^{DL} = \frac{\rho_{jk}^{DL}tr\left(R_{jk}^{DL}\Psi_{jk}^{DL}R_{jk}^{jDL}\right)p_{jk}^{DL}}{\underbrace{\sum_{l=1}^{L}\sum_{i=1}^{K_l}\left(\rho_{DLi}tr\left(R_{lk}^{l}\Psi_{lk}^{l}R_{lk}^{l}\right)/tr\left(R_{lk}^{l}\Psi_{lk}^{l}R_{lk}^{l}\right)\right)} + \underbrace{\sum_{(l,i)\epsilon p_{jk}\backslash(j,k)}\left(\rho_{DLi}p_{jk}\tau_{p}\left(R_{jk}^{l}\Psi_{lk}^{l}R_{lk}^{l}\right)/tr\left(R_{lk}^{l}\Psi_{lk}^{l}R_{lk}^{l}\right)\right)} + \sigma_{DL}^{2}} \tag{28}$$

Where $\Psi_{jk}^{DL}\Psi_{li}^{DL}$ define in (9) and (10) for UL as similar is here. In the denominator, the first term is non-coherent interference and the second term is coherent interference having spatially uncorrelated factor $R_{li}^{j} = \beta_{li}^{j}I_{M_j}$. The SE of DL is analyzed in the next section by taking the same combing vectors $\mathbf{V}_{jk}^{\mathrm{ULM-MMSE}} = [\mathrm{v}_{j1} \cdots \mathrm{v}_{j}\mathrm{k}_{j}]$ in precoding schemes based on MMSE channel are:

4. Results and Discussion

In this section, SE expression for UL and DL evaluated in previous sections are simulated and validated in a proposed scenario for the massive MIMO cellular network. The calculation of SE with M-MMSE, S-MMSE, RZF, ZF, MR combining and precoding schemes by taking M number of antennas having simulation parameters of Table 6.

The spectral efficiency of UL and DL for BS and UEs according to listed parameters in Table 6 is simulated as

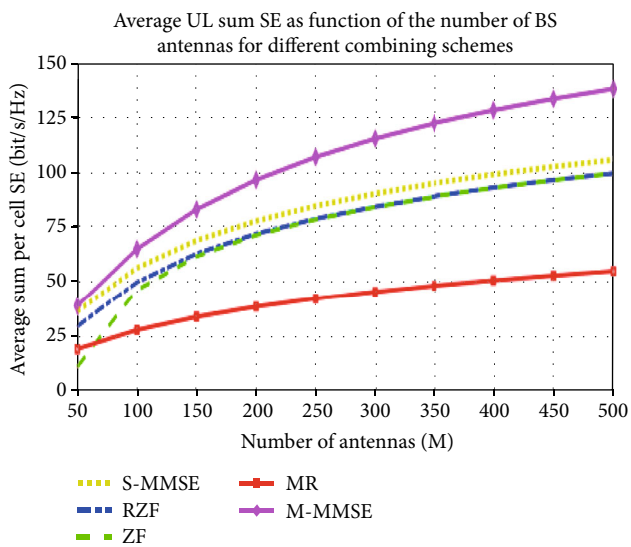

Figure 6: Desired Spectral Efficiency: Interference from other cell and noise added to the signal during UL Transmission.

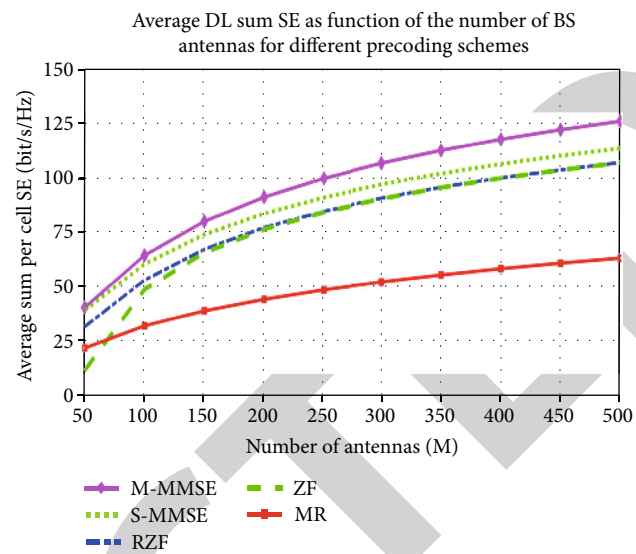

Figure 7: Desired Spectral Efficiency: Interference from other cell and noise added to the signal during DL transmission.

$$\mathbf{V}_{jk}^{\mathrm{DLM}-MMSE} = \left[\mathrm{v}_{j1} \cdots \mathrm{v}_j \mathrm{k}_j\right] = \begin{cases} V_{JK}^{M-MMSE} \; of\, M-MMSE\, precoding \\ V_{JK}^{S-MMSE} \qquad of\, S-MMSE\, precoding \\ V_{jk}^{RZF} \qquad of\, RZF\, precoding \\ V_{JK}^{ZF} \qquad of\, ZF\, precoding \\ V_{JK}^{MR} \qquad of\, MR\, precoding \end{cases} \tag{29}$$

per table sequence. Simulations are based on Figure 1, Tables 6 and Algorithm 1 and the optimized result is discussed in section 4.

4.1. Channel Estimators Comparison. The full potential of massive MIMO systems cannot be achieved without the selection of the best suitable channel estimation at the time of UL pilot transmission. As per the proposed scenario BS j estimates the channel of UE k and another cell transmits the same pilot signal. The effective SNR as per Table 5 is taken as it varied from −10 dB to 20 dB. In Figures 4–5, the results of the number of complex multiplication and MMSE vs number of antennas in the multi-cell scenario with MMSE, EW-MMSE, and LS channel estimators are shown. These estimators are numerically computed in section A of the methodology segment while Lemma 1 and Lemma 2 are considered for the EW-MMSE and LS, respectively. As mentioned in [11] that the MMSE channel estimator has superior SE as compared to other estimators having greater complexity in the computation. The statistical characteristics obtained from the MMSE estimator are fine as the Minimum means square error decreases gradually with the increment in effective SNR as result shown in Figure 5. This is tested in our models of channel estimation and found the same patron as termed in [11]. Meanwhile, our model is based on SE and required minimum MMMSE other than the complexity. In this regard, the result publicized in Figure 5 also depicts that we can able to compute better SE for our model while ignoring the result of Figure 4 as the MMSE estimator is complex.

4.2. Results for SE of UL Combining Schemes. The results of SE with different combining schemes are shown in Figure 6. The proposed model has better improvement in SE as compared to previous work done in [19]. The SE of a system is gradually increased with the number of antennas and cells as Figure 6 demonstrates that multicell MMSE (M-MMSE) has greater SE than single-cell MMSE(S-MMSE) having increment in SE by increasing of antennas. As literature highlights that the SE of UL massive MIMO systems has great intention in channel estimation instead of combing schemes. Meanwhile, the results of our proposed model are simply compared with the MMSE combining scheme of [23] after comprehensive numerical computation of channel estimation. The summary of improvement in SE with previous work is given in Table where our proposed MMSE estimator for multicell M-MMSE has great augmentation in SE compared to given combing schemes and M-MMSE given in [23] as well.

Table 7: Comparison: Results in Figure 4 & past works.

Precoding Schemes	Results [24]		Results [25]		Results [26]		Results (proposed model)	
	EE Bit/Hz Per cell	M	EE Bit/Hz Per cell	M	EE Bit/Hz Per cell	M	EE Bit/Hz Per cell	M
M-MMSE	105	500	110	500	—	128	125	500
S-MMSE	—	500	—	500	—	128	110	500
RZF	—	500	108	500	110	128	105	500
RF	103	500	—	500	110	128	105	500
MR	58	500	45	500	85	128	65	500

Table 8: Comparison: Results in Figure 3 & past works.

Combining schemes	Results (proposed model)		Results [23]	
	EE Bit/Hz per cell	M	EE Bit/Hz per cell	M
M-MMSE	140	500	33	100
S-MMSE	105	500	—	—
RZF	90	500	—	—
RF	90	500	—	—
MR	52	500	—	—

4.3. Results for SE of DL Precoding Schemes. Figure 7 illustrates the achievable average sum of SE per cell against the proposed massive MIMO system for five precoding schemes. As per K user and effective SNR is given in Table 5, the average SE per cell increases as the number of antennas grows. It indorses the dramatic benefits of implantation in large-scale antennas in BS. We also observed that at the same configuration, the desired average SE rate with MMSE precoding is approximately doubled with the MR scheme. The comparison of past work in Table 7 also shows that the MMSE precoding scheme is always better than other schemes and ultimately a top choice for a massive MIMO system.

To evaluate the performance (as per Figure 7) of our proposed massive MIMO system precoder over the rest of the schemes, the simulation result of M_MMSE matched with from [24, 25], RZF with from [25, 26], RF with from [20, 22], and MR with from [20–27] are provided in Table 8. The numerical expression and simulation results show the achievable average sum of SE per cell is increased as compared to past work done [24–26] after considering the proposed numerical expression.

The computed results of the proposed models are appropriate to endorse that the massive MIMO systems can enhance SE in a 5G cellular network. The proposed model is applicable for both UL and DL communication while the UL SE with the MMSE estimator is compared with EW-MMSE and LS. In the end, the maximum-ratio (MR) precoding scheme is modelled for the augmentation of DL SE whereas the latest work presented in the [22] has not considered the mentioned points. As mentioned, the SE of a system is gradually increasing with the number of antennas and cells. It demonstrates that the multicell MMSE (M-MMSE) has greater SE than single-cell MMSE(S-MMSE) having an increment in SE with the increasing number of antennas. The results presented in [19] are tested only for M-MMSE where we analyzed and tested for different combining schemes like M-MMSE, S-MMSE, RZF, RF, and MR. On the other hand, we considered 500 antennas although it increases the power consumption but high numbers of M have comparatively high EE as shown in Table 7. As there is a need to design a massive MIMO system where EE performance should be reviewed using practical measurements. In the work presented in [24–26], energy consumption models include only radiated power whereas the power consumption of radio frequency circuits is not included. In our previous work [28], the power consumption modelling for the massive MIMO systems has been demonstrated. We have considered and extended our previous work [28] by modelling the numbers of antenna estimation, assessment of maximum users and the practical effective transmit power and circuit power.

5. Conclusion

In this work, we have augmented an optimal SE per cell in the proposed massive MIMO system and computed MMSE channel estimation with their different combining and precoding schemes. As a first step, we have figured out a multi-cell scenario and computed the expressions for uplink and downlink transmission and then recommended a realistic, efficient and applicable model. We have computed an MMSE channel estimator instead of EW-MMSE and LS that can enhance the achievable average sum of SE per cell based on the above-mentioned schemes. The simulation results have revealed remarkable implications.

The research was fundamentally originated upon MMSE channel estimation after examining EW-MMSE and LS estimators, where MMSE found the more complex but exceptionally improved estimator to enhance the SE per cell. The results of MMSE combining and precoding schemes are produced by monte Carlo simulations in MATLAB. Although the MMSE was the optimum channel estimator among all, it is also observed that MR was less complex at all. In this regard, the complex computations of MMSE are taken into account because the variance in results is relatively small and the improvement in SE is big. M-MMSE, S-MMSE, RZF, ZF, MR combing and precoding schemes

for UL and DL are tested with the proposed numerical expressions by taking the same vectors where M-MMSE has found the best option to deal with SE. The results with MR precoding are not much good but it can operate under intercell interference with less complexity in the computation of channel estimation. The conclusions of this work specify that the massive MIMO system can develop by optimizing channel estimation for the augmentation of SE in UL and DL transmissions. We can recapitulate that some complex computations of MMSE channel estimators can augment the average sum of SE per cell as results shown in our model.

Data Availability

No data were used to support this study.

Conflicts of Interest

The authors declare no conflict of interest.

Authors' Contributions

Rao Muhammad Asif, Mustafa Shakir, Ateeq Ur Rehman contributed to actualization, validation, methodology, formal analysis, investigation, software, and initial draft. Muhammad Shafiq, Rehan Ali Khan, Wali Ullah Khan contributed to actualization, validation, methodology, formal analysis, investigation, and initial draft. All authors read and approved the final version.

References

[1] Y. Liu, C. Wang, J. Huang, J. Sun, and W. Zhang, "Novel 3-D nonstationary MmWave massive MIMO Channel models for 5G high-speed train wireless communications," *IEEE Transactions on Vehicular Technology*, vol. 68, no. 3, pp. 2077–2086, 2019.

[2] A. U. Rehman, J. Aimin, A. Rehman, and A. Paul, "Weighted Based Trustworthiness Ranking in Social Internet of Things by using Soft Set Theory," in *IEEE 5th International Conference on Computer and Communications (ICCC)*, pp. 1644–1648, Chengdu, China, 2019.

[3] R. M. Asif, J. Arshad, M. Shakir, S. M. Noman, and A. U. Rehman, "Energy Efficiency Augmentation in Massive MIMO Systems through Linear Precoding Schemes and Power Consumption Modeling," *Wireless Communications and Mobile Computing*, vol. 2020, 13 pages, 2020.

[4] R. Chataut, R. Akl, and U. K. Dey, "Least Square Regressor Selection Based Detection for Uplink 5G Massive MIMO Systems," in *IEEE 20th wireless and microwave technology conference (WAMICON)*, pp. 1–6, Cocoa Beach, FL, USA, 2019.

[5] B. Kang, J. H. Yoon, and J. Park, "Low-complexity massive MIMO detectors based on Richardson method," *ETRI Journal*, vol. 39, no. 3, pp. 326–335, 2017.

[6] A. U. Rehman, R. A. Naqvi, A. Rehman, and A. Paul, "Muhammad Tariq Sadiq, Dildar Hussain A Trustworthy SIoT Aware Mechanism as an Enabler for Citizen Services in Smart Cities," *Electronics*, vol. 9, no. 6, p. 918, 2020.

[7] E. Björnson, J. Hoydis, and L. Sanguinetti, "Massive MIMO has unlimited capacity," *IEEE Transactions on Wireless Communications*, vol. 17, no. 1, pp. 574–590, 2018.

[8] J. Singh and D. Kedia, "Spectral efficient precoding Design for Multi-cell Large MU-MIMO system," *IETE Journal of Research*, pp. 1–16, 2020.

[9] J. Arshad, A. Rehman, A. U. Rehman, R. Ullah, and S. O. Hwang, "Spectral efficiency augmentation in uplink massive MIMO systems by increasing transmit power and uniform linear array gain," *Sensors*, vol. 20, no. 17, p. 4982, 2020.

[10] H. Yang and T. L. Marzetta, "Performance of conjugate and zero-forcing beamforming in large-scale antenna systems," *IEEE Journal on Selected Areas in Communications*, vol. 31, no. 2, pp. 172–179, 2013.

[11] S. Hassan, N. Tariq, R. A. Naqvi, A. U. Rehman, and M. K. A. Kaabar, "Performance Evaluation of Machine Learning-Based Channel Equalization Techniques: New Trends and Challenges," *Journal of Sensors*, vol. 2022, 14 pages, 2022.

[12] A. Thakur and R. C. Mishra, "Performance Analysis of Energy-Efficient Multi-Cell Massive MIMO System," in *10th International Conference on Computing, Communication and Networking Technologies (ICCCNT)*, Kanpur, India, 2019.

[13] S. Al-Mogren, "Energy Adaptive Approach In a Multi-Channel Dissemination-Based Network," in *New Technologies, Mobility and Security*, pp. 1–6, Tangier, Morocco, 2008.

[14] R. Mubashar, M. A. B. Siddique, A. U. Rehman, A. Asad, and A. Rasool, "Comparative performance analysis of short-range wireless protocols for wireless personal area network," *Iran Journal of Computer Science*, vol. 4, no. 3, pp. 201–210, 2021.

[15] H. B. Almelah and K. A. Hamdi, "Spectral efficiency of distributed large-scale MIMO systems with ZF receivers," *IEEE Transactions on Vehicular Technology*, vol. 66, no. 6, pp. 4834–4844, 2017.

[16] A. Ahmed, Q. Z. Ahmed, A. Almogren, S. K. Haider, and A. U. Rehman, "Hybrid precoding aided fast frequency-hopping for millimeter-wave Communication," *Access*, vol. 9, pp. 149596–149608, 2021.

[17] Y. Wang, G. Zhu, M. Li et al., "Water pollutants p-cresol detection based on au-ZnO nanoparticles modified tapered optical fiber," *IEEE Transactions on Nanobioscience*, vol. 20, no. 3, pp. 377–384, 2021.

[18] A. G. Leal-Junior, A. Frizera, C. Marques et al., "Polymer optical fiber for angle and torque measurements of a series elastic actuator's spring," *Journal of Lightwave Technology*, vol. 36, no. 9, pp. 1698–1705, 2018.

[19] V. Chien, C. M. Trinh, and E. Björnson, "Large-scale-fading decoding in cellular massive MIMO systems with spatially correlated channels," *IEEE Transactions on Communications*, vol. 67, no. 4, pp. 2746–2762, 2019.

[20] H. Q. Ngo, E. Larsson, and T. Marzetta, "Energy and spectral efficiencyof very large multiuser MIMO systems," *IEEE Transactions on Communications*, vol. 61, no. 4, pp. 1436–1449, 2013.

[21] X. Chen, X. Wang, and X. Chen, "Energy-Efficient optimization for wireless information and power transfer in large-scale MIMO systems employing energy beamforming," *IEEE Wireless Communications Letters*, vol. 2, no. 6, pp. 667–670, 2013.

[22] Y. Xin, D. Wang, J. Li, H. Zhu, J. Wang, and X. You, "Area spectral efficiency and area energy efficiency of massive MIMO cellular systems," *IEEE Transactions on Vehicular Technology*, vol. 65, no. 5, pp. 3243–3254, 2016.

Hindawi
Journal of Sensors
Volume 2022, Article ID 3852243, 12 pages
https://doi.org/10.1155/2022/3852243

Research Article

IIPA-Net: Joint Illumination-Invariant and Pose-Aligned Feature Learning for Person Reidentification

Senquan Yang,[1,2] **Fan Ding**,[1] **Haoxiang Wen**,[1] **Pu Li**,[1,3] **and Songxi Hu**[1,3]

[1]*School of Intelligent Engineering, Shaoguan University, Shaoguan 512005, China*
[2]*Foshan Nanhai Guangdong Technology University CNC Equipment Cooperative Innovation Institute, Foshan 528225, China*
[3]*Guangdong Provincial Key Laboratory of Technique and Equipment for Macromolecular Advanced Manufacturing, South China University of Technology, 510641, China*

Correspondence should be addressed to Pu Li; lipu_300@sgu.edu.cn

Received 3 March 2022; Revised 9 April 2022; Accepted 26 May 2022; Published 21 June 2022

Academic Editor: Han Wang

Person reidentification (re-id) has gained significant progress and aroused great interest in computer vision. However, due to the effect of weak illumination and poor alignment, person re-id is still a challenging task. Many previous works focus on either illumination enhancement methods or pose estimation. However, those methods are difficult to apply in real-world scenarios, which usually contain various interference factors. To improve the performance of re-id, we propose an Illumination-Invariant and Pose-Aligned Network (IIPA-Net). The illumination change is handled by a retinex decompose network, and the pose variation problem is solved by a local feature matching method. Based on the multimodal nature of a person, we propose a part attention module to optimize the global feature. Finally, a data-driven training strategy is proposed to train the proposed architecture effectively. Experiments show that the proposed framework outperforms other state-of-the-art approaches on both normal- and low-light datasets.

1. Introduction

Person reidentification (re-id) is aimed at identifying a specific person (probe query image) from a gallery of candidate images captured by multiple cameras with overlap or nonoverlap fields of view. The increasing need for safety and security, combined with the growing availability of surveillance cameras, makes person reidentification an increasingly explored area [1]. However, it is very challenging since the interest person images captured by surveillance cameras usually have significant variations in different viewpoints, illumination, human pose, and so on [2]. Low resolution, partial occlusions, and blurring increase the difficulty of person re-id [3].

Since person images are captured by different cameras under unknown lighting conditions, the appearance of the same person contains various variants, making the re-id task extremely difficult. In order to eliminate the effect of illumination, many methods rely on the statistics of color distribution and project image to color constant space [4]. However, the prior information of lighting is unpredictable in real-world scenarios. An alternative solution is to simulate the real-world illumination and use data augmentation techniques, which is expensive and needs a lot of labeled data [5]. Pose misalignment, which is caused by changed viewpoint or inaccurate detection boxes, is another interference of person re-id framework [6]. A straightforward solution to this pose variation is to apply human pose estimation, which parses a person image into different semantic parts. However, pose estimation requires massive labeled data to train the model [7]. What is more, the re-id accuracy degrades substantially for inaccurate estimation. Figure 1 shows some examples of illumination change and pose misalignment.

Convolutional neural networks (CNNs), which have powerful representation and invariant embedding capabilities, have boosted the performance of person re-id [8]. CNN-based person re-id methods can be divided into two aspects: discriminative feature representation learning and deep metric learning [9]. In the first category, majority of the methods generally concentrate on extracting discriminative

(a) Illumination change

(b) Pose variation

Figure 1: Examples of challenging images in re-id.

features, then formulate the person re-id as a classification problem [10]. In the second category, a robust metric between positive (the same) and negative (the different) persons is learned to deal with the matching problem [11]. In this paper, we focus on extracting discriminative feature representation. To achieve this aim, we propose a joint CNN framework that couples global and local feature learning to suppress interference, especially illumination and pose variations. Firstly, motivated by deep retinex illumination decomposition [12], we adopt a lightweight estimation to eliminate the effect of illumination and enhance the global person feature. Secondly, inspired by AlignedReID++ [13], which aligns local information to learn more discriminative features, we introduce a local feature matching to align different parts of person image, which is able to solve the pose variation problem. We find that the illumination-invariant feature can guide the local feature matching to align different person image parts. Thirdly, since the detected person has two significant modes [14], we concatenate the low-level feature of CNNs and the two-peak Gaussian map to design an attention mechanism. Consequently, the proposed IIPA-Net can boost the performance of the re-id in both normal- and low-light datasets. In summary, the contributions of this paper are threefold:

(i) We build a novel network framework, which contains a retinex decomposition net and a weight-shared Resnet50 backbone CNN and achieves illumination-invariant and pose-aligned re-id

(ii) We propose a part attention module to reweight the CNN output and extract the most informative parts of a person

(iii) A data-driven training strategy is introduced to train the network effectively and speed up the training process

2. Related Work

The main challenges of reidentification are changes in illumination, viewpoint, and pose across cameras. Many works focus on extracting the most discriminative visual feature of a person, including color [14], texture [15], and shape [16]. Kviatkovsky et al. [14] use shape context descriptors as a color-based signature to represent a person, which is divided into two significant modes. However, they assume that the silhouette of a person can be always obtained, which is not the case in real-world applications. Deep learning has revolutionized the techniques for person reidentification [17]. Li et al. [18] successfully apply deep learning to extract the features for person reidentification. Xiao et al. [19] propose a new deep learning framework that jointly handled both person detection and reidentification in a single convolutional neural network. Wu et al. [20] improve the discriminative feature representation of CNNs by exploiting unlabeled tracklets. The major limitation of this framework is that they either have handcrafted features or employ single scene images, thus making them less robust to various lighting conditions and changed human pose. Retinex theory is widely used for illumination estimation [21]. Many retinex-based re-id algorithms had achieved competitive performances [22, 23]. Specially, Liao et al. utilize the retinex transform and a scale invariant texture operator to handle illumination variations [23]. Huang et al. propose a retinex decomposition network to address the illumination variation problem and achieved a competitive re-id performance in low-light condition [22].

In [24], a new synthetic dataset, which contains hundreds of illumination conditions, is introduced to simulate the real-world lighting. The above methods reduced the adverse effects of illumination variant. However, they ignore the matching of local feature and failed to learn the aligned information, which effectively eliminate the influence of pose variant.

To reduce the negative impact of pose variant, some works apply human pose estimation to extract pixel-level body regions [8, 25]. Zheng et al. adopt the pose estimation confidence of input image to build a pose-invariant embedding (PIE) descriptor [8]. In [25], Zhao et al. represent a person with a discriminative feature, which is learned from different semantic regions of a person. On the other hand, some works focus on utilizing horizontal stripes or grids to extract pose-invariant features [13, 26]. Sun et al. design a Part-based Convolutional Baseline (PCB) network to learn discriminative part-level features [26]. Using the dynamic programming to match horizontal stripes of person images, Luo et al. propose a deep model to address the misalignment issue [13]. Additionally, Miao et al. propose an occluded person re-id framework by incorporating the pose information [27]. In spite of the great progress in re-id performance, the above methods still could be optimized by integrating the advantages of different architectures.

Different from existing frameworks, we focus on addressing issues of illumination and pose change simultaneously. Then, we propose a novel framework that is able to learn illumination invariance and pose alignment in a multitask manner.

3. Methodology

In this section, we firstly describe the retinex decomposition net and the part attention module. Then, the details of the proposed structure and training strategy are introduced.

3.1. Retinex Decomposition Net. To simulate the human color perception, retinex theory decomposes the observed image into two components: reflectance and illumination [21]. Mathematically, the source image $\mathbf{S}$ can be denoted as follows:

$$\mathbf{S} = \mathbf{R} \circ \mathbf{I}, \tag{1}$$

where $\mathbf{R}$ and $\mathbf{I}$ represent the reflectance and illumination components, respectively, and $^\circ$ represents element-wise multiplication. The reflectance map described the intrinsic person property and is invariant to light change.

Thus, it is active to extract illumination-invariant discriminative features from the reflectance map. The illumination map, which represents various light environments, is harmful to re-id performance and ignored in this paper.

Unlike deep retinex net [12] that performs both reflectance and illumination decomposition to enhance low-light images, we only perform retinex decomposition net to extract the consistent feature of a person. As shown in Figure 2, the retinex decomposition net includes 8 layers. The first layer is a 3×3 convolutional layer, which extracts convolutional features from the input image. The second to sixth layers are 3×3 convolutional layers with a Relu activation function. The seventh layer is a 3×3 convolutional layer which maps $\mathbf{R}$ and $\mathbf{I}$ from feature space. The last layer is a sigmoid function that normalizes $\mathbf{R}$ and $\mathbf{I}$ to $[0, 1]$.

To extract $\mathbf{R}$ from different lightness images, the decomposition network is fed in paired normal/low-light images each time. During the training stage, the paired images, instead of their corresponding ground truth, are taken to train the retinex decomposition net. However, it can predict $\mathbf{R}$ and $\mathbf{I}$ in the test stage.

The loss L_{R} for retinex decomposition net consists of reconstruction loss L_{recon} and invariable reflectance loss L_{ir}:

$$L_{\mathrm{R}} = L_{\mathrm{recon}} + \lambda_{\mathrm{ir}} L_{\mathrm{ir}}, \tag{2}$$

where λ_{ir} is used to balance the consistency of reflectance. The reconstruction loss L_{recon} is defined as

$$L_{\mathrm{recon}} = \sum_{i=\mathrm{low,normal}} \sum_{j=\mathrm{low,normal}} \lambda_{ij} L_{\mathrm{ir}} \left\| \mathbf{R}_i \circ \mathbf{I}_j - \mathbf{S}_j \right\|_1, \tag{3}$$

where $\mathbf{S}_{\mathrm{low}}$ and $\mathbf{S}_{\mathrm{normal}}$ denote the input low-light and normal-light images, respectively. $\mathbf{R}_{\mathrm{low}}$ and $\mathbf{I}_{\mathrm{low}}$ denote the reflectance and illumination of $\mathbf{S}_{\mathrm{low}}$, as well as $\mathbf{R}_{\mathrm{normal}}$ and $\mathbf{I}_{\mathrm{normal}}$ of $\mathbf{S}_{\mathrm{normal}}$. The invariant reflectance loss L_{ir} is defined as

$$L_{\mathrm{ir}} = \left\| \mathbf{R}_{\mathrm{low}} - \mathbf{R}_{\mathrm{normal}} \right\|_1. \tag{4}$$

3.2. Part Attention Module. In order to extract discriminative features, many re-id methods introduce the attention mechanism to highlight the informative parts of person images, while suppressing cluttered background [9, 28]. The goal of the attention mechanism is to produce a saliency map to reweight CNN output. Given a 3-D $X \in \mathbb{R}^{C \times H \times W}$, where C, H, and W indicate the number of pixels in the channel, height, and width dimensions, respectively, the reweight process can be formulated as

$$\mathbf{Y} = A(\mathbf{X}) \odot \mathbf{X}, \tag{5}$$

where $\mathbf{Y}$ is the reweighted map and $A(\mathbf{X})$ is the output of the attention module. Combined with the state-of-the-art detector, there is an intuitive assumption that the detected persons lie in the middle of images. In real-world scenarios, a person usually has different clothing for lower and upper parts. Based on their multimodal nature, we introduce a two-peak Gaussian map M_f, defined as Equation (6), to deal with the intradistribution of person appearance:

$$M_f = (2\pi)^{-1/2} |\Sigma|^{-1/2} \left(e^{-1/2(r-\mu_1)^T \Sigma^{-1} (r-\mu_1)} + e^{-1/2(r-\mu_1)^T \Sigma^{-1} (r-\mu_1)} \right), \tag{6}$$

where $\mu_1 = [H/3, W/2]$ and $\mu_2 = [2 \times H/3, W/2]$ represent the peak centers of the Gaussian map.

As shown in Figure 3, we concatenate M_f and the 4th layer of Resnet-50. Subsequently, six 3×3 convolution layers are added to extract the discriminative feature. Finally, a softmax classifier is implemented with a Fully Connected (FC) layer.

3.3. IIPA-Net Architecture. As shown in Figure 4, the proposed IIPA-Net can be divided into two parts: global branch and local branch.

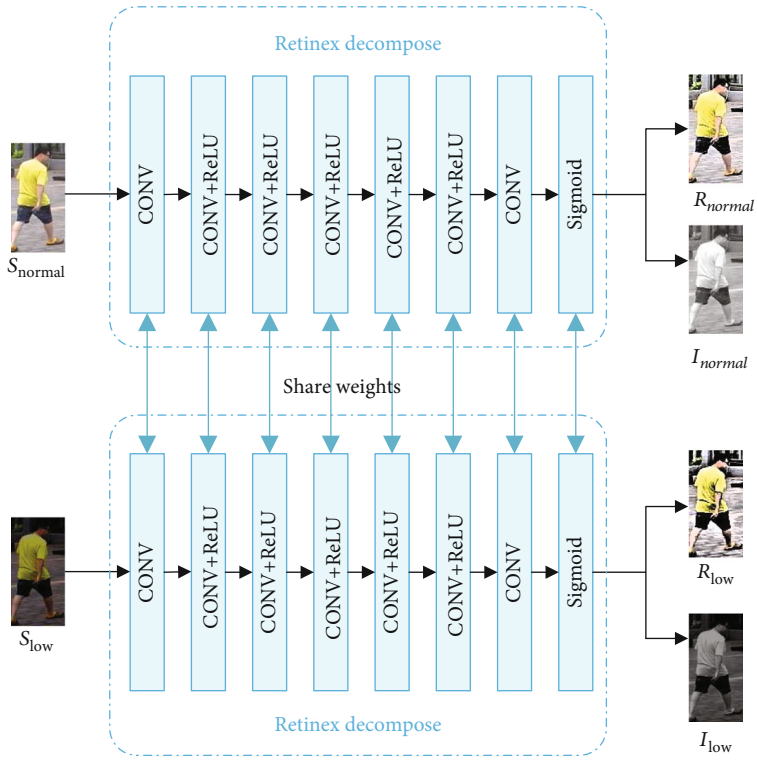

Figure 2: Retinex decomposition net.

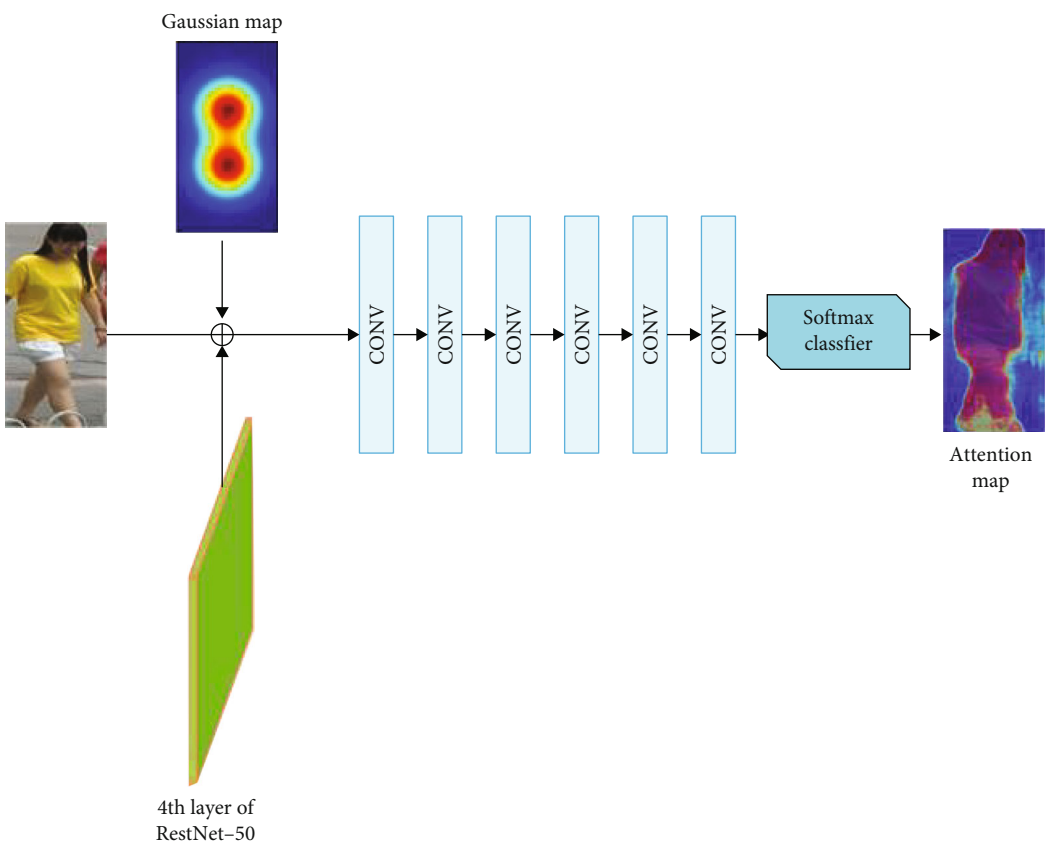

Figure 3: The proposed part attention module.

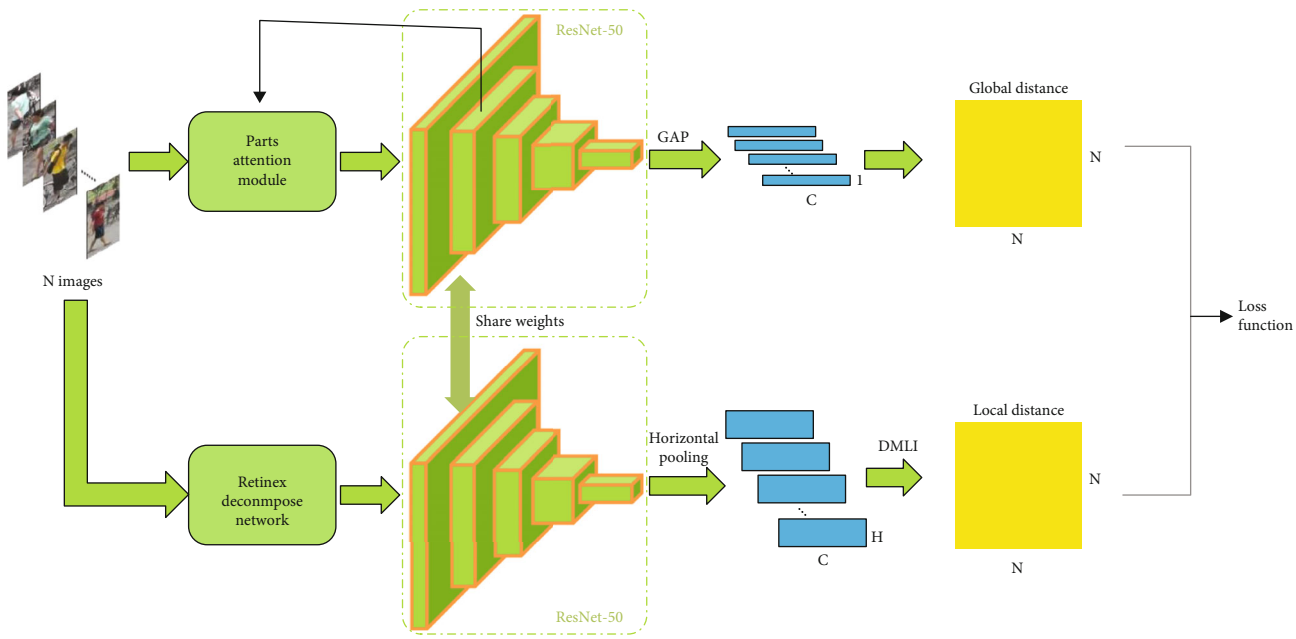

Figure 4: The proposed network architecture.

For the first branch, the most discriminative image parts of a person are extracted by the part attention module. In the second branch, the person images are enhanced by preserving the reflectance map of retinex decomposition net. Both of the two branches are sent into the weight-shared Resnet50 backbone CNNs, which makes the proposed model more flexible and easy to train. The output of Resnet50 is a$\mathbb{R}^{c\times h\times w}$ feature map, where c represents the feature channel and $h \times w$ is the spatial size. We extract a global discriminative feature vector $I \in \mathbb{R}^{c\times 1}$ using Global Average Pooling (GAP). Then, the global feature distance can be calculated by

$$d_I(A, B) = \|I_A - I_B\|_2, \tag{7}$$

where I_A and I_B denote the global feature of images A and B. The global feature is able to learn holistic information from the person image. However, it fails to address the pose-misalignment issue for the reason that the local representation is still unexploited. To learn the pose-aligned local feature, the output feature map of Resnet50 is transferred into $c \times h$ size using horizon horizontal average pooling. Let $P_A = \{p_A^1, p_A^2, \cdots, p_A^h\}$ and $P_B = \{p_B^1, p_B^2, \cdots, p_B^h\}$ denote the local feature of images A and B. We can have the distance of the ith vertical part of A and jth vertical part of B as follows:

$$d(i, j) = \frac{e^{\|p_A^i - p_B^i\|_2} - 1}{e^{\|p_A^i - p_B^i\|_2} + 1}. \tag{8}$$

We further have the distance matrix D, where its elements are $d(i, j)$. As described in [13], the local pose-aligned feature distance $d_p(A, B)$ can be derived by dynamically matching local information (DMLI), which could dynamically align different part features. Finally, we obtain the total distance of A and B by

$$d(A, B) = d_I(A, B) + d_p(A, B). \tag{9}$$

The total loss function of the framework is

$$L_{\text{total}} = L_{ID} + L_T^I + L_C^P, \tag{10}$$

where L_{ID} and L_T^I denote softmax loss and triplet loss [29] of the global feature and L_C^P denotes the circle loss [30] of the local pose-aligned feature. The performance of different loss functions is described in Section 4.3.

3.4. Training the Network. Since there is a lack of explicit ground truth for the training part attention module and retinex network, it is difficult to optimize the network for various scenes. Therefore, we try to train the network in a date-driven way. The whole network is trained in four stages, as illustrated in Algorithm 1.

(i) First, the backbone network, Resnet-50, is initialized by the ImageNet [31] pretrained model and trained to convergence under the supervision of triplet loss

(ii) Second, the synthetic low-light image sets based on PASCAL VOC, together with their original images, are fed to the Retinex decompose network, as described in Section 3.3. This training step is finished after 200 epochs

(iii) Third, all the layers in Resnet-50 are fixed; only the part attention module is trainable. Then, the IIPA-Net is retained with the softmax and triplet loss on

1. The shared-weights Resnet-50 is trained to convergence with triplet loss.
2. All synthetic images, together with their original images, are fed into the Retinex decomposition network.
3. Parts attention module is trained using the training images set.
4. The whole network is fine-tuned with Equation (10).

Algorithm 1: Training steps of the proposed network.

(a) Low-light Duke

(b) Low-light Market

Figure 5: Examples of synthetic low-light image.

the training set. The learning rate is decayed for 40 epochs

(iv) Finally, we set all the layers trainable and fine-tune the IIPA-Net to convergence again

4. Experiments

4.1. Datasets and Evaluation Measures. Our experiments are based on two real-world and popular person re-id datasets: Market1501 [32] and DukeMTMC-reID [33]. To better present the advantages of the proposed illumination-invariant feature, we adopt two manual low-light re-id datasets named low-light Market and low-light Duke. The Market1501 includes 32,668 images of labeled people captured by six cameras. Specially, there are 12,936 images of 751 identities in the training set and 19,732 images of 750 identities in the testing set. The DukeMTMC-reID contains 25,272 images, which are extracted from the DukeMTMC dataset [34] captured by eight cameras. There are 6,522 images of 702 identities in the training set and 18,750 images of 1110 identities in the testing set. The low-light Market and low-light Duke are built from Market1501 and DukeMTMC-reID, respectively. Following [22], we use gamma correction to simulate low-light conditions. Each image in the datasets is processed with a gamma value, which is randomly picked from $\{1, 2, 3, 4\}$. Figure 5 shows examples of synthetic low-light images. To evaluate the performance of different algorithms, we use Cumulative Matching Characteristic (CMC) curves and mean Average Precision (mAP) [32] as the evaluation criteria. CMC is defined as a function of Rank-r [35].

$$q(r) = \frac{|C(r)|}{|\mathscr{P}_g|}, \tag{11}$$

where $|\mathscr{P}_g|$ represents the total number of person images in the gallery, and the query set $C(r)$ is defined as

$$C(r) = \{p_i : \text{rank}\ (p_i) \leq r\}, \quad \forall p_i \in \mathscr{P}_g. \tag{12}$$

mAP is calculated based on the Average Precision (AP) and defined as

$$\text{mAP} = \frac{\sum_{k=1}^{n} \text{AP}(k)}{n}, \tag{13}$$

where $\text{AP}(k)$ represents the precision-recall curve area of the kth query and n represents the size of the query set.

4.2. Experimental Setup. We implement all experiments using an Intel Xeon e5-2630 v3 2.4 GHz machine with

(a) Normal-light example (b) Low-light example

Figure 6: Illustration for the parts attention module. The first column shows the input images. The second and third columns show the attention map results of normal and two-peak Gaussian.

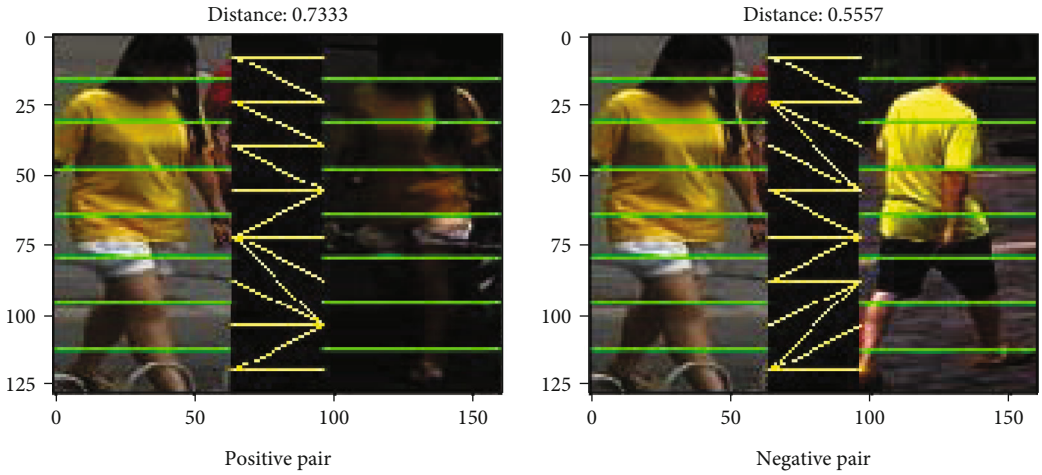

(a) Aligned results of baseline

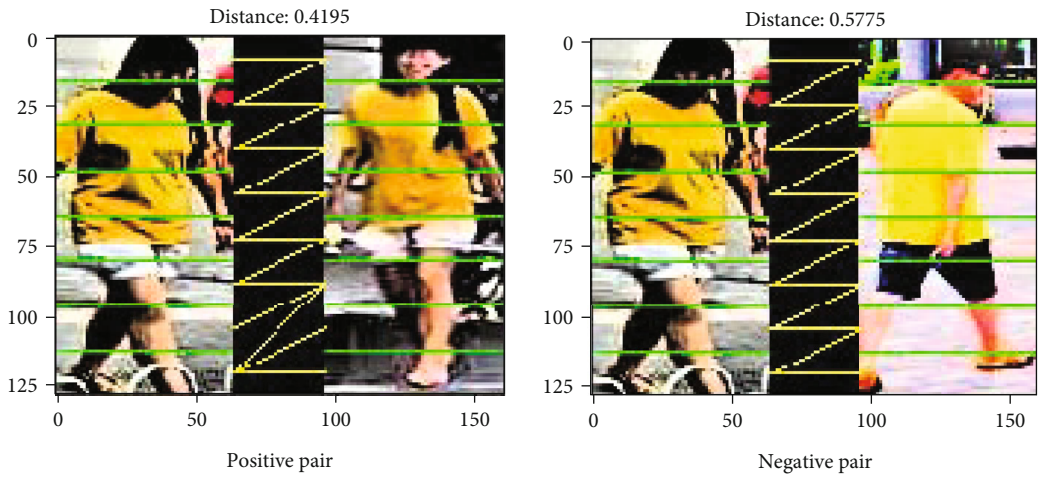

(b) Aligned results of our framework

Figure 7: The example aligned results of a positive pair and a negative pair from low-light Market.

32 GB RAM and one NVIDIA GTX Titan 12 GB GPU. The training patch size is set to be 32; λ_{ir} is set to be 0.001. λ_{ij} is set to 1, when $i = j$. Otherwise, λ_{ij} is 0.001. Each input image is resized to 256×128. Random horizontal flipping and cropping tricks are preformed to augment data. We use Adam optimizer with learning rate 10^{-4}.

4.3. Experimental Results. In this subsection, we firstly evaluate the part attention module. The two-peak Gaussian map can better guide the main body information of a person. Then, the effect of low light is analyzed. We can see that the low-light condition has a negative impact on pose alignment. Then, we evaluate the performance of our proposed IIPA-Net compared with other state-of-the-art re-id methods.

4.3.1. Evaluation of Part Attention. To better illustrate the effect of the proposed part attention module, we visualize the attention maps of the model with normal and two-peak Gaussian maps. In Figure 6, we can observe that the two-peak Gaussian map can pay attention to both upper and down parts of a person, while the normal one only to either upper (Figure 6(a)) or down (Figure 6(b)) part. The introduction of two-peak Gaussian makes part attention work more effective with the multimodal nature of a person. Figure 6 third columns show that the proposed part attention is able to produce similar predicted attention under different light conditions.

4.3.2. Effect of Low Light. As shown in Figure 7(a), using AlignedReID++ [13] as the baseline model, the fifth block of the left image is aligned to the fourth and sixth blocks of the right image and the distance of the two images is 0.7333, which is greater than the negative pair (0.5557). However, after decomposing the illumination, our proposed method is able to align the head, chest, foot, etc., of the positive pair images, and the distance is reduced to 0.4195, which is less than the negative pair (0.5775), as illustrated in Figure 7(b). The wrong connections of the baseline can be attributed to the negative impact of the low illumination. This indicates that the proposed approach eliminates the effect of weak illumination and learns the illumination-invariant features.

4.3.3. Performance of Different Loss Functions. We train four models with softmax+triplet loss ($L_{ID} + L_T^I + L_T^P$), softmax +instance [36] loss ($L_{ID} + L_I^I + L_I^P$), softmax+circle loss ($L_{ID} + L_C^I + L_C^P$) and the proposed loss. The performance on Market1501 is presented in Table 1. L^I and L^P represent the loss of the global and local features, respectively. We can observe that Softmax+Instance and Softmax+Circle loss achieve the similar Rank-1 accuracy. Compared with Softmax+Triplet, the proposed loss improves the Rank-1 and mAP arropminately 0.3 and 0.2, respectively. We believe that the Circle loss works on some hard local features.

4.3.4. Comparison with State-of-the-Art. To evaluate the performance of the proposed IIPR-Net, we report the experimental results with some state-of-the-art methods. Our baseline is AlignedReID++ [13], which focuses on solving the pose change problem. In order to demonstrate the advantage of the proposed framework, we also report the results of baseline with a low-light enhancement method. Both training and testing image sets are enhanced with MSRCP [37] and then fed into the baseline.

As shown in Table 2, our proposed framework outperforms most state-of-the-art methods on all four datasets. Specially, the proposed framework achieves 96.2% Rank-1 for Market1501 and 90.8% Rank-1 for Duke MTMC-reID, outperforming other attention-based methods, i.e., MHN-6 [9] and DSA [38]. Although FlipReID [39] and st-ReID [40] achieve the best performance, the extra data, for instance, spatial and temporal information, are utilized to train the network. For low-light Market and Duke datasets, the Rank-1 accuracy of the proposed method is increased by 10.1% and 11.2%, and the mAP increased by 9.5% and 6.0%, respectively. This demonstrates that our joint framework not only eliminates the impact of low light but also explores pose-invariant local features for person re-id. Figure 8 depicts five examples of queries together with the top 10 retrieved results of baseline and IIPA-Net on the low-light Market dataset. As we can see, the IIPA-Net

Table 1: The performance of different loss functions on Market1501.

Loss function	Rank-1	mAP
$L_{ID} + L_T^I + L_T^P$	95.9	90.1
$L_{ID} + L_I^I + L_I^P$	95.7	89.8
$L_{ID} + L_C^I + L_C^P$	95.6	90.0
$L_{ID} + L_T^I + L_C^P$	**96.2**	**90.3**

Bold: best results.

Table 2: Experiment results of our framework compared to other state-of-the-art methods.

Dataset	Method	Rank-1	mAP
Market1501	IDE [41]	85.3	68.5
	Baseline [13]	92.8	89.4
	PCB [26]	92.3	77.4
	MHN-6 [3]	95.1	85.0
	DSA [38]	95.7	87.6
	FlipReID [39]	95.8	94.7
	st-ReID [40]	**98.0**	**95.5**
	IIPA-Net	96.2	90.3
DukeMTMC-ReID	IDE [41]	73.2	52.8
	Baseline [13]	80.7	68.0
	PCB [26]	81.7	66.1
	MHN-6 [3]	89.1	77.2
	DSA [38]	86.2	74.3
	FlipReID [39]	93.0	90.7
	st-ReID [40]	**94.5**	**92.7**
	IIPA-Net	90.8	83.3
Low-light Market	Baseline [13]	33.4	14.1
	Baseline+MSRCP	49.4	15.7
	PCB [26]	48.5	16.2
	IIPA-Net	**60.5**	**27.7**
Low-light Duke	Baseline [13]	36.2	12.4
	Baseline+MSRCP	40.4	18.3
	PCB [26]	48.4	21.0
	IIPA-Net	**51.6**	**24.3**

Bold: best results.

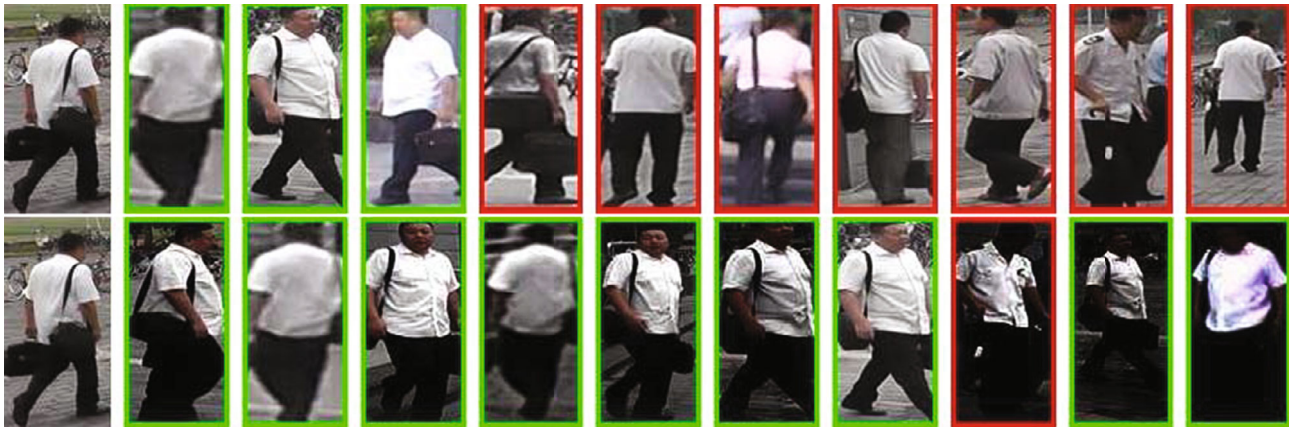

(a)

(b)

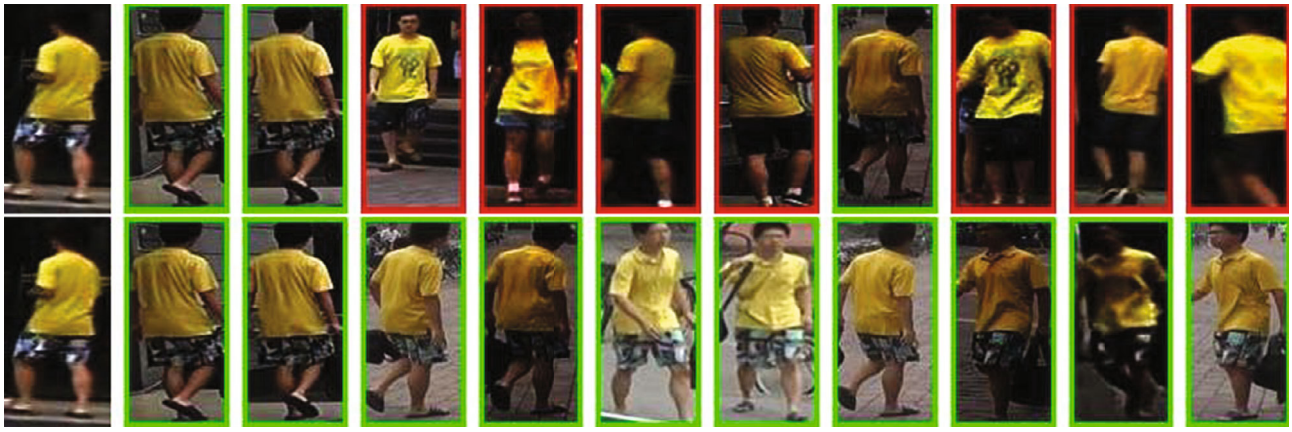

(c)

Figure 8: Continued.

(d)

(e)

Figure 8: Retrieved results of baseline and IIPA-Net on the low-light Market dataset. The first column images are the query. For each example, the upper row images are the results of baseline and the lower row images are of IIPA-Net. The images with a green border are the correct retrieved results, and those with a red border are the incorrect results.

Table 3: Ablation study on normal- and low-light market datasets.

Condition	Method	Rank-1	mAP
Normal	Ours w/o attention	94.4	89.5
	Ours w/o retinex	92.6	88.3
	Ours	**96.2**	**90.3**
Low light	Ours w/o attention	44.7	17.3
	Ours w/o retinex	56.3	22.4
	Ours	**60.5**	**27.7**

w/o: without; bold: best results.

outperforms the baseline and accurately retrieves the target in spite of illumination and pose variants.

4.3.5. Ablation Study. To verify the contribution of each component, we perform the ablation study on normal- and low-light Market datasets. Table 3 shows the results of each component of IIPA-Net. We note that the attention component achieves better results on the Market1501 dataset. However, retinex is better in low-light conditions. The combination of the retinex and attention achieves the best performance on both datasets. The reason is that IIPA-Net is able to learn both illumination and pose-invariant features.

5. Conclusions

In this paper, we proposed a jointly illumination-invariant and pose-aligned learning framework for person re-id. Motivated by retinex theory, we introduce a retinex decomposition net to eliminate the impact of different lights and extract an illumination-invariant feature. To tackle the problems of pose alignment, dynamically matching local information is utilized to align local feature, which is transferred from the deep learning feature map. Based on the nature of a person, we proposed a part attention mechanism to extract the most discriminative global feature. The joint framework is trained in a four-stage fashion. Experiments demonstrate that the proposed framework achieves better performance on both normal- and low-light datasets. In the future, we will focus on long-term re-id scenarios which present more complex scene variations.

Data Availability

All data included in this study are available from the corresponding author upon request.

Conflicts of Interest

The authors declare that there are no conflicts of interest regarding the publication of this article.

Acknowledgments

This work was partially supported by the National Natural Science Foundation of China under Grant 52105268, Natural Science Foundation of Guangdong Province under Grant 2022A1515011409, Key Platforms and Major Scientific Research Projects of Universities in Guangdong under Grants 2019KTSCX161 and 2019KTSCX165, Key Projects of Natural Science Research Projects of Shaoguan University under Grants SZ2020KJ02 and SZ2021KJ05, Project of Guangdong Provincial Key Laboratory of Technique and Equipment for Macromolecular Advanced Manufacturing under Grant 2020kfkt07, and the Science and Technology Program of Shaoguan City of China under Grants 2019sn056, 200811094530423, 200811094530805, and 200811094530811.

References

[1] M. Ye, J. Shen, G. Lin, T. Xiang, L. Shao, and S. C. H. Hoi, "Deep learning for person re-identification: a survey and outlook," *IEEE Transactions on Pattern Analysis and Machine Intelligence*, vol. 44, no. 6, pp. 2872–2893, 2022.

[2] R. Quan, X. Dong, Y. Wu, L. Zhu, and Y. Yang, "Auto- reid: searching for a part-aware convnet for person re- identification," in *2019 IEEE/CVF International Conference on Computer Vision (ICCV)*, pp. 3749–3758, Seoul, Korea (South), 2019.

[3] Y. Wu, Y. Lin, X. Dong, Y. Yan, W. Bian, and Y. Yang, "Progressive learning for person re-identification with one example," *IEEE Transactions on Image Processing*, vol. 28, no. 6, pp. 2872–2881, 2019.

[4] R. Prates, C. R. S. Dutra, and W. R. Schwartz, "Predominant color name indexing structure for person re-identification," in *2016 IEEE International Conference on Image Processing (ICIP)*, pp. 779–783, Phoenix, AZ, USA, 2016.

[5] A. J. Ma, J. Li, P. C. Yuen, and P. Li, "Cross-domain person reidentification using domain adaptation ranking svms," *IEEE Transactions on Image Processing*, vol. 24, no. 5, pp. 1599–1613, 2015.

[6] C. Su, J. Li, S. Zhang, J. Xing, W. Gao, and Q. Tian, "Pose-driven deep convolutional model for person re- identification," in *2017 IEEE International Conference on Computer Vision (ICCV)*, pp. 3980–3989, Venice, Italy, 2017.

[7] J. Miao, Y. Wu, P. Liu, Y. Ding, and Y. Yang, "Pose-guided feature alignment for occluded person re-identification," in *2019 IEEE/CVF International Conference on Computer Vision (ICCV)*, pp. 542–551, Seoul, Korea (South), 2019.

[8] L. Zheng, Y. Huang, H. Lu, and Y. Yang, "Pose-invariant embedding for deep person re-identification," *IEEE Transactions on Image Processing*, vol. 28, no. 9, pp. 4500–4509, 2019.

[9] B. Chen, W. Deng, and J. Hu, "Mixed high-order attention network for person re-identification," in *2019 IEEE/CVF International Conference on Computer Vision (ICCV)*, pp. 371–381, Seoul, Korea (South), 2019.

[10] E. Ristani and C. Tomasi, "Features for multi-target multi-camera tracking and re-identification," in *2018 IEEE/CVF Conference on Computer Vision and Pattern Recognition*, pp. 6036–6046, Salt Lake City, UT, USA, 2018.

[11] Y. Lin, L. Zheng, Z. Zheng et al., "Improving person re-identification by attribute and identity learning," *Pattern Recognition*, vol. 95, no. C, pp. 151–161, 2019.

[12] W. Chen, W. Wenjing, Y. Wenhan, and L. Jiaying, "Deep retinex decomposition for low-light enhancement," in *British Machine Vision Conference*, British Machine Vision Association, 2018.

[13] H. Luo, W. Jiang, X. Zhang, X. Fan, J. Qian, and C. Zhang, "AlignedReID++: dynamically matching local information for person re- identification," *Pattern Recognition*, vol. 94, pp. 53–61, 2019.

[14] I. Kviatkovsky, A. Adam, and E. Rivlin, "Color invariants for person reidentification," *IEEE Transactions on Pattern Analysis and Machine Intelligence*, vol. 35, no. 7, pp. 1622–1634, 2013.

[15] L. Ma, T. Tan, Y. Wang, and D. Zhang, "Personal identification based on iris texture analysis," *IEEE Transactions on Pattern Analysis and Machine Intelligence*, vol. 25, no. 12, pp. 1519–1533, 2003.

[16] X. Wang, G. Doretto, T. Sebastian, J. Rittscher, and P. Tu, "Shape and appearance context modeling," in *IEEE International Conference on Computer Vision*, pp. 1–8, Rio de Janeiro, Brazil, 2007.

[17] E. Ahmed, M. Jones, and T. K. Marks, "An improved deep learning architecture for person re-identification," in *Computer Vision and Pattern Recognition*, pp. 3908–3916, Boston, MA, USA, 2015.

[18] W. Li, R. Zhao, T. Xiao, and X. Wang, "Deepreid: deep filter pairing neural network for person re-identification," in *IEEE International Conference on Computer Vision*, pp. 152–159, Columbus, OH, USA, 2014.

[19] T. Xiao, S. Li, B. Wang, L. Lin, and X. Wang, "Joint detection and identification feature learning for person search," in *2017 IEEE Conference on Computer Vision and Pattern Recognition (CVPR)*, pp. 3376–3385, Honolulu, HI, USA, 2017.

[20] Y. Wu, Y. Lin, X. Dong, Y. Yan, W. Ouyang, and Y. Yang, "Exploit the unknown gradually: one-shot video-based person re-identification by stepwise learning," in *2018 IEEE/CVF Conference on Computer Vision and Pattern Recognition*, pp. 5177–5186, Salt Lake City, UT, USA, 2018.

[21] E. H. Land, "The retinex theory of color vision," *Scientific American*, vol. 237, no. 6, pp. 108–128, 1977.

[22] Y. Huang, Z. J. Zha, X. Fu, and W. Zhang, "Illumination-invariant person re-identification," in *Proceedings of the 27th ACM International Conference on Multimedia, MM '19*, pp. 365–373, Nice France, 2019.

[23] S. Liao, Y. Hu, X. Zhu, and S. Z. Li, "Person re- identification by local maximal occurrence representation and metric learning," in *2015 IEEE Conference on Computer Vision and Pattern Recognition (CVPR)*, pp. 2197–2206, Boston, MA, USA, 2015.

[24] S. Bak, P. Carr, and J. F. Lalonde, "Domain adapta- tion through synthesis for unsupervised person re- identification," in *Computer Vision – ECCV 2018*, V. Ferrari, M. Hebert, C.

Sminchisescu, and Y. Weiss, Eds., pp. 193–209, Springer International Publishing, Cham, 2018.

[25] H. Zhao, M. Tian, S. Sun et al., "Spindle net: person re-identification with human body region guided feature decomposition and fusion," in *2017 IEEE Conference on Computer Vision and Pattern Recognition (CVPR)*, pp. 907–915, Honolulu, HI, USA, 2017.

[26] Y. Sun, L. Zheng, Y. Yang, Q. Tian, and S. Wang, "Beyond part models: person retrieval with refined part pooling (and a strong convolutional baseline)," in *Proceedings of the European conference on computer vision (ECCV)*, pp. 480–496, Munich, Germany, 2018.

[27] J. Miao, Y. Wu, and Y. Yang, "Identifying visible parts via pose estimation for occluded person re-identification," *IEEE Transactions on Neural Networks and Learning Systems*, no. article 3059515, pp. 1–11, 2021.

[28] W. Li, X. Zhu, and S. Gong, "Harmonious attention network for person re-identification," in *2018 IEEE/CVF Confer- ence on Computer Vision and Pattern Recognition*, pp. 2285–2294, Salt Lake City, UT, USA, 2018.

[29] A. Hermans, L. Beyer, and B. Leibe, "In defense of the triplet loss for person re-identification," 2017, http://arxiv.org/abs/1703.07737.

[30] Y. Sun, C. Cheng, Y. Zhang et al., "Circle loss: a unified perspective of pair similarity optimization," in *2020 IEEE/CVF Conference on Computer Vision and Pattern Recognition (CVPR)*, pp. 6397–6406, Seattle, WA, USA, 2020.

[31] O. Russakovsky, J. Deng, H. Su et al., "Imagenet large scale visual recognition challenge," *International Journal of Computer Vision*, vol. 115, no. 3, pp. 211–252, 2015.

[32] L. Zheng, L. Shen, L. Tian, S. Wang, J. Wang, and Q. Tian, "Scalable person re-identification: a benchmark," in *2015 IEEE International Conference on Computer Vision (ICCV)*, pp. 1116–1124, Santiago, Chile, 2015.

[33] Z. Zheng, L. Zheng, and Y. Yang, "Unlabeled samples generated by gan improve the person re-identification baseline in vitro," in *2017 IEEE International Conference on Computer Vision (ICCV)*, pp. 3774–3782, Venice, Italy, 2017.

[34] E. Ristani, F. Solera, R. Zou, R. Cucchiara, and C. Tomasi, "Performance measures and a data set for multi-target, multi-camera tracking," in *2016 European Conference on Computer Vision (ECCV)*, G. Hua and H. J'egou, Eds., pp. 17–35, Springer International Publishing, Cham, 2016.

[35] P. Grother, R. J. Micheals, and P. J. Phillips, "Face recognition vendor test 2002 performance metrics," in *Proceedings of the 4th International Conference on Audio- and Video-Based Biometric Person Authentication, AVBPA'03*, pp. 937–945, Guildford, UK, 2003.

[36] Z. Zheng, L. Zheng, M. Garrett, Y. Yang, M. Xu, and Y. D. Shen, "Dual-path convolutional image-text embeddings with instance loss," *ACM Transactions on Multimedia Computing, Communications, and Applications*, vol. 16, no. 2, pp. 1–23, 2020.

[37] A. B. Petro, C. Sbert, and J. M. Morel, "Multiscale retinex," *Image Processing On Line*, vol. 4, pp. 71–88, 2014.

[38] Z. Zhang, C. Lan, W. Zeng, and Z. Chen, "Densely semantically aligned person re-identification," in *2019 IEEE/CVF Conference on Computer Vision and Pattern Recognition (CVPR)*, pp. 667–676, Long Beach, CA, USA, 2019.

[39] X. Ni and E. Rahtu, "Flipreid: closing the gap between training and inference in person re-identification," in *2021 9th European Workshop on Visual Information Processing (EUVIP)*, pp. 1–6, Paris, France, 2021.

[40] G. Wang, J. Lai, P. Huang, and X. Xie, "Spatial-temporal person re-identification," *Proceedings of the AAAI Conference on Artificial Intelligence*, vol. 33, pp. 8933–8940, 2019.

[41] L. Zheng, Y. Yang, and A. Hauptmann, "Person re- identification: past, present and future," 2016, http://arxiv.org/abs/1610.02984.

Hindawi
Journal of Sensors
Volume 2022, Article ID 6730677, 14 pages
https://doi.org/10.1155/2022/6730677

Research Article

A Load Forecasting Algorithm for Power Internet of Things Using Training Data Dimension Expansion and Ensemble Learning Technique

Chang Liu, Wei Rao, Jin Wang, Zeyang Tang, Chang Liu, Jie Wang, Li Tian, Liang Zhou, and Jiangpei Xu

State Grid Hubei Electric Power Research Institute, Wuhan 430000, China

Correspondence should be addressed to Chang Liu; 12612209@qq.com

Received 28 April 2022; Accepted 3 June 2022; Published 20 June 2022

Academic Editor: Han Wang

With the development of the power internet of things (IOT), load forecasting will play an important role the power system. It can optimize the power generation planning and improve the economical operation of power IOT. In this paper, a new loading forecasting algorithm for power IOT is proposed using training data dimension expansion and ensemble learning. In the offline phase, the obtained meteorological data and time information is normalized to remove the unit effect at first. Then, the Hampel filter is used to cope with the outliers of the meteorological data from sensors. Through the preprocessing, the fingerprint of the training data is constructed. Next, the matrix multiplication method is proposed to expand the dimension of training data fingerprint information. Finally, the ensemble learning combining multiple long short-term memory (LSTM) networks are proposed to obtain multiple power load forecasting models and corresponding weight coefficients. In the online phase, the obtained meteorological data and time information are preprocessed to form the input of and power load forecasting models. The final power load forecasting is obtained by linear weighted sum method with intermediate forecasting result. In the proposed algorithm, more features of training data can be obtained by the data dimension expansion. Moreover, the ensemble learning using LSTM can make fully use of the timing sequence of training and improve the generalization performance of offline training. Experiment results illustrate that the proposed algorithm has better forecasting performance than existing methods.

1. Introduction

With the increasing requirement of energy consumption, a clean, low-carbon, safe, and shared power system has received many attentions for both academic and industry [1, 2]. The new energy revolution called "energy + Internet" becomes a research hotspot [3]. In China, the State Grid Corporation began to develop the ubiquitous power internet of things (IOT) for smart grid in 2019 [3]. The power IOT connects people and devices that are related to the power grid. By collecting device-related data using sensor, the data is sent to the server which is processed by big data analysis, cloud computing, and artificial intelligence technologies. It effectively integrates communication infrastructure resources and power system infrastructure resources which can realize the interconnection of all things in the power system. Now, the power IOT can promote the efficiency of energy services and new energy consumption dramatically. In [4], an architecture for ubiquitous power IOT is proposed which brings great convenience to the collection, transmission, processing, and storage of data. In [5], the characteristics of power IOT, its application, and the needs of smart grid for communication coverage and data acquisition are proposed.

For the requirement of power IOT construction, power load forecasting plays an important role in the operation planning of power system. The authors of [6] proposed a load forecasting method by two groups of features. The half-hour electrical load variables obtained from the smart

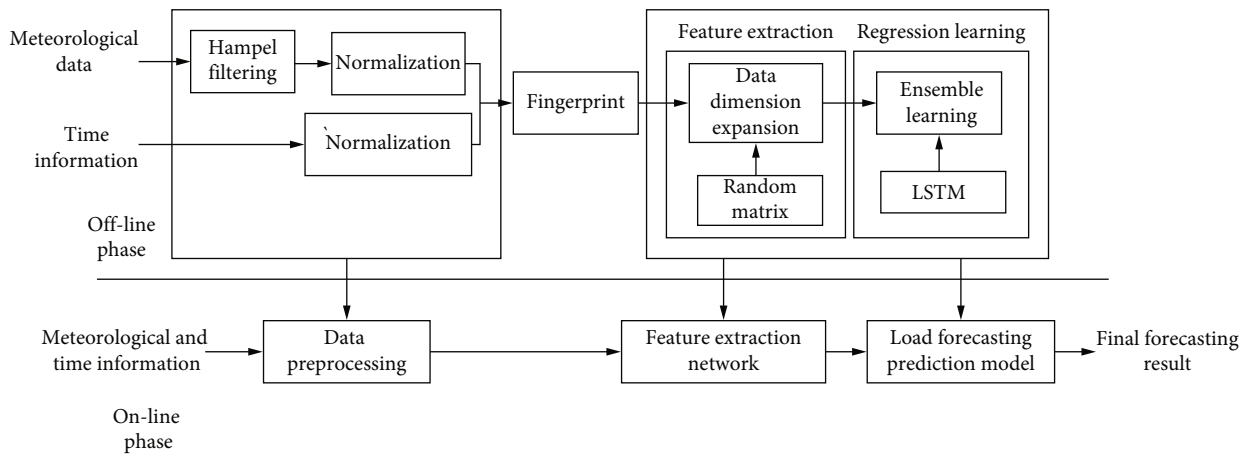

Figure 1: The block diagram of the proposed algorithm.

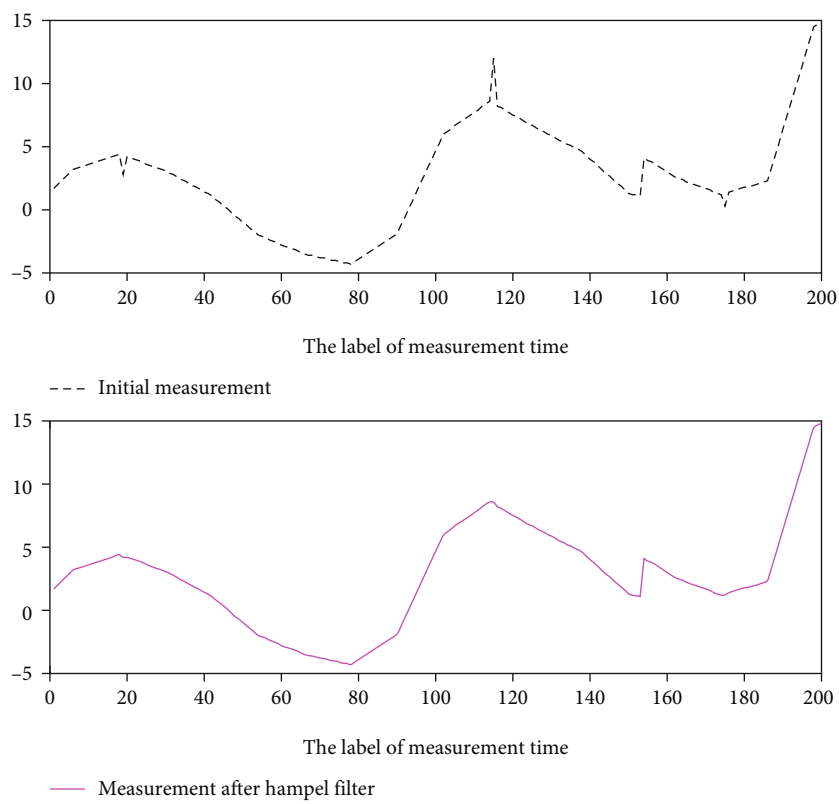

Figure 2: The description of temperature information process by Hampel filter.

meters through the IOT technology together with the lagged load and calendar variables are used for short-term load forecasting by multilayer perceptron neural networks. In [7], an ultrashort term load forecasting method for the power IOT is proposed by federated learning. It learns the model parameters from the data distributed in multiple edge nodes. Since rapid and accurate power load forecasting can optimize the power generation planning and improve the economical operation of power IOT, it is urgent to study the load forecasting technique for power IOT [8].

Recently, the load forecasting is performed with different kinds of techniques in the literature which can be broadly divided into two groups: traditional and artificial intelligence-based techniques.

For traditional technique, the statistical method is mostly used for load forecasting. In [9], considering the load forecast is a conditional expectation of load given the time, weather conditions, and other explanatory variables; load forecasting can be calculated directly from given parameters. In [10], the general exponential smoothing is used to develop an adaptive load forecasting system using observed values of integrated hourly demand. In [11], a modified autoregressive moving average- (ARMA-) based method with non-Gaussian process is used to improve the

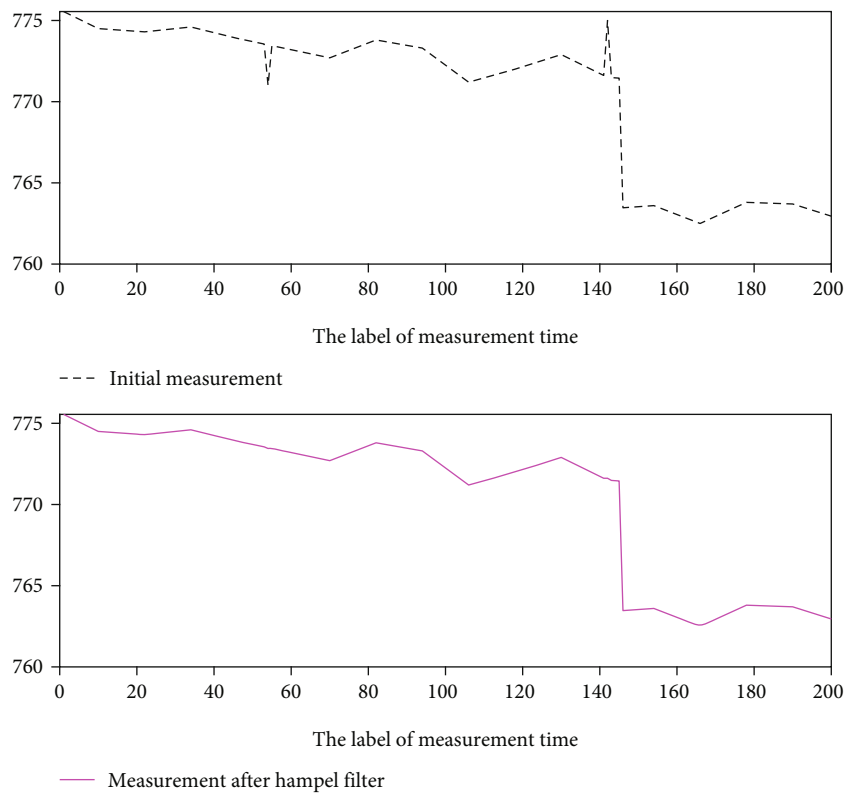

Figure 3: The description of pressure information process by Hampel filter.

forecasting performance. Note that due to characteristics of nonlinear features of time series univariate load data, this kind of technique does not always perform well.

In order to cope with the limits of traditional technique, artificial intelligence-based technique is developed. First, some machine learning-based methods are proposed. In [12], a kernel-based support vector regression (SVR) method is used for load forecasting by choosing kernel function. In [13], the artificial neural network (ANN) is used to obtain the load forecasting model for weekdays and weekends, respectively. Now, with the development of machine learning theory, some deep learning methods are used for load forecasting, because it has greater number of hidden layers to deal with the complicated nonlinear patterns. In [14], a multiscale convolutional neural network with time cognition is proposed for load forecasting. Since the recurrent neural network (RNN) is effective to capture non-stationary training data, a pooling-based deep RNN in [15] is proposed to solve the overfitting problem in load forecasting. Note that vanishing gradient and exploding gradient problem arise in RNN can reduce the prediction accuracy. Thus, the long short-term memory (LSTM) network has been taken into account to solve these problems. In [16], an effective methodology using the LSTM network is developed to make a precise forecasting under more complex time series load data condition.

According to the above discussion, we continue to study deep learning-based load forecasting algorithm. Since the time and meteorological data, such as wind speed, temperature, and pressure, are critical affect the power consumption [17], in this paper, a deep learning technique is used to training the relationship between the above factors and power load. The contributions of this paper can be summarized as follows:

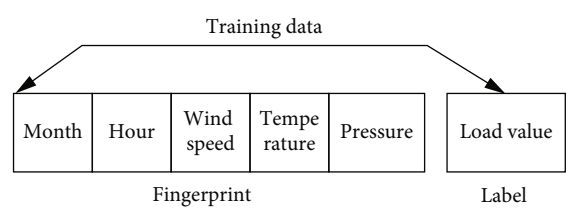

Figure 4: The description of the training data.

(1) A deep learning-based load forecasting algorithm is proposed by LSTM. It can effectively avoid the insensitivity of training data time series in the prediction process

(2) For data preprocessing, the Hampel filter can eliminate the outlier caused by sensor noise. Moreover, the feature extraction network using random matrix multiplication can obtain better feature representation which can improve the offline training performance

(3) For regression learning, the ensemble learning framework which combines multiple LSTM networks is used to train the relationship between the

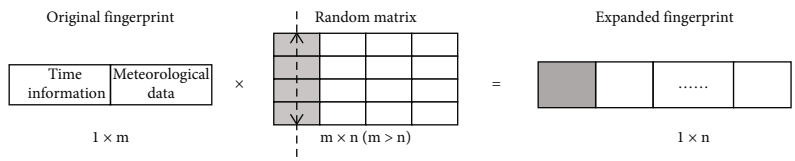

Figure 5: The schematic diagram of the proposed dimension expansion.

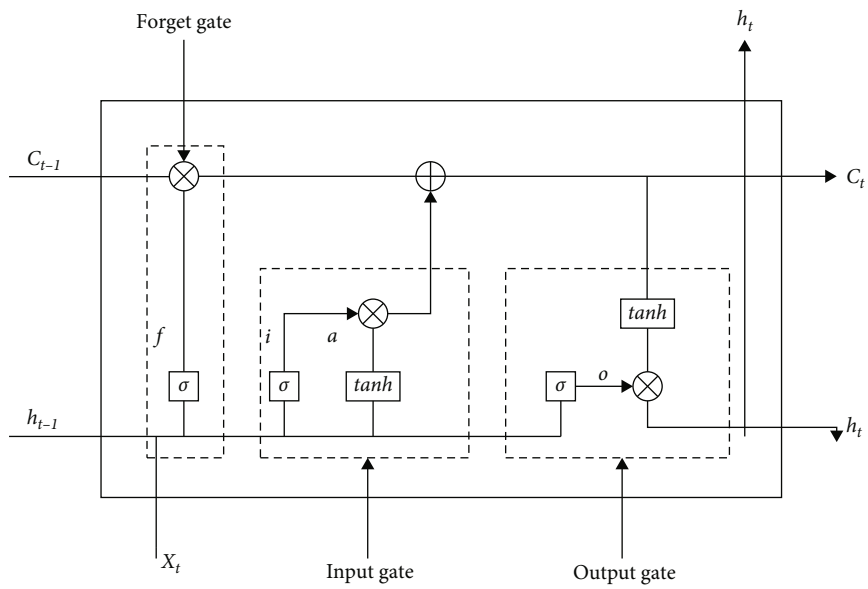

Figure 6: The description of LSTM architecture.

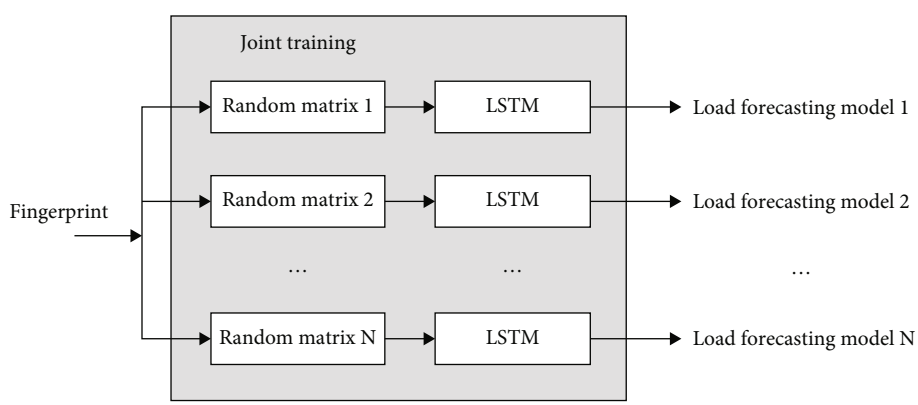

Figure 7: Flowchart of the proposed regression learning.

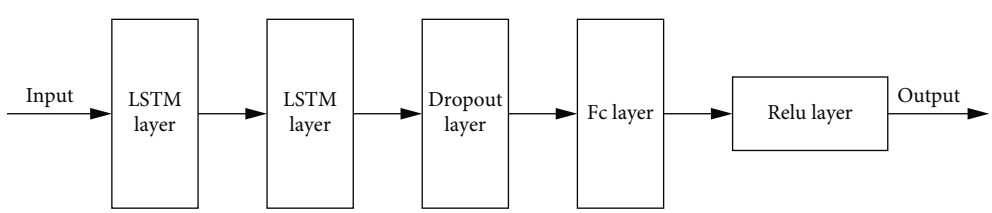

Figure 8: The description of LSTM network.

measurements and load. It can reduce the risk of falling into local optimal solutions and improve the generalization performance

(4) Feature extraction network (random matrix) and regression learning network (LSTM network) are combined for joint learning and optimization. Thus,

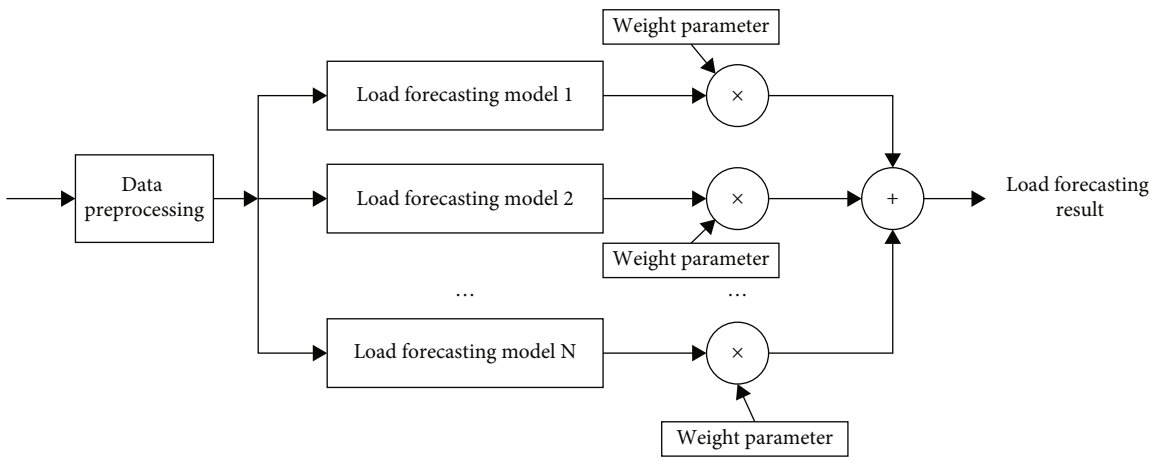

Figure 9: The block diagram of the online phase description.

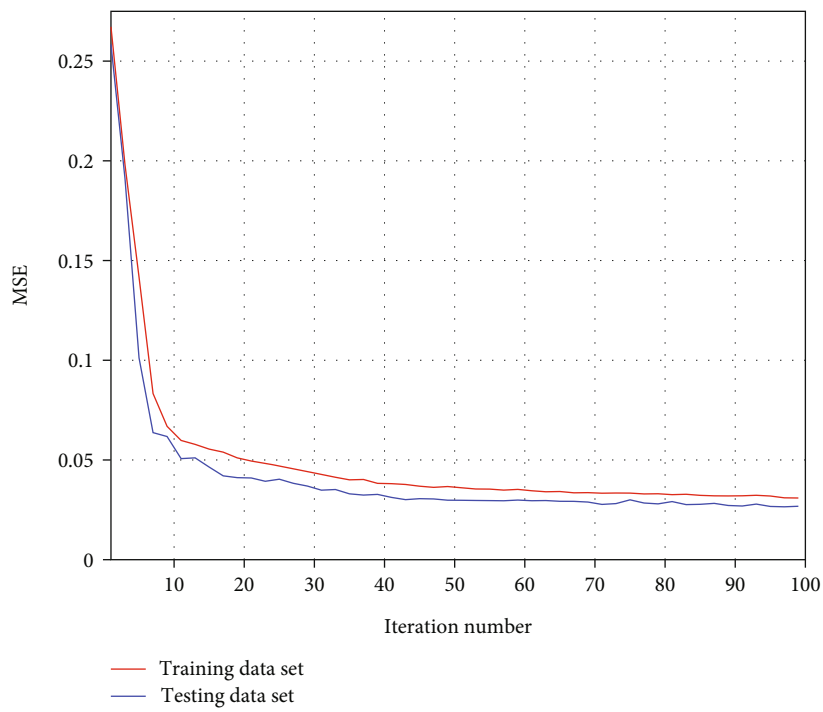

Figure 10: The description of the training performance of the proposed algorithm.

the optimal parameters in the global sense can be obtained, and the final load forecasting performance can be improved

The remainder of this paper is organized as follows. Section 2 gives the algorithm framework. The offline phase description and the online phase description of the proposed algorithm are explained in Sections 3 and 4, respectively. Field test and performance analysis are illustrated in Section 5, and conclusions are drawn in Section 6.

2. Algorithm Framework

According the block diagram shown in Figure 1, the proposed algorithm contains two main phases: offline training phase and online forecasting phase. For offline training phase, it contains three important steps: (1) training data preprocessing, (2) feature extraction using dimension expansion, and (3) regression learning using ensemble learning. For another, in the online forecasting phase, after the similar preprocessing of the obtained data, the trained feature extraction network and forecasting model are used to estimate the final load forecasting result. In the following, each step of the proposed algorithm will be described in detail.

3. Offline Phase Description

3.1. Training Data Preprocessing. In this step, data normalization and outlier detection are used for data preprocessing. First, as we know, some measurement environments and the

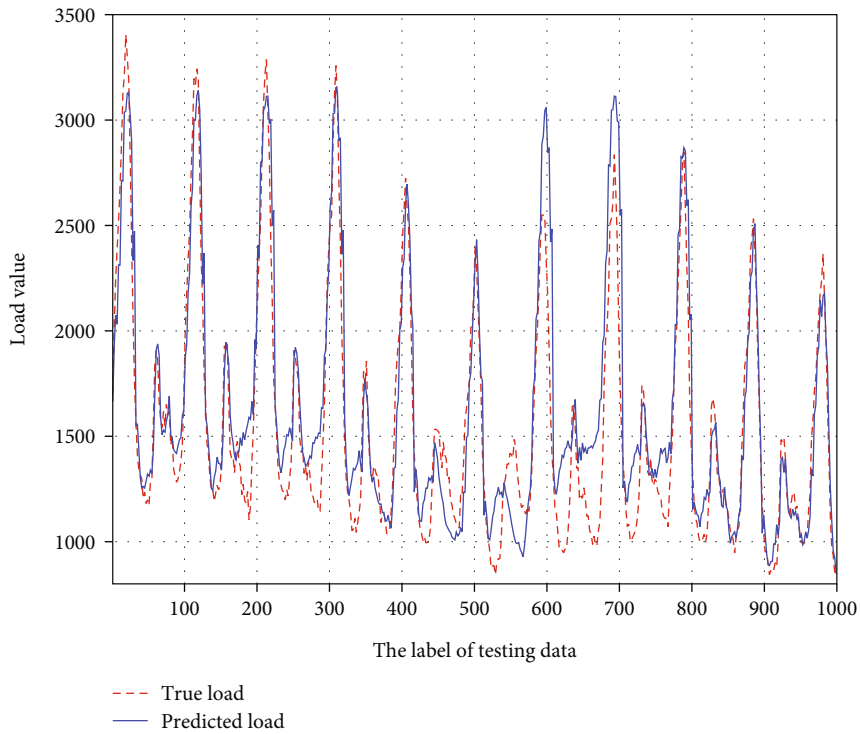

Figure 11: The load forecasting description of the proposed algorithm.

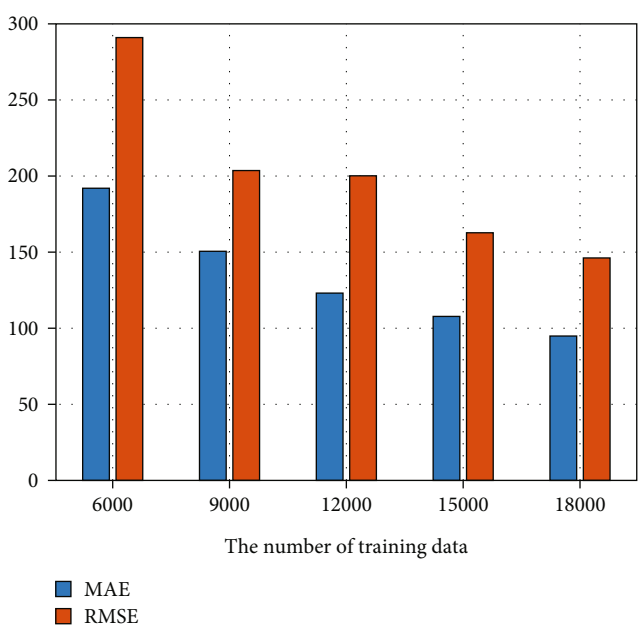

Figure 12: MAE and RMSE description of the proposed algorithm.

sensor noise may lead some measurements become outlier in the data collection. In the paper, the Hampel filter is used to remove these outliers [18]. For a given vector $x = \{x_1, x_2, \cdots, x_n\}$, the observation window of each measurement is defined at first. Assume the half-length of the window is k; the total length of the defined window is calculated as $2k + 1$ (including the given measurement). Then, the median of all measurement data in the window is calculated as

$$\overline{x_i} = \text{median}(x_{i-k}, x_{i-k+1}, \cdots, x_i, \cdots, x_{i+k-1}, x_{i+k}). \quad (1)$$

The standard deviation of each measurement for the absolute value of the median is written as

$$e_i = 1.4286\text{median}(|x_{i-k} - \bar{x}_i|, \cdots, |x_{i+k} - \bar{x}_i|), \quad (2)$$

After filter, the measurement can be described as

$$b_i = \begin{cases} x_i(|x_i - \bar{x}_i| \leq 3\, e_i, \\ \bar{x}_i(|x_i - \bar{x}_i| \geq 3\, e_i. \end{cases} \quad (3)$$

If the measurements exceed three times of the obtained standard deviation, the median is used to substitute the measurement data.

Taking the temperature and pressure information as an example, Figures 2 and 3 describe the measurement data preprocessing results. It can be seen that after Hampel filter process, some outliers are removed. Thus, Hampel filter has effects on outlier deletion.

Next, the collected meteorological data and time information are scaled in order to lead them fall into a special range. In this paper, the min-max method is used to make the obtained data information into [0 1] range which can be given by [19]

$$x_n' = \frac{x_n - x_{\min}}{x_{\max} - x_{\min}}, \quad (4)$$

where x_n, x_n' describe the original and normalized data, respectively, and $x_{\max}$ and $x_{\min}$ are the maximum and minimum values of this kind of given data.

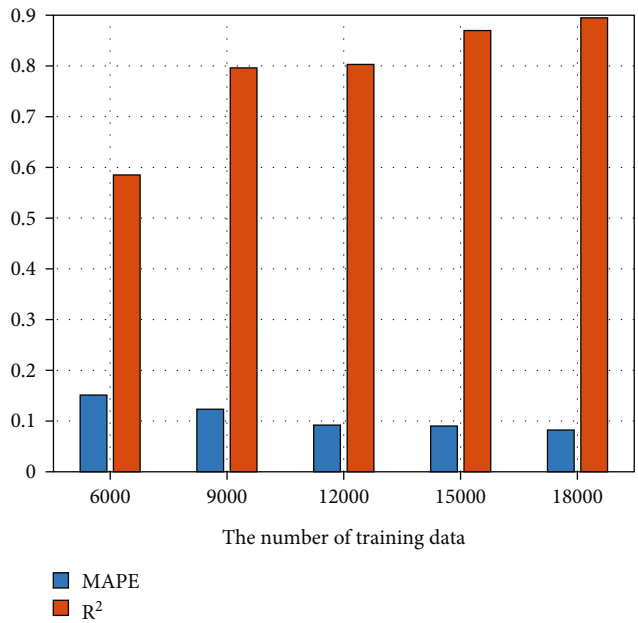

Figure 13: MAPE and R^2 description of the proposed algorithm.

Table 1: Statistical error analysis of the proposed algorithm with different numbers of LSTM.

	2	4
MAE	94.8697	86.64721
RMSE	146.1882	130.1099
MAPE	0.08238	0.07374
R^2	0.8949	0.91678

The purpose of data normalization is to remove the unit effects for the following training. Through this process, different kinds of data are at the same level. And the comprehensive evaluation and analysis can be carried out.

Thus, through the above preprocessing, the fingerprints of training data are described in Figure 4, where the fingerprint contains time information (month, hour) and meteorological data (wind speed, temperature, and pressure). The size of fingerprint is five dimensions. The label of training data is actual load.

3.2. Feature Extraction Using Training Data Dimension Expansion. After the data preprocessing, in the next, the training data expansion is used to obtain more features for training. Traditional data dimension expansion for deep learning contains random augmenter and lower-bound cropper [20]. The idea of random augmenter is to randomly generate a binary mask that can be multiplied by the data vector. The lower-bound cropper augmentation technique leverages this observation to increase the training data size. In particular, for a given collected data vector, any entry whose value is less than a certain threshold is a candidate to be removed (set to zero). All combinations of these entries can then be added to form the new training data. As shown in Figure 5, in this step, the random matrix is proposed to expand the dimension of the fingerprint.

Assume the original fingerprint is defined as A with size $1 \times m$; in order to expand the dimension of a vector, a random matrix B is defined for multiplication operation. In order to meet the requirement of calculation rule and dimension expansion, the size should be $m \times n$ (where $n > m$). The optimal element can be obtained from the training with following regression learning.

At last, the expanded fingerprint can be written as

$$C = A * B, \tag{5}$$

where the size of C is n. Each element is obtained by multiplying vector with matrix.

Note that since the size of expanded fingerprint is larger than that of the original fingerprint and the element can be determined with the offline training, more detailed feature for training data can be obtained through above dimension expansion.

3.3. Regression Learning Using Ensemble Learning. In this section, in order to improve the training performance of the offline phase, ensemble learning framework is proposed for regression learning [21]. Moreover, the LSTM network is chosen as the sublearner which can make fully use of the time series of the training data.

First, some basic knowledge of LSTM network is described [22]. According to the LSTM architecture shown in Figure 6, it contains four basic components: cell, input gate, output gate, and forget gate. The function of each component is described as follows. Cell is the core of the compute node. The information can be transferred over random time intervals through the cell. The gate traces the flow of the input and output data from the cell. The input gate and output gate are used to control the input and output. The forget gate is used to control the retention degree of historical information. Moreover, the sigmoid activation function is introduced to make the output between [0, 1]. When the output is 0, it means that all the information in the previous state is discarded. When the input gate is 1, all information in the previous state is retained.

A unit of LSTM is defined as

$$\begin{aligned} i_t &= \sigma(W_{xi}x_t + W_{hi}h_{t-1} + b_i), \\ f_t &= \sigma\left(W_{xf}x_t + W_{hf}h_{t-1} + b_f\right), \\ o_t &= \sigma(W_{xo}x_t + W_{ho}h_{t-1} + b_o), \end{aligned} \tag{6}$$

Input is defined as

$$g_t = \tanh\left(W_{xc}x_t + W_{hc}h_{t-1} + b_c\right) \tag{7}$$

Cell update is defined as

$$\begin{aligned} c_t &= f_t \circ c_{t-1} + i_t \circ g_t, \\ h_t &= o_t \circ \tanh\left(c_t\right). \end{aligned} \tag{8}$$

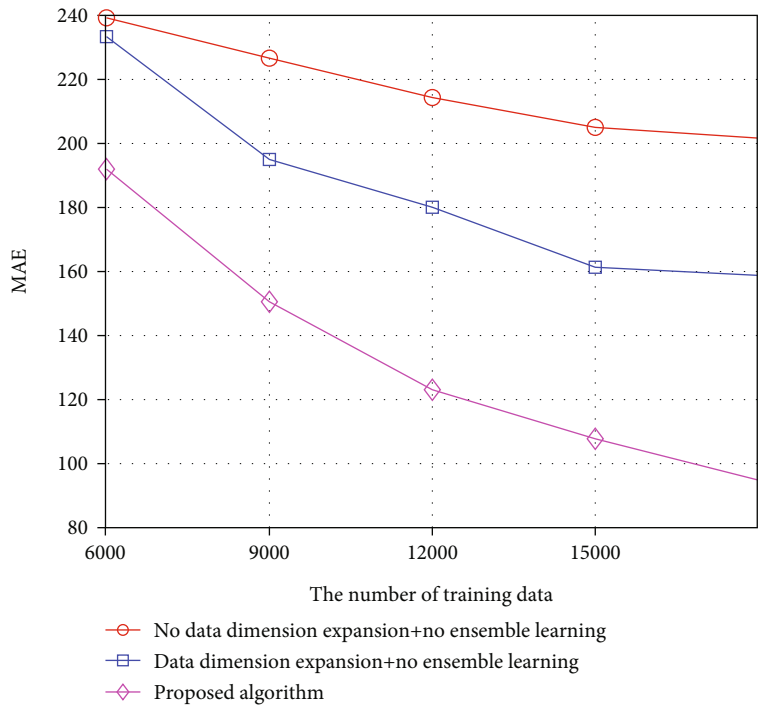

Figure 14: MAE comparison of different algorithms.

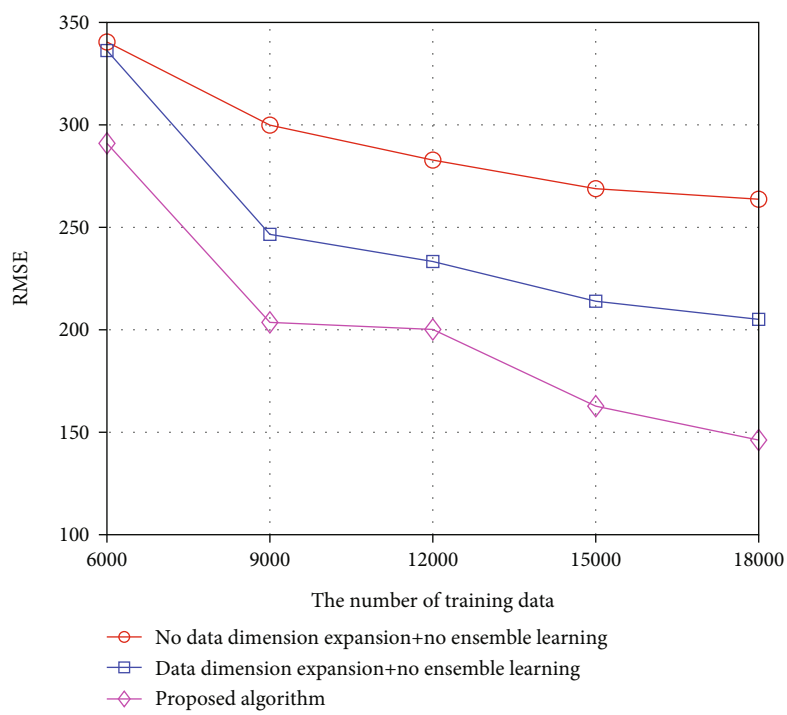

Figure 15: RMSE comparison of different algorithms.

where σ is sigmoid activation function; $\circ$ is the Hadamard product; x_t and h_t are described as the input and output of the current node; W_{xi}, W_{hi}, W_{xf}, and W_{hf} represent weight matrix; b_i, b_f, b_o, and b_c are the biased values; i_t, f_t, and o_t describe the results of input gate, output gate, and forget gate, respectively; g_t is the update condition; and x_t is the data input.

Second, the regression learning using ensemble learning framework is proposed. As we all know, an ensemble with a

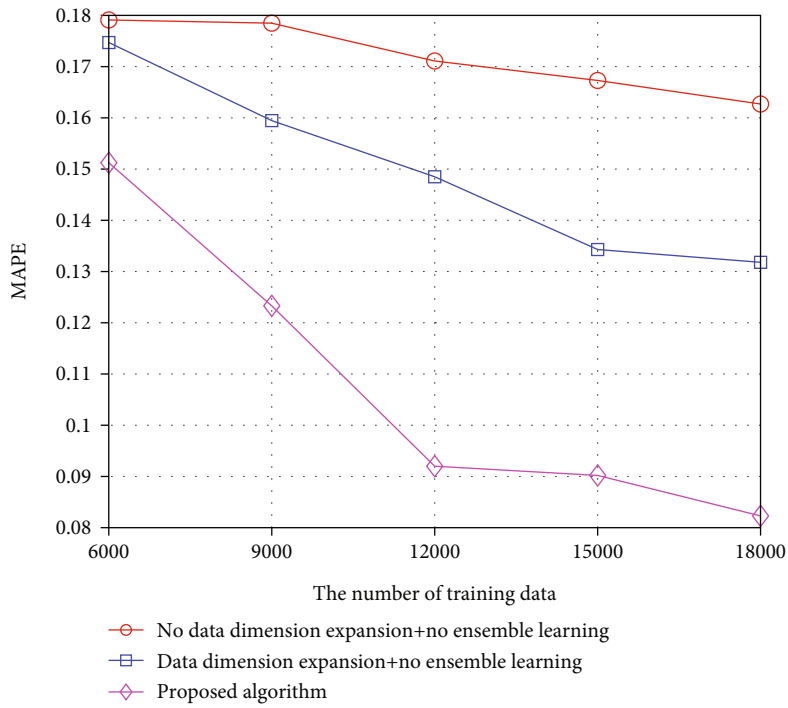

Figure 16: MAPE comparison of different algorithms.

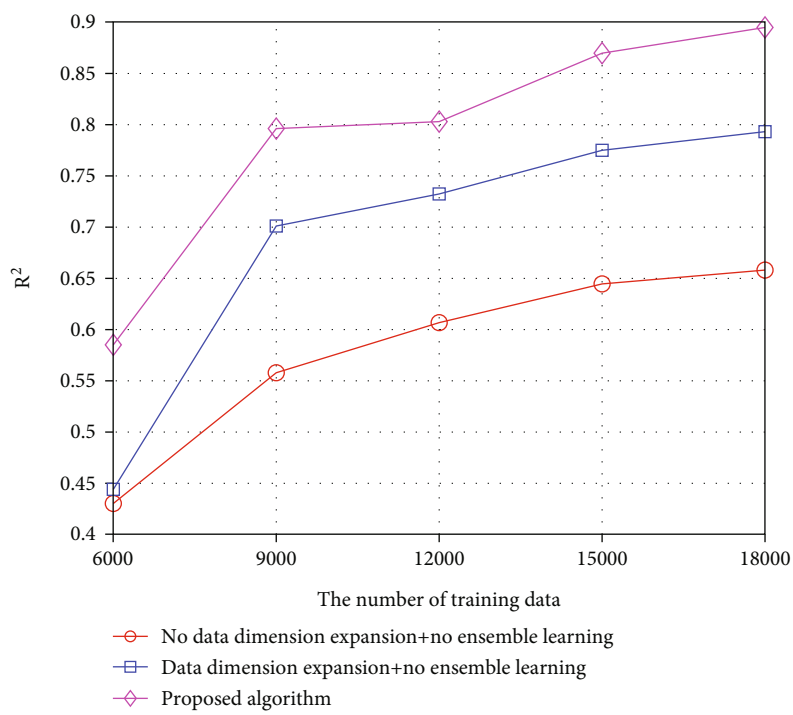

Figure 17: R^2 comparison of different algorithms.

number of sublearners has much stronger generalization ability than that of sublearners. Sublearners are usually generated from training data by a basic learning algorithm such as neural network, SVM, or other machine learning approaches. The diversity of each sublearner is vital to training performance of ensemble learning. Therefore, most ensemble methods use some effective strategies to improve the diversity of sublearners [23, 24]. Three main kinds of ensemble learning contain Adaboost, bagging, and boosting. As shown in Figure 7, by the data normalization and Hampel filter preprocessing in Section 3.1, the obtained fingerprint is used for data dimension expansion and regression learning. For each sublearner, the random matrix is generated at first and then the LSTM is used for regression learning. The task of learning is to obtain the

optimal element of random matrix and the parameters of LSTM network. At last, the feature extraction network with optimal element-based random matrix and the load forecasting model is given. In the offline phase, more sublearners are used for regression learning.

Figure 8 shows the proposed framework of LSTM network. It can be seen that it contains two LSTM layers, one dropout layer, one full connection (FC) layer, and RELU layer. Both function and parameters of each layer are described as follows:

(1) LSTM layer: for the first layer, the length of the state vector unit is 8, the time stride is 1, and the activation function is tanh. For the second LSTM layer, the length of the state vector unit is 16 and the time stride is 1

(2) Dropout layer: the aim of this layer is to reduce the number of actual training parameters by disconnecting neural network randomly. In this paper, the parameter is chosen as 0.1

(3) FC layer: in this layer, it can map the feature from one space to another. The activation function is chosen as RELU

(4) RELU layer: the aim of this layer is to mitigate the effect of overfitting

At last, the weight parameter is chosen for online forecasting data fusion. In this paper, the weight parameter is determined with the offline training error. If the offline training error of the sublearner is small, the corresponding weight parameter is larger. Otherwise, the weight parameter is small. For ith sublearner, the weight parameter can be described as

$$w_i = \frac{1/e_i}{\sum_i 1/e_i}, \tag{9}$$

where e_i is the training error of the ith sublearner.

Note that in the proposed offline training, the random matrix is chosen as the feature extraction network. The feature extraction network and regression learning network are combined with each other for offline training. Thus, the performance of offline phase can be improved.

4. Online Phase Description

In this section, when the meteorological data and time information are obtained, the load forecasting model is used for load forecasting. According to the block diagram shown in Figure 9, the load forecasting process is described as follows:

First, based on the obtained time information and meteorological data, the data preprocessing proposed in offline phase is used to construct the fingerprint by normalization and Hampel filtering. Then, the fingerprint is chosen as the input data for each load forecasting model. At last, the final load is estimated by the linear weighting method which is given by

Figure 18: The figure of raspberry pi.

$$\hat{g} = \sum_i w_i g_i, \tag{10}$$

where g_i is the intermediate load forecasting of the ith load forecasting model.

5. Experiment Results and Performance Analysis

5.1. Experiment Parameter and Environment. In the experiment, the training data are chosen for a community of Suzhou, Jiangsu Province. All the measurement data are collected with the time interval of 15 min in 24 hours. The procedures are based on Windows 10 operating system Python 3.7. The pandas, numpy, and matplotlib library routines in Anaconda and Keras training framework are chosen for offline training.

5.2. Performance Evaluation Index. In this paper, the mean absolute error (MAE), mean absolute percentage error (MAPE), root mean square error (RMSE), and determinate coefficient (R^2) are chosen for performance evaluation which are shown in (11)–(14). The above performance evaluation indexes describe the forecasting performance from different aspects. The MAE is defined as the average absolute error between the predicted value and the observed value. The MAPE is the percentage value description of the MAE. The RMSE represents the standard deviation of the difference between the predicted value and the observed value. The determination coefficient is used to evaluate the fitting degree of regression model coefficients. The higher the value is, the better the model is.

$$\mathrm{MAE} = \frac{1}{N}\sum_{n=1}^{N}|\hat{q}_n - q_n|, \tag{11}$$

$$\mathrm{MAPE} = \frac{100\%}{N}\sum_{n=1}^{N}\left|\frac{\hat{q}_n - q_n}{q_n}\right|, \tag{12}$$

$$\mathrm{RMSE} = \sqrt{\frac{\sum_{n=1}^{N}(\hat{q}_n - q_n)^2}{N}}, \tag{13}$$

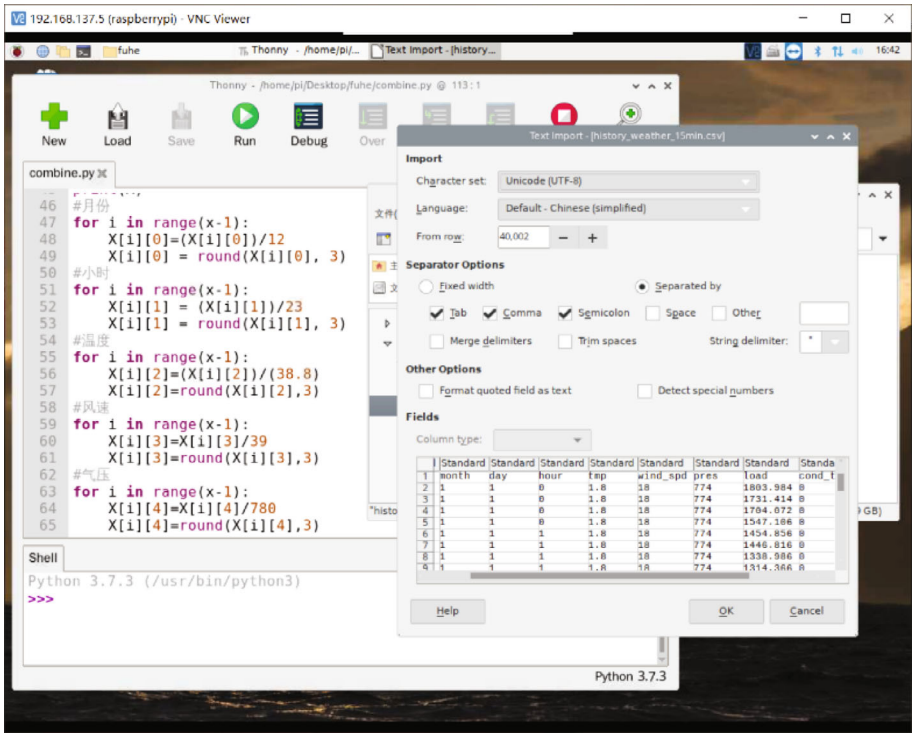

Figure 19: The description of testing data import.

$$R^2 = \frac{\sum_{n=1}^{N}(\hat{q}_n - \bar{q})^2}{\sum_{n=1}^{N}(q_n - \bar{q})^2}, \tag{14}$$

where q_n and $\hat{q}_n$ describe the true and forecasting of the load, $\bar{q}$ is the mean of the load forecasting, and N is the number of load to be forecasting.

5.3. Performance Description of the Proposed Algorithm

5.3.1. The Description of Training Performance. In this experiment, the parameter of the running computer is given as follows: CPU—AMD R7-5800H, GPU—Nvidia RTX 3050 4G, Memery—16G, and software platform—Pycharm (Python 3.9.7)+TensorFlow 2.1.0+Keras 2.3.1. There are 18000 measurements for the experiment where the ratio between training data and testing data is 0.8 : 0.2. Figure 10 shows the training performance of the proposed algorithm, where the parameter of data dimension expansion is 16. We can find that when the number of iterations increases, the MSE of load forecasting will gradually decrease. Taking the iteration number is 80 as an example, the MSE approaches the minimum value of 0.032 which means the loss function converges. Therefore, under this iterative condition, the load forecasting model obtained from offline learning can be used for online prediction estimation.

5.3.2. Performance Description of the Proposed Algorithm. In this section, the forecasting performances of the proposed algorithm with different parameters are described. Taking the number of training data as 18000 as an example, Figure 11 illustrates the true and forecasting load under different times, when the parameter of data dimension expansion is 16 and the number of LSTM is 2. It can be seen that under different time and meteorological data conditions, the load is changed dramatically, but the load forecasting can be also close to the actual value no matter how the actual load changes. In order to describe the algorithm performance more clearly, Figures 12 and 13 show the statistical error of the load forecasting. When the number of training data increases, the forecasting error will decrease and the forecasting performance can be improved. From the figures, when the number of training data is 18000, the MAE and RMSE are only 94.87 and 146.19, respectively. If the number of training data is more than 9000, the parameter R^2 is close to or larger than 0.8. Therefore, through the statistical analysis, it can be concluded that the proposed algorithm can fully satisfy for practical application.

Table 1 describes the statistical error analysis with different numbers of LSTM, when the number of training data is 18000. As expected, when the number of LSTM increases, the load forecasting performance can be improved dramatically. Thus, without considering the training time cost, it is a better method to increase number of LSTM for performance improvement.

5.4. Performance Comparison. In this section, there are two existing load algorithms: (1) the training data is straightly used for training with LSTM (no data dimension expansion+no ensemble learning), and (2) the training data dimension is expanded at first, and then the LSTM is used for training (data dimension expansion+no ensemble learning) chosen for algorithm comparison. Figures 14–17 describe the statistical error comparison of different

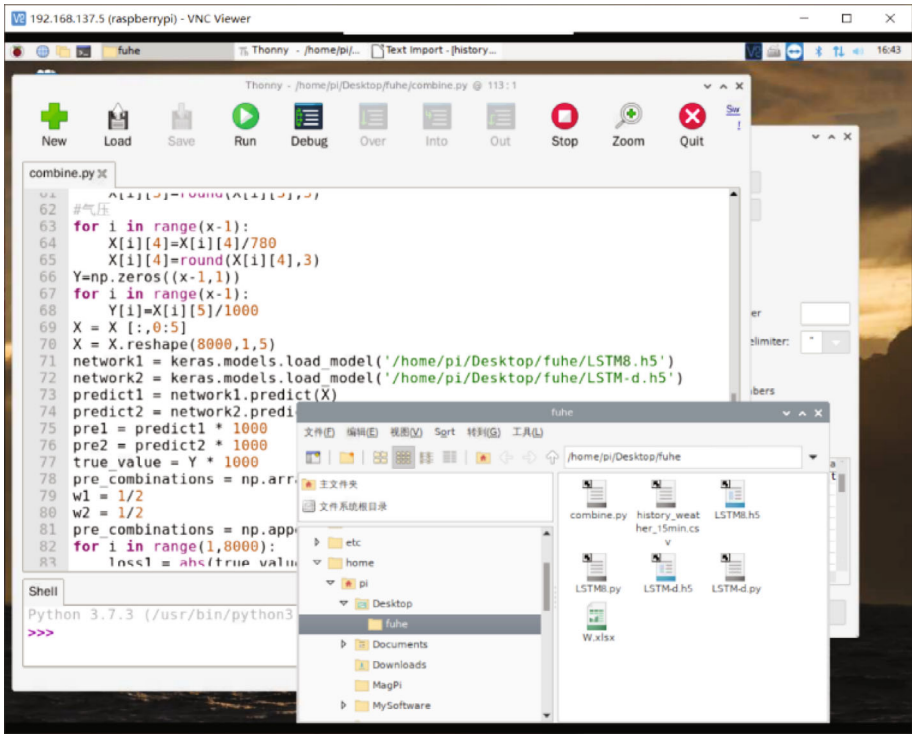

Figure 20: The description of load forecasting model import.

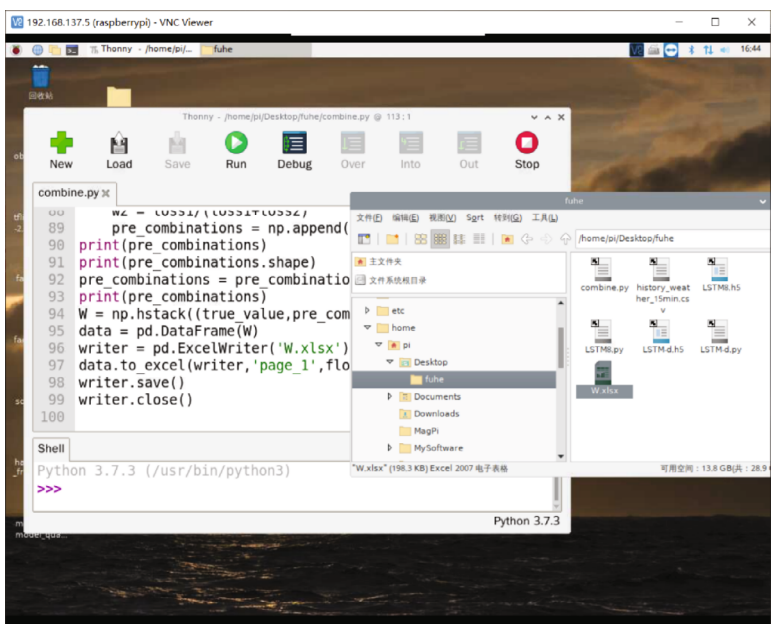

Figure 21: The description of load forecasting save.

algorithms, respectively. From the experiment results, it can be seen that the load forecasting performance of all three algorithms becomes better, when the number of training data increases. Taking 15000 training data as an example, the MAE, RMSE, MAPE, and R^2 of the algorithm are 107.76, 162.73, 0.09, and 0.87, respectively. However, the four error statistical parameters of the data dimension expansion+no ensemble learning method, which the performance is more close to the proposed algorithm, are 161.34, 213.94, 0.13, and 0.78. Thus, according to the statistical error analysis, the proposed algorithm has the best load forecasting performance among three methods. The reason can be concluded as follows. The data dimension expansion technology can describe the feature of training data more clearly. Moreover, the ensemble learning can improve the efficiency of offline learning.

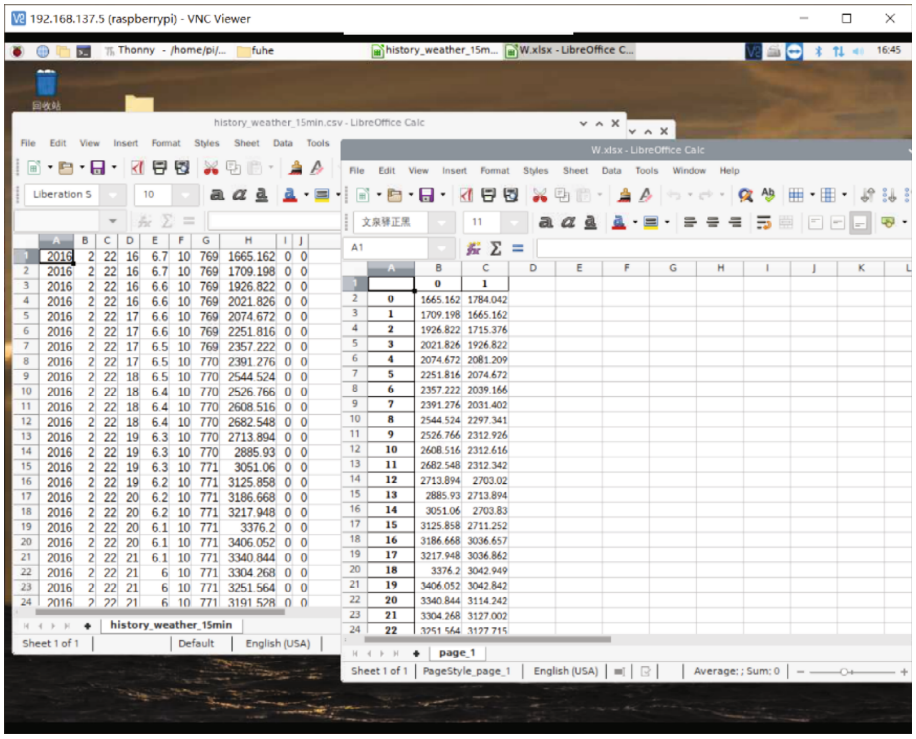

Figure 22: The output description of the load forecasting.

5.5. Hardware Transplantation Experiment. In order to show the performance of the proposed algorithm for practical application, in this paper, the raspberry pi shown in Figure 18 is used for hardware transplantation [25]. First, the deep learning tools, such as Tensorflow and Keras, are installed, and then, all the libraries for the experiment are configured. In the following, the transplantation are described by the trained load forecasting model and testing data.

According to Figure 19, the testing data set "history_weather_15min.csv" is imported in raspberry pi. The month, hour, wind speed, temperature, and pressure in the testing data are chosen for the load forecasting. Then, the obtained load forecasting model in the offline phase is loaded in the hardware platform which is shown in Figure 20. At last, the actual load and load forecasting are written in files "W.xlsx." From the output shown in Figures 21 and 22, columns B and C describe the actual load and load forecasting, respectively.

6. Conclusions

In this article, a deep learning-based loading forecasting algorithm for power IOT is proposed. In the proposed algorithm, two data preprocessing, min-max normalization and hampel filter, are used to construct the fingerprint of the training data. Then, matrix multiplication method is proposed to extract the fingerprint feature by dimension expansion. Finally, the ensemble learning using multiple LSTM networks is proposed for offline training and obtain power load forecasting models. In the proposed algorithm, the data dimension expansion can obtain more features for training data. The ensemble learning using LSTM can make fully use of the timing sequence of training and improve the generalization performance. The experiment is carried out to evaluate the forecasting performance. Through the experiment results, it can be seen that the proposed algorithm has better load forecasting performance than chosen existing approaches.

Data Availability

The data used to support the findings of this study are available from the corresponding author upon request.

Conflicts of Interest

The authors declare that they have no conflicts of interest.

Acknowledgments

This work is supported by the National Natural Science Foundation of China (No. 61771256).

References

[1] J. H. Enslin, "Power system infrastructure: do we face a complete power-electronics-based power system and energy-storage infrastructure?," *IEEE Power Electronics Magazine*, vol. 3, no. 2, pp. 42–45, 2016.

[2] F. Rahimi, A. Ipakchi, and F. Fletcher, "The changing electrical landscape: end-to-end power system operation under the transactive energy paradigm," *IEEE Power and Energy Magazine*, vol. 14, no. 3, pp. 52–62, 2016.

[3] L. Wang, L. Zhang, C. Xu, H. Wu, Y. Li, and H. Sun, "Three-dimensional maturity model of regional power users against the background of the ubiquitous power internet of things," *IEEE Access*, vol. 8, pp. 20215–20223, 2020.

[4] Z. Zhai, L. Jia, Y. Wang, Y. Ma, W. Jing, and Z. Zhang, "Research on ubiquitous power internet of things architecture," in *2019 IEEE 3rd Conference on Energy Internet and Energy System Integration (EI2)*, pp. 435–439, Changsha, China, 2019.

[5] Q. Wang and Y. G. Wang, "Research on power internet of things architecture for smart grid demand," in *2018 2nd IEEE Conference on Energy Internet and Energy System Integration*, pp. 1–9, Beijing, China, 2018.

[6] M. Imani and H. Ghassemian, "Electrical load forecasting using customers clustering and smart meters in internet of things," in *2018 9th International Symposium on Telecommunications (IST)*, pp. 113–117, Tehran, Iran, 2018.

[7] J. Li, Y. Ren, S. Fang, K. Li, and M. Sun, "Federated learning-based ultra-short term load forecasting in power internet of things," in *2020 IEEE International Conference on Energy Internet (ICEI)*, pp. 63–68, Sydney, NSW, Australia, 2020.

[8] A. Y. Saber and T. Khandelwal, "IoT based online load forecasting," in *2017 Ninth Annual IEEE Green Technologies Conference (GreenTech)*, pp. 189–194, Denver, CO, USA, May 2017.

[9] W. Charytoniuk, M. S. Chen, and P. Van Olinda, "Nonparametric regression based short-term load forecasting," *IEEE Transactions on Power Systems*, vol. 13, no. 3, pp. 725–730, 1998.

[10] W. Christiaanse, "Short-Term load forecasting using general exponential smoothing," *IEEE Transactions on Power Apparatus and Systems*, vol. PAS-90, no. 2, pp. 900–911, 1971.

[11] S.-J. Huang and K.-R. Shih, "Short-term load forecasting via ARMA model identification including non-Gaussian process considerations," *IEEE Transactions on Power Systems*, vol. 18, no. 2, pp. 673–679, 2003.

[12] J. Che and J. Wang, "Short-term load forecasting using a kernel-based support vector regression combination model," *Applied Energy*, vol. 132, pp. 602–609, 2014.

[13] S. Singh, S. Hussain, and M. A. Bazaz, "Short term load forecasting using artificial neural network," in *2017 Fourth International Conference on Image Information Processing (ICIIP)*, pp. 1–5, Shimla, India, December 2017.

[14] Z. Deng, B. Wang, Y. Xu, T. Xu, C. Liu, and Z. Zhu, "Multi-scale convolutional neural network with time-cognition for multi-step short-term load forecasting," *IEEE Access*, vol. 7, pp. 88058–88071, 2019.

[15] H. Shi, M. Xu, and R. Li, "Deep learning for household load forecasting-a novel pooling deep RNN," *IEEE Transactions on Smart Grid*, vol. 9, no. 5, pp. 5271–5280, 2018.

[16] M. S. Hossain and H. Mahmood, "Short-term load forecasting using an LSTM neural network," in *2020 IEEE Power and Energy Conference at Illinois (PECI)*, pp. 1–6, Champaign, IL, USA, February 2020.

[17] M. Jawad, M. S. A. Nadeem, S. Shim et al., "Machine learning based cost effective electricity load forecasting model using correlated meteorological parameters," *IEEE Access*, vol. 8, pp. 146847–146864, 2020.

[18] S. Bhowmik, B. Jelfs, S. P. Arjunan, and D. K. Kumar, "Outlier removal in facial surface electromyography through Hampel filtering technique," in *2017 IEEE Life Sciences Conference (LSC)*, pp. 258–261, Sydney, NSW, Australia, 2017.

[19] N. Singh and P. Singh, "Exploring the effect of normalization on medical data classification," in *2021 International Conference on Artificial Intelligence and Machine Vision (AIMV)*, pp. 1–5, Gandhinagar, India, 2021.

[20] H. Rizk, M. Torki, and M. Youssef, "CellinDeep: robust and accurate cellular-based indoor localization via deep learning," *IEEE Sensors Journal*, vol. 19, no. 6, pp. 2305–2312, 2019.

[21] G. I. Webb and Z. Zheng, "Multistrategy ensemble learning: reducing error by combining ensemble learning techniques," *IEEE Transactions on Knowledge and Data Engineering*, vol. 16, no. 8, pp. 980–991, 2004.

[22] W. Kong, Z. Y. Dong, Y. Jia, D. J. Hill, Y. Xu, and Y. Zhang, "Short-term residential load forecasting based on LSTM recurrent neural network," *IEEE Transactions on Smart Grid*, vol. 10, no. 1, pp. 841–851, 2019.

[23] F. Huang, G. Xie, and R. Xiao, "Research on ensemble learning," in *2009 International Conference on Artificial Intelligence and Computational Intelligence*, pp. 249–252, Shanghai, China, 2009.

[24] N. Alon, A. Gonen, E. Hazan, and S. Moran, "Boosting simple learners," in *Proceedings of the 53rd Annual ACM SIGACT Symposium on Theory of Computing*, pp. 481–489, New York, NY, USA, 2021.

[25] A. Nadjaran Toosi, J. Son, and R. Buyya, "CLOUDS-Pi: a low-cost raspberry-pi based micro data center for software-defined cloud computing," *IEEE Cloud Computing*, vol. 5, no. 5, pp. 81–91, 2018.

Hindawi
Journal of Sensors
Volume 2023, Article ID 9850274, 1 page
https://doi.org/10.1155/2023/9850274

Retraction

Retracted: Subdivision of Artistic Objectives of Oil Painting Creation under the Evaluation of Deep Learning Model

Journal of Sensors

Received 8 August 2023; Accepted 8 August 2023; Published 9 August 2023

This article has been retracted by Hindawi following an investigation undertaken by the publisher [1]. This investigation has uncovered evidence of one or more of the following indicators of systematic manipulation of the publication process:

(1) Discrepancies in scope
(2) Discrepancies in the description of the research reported
(3) Discrepancies between the availability of data and the research described
(4) Inappropriate citations
(5) Incoherent, meaningless and/or irrelevant content included in the article
(6) Peer-review manipulation

The presence of these indicators undermines our confidence in the integrity of the article's content and we cannot, therefore, vouch for its reliability. Please note that this notice is intended solely to alert readers that the content of this article is unreliable. We have not investigated whether authors were aware of or involved in the systematic manipulation of the publication process.

Wiley and Hindawi regrets that the usual quality checks did not identify these issues before publication and have since put additional measures in place to safeguard research integrity.

We wish to credit our own Research Integrity and Research Publishing teams and anonymous and named external researchers and research integrity experts for contributing to this investigation.

The corresponding author, as the representative of all authors, has been given the opportunity to register their agreement or disagreement to this retraction. We have kept a record of any response received.

References

[1] M. Wu, "Subdivision of Artistic Objectives of Oil Painting Creation under the Evaluation of Deep Learning Model," *Journal of Sensors*, vol. 2022, Article ID 6825863, 6 pages, 2022.

Hindawi
Journal of Sensors
Volume 2022, Article ID 6825863, 6 pages
https://doi.org/10.1155/2022/6825863

Research Article

Subdivision of Artistic Objectives of Oil Painting Creation under the Evaluation of Deep Learning Model

Meishuang Wu

Arts of Department, Xi'an Jiaotong University City College, Xi'an 710018, China

Correspondence should be addressed to Meishuang Wu; jyiyi.1985.12.10@stu.xjtu.edu.cn

Received 24 March 2022; Accepted 12 May 2022; Published 9 June 2022

Academic Editor: Han Wang

In order to fully segment and classify the artistic objectives of painting and realise the needs of automatic classification and retrieval of painting by computer, this paper proposes to establish convolution neural network with dual core compression activation module and deep separation convolution. The DKSE module is constructed based on the structural features of SKNet. SKNet extracts the overall image and detail features, SENet enhances the channel features. Using DKSE module and depth separable convolution, a convolution neural network is established to classify paintings. DKSE module can effectively improve the classification performance of the model, fully extract the overall and local detail features of oil painting images, and provide better classification accuracy than the traditional network model.

1. Introduction

In recent years, with the rapid development of the digitisation of oil paintings, how to establish and manage digital libraries and digital museums of oil paintings? It has become a hot research issue at present, and the processing technology of the images of written oil paintings is the key to this research problem. How to discover the digital laws behind these paintings and how to effectively analyse, identify, and classify the authors and artistic styles of oil paintings are increasingly becoming hot research issues [1].

There is a large body of literature on the use of computer technology to analyse and study art paintings, but the following problems still exist in the study of oil paintings:

(1) The existing results in art painting mainly simulate natural images in oil and pastel painting or analyse art styles for western paintings such as oil painting [2]. As a unique art form, Chinese painting has a very different mood and flavour compared to other art styles (such as oil painting, cartoon, and chalk painting), so some of the existing research on Western painting cannot be directly applied to the analysis of oil painting

(2) At present, there are only a few studies on oil painting, but the main ones are as follows: [3] extracted the overall and local features and proposed the entropy balance (fusion) algorithm to classify the authors of Chinese paintings. [4] studied the different depth information features of paintings at different scales and frequency bands in the wavelet domain in order to classify paintings. [5] designed a related algorithm to classify the paintings of Shen Zhou, Tang Yin, Zhang Daqian, and other Chinese painting artists. The algorithm first extracts wavelet features from the paintings and designs a Mixtures of Hidden Markov Models (MHMM) to classify the painters for the study. [6] proposed an algorithm for classifying Chinese oil paintings into two categories, namely, Chinese painting and brushwork, by first extracting the underlying features such as colour and texture and then using a support vector machine for classification. [7] proposed the adaptive selection of composite features and the optimisation of the description of ink painting styles. It also described the style of Chinese painting by extracting multiple underlying heterogeneous visual features and made classification predictions for Chinese painting

authors. [8] proposed a colour conversion algorithm to convert photographs into Chinese ink paintings. Most of the current work on Chinese paintings has focused on content-based image analysis and retrieval (content-based image analysis), but the following problems exist

(1) There are limitations to the adaptability of any image content features. For example, the stroke of a horse is certainly different from the stroke of a leaf [9], and it would be blinding to analyse the direction and force distribution of the stroke without considering the conditions under which each stroke is produced

(2) Existing content-based studies consider all the information in the painting, which makes the focus of the study more fragmented and susceptible to interference from noisy information [10]

In response to the above problems, this paper defines the artistic objects in Chinese painting as "artistic objects," such as flowers, birds, figures, and trees in Chinese painting, which are relatively stable units used by painters to express artistic forms and emotions and are the carriers of artistic style features in paintings. In turn, this paper proposes a framework for the interactive segmentation and identification of the main artistic objects in Chinese painting, in order to digitally quantify and analyse the artistic objects and extract the high-level semantic information that best reflects the artist's artistic style [11].

Firstly, a simple linear iterative clustering (SLIC) algorithm is proposed to segment the superpixel grid based on the degree of difference in colour and position between pixels; secondly, a maximum similarity region fusion algorithm (MSRMAO) is proposed to segment the art targets interactively, i.e., to segment the whole painting into a series of art targets, such as horses and figures, in order to extract the relatively Finally, a support vector machine based fusion algorithm is proposed to learn and recognise the extracted art targets, thus realising the analysis and recognition of artistic style of painting based on art targets.

2. Convolutional Neural Network-Based Classification of Writing Oil Paintings

2.1. DKSE Modules. The dual core compression activation (DKSE) module combines the features of the SE module and the SK module to better enhance the overall style and local detail of the extracted paintings and consists of four submodules, split, squeeze, excitation, and scale, as shown in Figure 1, with the expression

$$\mathbf{V} = \sum_{i=1}^{N} \mathbf{U}_i \cdot F_{\mathrm{ex}}\left(F_{\mathrm{sq}}\left(F_{\mathrm{gp}}(\mathbf{U})\right)\right), \tag{1}$$

where $\mathbf{U}$ is the fused feature map on the DKSE module branch, $F_{\mathrm{gp}}(-)$ is the global average pooling (GAP) operation, $F_{\mathrm{sq}}(-)$ is the channel compression process, $F_{\mathrm{ex}}(-)$ is the channel feature activation operation, N is the number of DKSE module branches, and $N = 2$ in this paper.

(1) *Submodule Split*. For an intermediate Eigenmap $x \in \mathbf{R}^{H' \times W' \times C'}$, a convolutional mapping uses two convolutional kernels of different sizes, i.e.,

$$\begin{aligned} F_1 &: \mathbf{X} \longrightarrow \mathbf{U}_1 \in \mathbf{R}^{H \times W \times C}, \\ F_2 &: \mathbf{X} \longrightarrow \mathbf{U}_2 \in \mathbf{R}^{H \times W \times C}, \end{aligned} \tag{2}$$

where H', W', and C' denote the height, width, and number of channels of the feature map $\mathbf{X}$, respectively. F_1 and F_2 are the mapping processes processed by convolutional kernel convolution mapping, batch normalization (BN), and ReLU excitation function, respectively. H, W, and C denote the height, width, and number of channels of the feature map after and operations, respectively. W and C denote the height, width, and number of channels of the feature map after operations F_1 and F_2, respectively. Convolution filters $\mathbf{w} = [w_1, w_2, \cdots, w_c, \cdots, w_C]$, where w_c denotes the parameters of the cth filter. The convolution mapping formula for each filter on the ith branch for the intermediate feature map $\mathbf{X}$ is

$$\begin{aligned} \mathbf{u}'_{ic} &= \mathbf{w}_{ic} \times \mathbf{X} = \sum_{k=1}^{c'} \mathbf{w}_{ic}^{k} \times \mathbf{X}^{k} + b_{ic}, \\ \mathbf{u}_{ic} &= \delta\left(\mathbf{u}'_{ic}\right)\Big), i = 1, \cdots, N, \end{aligned} \tag{3}$$

where c' denotes the number of channels in the filter and feature map, b_{ic} denotes bias, $\aleph(.)$ denotes batch normalisation, $\delta(\mathbf{X}') = \max\,(0, \mathbf{X}')$ is the ReLU function operation, and $\mathbf{X}' = \aleph(\mathbf{u}'_{ic})$, $\mathbf{U}_i = [\mathbf{u}_{i1}, \mathbf{u}_{i2}, \cdots, \mathbf{u}_{iC}]$.

(2) After the split operation, two new feature maps $\mathbf{U}_1$ and $\mathbf{U}_2$ are obtained, and the feature information of the two feature maps is fused by summing the corresponding elements, i.e.

$$\mathbf{U} = \mathbf{U}_1 + \mathbf{U}_2. \tag{4}$$

The fused feature map $\mathbf{U}$ combines the feature information from $\mathbf{U}_1$ and $\mathbf{U}_2$ and uses global average pooling to pool the global spatial feature nodes in each feature channel. The global average pooling compresses the feature map $\mathbf{U}$ space information into C channel descriptors, generating a statistic $\mathbf{S} \in \mathbf{R}^C$ that describes the feature channel information. The cth element of the statistic $\mathbf{S}$ is calculated by compressing the $\mathbf{U}$ space information as

$$\mathbf{S}_c = F_{\mathrm{gp}}(\mathbf{U}_c) = \frac{1}{H \times W} \sum_{i=1}^{H} \sum_{j=1}^{W} \mathbf{U}_c(i, j). \tag{5}$$

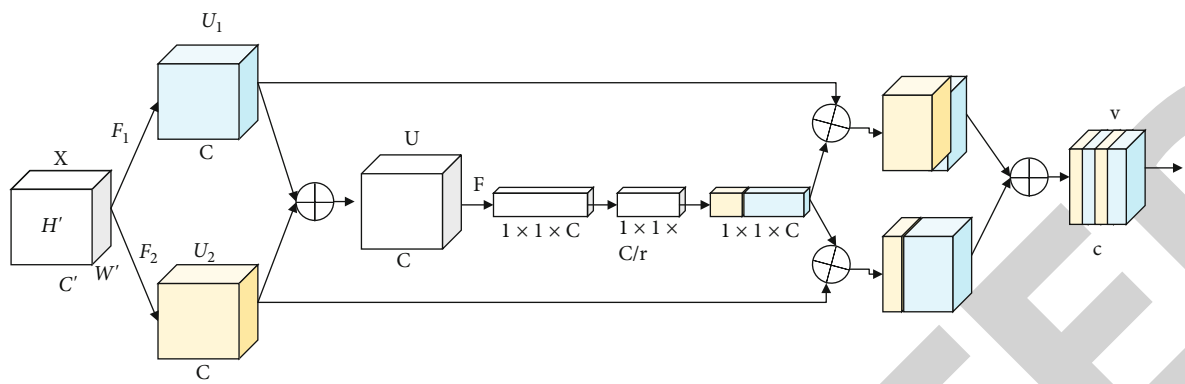

Figure 1: DKSE module.

(3) The submodule excitation is used to enhance the style features extracted from each type of painting and to reduce the information of the less useful features, the channel dimension of the globally averaged pooled feature map is reduced to $1/r$ of the original channel by a 1×1 convolution operation, r is the rate of decline, then after BN processing and ReLU function activation, the number of channels is increased to the original number by a 1×1 convolution operation, and finally, the normalized weights between (0, 1) are obtained through a Sigmoid gate mechanism to obtain the stylistic feature information of each type of written oil painting

$$\mathbf{Z} = F_{\mathrm{ex}}(\mathbf{S}) = \sigma\left(\mathbf{W}_2 F_{\mathrm{sq}}(\mathbf{S})\right) = \sigma(\mathbf{W}_2 \delta(\aleph(\mathbf{W}_1 \mathbf{S}))). \tag{6}$$

(4) The weights of $\mathbf{Z}$, obtained by squeeze and excitation operations, are the image features filtered by the primary features and suppressed by the secondary features, weighted and summed with $\mathbf{U}_1$ and $\mathbf{U}_2$, respectively

$$\mathbf{V}_c = \mathbf{u}_{1c} \cdot \mathbf{Z}_c + \mathbf{u}_{2c} \cdot \mathbf{Z}_c. \tag{7}$$

2.2. Convolutional Neural Network Structure. A CNN was built using the MobileNetV1 network structure, using depth-separable convolution and the DKSE module, with the first layer using null convolution to extract features from the original painting. Compared with normal convolution, the cavity convolution has a larger perceptual field than normal convolution and can maintain more internal data structure and information of the original painting. The depthwise convolution consists of a depthwise convolution and a pointwise convolution, and the DKSE module embedded in the depthwise convolution is given by

$$\mathbf{Y}(\mathbf{X}) = [Y_1.Y_2.Y_3](\mathbf{X}), \tag{8}$$

where $Y_1 : \mathbf{R}^{H' \times W' \times C'} \longrightarrow \mathbf{R}^{H/s \times W'/s \times C'}$ is the depth convolution operation, $Y_2 : \mathbf{R}^{H/5 \times W/s \times C'} \longrightarrow \mathbf{R}^{\mathbf{H}^{-} \times W/s \times iC'}$ is the point-by-point convolution operation, $Y_3 : \mathbf{R}^{H'/* \times W'/s \times C'} \longrightarrow \mathbf{R}^{H \times W \times C}$ is the DKSE module operation, s denotes the depth convolution to reduce the dimensionality of the feature map, and t denotes the point-by-point convolution to process the number of channels of the feature map. Each deep and point-by-point convolution operation is followed by BN and ReLU excitation function processing.

3. Experimental Results

The content and style representations can be well separated in the convolutional neural network used in this paper's algorithm, so that the two representations can be processed independently to produce new perceptually meaningful images [12]. The following is an image of the effect of the oil painting implemented according to the coding, where we combine different representations of the image content with multiple stylistic representations of the oil painting artwork. The effect of combining different images with various oil paintings is shown in Figure 2.

An influential factor in image stylisation is the ratio of content to style, i.e., α/β. Figure 3 shows a composite image of the content image (d) in Figure 4 stylised by choosing 1×10^{-2}, 1×10^{-4}, and 1×10^{-6} sand drawings, respectively, for α/β. The ratio of content to style $\alpha\,\beta$ decreases sequentially from the three images in Figure 3, i.e., but the content shown is not easily identifiable. A compromise approach is usually used to adjust the ratio between content and style to create a visually more pleasing image.

Another influential factor in image stylisation is the choice of convolutional feature layers. As stated above, style representations are multiscale representations containing multiple layers of neural networks, and the number and location of these layers determine the local scale of style matching, resulting in different visual experiences. Matching style representations to higher layers in the network can keep the local image structure at an increasing scale, leading to a smoother and more sustained visual experience [13]. As a result, stylised images typically match style representations to the highest layer in the network. To analyse the effect of using different layers to match content features, we set the other parameters to the same number (1×10^{-4}) to style the images for transfer, as shown in Figure 3. When

Figure 2: Synthesis of images of different contents with stylised sand drawings.

Conv1_2 Layer (a) Conv3_2 (b) Conv5_2 (c)

Figure 3: Effect of matching different content feature layers.

(a) (b) (c)

Figure 4: Graph of the effect of different ratios of α to β.

matching content on the lower layers of the network, the algorithm matches most of the detailed pixel information in the photo, and the resulting sand painting image looks and feels like a mixture of textures from the artwork on the picture (e.g., Conv1_2); in Figure 4(b) which is Conv3_2, when matching content features on the higher layers of the network, the detailed pixel information of the photo is not so strongly constrained, and the content of the building and with the sand painting textures are blended together (e.g., Conv5_2), and the fine structure of the image such as

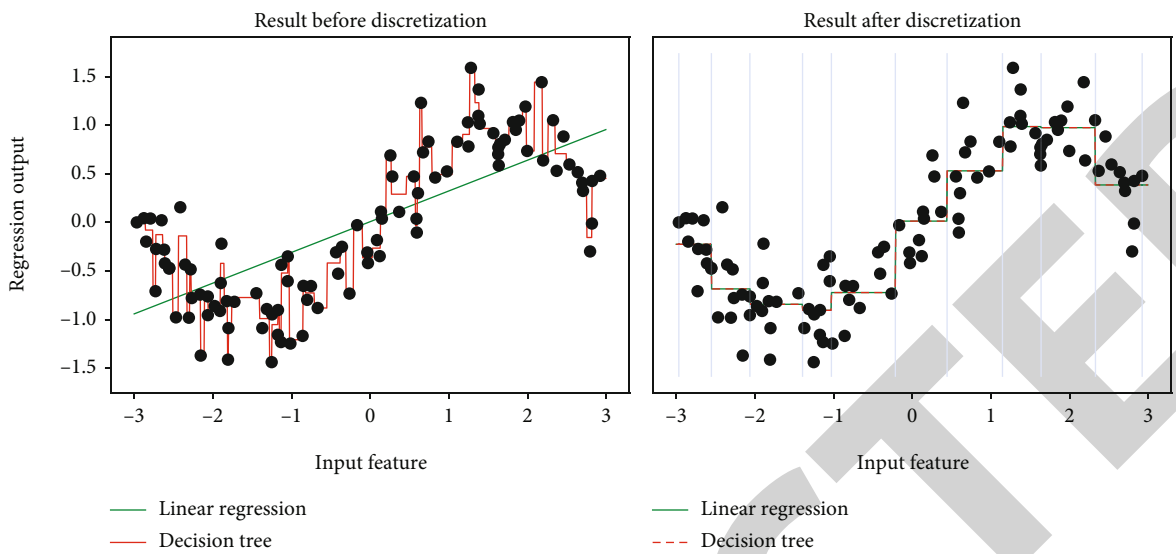

Figure 5: Different classification effects.

edges and colours change considerably, accentuating the stylistic features even more.

In recent years, there have been two commonly used methods for generating superpixels: algorithms based on graph theory and algorithms based on gradient ascent. The former is a constructed energy function minimisation problem, where the image is constructed as a weighted undirected graph, where the pixel points in the image correspond to graph nodes, the adjacency of two pixels represents an edge of the graph, and the weight of an edge is the degree of difference between neighbouring pixels. The graph is partitioned in such a way that the local similarity of the partitioned subgraphs is maximised, thus generating a super image. Algorithms such as SuperLattice [14], EGS [15], and Ncut [16] are included. The basic idea of the latter is to start from the initial seed points and cluster the pixels using certain criteria at each iteration until a stable state is reached, thus generating super pixels, including MeanShift [17], TurboPixel [18], and SLIC [19, 20] (simple linear iterative clustering). As shown in Figure 5, this algorithm uses a greedy strategy to segment the image using horizontal and vertical paths at a time at the minimum of the boundary cost map to obtain superpixels. This method maintains a regular image topology and produces a regular grid of superpixels with good segmentation accuracy and stability, while the number of superpixels can be artificially specified. However, the superiority of the superpixels produced by this method is highly dependent on the quality of the boundary map of the image [21–23].

As shown in Figure 6, the algorithm in this paper is a parameter-free iterative algorithm that converges the centroid to the point of maximum density by means of a probability density function. The method produces regular shaped superpixels that maintain good performance in terms of stability and resilience. However, the method is not fast, has no control over the number of superpixels, and suffers from oversegmentation problems. The level-set method for geometric flow starts by selecting an initial seed point and expands the area of the seed point through a curvature evolution model and a skeletonisation process to obtain grid-like superpixels. The algorithm's runtime is positively correlated with the image size, it can artificially specify the number of generated superpixels, the superpixels are regular in shape and retain the contour structure of the image, and it improves the undersegmentation problem. However, the shape of the generated superpixels is not controllable and does not allow for fast and high quality image segmentation for large resolution images [24].

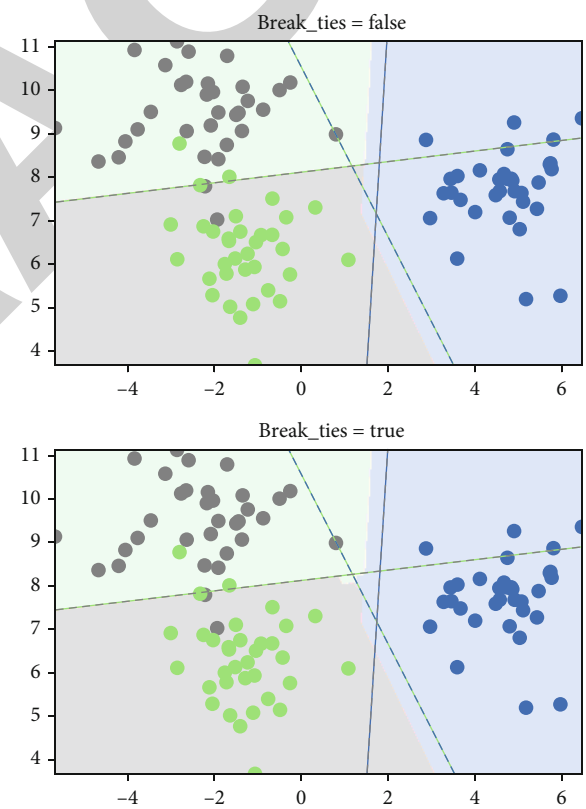

Figure 6: Clustering effect of different schemes.

Hindawi
Journal of Sensors
Volume 2023, Article ID 9848312, 1 page
https://doi.org/10.1155/2023/9848312

Retraction

Retracted: Research on Emergency Logistics Vehicle Route Scheduling and Optimization Method Based on Multi-Intelligent Decision System

Journal of Sensors

Received 19 December 2023; Accepted 19 December 2023; Published 20 December 2023

This article has been retracted by Hindawi following an investigation undertaken by the publisher [1]. This investigation has uncovered evidence of one or more of the following indicators of systematic manipulation of the publication process:

(1) Discrepancies in scope
(2) Discrepancies in the description of the research reported
(3) Discrepancies between the availability of data and the research described
(4) Inappropriate citations
(5) Incoherent, meaningless and/or irrelevant content included in the article
(6) Manipulated or compromised peer review

The presence of these indicators undermines our confidence in the integrity of the article's content and we cannot, therefore, vouch for its reliability. Please note that this notice is intended solely to alert readers that the content of this article is unreliable. We have not investigated whether authors were aware of or involved in the systematic manipulation of the publication process.

Wiley and Hindawi regrets that the usual quality checks did not identify these issues before publication and have since put additional measures in place to safeguard research integrity.

We wish to credit our own Research Integrity and Research Publishing teams and anonymous and named external researchers and research integrity experts for contributing to this investigation.

The corresponding author, as the representative of all authors, has been given the opportunity to register their agreement or disagreement to this retraction. We have kept a record of any response received.

References

[1] C. Ji, S. Liang, and Y. Yu, "Research on Emergency Logistics Vehicle Route Scheduling and Optimization Method Based on Multi-Intelligent Decision System," *Journal of Sensors*, vol. 2022, Article ID 2148785, 15 pages, 2022.

Hindawi
Journal of Sensors
Volume 2022, Article ID 2148785, 15 pages
https://doi.org/10.1155/2022/2148785

Research Article

Research on Emergency Logistics Vehicle Route Scheduling and Optimization Method Based on Multi-Intelligent Decision System

Chenlu Ji,[1,2] Shuyu Liang,[1,2] and Yating Yu[3]

[1]*Data Science Institute, Shandong University, Jinan 250100, China*
[2]*School of Mathematics, Shandong University, Jinan 250100, China*
[3]*Division of Regional and International Education, Kitami Institute of Technology, Hokkaido 090-8507, Japan*

Correspondence should be addressed to Shuyu Liang; liang_sy@email.sdu.edu.cn

Received 14 March 2022; Revised 8 April 2022; Accepted 20 April 2022; Published 8 June 2022

Academic Editor: Han Wang

Logistics distribution vehicle planning is an important issue in logistics transportation activities, and it is also a research hotspot in theoretical circles at home and abroad. At present, many studies have focused on establishing vehicle planning models and optimizing vehicle planning in different environments and have achieved rich results. As an important part of transportation production process, the efficiency of logistics distribution is very important to the whole production process. Especially for emergency logistics, every minute is very critical for emergency situations such as disaster relief. In order to improve the efficiency of emergency logistics, this paper applies multiagent technology to emergency logistics and puts forward an integrated modeling method of enterprise macromodeling, business process mesomodeling, and micromodel design. Using the agent-oriented system development method, an emergency logistics distribution vehicle planning model system is established. The development process of multiagent automatic trading system is described. The results show that it is feasible and effective to use multi-intelligent fuselage technology for emergency logistics distribution vehicle planning and decision-making. The algorithm proposed in this paper has advantages over the container order sequence processing scheme, and the total cost of order acceptance decreases sharply in the initial stage, which shows the practical convergence of the algorithm. The adjacency search method and Tabu search method deal with the calculation of total labor cost, and the Tabu neighborhood search algorithm obtains better results with lower labor cost.

1. Introduction

Logistics industry is developing rapidly in the direction of global integration and computerized operation. Logistics distribution is an important link connecting producers and consumers and plays an increasingly important role in the whole supply chain. With the development of social economy and the continuous improvement of people's demand, logistics distribution gradually has the characteristics of multi-variety, less batch, real time, and customization. A system requires logistics distribution to accurately realize "7R." Therefore, in addition to designing a reasonable and effective vehicle scheduling scheme according to the existing distribution orders, an important problem of logistics distribution is to dynamically form various real-time distribution schemes to meet people's needs under the influence of customers' real needs and random variables, and they need to meet the real and customized needs of real-time logistics distribution customers. As an important part of transportation and production process, logistics distribution is generally considered to include parts, assembly, distribution and other processes. With the rapid development of intensive and integrated logistics, it is necessary to comprehensively consider all aspects of logistics distribution in the research process. Starting with the optimization of logistics distribution system, this paper mainly optimizes the key specific links and technologies [1]. Many scholars believe that the decision of arranging vehicles from logistics distribution is the most important link to optimize logistics distribution system, and it is an indispensable part of the close combination of highly developed intelligent logistics distribution and e-commerce. I think it has attracted the attention of many

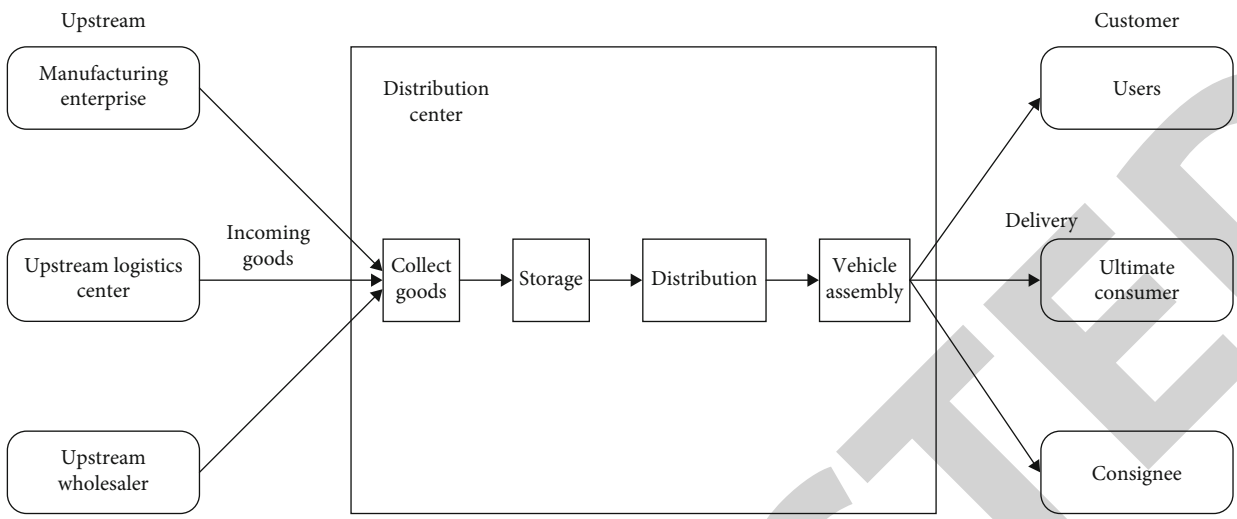

Figure 1: Schematic diagram of general operation flow of logistics distribution.

scholars. The research on intelligent vehicle scheduling technology in foreign countries started earlier and has been widely used in production and life [2]. Relatively speaking, the systematic research on intelligent political decision-making in China's academic circles is still at a critical stage of continuous exploration, which cannot meet the urgent needs of the rapid development of China's transportation industry and logistics industry. Especially in China, the research on intelligent decision-making of real-time logistics distribution vehicle dynamic scheduling is still in its initial stage [3]. In recent years, multiagent technology has become a hot issue in the field of artificial intelligence, and it is an important tool in the process of intelligent decision-making [4]. The emergence of technology also provides a research opportunity for scholars in the field of transportation and logistics to study the decision-making of logistics distribution vehicle scheduling system. It has the characteristics of reactivity, preaction, and sociality. In the field of complex problem solving, pattern is a new method to study problems. At the same time, pine is a granular system composed of multiple computing units, and its characteristics of cooperation, parallelism, robustness, scalability, and distributed solution have natural advantages in describing complex dynamic systems [5]. Therefore, it is widely used as a theoretical reference model for constructing various complex dynamic systems and plays an increasingly important role in the field of intelligent decision support systems. On the other hand, for solving complex problems that are difficult to obtain results by traditional methods, we can try to model and coordinate with the latest research theories and decision-making methods. After refining and summarizing the research results obtained by technical means, the theories can be enriched and then extended to other complex systems [6]. Based on the existing research results of logistics distribution vehicle scheduling theory, this paper will use technical means to study logistics distribution vehicle scheduling decision-making methods and provide new technologies and methods for logistics distribution business decision-making management.

2. Basic Theory

2.1. Overview of Logistics Distribution Vehicle Scheduling

2.1.1. Logistics Distribution and Its Mode

(1) The concept of logistics distribution [7]: logistics distribution refers to the logistics in which goods are sorted, packaged, divided, and assembled according to the needs of customers in a certain economic and reasonable area and arrived at the designated place in time. It is a link connected with important direct consumers in logistics activities. Distribution is an economic activity based on goods collection and distribution, which uses vehicles to transport according to customers' needs (such as goods type, quantity, and delivery time). Generally speaking, logistics distribution mainly includes the collection and distribution of goods, the assembly of vehicle-mounted goods, and the definition of distribution channels. The latter two parts are not only important contents of logistics distribution vehicle planning but also important technologies of logistics distribution [8], as shown in Figure 1.

(2) The model of logistics distribution: according to different enterprise entities, logistics distribution can be divided into five modes: individual distribution, outsourcing distribution, joint distribution, mixed distribution, and virtual logistics distribution [9]. Self-distribution means that enterprises establish their own distribution centers according to their own business strategies and scale and rely on their own network systems for distribution, such as the number of goods distributed and the configuration of commercial websites. Outsourcing distribution means that a company does not establish its own distribution center, entrusts other logistics companies

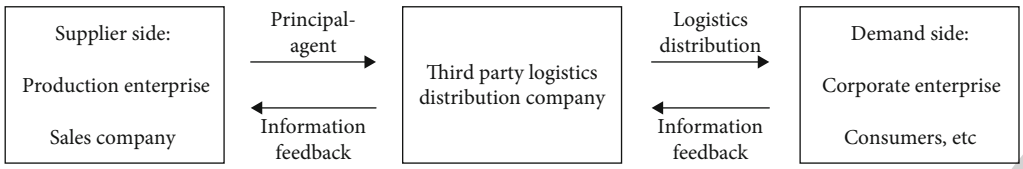

Figure 2: Outsourcing distribution mode.

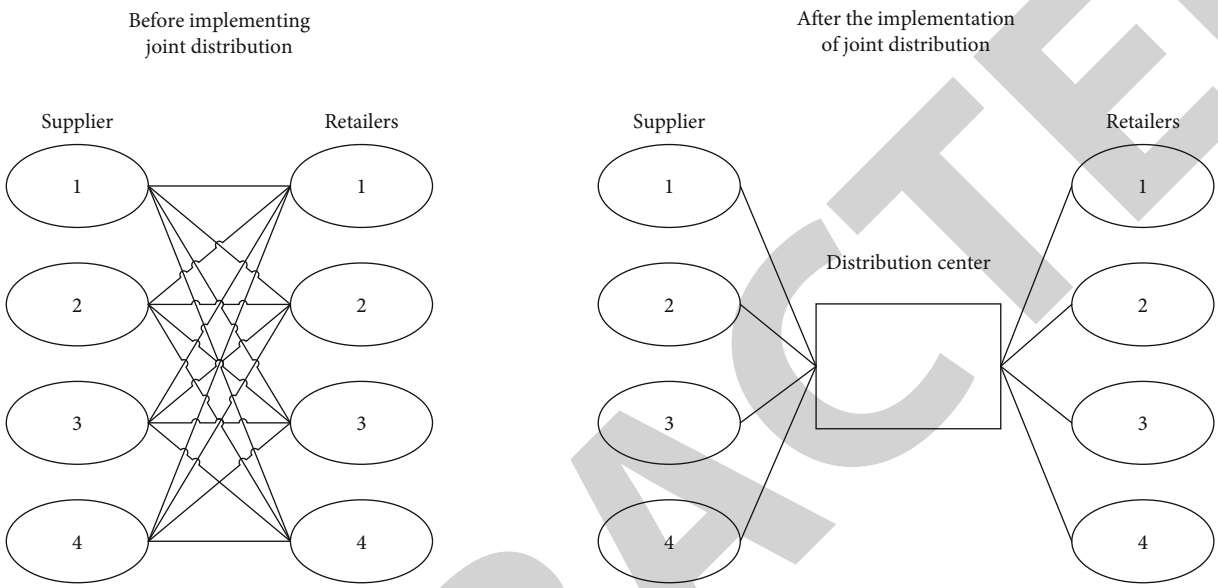

Figure 3: Effect of codistribution.

to trade in the form of contracts, and establishes long-term strategic alliances with external logistics distribution companies to achieve win-win cooperation. Enterprises adopting outsourcing distribution mode do not need to invest in logistics distribution, which can save a lot of construction resources and management costs, do not have to worry about related processes, and can also enjoy perfect logistics distribution services [10]. More importantly, you can invest important manpower and material resources to improve the core competitiveness of the company. Due to the specialization and globalization of production in many enterprises and multinational companies, logistics distribution is carried out in the form of outsourcing. The specific mode of outsourcing logistics distribution is shown in Figure 2.

Joint distribution is also called cooperative distribution. In the past, goods loaded by different vehicles were transported according to the type of goods, which was changed to "intensive goods and distribution," and all goods were loaded into distribution vehicles for unified distribution. Figure 3 shows the effect of codistribution.

Mixed distribution means that enterprises establish their own distribution system, and large-scale distribution adopts outsourcing mode of small-scale distribution, which can be implemented by outsourcing distribution companies. Based on this situation, the mixed mode can give full play to the advantages of enterprises in short-distance and long-distance distribution, save costs, and improve enterprise efficiency [11]. In addition, the company can control the distribution of goods and adapt to changes and market demands in time. Virtual logistics distribution mode is a new distribution concept in recent years, which refers to the mode of establishing dynamic alliance and realizing logistics distribution with the concept of virtual enterprise [12]. The specific flow is shown in Figure 4.

The key of virtual import mode is that the contact information of the whole distribution system is real-time and accurate, and the adjustment of all connections is synchronized correctly [13]. First of all, it needs the support of advanced computer and network technology.

Virtual logistics distribution mode has the advantages of low cost, high efficiency, and good quality assurance. That can make full use of various logistics distribution functions and avoid redundant construction. The main characteristics of virtual logistics distribution are virtualization, economy, flexibility, and efficiency. Virtual logistics distribution is an important direction of logistics development in the future.

2.1.2. Vehicle Scheduling Problem of Logistics Distribution. There are problems related to vehicle programming. Vehicle scheduling problem is the most important part of logistics distribution. For the actual situation of logistics distribution production process, the corresponding vehicle planning problems usually involve the assembly of goods, the level of configuration, and the arrangement of vehicle guidance. Cargo assembly problem is the application and extension

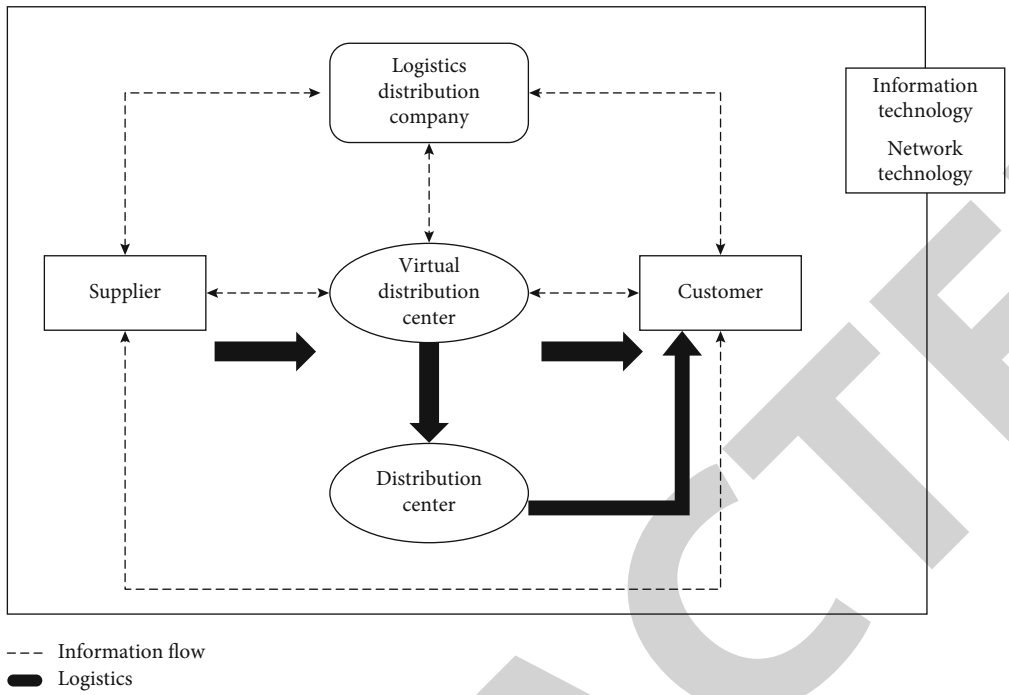

Figure 4: Virtual logistics distribution process.

of knapsack problem. The problem with the backpack is that the capacity of the backpack is fixed. N objects with different weights W_j ($j = 1, 2 \cdots N$, the same below), and P values are selected, and a combination is placed on the backpack to maximize the total value of the items. If an object is selected in the knapsack, the variable x is set to $x_j = 1$; otherwise, $x_j = 0$. This mathematical model is used to solve the object $x = [x_0, x_1 \cdots x_N]$, resulting in

$$\max \quad f(X) = \sum_{j=1}^{N} p_j x_i,$$
$$\text{s.t.} \quad \begin{cases} \sum_{j=1}^{N} w_j x_j \le W \\ x_j \in \{0, 1\}, (j = 1, 2, 3, \cdots, N), \end{cases} \tag{1}$$

Among these variables, one and can judge that the search space is $2n$. Goods assembly is the continuation and development of knapsack problem in logistics distribution vehicle scheduling problem, and it also increases some practical restrictions. The logistics center must follow several principles when deciding the loading scheme of goods distribution. Reasonable abstraction of these principles at a certain theoretical height has become the limiting condition of mathematical model. For example, in order to make full use of the load capacity of the vehicle, the volume and load capacity of the vehicle may be considered. This can be used as a full load limit. Secondly, the total load weight cannot reach the total load capacity of all vehicles, which can be used as a weight limit. Then, the total load shall not exceed the sum of the volumes that can be carried by all vehicles that can be used as vehicle volume limits. In addition, loading cargo can also be combined with light weight, and time priority can be considered to determine the loading limit of cargo. The mathematical model considers multiple objective functions and all constraints simultaneously, which is a multiobjective programming problem [14].

The scheduling problem has n people and n things. The cost for a person to do the j-th is C_{ij} $(i, j = 1, \cdots, n)$. People and objects must decide the corresponding distribution scheme, and the total cost of N objects must be controlled within the minimum matrix. $C = (C_{ij})\, N \times N$ is the assignment of coefficient matrices in the assignment problem. In practical problems, according to the specific meaning of C_{ij}, the meaning of C matrix is also different. The elements in line i represent the cost of doing different things for I people, and the elements in column j represent the cost of doing j things for different people. In fact, the C_{ij} element in matrix C and the cost for i to do J things are taken as grade indices. At this time, the C matrix is called the cost matrix. The essence of general assignment problem is to find the minimum objective function assignment scheme. In order to establish the mathematical model of general assignment problem, it is necessary to import the variable $n2$.

$$x_{ij} = \begin{cases} 1, & \text{indicates that the } i \text{ person is assigned to do the } j \text{ thing}, \\ 0, & \text{otherwise}, \end{cases} \tag{2}$$

Then the mathematical model of general assignment problem is as 2.

$$\min \quad f = \sum_{i=1}^{n}\sum_{j=1}^{n} c_{ij}x_{ij}$$

$$\text{s.t.} \quad \begin{cases} \sum_{i=1}^{n} x_{ij} = 0, & j = 1, \cdots, n(5A), \\ \sum_{j=1}^{n} x_{ij} = 1, & i = 1, \cdots, n(5B), \\ x_{ij} = 0 \text{ or } 1, & i, j = 1, \cdots, n(5C), \end{cases} \tag{3}$$

where min f is the objective function for minimizing the total cost of allocation. $(5A)$, $(5B)$, $(5C)$ are constraints, indicating that the person doing each thing is unique, one person must do only one thing, and the variable is 0 or 1. For any executable solution of the usual allocation problem, each column of the matrix does not have one element to satisfy the constraint $(5A)$. Only one element in each row satisfies the constraint $(5B)$. Usually, the allocation problem is $n!$, a viable solution. The scheduling of logistics distribution vehicle scheduling problem develops according to the allocation problem. It mainly includes two aspects: one is the cooperation between vehicles and drivers; the other is the matching of vehicle and shipping orders. Specific scheduling problems need to consider more elements than allocation problems, so they may be more complex.

2.2. Agent and Multiagent Theory

2.2.1. Concept and Structure of Agent. The concept of agent first appeared in the field of distributed artificial intelligence in 1980s, and its prototype is Hewitt's agent model. Academic research on agent-related topics is quite in-depth, and the most classic ones are the related "weak definition" and "strong definition" given by others [15].

Definition 1 (weak definition). Intelligent agent is usually a software system with the following characteristics.

(1) Autonomy: It is the ability of agents to operate and control their own behavior or internal state without direct intervention by individuals or other agents.

(2) Social ability: agents can exchange information with other agents through their communication language.

(3) Reaction ability: agents can perceive the environment, react for a certain time, and change the environment through actions.

(4) Activity: different from the instructions which are executed passively and mechanically by users in traditional applications, agent mainly detects and indicates the characteristics of the target automatically according to the changes of the environment.

Definition 2 (strong definition). According to researchers in the field of artificial intelligence intelligent fuselage, in addition to the above characteristics, it should also have the characteristics unique to ordinary people. For example, the abbreviations of belief, desire, intention, and BID, respectively, reflect the thinking state of cognition, emotion, and consciousness of agents. If the above definitions are weak or strong, they basically describe the characteristics of agents. R believes that the Soviet Union and Novig can deal with environmental problems by detecting the environment. Compared with object technology, it presents a higher degree of abstraction. Besides encapsulating attributes, events, and methods, it also provides the ability of thinking and decision-making. It has greater autonomy, stronger objectivity, flexible reactivity, objectivity, and sociality and can reflect the interaction with people.

2.2.2. Concept and Structure of Multiagent

(1) The concept of MAS: MAS is a system in which some semiautonomous or autonomous agents can communicate with other agents according to the language of a given protocol to solve complex problems. It has the characteristics of cooperation, parallelism, robustness, extensibility, distribution, and flexibility.

(2) The composition of MAS: this diagram shows the standard structure of the system, describes the connection of intelligent agents in the application system, reflects the information and control relationship between intelligent agents, and is used to reflect the distribution mode, information sharing, and storage mode of problem solving ability.

The interactive structure of MAS not only affects the free play but also directly affects the performance of the whole application system. It is usually divided into three types: distributed, centralized, and federated [16], as shown in Figure 5.

2.2.3. Multiagent Communication. The communication between each agent in MAS system is to coordinate their actions to achieve mutual communication and based on communication technology. In order to ensure the smooth communication between agents in the system, it is necessary to solve the communication mechanism, communication language, interaction management, and other related problems.

(1) Session management: realize the session management of both parties to ensure the correct communication content and cooperation process.

(2) Communication mechanism: the communication mechanism of MAS can be classified into low-level transport protocol and high-level dialog protocol. The transmission protocol refers to the low-level transmission mechanism used in communication. Interaction protocol can describe various response possibilities to messages and the basic process of interaction. And there are three kinds of communication institutions: direct communication, broadcast communication, public blackboard system, and federal system.

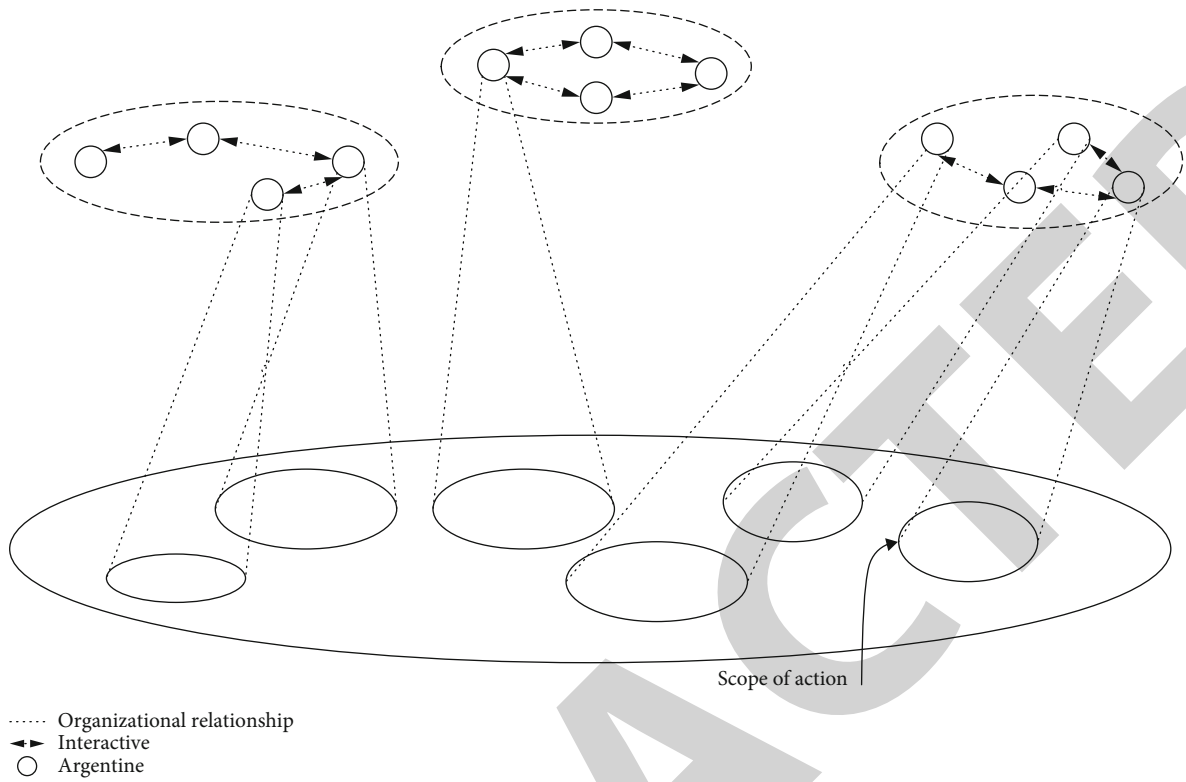

Figure 5: Standard MAS system structure.

(3) Communication mechanism: the communication mechanism of MAS can be classified into low-level transport protocol and high-level dialog protocol. The transmission protocol refers to the low-level transmission mechanism used in communication. Interaction protocol can describe various response possibilities to messages and the basic process of interaction. And there are three kinds of communication institutions: direct communication, broadcast communication, public blackboard system, and federal system.

Agent Communication Language (ACL) is a high-level language for multi-intelligence coordination negotiation and cooperation which is composed of communication instruction set and related structures. The communication command set and related structure include communication content, message parameters, and message body, and the content of the message body is the purpose of the sender's communication content. Classical ACL66 includes KQML (Knowledge Queryand Manipulation Language), FIPA Agent Communication Language (FIPA-ALL), and KIF (Knowledge Interchange Format) [17].

In the original operation, the target agent knowledge base and multiple license operations in the base are defined. In KQML, the meaning, associated attributes, and convention format of each basic behavior are maintained. There are mainly three types of behavior basic bodies: conversation basic bodies. The primitives of dialogue class are mainly ask everyone, ask if, exclude, ask one, deny and other primitives. Raw intervention and dialog mechanisms are used to intervene in the normal session process, terminate the session prematurely, and change the default session protocol. Original network and service words mainly include recording, broadcasting, and other original words. Through the interaction of messages, the negotiation and cooperation between agents are finally realized. In communication language KQML, the grammar, meaning, and pragmatic rules that both agents should follow in realizing communication between agents in MAS are the intermediates for agents to transmit information and exchange knowledge with each other.

3. Multiagent Modeling of Logistics Distribution Vehicle Scheduling

Agent is an idea and method to describe the world. In the research field of logistics vehicle planning and distribution, different levels of agents can be used to describe and express. This section simulates the scheduling of logistics transportation vehicles from macro-, meso-, and microaspects. On the macrolevel, using the theory of virtual logistics and business modeling, this paper constructs a business model of virtual logistics distribution and expounds it from four aspects: function, information, resources, and organizational vision. At the middle level, on the basis of analyzing the workflow of logistics distribution vehicle planning, the workflow model of logistics distribution vehicle planning is strengthened by using workflow theory and agent technology. At the microcosmic level, the classification of agents in MAS

logistics transportation vehicle scheduling system and the general structure and expression method of agent model are defined in detail. All kinds of models constructed by the above methods lay a basic framework and implementation platform for future research.

3.1. Agent Model Framework. The MAS system for planning logistics distribution vehicles should clarify the hierarchical structure of each component according to the previous macro- and mesoagent modeling. At the same time, each system configuration agent should decompose the current logistics distribution vehicle planning system into several entities, encapsulate these entities into agents, and then establish an agent system model [18].

Nowadays, individual agent modeling methods are mainly divided into function-based modeling methods and physics-based modeling methods. According to the present situation of logistics distribution vehicle planning system, this document adopts the method of combining functional modeling with physical modeling, which involves the management of physical entities such as vehicles, transportation orders and road network information, and the planning process of distribution centers and logistics distribution vehicles. Logical entities (such as planning) are uniformly decomposed into four different types of agents: management agents, task agents, resource agents, and computer agents.

(1) Management agent: manage agent monitors and processes global information, including order division, order cancellation, order modification, and planning. Let the management agent be responsible for the management, supervision, and control of the whole logistics distribution vehicle planning system. And in the case of emergency orders, the management agent will develop basic knowledge rules according to the plan, which will be used to improve the priority of emergency orders.

(2) Task-based agent: task-based agent maps the activities in the current logistics distribution vehicle planning system. The planning layer maps the distribution plan, and the operation layer maps the transportation order acceptance activities. The task agent will be dynamically generated here and then select the appropriate resources to complete its own processing and monitor the smooth execution of the task.

(3) Resource-based proxy: the asset type agent should be mapped to a unit or combination of units that can perform at least one function in the actual logistics distribution system. For example, a company's transportation department may provide its vehicles (teams), road network information, capabilities, status, task requirements, and environmental information provided by third-party vehicle platforms (teams) and other companies, judge current activities, and monitor resource status and activity implementation.

(4) Computer agent: computing agent mapping is based on the Tabu search algorithm, neural network, genetic algorithm, and immune algorithm to determine whether it can solve the problem.

Among the above four agents, agents can also be divided into entity agents and process agents in other ways. The first three belong to entity agents, and the last belongs to process agents. By using two agents, the functional flexibility of intelligent multilogistics distribution vehicle scheduling system can be improved.

As shown in Figure 6, in the process of logistics distribution vehicle scheduling, logistics distribution companies reasonably correspond to vehicles and transportation orders according to existing available vehicles and road network. Road transport information can be collected using the electronic map service of real-time Internet proxy. Here, the logistics distribution process of vehicle dispatching business is simplified as much as possible. The main objects of logistics distribution vehicle scheduling only include transportation order agent, vehicle agent, and road network information agent. Management objects and logical entities include coordination agent and vehicle scheduling agent, and the process of building agent structure model is described. In Figure 6, the coordination agent belongs to the management agent, the transportation receiving agent belongs to the task agent, the vehicle agent and the road network information agent belong to the resource agent, and the vehicle scheduling agent belongs to the calculation agent.

This graph only considers the negotiation between the vehicle scheduling agent and the vehicle agent, which simplifies the coordination process between the vehicle fleet agent and the vehicle agent. The vehicle agent directly negotiates the information of the transportation order with the agent dispatching the vehicle. The coordinating agent shall be regarded as the general agent provided in the system. Of course, agents will be generated dynamically in real time during the running of MAS system, but there is no specific analysis here.

4. Task Matching and Method of Multiagent Logistics Distribution Vehicle Scheduling

This section mainly studies the decomposition and matching methods of logistics distribution vehicle scheduling tasks. This paper focuses on how to combine the (personnel) vehicles needed to complete the distribution tasks with the distribution tasks on the basis of task decomposition. This section first introduces the task of planning logistics distribution vehicles and then decomposes the task of planning logistics distribution vehicles with reference to the method and thought of Labor Distribution Structure (WBS) in project management and puts forward the decomposition strategy of vehicle logistics distribution tasks and the planning ideas of corresponding tasks. Finally, the selection and evaluation method of vehicle (personnel) transportation request and corresponding relationship is proposed under the condition of incomplete actual information, and it is integrated into

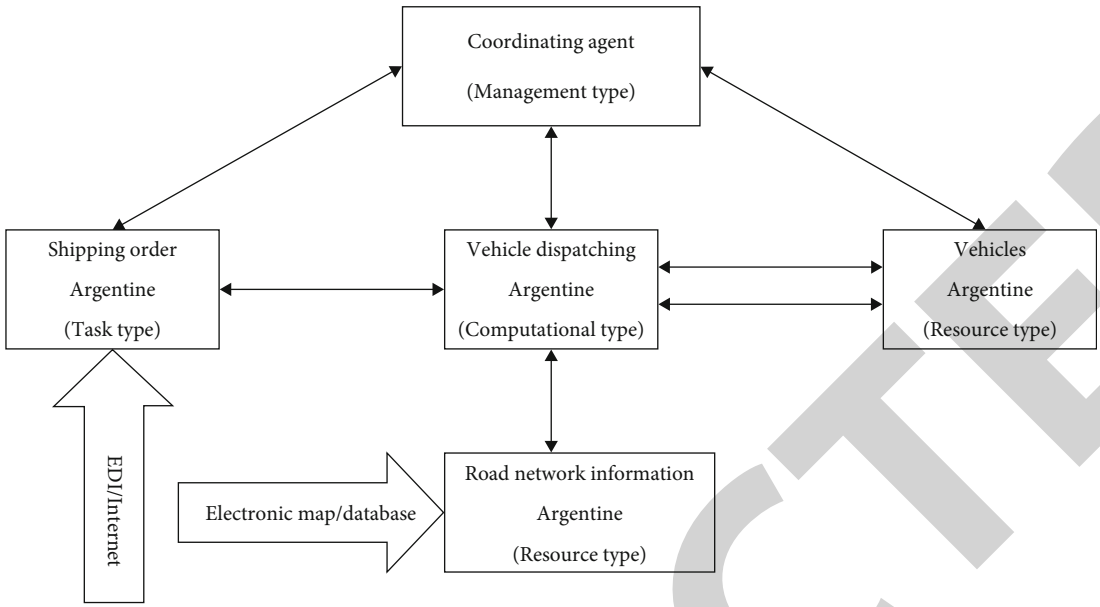

Figure 6: Agent framework of vehicle scheduling business process.

the logistics distribution vehicle scheduling system. An example is given to verify the effectiveness of this method, and the effectiveness of this method in transportation sequence and vehicle or personnel communication is illustrated.

4.1. Logistics Distribution Vehicle Scheduling Task Analysis. Logistics distribution center has irreplaceable special significance in logistics network system, so it must have the following basic logistics functions:

(i) Storage function: this mainly stores and maintains items that can be received in real time when needed.

(ii) Commodity adjustment function: the cyclical and seasonal changes of commodity demand can receive related commodities in different periods according to the adjustment of commodities.

(iii) Distribution and sale function: marketing methods related to commodity flow can be used to promote the flow of goods in the market.

(iv) Information management function: logistics distribution center is usually the central node of information processing and processing. It can play the role of central nervous system in the whole logistics process.

(v) Commodity distribution function: this is also the core and basic function of logistics distribution center. I guarantee that the goods will be delivered to the designated customers as required.

Generally speaking, the workflow of logistics distribution center can be summarized as shown in Figure 7.

Especially as a part of logistics distribution, the further decomposition of logistics distribution business shows that logistics distribution vehicle planning is a very important part of logistics distribution. In logistics distribution center, upstream manufacturing companies and parts wholesalers can collect, store, and spare parts through goods. Logistics distribution is a part of vehicle scheduling, which usually considers three tasks, including vehicle scheduling, scheduling, and obtaining road information. In the process of transporting vehicles and personnel, it is necessary to investigate the corresponding relationship between orders and vehicles or drivers and vehicle tasks. Ultimately, the problem lies in the choice of partners, whose selection methods and ideas are basically the same. The vehicle planning scheme of logistics distribution obtains the vehicle driving scheme through certain decision-making methods on the basis of obtaining relevant road information. The schematic diagram of logistics distribution vehicle planning in logistics distribution center is shown in Figure 8.

According to the above analysis ideas, we introduce the Labor Distribution Structure (WBS) method into the project management and further analyze the planning activities of logistics distribution vehicles.

4.2. Task Decomposition

4.2.1. Work Breakdown Structure. Work sharing structure (WBS) decomposes upper functional entities into upper subitems in the tree structure and then gradually decomposes them into independent work units. This is a project management tool that determines the tasks and tasks that each unit can perform and makes the project organization more effective. WBS theory is based on cybernetics, informatics, systems engineering, and so on. WBS can also be defined as a process to achieve a specific goal. The project will go from big activities to small activities, and all activities to be completed will be organized in a certain order. WBS's idea was

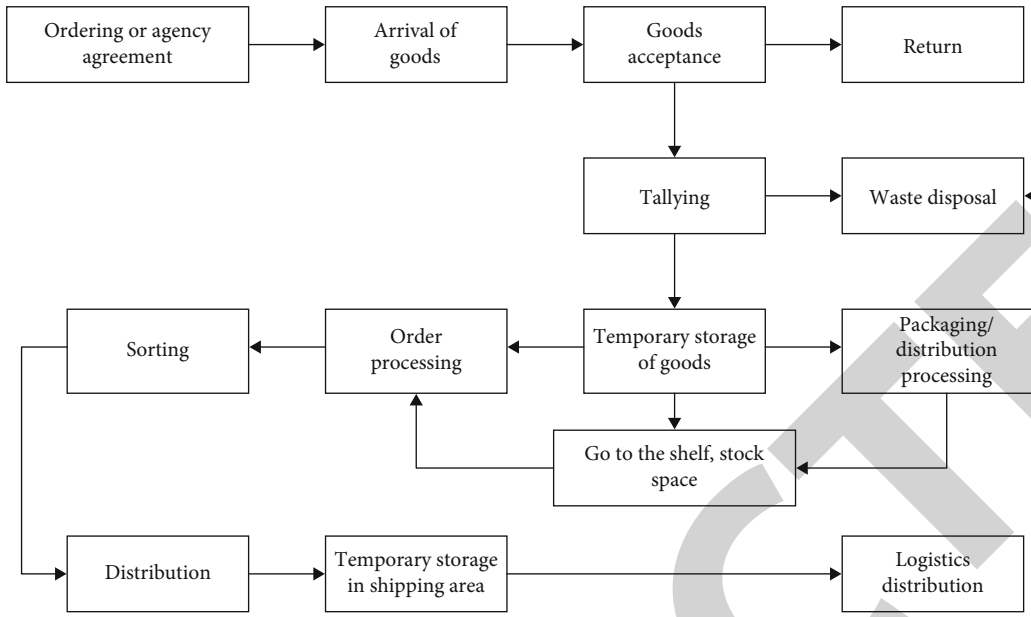

Figure 7: Schematic diagram of operation flow of logistics distribution center.

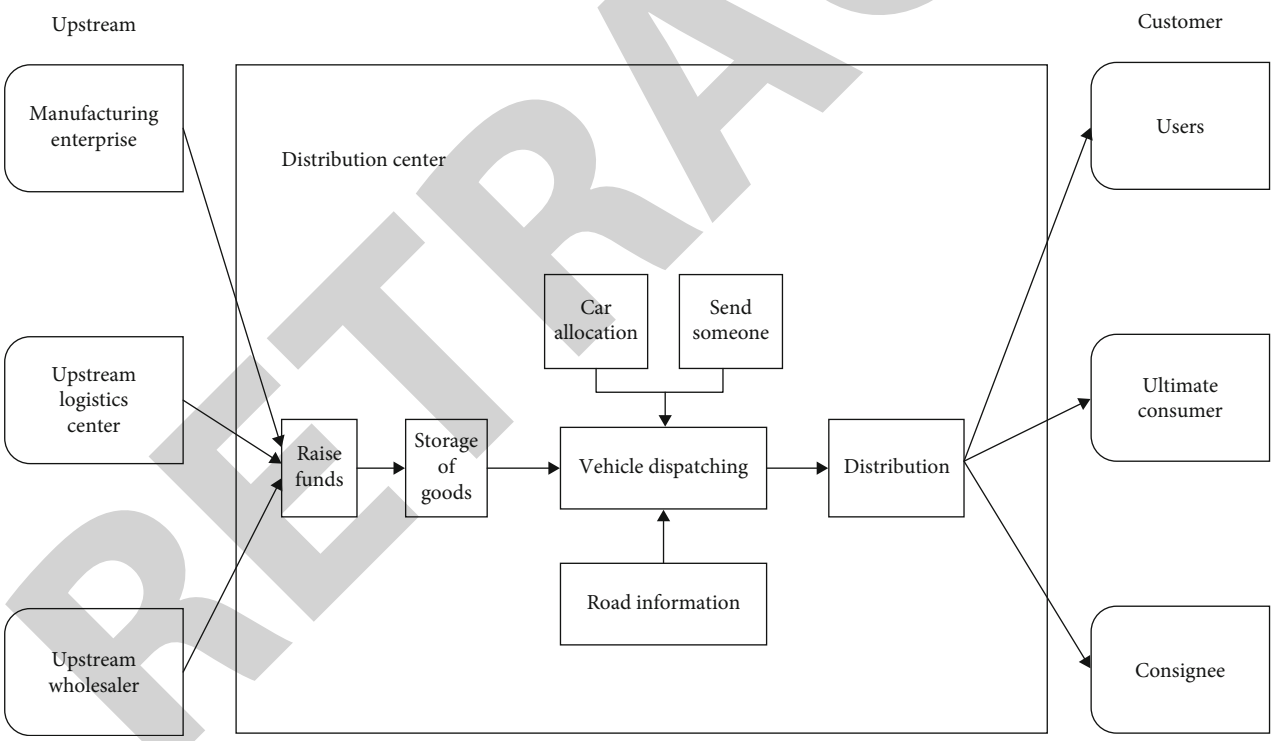

Figure 8: Schematic diagram of logistics distribution vehicle scheduling task.

originally proposed by the US Office of Defense Finance for the procurement and management of large-scale equipment procurement projects. The original WBS is limited to the product itself. Now, it has been renovated throughout the project life cycle. It is the main tool frequently used in project management [19].

As a core tool in the project management process, WBS is scientific and requires you to follow certain rules. In a word, the principles to be followed include the following aspects.

(1) The content should be consistent with the project (task), and the necessary components should not be disclosed. For each unit X, if it is decomposed into lower-level units $X_1, X_2, \cdots, X_n$, the following conditions should be met:

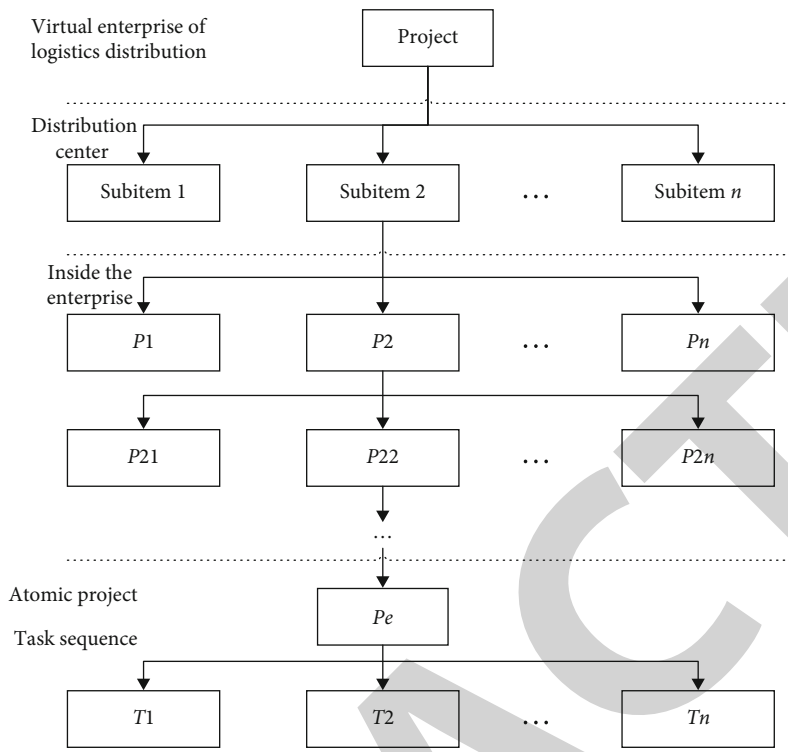

Figure 9: Project decomposition process of logistics distribution enterprises.

$$X = X_1 \bigcup X_2 \bigcup \cdots \bigcup X_i \bigcup \cdots \bigcup X_n, \quad (4)$$

$$X_i \bigcup X_j = \varnothing (i \neq j). \quad (5)$$

The sum of the costs of $X_1, X_2, \cdots, X_n$ of equations (4) and (5) is equal to the total cost of X, that is,

$$C_X = \sum C_{X_i}, \quad (6)$$

The duration of X is the combined duration of $X_1, X_2, \cdots, X_n$

(2) The decomposition of the working structure needs to ensure that it is linear. The Unit of Work X may belong to one of the Upper Unit X and two or more Upper Units X and Y that are not allowed to intersect.

$$X_i \subset X, X_i \not\subset Y \quad (7)$$

(3) Cells at the same level should have the same attributes. For example, $X_1, X_2, \cdots, X_n$ are all represented as functions, or all as elements, or all implementation procedures

(4) Ensure that the interface is clear and the responsibilities are clear. For each work unit, we need to be able to distinguish different work contents and different principles. Each project unit needs relatively strong independence and integrity. Control the interface and operation responsibility between each operation unit to a minimum and make it clear. Only in this way can we promote the concrete decomposition and implementation of the objectives and responsibilities of each project and promote the assessment of results and the analysis of responsibilities

(5) Flexibility should be ensured. The breakdown of work structure should promote the expansion of project scope and content and change the project structure in real time

4.2.2. Project Task Decomposition Process. Because of the characteristics of project management under the environment of logistics distribution vehicle planning and the actual needs in the process of logistics distribution operation, this paper proposes a top-down and bottom-up project activity decomposition method. The decomposition process is shown in Figure 9.

According to the above design task decomposition method and the logistics distribution process analyzed before, Figure 9 shows the work breakdown structure of logistics Distribution Company after project decomposition (we only decompose into subprojects, which can be subdivided into atomic projects). In addition, the decomposition of projects is different from the value analysis activities here. The latter involves extracting only a part of the target process, finding the main value-added activities in the target process, and eliminating the activities without value-

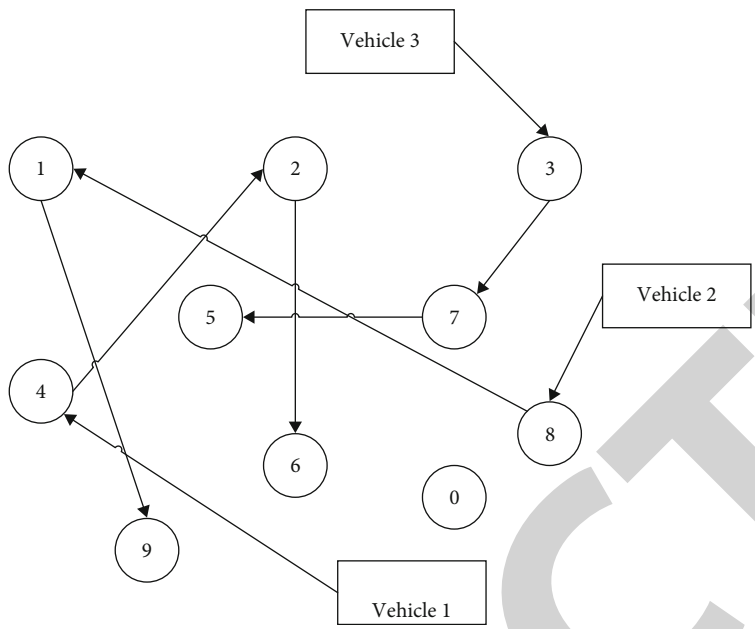

Figure 10: Conceptual model of vehicle scheduling in container port without central node.

added. The first method decomposes all project processes into independent and measurable activities and organizes the implementation of the project. The finer the granularity of the final decomposition of the project, the easier it is to create a plan. The divided activities are used for value analysis, which can control decision-making and project funds.

4.3. Mathematical Modeling of Vehicle Scheduling. In order to process the work order, the tractor must first run to the departure place for loading and unloading and meet the operation time window limit of the departure place. The tractor should wait for the operation time window to allow the container to be loaded into the tractor; after the operation is completed, the vehicle can drive to the destination. At the destination, loading and unloading operations must also be carried out within the allowed time.

From Figure 10, we can see that each marked node represents a task order, and each dotted line sequence guided by the trailer represents a sequence of orders completed by the trailer in sequence. Each arc does not represent the actual geographical connection, but represents the order for processing the order.

In order to establish a mathematical model, we assume that only two types of 20-foot and 40-foot boxes suitable for the United Nations are considered. Assuming that 20 feet and 40 feet are treated equally, each trailer can only carry one container. Different cash types will not affect the plan before and after the plan, but they are different in cost calculation. Each trailer has a predefined maximum working time or maximum number of orders processed. Each work instruction must meet all relevant working time limits. Only one tractor can be accessed at each node. All work orders for other lead-free vehicles are stored in Series 0.

The following are the decision variables:

$X_i(k_m) \in \{0, 1\}, i \in \{1, \cdots, N\}; k \in \{1, \cdots, k\}; \mathrm{m} \in \{1, \cdots, \mathrm{m}\}$. Set $X_i(k_{m-1})$ when the work order i of the k trailer is scheduled for the m processing operation; otherwise, take 0.

$X_{io} \in \{0, 1\}, i \in \{1, \cdots, N\}$. Set $X_{io} = 1$ when work order i is outsourced to a leased vehicle (where 0 represents another shipping company); otherwise, take O.

W_{km1} $(m \in \{1, \cdots, m\}; k \in \{1, \cdots, k\})$ represents the waiting time of the k trailer for the m-th run at the departure point.

$W_{km2}(m \in \{1, \cdots, m\}; k \in \{1, \cdots, k\})$ represents the waiting time of the k-th trailer for the m-th run at the destination.

The following are the parameters:

N denotes the number of jobs; k represents the number of tractors; M represents the maximum number of work orders that a car can handle in one day; P_i represents the cost of completing work order I with one's own vehicle, $i \neq \{1, \cdots, n\}$; S_i represents the cost required for the leased vehicle to complete the operating instruction i, $i \neq \{1, \cdots, n\}$; T_{mk0} indicates the start time of the m-th operation of the k-th trailer; T_{mk1} represents the start time of the k-th trailer and the m-th operation to reach the destination; T_{mk2} represents the last time of the m-th operation of the k-th trailer; D_{ij} represents the running time of the trailer from the destination of job i to the departure place of job j; D_i represents the running time of the trailer from the beginning to the end of the i-th operation; H_{i1} represents the processing time of the first job at the starting site; H_{i2} denotes the processing time of the i-th operation at the destination; R_{i0} represents the start time of the i-th operation and the start time of the operation time window; R_{i1} represents the start and end times of the i-th operation; R_{i2} refers to the start time of the operation time window at the end of operation i; R_{i3}

represents the final arrival time of the operation time window at the end of operation i; A_{k0} indicates the start time of the available time of the tractor; A_{K1} denotes the available time and end time of the tractor.

The time sequence of the m-th operation of the k-th trailer is shown in the figure. Establish the following mathematical model:

$$\text{Minimize} \quad \sum_{i=1}^{N} P_i \left(\sum_{k=1}^{K} \sum_{m=1}^{M} X_{ikm} \right) + \sum_{i=1}^{N} S_i X_{i0} \tag{8}$$

$$\text{s.t.} \quad \sum_{k=1}^{K} \sum_{m=1}^{M} X_{ikm} + X_{i0} = 1, \quad \text{for } i \in \{1, \cdots, N\}, \tag{9}$$

$$\sum_{i=1}^{N} X_{ik(m+1)} \leq \sum_{m=1}^{M} X_{ikm} \leq 1, \quad \text{for } k \in \{1, \cdots, k\} \text{ and } m \in \{1, \cdots, M-1\}, \tag{10}$$

$$T_{(m+1)k0} = T_{mk2}, \quad \text{for } k \in \{1, \cdots, k\} \text{ and } m \in \{1, \cdots, M-1\}, \tag{11}$$

$$T_{mk1} = T_{mk0} + \sum_{\substack{i=1, j=1 \\ i \neq j}}^{M} X_{ikm} X_{jk(m-1)} \left(D_{ji} + H_{i1} \right) + W_{mk1}, \quad \text{for } k \in \{1, \cdots, k\} \text{ and } m \in \{1, \cdots, M\}, \tag{12}$$

$$T_{mk2} = T_{mk1} + \sum_{i=1}^{N} X_{ikm} (D_i + H_{i2}) + W_{mk2}, \quad \text{for } k \in \{1, \cdots, k\} \text{ and } m \in \{1, \cdots, M\}, \tag{13}$$

$$A_{k0} \leq T_{mk0} \leq A_{k1} - (T_{mk2} - T_{mk0}), \quad \text{for } k \in \{1, \cdots, k\} \text{ and } m \in \{1, \cdots, M\}, \tag{14}$$

$$R_{i0} = \sum_{k=1}^{K} \sum_{m=1}^{M} X_{ikm} (T_{mk1} - H_{i1}) + X_{i0} R_{i0} \leq R_{i1}, \quad \text{for } i \in \{1, \cdots, N\}, \tag{15}$$

$$R_{i2} = \sum_{k=1}^{K} \sum_{m=1}^{M} X_{ikm} (T_{mk2} - H_{i2}) + X_{i0} R_{i2} \leq R_{i3}, \quad \text{for } i \in \{1, \cdots, N\}. \tag{16}$$

Here, Formula (8) is the objective function, which means that the total cost is the lowest, which is p for the same job. It is usually smaller than the S, which means it is more costly to complete on your own vehicle than to outsource a rental vehicle. Formula (9) indicates that each operation can only be assigned once. Formula (10) indicates that all operations must be arranged in an orderly manner on a specific tractor. Formulas (11) to (12) represent time series limits for each operation, Formula (13) indicates that all operations must be completed within the working time available to the tractor, and Formulas (14) and (15) represent time window limits at start and end, respectively.

4.4. Tabu Search Algorithm and Exchange Neighborhood Search Algorithm. Tabu search (TS) was first proposed by Glover, which is an extension of local neighborhood search. It is not only a global sequence optimization algorithm but also a simulation of human intelligent process. TS adopts the idea of local neighborhood search. In addition, the Tabu policy corresponding to flexible storage structure is introduced, Tabu and Tabu objects are defined, and some objects corresponding to the optimal local solution of recovery are marked instead of absolutely prohibiting loops. Avoid these objects as much as possible in additional iterative searches. The algorithm combines the characteristics of avoiding search deviation. Make sure there are different valid search paths. At the same time, set standards to despise, reward, and forgive various states. Tabu search is mainly used to solve various vehicle planning problems. Tabu search is very fast, but it depends on the initial solution to a great extent, so it is impossible to perform parallel search defined as GS.

4.4.1. Initial Solution Generation and Exchange Neighborhood Search Strategy. Suppose there are K Trailers and all workflows 1, 2, 3. Firstly, K task sequences are generated by random insertion as the initial solution, and the remaining task sequences are all the second ones. O in this work sequence, it is used as an object for ordering outsourced work. During the build of the initial solution, if a new work order cannot be entered for the current work sequence, the work order will be regenerated until all K trailers are assigned. Therefore, a $K+1$ task sequence is generated.

When the initial solution is generated, the adjacent switching structure is generated by using the switching neighborhood search method. This method uses two work sequences to exchange work orders and generates two new work sequences as new solutions: referred to herein as (0, 1), (1, 0), (1, 1), (0, 2), (2, 0), (2, 1), (1, 2), and (2, 2).

Here, (2, 1) means that two tasks in the first task sequence accept the request and are replaced by the second task sequence and one task in the second task sequence accepts the request and is replaced by the first task sequence. In addition, it is assumed that each work sequence can be exchanged with the 0th work sequence to generate a new solution.

4.4.2. Tabu Structure Table and Tabu Capacity Setting. During parsing, the Tabu table can hold the most recently changed workflow, and the capacity of the Tabu table can be preset. The Tabu table structure has two ways: One is to record the changed work tasks in each work sequence, and the other is to record the whole changed work sequence completely. In subsequent swap operations, operations that return preexisting work sequences are marked in a Tabu table and are therefore prohibited to improve recovery efficiency. If a new and better solution is generated by changing the workflow, it will be saved to the Tabu table and updated in real time, but the Tabu table capacity limits the number of Tabu templates that can save the workflow. Here, the Tabu

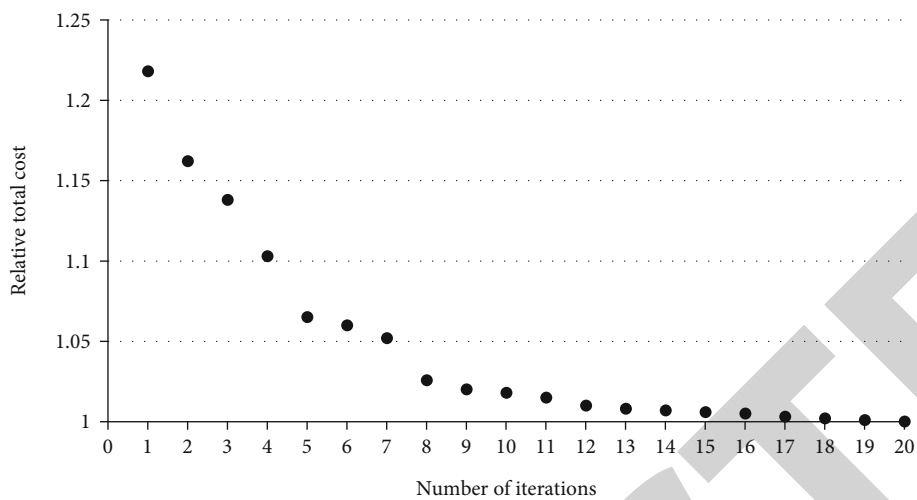

Figure 11: Trend of relative total cost on the first day with iteration times.

table adopts "first-out, first-out" update source, and the Tabu table capacity is set to 10.

4.4.3. Termination Criteria. When the total number of iterations reaches a given value or the current optimal solution does not change within a given number of consecutive iteration steps, the algorithm ends.

4.4.4. Algorithm. After generating the initial K solution through 3.1, according to the neighborhood exploration method described in this paper, first, the second O task sequence and the task sequence are exchanged. After completion, two random task exchanges are performed on a task sequence to obtain a better global executable task sequence. All replacement work acceptance orders are arranged in an ascending order of total cost.

Then, check the executability of the first candidate task sequence. First, make sure it exists in the Tabu table. If it does not exist in the Tabu table, it is saved as a better work sequence in the Tabu table and updated in real time. If you are already in the Tabu table, check the order of the second candidate task. The specific description is as follows.

(Step 1) Randomly generate the initial solution S, $S = SB$ (S is the best scheme at present).

(Step 2) Initialize the Tabu list and candidate task sequence (empty).

(Step 3) $m = 0$ (loop control).

(Step 4) Explore the neighborhood of S using the exchange neighborhood exploration method, update the list of candidate work sequences, and organize them in ascending order.

(Step 5) Assign the first update scheme to SS.

(Step 6) If $\{\text{cost}(SS) < \text{cost}(SB)\}$, go to step 8.

(Step 7) If $\{SS \text{ is taboo}\}$ selects the candidate's next work sequence, assign it to the SS and go to Step 6.

(Step 8) If $S = SS$, update the tabu table. If $\{\text{cost}(S) < \text{cost}(SB)\}$ is defined as $S = SB$, $m = m + 1$.

(Step 9) If the default value is exceeded (assuming m is the maximum number of jobs that the trailer can handle in a day), complete the program; otherwise, return to Step 4.

4.5. Example Analysis. Guangzhou Zhuozhi Logistics (Group) Co., Ltd. is a professional large-scale integrated logistics company providing full supply chain services. Zhuozhi Group Guangzhou Zhuozhi Logistics Service Co., Ltd. has more than 300 trucks and has rich experience in dangerous goods transportation and container transportation. Company vehicles are equipped with GPS satellite positioning system, which is used in vehicle fixed-point control, safety incident control, load distribution and inventory management, electronic information feedback, customer service, and so on. Zhuozhi Group has 6 terminal transit warehouses and 8 logistics distribution center warehouses with a total warehouse area of 50,000 square meters, mainly engaged in port container transportation and related activities.

(1) Algorithm effectiveness analysis: the algorithm is programmed in Delphi language and implemented in PIV1.66GHz microcomputer. The experimental data are collected from the data processing of commercial container orders by a company in Guangzhou from January to June, 2008, including the distribution of container orders, operating costs, and working hour constraints. In order to simplify the calculation of the problem, there is only one third-party alternative transportation company. $\alpha = 1$, $Q_{i1} = 100$, and $l = 0$.

The method in this paper is used to process the data of any two days, and the optimized processing results shown in Figures 11 and 12 are obtained.

Through analysis, it is found that in the initial stage of the iterative process, the algorithm proposed in this paper has advantages over the container order sequence processing scheme, and the total cost of order acceptance decreases

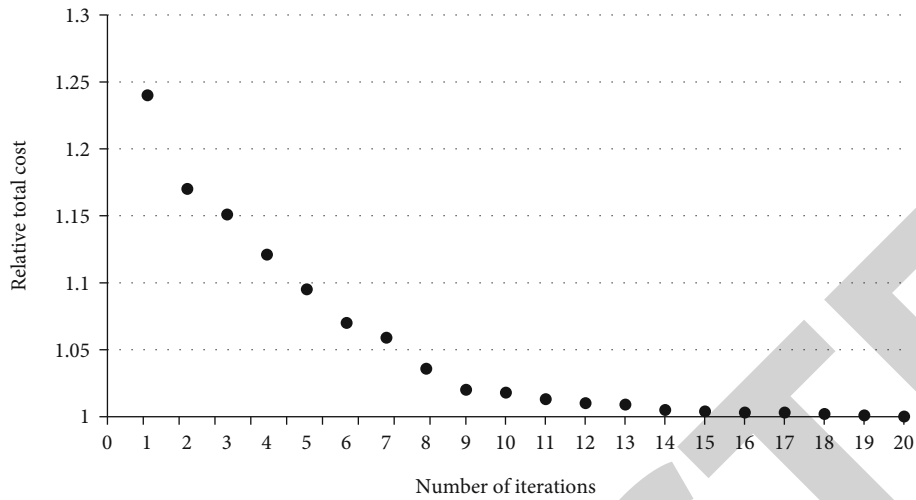

Figure 12: Trend of relative total cost on the second day with iteration times.

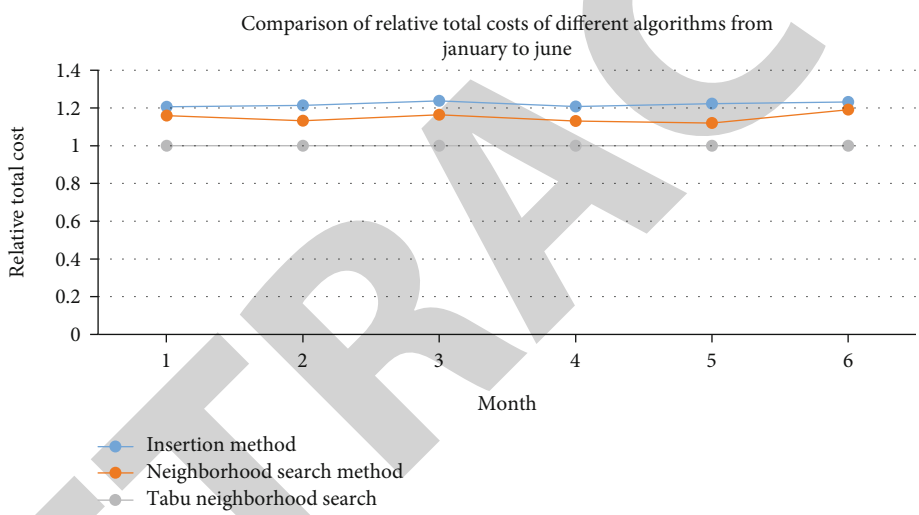

Figure 13: Comparison of relative total costs of different algorithms from January to June.

Table 1: Comparison of relative total cost between neighborhood search algorithm and Tabu search algorithm.

Month	Insertion method	Neighborhood search	Tabu neighborhood search
1	1.2064	1.1599	1.0000
2	1.2132	1.1315	1.0000
3	1.2375	1.1633	1.0000
4	1.2072	1.1310	1.0000
5	1.2226	1.1201	1.0000
6	1.2325	1.1905	1.0000

sharply in the initial stage, which shows the actual convergence of the algorithm. However, with the increase of iteration cycle, the optimization effect decreases and is not significant, especially in the ninth and tenth cycles, so it is best not to fall into local optimization in the subsequent cycles. The main reason to avoid prematurity of search algorithm is to avoid prematurity of exchange algorithm. Therefore, we prove that the algorithm proposed in this paper is effective and avoids local optimization to a certain extent.

(2) Algorithm optimization analysis: for comparison with other methods, all monthly data are divided

Hindawi
Journal of Sensors
Volume 2024, Article ID 9837823, 1 page
https://doi.org/10.1155/2024/9837823

Retraction

Retracted: Embedded Estimation Sequential Bayes Parameter Inference for the Ricker Dynamical System

Journal of Sensors

Received 23 January 2024; Accepted 23 January 2024; Published 24 January 2024

This article has been retracted by Hindawi following an investigation undertaken by the publisher [1]. This investigation has uncovered evidence of one or more of the following indicators of systematic manipulation of the publication process:

(1) Discrepancies in scope
(2) Discrepancies in the description of the research reported
(3) Discrepancies between the availability of data and the research described
(4) Inappropriate citations
(5) Incoherent, meaningless and/or irrelevant content included in the article
(6) Manipulated or compromised peer review

The presence of these indicators undermines our confidence in the integrity of the article's content and we cannot, therefore, vouch for its reliability. Please note that this notice is intended solely to alert readers that the content of this article is unreliable. We have not investigated whether authors were aware of or involved in the systematic manipulation of the publication process.

Wiley and Hindawi regrets that the usual quality checks did not identify these issues before publication and have since put additional measures in place to safeguard research integrity.

We wish to credit our own Research Integrity and Research Publishing teams and anonymous and named external researchers and research integrity experts for contributing to this investigation.

The corresponding author, as the representative of all authors, has been given the opportunity to register their agreement or disagreement to this retraction. We have kept a record of any response received.

References

[1] M. J. U. Rehman, R. Zafar, H. Dilpazir, M. F. Sohail, M. A. Khan, and R. Jahan, "Embedded Estimation Sequential Bayes Parameter Inference for the Ricker Dynamical System," *Journal of Sensors*, vol. 2022, Article ID 4540366, 8 pages, 2022.

Hindawi
Journal of Sensors
Volume 2022, Article ID 4540366, 8 pages
https://doi.org/10.1155/2022/4540366

Research Article

Embedded Estimation Sequential Bayes Parameter Inference for the Ricker Dynamical System

Muhammad Javvad Ur Rehman,[1] **Raheel Zafar**,[2] **Hammad Dilpazir**,[1] **Muhammad Farhan Sohail**,[1] **Muhammad Arslan Khan**,[3] **and Rifat Jahan**[4]

[1]*Department of Electrical Engineering, National University of Modern Languages, Pakistan*
[2]*Department of Software Engineering, National University of Modern Languages, Pakistan*
[3]*Department of Computer Science and Engineering, HITEC University, Museum Road, Taxila, Pakistan*
[4]*Department of Electronics and Telecommunication Engineering, Rajshahi University of Engineering and Technology (RUET), Rajshahi 6204, Bangladesh*

Correspondence should be addressed to Rifat Jahan; 1604048@student.ruet.ac.bd

Received 20 April 2022; Revised 13 May 2022; Accepted 23 May 2022; Published 8 June 2022

Academic Editor: Waliullah Khan

The dynamical systems are comprised of two components that change over time: the state space and the observation models. This study examines parameter inference in dynamical systems from the perspective of Bayesian inference. Inference on unknown parameters in nonlinear and non-Gaussian dynamical systems is challenging because the posterior densities corresponding to the unknown parameters do not have traceable formulations. Such a system is represented by the Ricker model, which is a traditional discrete population model in ecology and epidemiology that is used in many fields. This study, which deals with parameter inference, also known as parameter learning, is the central objective of this study. A sequential embedded estimation technique is proposed to estimate the posterior density and obtain parameter inference. The resulting algorithm is called the Augmented Sequential Markov Chain Monte Carlo (ASMCMC) procedure. Experiments are performed via simulation to illustrate the performance of the ASMCMC algorithm for observations from the Ricker dynamical system.

1. Introduction

It is possible to examine the dynamical characteristics of linear and nonlinear systems using state space modelling because it provides a consistent framework for doing so. The state space modelling process is divided into two stages: the development of a model that describes the underlying system dynamics over time, known as the state space model; and (ii) the development of a model that relates observations to state space variables, known as the measurement state model (also known as the measurement state model). The class of issues covered in this paper is the inference of unknown parameters, denoted by the symbol Ω, that regulate the dynamical system under consideration. As an example of a discrete-time stochastic system representing (i) and (ii), the discrete-time stochastic system is expanded to include Ω to solve the parameter inference issue and is given by

$$m_k = \Phi_{k-1,\Omega}(m_{k-1}, u_{k-1}), \tag{1}$$

$$y_k = \Psi_{k,\Omega}(m_k, v_k), \tag{2}$$

for $k = 1, 2, 3, \cdots, T$ with $m_0 \sim p_0$ represents the known prior distribution on the initial state space variable m_0; in (1) and (2), k represents a generic time step and T denotes the final time, $\Phi_{k-1,\Omega}(\cdot)$ represents the transfer function in the state space model with noise u_k, and $\Psi_{k,\Omega}(\cdot)$ represents the nonlinear and non-Gaussian measurement model. Both $\Phi_{k-1,\Omega}(\cdot)$ and $\Psi_{k,\Omega}(\cdot)$ are further known only up to the unknown parameter $\Omega \in R^p$ which is the object of inference. Additionally, in (1), u_{k-1} is assumed to be distributed

according to $F_\Omega(\cdot)$ which is again parameterized by the components of Ω. In other words, Ω represents the collection of all unknown parameters in the dynamical system of (1) and (2), which are to be inferred based on the observed data. The development of Bayesian parameter inference methodology for the above dynamical system is the key objective of this article.

Physical, biological, neuroscience, and object tracking systems are all examples of multidisciplinary fields in which the inference problems that govern the characteristics of nonlinear dynamical systems are applied [1–10]. The most commonly used statistical frameworks for finding solutions to parameter inference problems seem to be frequentist (or non-Bayesian) approaches that use maximum likelihood estimation (ML), such as the Expectation Maximization (EM) procedure [11–16]. It is computationally difficult to infer parameters for nonlinear dynamical systems using frequentist approaches. Furthermore, these procedures return just point estimates rather than the whole distribution, indicating parameter uncertainty. It is necessary to run the estimation method a large number of times, using uncertainty estimation techniques such as bootstrapping, to get estimates of uncertainty. This entails an increase in both the computational load and the intensity.

The posterior distribution of unknown parameters, on the other hand, is used to offer both a point estimate and a corresponding estimate of uncertainty when estimating unknown parameters using Bayesian approaches. The aim of Bayesian procedures in a dynamical system setup is to obtain the posterior of Ω, $p(\Omega|y_{1:T})$, given all observations up to the final time T, $y_{1:Y}$. The posterior $p(\Omega|y_{1:T})$ is generally difficult to obtain in closed form, so Bayesian computational algorithms are utilized to approximate it in the Monte Carlo sense. Markov chain Monte Carlo (MCMC) methods are the most frequently used approaches for estimating the posterior distribution when closed forms are not accessible, and they are the most accurate. Although Bayesian computational methods may be used to derive the posterior distribution of an unknown parameter, they are only justified in the limiting sense and can require a significant number of burn-ins before the MCMC algorithm converges [17–19]. In spite of this, certain computational methods are trivial to conceive and execute on computers, and standard packages are already available for many uncomplicated implementations of these procedures [20–22]. Some of the MCMC procedures are the Metropolis-Hastings (MH) algorithm, Gibbs sampler, and particle Markov Chain Monte Carlo (PMCMC) [23–25].

Several sequential Monte Carlo (SMC) approaches have been developed to address the constraints of the Markov Chain Monte Carlo (MCMC) algorithm for parameter estimation in dynamical systems. It is the core concept of SMC to utilise important samples to estimate the posterior of Ω at each k point in time and to propagate the samples sequentially via a suitable kernel. There exists an extensive literature on SMC methods (see, for example, [26–29]). The SMC-based parameter inference in nonlinear dynamical systems was first addressed in [30] where the Liu and West filter was developed. An artificial evolution of parameters for parameter Ω is used in the Liu and West filter and assumes a mixture of normal distribution for the posterior distributions, $p(\Omega|y_{1:k})$, for $k = 1, 2, \cdots, T$ within the mixture distribution. The tuning parameters govern the extent of the control of overdispersion of the mixture components [30, 31]. To minimize the weight degeneracy or particle decay, the main idea is to generate new samples from the posterior by fitting the mixture to the posterior. The Liu and West filter can generally be applied to any dynamical system, which is the main attraction of this procedure. However, due to the artificial evolution of the unknown parameter, the artificial variability is incorporated, which is the main drawback of this algorithm.

The aim of Bayesian procedures is to obtain the posterior of Ω, $p(\Omega|y_{1:T})$, given all observations up to time T, $y_{1:T}$. The posterior $p(\Omega|y_{1:T})$ is again difficult to obtain in close form, so Bayesian computational algorithms are utilized to approximate it in a Monte Carlo sense.

Another major class of SMC methods for parameter inference that does not introduce overdispersion in the posterior of Ω is particle learning algorithms [32, 33]. The original method is attributed to Storvik [34, 35] resulting in Storvik's filter (similar approaches are also proposed in [36, 37]). Storvik's filter assumes that the posterior distribution of Ω given $m_{0:k}$ and $y_{0:k}$ depends on a lower-dimensional set of sufficient statistics that can be recursively updated for each $k = 1, 2, \cdots, T$. This recursion for sufficient statistics is defined by $s_{k+1} = S(s_k, m_{k+1}, y_{k+1})$, leading to the generation of Ω samples according to $\Omega \sim p(\Omega|m_{0:k}, y_{1:k}) = p(\Omega|s_k)$ for each $k = 1, 2, \cdots, T$. Unlike the Liu and West filter, in Storvik's filter, there is no artificial evolution process for Ω and thus it does not suffer from overdispersion [38]. However, the crucial assumption in Storvik's filter is the availability of sufficient statistics s_k as well as the ability of sampling from the posterior $p(\Omega|s_k)$ given the sufficient statistics s_k.

Subsequent developments in SMC methods for parameter inference have extended the applicability of Storvik's filter to a variety of more general settings (see, for example, [39, 40]). The extended Liu and West (ELW) filter to estimate parameters and states [40] divides the parameter set to be inferred Ω, into two sets, Ω_0 and γ representing parameters without and with sufficient statistics, respectively. For the Ω_0 set, the ELW filter uses the Liu and West filter, where an artificial random error is introduced to the static parameter Ω_0. The set of parameters γ updated based on Storvik's filter $\gamma \sim p(\gamma|s_k(\Omega_0))$. The sufficient statistics $s_k(\Omega_0)$ are based on the static parameters. The rest of the parameters have the artificial evolution in which overdispersion is used. The overall set of parameters is represented as $\Omega = (\Omega_0, \gamma)$. The ELW filter applies to a wider class of state space models compared to Storvik's original procedure but suffers from two drawbacks, namely, (i) artificial overdispersion of the final posterior and (ii) the requirement of the existence of the sufficient statistic $s_k(\Omega_0)$ for γ and the ability of sampling from the posterior $p(\gamma|s_k(\Omega_0))$.

Development of statistical methods in specific ecological combines the nonlinear and near chaotic behavior of the

system response for various applications [41–44]. A detailed comparison of the inference problem for nonlinear ecology and epidemiology is given in [45]. Nonlinearity is an observer in the experimental research [46]. Although the objectives of epidemiologists and ecologists are different, both are concerned about the persistence of specific species. The mathematical explanations of the population dynamics are similar in both studies [45].

The aim and scope of this paper are to use the chaotic epidemiological or ecological model and perform parameter inference. There are two objectives. First is to perform the inference for the proposed application even if sufficient statistics are not available. Second is to use an online method to perform the parameter inference. Many researchers [47, 48] have discussed the relationship between statistics and chaos. The primary inference methodology used in this manuscript is developed in [49], which is a sequential MCMC (SMCMC) procedure to obtain the unknown parameter posterior inference in dynamical systems. However, then in [49], the proposed methodology was only applicable when the considered measurement model is linear and additive Gaussian noise. In this work, the measurement model of the Ricker dynamical system incorporates a non-Gaussian distribution, and the associated dynamical system (a special case of (1) and (2)) incorporates nonlinearities via the transfer function $\Phi_{k-1,\Omega}(\cdot)$. The appropriate SMCMC algorithm for inferring Ω is developed for the Ricker dynamical system subsequently.

The remainder of this paper is organized into the following sections: In Section 2, Ricker's model is discussed. In Section 3, details of the SMCMC procedure are given. The simulation experiments are given in Section 4. In the last section, Section 5, we state our conclusions, and potential future work is discussed.

2. Ricker's Model

Theoretical ecology relies heavily on mathematical models of competition. Several mathematical models have been suggested to date to characterize the growth of contending populations; some of them are detailed in [50–52], including discrete-time models [53, 54]. The wide range of biological factors that influence ecosystem behavior makes it difficult for researchers to come to a consensus on how to simulate the dynamics of competing populations. Numerous instances of competing species and techniques for mathematical modelling are discussed in one of the pioneering publications on interspecific interaction [55]. The scramble competition has been found to fit the Ricker model [56, 57]. From order to chaos, the Ricker model illustrates dynamics [20–58]. It would be fascinating to observe what dynamic modes emerge when two Ricker maps are joined.

The Ricker's model is a classical discrete population model. It gives the expected density or numbers of individual species at each next generation.

$$\widehat{m}_k = r m_{k-1} e^{-\widehat{m}_{k-1}+u_{k-1}}, u_k \sim \mathcal{N}\left(0, \sigma^2\right). \tag{3}$$

Ricker's model is often used to explain the dynamics of two populations that are linked through migrations [50–58]. As a result, nothing is known about how Ricker communities evolved. In the experimental setup, a noisy model is considered in equation (3); here k represents the time evolution variable. r is a parameter to represent the intrinsic growth rate of the population. The process noise is represented by u_{k-1}, which can also be considered environmental noise. Here the process noise has a zero mean, and the covariance parameter is σ^2. Suppose the dynamics of the population are modelled with Ricker's model, but it is not possible to know the exact population density at any time, so it is necessary to have a measurement model.

$$y_k \sim \text{Poisson}(\phi m_k). \tag{4}$$

Here y_k is the measurement parameter of the individual sampled at any time point k, and ϕ is the scale parameter.

By transforming $m_k = \log(\widehat{m}_k)$, it is seen that (3) becomes

$$m_k = \log(r) + \log(m_{k-1}) - m_{k-1} + z_k, \tag{5}$$

and the measurement model (4) becomes

$$y_k \sim \text{Poisson}(\phi e^{m_k}). \tag{6}$$

Using the transformed variables, equations (5) and (6) can be seen to be special forms of the general state space and measurement model equations given by (1) and (2), respectively. We have $\Phi_{k-1,\Omega}(\cdot) = \log(r) + \log(m_{k-1}) - m_{k-1}$, and $\Psi_{k,\Omega}(\cdot)$ is the Poisson probability density function with mean ϕe^{m_k}. Thus, the Ricker dynamical system has three underlying parameters that govern the system, namely, σ^2, $\log(r)$, and ϕ. In this paper, the latter two parameters are taken to be unknown, that is, $\Omega = [\log(r), \phi]$ and $\sigma^2 = 0.09$ is assumed fixed and known. True values of the parameters for our simulation studies are taken to be $\Omega = [\log(r), \phi] = [3.8, 0.7]$, which the same as given in [45].

3. An Augmented Sequential Markov Chain Monte Carlo Algorithm

Sequential Markov chain Monte Carlo algorithm working process is described in the subsequent text. Sequential updating characteristic of SMCMC is used in the proposed technique. The core notion is addressed in [59], which is focused on the Monte Carlo sum, but the cumulative filtering steps required for estimating the probability $p(y_k|y_{1:k-1}, \Omega)$ minimise. State variable m_k and unknown parameter Ω are supplemented at the time step of $k-1$ in [49]. Therefore, the likelihood function changes accordingly from $p(y_k|y_{1:k-1}, \Omega)$ to $p(y_k|m_{k-1}, \Omega)$. It is possible to achieve the analytical expression to avoid the need for cumulative filtering procedures. This is particularly useful when the amount of k is substantial.

The ASMCMC is an iterative procedure that starts from the initial time step $k = 1$, increases sequentially, and finally

ends when $k = T$. Within the k-th step of the ASMCMC procedure, posterior samples are obtained based on an underlying Markov chain Monte Carlo procedure. This Markov chain Monte Carlo procedure will be called the k-th time step Markov chain Monte Carlo procedure. The target of the k-th step MCMC procedure is the posterior, $p(\Omega, m_T|y_{1:k})$, at time step k. Thus, when $k = T$, we will have obtained samples from the desired posterior $p(\Omega, m_T|y_{1:k})$ as well as $p(\Omega, |y_{1:k})$ via marginalization. Details on the implementation of the k-th step Markov chain Monte Carlo procedure are as follows.

Assume that after the $(k-1)$-th time step MCMC procedure, M samples (i.e., particles) $\xi_{k-1}^j \equiv (\Omega_{k-1}^j, m_{k-1}^j), j = 1, 2, \cdots, M$ are available from the posterior density $p(\Omega, m_{k-1}|y_{1:k-1})$. A class of Gaussian mixture model (GMM) is fitted using $\xi_{k-1}^j, j = 1, 2, \cdots, M$ following the methodology outlined in [48–60]. This results in the estimated density $p_{Mix}(\Omega, m_{k-1}|y_{1:k-1})$ based on GMMs. The methodology developed and implemented in [48–60] ensures that the fitted GMM is close to the true posterior density $p(\Omega, m_{k-1}|y_{1:k-1})$, that is,

$$p_{Mix}(\Omega, m_{k-1}|y_{1:k-1}) \approx p(\Omega, m_{k-1}|y_{1:k-1}), \tag{7}$$

even though the exact form of the latter is unavailable.

To initialize the k-th time step MCMC procedure, the M samples $\xi_{k-1}^j, j = 1, 2, \cdots, M$ are taken to form the starting points of Mk-th step MCMC procedures, that is, $\Omega_{k-1}^j \equiv \Omega_k^{j,0}$ and $m_{k-1}^j \equiv m_{k-1,k}^{j,0}$ for $j = 1, 2, \cdots, M$. Some notations are developed here: denoted by $\Omega_g^{j,k}$ and $m_{k-1,k}^{j,g}$, respectively, to be the values of Ω and m_{k-1} at the g-th cycle of the k-th time step MCMC procedure initialized by ki_{k-1}^0 for $j = 1, 2, \cdots, M$. In other words, the Mk-th time step MCMC procedures initialized based on $\Omega_k^{j,0}$ form separate chains based on separate starting values; this entails that the M MCMC chains can be run in parallel for each time step $k = 1, 2, \cdots, T$.

For details of the steps involved within each k-th step MCMC procedure, we suppress the j notation. For a generic k-th step MCMC procedure (note that there are M of them), initialize $\xi_k^0 \equiv (\Omega_k^0, m_{k-1,k}^0)$ as above from outputs of the $(k-1)$-th chain. At step k of the kth step MCMC procedure, assume $(\Omega_k^g, m_{k-1,k}^g)$ is already available. To transit from $g \longrightarrow g+1$,

(i) Generate

$$\left(\Omega_k^*, m_{k-1,k}^*\right) \sim q\left(\Omega_k, m_{k-1,k}\middle|\Omega_k^g, m_{k-1,k}^g\right), \tag{8}$$

where $q(\cdot|\cdot)$ in equation (8) is proposal density.

(ii) Compute the acceptance probability

$$\alpha_k((\Omega^g, m^g), (\Omega^*, m^*)) = \min\{\mathbf{A}\cdot\mathbf{B}, 1\} \text{ here} \tag{9}$$

$$\mathbf{A} = \frac{p\left(y_k\middle|m_{k-1,k}^*, \Omega_k^*\right)\widehat{p}_{Mix}\left(\Omega_k^*, m_{k-1,k}^*|y_{1:k-1}\right)}{p\left(y_k\middle|m_{k-1,k}^g, \Omega_k^g\right)\widehat{p}_{Mix}\left(\Omega_k^g, m_{k-1,k}^g|y_{1:k-1}\right)} \tag{10}$$

$$\mathbf{B} = \frac{q\left(\Omega_k^g, m_{k-1,k}^g\middle|\Omega_k^*, m_{k-1,k}^*\right)}{q\left(\Omega_k^*, m_{k-1,k}^*\middle|\Omega_k^g, m_{k-1,k}^g\right)} \tag{11}$$

where $p(y_k|m_{k-1}^*, \Omega_k$ is the probability function of y_k given m_{n-1} and Ω as in ((13)).

Set $(\Omega_k^{k+1}, m_{k-1,k}^{k+1}) = (\Omega_k^*, m_{k-1,k}^*)$ with probability $\alpha_k((\Omega_k^g, m_{k-1,k}^g), (\Omega_k^*, m_{k-1,k}^*))$; otherwise, set

$$\left(\Omega_k^{k+1}, m_{k-1,k}^{k+1}\right) = \left(\Omega_k^g, m_{k-1,k}^g\right). \tag{12}$$

Continue the iteration from $k+1 \longrightarrow k+2$.

The aforementioned Markov chain will converge as $k \longrightarrow \infty$ to the stationary (and target) distribution determined by the numerator of the expression $\mathbf{A}$ in (10), namely, $p(y_k|m_{k-1}, \Omega)\widehat{p}_{Mix}(\Omega, m_{k-1}|y_{1:k-1})$. Since

$$\begin{aligned} &p(y_k|m_{k-1}, \Omega)\widehat{p}_{Mix}(\Omega, m_{k-1}|y_{1:k-1}) \\ &\quad \approx p(y_k|m_{k-1}, \Omega)p(\Omega, m_{k-1}|y_{1:k-1}) \propto p(\Omega, m_{k-1}|y_{1:k}). \end{aligned} \tag{13}$$

The target density of the k-th step MCMC procedure is the posterior density of (Ω, m_{k-1}) given $y_{1:k}$, where the first approximate equality is due to ((7)). In our previous work [49], $p(y_k|m_{k-1}, \Omega)$ was available in closed form due to a linear measurement model and additive noise variables distributed as Gaussian in both the state space and measurement models. In the present context,

$$p(y_k|m_{k-1}, \Omega) = \int_{m_k} \Psi_{k,\Omega}(y_k|m_k)p(m_k|m_{k-1}, \Omega)dm_k. \tag{14}$$

Subsequently, after the burn-in period B, samples of $\Omega_k^{g^*}$ only are collected for a large value of $g^* \geq B$, whereas the samples of $m_{k-1}^{g^*}$ are discarded. MCMC theory and the marginalization property ensure that $\Omega_k^{g^*}$ is distributed according to the posterior $p(\Omega|y_{1:k})$. Since there are M parallel MCMC chains, M such samples of Ω, namely, $\{\Omega_k^{g^*,j}\}_{j=1}^M$, are collected in this way. Subsequently, pure filtering steps as in given in ((15)) are performed to get the samples of m_k from $p(m_k|y_{1:k}, \Omega)$ for each Ω in the collection $\{\Omega_k^{g^*,j}\}_{j=1}^M$ [48]. Hence, the particle pairs $\{\Omega_k^{g^*,j}, m_k^j\}_{j=1}^M$ constitute M samples from the joint posterior density $p(\Omega, m_k|y_{1:k})$ and can serve as the input for the next $(n+1)$-st time step of the ASMCMC Algorithm 1.

$$w_k^j \propto \frac{p\left(y_k\middle|m_k^j, \Omega\right)p\left(m_k^j\middle|m_{k-1}^j, \Omega\right)}{q\left(m_k^j\middle|m_{k-1}^j, y_k, \Omega\right)} \text{for} j = 1, 2, \cdots, M. \tag{15}$$

$[\{m_T^j, \Omega_T^j\}_{j=1}^M]$=ASMCMC $[\{m_0^j, \Omega_0^j\}_{j=1}^M]$
Initialize with M initial value (Ω_0^j, m_0^j) prior density $p_0(\Omega, m_0)$.
Start for k=1:T
    $[\{m_k^j, \Omega_k^j\}_{j=1}^M]$=AMCMC $[\{m_{k-1}^j, \Omega_{k-1}^j\}_{j=1}^M, y_k]$
    DO: M Parallel MCMC chains initialized from M pairs $(\Omega_{k-1}^j, m_{k-1}^j)$, $j = 1, 2, \cdots, M$.
    For the generic j-th chain:
    Start with $(\Omega^0, m^0) \equiv (\Omega_{k-1}^i, m_{k-1}^i)$ (prior value).
    for k=1:B (burn-in chains)
        Generate samples $(\Omega^*, m^*) \sim q(\Omega^*, m^* | \Omega^{k-1}, m^{k-1})$.
        Compute the acceptance probability $\alpha_k = \min\{\mathbf{A} \cdot \mathbf{B}, 1\}$ as in (9) and (10).
        Set $(\Omega^g, m^g) = (\Omega^*, m^*)$ with probability α_k
        Else $(\Omega^g, m^g) = (\Omega^{k-1}, m^{(k-1)})$ with probability $1 - \alpha_k$
    end for
    Obtain $\Omega^B \equiv \Omega_k^j$, from $j = 1, 2, \cdots, M$ chains.
    $m_k^j \sim p(m_k^j | y_{1:k}, \Omega_k^j)$ Samples are based (12)
    Mixture fitting $\widehat{p}_{Mix}(\Omega, m_k | y_{1:k})$
    Output: $\{\Omega_k^j, m_k^j\}_{i=1}^M$ and fitted mixture model $\widehat{p}_{Mix,n} \equiv \widehat{p}_{Mix}(\Omega, m_k | y_{1:k})$.
The posterior distribution $p(\Omega | y_{1:T})$ is based on the collected samples of Ω_T^j.
end for

Algorithm 1: Augmented sequential MCMC procedure.

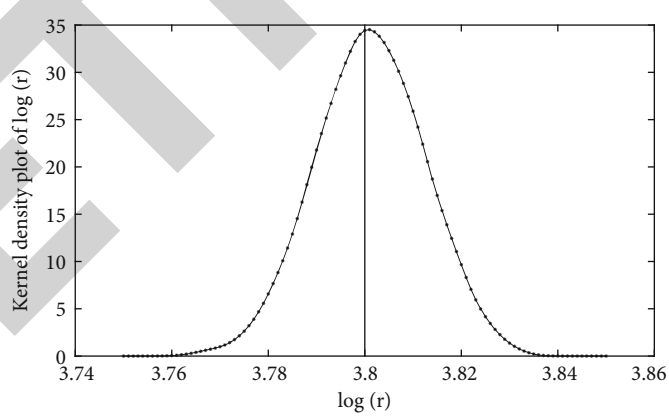

Figure 1: The estimated density curves are based on final posterior samples of the parameter log (r) at the completion of the ASMCMC.

4. Results and Discussion

In this section, the ASMCMC methodology is used for parameter inference in the Ricker dynamical system. The y-observations were generated from the time-discretized Ricker's model (state space model given by (5) and the measurement model given by (6)) using the initial point mass prior at $m_0 = 7$. Starting from the initial state values generated from the prior, the state and measurement systems are updated at every fixed time step of $k = 1, 2, \cdots, T = 10$. The true value for Ω is taken as $\Omega = [\log(r), \phi] = [3.8, 0.7]$, which is the same as the choice made in [45]. The burn-in B was set at $B = 5000$. The estimated posterior density curves are obtained based on the final posterior samples of $\Omega = [\log(r), \phi]$ at the completion of the ASMCMC algorithm. These density curves are given in Figures 1 and 2 for the parameters $\log(r)$ and ϕ, respectively. In Figure 1, estimated density curves based on final posterior samples of

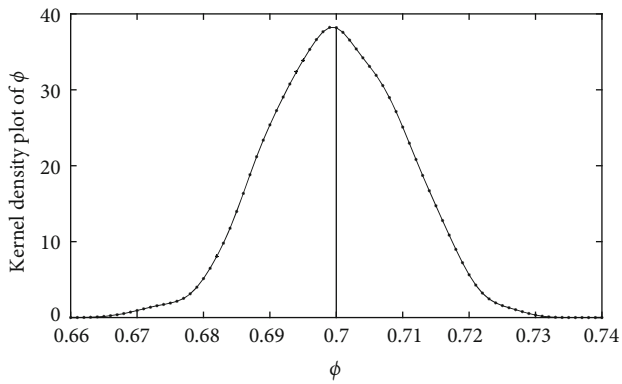

Figure 2: The estimated density curves are based on final posterior samples of the parameter ϕ at the completion of the ASMCMC.

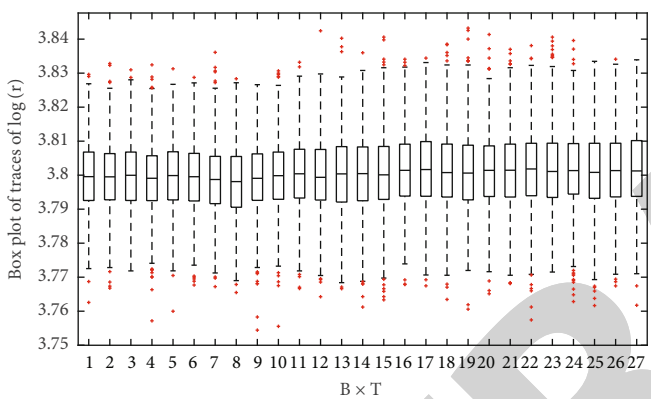

Figure 3: Boxplot trajectories representing the distribution of $p(\Omega|y_{1:k})$ based on the ASMCMC algorithm. The boxplots are constructed based on the M final iterates $\log(r)_k^{j,B}$.

Table 1: Simulation parameters.

Variable	Value	Description
$\log(r)$	3.8	True value of parameter
ϕ	0.7	True value of parameter
m_0	7	Prior of state variable
B	5000	Burn-in period

the parameter $\log(r)$ at the completion of the ASMCMC are presented. The vertical solid black line represents the true value of the parameter $\log(r) = 3.8$, whereas the estimated density curves based on the final posterior samples of the parameter ϕ at the completion of the ASMCMC are presented in Figure 3. The vertical solid black line represents the true value of the parameter $\phi = 0.7$. We note that the true values of the parameters are well within the support of their respective posterior densities, which gives credence to the parameter inference methodology using the ASMCMC procedure. The following Table 1 represents the simulation parameters considered in the experimental setup.

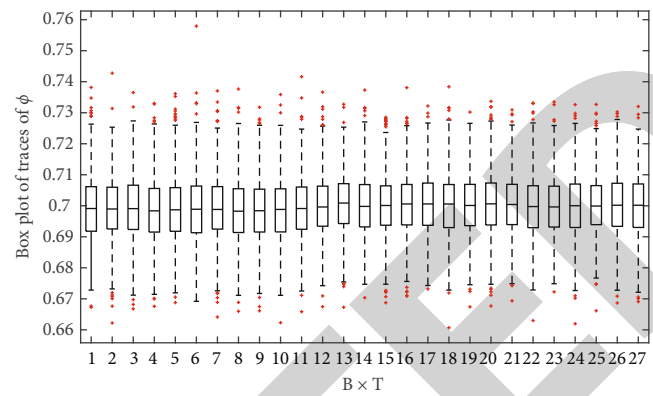

Figure 4: Boxplot trajectories representing the distribution of $p(\Omega|y_{1:k})$ based on the ASMCMC algorithm. The boxplots are constructed based on the M final iterates $\phi_k^{j,B}$.

To illustrate the convergence of the ASMCMC procedure, boxplot trajectories represent the distribution of $p(\Omega|y_{1:k})$ for $k = 1, 2, \cdots, T$ can be plotted. These boxplots are constructed based on the M final iteration $\Omega_k^{g^*,j}$ for $j = 1, 2, \cdots, M$, collected after burn-in. Figure 3 shows that the boxplot trajectories based on posterior samples of $\log(r)$. Figure 3 indicates that these boxplot trajectories have stabilized long before reaching the final time point $T = 10$. In other words, the posterior $p(\log(r)|y_{1:k})$ changes much when k approaches the final time point T, which can be taken as an indication that the estimate of $p(\log(r)|y_{1:k})$ based on the ASMCMC sampler has converged. A similar boxplot trajectory plot (shown in Figure 4) is obtained for ϕ which indicates that the convergence of its posterior distribution has been achieved.

5. Conclusion

The dynamical system based on Ricker's model is an example of a nonlinear and non-Gaussian system that has applications in ecology and epidemiology. We develop the ASMCMC algorithm for the Ricker dynamical system to perform Bayesian parameter inference. We observe that the posteriors encompass the true parameter values used to simulate observations from the Ricker dynamical system. Our future work will be to investigate the performance of the ASMCMC algorithm when σ^2 is unknown as well and for high-dimensional dynamical systems that appear in ecology and epidemiology.

Symbols

m_k:	State variable
y_k:	Observation variable
$\Phi_{k-1,\Omega}(\cdot)$:	State model
$\Psi_{k,\Omega}(\cdot)$:	Measurement model
T:	Final time point
k:	Time variable
u_{k-1}:	State noise

v_k:	Observation noise
Ω:	Unknown parameters
$p(\cdot\|\cdot)$:	Probability density function
$q(\cdot\|\cdot)$:	Proposal distribution
$y_{1:k}$:	Observation vector for time point 1 to k
s_k:	Sufficient statistics at k-th time point
w_k^j:	Weights vector at time point k
B:	Burn-in period
$\{\log(r), \phi\}$:	Unknown parameters of Ricker dynamical system
ξ_{k-1}^j:	Augmented particles of unknown state and parameters.

Data Availability

This paper does not require any dataset whereas the simulated data is used using MATLAB tool.

Conflicts of Interest

Authors of this article have no conflict of interest publishing this article in Journal of Sensors.

References

[1] M. Eder, M. Reip, and G. Steinbauer, "Creating a robot localization monitor using particle filter and machine learning approaches," *Applied Intelligence*, vol. 52, no. 6, pp. 6955–6969, 2022.

[2] M. Breakspear, "Dynamic models of large-scale brain activity," *Nature Neuroscience*, vol. 20, no. 3, pp. 340–352, 2017.

[3] Y. Shoukry, P. Nuzzo, A. Puggelli, A. L. Sangiovanni-Vincentelli, S. A. Seshia, and P. Tabuada, "Secure state estimation for cyber physical systems under sensor attacks: a satisfiability modulo theory approach," *IEEE Transactions on Automatic Control*, vol. 62, no. 10, pp. 4917–4932, 2017.

[4] Y. Fang, C. Wang, W. Yao, X. Zhao, H. Zhao, and H. Zha, "On-road vehicle tracking using part-based particle filter," *IEEE Transactions on Intelligent Transportation Systems*, vol. 20, no. 12, pp. 4538–4552, 2019.

[5] S. S. Moghaddasi and N. Faraji, "A hybrid algorithm based on particle filter and genetic algorithm for target tracking," *Expert Systems with Applications*, vol. 147, article 113188, 2020.

[6] J. Liu, M. Ahmed, M. A. Mirza et al., "Rl/drl meets vehicular task offloading using edge and vehicular cloudlet: a survey," *IEEE Internet of Things Journal*, vol. 9, no. 11, pp. 8315–8338, 2022.

[7] L. Yan, D. Zhou, M. Fu, and Y. Xia, "State estimation for asynchronous multirate multisensor dynamic systems with missing measurements," *IET Signal Processing*, vol. 4, no. 6, pp. 728–739, 2010.

[8] A. Mahmood, A. Ahmed, M. Naeem, and Y. Hong, "Partial offloading in energy harvested mobile edge computing: a direct search approach," *IEEE Access*, vol. 8, pp. 36757–36763, 2020.

[9] W. U. Khan, M. A. Jamshed, E. Lagunas et al., "Energy efficiency optimization for backscatter enhanced noma cooperative V2X communications under imperfect CSI," 2022, http://arxiv.org/abs/2202.01592.

[10] W. U. Khan, T. N. Nguyen, F. Jameel et al., "Learning-based resource allocation for backscatter-aided vehicular networks," *IEEE Transactions on Intelligent Transportation Systems*, pp. 1–15, 2021.

[11] Y. M. Zhang, H. Wang, H. P. Wan, J. X. Mao, and Y. C. Xu, "Anomaly detection of structural health monitoring data using the maximum likelihood estimation-based Bayesian dynamic linear model," *Structural Health Monitoring*, vol. 20, no. 6, pp. 2936–2952, 2021.

[12] Y. Amidi, B. Nazari, S. Sadri, and A. Yousefi, "Parameter estimation in multiple dynamic synaptic coupling model using Bayesian point process state-space modeling framework," *Neural Computation*, vol. 33, no. 5, pp. 1269–1299, 2021.

[13] Z. Ghahramani and S. T. Roweis, "Learning nonlinear dynamical systems using an EM," *Advances in Neural Information Processing Systems*, vol. 11, pp. 431–437, 1999.

[14] S. Colonnese, S. Rinauro, and G. Scarano, "Fast maximum likelihood scale parameter estimation from histogram measurements," *IEEE Signal Processing Letters*, vol. 18, no. 8, pp. 474–477, 2011.

[15] A. Mahmood, A. Ahmed, M. Naeem, M. R. Amirzada, and A. Al-Dweik, "Weighted utility aware computational overhead minimization of wireless power mobile edge cloud," *Computer Communications*, vol. 190, pp. 178–189, 2022.

[16] W. Ullah Khan, E. Lagunas, Z. Ali et al., "Opportunities for physical layer security in UAV communication enhanced with intelligent reflective surfaces," 2022, http://arxiv.org/abs/2203.16907.

[17] F. Septier and G. W. Peters, "Langevin and Hamiltonian based sequential MCMC for efficient Bayesian filtering in high-dimensional spaces," *IEEE Journal of Selected Topics in Signal Processing*, vol. 10, no. 2, pp. 312–327, 2016.

[18] Z. Khan, T. Balch, and F. Dellaert, "MCMC-based particle filtering for tracking a variable number of interacting targets," *IEEE Transactions on Pattern Analysis and Machine Intelligence*, vol. 27, no. 11, pp. 1805–1819, 2005.

[19] N. De Freitas, A. Doucet, and N. Gordon, *An Introduction to Sequential Monte Carlo Methods*, Springer Verlag, SMC Practice, 2001.

[20] G. L. Jones and Q. Qin, "Markov chain Monte Carlo in practice," *Annual Review of Statistics and Its Application*, vol. 9, 2021.

[21] D. J. Lunn, A. Thomas, N. Best, and D. Spiegelhalter, "Winbugs-a Bayesian modelling framework: concepts, structure, and extensibility," *Statistics and Computing*, vol. 10, no. 4, pp. 325–337, 2000.

[22] J. K. Kruschke and T. M. Liddell, "Bayesian data analysis for newcomers," *Psychonomic Bulletin & Review*, vol. 25, no. 1, pp. 155–177, 2018.

[23] T. Lux, "Bayesian estimation of agent-based models via adaptive particle Markov chain Monte Carlo," *Computational Economics*, pp. 1–27, 2021.

[24] J. M. Bardsley and T. Cui, "A Metropolis-Hastings-within-Gibbs sampler for nonlinear hierarchical-Bayesian inverse problems," in *2017 MATRIX Annals*, pp. 3–12, Springer, Cham, 2019.

[25] C. Andrieu, A. Doucet, and R. Holenstein, "Particle Markov chain Monte Carlo methods," *Journal of the Royal Statistical Society: Series B (Statistical Methodology)*, vol. 72, no. 3, pp. 269–342, 2010.

[26] M. Speich, C. F. Dormann, and F. Hartig, "Sequential Monte-Carlo algorithms for Bayesian model calibration–a review and

Hindawi
Journal of Sensors
Volume 2023, Article ID 9756492, 1 page
https://doi.org/10.1155/2023/9756492

Retraction

Retracted: Dynamic Evaluation and Prediction for Macroeconomic Based on IGA-LSSVM

Journal of Sensors

Received 8 August 2023; Accepted 8 August 2023; Published 9 August 2023

This article has been retracted by Hindawi following an investigation undertaken by the publisher [1]. This investigation has uncovered evidence of one or more of the following indicators of systematic manipulation of the publication process:

(1) Discrepancies in scope
(2) Discrepancies in the description of the research reported
(3) Discrepancies between the availability of data and the research described
(4) Inappropriate citations
(5) Incoherent, meaningless and/or irrelevant content included in the article
(6) Peer-review manipulation

The presence of these indicators undermines our confidence in the integrity of the article's content and we cannot, therefore, vouch for its reliability. Please note that this notice is intended solely to alert readers that the content of this article is unreliable. We have not investigated whether authors were aware of or involved in the systematic manipulation of the publication process.

Wiley and Hindawi regrets that the usual quality checks did not identify these issues before publication and have since put additional measures in place to safeguard research integrity.

We wish to credit our own Research Integrity and Research Publishing teams and anonymous and named external researchers and research integrity experts for contributing to this investigation.

The corresponding author, as the representative of all authors, has been given the opportunity to register their agreement or disagreement to this retraction. We have kept a record of any response received.

References

[1] X. Bai, "Dynamic Evaluation and Prediction for Macroeconomic Based on IGA-LSSVM," *Journal of Sensors*, vol. 2022, Article ID 6823102, 7 pages, 2022.

Hindawi
Journal of Sensors
Volume 2022, Article ID 6823102, 7 pages
https://doi.org/10.1155/2022/6823102

Research Article

Dynamic Evaluation and Prediction for Macroeconomic Based on IGA-LSSVM

Xiaolong Bai

School of Management University of Liverpool, Liverpool, L697ZX Merseyside, UK

Correspondence should be addressed to Xiaolong Bai; xiaolong.bai18@student.xjtlu.edu.cn

Received 12 April 2022; Revised 7 May 2022; Accepted 13 May 2022; Published 8 June 2022

Academic Editor: Han Wang

Among all statistics, government statistics plays an extremely important role in socioeconomic activities, while the continuous changes of external factors bring new challenges to government statistics and have a great impact on the quality of statistics. With the rapid development of the economy and the maturity of the market economy system, the demand for government statistics from all walks of life has become more and more vigorous. In order to effectively improve the accuracy of macroeconomic outflow forecasting and further secure economic production, a weighted least squares support vector machine (LS-SVM) optimized with the immune genetic algorithm (IGA) is proposed to build a macroeconomic outflow forecasting model. For the nonlinearity, time-varying, and complexity of the economic outflow system, a new weighted strategy function is proposed to improve the LS-SVM, and then the IGA is introduced to optimize the improved LS-SVM with the kernel parameter δ and the regularization parameter γ. Finally, an experimental analysis is conducted using economic emergence data from economic history. The results show that the maximum relative error of forecasting using the model is 2.763%, the minimum relative error is 0.705%, the average relative error is 1.3298%, and the model has faster convergence, stronger generalization ability, and higher forecasting accuracy than other forecasting models.

1. Introduction

With the change of economic development mode and the continuous change of demand structure, China's economic system is gradually moving towards the market economy system, and the interests of subjects are becoming more and more diversified [1]. The accuracy of individual indicators is no longer the only criterion for assessing the quality of data, and the data of different macroeconomic statistical indicators should be in a mutually coordinated relationship [2]. For this reason, both academic circles and government statistical departments have increased the exploration of statistical data quality assessment methods from the perspective of data coordination [3].

The quality of government statistics is directly related to the accuracy of national macroeconomic control and the correctness of the development strategy of each economic entity, but the quality of Chinese government statistics has always been the core topic of socioeconomic activities and statistical work, and has been concerned by many scholars at home and abroad, becoming a difficult problem in the statistical field [4]. In addition to affecting economic activities, the quality of government statistics also directly reflects the credibility of the government [5]. Accurate, comprehensive, fast, and effective statistics can enhance the credibility of the government and play a very important role in the public's access to information and correct decision-making [6].

In recent years, China's economy has experienced unprecedented sustained and rapid growth, and as China's economic strength and international influence continue to grow, the quality of macroeconomic statistics as a measure of economic development has also attracted widespread attention from people at home and abroad [7]. However, scholars at home and abroad as well as people from all walks of life are constantly questioning the main macroeconomic statistics of China [8]. In order to make the majority of data users better understand the macroeconomic data of China, and to further align the macroeconomic statistics of China with international standards and enhance their international comparability, this paper considers it necessary to try to

conduct an in-depth and systematic assessment of the data quality of the five major macroeconomic indicators of China from a new perspective [9]. This paper believes that it is necessary to try to conduct an in-depth assessment of the data quality of the five major macroeconomic indicators of China from a new perspective and draw corresponding conclusions from them, in order to provide some reference for the future economic decision-making and bring convenience to the data users [10].

Wu and Ning (2018) pointed out that the official GDP data published in China since 1998 are suspected to be overestimated and biased much more than the errors caused by statistical technical difficulties, and that the official GDP growth rate does not reflect the real economic results, and the paper gives a true assessment of the economic growth in China [11, 12]. Blanchard [13] assessed the quality of Chinese energy statistics from 1990 to 2000 based on the assumption that energy data should be coherent between different items within energy data and concluded that energy data in the early 1990s were relatively accurate and reliable, but the quality of data has declined since the mid-1990s. Gupta and Kabundi [14] selected 10 core macroeconomic indicators and assessed the accuracy of GDP data by constructing a fixed-effects variable intercept model using panel data for 28 regions in China from 1984 to 2001. It was found that the regions did not find a basis for long-run errors in GDP data throughout the study period of 1984-2001. Sagaert et al. [15] constructed an econometric model based on the *C-D* production function and selected relevant indicator data from 1978 to 2004 to evaluate the accuracy of GDP by calculating traditional statistics such as COOK and W-K, which were calculated to obtain questionable GDP data for 1978, 1984-1986, and 1991. An et al. [16] constructed a data quality diagnosis method based on robust MM estimation based on *C-D* production function and evaluated the accuracy of Chinese GDP data from 1978 to 2008 and concluded that Chinese GDP data were relatively reliable.

Summarizing the domestic and international literature, it is found that in terms of model estimation methods, most scholars still use the ordinary least squares method to estimate model parameters; however, OLS regression is vulnerable to the influence of a few outliers in the data set; thus, the model estimation results are inaccurate, and the residuals obtained according to the fitted model cannot detect all outliers [17]. In recent years, statisticians have begun to pay attention to robust estimation methods and establish data quality assessment models based on robust estimation methods, which can effectively solve the drawback of multiple outliers masking that often occurs in OLS methods.

2. Related Work

Although foreign research on macroeconomics has been relatively mature, domestic research on macroeconomics is relatively rare, and there is no systematic introduction and research in related fields, and most of the literature is only a simple introduction to macroeconomics and simple application in the field of auditing. This indicates that the law has not attracted sufficient attention of domestic scholars, and there is still a considerable gap with foreign countries in this regard.

In terms of assessing the quality of audited financial data, Azis et al. [18] gives the origin and meaning of macroeconomics, then uses the annual financial data of a university to illustrate how to use macroeconomics to assess the data, suggests that analyzing the first two digits of the data can give more accurate results than analyzing only the first digit of the data, and finally summarizes the specific steps of using macroeconomics in the field of auditing [19]. From the daily experience of CPAs, with the help of Excel tools, it was found that the main financial data published by Chinese listed companies are well in line with macroeconomics, and the data that do not comply with this law can only indicate signs of fraud, which provides strong evidence for auditors to detect financial fraud. Forrester [20] briefly summarizes the application of macroeconomics in the security market, followed by a detailed description of the sample selection described in the article, and finally applies the macroeconomic goodness-of-fit test and statistical tests to investigate whether there is artificial manipulation of profits in the annual accounting statement net profits of 3570 listed companies on the Shanghai and Shenzhen exchanges in China between 2000 and 2002. McAlinn et al. [6] identifies fraudulent practices in auditing finances and applies existing foreign experience to Chinese auditing research. Rossi and Sekhposyan [8] explains the scope and steps of macroeconomics in the field of auditing, specifies how to apply the law through actual financial data, and suggests that computer-related software can be used to analyze whether the data conforms to macroeconomics. Zheng-wan et al. [11] suggests that with the development of modern information technology, the audit model has evolved into a data-based audit and then introduces the basic principles of macroeconomics, the conditions of use, and the steps of analysis. Wu and Ning [12] briefly introduced the meaning of macroeconomics and its scope of use and proposed that macroeconomics is a useful supplement to audit sampling techniques based on the analysis of the shortcomings of audit sampling. The macroeconomics and correlation coefficients are combined with the quarterly and annual financial data of balance sheet and income statement of listed companies, and the Excel software is used to check the authenticity of the financial data of listed companies.

From the above literature review, it can be seen that the research on macroeconomics in China started relatively late compared with that in foreign countries, and it is far less extensive and deeper than the research already conducted in foreign countries. According to the existing research in China, most of the articles only focus on the existence of fraud and artificial manipulation of financial data in the field of auditing.

3. Diagnosis of the Quality of Macroeconomic Statistics

3.1. Trend-Fitting Diagnostic Method. The existing trend-fitting diagnostic method assesses the coordination between data by calculating the error rate between the actual

statistical values of the explanatory variables in period t and the estimated values obtained according to the model, and if the error rate exceeds the permissible error range set by itself, the data in that period are considered to be inconsistent, and the credibility of this data is doubtful. The specific formula is as follows:

$$\delta_t = \frac{y_t - \widehat{y}_t}{y_t}, \tag{1}$$

where δ_t represents the error rate, y_t represents the actual statistical value, and $\widehat{y}_t$ represents the estimated value.

From reading the extensive literature, it is found that statisticians generally consider macroeconomic data estimates to be suspect when they deviate from the actual values by more than 5%. In this paper, based on the previous research, the maximum allowable error rate is also set to 5%.

3.2. Statistical Diagnosis Method. Robust regression by itself enables the estimation results to be more resistant to outliers and reduce the impact of outliers on the estimation results when there are outliers in the data set, but it also enables the identification of the type of outliers and the diagnosis of data quality through the robust residual-robust distance diagnostic plot (RR-RD diagnostic plot). The vertical axis of the RR-RD diagnostic plot is the standardized robust residuals $\mathrm{RR}_t = e_t/\widehat{\sigma}_S$, and the horizontal axis is the robust martingale distance RD_t in the independent variable X-space.

$$\mathrm{RD}_t = \sqrt{(x_t - \mu_{\mathrm{MCD}})' \sum_{\mathrm{MCD}}^{-1} (x_t - \mu_{\mathrm{MCD}})\mathrm{RD}_t^2 \sim \chi^2_{(p)}}, \quad t = 1, 2, \cdots, n. \tag{2}$$

In equation (2), the μ_{MCD} mean vector and covariance matrix $\sum_{\mathrm{MCD}}$ are robust estimates obtained from MCD estimation to resist the effect of outliers on the estimation results, and p refers to the number of explanatory variables in the model.

Based on the RR-RD diagnostic chart, it is possible not only to diagnose which data points are outliers but also to identify the type of outliers. On the vertical axis, under the assumption that the residuals obey a normal distribution, this data point can be regarded as an outlier in terms of Y if $\mathrm{RR}_t < -\sqrt{x^2_{1.0795}}$ or $\mathrm{RR}_t > \sqrt{x^2_{1.0795}}$, RR_t. The critical value $\pm$ 2.24, where 2.24 is the maximum distance allowed to deviate in the Y direction, is the maximum allowed deviation distance in the later section. On the horizontal axis, this data point can be considered an outlier on the X side if $\mathrm{RD}_t > \sqrt{x^2_{p.0795}}$ (p is the number of explanatory variables in the model), and this robust distance is considered to be overleveraged. The RR-RD diagnostic plot divides the data points into four categories.

$|\mathrm{RR}_t|$ and RD_t are small for normal values, $|\mathrm{RR}_t|$ is large and RD_t is small for longitudinal outliers, $|\mathrm{RR}_t|$ and RD_t are both large for bad leverage points, and $|\mathrm{RR}_t|$ is small and RD_t is large for good leverage points. Among the four types of data points, normal values and good leverage points are consistent with the overall trend of the data set and do not lead to the degradation of data quality, but longitudinal outliers and bad leverage points are far from the overall trend of the data set from X-space or Y-space, and the presence of these two types of data points increases the standard error of the regression coefficients, which leads to the degradation of data quality.

4. Improving LS-SVM

The basic idea of weighted LS-SVM is to set different weights for each training sample according to the degree of influence on the modeling. The author constructs a new weighting strategy function by considering the time factor and the similarity between samples:

$$g_i = \lambda_i g_{T_i} + (1 - \lambda_i) g_{Di}, \tag{3}$$

where g_i is the importance of the i-th sample, which is composed of 2 parts, such as the time weight function g_{T_i} and the similarity function g_{Di}, $\lambda_i \in [0, 1]$ is used to adjust the weights of both, g_{T_i} is taken according to the time of the training sample from the test sample, the closer the training sample is to the test sample, the more important it is, g_{Di} is taken according to the Euclidean distance of the training sample from the test sample, and the closer the training sample is to the test sample, the more important it is. The closer the training sample is, the more important it is.

Using x_i, y_i as the input and output of the model, the improved LS-SVM can be described as solving the following minimum problem:

$$\min_{w,b,e}(w, e) = \frac{1}{2} w^T w + \frac{1}{2}\gamma \sum_{k=1}^{N} g_i e_i^2, \tag{4}$$

where w is the weight vector, $\gamma > 0$ is the regularization parameter, and e_i is the error variable.

$$s.t. y_i = w f(x_i) + b + e_i, i = 1, 2, \cdots, N, \tag{5}$$

where $f(x_i)$ denotes the nonlinear mapping of the sample to the high-dimensional feature space, and b is the bias value.

The Lagrangian multiplier α_i is introduced to construct the following Lagrangian function:

$$L(w, b, e, \alpha) = J(w, e) - \sum_{k=1}^{N} \alpha_i \{w^T f(x_i) + b + e_i - y_i\}. \tag{6}$$

The improved LS kuuch matrix can be obtained by combining the optimized SVM Kuhn matrix:

$$\begin{bmatrix} \alpha \\ b \end{bmatrix} = \begin{bmatrix} 0 & 1^{\mathrm{T}} \\ 1 & \Omega + V_\gamma \end{bmatrix}^{-1} \begin{bmatrix} 0 \\ y_N \end{bmatrix}, \tag{7}$$

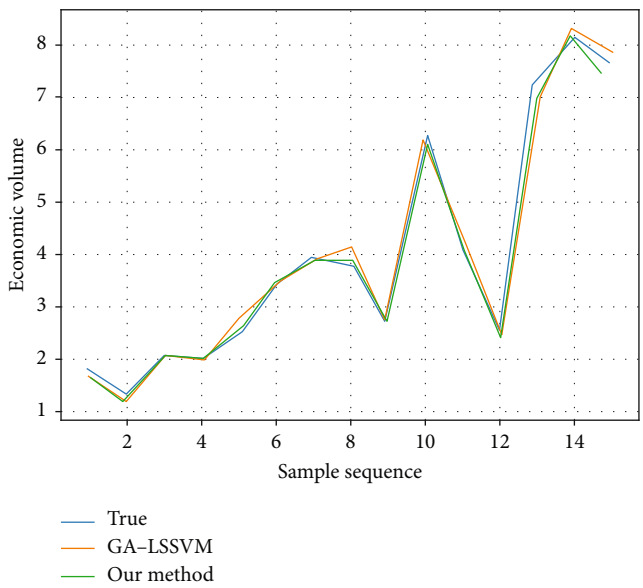

Figure 1: Comparison of prediction values and practical ones.

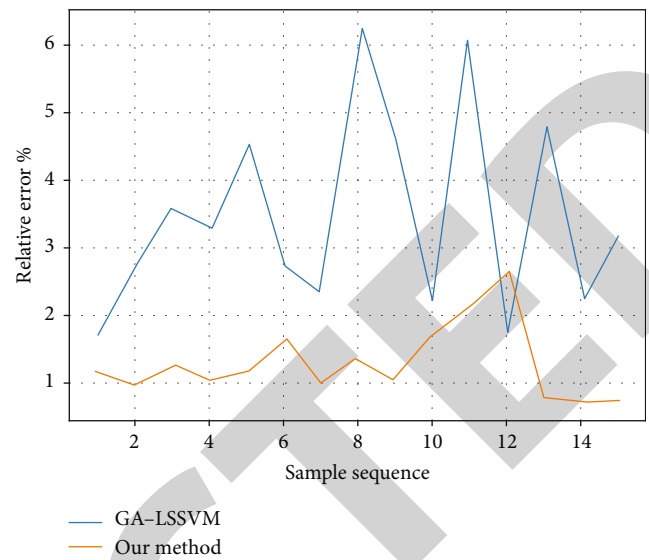

Figure 2: Relative errors of prediction values.

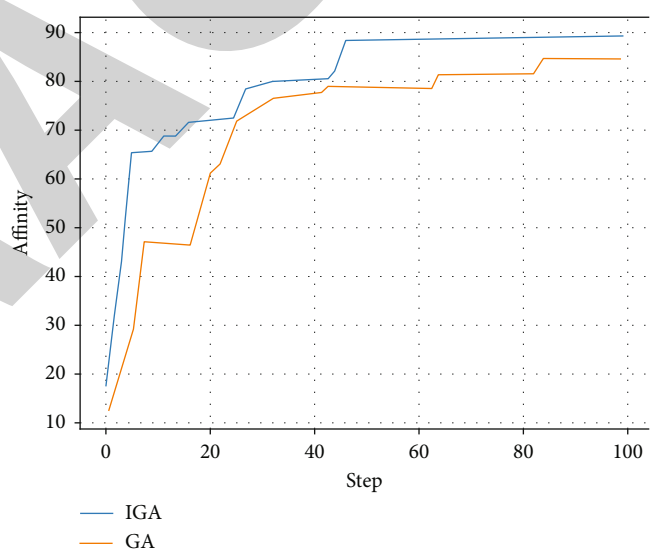

Figure 3: Comparison in terms of optimization speed between IGA and GA.

where $V_\gamma = \text{diag}\{1/\gamma g_1, \cdots, 1/\gamma g_N\}$; $y^{TN} = [y_1, \cdots, y_N]$, $1^T = [1_1, \cdots, 1_N]$, Ω is the kernel matrix, and its elements $K(x_i, y_i) = f(x_i)^T f(x_j)$ are called kernel functions.

The author selects the radial basis function (RBF) $K(x_i, x_j) = \exp[-(x - x_i)^2/\delta_2]$ and finally obtains the improved LS-SVM fitting model as

$$\phi(x) = \sum_{i=1}^{L} \alpha_i K(x_i, x) + b. \tag{8}$$

The time weights are determined based on the properties of the normal distribution, i.e., $g_{Ti} = \exp(-(t_i - t)^2/2\beta)$, where t_i is the sampling moment of the i-th training sample, t is the sampling moment of the current test sample, and β is determined based on the distribution of the sample prediction error.

The similarity weights are determined by nonlinear interpolation. Let the similarity weight of the training sample with the smallest Euclidean distance from the predicted sample be 1 and the similarity weight of the training sample with the largest Euclidean distance from the predicted sample be 0. The nonlinear interpolation function selects $g_D = e^{-t^2/2\beta}$, t_j as the sampling moment of the j-th test sample, and then the similarity weights of the other training samples are determined by nonlinear interpolation of the normal distribution function [21, 22].

5. IGA-LSSVM-Based Economic Outflow Prediction

The model needs to normalize the sample data with inconsistent magnitudes before making predictions, and the normalization interval chosen by the author is [0.1, 0.9], and the normalization formula is as follows:

$$Y = \frac{X - X_{\min}}{X_{\max} - X_{\min}} \times 0.8 + 0.1, \tag{9}$$

where $X, X_{\min}$ and $X_{\max}$ are the sample data, the minimum value in the sample data, and the maximum value in the sample data, respectively, and Y is the normalized data. After the prediction operation is completed, the predicted data are normalized by the inverse normalization formula:

$$X = X_{\min} + \frac{(Y - 0.1)(X_{\max} - X_{\min})}{0.8} \times 0.8. \tag{10}$$

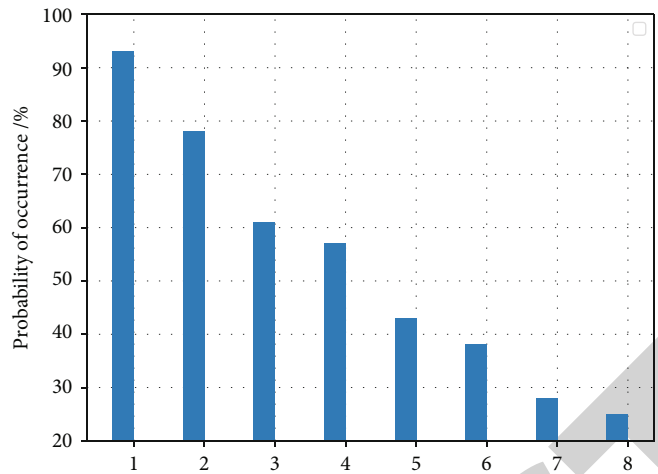

Figure 4: Probability distribution of Benford's law.

The specific steps of economic outflow prediction based on IGA-LSSVM are as follows:

Step 1. Determine the input and output layers of the model and obtain the sample data and then preprocess the sample data according to equation (9).

Step 2. Select the optimal kernel parameter δ and the optimal regularization parameter γ of LS-SVM using IGA and then train the model based on the training sample set to obtain the IGA-LSSVM-based gas outflow prediction model.

Step 3. The trained IGA-LSSVM model is used to predict the prediction sample set, and after the prediction is completed, the inverse normalization process is performed according to equation (10), and then the error analysis is performed [23, 24].

6. Economic Outflow Prediction Test and Analysis

There are many factors affecting the economic outflow, and the model is compared with the weighted LS-SVM proposed in the literature [25] based on the prediction error of the sample. 2 prediction methods are chosen RBF, the same optimal model parameters are selected by IGA optimization, and the prediction results and the relative error of prediction are shown in Figures 1 and 2. From Figure 2, it can be seen that the maximum relative error of the prediction using the IGA-LSSVM-based economic outflow prediction model is 2.763%, the minimum relative error is 0.705%, and the average relative error is 1.3298%.

In contrast, the maximum relative error of the prediction using the weighted LSSVM prediction model proposed in the literature [13] based on the prediction error of the sample is 6.263%, the minimum relative error is 1.759%, and the average relative error is 3.4897%. The above prediction results show that the economic outflow prediction model based on IGA-LSSVM established in the paper has stronger generalization ability and higher prediction accuracy, which is a reasonable and reliable method for predicting economic outflows [26].

Table 1: Expected probability of occurrence of the numbers 0-9 in the first four digits of different data.

Number	$P(d_1)$	$P(d_2)$	$P(d_3)$	$P(d_4)$
1	0.31003	0.12001	0.10188	0.10017
2	0.18908	0.11988	0.10122	0.10013
3	0.13001	0.10886	0.10006	0.10009
4	0.12434	0.10463	0.10057	0.10006
5	0.09612	0.10336	0.10013	0.09997
6	0.07686	0.09987	0.09985	0.09987
7	0.06813	0.09337	0.09961	0.09985
8	0.05659	0.90009	0.09842	0.09983
9	0.04687	0.88000	0.09826	0.09981
Total	1.00000	1.00000	1.00000	1.00000

Figure 3 shows the comparison of the optimization process of IGA and GA. It can be seen that IGA is significantly better than GA in the whole parameter search process, reaching the optimum in 45 generations, while GA reaches the optimum only in 83 generations.

7. Macroeconomics in Statistical Data Quality Assessment

If the distribution pattern of the sample data does not match with the theoretical distribution pattern described by macroeconomics, we can assume that the phenomenon may be caused by human factors, i.e., there are artificial fabrication, falsification, and deliberate concealment to a certain extent, and then we can assume that the data may be problematic. The macroeconomics is given in different data.

Macroeconomics gives the probability distribution of the first digit d_1 in the different data as

$$P(d_1) = \frac{\int_{d_1}^{d_1+1} P(x)dx}{\int_1^{10} P(x)dx} = \log_{10}\left(1 + \frac{1}{d_1}\right), d_1 = 1, 2, 3, \cdots, 9. \tag{11}$$

The $P(d_1)$ represents the probability of nonzero numbers appearing in the first place of different data, and the probability distribution is shown in Figure 4.

With the continuous research on macroeconomics, the probability distribution of the second digit d_2, the third digit d_3, and the fourth digit d_4 in a data has been gradually explored, and the logarithmic law can be extended to higher digits ②. Based on the studied logarithm law, we can obtain the probability of the first, second, third, and fourth digits of numbers 0-9, as shown in Table 1, where $P(d_n)$ denotes the probability of occurrence of each digit in the nth position.

For example, when the first digit is 1, the probability of occurrence is 31.003%, while when the first digit is 9, the probability of occurrence is only 4.687%, and the gap between the maximum and minimum probabilities is as high as 26.133%; the probability of occurrence of the second digit is obviously much more concentrated than that of the first digit, with a maximum probability of 12.001% and a minimum probability of 8.8%. The probability of the second digit is much more concentrated than that of the first digit, with a maximum probability of 12.001% and a minimum probability of 8.8%, and the gap between them is reduced from 26.133% to 3.201%; the probability of the third digit is even more concentrated, fluctuating around 10%; the fourth digit is more obvious. We can thus see that as the number of digits in the sample increases, the probability of each digit appearing 0-9 tends to be more and more consistent, i.e., the probability of each digit appearing is equal to 0.1, as is commonly believed.

8. Conclusion

Although the model-based abnormal numerical observation and parameter stability analysis method is more scientific than the first three methods, when using this method, we must first ensure that all the data used in the model are real and reliable; in solving practical problems, we can first apply macroeconomic tests to the statistical data to be evaluated, and when abnormal data are found, we can carefully check these figures in a targeted manner. When anomalous data are found, these figures can be carefully checked to see if there is any artificial manipulation, thus ensuring the quality of the statistics. In this paper, based on the macroeconomic dynamic assessment and prediction of IGA-LSSVM, from the perspective of feasibility, most of the statistics in real life have a specific distribution law, and this distribution law has some inherent connection with the theoretical distribution law of macroeconomics; so, when assessing the quality of major statistics in China, we can make reference to macroeconomics and expect to get better results.

Data Availability

The experimental data used to support the findings of this study are available from the corresponding author upon request.

Conflicts of Interest

The author declares that he/she has no conflicts of interest regarding this work.

References

[1] H. Fu and D. D. Shi, "Study on gas emission prediction model based on IGA-LSSVM," *China Safety Science Journal*, vol. 23, no. 10, pp. 51–55, 2013.

[2] Q. Wang and X. M. Tian, "Soft sensing based on improved GA-LSSVM," *Transactions of Beijing Institute of Technology*, vol. 32, no. 10, pp. 1031–1035, 2012.

[3] Z. H. Wang and N. Qiao, "Prediction model of coal and gas outburst intensity based on IGA-LSSVM," *Journal of Liaoning Technical University: Natural Science*, vol. 34, no. 7, pp. 791–796, 2015.

[4] F. H. S. Dongdong, "Study on gas emission prediction model based on IGA-LSSVM," *China Safety Science Journal*, vol. 23, no. 10, pp. 51–55, 2013.

[5] A. D'Agostino, L. Gambetti, and D. Giannone, "Macroeconomic forecasting and structural change," *Journal of Applied Econometrics*, vol. 28, no. 1, pp. 82–101, 2013.

[6] K. McAlinn, K. A. Aastveit, J. Nakajima, and M. West, "Multivariate Bayesian predictive synthesis in macroeconomic forecasting," *Journal of the American Statistical Association*, vol. 115, no. 531, pp. 1092–1110, 2020.

[7] F. Bräuning and S. J. Koopman, "Forecasting macroeconomic variables using collapsed dynamic factor analysis," *International Journal of Forecasting*, vol. 30, no. 3, pp. 572–584, 2014.

[8] B. Rossi and T. Sekhposyan, "Macroeconomic uncertainty indices based on nowcast and forecast error distributions," *American Economic Review*, vol. 105, no. 5, pp. 650–655, 2015.

[9] B. Bok, D. Caratelli, D. Giannone, A. M. Sbordone, and A. Tambalotti, "Macroeconomic nowcasting and forecasting with big data," *Annual Review of Economics*, vol. 10, no. 1, pp. 615–643, 2018.

[10] Z. H. A. N. G. Zhengwan, Z. H. A. N. G. Chunjiong, L. I. Hongbing, and X. I. E. Tao, "Multipath transmission selection algorithm based on immune connectivity model," *Journal of Computer Applications*, vol. 40, no. 12, p. 3571, 2020.

[11] Z. Zheng-wan, W. Di, and Z. Chun-Jiong, "Study of cellular traffic prediction based on multi-channel sparse LSTM," *Computer Science*, vol. 48, no. 6, pp. 296–300, 2021.

[12] D. Wu and S. Ning, "Dynamic assessment of urban economy-environment-energy system using system dynamics model: a case study in Beijing," *Environmental Research*, vol. 164, pp. 70–84, 2018.

[13] O. Blanchard, "On the future of macroeconomic models," *Oxford Review of Economic Policy*, vol. 34, no. 1-2, pp. 43–54, 2018.

[14] R. Gupta and A. Kabundi, "A large factor model for forecasting macroeconomic variables in South Africa," *International Journal of Forecasting*, vol. 27, no. 4, pp. 1076–1088, 2011.

Hindawi
Journal of Sensors
Volume 2023, Article ID 9850854, 1 page
https://doi.org/10.1155/2023/9850854

Retraction

Retracted: Research on Agricultural Economic Early Warning Based on Genetic Algorithm and SVM

Journal of Sensors

Received 8 August 2023; Accepted 8 August 2023; Published 9 August 2023

This article has been retracted by Hindawi following an investigation undertaken by the publisher [1]. This investigation has uncovered evidence of one or more of the following indicators of systematic manipulation of the publication process:

(1) Discrepancies in scope
(2) Discrepancies in the description of the research reported
(3) Discrepancies between the availability of data and the research described
(4) Inappropriate citations
(5) Incoherent, meaningless and/or irrelevant content included in the article
(6) Peer-review manipulation

The presence of these indicators undermines our confidence in the integrity of the article's content and we cannot, therefore, vouch for its reliability. Please note that this notice is intended solely to alert readers that the content of this article is unreliable. We have not investigated whether authors were aware of or involved in the systematic manipulation of the publication process.

Wiley and Hindawi regrets that the usual quality checks did not identify these issues before publication and have since put additional measures in place to safeguard research integrity.

We wish to credit our own Research Integrity and Research Publishing teams and anonymous and named external researchers and research integrity experts for contributing to this investigation.

The corresponding author, as the representative of all authors, has been given the opportunity to register their agreement or disagreement to this retraction. We have kept a record of any response received.

References

[1] X. Bian, X. Lv, and J. Tian, "Research on Agricultural Economic Early Warning Based on Genetic Algorithm and SVM," *Journal of Sensors*, vol. 2022, Article ID 3109468, 6 pages, 2022.

Hindawi
Journal of Sensors
Volume 2022, Article ID 3109468, 6 pages
https://doi.org/10.1155/2022/3109468

Research Article

Research on Agricultural Economic Early Warning Based on Genetic Algorithm and SVM

Xueyong Bian,[1] Xuzi Lv,[2] and Jie Tian[3]

[1]*School of Management Science and Engineering, Guizhou University of Finance and Economics, Guiyang 550000, China*
[2]*School of Education, Guizhou Normal University, Guiyang 550000, China*
[3]*School of Economics, Hebei GEO University, Shijiazhuang 050000, China*

Correspondence should be addressed to Xuzi Lv; bxy3729230@mail.gufe.edu.cn

Received 29 March 2022; Accepted 28 April 2022; Published 7 June 2022

Academic Editor: Han Wang

Agriculture is unique in that the industry is subject to a certain level of uncertainty due to seasonal and other factors, and its risk level is significantly higher than that of other industries. Therefore, it is necessary to establish an appropriate financial early warning model to predict, analyze, and control its financial risks. The article uses a genetic algorithm and support vector machine-based economic forecasting model for agribusinesses to adapt its own pollutant weights in a practical application environment to improve the forecasting accuracy. This model first uses a genetic algorithm to train a feature weight vector of current data so that the weights are adapted to the current prediction problem and then uses this feature weight vector to apply to SVM model training. It is found that 62.79% of the listed agricultural companies are in warning status, and their development is not optimistic. The article provides new ideas for the subsequent research on financial warning methods and also expands the boundaries of theoretical research for the research system of financial warning problems and enriches the experience and evidence of practical research.

1. Introduction

Since China's social economy is inextricably linked with agricultural development, agricultural development has also received national attention. At the current level of development, the number of listed green agricultural companies is increasing, which is an important help to China's social and economic development [1]. However, there are still more shortcomings in the development process, especially, many listed green agriculture companies do not clearly carry out investment planning in order to obtain more economic benefits; so, there are more problems in financial management, leading to financial risks [2]. Although opportunities and risks coexist, as long as green agricultural listed companies can establish risk early warning mechanism and use it to do a good job in financial management, they can avoid the impact caused by financial risks and can also effectively solve financial risks when they occur, thus effectively reducing economic losses [3].

In the past 10 years, there are 547 listed companies in Shanghai and Shenzhen A-shares that have been specially handled by SFC, among which there are 17 listed agricultural companies, such as Xiangli, Nongfa Seed, Pingtan Development, Zhonglu B, and ST Jinggu [4]. In addition, in recent years, financial fraud cases of listed agricultural companies have been frequent, such as the well-known "scallop exodus" financial fraud of the Swertia Island Group, the financial fraud case of Wanfushengke (now renamed as Jiawo), the abnormal trading case of Pingtan Development, and the illegal disclosure cases of [3]. All the above cases are staggering, they all show that the actual financial situation of listed agricultural companies is not good, and some companies are even on the verge of bankruptcy [4]. Therefore, it is crucial to analyze the reasons for the formation of financial crises in agricultural listed companies and construct a financial early warning model in line with them, so that the possible financial risks can be predicted and controlled [5].

Foreign scholars have made a great breakthrough in the research methods for the construction of financial early warning models [6]. The earliest research on financial early warning models using statistical methods was conducted by [7], and the study proposed a univariate model. On the basis of their research, [8] proposed a more improved univariate model, which is simple and easy to use, but its discriminative accuracy is not high. Several other scholars applied the logit model and its improved model to financial distress studies, which provided the theoretical basis for subsequent studies [9]. On the other hand, Nagasubramanian et al. [8] and Yu [9] used the research method of AdaBoosted decision tree and combinatorial model to study the determinants affecting financial distress. It is evident from the above literature that although foreign scholars have conducted a large number of constructive studies on financial early warning methods, there are fewer studies that combine these theoretical methods with applications in particular industries [10]. Most of the domestic scholars have improved the existing models based on foreign scholars' research or compared the existing models and applied them to the financial early warning of Chinese listed companies. Some scholars have used logistic regression models to conduct early warning analysis on the financial situation of listed companies [11]: conducted an early warning analysis of the financial crisis of listed companies by establishing a multiple probability ratio regression model (Probit). [12] used the additional momentum method, conjugate gradient method, and *L-M* optimization method to construct a prediction model for the financial crisis of listed companies [13]. The agricultural industry has certain special characteristics in terms of operational risk compared with other industries, and most of the existing studies on the establishment and comparison of financial early warning models for listed agricultural companies are limited to traditional methods (e.g., univariate models, multivariate models, logit models, and artificial neural network models) and rarely use more advanced methods combined with computer networks (e.g., unit learning framework models, rough set models, decision tree models, gradient advancement models, and fuzzy OSVR methods) to conduct empirical studies [14]. For example, [15] used univariate analysis and multivariate analysis to study the financial distress of agricultural listed companies, and [16] conducted a financial warning study on agricultural listed companies based on survival analysis method. [17] illustrated how traditional accounting indicators can be applied to financial early warning of agricultural listed companies. [18] constructed a logistic regression analysis model based on EVA theory and also conducted an early warning on the financial crisis of agricultural listed companies.

2. Fundamentals and Prediction Model

2.1. Basic Theory of SVM. Support vector machine is a new type of generalized classifier based on statistical learning theory. It is widely used in various supervised learning scenarios because it minimizes structural risk, has good generalization ability, and can make samples linearly indistinguishable in the low-dimensional input space by mapping them to the higher space after introducing kernel functions. In recent years, many studies have applied SVM to various prediction analysis problems, and its prediction ability is even better than that of BP neural network methods and RBF neural networks when performing small sample data prediction.

Let sample $(x_1, y_1), (x_2, y_2), \cdots, (x_k, y_k) \in R^N \times R$, where x_i is the input data, y_i corresponds to the label, and k is the total number of data; then, its minimization objective function can be expressed as

$$R(\omega) = \min_{\omega,b,\zeta}\left[\frac{1}{2}\omega^2 + C\sum_{i=1}^{n}\zeta_i\right], \quad \text{s.t.}\begin{cases}\omega^{\mathrm{T}}\varphi(x_i) + b \geq 1 - \zeta_i,\\ \zeta_i \geq 0, i = 1, \cdots, n,\end{cases} \tag{1}$$

where C is a penalty factor balancing the empirical risk of the model with model complexity, ζ is a nonnegative relaxation variable, and $\varphi(x_i)$ is a function related by the kernel function $\mathrm{K}(x_i, x_j) = \varphi(x_i)^{\mathrm{T}}\varphi(x_j)$.

The above optimization problem is transformed into a dyadic problem by the Lagrangian method.

$$\min\left[\frac{1}{2}\alpha^{\mathrm{T}}Q_\alpha - \mathbf{e}^{\mathrm{T}}\alpha\right], \quad \text{s.t.}\begin{cases}\mathbf{y}^{\mathrm{T}}\alpha = 0,\\ 0 \leq \alpha_i \leq C, i = 1, \cdots, n.\end{cases} \tag{2}$$

Finally, the decision function can be obtained:

$$\operatorname{sgn}\left(\sum_{i=1}^{n} y_i\alpha_i K(x_i, x) + \rho\right). \tag{3}$$

When the model is predicted with the input data x, the corresponding prediction can be calculated by the above equation.

2.2. Genetic Algorithm Optimized SVM Model. In the field of machine learning for data mining, high-dimensional data usually requires feature selection for dimensionality reduction to avoid subjecting the model to dimensional disasters, which makes feature selection an important part of the data preprocessing step of machine learning algorithms.

The genetic algorithm is an iterative optimization algorithm that simulates the evolutionary patterns of species. It optimizes the candidate solution by simulating the mutation and reproduction of biological populations. Since genetic algorithms have the feature of global optimization search, they are widely used in various fields. The flow chart of the genetic algorithm is shown in Figure 1.

In optimizing the SVM model using the genetic algorithm, by selecting a vector $v = (\mathrm{v1}, \mathrm{v2}, \mathrm{v3}, \cdots, \mathrm{vm})$ consisting of deflators for each dimension as the population individuals, the training set data is trained with the feature

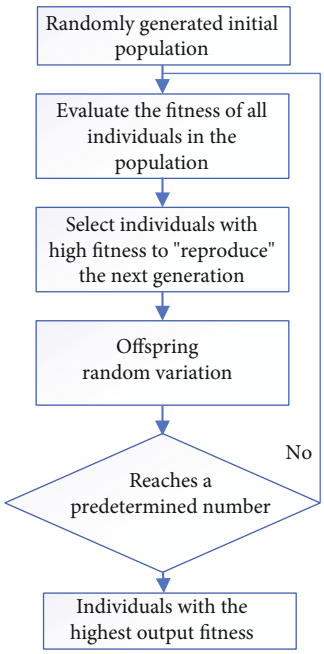

Figure 1: The flow chart of the genetic algorithm.

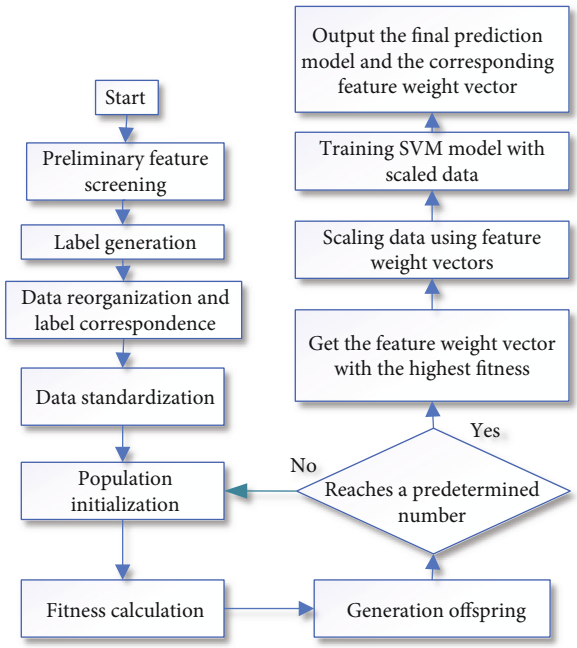

Figure 2: Flow chart of the prediction model.

weight vector v deflated data $x' = x \times v^T$ supplying the SVM model, and its F1 score on the validation set is used as the individual fitness [19, 20].

The process of optimizing the feature weight vectors by the genetic algorithm is to adapt the SVM model to the characteristics of the validation set data distribution. When the optimization results are put on the test set for validation, the performance of the model on the test set will degrade compared to the validation set due to overfitting because the validation set data distribution is not exactly the same as the test set data distribution. This degradation itself is due to overfitting and can be suppressed by adjusting the population size, number of iterations, and degree of variation parameters of the genetic algorithm [21–23].

In summary, the complete process of training an agribusiness economic forecasting model based on genetic algorithm and SVM using the original agribusiness economic data x and national three-level agribusiness economic criteria is shown in Figure 2.

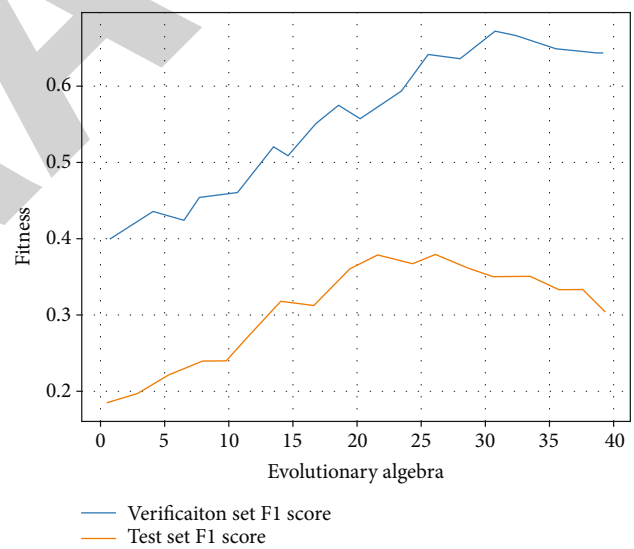

Figure 3: Genetic algorithm adaptation curve.

3. Experimental Results and Analysis

The experiments are based on more than 1,000 historical data from agricultural enterprises, and the predictions are made separately for the agribusiness economies of interest to the plant and compared with the results predicted by traditional SVM [24].

Since the overfitting problem of the model can be mitigated by increasing the number of data in the validation set and ensuring that the data distribution of the validation set is close to the situation when it is actually applied (test set), the data were divided into training set, validation set, and test set in the ratio of 3 : 5 : 2 when segmenting the data [25, 26].

Given a population size of 10 in the genetic network and a variation range of 0 to 0.1, the appropriate number of iterations was determined by testing and observing the fitness on the validation set and the fitness on the test set with the number of iterations. The effect graph obtained from the experiment is shown in Figure 3.

The fitness of the validation set in Figure 3 increases with the number of evolutionary generations in a small oscillation and reaches a stable value around 40 generations, while the fitness of the test set reaches its maximum around the 23rd generation. The optimal number of iterations is conservatively taken to be 20 in order to avoid the effect of randomness of the experiment [27].

Table 1: Sample statistics of positive cases.

Prediction target	Total phosphorus	Total nitrogen	BOD5	COD
Proportion of positive cases/%	22.4	64.1	19.2	51.3

Table 2: Forecast results.

Prediction target	Accuracy rate/%		Recall rate/%	
	Traditional SVM	Improved SVM	Traditional SVM	Improved SVM
Total phosphorus	79.2	86.5	69.5	73.6
Total nitrogen	68.9	79.2	66.5	76.8
BOD5	80.1	86.2	71.8	75.1
COD	73.2	74.8	72.1	75.6

Since the agribusiness economy was in line with the agribusiness economy criteria most of the time except for a few cases, the data showed a tendency to be unbalanced, and the labeling balance of this data according to the four prediction objectives is shown in Table 1.

Category imbalanced samples are prone to model overfitting and also prone to higher model correctness and lower recall and accuracy, which has no practical meaning. For example, if there are 100 positive cases and 900 negative cases in the data, the model is trained to always return new samples to predict the results as negative cases; although, the correct rate is as high as 90%, but there is no reference value for practical problems. There are 2 main types of methods to solve the category imbalance problem: undersampling and resampling. Undersampling makes the number of positive and negative cases close to each other by removing the majority of samples, but it is easy to result in too few samples and overfitting; resampling balances the number of positive and negative cases by repeating a small number of samples, but simply repeating a small number of samples will make the information amplified and the model learns too "special" information. In the SVM model parameters in the sklearn library, we set the class_weight parameter to "balanced" and use the weighting method to make the majority class and the minority class in the weighted balance, which can play an equally large role in the loss function of the SVM training process and alleviate the impact of the data. The impact of the class imbalance on the model is mitigated.

In the formal experiments, more than 1,000 agribusiness economic data were predicted according to the agribusiness economy using a genetic algorithm and SVM-based agribusiness economic prediction model and a traditional linear SVM model, respectively. The parameters of the genetic algorithm were referred to the previous tests, and the population size was taken as 10, the variance range was 0-0.1 (uniform distribution), and the number of iterations was 20. The parameters of the SVM model for both are $C = 1.0$, $\text{tol} = 0.0001$, and $\text{class\_wight} = \text{balanced}$. The correctness and recall of the predictions are shown in Table 2.

As can be seen from Table 2, in terms of agribusiness economic indicators, two agribusiness economic indicators, total phosphorus and BOD5, are better predictors and easier to predict, while agribusiness economic and COD are relatively more difficult to predict. In terms of model comparison, the improved SVM outperforms the traditional SVM in predicting all agribusiness economic indicators, especially in the prediction of agribusiness economic indicators, which has a very great improvement. It shows that the practice of optimizing feature weight vectors by the genetic algorithm to achieve some degree of feature selection can indeed improve the prediction performance of the classifier.

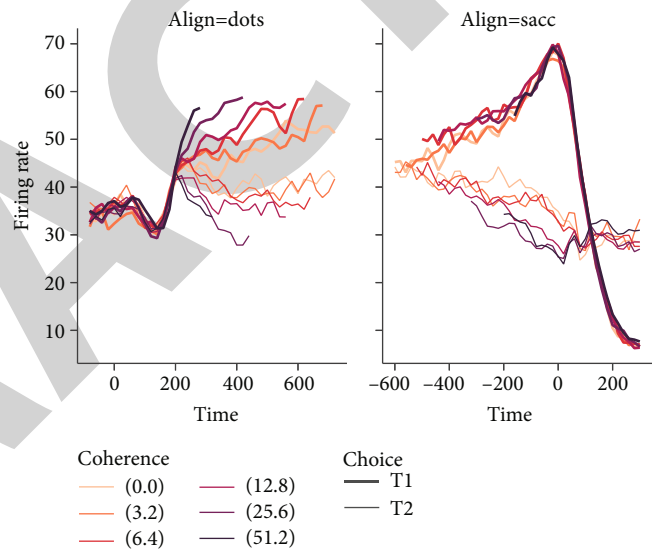

Figure 4: Effect of various economic projections for different agricultural companies.

The effects of various economic predictions of different agricultural companies are shown in Figure 4. It can be known that in green agricultural listed companies, the financial risks caused by external factors are often not controllable by human, such as changes in the market environment and the influence of political situation. Each country has policy restrictions for overseas investment, including foreign investment, investment ratio, and approval system, which leads to the macroeconomic environment that has an impact on the company's financial risk, which in addition to this includes social culture and resource environment.

These external factors can have a huge impact on the company's finances, especially in the complex market environment, where supply and demand are changing at all times, and the increase in rivals and products can lead to the company facing sales difficulties and other situations, and despite internal coping strategies, wrong decisions can still drive the company into financial difficulties.

4. Conclusion

It is only important to establish an appropriate financial early warning model for prediction, analysis, and control of agricultural economic risks. In this paper, we use a genetic algorithm and support vector machine-based economic forecasting model for agricultural enterprises to improve the accuracy of forecasting by adapting pollutant weights in a practical application environment. It provides new ideas for the subsequent research of financial early warning methods and also expands the boundaries of theoretical research and enriches the experience and evidence of practical research for the research system of financial early warning problems.

Data Availability

The experimental data used to support the findings of this study are available from the corresponding author upon request.

Conflicts of Interest

The authors declared that they have no conflicts of interest regarding this work.

References

[1] Y. Zhang, "Food safety risk intelligence early warning based on support vector machine," *Journal of Intelligent & Fuzzy Systems*, vol. 38, no. 6, pp. 6957–6969, 2020.

[2] J. S. Chou, M. Y. Cheng, Y. W. Wu, and A. D. Pham, "Optimizing parameters of support vector machine using fast messy genetic algorithm for dispute classification," *Expert Systems with Applications*, vol. 41, no. 8, pp. 3955–3964, 2014.

[3] L. Guo and Y. Zhao, "Research and verification analysis on early warning model through support vector machine algorithm," in *2021 IEEE International Conference on Electronic Technology, Communication and Information (ICETCI)*, pp. 211–213, Changchun, China, 2021, August.

[4] J. Su, X. Wang, S. Zhao, B. Chen, C. Li, and Z. Yang, "A structurally simplified hybrid model of genetic algorithm and support vector machine for prediction of chlorophyll a in reservoirs," *Water*, vol. 7, no. 12, pp. 1610–1627, 2015.

[5] X. J. Wang, G. T. Zeng, K. X. Zhang, H. B. Chu, and Z. S. Chen, "Urban real estate market early warning based on support vector machine: a case study of Beijing," *International Journal of Computational Intelligence Systems*, vol. 13, no. 1, pp. 153–166, 2020.

[6] S. Liu, H. Tai, Q. Ding, D. Li, L. Xu, and Y. Wei, "A hybrid approach of support vector regression with genetic algorithm optimization for aquaculture water quality prediction," *Mathematical and Computer Modelling*, vol. 58, no. 3-4, pp. 458–465, 2013.

[7] T. Li, J. Yang, and Z. Chen, "The early warning and prediction method of flea beetle based on maximum likelihood algorithm ensembles," in *2010 Sixth International Conference on Natural Computation*, vol. 4, pp. 1901–1905, Yantai, 2010, August.

[8] K. Nagasubramanian, S. Jones, S. Sarkar, A. K. Singh, A. Singh, and B. Ganapathysubramanian, "Hyperspectral band selection using genetic algorithm and support vector machines for early identification of charcoal rot disease in soybean stems," *Plant Methods*, vol. 14, no. 1, pp. 86–113, 2018.

[9] X. Yu, "Disaster prediction model based on support vector machine for regression and improved differential evolution," *Natural Hazards*, vol. 85, no. 2, pp. 959–976, 2017.

[10] R. Kolachian and B. Saghafian, "Hydrological drought class early warning using support vector machines and rough sets," *Environmental Earth Sciences*, vol. 80, no. 11, pp. 1–15, 2021.

[11] R. C. Deo, O. Kisi, and V. P. Singh, "Drought forecasting in eastern Australia using multivariate adaptive regression spline, least square support vector machine and M5Tree model," *Atmospheric Research*, vol. 184, pp. 149–175, 2017.

[12] Z. H. A. N. G. Zhengwan, Z. H. A. N. G. Chunjiong, L. I. Hongbing, and X. I. E. Tao, "Multipath transmission selection algorithm based on immune connectivity model," *Journal of Computer Applications*, vol. 40, no. 12, pp. 3571–3577, 2020.

[13] P. An, Z. Wang, and C. Zhang, "Ensemble unsupervised autoencoders and Gaussian mixture model for cyberattack detection," *Information Processing & Management*, vol. 59, no. 2, article 102844, 2022.

[14] M. Fallah Shams, H. Jahangirnia, R. Gholami Jamkarani, H. Kordlouie, and R. Derakhshani, "Designing credit risk early-warning system for individual and corporate customers of the bank using multiple logit comparison model and survival function," *International Journal of Finance & Managerial Accounting*, vol. 7, no. 25, pp. 163–177, 2022.

[15] I. R. Morales, D. R. Cebrián, E. F. Blanco, and A. P. Sierra, "Early warning in egg production curves from commercial hens: a SVM approach," *Computers and Electronics in Agriculture*, vol. 121, pp. 169–179, 2016.

[16] Y. Wu and X. Long, "Research of groundwater environment early warning based on intelligent algorithm," in *2012 International Conference on Computer Science and Electronics Engineering*, vol. 1, pp. 536–540, Hangzhou, China, 2012, March.

[17] L. Sun, Y. Qiandi, D. Peng, S. Subramani, and X. Wang, "Fogmed: a fog-based framework for disease prognosis based medical sensor data streams," *Computers, Materials & Continua*, vol. 66, no. 1, pp. 603–619, 2021.

[18] Q. Zhiguo, H. Sun, and M. Zheng, "An efficient quantum image steganography protocol based on improved EMD algorithm," *Quantum Information Processing*, vol. 20, no. 2, pp. 1–29, 2021.

[19] Z. H. A. N. G. Zheng-wan, W. U. Di, and Z. H. A. N. G. Chunjiong, "Study of cellular traffic prediction based on multichannel sparse LSTM," *Computer Science*, vol. 48, no. 6, pp. 296–300, 2021.

[20] Q. Zhiguo, S. Chen, and X. Wang, "A secure controlled quantum image steganography algorithm," *Quantum Information Processing*, vol. 19, no. 10, pp. 1–25, 2020.

[21] J. Su, X. Wang, Y. Liang, and B. Chen, "GA-based support vector machine model for the prediction of monthly reservoir

Hindawi
Journal of Sensors
Volume 2023, Article ID 9837074, 1 page
https://doi.org/10.1155/2023/9837074

Retraction

Retracted: Efficiency Analysis and Utilization of College Sports Equipment Based on Intelligent Computing

Journal of Sensors

Received 8 August 2023; Accepted 8 August 2023; Published 9 August 2023

This article has been retracted by Hindawi following an investigation undertaken by the publisher [1]. This investigation has uncovered evidence of one or more of the following indicators of systematic manipulation of the publication process:

(1) Discrepancies in scope
(2) Discrepancies in the description of the research reported
(3) Discrepancies between the availability of data and the research described
(4) Inappropriate citations
(5) Incoherent, meaningless and/or irrelevant content included in the article
(6) Peer-review manipulation

The presence of these indicators undermines our confidence in the integrity of the article's content and we cannot, therefore, vouch for its reliability. Please note that this notice is intended solely to alert readers that the content of this article is unreliable. We have not investigated whether authors were aware of or involved in the systematic manipulation of the publication process.

Wiley and Hindawi regrets that the usual quality checks did not identify these issues before publication and have since put additional measures in place to safeguard research integrity.

We wish to credit our own Research Integrity and Research Publishing teams and anonymous and named external researchers and research integrity experts for contributing to this investigation.

The corresponding author, as the representative of all authors, has been given the opportunity to register their agreement or disagreement to this retraction. We have kept a record of any response received.

References

[1] C. Li, J. Wang, and Q. Yu, "Efficiency Analysis and Utilization of College Sports Equipment Based on Intelligent Computing," *Journal of Sensors*, vol. 2022, Article ID 7497555, 10 pages, 2022.

Hindawi
Journal of Sensors
Volume 2022, Article ID 7497555, 10 pages
https://doi.org/10.1155/2022/7497555

Research Article

Efficiency Analysis and Utilization of College Sports Equipment Based on Intelligent Computing

Chunping Li,[1] Jie Wang,[2] and Qingding Yu[1]

[1]*School of Physical Education, Nanchang University, Nanchang 330000, China*
[2]*School of Economics and Management, Nanchang University, Nanchang 330000, China*

Correspondence should be addressed to Qingding Yu; 171849018@masu.edu.cn

Received 21 March 2022; Revised 13 April 2022; Accepted 23 April 2022; Published 29 May 2022

Academic Editor: Han Wang

Under the background of the new curriculum standard, promote the all-round development of moral education, intellectual education, physical education, aesthetic education, and labor education. Children's health exercise also makes physical education one of the subjects that schools and parents attach importance to. Different from the teaching methods of other disciplines, physical education is carried out outdoors and has high requirements for equipment and facilities, which is not only related to the effective implementation of physical education but also related to students' enthusiasm for outdoor physical exercise. It is actually a powerful theoretical support for physical education. With the frequent loss, damage, and lack of sports equipment in colleges and universities, people do not think: how can we manage the equipment efficiently and orderly and keep its integrity? It can be seen that the effective use of school sports equipment and facilities in the new period should grasp the research core, clarify the research direction and goal, and provide strong support for the continuous innovation of school sports education. The management of sports equipment is an important part of the daily work of schools. All schools have formulated management systems and use norms, but from the long-term practice, it is obvious that the implementation of the system and use norms is not ideal, and various management systems and norms become a mere formality. Even physical education teachers do not strictly follow this requirement, resulting in the management process of sports equipment and facilities in trouble. It can be seen that the management of sports equipment is not strictly controlled, and it is difficult to implement it, which limits the application value and effectiveness of sports equipment, and students are prone to safety problems in class. Therefore, the school should employ full-time personnel to manage sports equipment, which also improves the attention of the personnel to equipment management. For equipment damage, many students use equipment wrongly and damage equipment, so reasonable use of equipment and facilities can prolong the service life of equipment and facilities. However, physical education teachers usually do not demonstrate the use of equipment scientifically in the teaching process and lack guidance to students, which leads to many students not paying enough attention to the use of equipment, such as kicking basketball, sitting on a stool with basketball, and inflating football; these are the reasons that lead to the damage of equipment. We can through the intelligent optimization of the management mode of sports equipment for a qualified management delay the service life of equipment.

1. Introduction

With the continuous development and progress of society, people's value of sports has become increasingly prominent, and more and more people realize the importance of strengthening their bodies and ensuring their health. Therefore, many people will choose to participate in various sports activities to enhance their physical fitness, and many schools also buy many sports equipment that make students full of interest. However, it is against this background that various sports equipment in schools frequently have problems. Literature [1] reveals the management status of sports equipment room in colleges and universities, and literature [2] puts forward the application of intelligent management of sports equipment. Literature [3] and literature [4] talk about the design and implementation of sports equipment sharing management and the exploration of management system. Literature [5] discusses why sports equipment frequently

appears to have problems in recent years; reference [6] analyzes the countermeasures of classified management of sports equipment in colleges and universities and analyzes the tentative plan of diverted management of equipment in literature [7]. Literature [8] optimizes the purchase and management of sports equipment and concretely carries out the reform of "six-oriented" sports equipment management in [9]. Reference [10] talks about fiber-reinforced composites that can increase the performance of equipment, and reference [11] optimizes the material to prolong the service life of equipment. Analysis and research of new materials are discussed [12] in the manufacturing process of sports equipment. Reference [13] expounds the application of computer technology in gymnasium equipment management [14], intelligent optimization algorithm [15], and intelligent optimization algorithm of road strength planning. Literature [16] discusses the design and implementation of college sports equipment sharing management system; literature [17] uses the five-routine method to thoroughly study the management of school sports equipment. Reference [18] presents the preparation of waterborne polyurethane and its application in sports equipment. This material [19] is optimized to prolong the service life of equipment. Literature [20] talks about the interest of primary school sports equipment to stimulate children, literature [21] talks about the application value of high-performance composite materials to sports competition, and literature [22] teaches them how to scientifically manage equipment and facilities. Literature [23] talks about the influence of the choice of sports equipment on physical education. The influence of intelligent optimization method on various applications is adopted in references [24, 25].

2. The Management Status and Solutions of Sports Equipment

2.1. Current Situation of School Sports Equipment Management

2.1.1. Wear Degree of Sports Equipment. At present, there is no strict implementation plan for the management of school sports equipment in China. According to the requirements of physical education teachers, after the study of physical education class content, the remaining time will be spent by the class sports committee members entering the sports equipment room to borrow the sports equipment needed by physical education class, and the management personnel responsible for managing the equipment only require students to fill in simple borrowing information, such as class and name, that is, to distribute sports equipment to them. When the equipment is returned after the physical education class, the administrator only counts the number and category of sports equipment and puts it into the sports storage room, but ignores the wear and tear of sports equipment. After a long time, students will not care for sports equipment.

2.1.2. Sports Equipment Management Is Not Strict. Although there is a corresponding management system for the management of sports equipment, the managers do not strictly and seriously manage the equipment. If almost all sports equipment in the management system "requires the consent of the school administration to be outsourced and must be registered, such as the necessity of claiming compensation for damage or loss," although many schools only provide an arbitrary number of equipment in terms of quantity, type, etc., which is not clearly listed when actually outsourcing. If damage or loss occurs, it is often due to the situation, so it cannot solve the problem.

2.1.3. Lack of Funds for Sports Equipment Procurement. Due to the limited funds of schools, reasonable equipment procurement is also an important link in the management of sports equipment. When purchasing, the lack of equipment is mainly purchased by managers, without checking whether the equipment is qualified in performance and whether the price is reasonable. Under the influence of various factors, management loopholes often appear, especially the accounting of procurement funds. If there is a mistake in purchasing funds, it will greatly consume manpower and material resources and seriously affect the effective utilization rate of sports equipment. This kind of management flaws proves that the previous management methods have great defects, and there is a lack of strong communication between various departments.

2.1.4. Improper Use in Teaching. The correct use of sports equipment can prolong the service life of the equipment, while some physical education teachers allow students to use the equipment in class without considering its correct use, which may cause serious damage. For example, some students sit on basketball as a stool, scrape badminton rackets on the ground, and damage bows and arrows with improper techniques. These improper use methods undoubtedly greatly shorten the life of sports equipment. The survey found that more than 30% of sports equipment in many schools were damaged due to improper use.

2.2. Solutions. In order to improve the management efficiency of school sports equipment, we must build an intelligent sports equipment management system, which is mainly divided into two aspects: on the one hand, it is a student management system, which is mainly aimed at students; on the other hand, it is an equipment administrator system, which is mainly aimed at the staff of sports equipment management. Students can clearly see the real-time information of sports equipment by creating personal accounts and inputting basic information such as name, class, and student number in the system, determine the return period of sports equipment, and avoid the adverse effects of delayed return on the work of staff. Staff can register the actual use of sports equipment by using the intelligent management system, such as the borrowing and returning information of equipment and wear and tear. By exchanging information between the intelligent management system and the internal management system of the school, the school administrators can know the damage degree of the equipment with the help of the system, so as to make the corresponding procurement plan in time. Data sharing provides a new way of thinking for the management of sports equipment in colleges and universities. Through the sharing of sports equipment, the role of sports equipment can be brought into

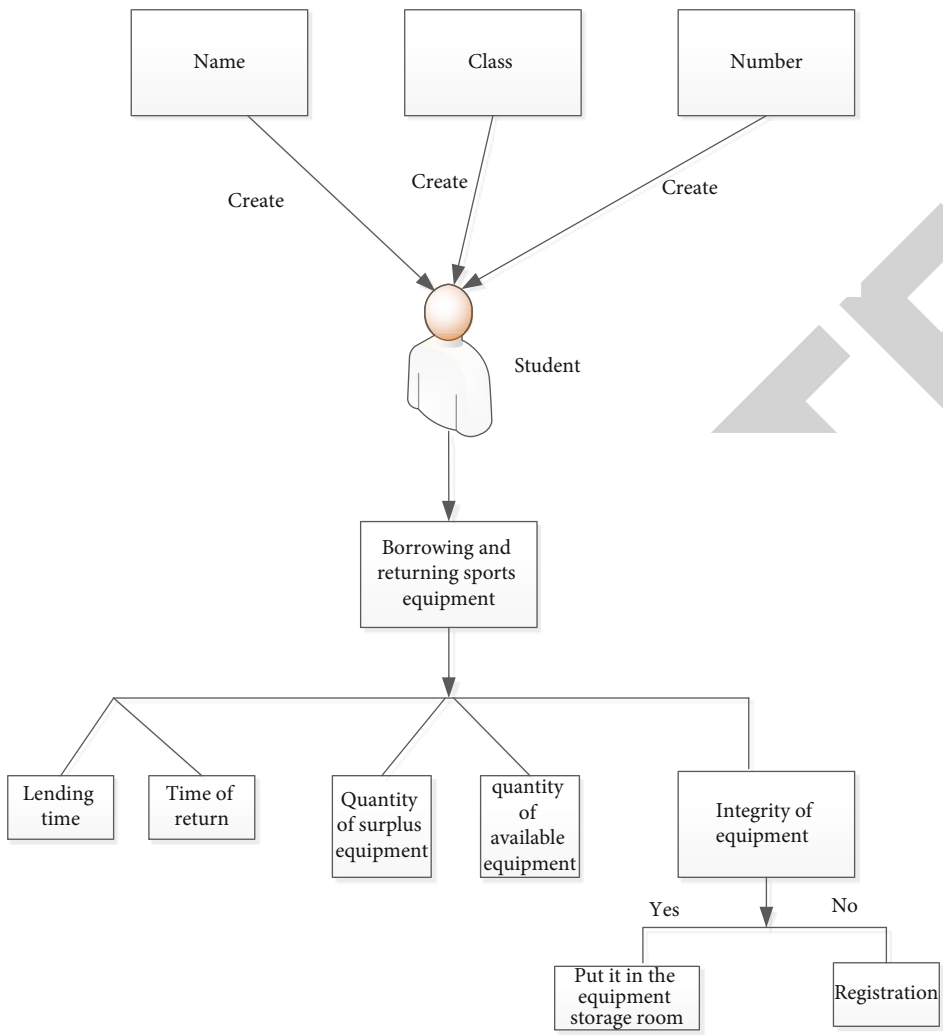

Figure 1: Student management system.

full play. The student management system is shown in Figure 1, and the sports equipment sharing system is shown in Figure 2.

3. Optimize Management Efficiency

3.1. Material Planning Management Optimization Measures. From the process of ordering sports equipment, the main factors that can improve the equipment cost are economic order quantity, purchase quantity, first order quantity, supplementary order point, and safety inventory. Therefore, this paper will consider the above factors to optimize the planning management of sports equipment.

$$TC = \frac{CD}{Q} + PH\frac{Q}{2}, \tag{1}$$

where D is the planned annual demand, Q is the order quantity, C is the cost, and P is the order unit price.

Take the partial derivative equal to 0:

$$\frac{\partial TC}{\partial Q} = \frac{-DC}{Q^2} + \frac{PH}{2} = 0. \tag{2}$$

Seek economic order quantity:

$$Q^* = \sqrt{\frac{2D\,C}{PH}}. \tag{3}$$

Because students will use the same equipment at the same time in class, it brings the problem of equipment inventory demand. According to the square root rule, the comprehensive standard deviation of total equipment demand is equal to the square root of the sum of variances of subsets of demand in each class:

$$\partial = \sqrt{\left(\partial_1^2 + \partial_2^2 + \partial_3^2 + \cdots + \partial_n^2\right)}. \tag{4}$$

Standard deviation of average equipment ordering cycle:

$$\partial = \sqrt{\mathrm{LT}}. \tag{5}$$

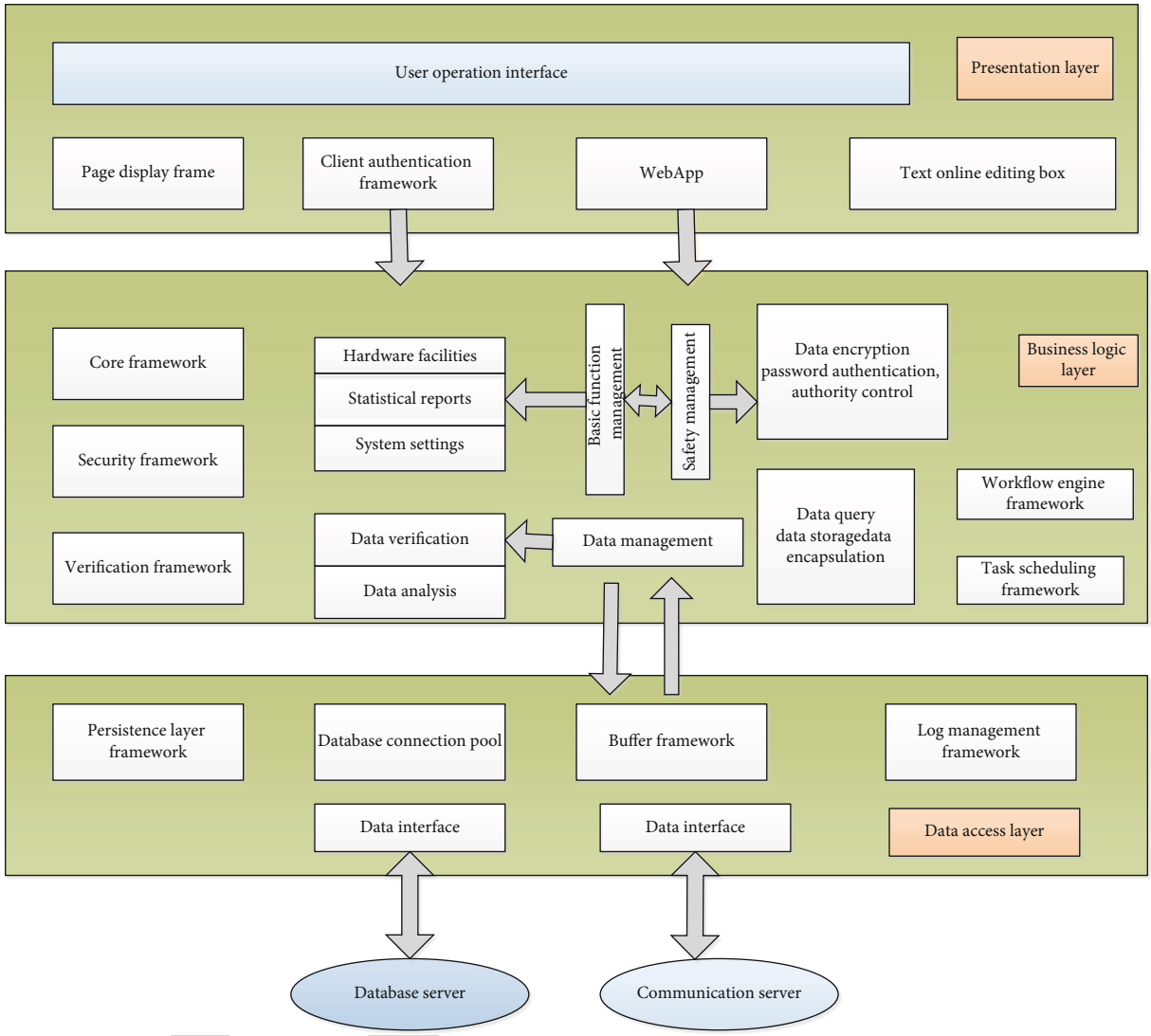

Figure 2: Data sharing system diagram of sports equipment data.

Table 1: Data sheet of sports equipment supply.

Category	Ball games	Shooting	Running	Running
Quotation	1200	23000	1000	1100
Freight	50	80	20	20
Warranty period	1 year	1 year	1 year	1 year
Qualified rate	98.6%	98.9%	99.2%	99.3%
Enterprise credit	Excellent	Excellent	Excellent	Excellent

Table 2: Table of retained individual volume and iteration times.

Parent	20%	20%	30%	30%	40%
Child	12%	15%	12%	10%	12%
Optimal iteration times	45	65	30	86	45

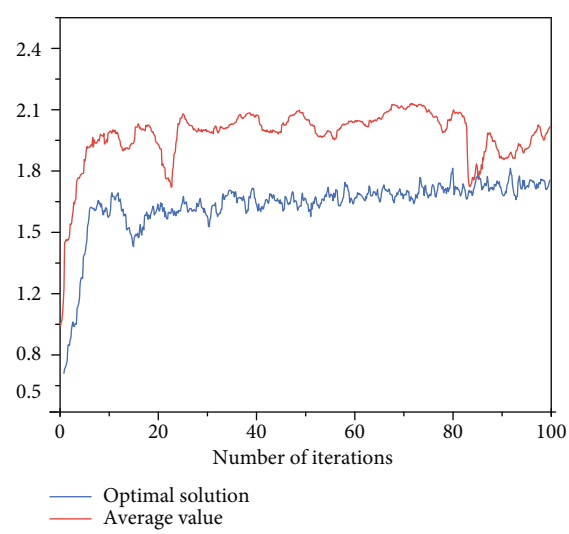

Figure 3: Simulation result diagram.

Table 3: Classification and comparison table.

Method factors	Importance classification	ABC classification		
	Importance to the normal use of equipment	Price and quantity of equipment		
	Important factors of equipment	Category	Quantity	Price
Grades	General: small inventory	A	10%	70%
	More important: proper inventory	B	20%	20%
	Very important: large inventory	C	70%	10%
Advantages	Equipment is supportable	Simple distinction, heavy management and small workload		
Disadvantages	The workload of statistical analysis is heavy	Great limitation		

Table 4: Elements of optimized classification model.

Thoughts	Multiple classification control methods are optimized			
Objects	Use material support		Price cost	
	Normal	Equipment quality	Equipment price	Equipment wear degree
Problems to be solved	The classification workload is heavy and the equipment is not guaranteed			
Expected goals	Whether the equipment is used normally and whether the inventory of equipment is safe			
Implementation methods	Importance classification combined with ABC classification			
Theoretical support	Relationship between price cost and material support rate			

Average fixed equipment cycle after correction:

$$\mathrm{LT} = \mathrm{LT} + \sqrt{\mathrm{LT}}. \tag{6}$$

Supplementary order demand:

$$\lambda = \mathrm{FS} \times \mathrm{FH} \times QA \times \mathrm{LT} \times \frac{\mathrm{UUR}}{100}. \tag{7}$$

FS is the quantity of equipment, FH is the average daily utilization rate, LT is the average order cycle, and URR is the failure replacement rate.

Standard deviation of prefetch equipment support ratio to average draft 1.65:

$$\text{Then the safety stock} = 1.65 \times \sqrt{\lambda}. \tag{8}$$

Safety stock model:

$$S = p\sqrt{\sigma_q^2(1) + \sigma_1^2(q)}. \tag{9}$$

Safety inventory directly affects the guarantee rate and availability rate of sports equipment. The safety inventory model is established by analyzing the inventory data, ordering cycle, demand, and guarantee rate of equipment.

3.2. Basic Algorithms

3.2.1. Particle Swarm Optimization Algorithm for Sports Equipment. Suppose n particles are initialized and each particle contains k scatter points, then for the i-th particle of generation t, formula (10) denotes its position vector p_i^t, and formula (11) denotes its velocity vector v_i^t.

$$p_i^t = [(p(1,x), p(1,y), p(1,z)), \cdots, (p(k,x), p(k,y), p(k,z))]_{(t,i)}^T, \tag{10}$$

$$v_i^t = [(v(1,x), v(1,y), v(1,z)), \cdots, (v(k,x), v(k,y), v(k,z))]_{(t,i)}^T. \tag{11}$$

Particles will generate memories, and then, choose the best position in the process of each iteration I and share the best position.

The particle position after the next iteration is determined according to the velocity update formula shown in formula (12) and the position update formula shown in formula (13).

$$v_i^{t+1} = \omega V_i^t + c_1 r_1 \left(p_i^{\text{best}} - p_i^t\right) + c_2 r_2 \left(g_i^{\text{best}} - p_i^t\right), \tag{12}$$

$$p_i^{t+1} = p_i^t + v_i^{t+1}. \tag{13}$$

After each iteration, the individual optimal position and the global optimal position are updated, and the updating rules are

$$p_{t+1}^{\text{best}} = \begin{cases} p_t^{\text{best}}; f\left(p_{t+1}^{\text{best}} \geq f\left(p_t^{\text{best}}\right)\right), \\ p_{t+1}^{\text{best}}; f\left(p_{t+1}^{\text{best}}\right) < f\left(p_t^{\text{best}}\right), \end{cases} \tag{14}$$

$$g_{t+1}^{\text{best}} = \begin{cases} g_t^{\text{best}}; f\left(g_{t+1}^{\text{best}} \geq f\left(g_t^{\text{best}}\right)\right), \\ g_{t+1}^{\text{best}}; f\left(g_{t+1}^{\text{best}}\right) < f\left(g_t^{\text{best}}\right). \end{cases} \tag{15}$$

3.2.2. Genetic Optimization Algorithm for Sports Equipment. For the t-th iteration, if the genome of the i-th individual contains k genotypes, its coding method is as shown in

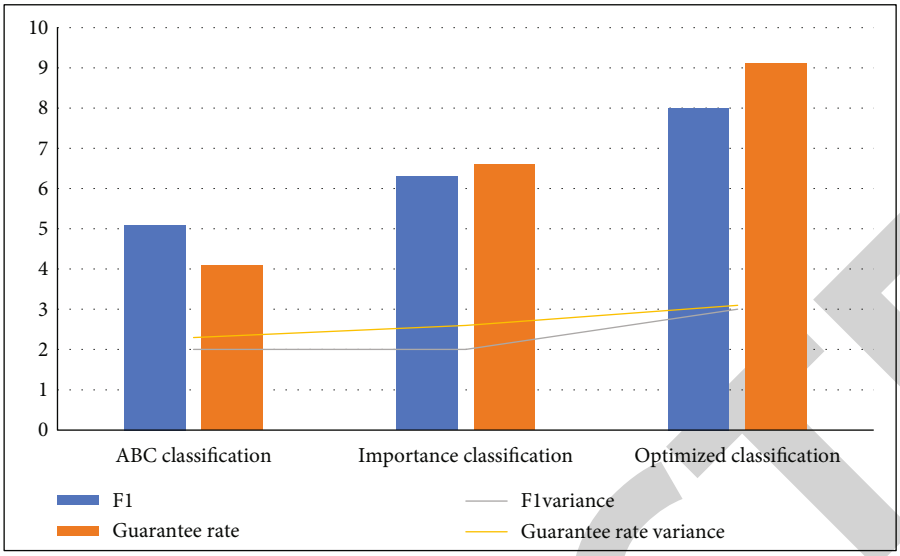

Figure 4: Comparison diagram of classification.

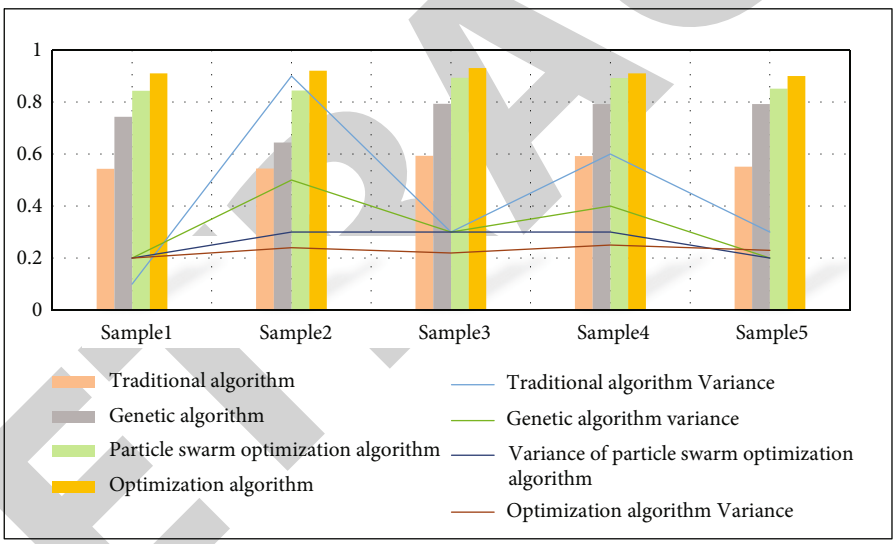

Figure 5: Accuracy comparison chart.

$$S_i^t = \left\{ [(p(1,x), p(1,y), p(1,z)), \cdots, (p(k,x), p(k,y), p(k,z))]_{(t,i)}^T \right\}_{(t,i)}. \tag{16}$$

In this paper, the roulette algorithm is used to select equipment individuals, and the survival probability T_i of the i-th individual in this round of survival competition is shown in formula (16).

3.2.3. Improved Particle Algorithm Combined with Genetic Algorithm. The particles whose fitness reaches the optimal value blend with each other and accelerate the local convergence speed; mutate the particles with poor fitness and improve the global search ability, such as

$$P_c = \frac{f_{\max} - f_i}{f_{\max} - f_{\min}}, \tag{17}$$

$$P_m = \frac{f_i - f_{\min}}{f_{\max} - f_{\min\ i}}. \tag{18}$$

Mutation operation:

$$P_m = k_p \times P_m. \tag{19}$$

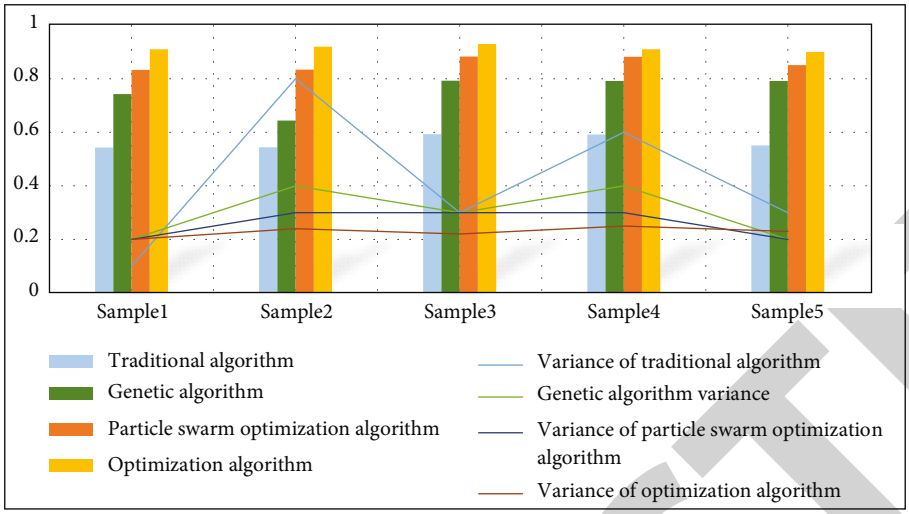

Figure 6: Comparison chart of recall rate.

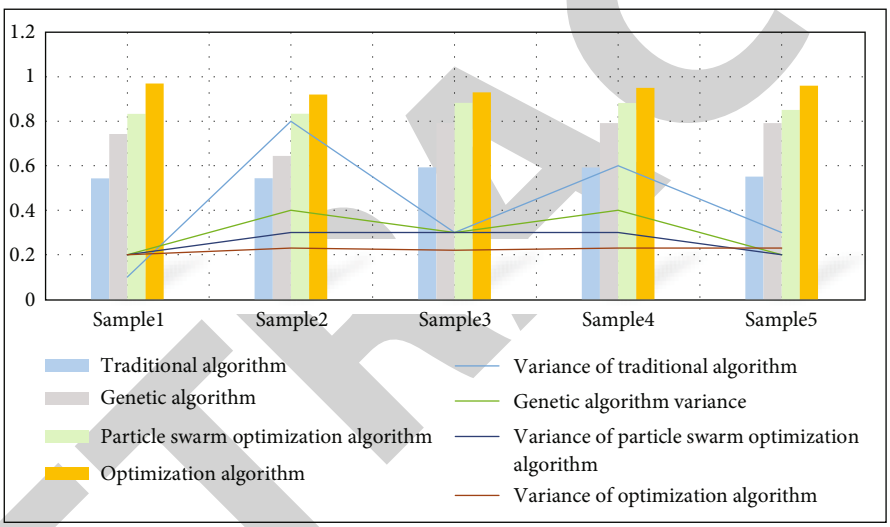

Figure 7: Comparison of $F1$ values.

k_p is a random parameter in the range of $(0, 1)$, which is used to improve the uncertainty of mutation.

Set dynamic inertia weights:

$$\omega_f = \omega_s\left(\frac{f_i - \bar{f}}{f_{\max} - f_{\min}} + 1\right),$$
$$\omega = \begin{cases} \omega_{\max}, \\ \omega_f, \\ \omega_{\min}, \end{cases} \quad \omega_{\max} \geq \begin{cases} \omega_f > \omega_{\max}, \\ \omega_f \geq \omega_{\min}, \\ \omega_f < \omega_{\min}, \end{cases} \tag{20}$$

where $\bar{f}$ the average fitness is the value of particles and ω_s is the standard inertia weight value.

The expression of step factor r relative to fitness value obtained by undetermined coefficient method is shown in the formula:

$$r = \frac{f_i - \bar{f}}{f_{\max} - \bar{f}} + 1\left(f_i > \bar{f}\right),$$
$$r = \frac{f_i - f_{\min}}{2\left(\bar{f} - f_{\min}\right)} + \frac{1}{2}\left(f_i < \bar{f}\right). \tag{21}$$

The improved particle velocity update formula v_i^{t+1} is shown in formula (22), and the position update formula is shown in formula (23):

$$v_i^{t+1} = r \bullet v_i^{t+1}, \tag{22}$$

$$p_i^{t+1} = p_i^t + v_i^{t+1}. \tag{23}$$

4. Experiments and Results

4.1. Experimental Testing

4.1.1. Contents of the Experiment. After processing the original data of the school in this experiment, there are five

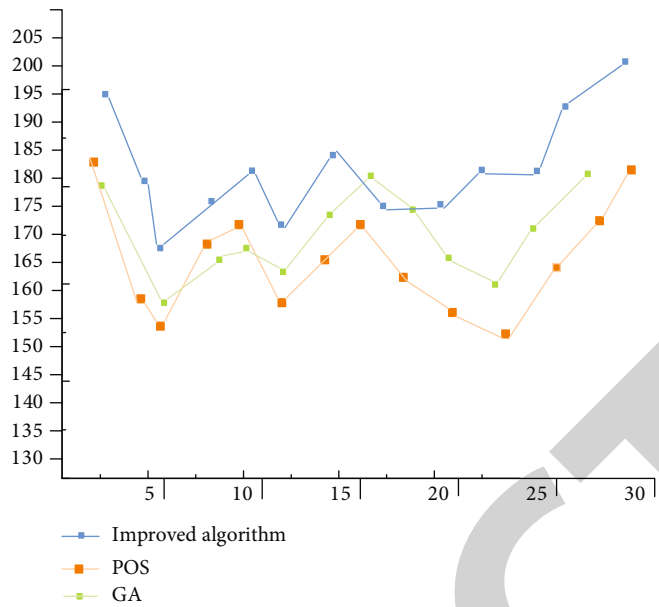

Figure 8: Algorithm comparison experiment.

indexes of purchased sports equipment, which are quotation, freight, warranty period, qualified rate, and enterprise credit supply data of sports equipment, as shown in Table 1.

4.1.2. Data Cleaning. Before calculation, there may be missing values and wrong data in the data. If the data is directly analyzed in this way, it will cause errors in the operation results. Therefore, before operation, it is necessary to clean the data set to improve the analysis quality of operation.

(1) Error data processing: this kind of error occurs because the business in the system is not perfect, and it is directly written into the background database without judgment after receiving the input, such as inputting numerical data into full-angle digital characters. This kind of data can be found and modified by writing SQL statements

(2) Missing value processing: some of the data values of enterprises are 0. In view of this situation, interpolating the missing values with the most possible values will cause less information loss than deleting all incomplete samples. Therefore, we must first find the missing value and fill it with the average value of this kind of data

4.2. Simulation Experiment. In this experiment, the population size is 1000, the maximum genetic algebra is 100 generations, and the variation probability is 0.01.

(1) Blending experiment: parent-child fusion needs to select the appropriate number of parent-child excellent individuals and child-child excellent individuals. From the experimental results in Table 2, it can be seen that when 30% of the optimal parent-child individuals and 12% of the optimal child-child individuals are preserved, the faster the genetic algorithm can get the optimal solution

(2) Example simulation, as shown in Figure 3

4.3. Comparison of Taxonomy

4.3.1. Traditional Taxonomy. To optimize the inventory control of sports equipment, the administrator classifies and optimizes the equipment with importance classification and ABC classification. First, the valuables of equipment are regarded as the main classification criteria, then classified according to price, and finally classified according to wear degree.

Comparative analysis of importance classification and ABC classification is shown in Table 3.

From Table 3, we know that the two classifications have their own advantages and disadvantages. If they are comprehensively improved, they will achieve efficient guiding significance in the management of sports equipment.

4.3.2. Improved Taxonomy. Combining the two classifications in Table 4 will produce a more optimized classification model, as shown in Table 4.

Comparative analysis of the $F1$ value and guarantee rate of improved classification, importance classification, and ABC classification is shown in Figure 4.

4.4. Model Comparison. The traditional management mode, genetic algorithm, particle swarm optimization algorithm, and the combination of the two optimization algorithm models are compared in accuracy, recall, and $F1$ equivalence, as shown in Figures 5–7.

Compare the accuracy of five batches of sports equipment according to genetic algorithm model, particle swarm

optimization algorithm, optimization algorithm, and traditional management model, as shown in Figure 5.

Compare the recall rates of five batches of sports equipment according to genetic algorithm model, particle swarm optimization algorithm, optimization algorithm, and traditional management model, as shown in Figure 6.

Five batches of sports equipment are compared in $F1$ according to genetic algorithm model, particle swarm optimization algorithm, optimization algorithm, and traditional management model, as shown in Figure 7.

4.5. Comparative Experiment of Optimization Algorithm. The genetic algorithm and particle algorithm are improved to achieve the optimal fitness, as shown in Figure 8.

By contrast experiments, the improved algorithm can achieve the best fitness with the least number of iterations and consumes the least time.

To sum up, from the experiment and experimental results, we can see that the improved genetic algorithm proposed in this paper can choose a better sports equipment supplier for schools to a certain extent, so as to purchase better equipment, greatly increase the service life of equipment, and then help schools save costs.

5. Conclusion

Under the background of the new era, physical education is no longer an unimportant subject before, but the focus of parents on whether their children take healthy exercise in school. In the physical education classroom, the management of sports equipment is particularly important. This paper mainly studies and analyzes whether the equipment is used normally, whether the equipment is safe, whether the inventory of the school equipment room is safe, and how to purchase the equipment reasonably:

(1) According to the current situation of sports equipment, put forward solutions, and use intelligent system to register and share data on the borrowing and returning of sports equipment

(2) Combining particle swarm optimization and genetic algorithm to calculate the guarantee rate of equipment and get the optimal algorithm to ensure the normal and safe use of equipment and whether there is a safe inventory for students to use

(3) According to the simulation experiment, it is known that the optimal fitness gets the least iteration times, which helps schools to purchase sports equipment with better quality and higher cost performance to a certain extent

(4) Optimize the classification algorithm model, synthesize the traditional classification model, and classify and store the equipment, which can greatly increase the service time of the equipment to a certain extent

(5) By comparing genetic algorithm, particle swarm optimization algorithm, optimization algorithm, and traditional algorithm model, it is obvious that the indexes of optimization algorithm are superior to the other three algorithms

Data Availability

The experimental data used to support the findings of this study are available from the corresponding author upon request.

Conflicts of Interest

The authors declared that they have no conflicts of interest regarding this work.

References

[1] C. Jianchang, "Investigation and analysis on the current situation of sports equipment room construction-taking Guangdong colleges and universities as an example," *Sports Boutique*, vol. 37, no. 2, pp. 1–3, 2018.

[2] L. Yuanhong, "Strategic analysis of rational application of intelligent management in sports equipment," *Contemporary Sports, Science and Technology*, vol. 10, no. 6, pp. 60–62, 2020.

[3] Y. Bing, "Design and implementation of sports equipment sharing management system in colleges and universities," *Journal of Bohai University (Natural Science Edition)*, vol. 42, no. 2, pp. 175–180, 2021.

[4] Y. Lan, M. Jie, and P. Min, "Exploration and research on sports equipment management system in colleges and universities," *Computer Knowledge and Technology*, vol. 13, no. 7, pp. 118-119, 2017.

[5] L. Peng, "Discussion on the causes of frequent problems in sports equipment recently," *Contemporary Sports, Science and Technology*, vol. 5, no. 27, pp. 178–181, 2015.

[6] J. Yanzhou, "Classified management and countermeasure analysis of sports equipment in colleges and universities," *Reading and Writing (Education and Teaching Journal)*, vol. 11, no. 6, pp. 58–247, 2014.

[7] Y. Shihai, "Tentative idea and attempt of sports equipment diversion management," *Physical Education*, vol. 34, no. 4, pp. 57-58, 2014.

[8] C. Yajin, "Research on the countermeasures of optimizing the purchase and management of sports equipment in colleges and universities," *Sports Research and Education*, vol. 26, no. S2, pp. 16-17, 2011.

[9] K. Fujun, "Six transformations of school sports equipment management," *Physical Education Teachers and Friends*, vol. 35, no. 1, pp. 40-41, 2012.

[10] Q. Jianing, "Simulation study on performance of fiber reinforced composite sports equipment," *Aging and Application of Synthetic materials*, vol. 50, no. 5, pp. 98-99, 2021.

[11] W. Xiaoyan, "Optimization and improvement of structural stiffness of sports equipment by carbon fiber composites," *Synthetic Fiber*, vol. 50, no. 10, pp. 45–47, 2021.

[12] W. Wen and Z. Yujuan, "Design analysis and research of new materials in sports equipment manufacturing process," *Mechanical Design*, vol. 38, no. 10, pp. 164-165, 2021.

[13] X. Lihong, "Application of computer technology in gymnasium equipment management," *Information Record Materials*, vol. 22, no. 1, pp. 92-93, 2021.

Hindawi
Journal of Sensors
Volume 2023, Article ID 9802327, 1 page
https://doi.org/10.1155/2023/9802327

Retraction

Retracted: Integrated Evaluation of Corporate Investment Decision Performance Based on Fuzzy Sets and BP Neural Networks

Journal of Sensors

Received 8 August 2023; Accepted 8 August 2023; Published 9 August 2023

This article has been retracted by Hindawi following an investigation undertaken by the publisher [1]. This investigation has uncovered evidence of one or more of the following indicators of systematic manipulation of the publication process:

(1) Discrepancies in scope
(2) Discrepancies in the description of the research reported
(3) Discrepancies between the availability of data and the research described
(4) Inappropriate citations
(5) Incoherent, meaningless and/or irrelevant content included in the article
(6) Peer-review manipulation

The presence of these indicators undermines our confidence in the integrity of the article's content and we cannot, therefore, vouch for its reliability. Please note that this notice is intended solely to alert readers that the content of this article is unreliable. We have not investigated whether authors were aware of or involved in the systematic manipulation of the publication process.

Wiley and Hindawi regrets that the usual quality checks did not identify these issues before publication and have since put additional measures in place to safeguard research integrity.

We wish to credit our own Research Integrity and Research Publishing teams and anonymous and named external researchers and research integrity experts for contributing to this investigation.

The corresponding author, as the representative of all authors, has been given the opportunity to register their agreement or disagreement to this retraction. We have kept a record of any response received.

References

[1] J. Du, "Integrated Evaluation of Corporate Investment Decision Performance Based on Fuzzy Sets and BP Neural Networks," *Journal of Sensors*, vol. 2022, Article ID 7628124, 7 pages, 2022.

Hindawi
Journal of Sensors
Volume 2022, Article ID 7628124, 7 pages
https://doi.org/10.1155/2022/7628124

Research Article

Integrated Evaluation of Corporate Investment Decision Performance Based on Fuzzy Sets and BP Neural Networks

Jiang Du

Claro M. Recto Academy of Advanced Studies, Lyceum of the Philippines University, Manila 0900, Philippines

Correspondence should be addressed to Jiang Du; du.jiang@lpunetwork.edu.ph

Received 1 April 2022; Accepted 5 May 2022; Published 28 May 2022

Academic Editor: Han Wang

Enterprise investment decision performance evaluation is a complex system, which is affected by many factors. Based on the consideration of corporate strategy and stakeholders, a six-level index system is designed to evaluate the performance of corporate investment decision-making. The index-selection method combining benchmarking management and principal component analysis is established, and the enterprise management index analysis method based on neural network and fuzzy decision-making is designed. The multiattribute decision-making problem in enterprise performance evaluation is solved by using the triangular fuzzy-weighted Einstein-Bonferroni mean (TF-WEBM). The algorithm is suitable for multiattribute decision-making in a triangular fuzzy environment. Finally, the effectiveness of this method is verified by an enterprise performance evaluation example.

1. Introduction

The evaluation of enterprise investment decision performance is very important to the implementation of enterprise strategy, and strategic motivation is the most important motivation to evaluate enterprise investment decision performance [1]. Corporate governance is an important aspect that affects the performance evaluation of corporate investment decision-making, and the stakeholder corporate governance model is the development trend of corporate governance. Based on these two basic theoretical motivation assumptions, we discuss the performance evaluation index system of enterprise investment decision-making [2]. As an important tool for strategy implementation, enterprise performance evaluation inevitably varies from enterprise to enterprise and from stage to stage. It is a multilevel complex system [3].

Strategic management focuses on how to make enterprises use appropriate strategies to maintain competitive advantage. Its competitive situation has increased exponentially in recent years. However, Zhang et al. [4] pointed out that strategic management research has been criticized for paying too much attention to analysis. In addition, its high management preference, neglect of learning behavior, and insufficient attention to learning behavior are also the main reasons for criticism [5]. It is pointed out that the focus of organizational learning research is the process, which may be a disadvantage in providing insights. Muriana et al. [6] argued that organizational learning is the basis for achieving sustainable competitive advantage and is a key variable for improving business management. Ang and Quek [7] stated that companies that are able to learn have a better chance of perceiving events and trends in the marketplace.

In addition, several studies provide evidence of a positive correlation between organizational learning and firm performance. For example, Kuo et al. [8] found that the direction of learning had a direct impact on firm performance [9]. Similar results were obtained by Wang et al. [10] using a cultural learning approach. Corporate performance appraisal is not only a result of a certain stage of market economy development, it is also a scientific approach and an effective tool that provides a role in regulating companies in a mature market economy [11]. While learning from successful business management experiences in foreign market economies is the direction of modern business management, the application of business performance assessment to the supervision and control of enterprises is also an important tool.

As one of the tools of modern corporate management, performance assessment is being tested by the rapid development of the economy and the constant renewal of corporate management models and is receiving wider attention and more in-depth discussion [12].

For China's enterprise performance appraisal work, understanding how to comply with the changes in China's economic and social environment and international trends and establishing a performance appraisal system suitable for China's economic development are effective ways to improve enterprise performance [13]. At the same time, the enterprise performance appraisal system has particularly important business significance in improving the health and management level of enterprises, enhancing their competitiveness, and further improving the quality of economic development [14].

Therefore, enterprise performance assessment based on the triangular fuzzy information is a classical multiattribute decision problem [15]. In this paper, we study the multiattribute decision problem of enterprise performance evaluation under the triangular fuzzy information. We develop a process for multiattribute decision-making in a triangular fuzzy environment using the triangular fuzzy-weighted Einstein-Bonferroni mean (TF-WEBM) operator. Finally, an example of enterprise performance evaluation is given to validate the developed method [16].

2. Construction and Selection of Indicator Systems

2.1. Construction of the Indicator System. Based on the strategy and stakeholder theory, the evaluation of shareholders, employees, related enterprises (upstream and downstream enterprises), society, and intellectual capital are integrated into the evaluation index system. The frequency statistics method, theoretical analysis method, and expert consultation method are used to set and screen the indicators, adjust the indicators, and establish a general indicator system for evaluating the performance of corporate investment decisions [17].

NPV is based on option NPV+C(value of the option),($C = At.N(d1) + I_t e^{-Rt}.(d2)$, = present value of investment return =Atexercise price of option= $\sum_{10+1}^{T} A(t).(1+r)^t$, I_t= additional investment$I_t(0)$; $d1 = [I_n(\mathrm{At}/I_t) + (R + \sigma^2/2t]/(\sigma.t^{1/2})d2 = d1 - \sigma.t^{1/2}$; R the risk rate; r is the risk discount rate; $A(t)$ is the net cash flow; σ is the expected return volatility; t is option maturity time), modified economic value added (REVA), return on intellectual capital, modified internal rate of return (RIRR), intellectual capital efficiency contribution rate, capital conservation and appreciation rate, net sales margin, payback period, cost reduction rate, earnings per share, current asset turnover, accounts receivable turnover, inventory turnover, ratio of net cash flow to REVA, asset-generating rate, net asset-generating rate, cost margin, net cash flow, return on debt, cost reduction rate, upstream corporate cost profitability, growth rate of knowledge, and intellectual assets contribution value [18].

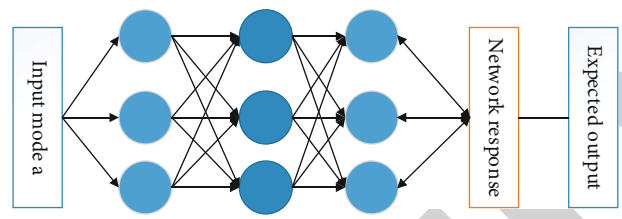

Figure 1: Neural network structure.

2.2. Benchmarking-Based Indicator System Screening. There are many mathematical methods for selecting indicators for evaluating the performance of enterprise investment decisions, including affiliation analysis, correlation analysis, discriminative power analysis, and grey correlation analysis. The principal component analysis is used here to select indicators at each level. The principal component analysis requires a large number of samples, and the company's own historical data is easy to obtain and can meet the conditions, in line with the principles of cost minimisation and efficiency. Using the principal component analysis, k principal components are obtained, and the variance contribution of the k values is determined by $\sum_{g=1}^{k}\lambda_g / \sum_{g=1}^{p}\lambda_g$ retaining 85%. The indicators in the retained principal components are judged, and those with smaller coefficients are screened out, while those with larger coefficients are retained, i.e., the principal component indicators. In the practice of investment decision performance of enterprises, it should be determined in conjunction with the theory and practice of enterprise management.

3. Fuzzy Integrated Evaluation Model

The factors affecting the performance of investment decisions are divided into several subsystems according to the attributes of the objectives, the evaluation set U is composed of all evaluation indicators, and the set of evaluation indicators is divided into n subsets according to each objective that cannot be subdivided, $U = \{U_1, U_2, \cdots; U_n\}$, and satisfies

$$\bigcup_{i=1}^{n} U_i \neq U, U_i \cap U_j = \varnothing (i \neq j \quad i, j \in \{1, 2, \cdots; n\}). \tag{1}$$

Let the i-th subset be $U_i = u_{i1}, u_{12}, \cdots; u_{ik}\}$; then the characteristic values of the evaluation indicators of the m samples can be represented by the following matrix:

$$\begin{aligned} X(i) &= \begin{bmatrix} x_{11}(i) & x_{12}(i) & \cdots & x_{1m}(i) \\ x_{21}(i) & x_{22}(i) & \cdots & x_{2m}(i) \\ & \cdots & & \\ x_{k1}(i) & x_{k2}(i) & \cdots & x_{km}(i) \end{bmatrix} \\ &= [X_1(i), X_2(i), \cdots X_k(i)] \\ &= [x_{kj}(i)] x_m, \end{aligned} \tag{2}$$

where $X_k(i)(k \in \{1, 2, \cdots; h\})$ represents the eigenvectors of

Table 1: Data for evaluating the performance of corporate investment decisions.

Project	Index								
	A1	A2	A3	A4	A5	A6	A7	A8	A9
1	0.055	0.24	0.25	0.87	0.07	0.08	0.07	0.12	0.75
2	0.087	0.55	0.27	0.90	0.11	0.88	0.06	0.27	0.78
3	0.07	0.40	0.035	0.81	0.13	0.70	0.074	0.25	0.81
4	0.05	0.45	0.037	0.87	0.27	0.72	0.078	0.26	0.88
5	0.08	0.48	0.057	0.89	0.37	0.78	0.074	0.27	0.89
6	0.09	0.50	0.058	0.90	0.40	0.79	0.075	0.30	0.90

the m samples corresponding to the indicators $U_{ik} \in U_i$ and $X_k(i) \neq (x_{k1}(i), x_{k2}(i), \cdots x_{km}(i))$.

According to the different types of evaluation indicators (cost, benefit, moderate, interval, etc.), different affiliation functions are used to transform the matrix of eigenvalues into the following affiliation matrix (evaluation matrix).

$$\begin{aligned} R(i) &= \begin{bmatrix} r_{11}(i) & r_{12}(i) & \cdots & r_{1m}(i) \\ r_{21}(i) & r_{22}(i) & \cdots & r_{2m}(i) \\ & \cdots & & \\ r_{k1}(i) & r_{k2}(i) & \cdots & r_{km}(i) \end{bmatrix} \\ &= R_1(i), R_2(i), \cdots; R_k(i)] \\ &= l_{kj}(i) l_{k\times m}, \end{aligned} \tag{3}$$

where $r_{kj}(i)$ is the affiliation of the sample p_j corresponding to u_{kj} of u_i and $r_{kj}(i) \in [0, 1]$; $Rj(i)$ is the one-sample evaluation of the h indicators corresponding to p_j and $Rj(i) = (r_{1j}(i), r_{2j}(i), \cdots; r_{kj}(i))^T$.

Let the weight coefficients of the k indicators of the subset u_i be $A(i) \neq (a_1(i), a_2(i), \cdots; a_k(i))$ as the value of the weight coefficient corresponding to the k-th evaluation indicator and

$$a_k(i) \geq 0, \sum_{k\neq j}^{h} a_k(i) = 1. \tag{4}$$

4. Triangular Fuzzy Information Theory

This section will briefly introduce some basic concepts and fundamental operations related to trigonometric fuzzy numbers.

Definition 1. A triangular fuzzy number a can be defined by a triplet as (a^L, a^M, a^U). The membership function is defined as

Table 2: Fuzzy integrated evaluation and BP neural network model training results.

Project	Actual output	Ideal output	Achievements
1	0.6425	0.65478	Medium
2	0.9478	0.9587	Excellent
3	0.8714	0.9478	Good
4	0.5741	0.5471	Poor
5	0.5781	0.5897	Poor
6	0.9001	0.9854	Excellent
7	0.9547	0.9247	Excellent
8	0.5574	0.5587	Poor
9	0.8241	0.8574	Good
10	0.5741	0.5574	Medium

$$\mu(x) = \begin{cases} 0, & x < a^L, \\ \dfrac{x - a^L}{a^M - a^L}, & a^L \leq x \leq a^M, \\ \dfrac{x - a^U}{a^M - a^U}, & a^M \leq x \leq a^U, \\ 0, & x \geq a^U, \end{cases} \tag{5}$$

where $0 < a^L \leq a^M \leq a^U$, a^L and a^U denote the lower and upper limits of $\tilde{a}$, respectively, and a^M denotes the modal value.

Definition 2. Let $\tilde{b} = [b^L, b^M, b^U]$ and $\tilde{a} = [a^L, a^M, a^U]$ be two triangular fuzzy numbers; then the degree of probability that $a \geq b$ is

$$\begin{aligned} p(a \geq b) &= \lambda \max 1 - \max \frac{b^M - a^L}{a^M - a^L + b^M - b^L, 0} \\ &(1 - \lambda) \max \left\{ 1 - \max \left[\frac{b^U - a^M}{a^U - a^M + b^M - b^M}, 0 \right], 0 \right\}. \end{aligned} \tag{6}$$

The λ value is an indicator of the attitude of the rating, which reflects the risk attitude of the decision-maker. If $\lambda > 0.5$, the decision-maker is a risk lover; if $\lambda = 0.5$, the

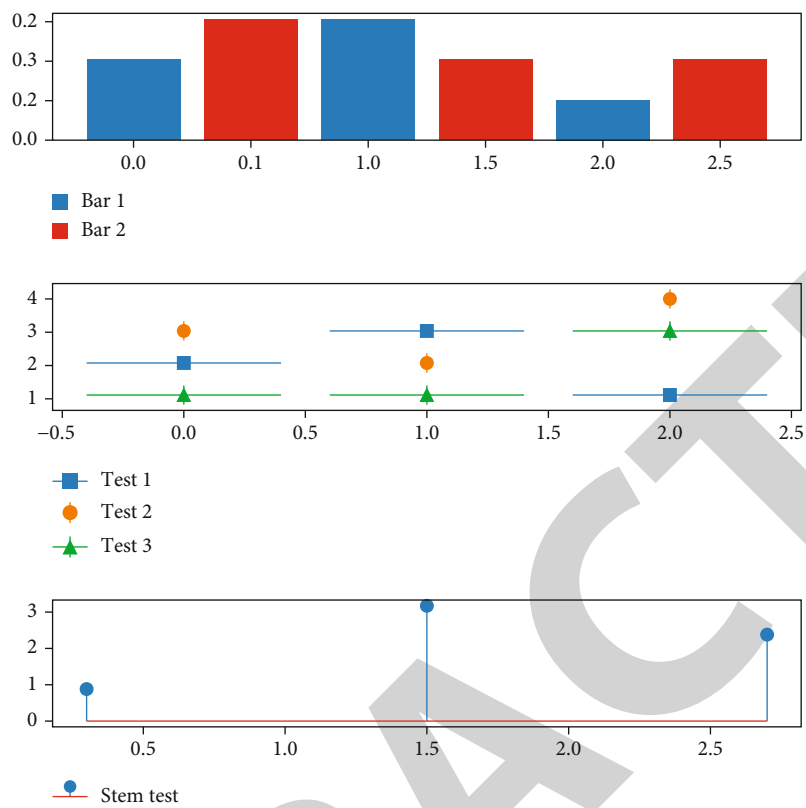

Figure 2: Development utilisation rates of different companies.

decision-maker is risk-neutral; if $\lambda < 0.5$, the chooser is risk-averse.

However, the Bonferroni mean (BM) operator and the Einstein operator are usually used in cases where the input parameters are nonnegative real numbers. Kumar and Ravi [16] extended the BM and Einstein operators to accommodate the case where the input parameters are triangular fuzzy numbers and proposed the triangular fuzzy Einstein-Bonferroni mean (TF-EBM) operator.

Considering that the input parameters may have different importance, Zhang et al. [19] further proposed the triangular fuzzy-weighted Einstein-Bonferroni mean (TF-WEBM) operator.

Definition 3. $a_i = [a_i^L, a_i^M, a_i^U](i = 1, 2, \cdots, n)$ is a set of triangular fuzzy numbers, and $p, q > 0, \omega = (\omega_1, \omega_2, \cdots, \omega_n)^{\mathrm{T}}$ is a weight vector of $a_i = [a_i^L, a_i^M, a_i^U](i = 1, 2, \cdots, n)$; ω_i expresses the importance of $\tilde{a}_i$, $\omega_i > 0(i = 1, 2, \cdots, n)$, and $\sum_{i=1}^{n} \omega_i = 1$.

5. A Comprehensive BP Neural Network Evaluation Model Based on Fuzzy Evaluation

The artificial neural network is a complex network composed of a large number of widely connected simple information units (called neurons). It is used to simulate the structure and behavior of the human brain neural network. The neural network is good at making decisions in approximate, uncertain, and even conflicting knowledge environments. Theoretically, the three-layer BP network can approximate any mapping relationship with any accuracy (Figure 1) [17, 20].

The number of neurons in the middle layer is determined according to the empirical formula $p \le n \times (q + 3) + 1$. The input layer weight factor w_{ij} and the output layer weight factor v_{jt} are adjusted by a large number of sample training. The input of the intermediate layer unit is $s_j = \sum_{i \neq 1}^{n} W_{ij} a_i - \rho$, and the output of the intermediate layer is the connection right of the input layer to the intermediate layer; θ_j is the threshold of the intermediate layer unit; p is the number of intermediate units; n is the number of input layer units; q is the number of the output layer. The neuron transformation function $f(x)$ is a sigmoid function. Following the same propagation idea, the input L_t and output C_t of the middle layer are calculated [18, 21, 22].

$\Delta_{v_{jt}} = \alpha . d_{t\,b}^{k\,k}, \Delta_t \gamma = \alpha . d_t^k, \Delta w_{ij} = \beta . e_j^k . \alpha_i^k, \Delta j_\theta = \beta \cdot e_j^k$ is the connection weight from the middle layer to the output layer and the threshold value of the output unit. The neuron feedback correction formula is as follows: α and β are the learning efficiency coefficients between 0 and 1, and k is the number of sample coefficients, where $d_t^k = (y_t^k - C_t^k) f'(L_t)$, $e_j^k = [\sum_{t \neq}^{q} v_{jt} d_t^k] f'(s_j)$. The use of the additional momentum method $(\Delta_W(N) = \mathrm{d} + \eta_W(N - 1)$ $(\eta$ is the momentum

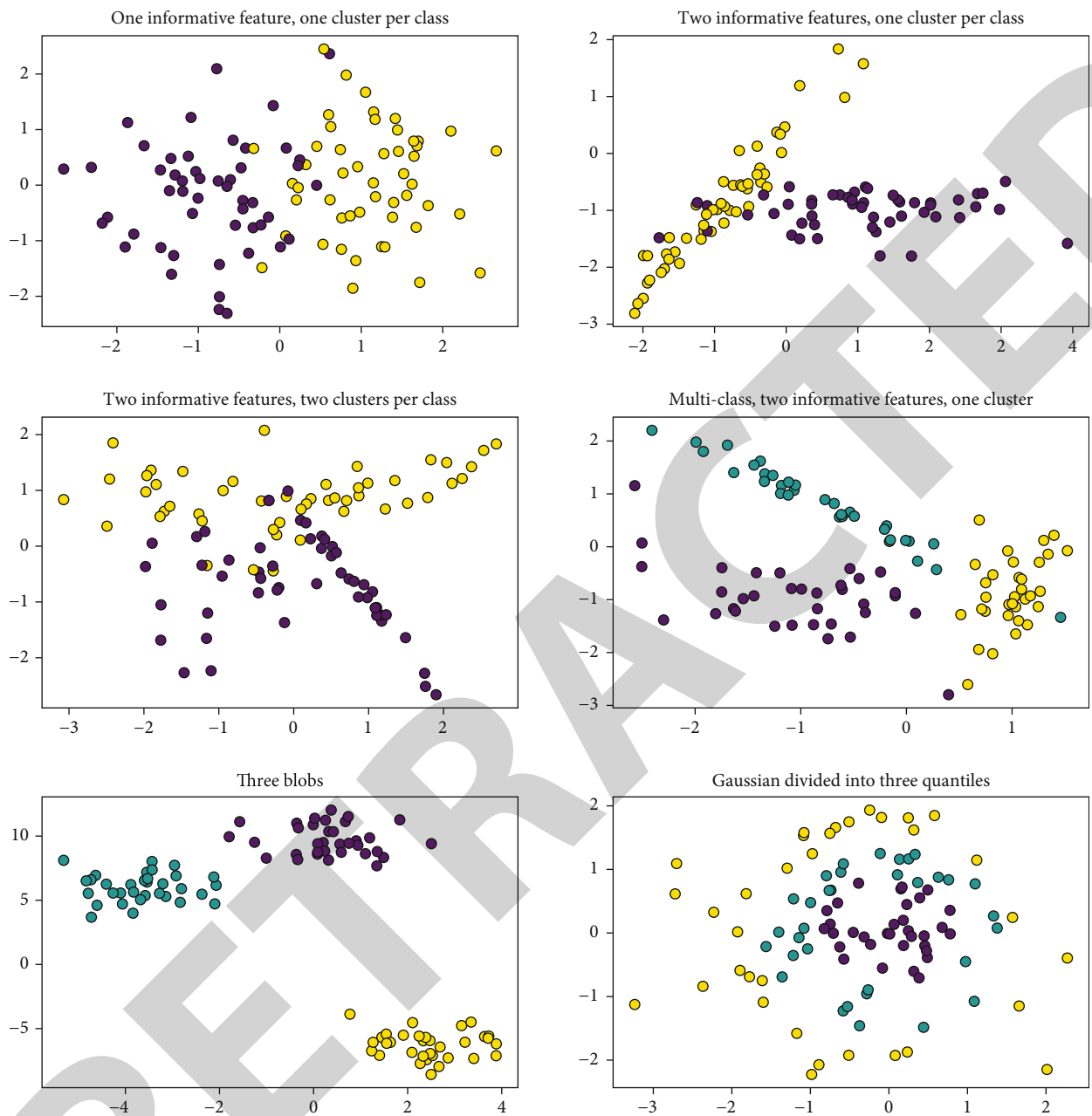

Figure 3: Cluster analysis of customers from different companies.

factor, generally between 0.9 and 0.98) can prevent the emergence of local minima and accelerate the convergence process of network learning and training.

The trained neural network is stored in the knowledge base for evaluating other evaluation objects. The result (vector) can be obtained by inputting the value vector (matrix) of the attribute of the object to be evaluated. Therefore, the neural network at this time is called the neural network comprehensive evaluation model. The connection weight coefficient and internal threshold of the neural network are the model parameters. Fuzzy evaluation samples and evaluation results provide training samples for the training of the model, and the trained model is used for the comprehensive evaluation of enterprise investment decision-making performance [23–25].

6. Empirical Analysis

A company is a large modern coal chemical company that produces metallurgical coke and a variety of coal chemical products. By combining the scope of data provided by the industry and the analysis of time series investment indicators of the coking industry, the benchmarking method was applied, and the experts' judgement analysis of the energy and coal chemical industry was used to obtain the return on investment, the growth rate of the value of contribution

of knowledge and intellectual assets, the R&D (research and development) cost rate, the production and sales rate of new products, the relative market share, the staff retention rate (employee satisfaction), the product production cycle efficiency, and the product (A,…, A9 in order). After eliminating the irregular index data items, the BP neural network model was trained by using the data of 10 items of relevant indexes and their fuzzy comprehensive evaluation results in 2000 in the coking industry (Table 1) [26], with a convergence accuracy of 0.001. The fuzzy evaluation and the neural network were validated against each other, the results were more satisfactory and improved the processing effect of the samples before model training compared with the single method, and the types of actual output, ideal output, and performance are shown in Table 2.

Indicators at the level of technological innovation are as follows: the total investment rate in intangible assets, return on investment in innovative products, R&D expenditure rate, rate of innovative products, rate of sales of innovative products, share of employees in R&D activities in the enterprise, labour productivity of new products, market share of new products, growth rate of sales revenue of new products, ratio of sales revenue of new products to total sales revenue, market volume of new products, growth rate of R&D expenditure, ratio of R&D expenditure to enterprise ratio of R&D expenses to enterprise sales revenue, ratio of R&D expenses to enterprise net profit, new product R&D expense rate, cost reduction R&D efficiency rate [27], product quality R&D efficiency rate, new product value added as a proportion of total product value added, reduction in production cost due to adoption of new technology, product innovation cycle, product quality R&D efficiency rate, new product contribution rate, new product R&D expense rate, speed of new product development, new product development, new product development capacity, and product quality research and development cost rate, as shown in Figure 2.

As shown in Figure 3, the different customer clusters can be analysed to know the customer level indicators. Customers include internal customers and external customers of the enterprise; external customers are commonly referred to as customers, and internal customers are referred to as internal employees. The ultimate goal is to satisfy external customers, and external customer satisfaction is closely related to internal customer satisfaction, which is the basis for external customer satisfaction, which in turn will lead to increased internal customer satisfaction. Internal customer indicators are as follows: staff retention rate (staff satisfaction), staff labour efficiency, total labour productivity, staff turnover rate, talent development growth rate, staff opinion adoption rate, staff training cost, staff knowledge, staff competence, and staff suggestion ability. External customer (commonly referred to as "recipients of products and services") indicators are market share, customer retention, customer profitability, customer acquisition, on-time product delivery, increase/decrease in sales from existing customers, repair rate, return rate, and length of time to resolve customer complaints.

7. Conclusions

An enterprise management index system based on neural network and fuzzy decision analysis is designed, and the multidependent decision-making problem in enterprise performance evaluation is solved by using triangular fuzzy theory. Finally, taking enterprise performance evaluation as an example, the effectiveness of this method is verified, in terms of social investment and donation rate, waste recovery rate, product energy intensity, success rate in dealing with environmental problems, public policy participation, pollution cost rate, average annual product life cycle cost, product raw material intensity, product service intensity, raw material recyclability, and product emission efficiency.

Data Availability

The experimental data used to support the findings of this study are available from the corresponding author upon request.

Conflicts of Interest

The author declared no conflicts of interest regarding this work.

References

[1] M. Khashei, S. R. Hejazi, and M. Bijari, "A new hybrid artificial neural networks and fuzzy regression model for time series forecasting," *Fuzzy Sets and Systems*, vol. 159, no. 7, pp. 769–786, 2008.

[2] X. Deyun, W. Zongjun, and C. Rongda, "Strategic performance measurement of investment decision-making based on fuzzy set and neural network," in *Proceedings. 2005 First International Conference on Neural Interface and Control, 2005*, pp. 163–166, Wuhan, China, 2005.

[3] R. J. Kuo, C. H. Chen, and Y. C. Hwang, "An intelligent stock trading decision support system through integration of genetic algorithm based fuzzy neural network and artificial neural network," *Fuzzy Sets and Systems*, vol. 118, no. 1, pp. 21–45, 2001.

[4] L. Zhang, A. Yang, and W. Dai, "Investment decision-making based on fuzzy and artificial neural network," in *Third international conference on natural computation (ICNC 2007)*, vol. 3, pp. 297–300, Haikou, China, 2007.

[5] M. Khashei, M. Bijari, and G. A. R. Ardali, "Improvement of auto-regressive integrated moving average models using fuzzy logic and artificial neural networks (ANNs)," *Neurocomputing*, vol. 72, no. 4-6, pp. 956–967, 2009.

[6] C. Muriana, T. Piazza, and G. Vizzini, "An expert system for financial performance assessment of health care structures based on fuzzy sets and KPIs," *Knowledge-Based Systems*, vol. 97, pp. 1–10, 2016.

[7] K. K. Ang and C. Quek, "Stock trading using RSPOP: a novel rough set-based neuro-fuzzy approach," *IEEE Transactions on Neural Networks*, vol. 17, no. 5, pp. 1301–1315, 2006.

[8] R. J. Kuo, S. C. Chi, and S. S. Kao, "A decision support system for selecting convenience store location through integration of fuzzy AHP and artificial neural network," *Computers in Industry*, vol. 47, no. 2, pp. 199–214, 2002.

[9] D. Enke and N. Mehdiyev, "Stock market prediction using a combination of stepwise regression analysis, differential evolution-based fuzzy clustering, and a fuzzy inference neural network," *Intelligent Automation & Soft Computing*, vol. 19, no. 4, pp. 636–648, 2013.

Hindawi
Journal of Sensors
Volume 2022, Article ID 4173346, 14 pages
https://doi.org/10.1155/2022/4173346

Research Article

AI-Enabled Energy-Efficient Fog Computing for Internet of Vehicles

Hira Tariq,[1] Muhammad Awais Javed,[1] Ahmad Naseem Alvi,[1] Mozaherul Hoque Abul Hasanat,[2] Muhammad Badruddin Khan,[2] Abdul Khader Jilani Saudagar,[2] and Mohammed Alkhathami[2]

[1]*Department of Electrical and Computer Engineering, COMSATS University Islamabad (CUI), Islamabad 45550, Pakistan*
[2]*Information Systems Department, College of Computer and Information Sciences, Imam Mohammad Ibn Saud Islamic University (IMSIU), Riyadh 11432, Saudi Arabia*

Correspondence should be addressed to Mozaherul Hoque Abul Hasanat; mhhasanat@imamu.edu.sa

Received 16 March 2022; Revised 24 April 2022; Accepted 10 May 2022; Published 26 May 2022

Academic Editor: Han Wang

Future autonomous electric vehicles (EVs) are equipped with several IoT sensors, smart devices, and wireless adapters, thus forming an Internet of Vehicles (IoVs). These intelligent EVs are envisioned to be a promising solution for improving transportation efficiency, road safety, and driving experience. Vehicular fog computing (VFC) is an evolving technology that allows vehicular application-related tasks to be offloaded to nearby computing nodes and process them quickly. A major challenge in the VFC system is to design energy-efficient task offloading algorithms. In this paper, we propose an optimal energy-efficient algorithm for task offloading in a VFC system that maximizes the expected reward function which is derived using the total energy and time delay of the system for the computation of the task. We use parallel computing and formulate the optimization problem as semi-Markov decision process (SMDP). Bellman optimal equation is used in value iteration algorithm (VIA) to get an optimal scheme by selecting the best action for the current state that maximizes the energy-based reward function. Numerical results show that the proposed scheme outperforms the greedy algorithm in terms of energy consumption.

1. Introduction

Recently, autonomous and connected electric vehicles also known as the Internet of Vehicles (IoVs) have gained extensive attention and flourished as a promising technology by bringing convenience to society by solving the traffic issues like accidents [1], congestion, and environmental pollution [2]. By 2035, it is estimated that around 25% of autonomous vehicles will be on-road [3]. Nowadays, a large number of sensors, smart devices, and controllers are deployed in vehicles to facilitate the drivers and passengers for autonomous driving, infotainment, and natural language processing [4].

According to an estimate in 2020, every day around 4000 GB of data is produced by the vehicles [5]. Due to these smart sensors and controllers, the IoVs consume an enormous amount of power for the processing of data generated by the smart devices [6, 7]. As the vehicles have limited resources of energy and computational power, the computation of smart applications that cannot be managed locally needs to be offloaded to the helping nodes [8].

With the development in the technology of computation and communication [9], the vehicles can be both task producer and service provider nodes. This concept brings the computation capabilities near the proximity of task producer vehicles with the help of Vehicular to Vehicular (V2V) and Vehicular to Infrastructure (V2I) communication [10].

Vehicular fog computing is a novel technique for computing tasks and uses computational resources of both moving and parked vehicles [11]. The basic concept behind VFC is to install resource units (RUs) on connected vehicles so that these vehicles act as fog nodes and deliver their services of communication and computing, according to the

requirements [12]. To enable communication of tasks to the vehicular fog nodes, vehicles are armed with different types of network interface components. Vehicular fog nodes communicate with devices and the Internet via cellular network or IEEE 802.11p [13].

VFC is thus a proficient method for low latency tasks and smart IoV applications. However, vehicular fog nodes have limited computation capability of RU's and bandwidth of communication; hence, it is not possible to process all the tasks and satisfy computation latency requirements by the VFC. To solve this issue, vehicles are also connected to the cloud servers in the form of remote cloud (RC) using cellular communications [14]. Vehicles can transfer the tasks to the RC and avail the opportunity of powerful computational resources. However, long distance between RC and vehicles suffers from challenges of high latency and high-power consumption due to the transfer of tasks to the RCs. To assure reliable computing services to the EVs, the three-tiered VFC architecture is considered in this paper. This architecture includes task producer devices, vehicular fog nodes, and the remote cloud as shown in Figure 1 [15].

In this paper, we propose an optimal energy-efficient algorithm for task offloading in a VFC system that minimizes the energy consumption of the system. We propose an energy-based reward function for the considered problem and utilize parallel offloading. Vehicles with the tasks divide it into several parts and offload it to the neighboring vehicles for processing. One part of the task is computed locally, and the rest of the parts are offloaded to the remaining other cooperative vehicles such that the energy efficiency of the whole system is maximized.

The main contribution of our work is summarized as follows:

(i) We propose a novel reward function that considers the energy of the system for parallel task offloading

(ii) We formulate the problem of task offloading as semi-Markov decision process (SMDP) that consider factors such as (1) arrival of task, (2) departure of task, (3) arrival of the vehicle, and (4) departure of the vehicle

(iii) The state space, actions, reward, and transition probabilities of the VFC system are analyzed and defined to obtain the optimal policy, which determines the best action for the specific state for task offloading

(iv) We used the iterative algorithm to solve the optimal task offloading problem and increased the long-term expected reward in the form of saved energy and time

(v) We compare the results of the proposed technique with a greedy algorithm and show significant performance gains

The rest of the paper is organized as follows. Section 2 provides the related literature review. In Section 3, we describe the system model of the VFC system. In Section 4, we formulate the problem as an SMDP optimization problem. The solution to the optimization problem is given in Section 5 as an iterative algorithm. Section 6 presents the numerical results and analysis of the performance. Finally, in Section 7, conclusion and future work are presented.

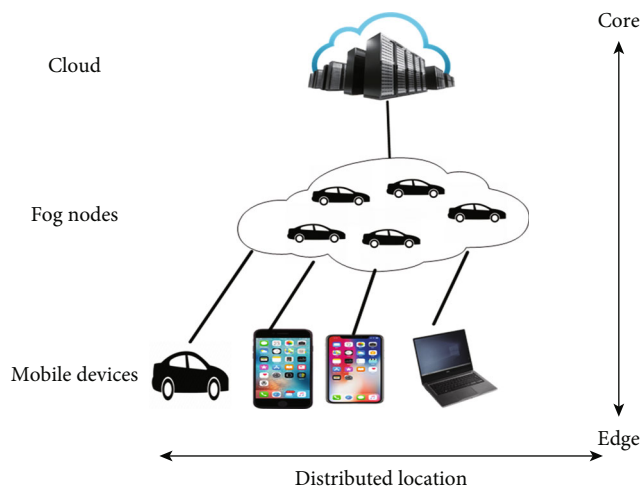

Figure 1: Basic three-tier architecture of VFC.

2. Related Work

In recent years, few works have been carried out to investigate the task offloading problem in vehicular fog computing. Wu et al. in [16] proposed a task offloading policy for the VFC and used IEEE 802.11p protocol for the transmission of tasks. Tasks are divided based on priorities according to the delay requirements. The problem is formulated as SMDP, and the task offloading scheme is presented to maximize the long-term reward in the form of reduction of processing time of a prioritized task. To solve this problem, iterative algorithm is used.

In [17], the authors improve the efficiency of application-aware offloading by proposing a VFC system in which public vehicles such as buses are being used as fog servers. A priority queuing system is applied to model the VFC for the application-aware delay requirements. The problem is formulated as SMDP. An application-aware task offloading policy is proposed to obtain the maximum long-term award of the VFC model.

In [18], a novel offloading scheme has been proposed to minimize the cost of energy consumption, failure in offloading, and service latency of the VFC network. At first, the overloaded cloudlet node has been determined, and then, an offloading policy has been introduced to determine which task will be offloaded and for the selection of vehicular node to place the offloaded task.

A game-theoretic approach can be used to overcome the demand-resource mismatch by minimizing the usage of resource energy and reducing the response time. The proposed resource allocation model has outperformed the state-of-the-art VFC models in terms of improved performance for the vehicles by keeping reducing the energy consumption [19].

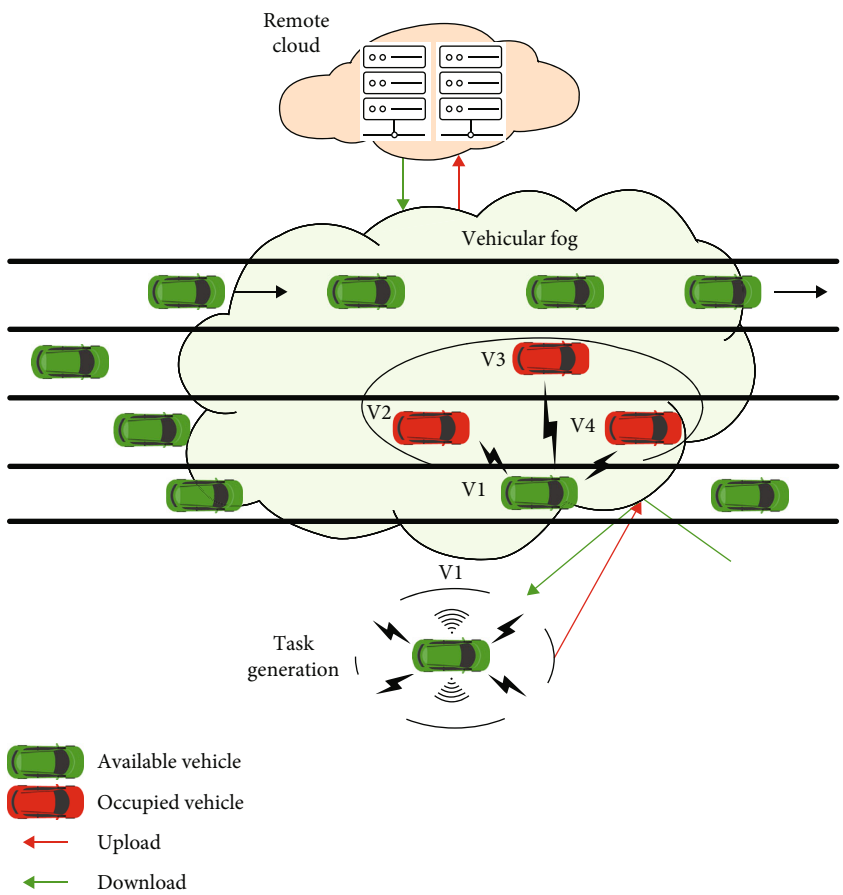

Figure 2: System model.

A distributed scheduler scheme for the energy consumption minimization for computing has been presented in [20]. The proposed model maximizes the efficiency of the system as well as maintains the quality of service. In [21], the authors show that the long-term reward of the VFC system can be increased by using an optimal task offloading strategy that uses the computation and transmission delays and available RUs. An iterative algorithm is used to solve the problem which is formulated as SMDP.

The work in [22] proposed the concept of VFC in which the electric vehicles are used as fog nodes and used to save energy for mobile devices. They used the Markov decision process to formulate the resource allocation problem and used dynamic programming to solve this problem. In [23], the authors proposed an efficient incentive mechanism based on the contrast matching approach for the problems of task offloading and computational resource allocation problems in the VFC system. By this approach, the base stations offload the task to nearby vehicles and minimize the task delays by using the underutilized resources of the vehicles.

The work in [24] proposed a deep dynamic reinforcement learning algorithm by exploiting the Markov decision process. They used reinforcement learning to get an offloading decision that minimizes the cost of the VFC system consisting of consumption of energy and service delay. In [25], Liu et al. presented a three-layered architecture for service offloading in the VFC system consisting of vehicular fog, fog server, and central cloud. They formulated the probabilistic task offloading problem to minimize the energy consumption payment cost and the execution delay and solved it by the iterative coordination process.

In [26], a task offloading policy for the VFC system is proposed that considers the task priority, vehicle mobility, and the availability of service by the vehicles. The priority-based task offloading policy was formulated as MDP and solved by a soft actor-critic-based deep reinforcement learning algorithm to maximize the entropy of policy and the reward.

To achieve the benefits prevailed by vehicular fog computing (VFC), the authors in [27] have presented a three-layer VFC model to minimize the response time of the vehicles. The problem has been formulated as a real-time optimization problem for the effective management of decentralized traffic.

Different from the work in the literature that studied the task offloading scheme in VFC system, we develop an energy-efficient task offloading scheme in VFC system to maximize the long-term reward by using the parallel computing and computing one part of the task request locally and offloading the remaining task to the vehicular fog nodes.

We utilize vehicular fog computing model in [21] as basis of our work; however, there are two major differences from the previous work. The first difference is the consideration of local computing at the task-generating vehicle as well as remote cloud computing whereas [21] only considers resources from other cooperative vehicles. The second

Table 1: List of important notations used in the paper.

Notations	Description
K	Maximum vehicles in the VFC system
R	Available RUs
M_R	Maximum number of RUs that can be allotted to a task request
S	Maximum number states
λ_c	Vehicle arrival rate
μ_c	Vehicle departure rate
λ_h	Task request arrival rate
μ_h	Task request service rate
n_i	Total request tasks serviced by i RUs
T	Task request arrival
D_i	The departure of the task request serviced by i number of RUs
C_{+1}	Vehicle's arrival
C_{-1}	Departure of vehicle
ω_e	Income weightage of energy
ω_d	Income weightage of time
β_e	Price per energy saving
β_d	Price per delay saving
ζ	Cost for transmission of task request
d_c	Transmission time between VFC to RC
d_f	Transmission time between requested vehicles to VFC
I	Total income of system
P_c	Computation power of RUs
P_t	The transmission power of vehicles
η	Punishment to the VFC system due to vehicle departure
γ	Discount factor
α	The factor of continuous discount
ϵ	Threshold value
θ	Convergence rate

difference is that the focus of our work is on energy efficiency, and hence, we propose a new reward function that considers energy consumption of the vehicular computing node.

3. System Model

In the present section, we present the system model inspired by [21] as shown in Figure 2. For computing, VFC is a recent paradigm that has been furnished several applications that required high computation and time-critical applications by offering the computing resources for the processing. All the vehicles, in the VFC, have a processor with a RU and also a source of a task; i.e., the vehicles can offload their computation tasks between each other. Since the arrival and departure of the vehicles from the VFC are random, the resources of computation change randomly in the VFC system. We assumed that all vehicles have the same virtualized RUs, and also, they are conscious of the accessible RUs in the system through communication with other vehicles in real time. When a task request arrives at the system, it has to be decided whether to accept this request or transfer it to the remote cloud (RC) according to the availability of the resources. If the request is accepted by the VFC system, the system decides to allocate the number of RUs according to available RUs.

For the illustration, we consider an example present in Figure 2. Vehicle $V1$ generates a task and is accepted by the VFC system as there are sufficient available resources; the task is then divided into four equal subtasks; one part is computed by $V1$ itself and the remaining three parts are offloaded to the three RUs, i.e., $V2$, $V3$, and $V4$. If there are no available RUs, the task is transferred to the RC for the computation. After the computation, the result is feedback to the $V1$. The vehicles arrive and depart the system according to the Poisson process. The arrival rate of the vehicle is λc, and the departure rate of the vehicle is μc. The maximum number of vehicles that the

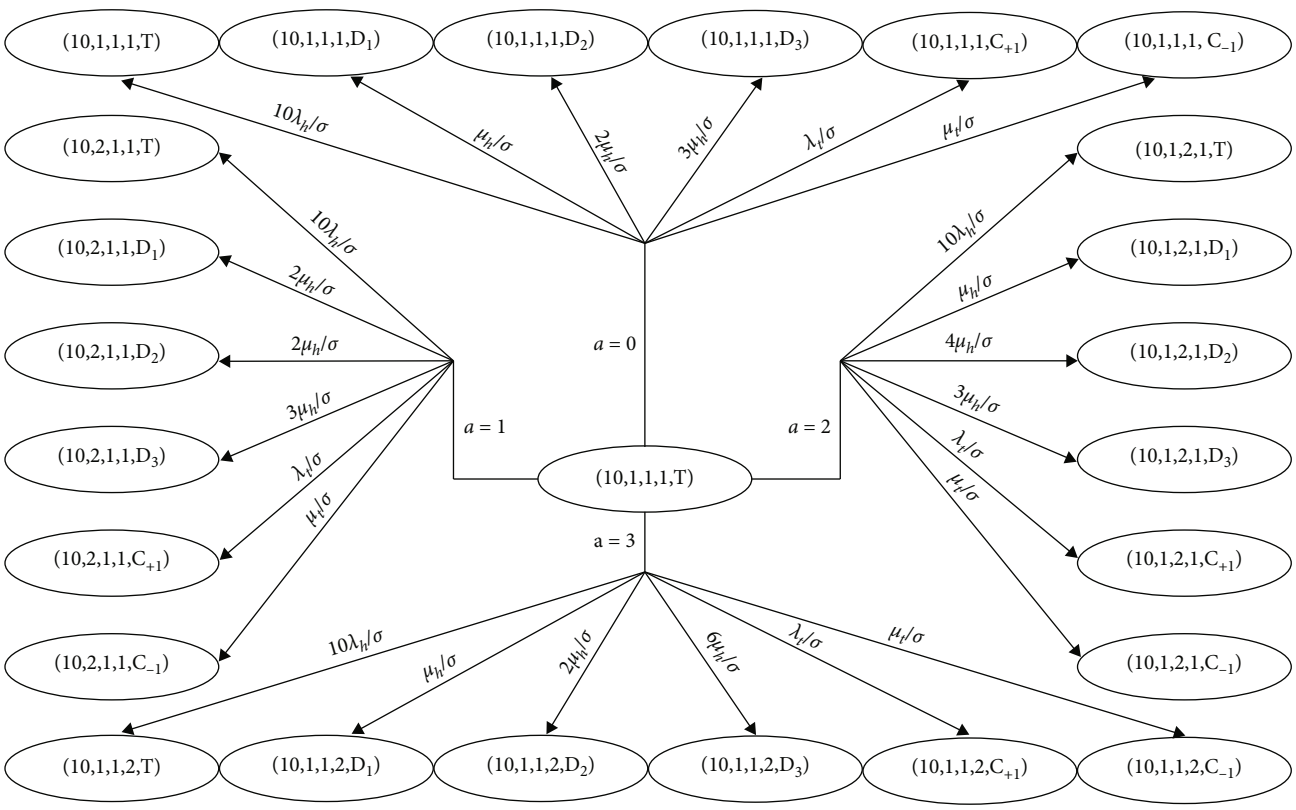

Figure 3: State transition diagram.

Input: state-space S, action space Λ, reward $R(s, a)$, transition probability $P(s' \mid s, a)$, rate of convergence ϵ
Output: the optimal policy π^*
Initialization: set value function $V(s) = 0$ for all $s \in S$ and $m = 0$
1. **For** every state $s \in S$
2. $\widehat{V}_{m+1}(s) = \max_{a \in A}[\widehat{R}(s, a) + \widehat{\gamma}\sum_{s' \in S}\widehat{P}(s' \mid s, a)\widehat{V}_m(s')]$
3. **If**$\|\widehat{V}_{m+1} - \widehat{V}_m\| < \epsilon$**then**
4. **For** each system state $s \in S$**do**
5. $'\pi^*(s)' = \arg\max_{a \in A}[\widehat{R}(s, a) + \widehat{\gamma}\sum_{s' \in S}\widehat{P}(s' \mid s, a)\widehat{V}_{m+1}(s')]$
6. **Else**
7. $m + +8$ back to line 1
9. Return the optimal policy π^*

Algorithm 1: VIA.

VFC system can handle is denoted as K, and we assume that available RUs in the system are R which fluctuate according to the departure and arrival of the vehicle. The number of RUs R in the VF cannot surpass the maximum number of vehicles K, i.e., $R \leq K$. Task arrival rate and service rate also follow the poison distribution denoted as λ_h and μ_h, respectively. The computing service rate is μ_h when only one RU process the task for i RU service rate $i\mu_h$.

4. Problem Formulation

In this section, we formulate the problem of task offloading by using SMDP. The number of available RUs in the VFC system changes by the events of departure and arrival of tasks and vehicles. When a task request from the vehicle arrives at the system, the system allocates the different number of RUs or transfer it to the RC for processing. The system achieves a reward as a result of task offloading decision which depends on the energy saved and computation time for the processing of the task.

In this SMDP model, the state is a set consist number of available and occupied RUs under different events. An action indicates the choices for decisions for different states. The reward reflects the advantage of the system in terms of energy and time for different states and actions. The probabilities of transition from one state to another under different actions

are described by transition probabilities. The notations used in this section are summarized in Table 1.

4.1. States. The system state S indicates the available resources present in the VFC system in the form of RUs, the number of requests processed by various numbers of RUs, and the events of requests and vehicles [21], i.e.,

$$S = \{s \mid s = (R, n_1, n_2, \cdots, n_{M_R}, e)\}, \tag{1}$$

where R is the available RUs in the system and n_i denotes the quantity of task request served by the i resource units $1 \le i \le M_R$, and e is a particular event that belongs to the E set

$$E = \{T, D_1, D_2, \cdots, D_{M_R}, C_{+1}, C_{-1}\}. \tag{2}$$

Here, T denotes the task's arrival, M_R denotes the maximum RUs the system of VFC can assign to the task, D_i is the departure of the task that was serviced and accomplished by i RUs, C_{+1} denotes vehicle's arrival rate, and C_{-1} denotes the departure of the vehicle. The overall sum of vehicles K should be greater than the number of RUs in the system. The allocated RUs to the in the system can be calculated by $\sum_{i=1}^{M_R} i.n_i$ that should always be less than the available RUs in the system at any state, i.e., $\sum_{i=1}^{M_R} i.n_i \le R$. Moreover, the remaining number of available RUs is measured from $R - \sum_{i=1}^{M_R} i.n_i$.

4.2. Actions. Action in the VFC system indicates the different possibilities of decision that the system can be taken according to the specific event of the current state [21]. Action based on the state s belongs to the set Λ and is denoted by $a(s)$

$$\Lambda = \{-1, 0, 1, 2, \cdots, M_R\}, \tag{3}$$

where $a(s) = -1$ shows the case when the task is completed and depart the system; no action of allocation of RUs is taken similarly when a vehicle arrives or departs, only the VFC system is updating its information about the available RUs. When the task request arrived, there are two options; either the request is accepted or transfer it to the RC; $a(s) = 0$ indicates the action when the task has arrived and there are no available RUs in the system and transfer it to the RC; $a(s) = i$ means that the task arrives and i RUs allocated for the processing of the task. The relationship between action and events is shown in the equation below.

$$\Lambda = \begin{cases} \{-1\}, & e = \{D_1, D_2, \cdots, D_{M_R}, C_{+1}, C_{-1}\}, \\ \{0, 1, 2, \cdots, M_R\}, & e = T. \end{cases} \tag{4}$$

4.3. Rewards. The reward reflects the advantage of the system of VFC after various actions undertaken for several states. As the main purpose of the system is to cut off the energy consumption and execution time of the tasks in the system by saving power and increasing the processing speed, the reward comprises both, the total income and cost of the system [21]. When an action is performed at a specific state s, the system earns an instant income $I(s, a)$.

The state s remains for a certain time till the next event is occurring, and state s is transitioned to the next state s'. This time is known as the cost $G(s, a)$ of the system. The difference of the income $I(s, a)$ and the cost $G(s, a)$ is known as reward $R(s, a)$.

$$R(s, a) = I(s, a) - G(s, a). \tag{5}$$

The income and cost of the system are derived below.

4.3.1. Income. The income of the system depends on different events and actions because the state is changed by the occurrence of the events. The income of the VFC system can be described as follows:

$$\begin{cases} \left[\omega_e \beta_e \left(P_c\left(\frac{1}{\mu_h}\right) - P_t d_f - P_c\left(\frac{1}{(i+1)\mu_h}\right)\right) + \omega_d \beta_d \left(\left(\frac{1}{\mu_h}\right) - d_f - \left(\frac{1}{(i+1)\mu_h}\right)\right) - \zeta d_f\right], & a = i, e = T, \\ \left[\omega_e \beta_e \left(P_c\left(\frac{1}{\mu_h}\right) - P_t d_f\right) + \omega_d \beta_d \left(\left(\frac{1}{\mu_h}\right) - d_f - d_c\right) - \zeta\left(d_{f+} d_c\right)\right], & a = 0, e = T, \\ 0, & a = i, e = \{D_1, D_2, \cdots, D_{M_R}, C_{+1}\}, \\ 0, & a = i, e = \{C_{-1}\}, \sum_{i=1}^{M_R} i.n_i < R, \\ -\eta, & a = i, e = \{C_{-1}\}, \sum_{i=1}^{M_R} i.n_i = R. \end{cases} \tag{6}$$

Table 2: Values of parameters in the VFC system.

Parameter	Value	Parameter	Value
P_c	4.4 W	β_e	2
P_t	1.8 W	β_d	2
d_f	2 ms	α	0.1
d_c	4 ms	K	6-14
ω_e	0.7	M_R	3
ω_d	0.3	ζ	2
η	18	θ	10
λ_h	2-9	λ_c	9
μ_h	8, 16	μ_h	8

The income function is explained below.

(1) $a = i, e = T$. When a task request arrives and is accepted by the system when resources are sufficient for the task, the system assigns i RUs to complete the request of the task; one part is computed locally by the requested vehicle so that no energy is wasted in idle. The instant income that can be earned by the VFC system is $[\omega_e\beta_e(P_c(1/\mu_h) - P_t d_f - P_c(1/((i+1)\mu_h))) + \omega_d\beta_d((1/\mu_h) - d_f - (1/((i+1)\mu_h))) - \zeta d_f]$ while $(P_c(1/\mu_h) - P_t d_f - P_c(1/((i+1)\mu_h)))$ is the energy saved and $((1/\mu_h) - d_f - (1/((i+1)\mu_h)))$ is the time saved during the processing of tasks in the VFC system. ω_d and ω_e are the weightage to the saved time and energy according to the various purposes; they can be predefined where $\omega_d + \omega_d = 1$. β_d and β_e are the saved price per unit time and energy to convert the energy and time into revenue. The cost of transferring the task to the VFC system and receiving the result from it is denoted as ζd_f and is known as the transfer expense. P_c and P_t are the computation and transmitting power, respectively. $P_c(1/((i+1)\mu_h))$ is the energy consumed when i RUs are assigned to the task request $i+1$ RUs process the task, as the requested vehicle also processes one part of the task. The total service time for the processing of the task is $(1/((i+1)\mu_h))$.

(2) $a = 0, e = T$. When a task request arrives and there are not sufficient resources in the VFC system, the request is not accepted by the system and transferred to the RC for processing. $[\omega_e\beta_e(P_c(1/\mu_h) - P_t d_f) + \omega_d\beta_d((1/\mu_h) - d_f - d_c) - \zeta(d_{f+}d_c)]$ is the immediate reward earned by the system when a task is processed by the remote cloud. Here, ζd_f and $d\zeta_c$ are the cost of transfer expense. ζd_c denotes the cost of transferring the task to the RC and receiving the result from the cloud. Remote cloud has a very large computation capability so the computation energy and time are not considered and have not affected the energy of the VFC system. But the delay is very large, so it is not a wise decision to transfer the task to the RC.

(3) $a = -1, e = \{D_1, D_2, \cdots, D_{M_R}, C_{+1}\}$. For the events of the arrival of the vehicle and the task's departure, there is no income as the system takes no action.

(4) $a = -1, e = \{C_{-1}\}, \sum_{i=1}^{M_R} i.n_i < R$. The system does not gain any reward when the vehicle departs the system and there are enough RUs to be allocated.

(5) $a = -1, e = \{C_{-1}\}, \sum_{i=1}^{M_R} i.n_i = R$. When the vehicle departs the VFC system and all the RUs already occupied and processing a task at this moment, the departure of the vehicle disturbs the processing, and the system has to pay a penalty of η.

4.3.2. Cost. To formulate the long-term cost, the discounted cost model is used from [28]. $G(s, a)$ is the expected discounted cost of the system during the duration when the state is transitioned from one state to another by taking an action and defined as

$$G(s, a) = k(s, a)\rho(s, a), \tag{7}$$

where $\rho(s, a)$ is the expected service time when system state s is changed to next state s' by taking an action a; this is assumed to be exponentially distributed according to [28]

$$G(s, a) = k(s, a)E_s^a\left\{\int_0^\tau e^{-\alpha t}dt\right\} = k(s, a)E_a^s\left\{\frac{1 - e^{-\alpha\tau}}{\alpha}\right\} = \frac{k(s, a)}{\alpha + \sigma(s, a)}, \tag{8}$$

where $k(s, a)$ is the expected service time's cost rate for the state s and action a that is characterized as a function of total occupied RUs, i.e.,

$$k(s, a) = \sum_{i=1}^{M_R} i \cdot n_i. \tag{9}$$

α is the factor of discount, and $\sigma(s, a)$ is the expected event rate of the system for the state s and action a that can be calculated by adding all the rates of arrival and departure of vehicles and task requests. The arrival and departure rate of the vehicle is λ_c and μ_c, respectively, while the arrival rate of the request of task and departure rate of the task request depends on the various events and actions of the system calculated as below.

(1) $a = i, e = T$. With the arrival of the task request in the VFC system, the system assigns i RUs for the task processing. $R\lambda_c$ is the arrival rate of the task, and the rate of departure for the task request is $(\sum_{j=1}^{M_R} jn_j + i)u_h$ because the allocated number of RUs is $(\sum_{j=1}^{M_R} jn_j + i)$, under action i.

(2) $a = -1, e = D_i$. The system takes no action when a task departs from the system which is allocated by i RUs. The task request arrival rate is $R\lambda_c$, while the departure rate of the task is $(\sum_{j=1}^{M_R} jn_j - i)u_h$.

(3) $a = -1, e = C_{-1}$. When the vehicle leaves the VFC system, no action is taken by the system but the available number of vehicles decreased by 1; hence, $(R-1)\lambda_c$ is the task request arrival rate, while the departure rate of tasks is $(\sum_{j=1}^{M_R} jn_j)u_h$.

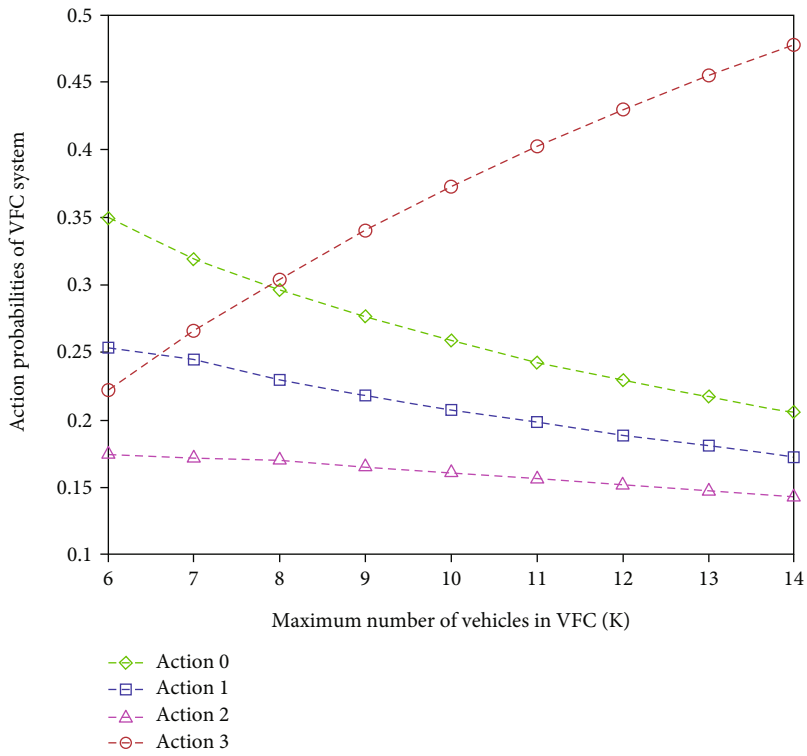

Figure 4: Action probabilities for the different numbers of maximum vehicles in the VFC system ($\lambda_h = 2$, $\mu_h = 8$).

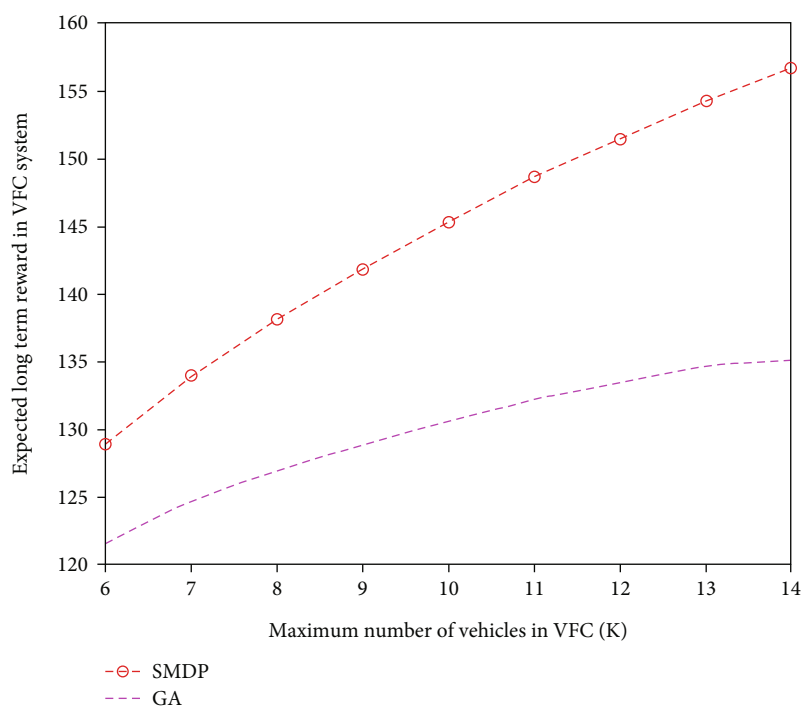

Figure 5: Reward for the VFC system for the different numbers of maximum vehicles ($\lambda_h = 2$ and service rate $\mu_h = 8$).

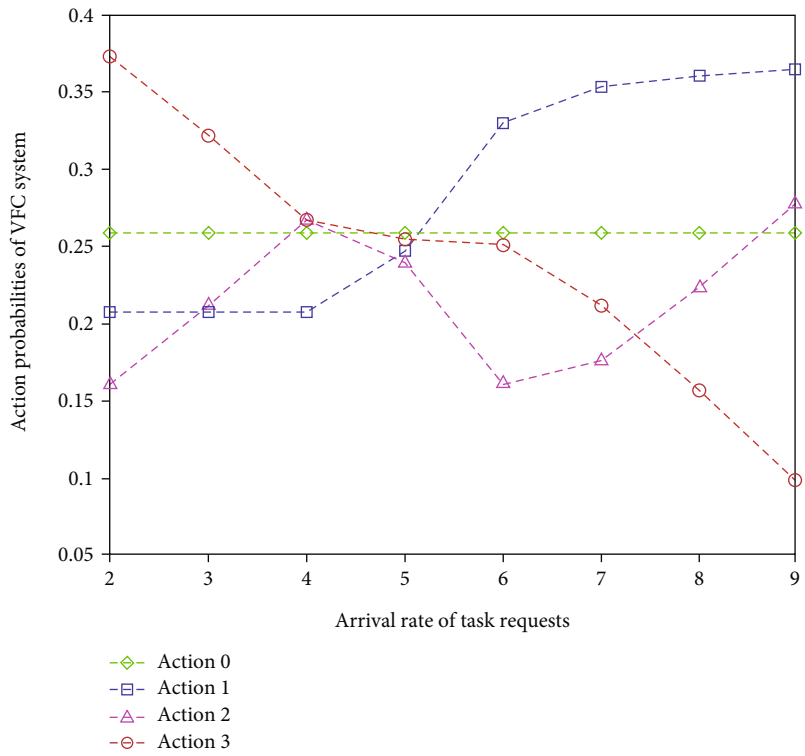

Figure 6: Action probabilities for different task request arrival rate λ_h ($K = 10$, $\mu_h = 8$).

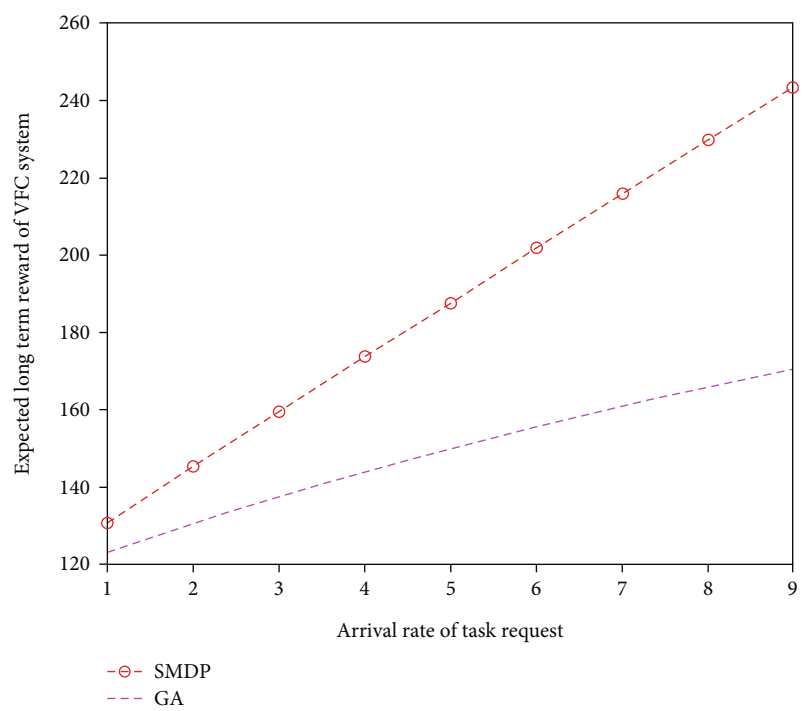

Figure 7: Reward for the VFC system for different numbers of different task request arrival rate λ_h ($K = 10$, $\mu_h = 8$).

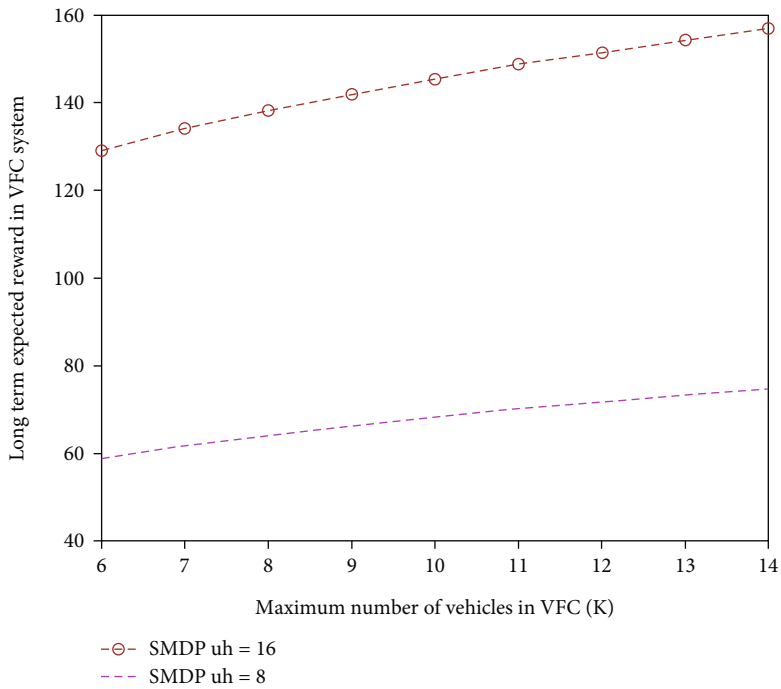

Figure 8: Reward of the VFC system for different service rates μ_h ($K = 6 - 14$, $\lambda_h = 2$).

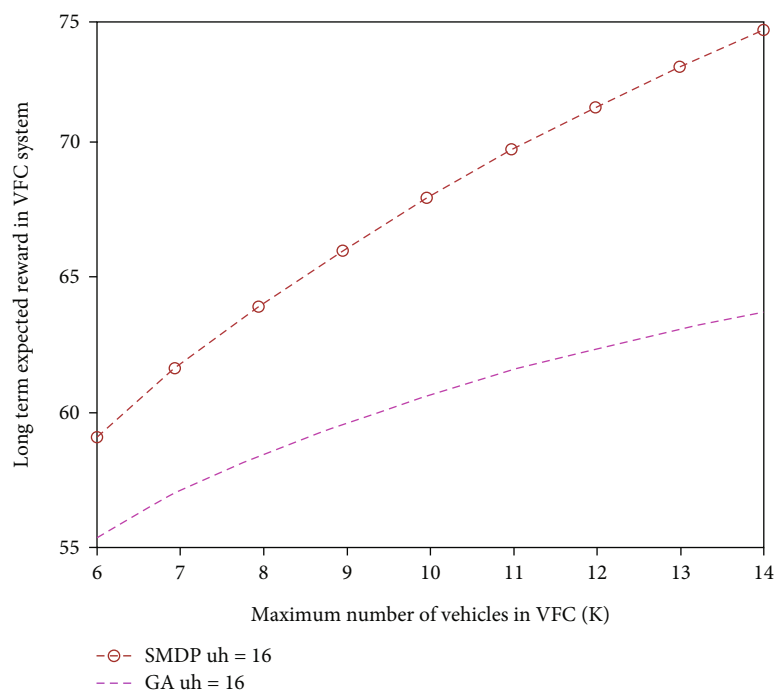

Figure 9: Reward for the VFC system for the different numbers of maximum vehicles K ($\lambda_h = 2$ and service rate $\mu_h = 16$).

(4) $a=-1, e=C_{+1}$. The system takes no action while the vehicle arrives, but there is an increment in the available number of vehicles by 1; hence, $(R+1)\lambda_c$ is the task request arrival rate, while the departure rate of tasks is ($\sum_{j=1}^{M_R} jn_j)u_h$.

The expected service rate $\sigma(s,a)$ for different events and action is calculated as

$$\sigma(s,a)=\begin{cases} R\lambda_c+\mu_c+\lambda_c+\left(\sum_{j=1}^{M_R} jn_j+i\right)u_h, e=T, a=i, \\ R\lambda_c+\mu_c+\lambda_c+\left(\sum_{j=1}^{M_R} jn_j-i\right)u_h, e=D_i, a=-1, \\ (R+1)\lambda_c+\mu_c+\lambda_c+\left(\sum_{j=1}^{M_R} jn_j\right)u_h, e=C_{+1}, a=-1, \\ (R-1)\lambda_c+\mu_c+\lambda_c+\left(\sum_{j=1}^{M_R} jn_j\right)u_h, e=C_{+1}, a=-1. \end{cases} \tag{10}$$

4.4. Transition Probability. The transition probability is the probability of going from the current state s to the future state s' after taking an action has been taken [21]. We have used the generalized SMDP transition probabilities [21]; however, the proposed work has an additional state for remote cloud computing.

The transition probability in the system of VFC can be explained by the ratio between the sum of all the events and the next event rate. The transition probability is denoted as $P(s'|s,a)$ and formulated as below:

(1) $s=(R,n_1,\cdots,n_N,T), a=i$

$$P\left(s'\mid s,a\right)=\begin{cases} \frac{R\lambda_h}{\sigma(s,a)}, s'=\left(R,n_1,\cdots,n_i+1,\cdots,n_{M_R},T\right), \\ \frac{(n_i+1)i\mu_h}{\sigma(s,a)}, s'=\left(R,n_1,\cdots,n_i+1,\cdots,n_{M_R},D_i\right), \\ \frac{n_j j\mu_h}{\sigma(s,a)}, i\neq j\, s'=\left(R,n_1,\cdots,n_i+1,\cdots,n_{M_R},D_j\right), \\ \frac{\lambda_c}{\sigma(s,a)}, s'=\left(R,n_1,\cdots,n_i+1,\cdots,n_{M_R},C_{+1}\right), \\ \frac{\mu_c}{\sigma(s,a)}, s'=\left(R,n_1,\cdots,n_i+1,\cdots,n_{M_R},C_{-1}\right). \end{cases} \tag{11}$$

(2) $s=(R,n_1,\cdots,n_N,T), a=0$

$$(P\left(s'\mid s,a\right)=\begin{cases} \frac{R\lambda_h}{\sigma(s,a)}, s'=\left(R,n_1,\cdots,n_i,\cdots,n_{M_R},T\right), \\ \frac{n_i i\mu_h}{\sigma(s,a)}, s'=\left(R,n_1,\cdots,n_i,\cdots,n_{M_R},D_i\right), \\ \frac{\lambda_c}{\sigma(s,a)}, s'=\left(R,n_1,\cdots,n_i,\cdots,n_{M_R},C_{+1}\right), \\ \frac{\mu_c}{\sigma(s,a)}, s'=\left(R,n_1,\cdots,n_i,\cdots,n_{M_R},C_{-1}\right). \end{cases} \tag{12}$$

(3) $s=(R,n_1,\cdots,n_N,D_i), a=-1$

$$P\left(s'\mid s,a\right)=\begin{cases} \frac{R\lambda_h}{\sigma(s,a)}, s'=\left(R,n_1,\cdots,n_i-1,\cdots,n_{M_R},T\right), \\ \frac{(n_i-1)i\mu_h}{\sigma(s,a)}, s'=\left(R,n_1,\cdots,n_i-1,\cdots,n_{M_R},D_i\right), \\ \frac{n_j j\mu_h}{\sigma(s,a)}, i\neq j\, s'=\left(R,n_1,\cdots,n_i-1,\cdots,n_{M_R},D_j\right), \\ \frac{\lambda_c}{\sigma(s,a)}, s'=\left(R,n_1,\cdots,n_i-1,\cdots,n_{M_R},C_{+1}\right), \\ \frac{\mu_c}{\sigma(s,a)}, s'=\left(R,n_1,\cdots,n_i-1,\cdots,n_{M_R},C_{-1}\right). \end{cases} \tag{13}$$

(4) $s=(R,n_1,\cdots,n_N,C_{-1}), a=-1$

$$P\left(s'\mid s,a\right)=\begin{cases} \frac{(R-1)\lambda_h}{\sigma(s,a)}, s'=\left(R-1,n_1,\cdots,n_i,\cdots,n_{M_R},T\right), \\ \frac{n_i i\mu_h}{\sigma(s,a)}, s'=\left(R-1,n_1,\cdots,n_i,\cdots,n_{M_R},D_i\right), \\ \frac{\lambda_c}{\sigma(s,a)}, s'=\left(R-1,n_1,\cdots,n_i,\cdots,n_{M_R},C_{+1}\right), \\ \frac{\mu_c}{\sigma(s,a)}, s'=\left(R-1,n_1,\cdots,n_i,\cdots,n_{M_R},C_{-1}\right). \end{cases} \tag{14}$$

(5) $s=(R,n_1,\cdots,n_N,C_{+1}), a=-1$

$$P\left(s'\mid s,a\right)=\begin{cases} \frac{(R+1)\lambda_h}{\sigma(s,a)}, s'=\left(R+1,n_1,\cdots,n_i,\cdots,n_{M_R},T\right), \\ \frac{n_i i\mu_h}{\sigma(s,a)}, s'=\left(R+1,n_1,\cdots,n_i,\cdots,n_{M_R},D_i\right), \\ \frac{\lambda_c}{\sigma(s,a)}, s'=\left(R+1,n_1,\cdots,n_i,\cdots,n_{M_R},C_{+1}\right), \\ \frac{\mu_c}{\sigma(s,a)}, s'=\left(R+1,n_1,\cdots,n_i,\cdots,n_{M_R},C_{-1}\right). \end{cases} \tag{15}$$

The state transition diagram is shown in Figure 3 which shows the state transition process takes current state $s = (10, 1, 1, 1, T)$ and shows it transitioned to the next states for different actions and events with the transition probability [21].

5. Solution

The solution of the above SMDP problem is presented in this section and find the solution to magnify the reward of the VFC system in a long term; by this we save energy and minimize the processing time. To solve the problem, value iteration algorithm is adopted. In the value iteration algorithm, Bellman optimal equation [21, 29] is used. In every iteration of all the states, maximum value function $V(s)$ is calculated for each action, i.e., $\Lambda \epsilon \{-1, 0, 1, 2, \cdots, M_R\}$. When $V(s)$ of every state is converging, the step is terminated. The Bellman optimal equation is shown below:

$$V_{M+1}(s) = \max_{a \in \Lambda} \left[R(s, a) + \gamma \sum_{s' \in S} P\left(s' \mid s, a\right) V_m\left(s'\right) \right]. \quad (16)$$

Here, $\gamma = \sigma(s, a)/(\alpha + \sigma(s, a))$ and known as discount function.

To transform the continuous-time semi-Markov decision process into a discrete-time process, a new parameter is defined $x = K\lambda_h + \lambda_c + \mu_c + K \cdot M_R \cdot \mu_h$ to normalize the reward, discount factor, and transition probabilities. The normalized equations are shown below.

$$\begin{gathered} \widehat{R}(s, a) = R(s, a) \frac{\alpha + \sigma(s, a)}{\alpha + x}, \\ \widehat{P}\left(s' \mid s, a\right) = \begin{cases} 1 - \dfrac{[1 - P(s \mid s, a)]\sigma(s, a)}{x}, & s' = s, \\ \dfrac{P\left(s' \mid s, a\right)\sigma(s, a)}{x}, & s' \neq s, \end{cases} \\ \widehat{\gamma} = \frac{x}{x + \alpha}. \end{gathered} \quad (17)$$

Thus, after normalization, the Bellman optimal equation becomes

$$\widehat{V}_{m+1}(s) = \max_{a \in \Lambda} \left[\widehat{R}(s, a) + \widehat{\gamma} \sum_{s' \in S} \widehat{P}\left(s' | s, a\right) \widehat{V}_m\left(s'\right) \right]. \quad (18)$$

Initially, the value function of all states was set to zero. Now, by Equation (18), the normalized value function of states is calculated by using values from the previous iteration. For example, the maximum value function $\widehat{V}_{m+1}(s)$ in $m + 1$th iteration is calculated by using the mth iteration. For finding the optimal policy π^*, the absolute difference between two succeeding iterations is computed for each state, i.e., $\|\widehat{V}_{m+1} - \widehat{V}_m\|$. The algorithm is stopped when the maximal absolute value is lower by the threshold $\epsilon = \theta(1 - \widehat{\gamma})/2\widehat{\gamma}$ and optimal scheme $\pi^*$is obtained.

$$\pi^*(s) = \max_{a \in \Lambda} \left[\widehat{R}(s, a) + \widehat{\gamma} \sum_{s' \in S} \widehat{P}\left(s' | s, a\right) \widehat{V}_m\left(s'\right) \right]. \quad (19)$$

If the threshold is greater than the maximum absolute value, the algorithm goes into the next iteration and continues till the optimal scheme of offloading is obtained. The pseudocode of the VIA is presented in Algorithm 1.

6. Simulation Results

The performance of our proffered scheme of task offloading has been evaluated in this section by conducting trials and getting experimental results. For the comparison, we compare our proposed scheme with the greedy algorithm (GA), which constantly tries to assign the maximum number of RUs to offload the task for processing [28]. We used the MATLAB R2019b tool for the experiments.

The parameters that have been used in the evaluation are exhibited in Table 2. The maximum number of RUs that can be assigned to the task for processing is $M_R = 3$; i.e., 1, 2, or 3 RUs can be assigned to task requests according to the availability of resources in the VFC system.

Action 1, action 2, and action 3 denote the number of assigned RUs to the tasks, while action 0 is the special scenario of sending the service request to the RC. For evaluation, different parameters are adjusted, for example, the number of maximum available vehicle K in the system of VFC, the arrival rate of the task requests λ_h, and service rate μ_h.

Figure 4 illustrates the relationship among the maximum number of vehicles K supported by the VFC system and transition probabilities of the different actions taken by the system when the request arrival rate $\lambda_h = 2$ and service rate $\mu_h = 8$. It is depicted from the figure that when the number of vehicles in the VFC system is low the transition probability for action 2 and action 3 is lower than the transition probabilities of action 0 and action 1. This is because when the number of vehicles is less the available resources in the form of RUs are also less and the VFC system allocates a smaller number of RUs to the task request. With the increment of the number of vehicles in the system, a decreasing trend in the transition probability of actions 0, 1, and 2 and an increase in the trend for action 3 can be seen. The system mostly assigns three RUs to the arriving requests to enhance the expected reward in the long term.

Figure 5 shows the comparison of our proposed scheme of SMDP-based algorithm with the GA scheme when $\lambda_h = 2$ and service rate $\mu_h = 8$. It can be observed that with the increment in the number of vehicles in the VFC system the expected reward of the VFC system increases since with the increase in the maximum number of vehicles the number of the completed tasks increased, and as a result, reward increased. The SMDP-based scheme has 19% improved performance in terms of reward than the GA as shown from the figure. This is because the GA tries to allocate maximum RUs without taking into account the expected reward of the VFC system.

Figure 6 depicts the relationship among the requests of the task arrival rate of λ_h and the transition probabilities of the actions taken by the system, when $K = 10$ and service rate $\mu_h = 8$. It could be noticed from the figure that the transition probability of action 3 is higher than all other actions when the task arrival rate is low because there is abundant computation capability in VFC. The system tries to assign the utmost number of RUs to the requested task to increase the long-term expected award. With the increase in the rate of the task, arrival requests in the transition probabilities of action 1 start increasing while for action 3 there is a decreasing trend because the VFC system starts taking conservative decisions according to the available resources and to get the maximum reward taking action 1 or 2 by this complete more tasks without transferring the requests to the RC. The transition probability of action 2 shows random behavior; in the beginning, it starts increasing and after some time shows the decreasing trend and at the end start increasing again according to the optimal policy to improve the expected reward.

Figure 7 demonstrates the relationship between λ_h and long-term reward of SMDP and compares it with the GA when $K = 10$ and service rate $\mu_h = 8$. The long-term expected reward shows an increasing trend with the increase in the rate of task arrival request because with the increment in the number of tasks request the completed task also increased, and as a result, long-term expected reward increases. Moreover, it can be conceivable from the figure that our proposed methods outperform the GA.

Figure 8 shows the comparison of the long-term reward of the system when μ_h changes from 16 to 8. It can be perceived from the figure that the expected reward for $\mu_h = 8$ is lower than that for $\mu_h = 16$ because the number of tasks computed is less when the rate of service is low. Moreover, when the service rate is high, processing of tasks by RUs is faster; as a result, the number of available RUs increases, and more tasks can be offloaded and gain more reward.

In Figure 9, there is a comparison of our proposed scheme of SMDP-based algorithm with the GA scheme when $\lambda_h = 2$ and service rate $\mu_h = 16$. It can be seen that our proposed scheme outperforms the GA and shows a similar trend as in Figures 5 and 7.

In this section, we present the performance of our work with the help of different experiments. We see that the proposed algorithm exhibits superior performance than the GA and gains more reward under different parameters; i.e., varying maximum numbers of vehicles in the VFC system, different service rates, and different rates of the task request, our scheme outperforms in all the cases.

7. Conclusion and Future Work

In this paper, we propose an optimal energy-aware task offloading technique for the Internet of Vehicles. When a vehicle with the task request arrives, the system decides for the allocation of computational resources, i.e., RUs, and divides the task according to the decision. We use parallel computing and save energy and minimize time delay for our VFC system and formulate the problem as an infinite horizon SMDP. The Bellman optimal equation is used in value iteration algorithm to get an optimal policy that amplifies the long-term expected reward that saved energy and time in this problem. The proposed scheme demonstrates the improved performance of the greedy algorithm as established by the substantial numerical results. In the future, we aim to consider mobility of the vehicles and dynamic wireless connectivity in task offloading.

Data Availability

Data is available from the corresponding author on request.

Conflicts of Interest

The authors declare no conflicts of interest.

Acknowledgments

The authors extend their appreciation to the Deanship of Scientific Research at Imam Mohammad Ibn Saud Islamic University for funding this work through Research Group no. RG-21-07-06.

References

[1] Q. Wu, S. Xia, P. Fan, Q. Fan, and Z. Li, "Velocity-adaptive V2I fair-access scheme based on IEEE 802.11 DCF for platooning vehicles," *Sensors*, vol. 18, no. 12, pp. 1–23, 2018.

[2] J. Han, A. Sciarretta, L. L. Ojeda, G. De Nunzio, and L. Thibault, "Safe-and eco-driving control for connected and automated electric vehicles using analytical state-constrained optimal solution," *IEEE Transactions on Intelligent Vehicles*, vol. 3, no. 2, pp. 163–172, 2018.

[3] M. A. Javed, S. Zeadally, and Z. Hamid, "Trust-based security adaptation mechanism for vehicular sensor networks," *Computer Networks*, vol. 137, pp. 27–36, 2018.

[4] G. Bresson, Z. Alsayed, L. Yu, and S. Glaser, "Simultaneous localization and mapping: a survey of current trends in autonomous driving," *IEEE Transactions on Intelligent Vehicles*, vol. 2, no. 3, pp. 194–220, 2017.

[5] Q. Wu, H. Ge, H. Liu, Q. Fan, Z. Li, and Z. Wang, "A task offloading scheme in vehicular fog and cloud computing system," *IEEE Access*, vol. 8, pp. 1173–1184, 2020.

[6] J. Zhao, Y. Liu, Y. Gong, C. Wang, and L. Fan, "A dual-link soft handover scheme for C/U plane split network in high-speed railway," *IEEE Access*, vol. 6, no. c, pp. 12473–12482, 2018.

[7] W. Xu, H. Zhou, N. Cheng et al., "Internet of vehicles in big data era," *IEEE/CAA Journal of Automatica Sinica*, vol. 5, no. 1, pp. 19–35, 2018.

[8] Q. Fan, N. Ansari, and X. Sun, "Energy driven avatar migration in green cloudlet networks," *IEEE Communications Letters*, vol. 21, no. 7, pp. 1601–1604, 2017.

[9] Y. Zhang, "Optimization strategy of mobile data transmission based on optimal crowd feedback," *EURASIP Journal on Embedded Systems*, vol. 2016, no. 1, Article ID 26, 2017.

[10] M. Báguena, C. T. Calafate, J. C. Cano, and P. Manzoni, "An adaptive anycasting solution for crowd sensing in vehicular environments," *IEEE Transactions on Industrial Electronics*, vol. 62, no. 12, pp. 7911–7919, 2015.

[11] X. Hou, Y. Li, M. Chen, D. Wu, D. Jin, and S. Chen, "Vehicular fog computing: a viewpoint of vehicles as the infrastructures," *IEEE Transactions on Vehicular Technology*, vol. 65, no. 6, pp. 3860–3873, 2016.

[12] Y. Bin Zikria, M. Khalil Afzal, and S. Won Kim, "Internet of multimedia things (Iomt): opportunities, challenges and solutions," *Sensors*, vol. 20, no. 8, 2020.

[13] M. Bagaa, A. Ksentini, T. Taleb, R. Jantti, A. Chelli, and I. Balasingham, "An efficient D2D-based strategies for machine type communications in 5G mobile systems," in *2016 IEEE Wireless Communications and Networking Conference*, vol. 2016, Doha, Qatar, 2016.

[14] J. Zhao, S. Ni, L. Yang, Z. Zhang, Y. Gong, and X. H. Yu, "Multiband cooperation for 5G HetNets: a promising network paradigm," *IEEE Vehicular Technology Magazine*, vol. 14, no. 4, pp. 85–93, 2019.

[15] R. K. Naha, S. Garg, D. Georgakopoulos et al., "Fog computing: survey of trends, architectures, requirements, and research directions," *IEEE Access*, vol. 6, pp. 47980–48009, 2018.

[16] Q. Wu, H. Ge, Q. Fan, W. Yin, B. Chang, and G. Wu, "Efficient task offloading for 802.11p-based cloud-aware mobile fog computing system in vehicular networks," *Wireless Communications and Mobile Computing*, vol. 2020, 12 pages, 2020.

[17] Z. Wang, Z. Zhong, and M. Ni, "Application-aware offloading policy using SMDP in vehicular fog computing systems," in *2018 IEEE international conference on communications workshops (ICC Workshops)*, pp. 1–6, Kansas City, MO, USA, 2018.

[18] R. Yadav, W. Zhang, O. Kaiwartya, H. Song, and S. Yu, "Energy-latency tradeoff for dynamic computation offloading in vehicular fog computing," *IEEE Transactions on Vehicular Technology*, vol. 69, no. 12, pp. 14198–14211, 2020.

[19] J. Klaimi, S. M. Senouci, and M. A. Messous, "Theoretical game approach for mobile users resource management in a vehicular fog computing environment," in *2018 14th International Wireless Communications & Mobile Computing Conference (IWCMC)*, pp. 452–457, Limassol, Cyprus, 2018.

[20] M. Shojafar, N. Cordeschi, and E. Baccarelli, "Energy-efficient adaptive resource management for real-time vehicular cloud services," *IEEE Transactions on Cloud computing*, vol. 7, no. 1, pp. 196–209, 2019.

[21] Q. Wu, H. Liu, R. Wang, P. Fan, Q. Fan, and Z. Li, "Delay-sensitive task offloading in the 802.11p-based vehicular fog computing systems," *IEEE Internet of Things Journal*, vol. 7, no. 1, pp. 773–785, 2020.

[22] H. M. Birhanie, M. A. Messous, S. M. Senouci, E. H. Aglzim, and A. M. Ahmed, "MDP-based resource allocation scheme towards a vehicular fog computing with energy constraints," in *2018 IEEE Global Communications Conference (GLOBECOM)*, pp. 1–6, Abu Dhabi, United Arab Emirates, 2018.

[23] Z. Zhou, P. Liu, J. Feng, Y. Zhang, S. Mumtaz, and J. Rodriguez, "Computation resource allocation and task assignment optimization in vehicular fog computing: a contract-matching approach," *IEEE Transactions on Vehicular Technology*, vol. 68, no. 4, pp. 3113–3125, 2019.

[24] Y. Wang, K. Wang, H. Huang, T. Miyazaki, and S. Guo, "Traffic and computation co-offloading with reinforcement learning in fog computing for industrial applications," *IEEE Transactions on Industrial Informatics*, vol. 15, no. 2, pp. 976–986, 2019.

[25] Z. Liu, P. Dai, H. Xing, Z. Yu, and W. Zhang, "A distributed algorithm for task offloading in vehicular networks with hybrid fog/cloud computing," *IEEE Transactions on Systems, Man, and Cybernetics: Systems*, pp. 1–14, 2021.

[26] J. Shi, G. S. Member, J. Du, and J. Wang, "Priority-aware task offloading in vehicular fog computing based on deep reinforcement learning," *IEEE Transactions on Vehicular Technology*, vol. 69, no. 12, pp. 16067–16081, 2020.

[27] Z. Ning, J. Huang, and X. Wang, "Vehicular fog computing: enabling real-time traffic management for smart cities," *IEEE Wireless Communications*, vol. 26, no. 1, pp. 87–93, 2019.

[28] S. Radhakrishnan, D. Kolippakkam, and V. S. Mathura, *Introduction to Algorithms*, MIT press, 2007.

[29] M. L. Puterman, *Markov Decision Processes: Discrete Stochastic Dynamic Programming*, John Wiley & Sons, 2008.

Hindawi
Journal of Sensors
Volume 2023, Article ID 9837069, 1 page
https://doi.org/10.1155/2023/9837069

Retraction

Retracted: Nonlinear Identification of PMSM Rotor Magnetic Linkages Based on an Improved Extended Kalman Filter

Journal of Sensors

Received 19 December 2023; Accepted 19 December 2023; Published 20 December 2023

This article has been retracted by Hindawi following an investigation undertaken by the publisher [1]. This investigation has uncovered evidence of one or more of the following indicators of systematic manipulation of the publication process:

(1) Discrepancies in scope
(2) Discrepancies in the description of the research reported
(3) Discrepancies between the availability of data and the research described
(4) Inappropriate citations
(5) Incoherent, meaningless and/or irrelevant content included in the article
(6) Manipulated or compromised peer review

The presence of these indicators undermines our confidence in the integrity of the article's content and we cannot, therefore, vouch for its reliability. Please note that this notice is intended solely to alert readers that the content of this article is unreliable. We have not investigated whether authors were aware of or involved in the systematic manipulation of the publication process.

Wiley and Hindawi regrets that the usual quality checks did not identify these issues before publication and have since put additional measures in place to safeguard research integrity.

We wish to credit our own Research Integrity and Research Publishing teams and anonymous and named external researchers and research integrity experts for contributing to this investigation.

The corresponding author, as the representative of all authors, has been given the opportunity to register their agreement or disagreement to this retraction. We have kept a record of any response received.

References

[1] T. Chen and B. Chen, "Nonlinear Identification of PMSM Rotor Magnetic Linkages Based on an Improved Extended Kalman Filter," *Journal of Sensors*, vol. 2022, Article ID 9477659, 8 pages, 2022.

Hindawi
Journal of Sensors
Volume 2022, Article ID 9477659, 8 pages
https://doi.org/10.1155/2022/9477659

Research Article

Nonlinear Identification of PMSM Rotor Magnetic Linkages Based on an Improved Extended Kalman Filter

Tao Chen[1,2] **and Bing Chen**[2]

[1]*School of Electrical Information Engineering, Henan University of Engineering, Zhengzhou 451191, China*
[2]*Henan Institute of Metrology, Zhengzhou 450000, China*

Correspondence should be addressed to Tao Chen; hact@haue.edu.cn

Received 25 February 2022; Revised 18 March 2022; Accepted 25 March 2022; Published 19 May 2022

Academic Editor: Han Wang

The permanent magnet synchronous motor (PMSM) has complex nonlinear, strongly coupled characteristics and the variation of motor parameters makes its control more difficult. Therefore, parameter identification is of great significance for the stable operation of its closed-loop control system. In this paper, a method based on an improved extended Kalman filter (EKF) for the identification of the rotor flux (ψ_f) of a permanent magnet synchronous motor is investigated for this nonlinear and strongly coupled model. Simulation results show that the method has a more fast convergence rate and more accurate identification result than traditional EKF algorithm.

1. Introduction

As the cost and price of rare earth permanent magnet materials continue to fall and motor design and manufacturing technology continues to develop, permanent magnet motors are gaining more and more attention for their small size, high efficiency, and high power density, with a wide range of applications from high-performance servo systems to aerospace systems [1]. In addition, the rotor magnetic field of permanent magnet motors is provided by permanent magnets, which do not need to be excited, and therefore have energy-saving features. In operation, the efficiency, reliability, and safety of permanent magnet motors are undoubtedly of great importance [2]. High-performance control technology and a perfect control system are therefore essential for the continued development of permanent magnet motors at high speed [3]. The vector control and direct torque control techniques originally used for induction motors have been successfully transferred to the control of permanent magnet motors with good results [4]. However, the implementation of high-performance control techniques such as vector control and direct torque control is dependent on the mathematical model of the motor, while the AC permanent magnet synchronous motor is a multivariable, strongly coupled, nonlinear system, whose parameters are constantly changing with time and there are certain coupling relationships between the parameters [5]. Therefore, in order to obtain high-performance control, it is necessary to provide the control algorithm with accurate motor parameters in real time, i.e., to carry out online parameter identification. On the other hand, in order to suppress the influence of measurement noise on the dynamic behavior of permanent magnet motors and to streamline the control system structure in order to further improve the control system performance, position sensor-free control techniques have been developed on the basis of vector control and direct torque control. When a position sensor is not present in the control system, the key variable of the motor's rotor angle must be identified [6].

PMSMs are widely used in AC servo drive systems for their fast response, good control performance, small size, and lightweight [7]. At present, the common parameter identification methods of PMSMs are Kalman filter identification [8], neural network identification method [9], and genetic algorithm. The Kalman filter is an efficient recursive filtering method that can estimate the state of a dynamic

system from a series of incomplete noise measurements. It mainly uses the dynamic information of the target and tries to remove the effect of noise to obtain a good estimate about the target [10]. The Kalman filter identification is based on the Kalman filter algorithm, is applicable to linear or nonlinear systems, and allows for model bias and measurement error in the system. Since its introduction, the Kalman filter has been widely used in the fields of navigation, process control, signal tracking, and system identification [11].

Until recently, the Kalman filter has been used in the control of AC permanent magnet synchronous motors, mainly to replace position sensors for position sensor-free control. The Kalman filter algorithm is used to estimate the angle and speed of the motor rotor independent of the initial rotor position [12].

Neural networks are highly parallel and nonlinear in their global action, and are highly adaptive and self-learning. They have been widely used in modelling, identification, and control of nonlinear systems. Compared with traditional BP and RBF networks, feedback neural networks are able to detect and identify time-varying patterns [13].

In order to improve the rotor flux identification accuracy and reduce the influence on the rotor flux identification results induced by stator resistance changes, the synchronous identification of rotor flux and stator resistance is realized for the first time by combining Kalman filter and feedback neural network. Firstly, the stator resistance and rotor flux calculated by EKF are used to train the feedback neural network off-line, and then the estimation errors of EKF algorithm are compensated by the trained feedback neural network [14]. The simulation results show that the method has high convergence and satisfactory parameter identification accuracy, and has good generalization ability.

2. Related Work

The extended Kalman filter is based on the Kalman filter algorithm, a recursive algorithm proposed by R.E. Kalman in 1960 for linear or nonlinear systems, which allows for measurement errors and model biases in the system and is robust to noise and is therefore widely used in industrial process control, navigation, and system identification [15]. The extended Kalman filter is divided into two processes: prediction and correction, where the prediction part is based on the estimation and covariance of the previous moment, and the correction part is based on the correction of the predicted system state from the measurement data [16].

The first studies on EKF in permanent magnet synchronous motor control without position sensors and parameter identification were carried out by [17], which implemented the hardware of the EKF algorithm for permanent magnet synchronous motors into the online algorithm and achieved good results in parameter identification and state estimation. In [18], the EKF was combined with an adaptive control algorithm to achieve accurate estimation of several parameters such as the speed, rotational inertia, friction coefficient, and load torque of the permanent magnet motor, and the sensitivity of the parameters of the EKF algorithm was analyzed with important parameters [19] .

The later development of EKF identification technology focuses on the reduction of the order of the identification model, which can significantly reduce the amount of data calculation, shorten the time required for the algorithm to run, simplify the system hardware implementation, and to a certain extent improve the performance of the motor control system, while ensuring a certain degree of accuracy [20].

3. Algorithmic Principles of the PMSM Mathematical Model

The mathematical model of the PMSM is described in terms of a reference coordinate system fixed to the rotor, i.e., the d-q rotating coordinate system, which is convenient for analyzing its steady-state and dynamic performance. The voltage equation in the d-q rotating coordinate system is

$$\begin{cases} u_q = R_s \dot{I}_q + p\psi_q + \omega_e \psi_d \\ u_d = R_s \dot{I}_d + p\psi_d - \omega_e \psi_q \end{cases}. \tag{1}$$

The equation for the magnetic chain is

$$\begin{cases} \psi_q = L_q i_q \\ \psi_d = L_d i_d + \psi_f \end{cases}, \tag{2}$$

where u_d, u_q are d, q-axis voltages; i_d, i_q are d, q-axis currents; L_d, L_q are d, q-axis inductances; R_s is the stator phase resistance; ω_e is the rotor electrical angular velocity; ψ_f is the chain of permanent magnet fundamental excitation field across the stator winding; ψ_d, ψ_q are the d, q-axis stator magnetic chain component; p is the differential operator. Without considering the torque equation, the mathematical model of a permanent magnet synchronous motor is a nonlinear, mutually coupled model of order 4, as can be seen from equations (1) and (2)

$$\begin{aligned} \dot{I}_d &= \frac{u_d}{L_d} - \frac{R_s}{L_d}\dot{I}_d + \frac{\psi_d}{L_d}\omega_e, \\ \dot{I}_q &= \frac{u_q}{L_q} - \frac{R_s}{L_q}\dot{I}_q - \frac{\psi}{L_q}\omega_e, \\ \dot{R}_s &= 0, \\ \dot{\psi}_f &= 0. \end{aligned} \tag{3}$$

4. Parametric Identification Systems and Identification Models

4.1. Parameter Recognition System. In modern motor drive and control technology, the rotor position is a critical variable. In the implementation of vector control algorithms, the rotor position needs to be transformed by coordinates; in the implementation of direct torque control algorithms, the rotor position needs to be estimated by the magnetic chain. The accuracy of the rotor position detection therefore has a significant impact on the performance of the PMSM

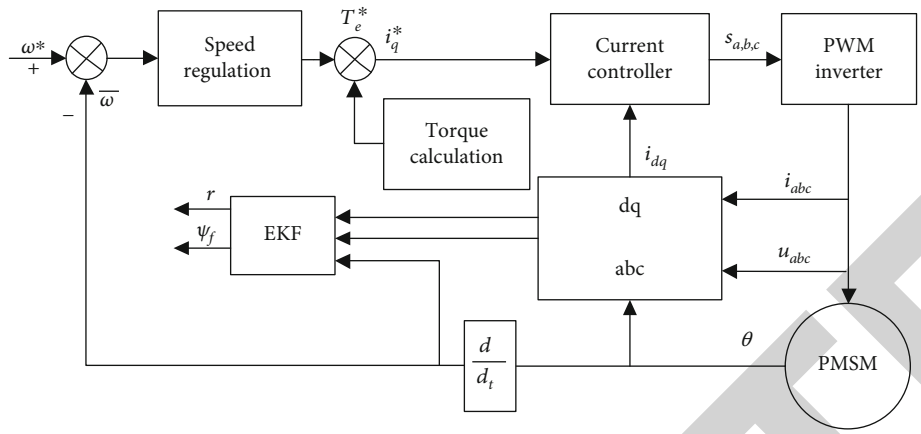

Figure 1: Parameter recognition system with position sensor.

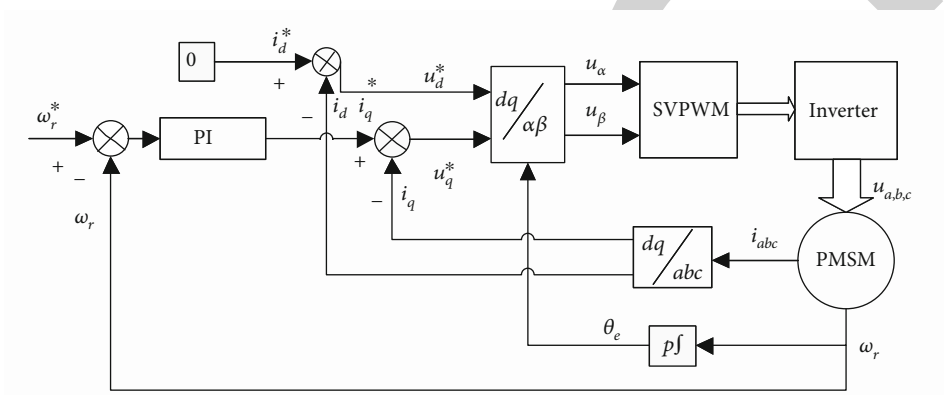

Figure 2: Dual closed-loop control model for PMSM AC servo system.

control system. A common method of collecting rotor position information is to install a mechanical position sensor, such as an optical rotary encoder, in the motor control system, which is connected to the motor and the rotor rotates the code plate to signal the rotor position. For parameter recognition systems, the rotor position is not only used in the vector control algorithm but is also an indispensable input to the EKF observer.

Figure 1 shows the EKF parameter recognition system with position sensor. The error signal obtained by comparing the given speed ω^* with the actual speed ω is used as input to the speed regulator, and the given torque T_e^* from the speed regulator is compared with the actual torque T to obtain the torque error signal, where the actual torque is calculated from the actual value of the cross-axis current component i_q. These reference values, together with the actual values of the detected three-phase stator currents, are processed by the hysteresis loop current controller and generate the switching state signals of the PWM inverter. At the same time, the stator current value $i^*{}_d$ and the input voltage value of the permanent magnet synchronous motor are transformed to obtain the current components i_q, i_d and voltage components u_d, u_q in the d and q axes, respectively, which are used as inputs to the EKF observer together with the actual speed. The rotor angle information used for the coordinate transformation in the above control process is provided by the position sensor.

4.2. Parameter Identification Models. In order to identify the parameters of a permanent magnet synchronous motor using the extended Kalman filter, an iterative computational model needs to be developed. Since a permanent magnet synchronous motor is a multivariable, strongly coupled, high-order nonlinear system, the process of parameter identification involves the inverse of a high-order matrix, and it is tedious and time-consuming to obtain the inverse of a matrix of order three or higher. In addition, in the conventional bit-trade sensor parameter recognition system, the rotor position variable is provided by the position sensor, which is equivalent to a reduced order of the system. During the identification of the individual parameters of the motor, the parameters themselves change slowly compared to the power transients, so that the parameters can be considered constant during each calculation cycle.

4.2.1. Discriminative Models in $\alpha\beta$ Coordinate Systems. For surface-mounted permanent magnet synchronous motors, it is convenient to use a two-phase stationary coordinate system with the stator field oriented in the EKF algorithm for

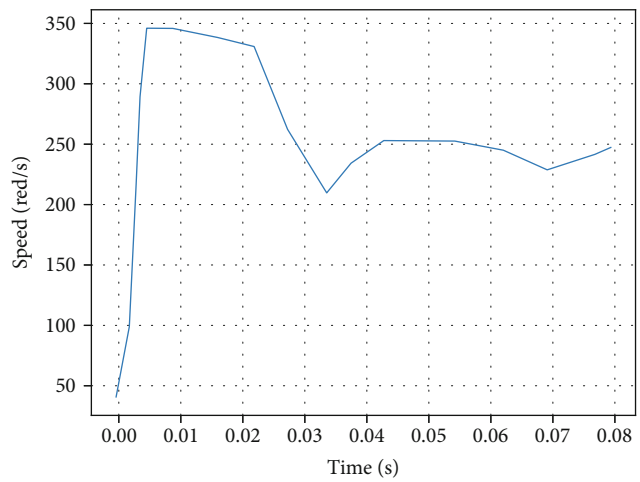

Figure 3: PMSM rotor speed.

parameter identification. At the same time, the control system contains a position sensor, so that rotor position and speed are known quantities. The identification model of the motor stator winding resistance can be divided into a second-order model and a third-order model, which are expressed as:

$$\begin{cases} \dfrac{dr}{dt} = 0 \\ \dfrac{di_\alpha}{dt} = -\dfrac{r}{L} i_\alpha + \dfrac{\lambda}{L}\omega \sin\theta + \dfrac{u_\alpha}{L} \end{cases},$$
$$\begin{cases} \dfrac{dr}{dt} = 0 \\ \dfrac{di_\beta}{dt} = -\dfrac{r}{L} i_\beta - \dfrac{\lambda}{L}\omega \cos\theta + \dfrac{u_\beta}{L} \end{cases}, \tag{4}$$
$$\begin{cases} \dfrac{dr}{dt} = 0 \\ \dfrac{di_\alpha}{dt} = -\dfrac{r}{L} i_\alpha + \dfrac{\lambda}{L}\omega \sin\theta + \dfrac{u_\alpha}{L} \\ \dfrac{di_\beta}{dt} = -\dfrac{r}{L} i_\beta - \dfrac{\lambda}{L}\omega \cos\theta + \dfrac{u_\beta}{L} \end{cases},$$

where r is stator phase resistance. Most of the above identification models are still nonlinear, and they can only be analyzed using the Kalman filter after they have been linearized by means of the Jacobi matrix. Taking the third-order identification model of the stator resistance as an example to find the relevant Jacobi matrix, the dynamic equation of the model can be expressed as follows

$$\begin{cases} \dot{x} = \phi(x, u) \\ z = c(x) \end{cases}, \tag{5}$$

where $\dot{x} = [r\ i_\alpha\ i_\beta]^T$ state vectors, $z = \begin{bmatrix} i_\alpha & i_\beta \end{bmatrix}^T$ measurement vectors, and$u = \begin{bmatrix} u_\alpha & u_\beta \end{bmatrix}^T$ input vectors.

After linearization, the discrete form of the dynamic equation is:

$$\begin{cases} x_{k+1} = \Gamma_k \delta x_k + w_k \\ z_k = \Delta_k \delta x_k + v_k \end{cases}. \tag{6}$$

The Jacobi matrix and the approximate discrete system matrix Γ_k and the measurement matrix Δ_k are obtained as follows

$$\Gamma_k = I + T_s \cdot \frac{\partial \phi(x, u)}{\partial x}_i : x = x_k = \begin{bmatrix} 1 & 0 & 0 \\ -\dfrac{i_\alpha T_s}{L} & 1 - \dfrac{rT_s}{L} & 0 \\ -\dfrac{i_\beta T_s}{L} & 0 & 1 - \dfrac{rT_s}{L} \end{bmatrix},$$
$$\Delta_k = \frac{\partial c(x)}{\partial x} = \begin{bmatrix} 0 & 1 & 0 \\ 0 & 0 & 1 \end{bmatrix}, \tag{7}$$

where T_s is the system sampling period.

4.2.2. Discriminative Model in d, q Coordinate System. For the parametric identification of surface-mounted permanent magnet synchronous motors, a two-phase rotating coordinate system with rotor field orientation can also be used. Again, the rotor position and speed signals required for the identification process are provided by the position sensors and are treated as known quantities. The reason for this is that the d-axis current is always controlled close to zero, making this term in the d-axis equation almost equal to zero, resulting in an equation with $-r\, i_d/L$ no state variables to be estimated, which naturally makes identification difficult. The stator resistance identification model using the q-axis equation can be expressed as follows

$$\begin{cases} \dfrac{dr}{dt} = 0 \\ \dfrac{di_q}{dt} = -\dfrac{r}{L} i_q - \omega i_d - \dfrac{\psi_f}{L}\omega + \dfrac{u_q}{L} \end{cases}. \tag{8}$$

The rotor flux identification model in $\alpha\beta$ coordinate systems and d, q coordinate system is similar with stator resistance identification model above mentioned.

5. Improved EKF Principle Analysis

Kalman filtering uses the statistical properties of Gaussian white noise signals to filter out the uninteresting components of the superimposed signal [21]. However, in motor filtering, the harmonic amplitude varies considerably when a high-capacity load is switched on, and the mean value is not zero, so the process noise in the system often does not conform to a Gaussian distribution. In this paper, a modified EKF filter module is used to replace the low-pass filter, and the harmonic current signal is introduced as process noise to reconstruct the noise signal. Since the classical Kalman

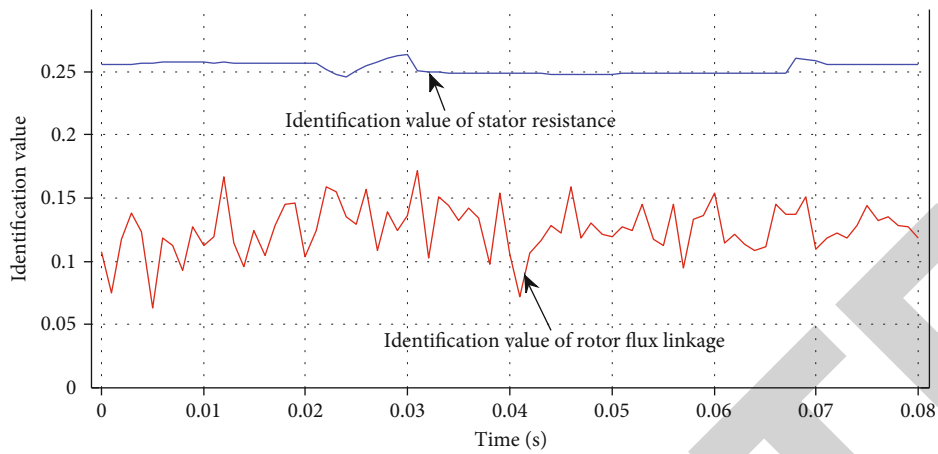

Figure 4: Identification of the stator resistance and rotor flux linage.

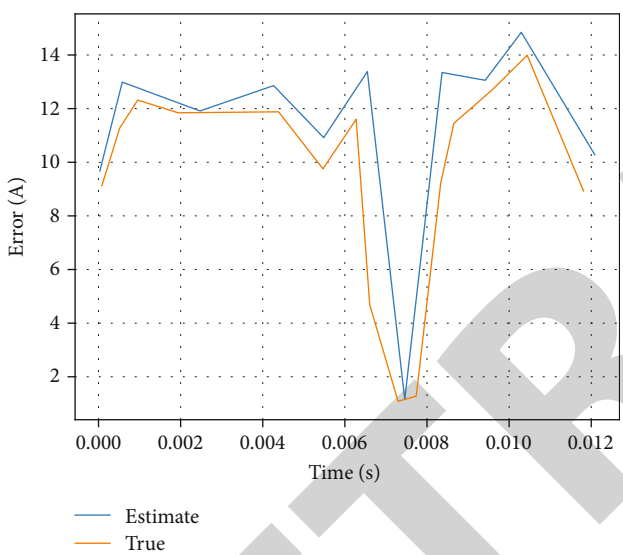

Figure 5: Error of i_q.

filter is not suitable for nonlinear systems, the extended Kalman filter is used, and the noise reconstruction is improved by introducing the harmonic current signal into the EKF filter module through a coordinate transformation. The extracted three-phase harmonic current $i^*_{\text{apff}-a}$, $i_{\text{apf}-b}$, $i_{\text{apff}-c}$ is transformed by coordinates and the harmonic current in stationary coordinates is $i^*_{\text{apf}-\alpha}$, $i^*_{\text{apf}-\beta}$ then

$$\begin{bmatrix} i^*_{\text{apf}-\alpha} \\ i^*_{\text{apf}-\beta} \end{bmatrix} = \sqrt{\frac{2}{3}} \begin{bmatrix} 1 & -\frac{1}{2} & -\frac{1}{2} \\ 0 & \frac{\sqrt{3}}{2} & -\frac{\sqrt{3}}{2} \end{bmatrix} \begin{bmatrix} i^*_{\text{apff}-a} \\ i_{\text{apf}-b} \\ i_{\text{apff}-c} \end{bmatrix}. \tag{9}$$

The coordinate transformation from two-phase stationary to two-phase rotating is

$$\begin{bmatrix} i^*_{\text{apf}-p} \\ i^*_{\text{ap f}-q} \end{bmatrix} = \begin{bmatrix} \cos\theta & \sin\theta \\ -\sin\theta & \cos\theta \end{bmatrix} \begin{bmatrix} i^*_{\text{apf}-\alpha} \\ i^*_{\text{ap f}-\beta} \end{bmatrix}. \tag{10}$$

Similarly, the load current is transformed to obtain the active current component i_q and the reactive current component i_d, which contain harmonic components, then, i_d, i_q can be expressed as

$$\begin{cases} \mathbf{x}_k = \mathbf{A}_k \mathbf{x}_{k-1} + \mathbf{W}_{k-1} \mathbf{w}_{k-1} \\ \mathbf{y}_k = \mathbf{H}_k \mathbf{x}_k + \mathbf{v}_k \end{cases},$$

$$\mathbf{x}^a_k = \begin{bmatrix} \mathbf{x}_k \\ \mathbf{w}_k \end{bmatrix}^{\mathrm{T}} = \begin{bmatrix} A_k & W_{k-1} \\ 0 & I \end{bmatrix} \begin{bmatrix} \mathbf{x}_{k-1} \\ \mathbf{w}_{k-1} \end{bmatrix} + \begin{bmatrix} 0 \\ I \end{bmatrix} \eta_{k-1}, \tag{11}$$

$$\mathbf{y}_k = [\mathbf{H}(k) 0] \begin{bmatrix} \mathbf{x}_k \\ \mathbf{w}_k \end{bmatrix} + \mathbf{v}_k.$$

As a result, the process and measurement noise of the system after state expansion are both white noise with zero mean, so that the conditions of the extended Kalman filter are satisfied and the reconstruction of the noise is feasible.

The improved EKF algorithm presented in this paper is implemented by using the motor parameters ψ_f calculated by the EKF to train feedback neural network off-line, and trained feedback neural network is used to compensate the estimation error in EKF algorithm. There are two steps to improve EKF algorithm by using feedback neural network, that is, feedback neural network training by EKF output parameters and joint estimation by feedback neural network and EKF.

6. Simulation and Implementation

The identification of the stator resistance R_s and the rotor magnetic linkage ψ_f of the PMSM were implemented using MATLAB.

(1) A simulation model of the dual closed-loop PMSM vector control system based on SVPWM is built in SIMILINK, and the model is shown in Figure 2

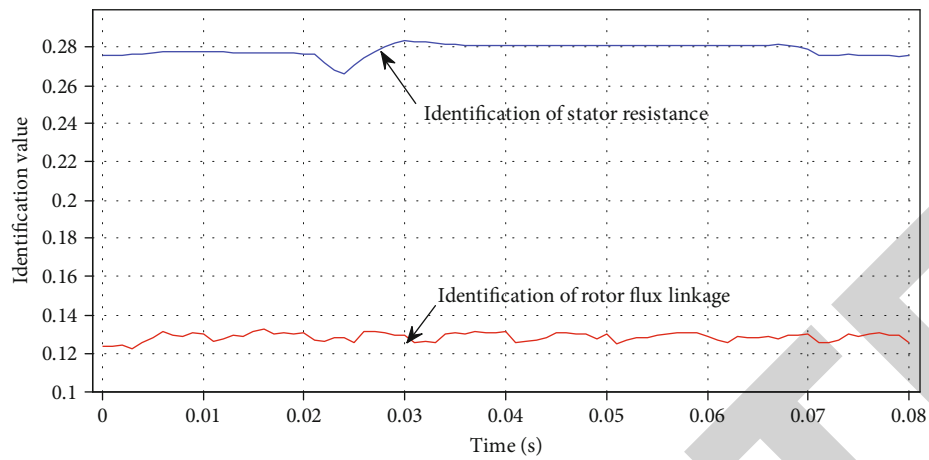

Figure 6: Identification results of improved extended Kalman filter.

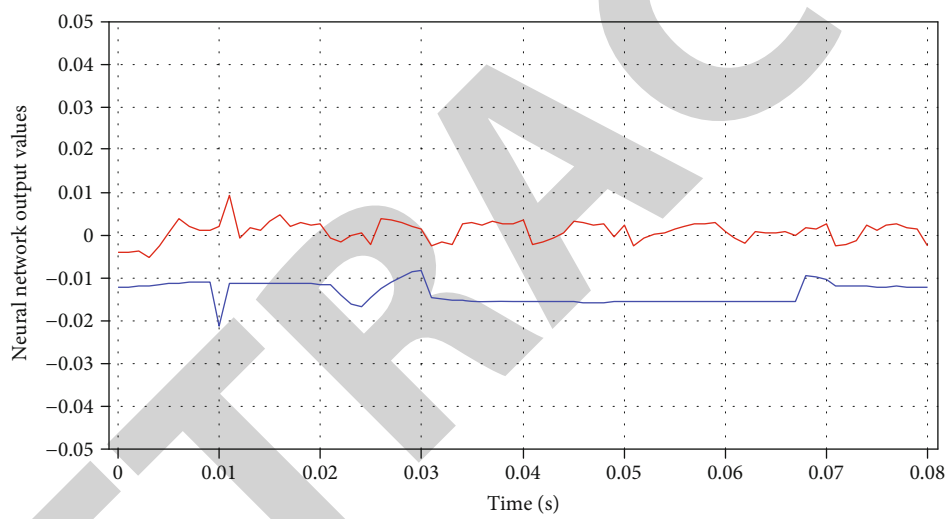

Figure 7: Neural network output values.

The rated parameters of this model motor are rated speed ω_N at 366.5 rad/s; rated torque T_N at 5 N-m; R_s at 0.28 Ω;ψ_f at 0.1278.

(2) Import the i_d, i_q, u_d, u_q data sets from the motor model output into a .mat file. Write MATLAB functions to call these data for the EKF algorithm to estimate the system state quantities and thus provide training samples for the Elman neural network

In order to ensure the representativeness of the training data, the given speed of the motor and the load perturbation were changed during the simulation, and the given speed is shown in Figure 3.

After the EKF algorithm, the identification values of the state variables are shown in Figure 4; the mean value of ψ_f is about 0.121 Wb, the standard deviation is 0.021, has a small amount variation and identification error; R_s falls from 0.257 to 0.246 a little around 0.025 s.

Figure 5 shows the error between the estimated and actual values of i_q with a load fluctuation, which is very small, at a maximum of 0.1%. The improved Kalman filter has very good convergence speed and accuracy, and the computational error is small enough to be used as a training sample for the Elman network.

(3) Design of Elman neural network. The network was designed with i_d, i_q as input, the error between estimation value and actual value of ψ_f, and R_s as output, and 15 neurons in the feedback network layer. The Elman network was trained for 200 time units with a target mean squared error of 0.000 5 and simulated using the sim(-) function

Figure 6 shows the identification results of improved extended Kalman filter (compensated by Elman neural network output), from which it can be seen that the proposed method has a higher identification accuracy and a smaller

identification standard deviation than traditional EKF output shown in Figure 4.

(4) To verify the generalization capability of the neural network. In the simulation model, the reference speed is set at 350 rad/s and the load is set 5 N-m at 0.01 s. In this case, i_d, i_q are taken as the input to identify the difference between estimation value and actual value of ψ_f and R_s. As can be seen from Figure 7, the output only has small fluctuations around 0.01 s. The network can identify the two errors well and has good generalization ability

7. Conclusions

(1) In the control system of permanent magnet synchronous motor, it often needs motor parameter identification to achieve better control performance. In order to improve the rotor flux identification accuracy and reduce the identification error induced by stator resistance changes, we propose an improved EKF algorithm to synchronously identify the rotor flux linkage and stator resistance of PMSM

(2) The research results show that the proposed improved EKF algorithm has high recognition accuracy and good generalization capability

(3) In practical systems, the accuracy of the system model and the correlation of noise cause the accumulation and transmission of errors in the calculation process, and the noise correlation is also considered in this paper

Data Availability

The experimental data used to support the findings of this study are available from the corresponding author upon request.

Conflicts of Interest

The authors declared that they have no conflicts of interest regarding this work.

Acknowledgments

This work was sponsored in part by Henan Province Science and Technology Project (no. 202102210293, no. 192102210076).

References

[1] A. Qiu, B. Wu, and H. Kojori, "Sensorless control of permanent magnet synchronous motor using extended Kalman filter," in *Canadian Conference on Electrical and Computer Engineering 2004 (IEEE Cat. No. 04CH37513)*, vol. 3, pp. 1557–1562, IEEE, 2004.

[2] S. Bolognani, L. Tubiana, and M. Zigliotto, "Extended Kalman filter tuning in sensorless PMSM drives," *IEEE Transactions on Industry Applications*, vol. 39, no. 6, pp. 1741–1747, 2003.

[3] X. Li and R. Kennel, "General formulation of Kalman-filter-based online parameter identification methods for VSI-fed PMSM," *IEEE Transactions on Industrial Electronics*, vol. 68, no. 4, pp. 2856–2864, 2021.

[4] G. H. B. Foo, X. Zhang, and D. M. Vilathgamuwa, "A sensor fault detection and isolation method in interior permanent-magnet synchronous motor drives based on an extended Kalman filter," *IEEE Transactions on Industrial Electronics*, vol. 60, no. 8, pp. 3485–3495, 2013.

[5] J. H. Kim, S. S. Lee, R. Y. Kim, and D. S. Hyun, "A sensorless control using Extended Kalman Filter for an IPM synchronous motor based on an extended rotor flux," in *IECON 2012-38th Annual Conference on IEEE Industrial Electronics Society*, pp. 1631–1636, IEEE, 2012.

[6] H. W. Sim, J. S. Lee, and K. B. Lee, "On-line parameter estimation of interior permanent magnet synchronous motor using an extended Kalman filter," *Journal of Electrical Engineering and Technology*, vol. 9, no. 2, pp. 600–608, 2014.

[7] Z. Peroutka, V. Smidl, and D. Vosmik, "Challenges and limits of extended Kalman Filter based sensorless control of permanent magnet synchronous machine drives," in *2009 13th European Conference on Power Electronics and Applications*, pp. 1–11, IEEE, 2009.

[8] D. Taibi, A. Titaouine, F. Benchabane, and O. Bennis, "Stability analysis of the extended Kalman filter for Permanent Magnet Synchronous Motor," *Journal of Applied Engineering Science & Technology*, vol. 1, no. 2, pp. 51–60, 2015.

[9] V. Smidl and Z. Peroutka, "Advantages of square-root extended Kalman filter for sensorless control of AC drives," *IEEE Transactions on Industrial Electronics*, vol. 59, no. 11, pp. 4189–4196, 2011.

[10] Z. Q. Zhu, X. Zhu, P. D. Sun, and D. Howe, "Estimation of winding resistance and PM flux-linkage in brushless AC machines by reduced-order extended Kalman Filter," in *2007 IEEE International Conference on Networking, Sensing and Control*, pp. 740–745, IEEE, 2007.

[11] P. Tety, A. Konate, O. Asseu, E. Soro, P. Yoboue, and A. R. Kouadjo, "A robust extended Kalman filter for speed-sensorless control of a linearized and decoupled PMSM drive," *Engineering*, vol. 7, no. 10, pp. 691–699, 2015.

[12] Z. H. A. N. G. Zhengwan, Z. H. A. N. G. Chunjiong, L. I. Hongbing, and X. I. E. Tao, "Multipath transmission selection algorithm based on immune connectivity model," *Journal of Computer Applications*, vol. 40, no. 12, p. 3571, 2020.

[13] S. Nadarajan, S. K. Panda, B. Bhangu, and A. K. Gupta, "Online model-based condition monitoring for brushless wound-field synchronous generator to detect and diagnose stator windings turn-to-turn shorts using extended Kalman filter," *IEEE Transactions on Industrial Electronics*, vol. 63, no. 5, pp. 3228–3241, 2016.

[14] Y. Li, M. Yang, J. Long, Z. Liu, and D. Xu, "Current sensorless predictive control based on extended Kalman filter for PMSM drives," in *2017 IEEE Transportation Electrification Conference and Expo, Asia-Pacific (ITEC Asia-Pacific)*, pp. 1–6, IEEE, 2017.

[15] H. Shu, C. Guo, Y. Song, X. Chen, and S. Luo, "Design of model predictive controllers for PMSM drive system based on the extended Kalman filter observer," *International Journal of Electric and Hybrid Vehicles*, vol. 11, no. 4, pp. 378–394, 2019.

Hindawi
Journal of Sensors
Volume 2022, Article ID 2022923, 15 pages
https://doi.org/10.1155/2022/2022923

Research Article

Crop Yield Maximization Using an IoT-Based Smart Decision

Amna Ikram,[1] Waqar Aslam,[2] Roza Hikmat Hama Aziz,[3] Fazal Noor,[4] Ghulam Ali Mallah,[5] Sunnia Ikram,[2] Muhammad Saeed Ahmad,[1] Ako Muhammad Abdullah,[6] and Insaf Ullah[7]

[1]*Department of Computer Science & IT, Government Sadiq College Women University, Bahawalpur, Pakistan*
[2]*Department of Computer Science & IT, The Islamia University of Bahawalpur, Bahawalpur 63100, Pakistan*
[3]*Department of Computer Science, College of Basic Education, University of Sulaimani, Kurdistan Region, Iraq*
[4]*Department of Computer and Information Systems, Islamic University of Madinah, Madinah 400411, Saudi Arabia*
[5]*Department of Computer Science, Shah Abdul Latif University, Khairpur Mir's, Pakistan*
[6]*University of Sulaimani, College of Basic Education, Computer Science Department, Sulaimaniyah, Kurdistan Region, Iraq*
[7]*Hamdard Institute of Engineering & Technology, Islamabad 44000, Pakistan*

Correspondence should be addressed to Waqar Aslam; waqar.aslam@iub.edu.pk and Insaf Ullah; insafktk@gmail.com

Received 2 March 2022; Revised 9 April 2022; Accepted 22 April 2022; Published 17 May 2022

Academic Editor: Waliullah Khan

Today, farmers are suffering from the low yield of crops. Though right crop selection is the main boosting key to maximize crop yield by doing soil analysis and considering metrological factors, the lack of knowledge about soil fertility and crop selection is the main reason for low crop production. In the changed current climate, the farmers having primitive knowledge about conventional farming are facing challenges about making sagacious decisions on crop selection. The selection of the same crop in every seasonal cycle makes the low soil fertility. This study is aimed at making an efficient and accurate system using IoT devices and machine learning (ML) algorithms that can correctly select a crop for maximal yield. Such a system is reliable as compared to the old laboratory testing manual systems, which bear the chances of human errors. Correct selection of a crop is predominantly a priority in agricultural arena. As a contribution, we propose an ML-based model, Smart Crop Selection (SCS), which is based on data of metrological and soil factors. These factors include nitrogen, phosphorus, potassium, CO2, pH, EC, temperature, humidity of soil, and rainfall. Existing IoT-based systems are not efficient as compared to our proposed model due to limited consideration of these factors. In the proposed model, real-time sensory data is sent to Firebase cloud for analysis. Its results are also visualized on the Android app. SCS ensembles the following five ML algorithms to increase performance and accuracy: Decision tree, SVM, KNN, Random Forest, and Gaussian Naïve Bayes. For rainfall prediction, a dataset containing historical data of the last fifteen years is acquired from Bahawalpur Agricultural Department. This dataset and an ML algorithm, Multiple Linear Regression leverages prediction of the rainfall in future, a much-desired information for the health of any crop. The Root Mean Square Error of the rain fall prediction model is 0.3%, which is quite promising. The SCS model is trained for 11 crops' prediction, while its accuracy is 97% to 98%.

1. Introduction

The agriculture sector is the lifeline of mankind and plays a vital role in economy. In conventional farming technique, crop selection was done by primitive knowledge of farmers. Mostly, farmers prefer to select the trendiest crop in their areas or the crop in their neighborhood. Due to a lack of scientific knowledge about farming and no rotation of crops, fertility of lands is affected adversely. Major factors contributing to the crop quality are soil nutrients, ground water level, and type of fertilizer used. A traditional farmer faces recurrent challenges. Soil acidity may increase due to selection of wrong crops and inadequate soil nutrients [1, 2]. The unpredictable climate is the main factor for effecting crop's quality and yield. Soil fertility is an important factor for right crop selection and its health.

The motivation behind our research is to find problems that farmers face to get good and healthy crops. To overcome the mentioned issues of agriculture, we propose an ML algorithm-based model, Smart Crop Selection (SCS) that uses IoT. It is aimed at overcoming few current farming issues that arise due to inefficient approaches. SCS considers metrological factors such as temperature, humidity, rainfall, CO2 level in air, soil pH, EC, and soil type, as depicted in Figure 1. The metrological factors directly affect the plant growth and production [3–5]. To check the soil fertility, soil analysis is performed. For soil analysis, the macro nutrients of soil, nitrogen, phosphorus, and potassium are considered. These three primary nutrients are very helpful for the well-being of plants and to prevent diseases. The soil pH shows the alkalinity of soil and regulates the soil nutrient availability for crops by controlling the chemical reactions and forms of nutrients. The higher and lower values of soil EC affect the plant growth. It also indicates the soil fertility, water quality, and salinity of soil. The CO2 level in air plays an important role for crop health. It is used in photosynthesis process of plants. The proposed model is applicable for two types of soil: loamy and clay. These types of soil have good humidity and moisture level required for most of the crops. Rainfall is also an important factor for crop health [6, 7]. Each crop may have different water requirement. It is highly useful to know the average amount of rainfall of the season before sowing the crop. Its prediction is difficult but machine learning algorithms show promising results. Moving towards precision agricultural techniques allows growth rate of crop yield from 50% to 90%. Precision agriculture is a systematic way to make reasonable decisions and optimal utilization of resources [2]. By such an approach, soil fertility is maintainable.

Towards precision agriculture, IoT can be a key enabler. An IoT-based farming system can create effective decision-making and avoid undesirable situations. An automation system in smart agriculture is not very expensive but more precise than traditional farming system. The structure of IoT systems is based on three layers: perception, network, and application. On perception layer, physical devices like sensors, RFID tags, and cameras are used for data collection. Network layer is used for data communication and forwarding. Application layer is used to combine IoT with specific domain of usage [3].

ML is an exciting application of Artificial Intelligence. It provides the ability to learn by experiences without any explicit program [8]. The proposed model is based on simple and cost-effective hardware that can be used by agriculture officers and farmers to get good productivity of crops. SCS model is trained by classifying dataset and tested subsequently. The accuracy and performance of an ML classifier depend only on the type and size of the dataset [9]. Our dataset used for training the model has 2200 instances for 11 crops. For dataset classification, five supervised ML algorithms (DT, SVM, KNN, RF, and NB) are used. To overcome the weaknesses of individual ML algorithm, they are ensembled for improved accuracy. Our experimental results show 97% to 98% accuracy on real-time testing. In contrast to the previous studies, SCS model has the following novelty aspects:

(i) In previous studies, limited parameters were used but in our proposed model, additional parameters related to soil and metrological factors are considered

(ii) Existing smart agriculture systems are based on costly and complex sensors, whereas we use inexpensive sensors

(iii) The laboratory system for soil analysis is time-consuming and expensive as compared to SCS. In existing research, soil samples are mostly collected manually and tested for fertility in laboratories. There is a risk of human error. For accurate results, an automated system should be developed, as done in our case

(iv) SCS estimates crop yields in totality

The rest of the paper is structured as follows. In Section 2, we summarize related works. In Section 3, we describe the proposed system. In Section 4, we have presented and discussed the results. In Section 5, conclusions are drawn.

2. Related Works

Crop selection by real-time sensing data and soil analysis attributes is a big contribution in research of smart agriculture. Bhojwani et al. proposed a model based on three modules: crop selection, crop management, and crop maturity. They used parameters soil moisture, temperature, humidity, air pressure, and air quality with weather conditions for better crop selection and health monitoring. A real-time sensory data was used for analysis on ThingSpeak application with KNN algorithm [10]. Patil et al. proposed a scientific approach for crop selection by using various sensors of temperature, soil, humidity, and infrared with microcontroller for collecting real-time data. Some data mining techniques are applied for data preprocessing and comparing real-time data with trained data for crop prediction. They also considered crop prices for crop prediction, listed on National Commodity and Derivative Exchange. The KNN classifier is applied for data analysis [11].

Majumdar et al. have focused on IoT-oriented agricultural methods for weather monitoring. The prediction methods are investigated for commercial and scientific perspectives, cost of IoT components, security threats, and dependency of weather parameters on irrigation of crops [12]. Imran suggested a smart irrigation and crop selection system based on the parameters like temperature, humidity, light intensity, and moisture level of soils. Experiments were performed on five types of soils (loamy, black, laterite, alluvial, and silt soil). Experimental results show that soil's characteristics of different lands can be used for crop selection. ThinkSpeak application is used for data analysis. An Android application is also designed to intimate the farmers about required water level of fields [13].

Rekha et al. proposed an IoT framework to improve farming methods for best use of land to increase crop production and profit maximization. A wireless sensor network

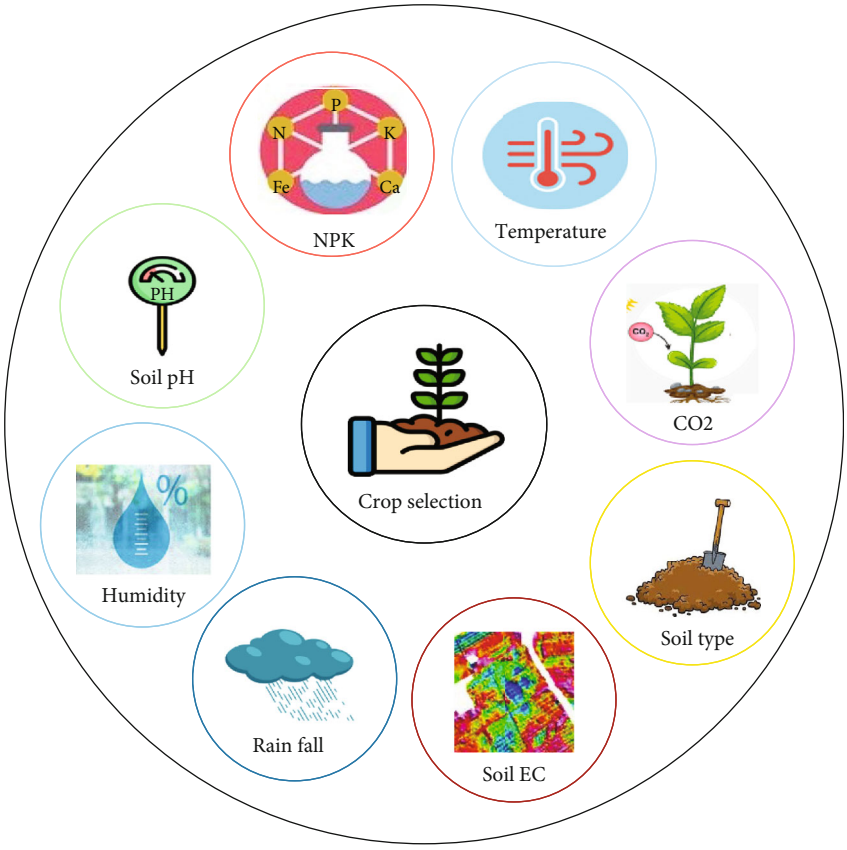

Figure 1: Real-time crop selection features.

Table 1: A brief comparison of SCS with contemporary works.

Citations	Objectives	Parameters	Methodology	Shortcomings
G Sai Pravallika et al., 2020 [31]	Crop selection	Temperature, moisture, humidity, and pH	No ML algorithm is applied. Simply compare the sensor data with the static data store in data base by SQL query to predict desirable crop.	Important parameters of soil fertility (NPK) are missing. An important factor rainfall is missing.
Bakthavatchalam et al., 2022 [21]	Crop prediction	Temperature, humidity, NPK, pH, and rainfall	Multilayer perceptron, JRip, Decision table	The performance metric results in Python are more reliable than in WEKA.
Waikar et al., 2020 [32]	Crop prediction	NPK, pH, and EC	SVM, Naïve Bayes, Artificial Neural Network, AdaBoost; Bagged Tree (Ensemble technique)	Results show less accuracy as compared to SCS. Important parameters, temperature, humidity, and rainfall, are missing
Jain and Ramesh, 2020 [33]	Crop selection	pH, NPK, and drainage capacity	RNN for weather prediction and Random Forest algorithm for crop selection	Random Forest is slow and inefficient for real-time predictions. Important parameters are missing.
A. Chlingaryan et al., 2020 [34]	Crop selection and fertilizer recommendation	Temperature, humidity, and water level	Linear Regression, Decision tree, K-Nearest Neighbors, and XGBoost	Limited parameters are considered for crop selection.

was deployed in the field to sense data for different parameters and for proper monitoring of field. The pH sensor was used to find the soil nutrients that helps to select the required fertilizer. An Android app was also developed to take proper farming decisions relating to irrigation with the help of weather conditions [14]. Mulge et al. proposed a crop prediction method for crop yield maximization and quality of crops by considering real-time data of metrological factors using ML algorithms: precipitation, temperature, humidity, and solar light [15].

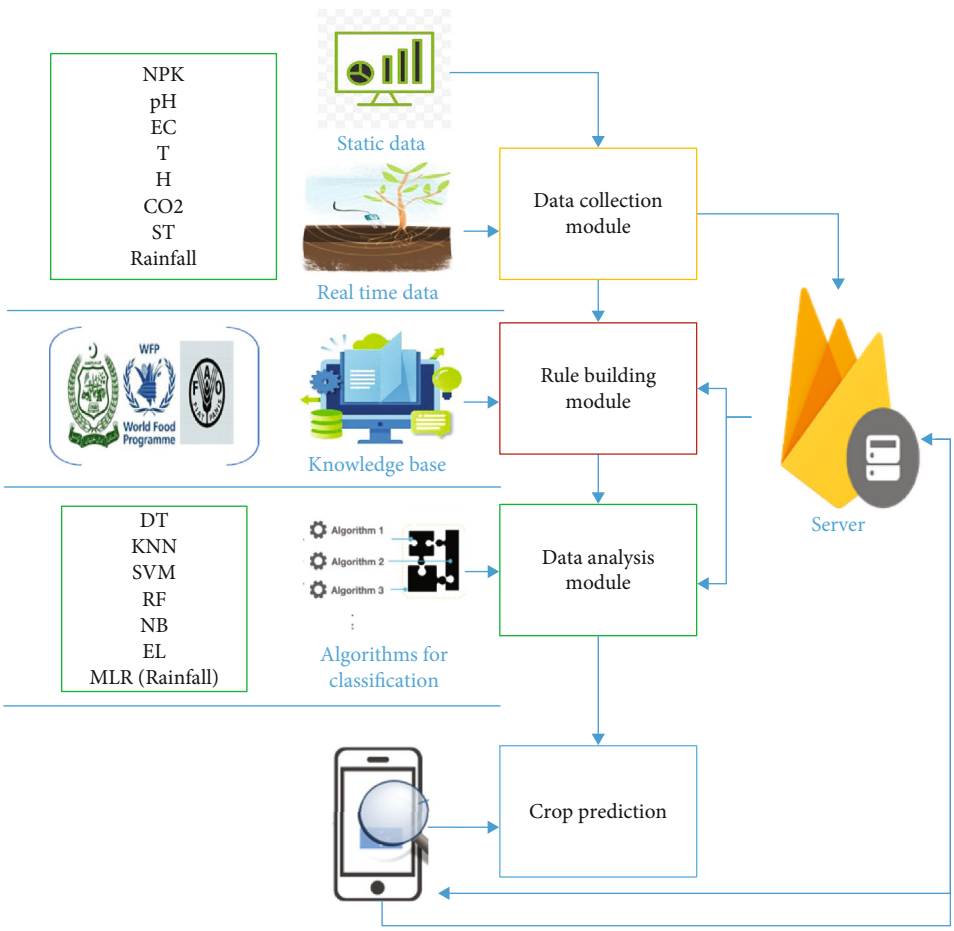

Figure 2: Process flow of SCS.

Table 2: Summary of the used symbols.

Symbol	Description
N	Nitrogen in soil
P	Phosphorous in soil
K	Potassium in soil
pH	Alkalinity of soil
T	Temperature of soil
H	Humidity of soil
EC	Electrical conductivity
DT	Decision tree
KNN	K-Nearest Neighbor
SVM	Support Vector Machine
RF	Random Forest
NB	Gaussian Naïve Bayes
MLR	Multiple Linear Regression
EL	Ensemble Learning

Nagasubramanian et al. proposed crop growth monitoring and disease detection by using cameras and IoT. Another work, ECPRC proposed an ensemble classification using SVM and CNN for data analysis and result prediction [16]. Paravalika et al. effectively predicted crops suitable to soil type. The used parameters are temperature, humidity, moisture, and pH [17]. Ram and Kumar predicted best crop by considering metrological and soil factors and using Ensemble Learning on Decision tree and Linear Regression [18]. Colombo-Mendoza et al. presented a design of smart farming system using IoT sensors for data collection and ML algorithms. A new data mining approach is used to combine two types of datasets: climate data and crop production data for crop yield prediction [19]. Khongdet et al. proposed a model for smart crop tracking and monitoring by storing real-time data from IoT devices. SVM is used for crop disease detection. Fertilizer recommendation is also performed on the basis of previous land data [20]. Bakthavatchalam et al. presented a smart module to recommend a suitable crop for farming that can maximize crop yield. WEKA tool is used for data analysis by ML algorithms. A decision table classifier and multilayer perceptron rule-based classifier JRip are used for classification [21].

Gupta and Nahar also proposed a two-tier ML model for crop yield prediction. In the first tier, a classifier, Adaptive K-Nearest Centroid Neighbor (aKNCN) is proposed to analyze the soil quality and classify the input soil samples into different classes based on soil properties. In the second tier, Extreme Learning Machine algorithm model is used for crop yield prediction [22]. A crop is predicted by using performance comparisons of three ML algorithms; KNN, SVM,

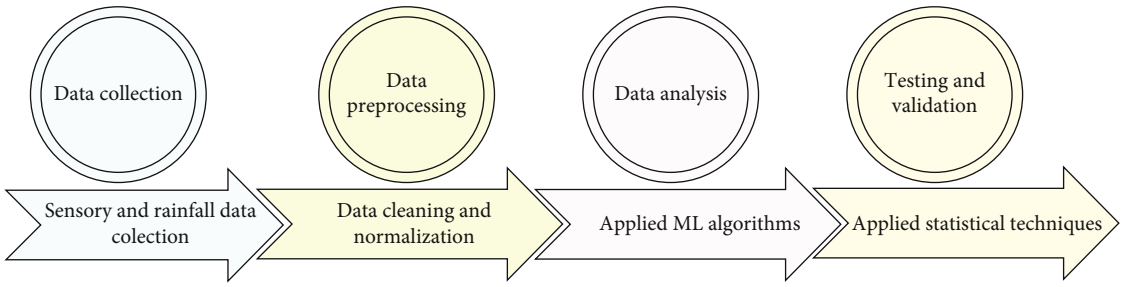

Figure 3: The architecture of SCS system.

1. Import libraries
2. Define variables and terms
3. Import datasets
4. Input rainfall data by user
5. Merge sensory dataset with rainfall prediction
6. Applied normalization
7. Applied split data
8. Applied classification algorithms
9. Evaluate results
10. Applied voting ensemble technique
11. Results output (selected crop)

Algorithm 1: Proposed algorithm for crop Selection Machine Learning (SCS) model.

Table 3: Sensors used in SCS.

Soil sensors	Specification	Description
Integrated soil sensor	Power supply	12 V-24 V
	Temperature measuring range	-45°C-115°C
	PH measuring range	3-9PH
	NPK measuring range	0-1999 mg/kg
	EC measuring range	0-10000 μs/cm
DHT11	Power supply	3.5 V to 5.5 V
	Measuring range	20-95%RH
	Accuracy	±1°C and ±1%
MQ135	Power supply	5 V
	Power consumption	150 mA
	Detect/measure	NH3, Nox, CO2, alcohol, benzene, smoke

and Decision tree [23]. Another model is trained for suitable crop selection and monitoring conditions in field for disease detection and weather analysis. CNN is used for disease detection [24]. On the network layer of IoT system, security issues and information leakages are pointed out [25–27]. Paul et al. have proposed a model for yield prediction by selecting suitable crop for sowing. An external dataset is acquired for soil analysis. Different micro and macro nutrients of the soil are considered. Rapid minor application is used for applying ML classification algorithms (KNN and Naïve Bayes) for training the dataset [28]. There is also proposal for rainfall forecasting. A metrological data including monthly rainfall details is used for validation [29]. In this work, four parameters are used: temperature, humidity, pH, and rainfall for crop selection. It also guides about the number of nutrients required for a particular crop. For dataset classification, Decision tree is applied and for rainfall prediction SVM is applied [30]. A comparison of existing research with SCS model is given in Table 1.

3. Proposed Model

The proposed system is based on real-time sensing of the soil parameters by sensors and the rain fall prediction on the basis of external dataset. The real-time data is saved in database on cloud, and ML algorithms are applied for further analysis and prediction as given in Figure 2. An Ensemble Learning (EL) technique is applied on some distinct ML algorithms, i.e., Decision tree, Naïve Bayes, Support Vector Machine, K-Nearest Neighbor, and Random Forest. For

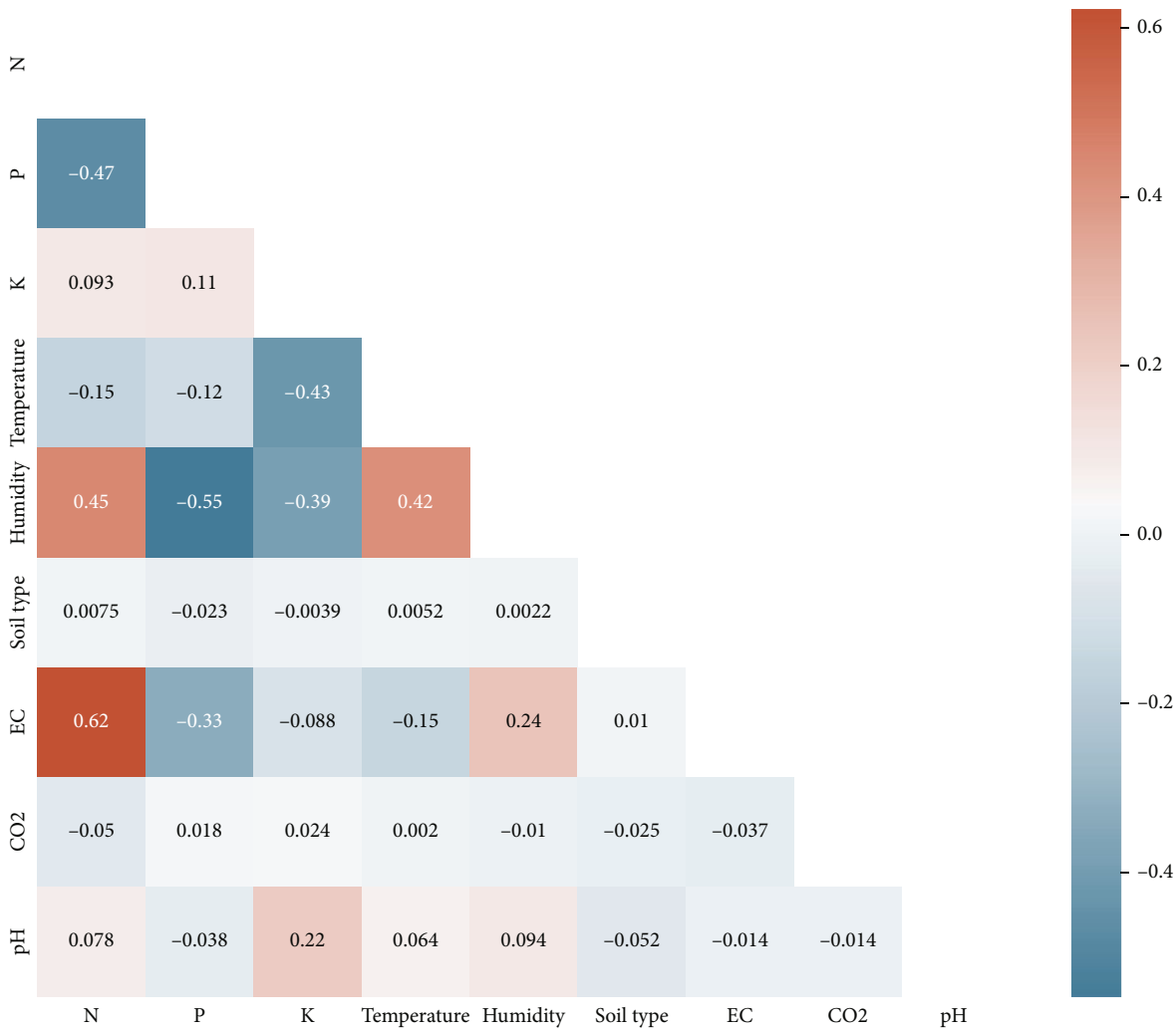

Figure 4: The correlation matrix of the data used.

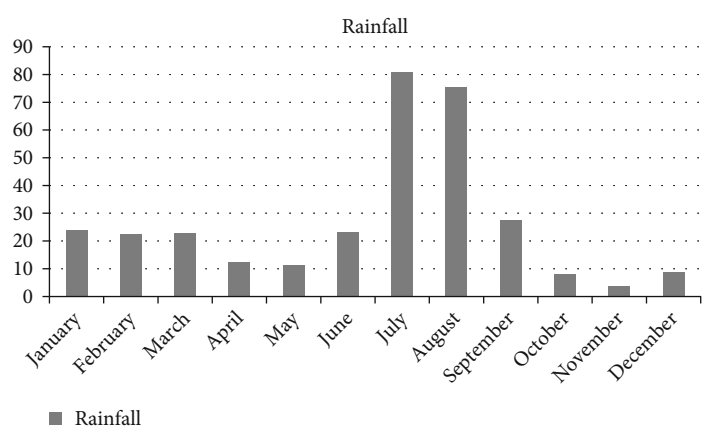

Figure 5: Average rainfall in Punjab.

rainfall prediction, a ML algorithm Multiple Linear Regression model is used. Python is used for implementation, as it is flexible. The proposed solution is based on real-time data sensing of major soil nutrient parameters such as NPK (nitrogen, phosphorus, and potassium) and other factors (T, H, pH, EC, CO2, soil type, and rainfall). In SCS, five ML algorithms are used due to their high performance and accuracy for results. We have shown the description of the

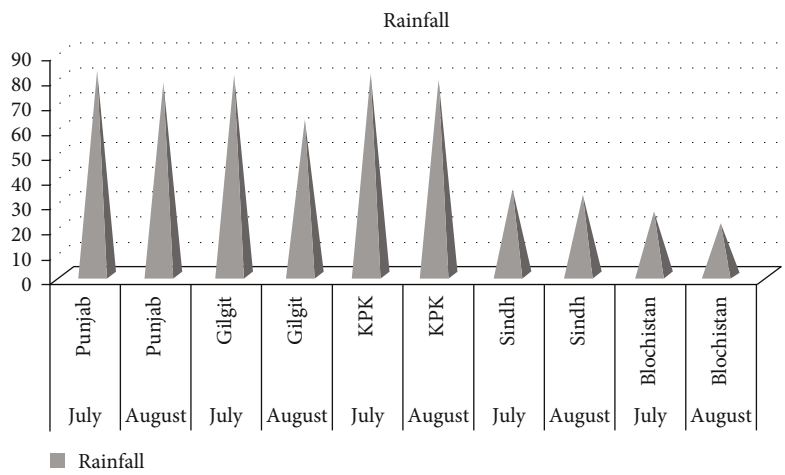

Figure 6: Average rainfall in different regions.

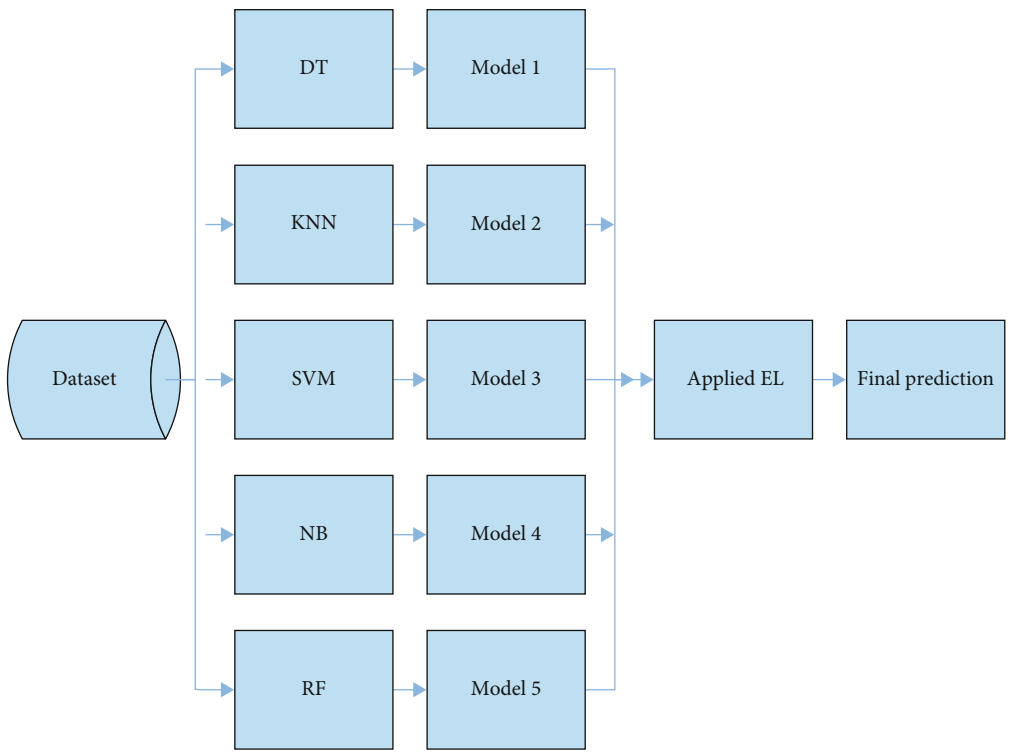

Figure 7: Layout used for the Ensemble technique.

used symbols in Table 2. The process flow of our proposed model comprises of different phases, which are discussed in Figure 3.

Data collection: two dataset are used in proposed model. One dataset is used for training the model, and the second one is used for testing and validation of the model. Real-time dataset is collected for NPK, pH, EC, T, and H by connecting NPK, pH, and EC sensors with Arduino microcontroller. The rainfall data of last 15 years is obtained from government website https://bakhabarkissan.com/. Experiments are performed on two types of soils: loamy and clay. Data preprocess: the real-time sensory data is usually in raw form. The data mining techniques are applied for data preprocessing. As real-time data is coming from different sensors so there could be chance of errors. For rainfall data, the same data mining techniques are applied as for sensory data. The preprocessing techniques are applied on dataset are given next.

Filling missing entries (cleaning) and feature scaling (normalization): in rainfall dataset, the user input is string based so data transformation technique is applied to convert string data into numeric form. Data analysis: after

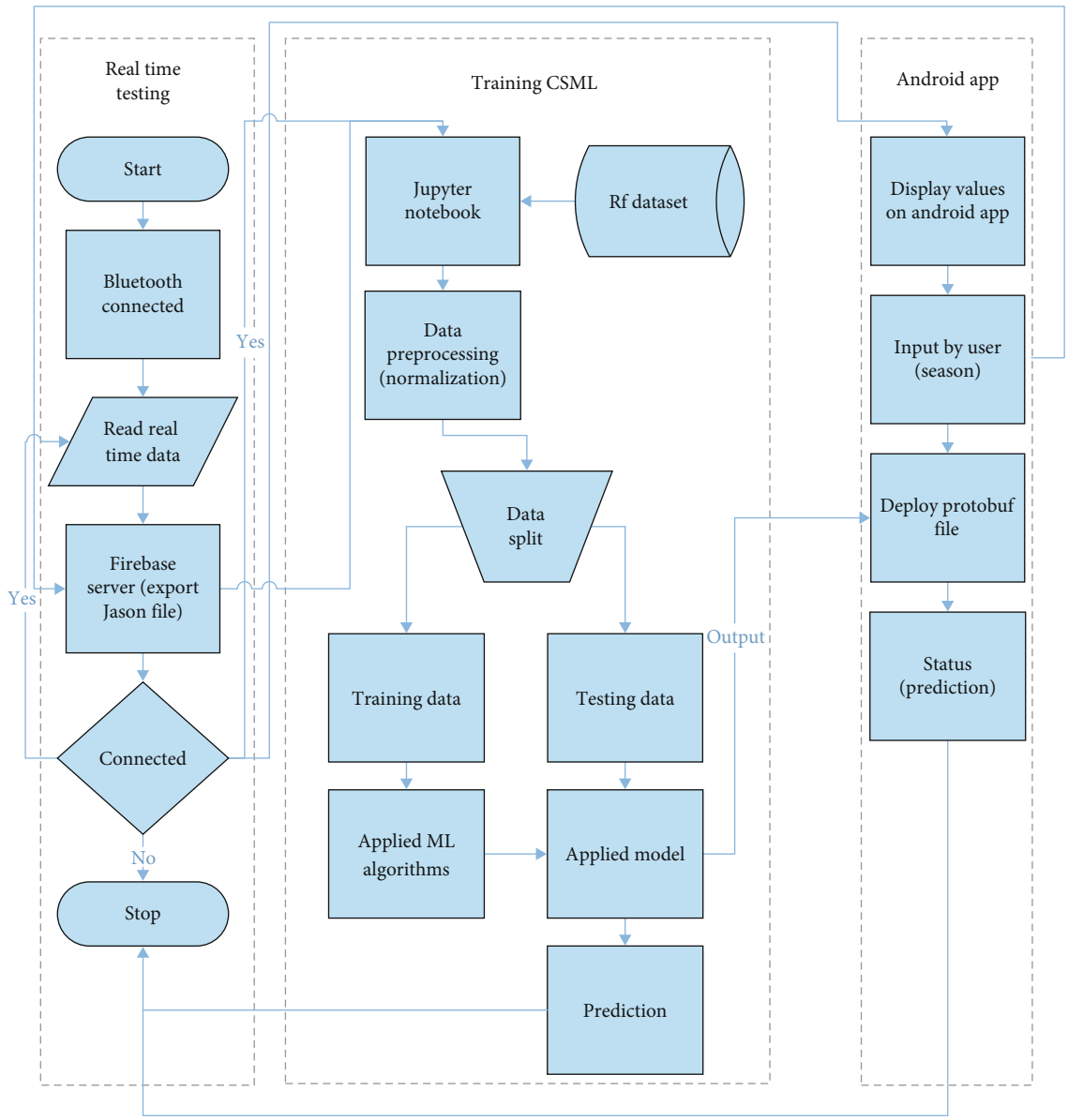

Figure 8: Workflow of SCS.

preprocessing the data, decision rules are applied on dataset. In decision rules, standard ranges of parameters are defined for each crop. ML algorithms are used for dataset training. The performance of each ML algorithms is compared and then applied voting Ensemble technique on applied algorithms for better performance and good accuracy. For testing and validation of the system, a real-time sensory dataset is used. For rain fall and soil type attributes, a user input acquired by Android app. For crop prediction, the results are displayed on an Android application. This is very efficient way to assist farmers. The proposed SCS model is described in Algorithm 1.

The architecture of SCS is shown in Figure 3. The SCS is based on four modules. In sensing module, real-time data is collected by sensors and send to Firebase cloud for storage. The external rainfall dataset is also used to get the predicted rainfall value on the basis of historical data. In the second module, working rules are applied to define the standard ranges for data classification. In the third module, ML algorithms are applied for classification and prediction of output. On the last step, final output is displayed on Android application.

We have considered various features for our proposed SCS including NPK, pH, temperature, humidity, EC, soil type, CO2, and rainfall. In proposed SCS, a 7 in 1 soil integrated sensor is used to perform data collection for major soil features like NPK, pH, T, M, and EC. To check CO2 level in air, MQ135 sensor is used. To calculate temperature and humidity, DHT11 sensor is used. For Bluetooth connectivity, HC-05 module is used. By integrating all these devices with Arduino Nano, a real-time data is send to cloud server [4]. The specifications of sensors are given in Table 3.

For prediction of right crop by our SCS model, the real-time dataset is collected by sensors. The dataset consists of

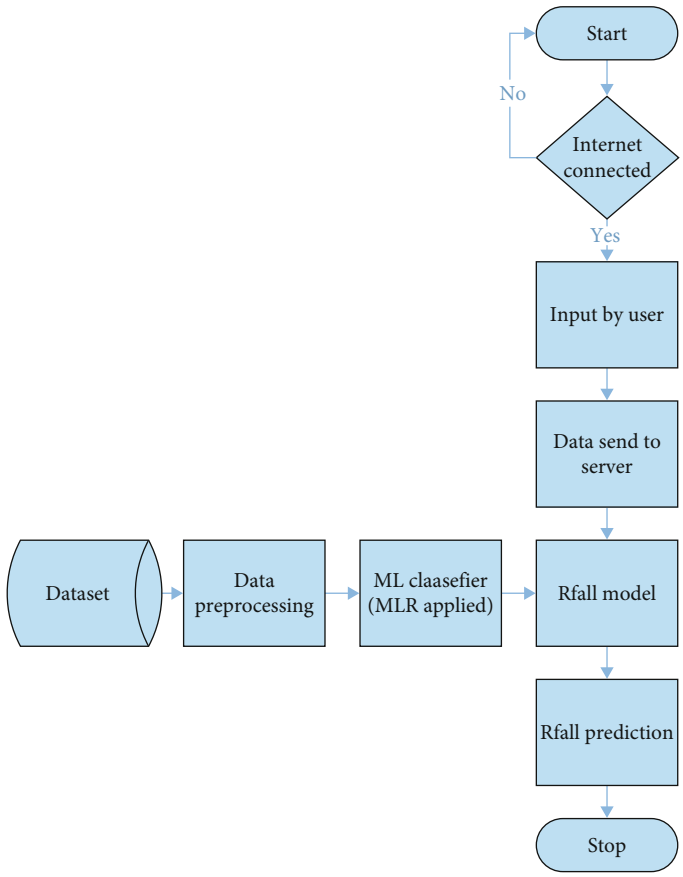

Figure 9: Workflow of the rainfall model.

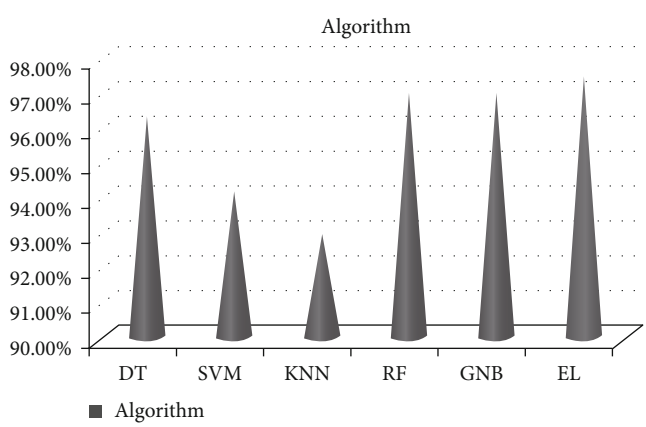

Figure 10: Accuracy comparisons of the ML algorithms with SCS.

ten features that have primary role in yield maximization. Each crop has different requirement of nutrients, temperature, humidity, and water. To train SCS model, we have selected 11 crops that are commonly used in different regions of Pakistan. For training the model, 2200 observations are used. The crop feature is used as a dependent variable in our model.

In Figure 4, correlation matrix of training dataset is given. A heat map is a good way of representing data visually as it is difficult to show large data into tabular form. In correlation matrix, the density and intensity of the variables are shown. Nitrogen and EC are showing higher correlation. All data is symmetrical from left to bottom. The dark red shows higher values, and dark blue shows low values. For heat map implementation, Python libraries are used. Rainfall data is collected from the local agricultural department of Bahawalpur region and government website of agriculture department. The collected data was in raw form. This data is based on the average rainfall of each month of each season of the last 15 years. It has 300 observations. The average rainfall in Punjab is shown in Figure 5. The average rainfall in the month of July and August is higher than remaining months in Punjab. In Figure 6, we also have juxtaposed the rainfall data of different regions of the country. The rainfall rate is higher in Punjab and KPK in the month of July and August than other provinces. These regions are more fertile than other regions of Pakistan. The soil fertility is also an important factor for crop maximization but it mainly depends on availability of water resources.

3.1. Soil Sampling. Soil samples are randomly chosen on the basis of availability. The soil samples were taken 4 to 6 inches below the earth surface. The loamy soil is considered best for sowing due to its structure having combination of soil particles of different soils. The clay soil has high capacity to absorb water. It is cold in winter and wet in summer. The

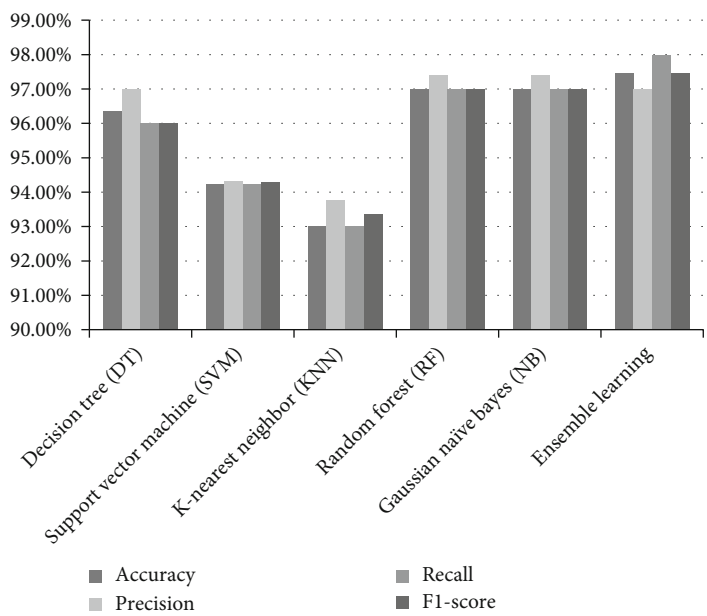

Figure 11: Statistical analysis of the ML algorithms with SCS.

purpose of getting soil samples of different soils is to check if the soil has adequate nutrients.

3.2. Used ML Algorithms. We used various ML algorithms including Decision tree (DT), Naïve Bayes (NB), Support Vector Machine (SVM), K-Nearest Neighbor (KNN), Random Forest (RF), and Ensemble Learning (EL) technique for crop prediction and Multiple Linear Regression (MLR) for rainfall forecasting. In the proposed SCS, these ML algorithms are used as the base models for dataset given in Figure 7.

3.3. Decision Rules. In our proposed SCS, decision rules are applied for data analysis and classification by ML algorithms to train the model. The ranges for each feature are defined to classify crops. We have designed working rules by getting the standard values of each factor for each crop. The first module of SCS is designed by connecting sensors with Arduino Nano. Every sensor is connected with separate Arduino. The real-time values are displayed on Android app by Bluetooth connectivity (HC-05 module) and sent to Firebase cloud database. The rainfall values are acquired from external dataset. The real-time data collected by sensors usually have some noise, missing values, and errors that can affect the decision by ML classifier algorithms. For accurate results and good accuracy, data preprocessing techniques should be applied. To remove missing entries, we have filled the fields with null entries and with the most frequent values. As all the features have different units to measure the magnitudes, so there is a need for data scaling. Two types of data scaling techniques used are normalization and standardization [35]. In SCS, normalization (Min–Max) technique is applied for data scaling. The algorithms using Euclidean distance (KNN and SVM) for data classification require data scaling. By this technique, all the feature data is converted into (0-1) range from the original range. The Min–MaxScaler method

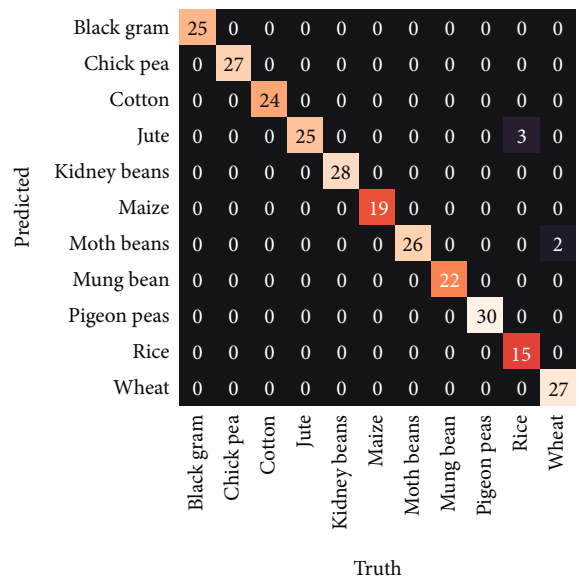

Figure 12: Confusion matrix of SCS.

is implemented from Scikit-learn library of Python [34, 36]. The normalized data is stored in variable x_s as follows:

$$x_s = \frac{(x - x_{\min})}{x_{\max} - x_{\min}}, \tag{1}$$

where x_s denotes scaled value of X and $x_{\min}$ and $x_{\max}$ refer to minimum and maximum values of X, respecitvely.

An Ensemble technique is applied on ML algorithms, which are used as base learners. The final result is based on the prediction of these algorithms. All applied base learner algorithms are appended together in an array.

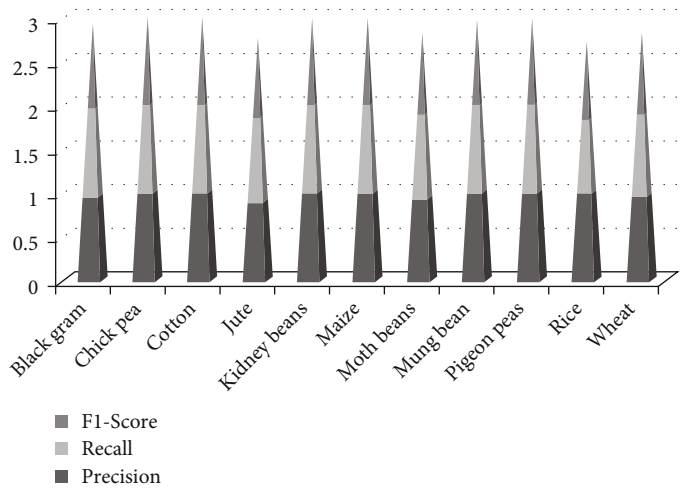

Figure 13: Performance metric of the classes.

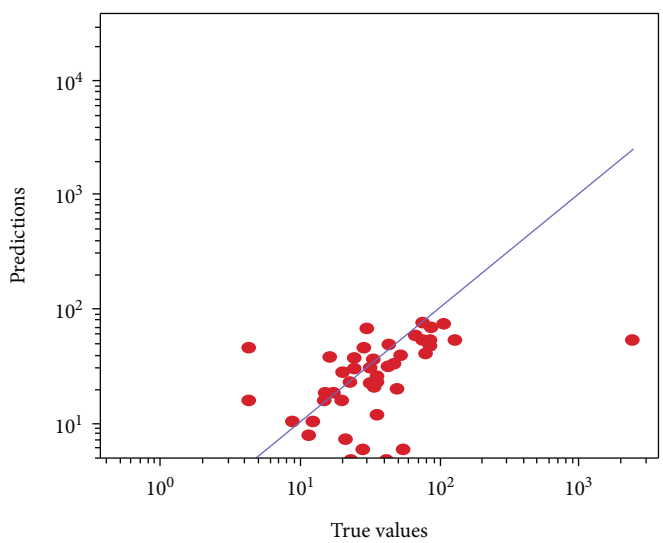

Figure 14: Rainfall: actual data vs. predicted data.

3.4. Workflow. In Figure 8, the whole workflow of model of SCS is shown. The data acquisition is performed by SCS hardware module by collecting real-time values of NPK, pH, EC and T, H, and CO2. SCS database is created in Firebase. When Bluetooth is connected with Android app, then real-time data is collected by sensors and sent to Firebase database. The real-time database exported a JSON file which we have converted into xsl and import into android studio. To train the SCS model, all working is performed in Jupyter Notebook using Python. An Android app is created to show SCS prediction values. A Protobuf file is exported to Android studio.

The workflow model for rainfall prediction is shown in Figure 9. ML algorithm MLR (Multiple Regression Model) [37, 38] is applied on rainfall data for the prediction of future values of rainfall. The dataset is based on average monthly rainfall of last 15 years. The parameters of dataset are year, month, season, and previous rain fall data. The calculated Root Mean Square Error is 0.3, and r^2 is 0.610132. The r^2 is used to show the percentage of variance of dependent variable to independent variable.

4. Performance Evaluations

By applying EL, we have improved the performance of our model by increasing the accuracy as compared to individual models. The accuracies are calculated by dividing all the true predictions calculated by algorithm with total number of dataset values.

$$\text{Accuracy} = \frac{\text{Tp} + \text{Tn}}{\text{Tp} + \text{Fp} + \text{Tn} + \text{Fn}}, \tag{2}$$

where Tp is the true positive, Tn is the true negative, Fp is the false positive, and Fn is the false negative. The classification error rate is calculated as follows:

$$\text{Error rate} = (1 - \text{accuracy}) \times 100. \tag{3}$$

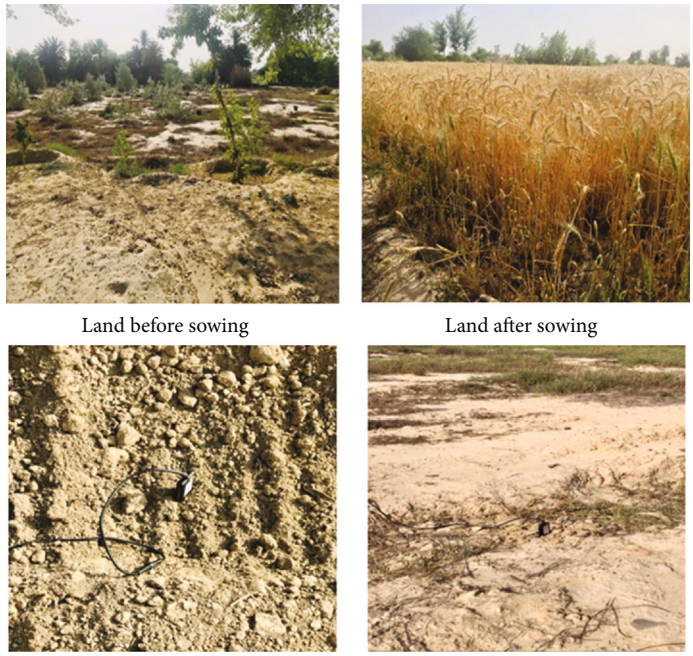

Figure 15: Agronomic measurement for SCS.

Figure 16: Android application for SCS.

Table 4: An accuracy comparison with existing approaches.

Citations	Year	Dataset size	Features selected	Approach	Accuracy
S. Parween et al. [39]	2021	Not mentioned	5	Naïve Bayes	96.00%
M. H. Kishan Das et al. [24]	2021	300	4	Decision tree	97.00%
R. Kumar and V. Singhal [40]	2022	298	3	XGBoost	92%
SCS (proposed model)	2022	2200	10	Ensemble Learning (DT, NB, SVM, KNN, and RF)	97.45%

The precision, recall, and F1-score are calculated to check the reliability of our model. Precision is calculated to show the accurate predictions in positive classes.

$$\text{Precision} = \frac{\text{Tp}}{\text{Tp} + \text{Fp}}. \tag{4}$$

Recall is calculated to predict how many positive cases our model can predict.

$$\text{Recall} = \frac{\text{Tp}}{\text{Tp} + \text{Fn}}. \tag{5}$$

For calculating F1-score, both precision and recall are combined,

$$\text{F1-score} = 2 \times \frac{\text{precision} \times \text{recall}}{\text{precision} + \text{recall}}. \tag{6}$$

We have compared the performances of ML algorithms. In Figure 10, we observe that performance of RF and NB algorithms has higher classification accuracy as compared to other algorithms KNN, DT, and SVM. This is because in Random Forest, multiple DTs are involved that make the decision boundary more stable and accurate. SVM is more suitable for binary classification.

In Figure 11, we have analyzed the accuracy, precision, recall, and F1-score of implemented algorithms. We observe RF, NB, and EL algorithms DT, SVM, and KNN in terms of accuracy, precision, recall, and F1-score in SCS system. To check class wise performance of SCS, a confusion metrics is given in Figure 12.

Confusion matrix is showing count of truly predicted instances and wrongly predicted instances of each class. By Equation (2), the accuracy of the whole model is calculated as

$$\text{Accuracy} = \frac{\text{sum of the truly predicted values}}{\text{sum of the total values}} = \frac{268}{275} = .9745. \tag{7}$$

The performance metrics of one output label class "black gram" is calculated by getting values from confusion matrix. By setting values Tp = 25, Tn = 250, Fp = 0, and Fn = 1 and applying formulas in Equations (2), (4), (5), and (6), the following values of performance metrics are determined: accuracy = 100, precision = 96%, recall = 100, and F1 − score = 98%.

Similarly, values of other classes are given in Figure 13.

The rainfall predicted data is given in Figure 14. We see that the values closer to diagonal line show correct prediction. We observe that most of our predicted values are closer to diagonal line. The diagonal line shows the actual values of rainfall data. The cross-validation technique is also performed for validity of the results. For k-fold, 5 splits are set to divide the data, and accuracy of each fold of model is displayed and validated.

Experiments are performed on two types of soil samples: loamy and clay. SCS recommended "wheat" crop for loamy soil and "lentils" crop for clay soil. The performance of SCS was also measured by direct observation of wheat crop using agronomic measurement given in Figure 15. The experiment was performed on 1 acre land of Bahawalpur region. By using SCS system, wheat crop was selected. The NPK value is maintained by adding required amount of fertilizer in the soil for yield maximization. A good yield and healthy crop are observed in the control field.

An interface is also designed on Android application to show the real-time sensory data and for input of rainfall data and soil type from user. Final crop prediction is displayed on the Android app. By connecting Bluetooth, the real-time values are received and sent to Firebase cloud for analysis. The decision support system displays final output of crop prediction on Android application given in Figure 16.

4.1. Comparison with Existing Approaches. In precision agriculture, a lot of work has been performed on crop selection using different features and dataset sizes. An accuracy comparison of our proposed SCS model with few representative works [24, 39, 40] is shown in Table 4.

4.2. Limitations. SCS seeks crop yield maximization through selection of the correct crop. Some limitations of proposed model are as follows:

(i) EL is computationally expensive

(ii) The performance of SCS varies with size of the dataset

(iii) Air pressure and light intensity can be considered as influential factors

(iv) The system is limited for few crops only

5. Conclusions

Farmers using traditional methods in agriculture face problems such as low crop yield due to unpredicted weather, wrong amount of water and nutrients, and wrong selection of crop. In previous research work, limited parameters were

used that are insufficient for high yield of crops. Our research is aimed at maximizing the crop yield by selecting suitable crop. We tackle this issue by applying technology methodically and evidence-based analysis. For instance, adding required amount of nutrients gives improved yields. Our work is based on selection of the influential parameters. The ML algorithms used in our proposed research give improved accuracy with less computational cost as compared to previous research. To facilitate farmers, an Android app is developed. The cost of our system is very low, and all the used sensors are easily available and easy to use.

In future, more parameters and crops can be added to this system. The more accurate and efficient ML algorithms like CNN and LSTM can also be studied. SCS model can be integrated with security to protect crop data. For crop monitoring, drone cameras can also be used. Fertilizer recommendation system can also be developed on the basis of real-time sensory data of soil nutrients.

Data Availability

All data generated or analyzed during this study are included in this published article.

Conflicts of Interest

The authors declare that they have no conflicts of interest to report regarding the present study.

References

[1] P. Kanchan and N. Shardoor, "Krashignyan: a farmer support system," *Asian Journal For Convergence In Technology (AJCT) ISSN-2350-1146*, vol. 7, no. 3, pp. 1–7, 2021.

[2] F. Javed, M. K. Afzal, M. Sharif, and B. S. Kim, "Internet of Things (IoT) operating systems support, networking technologies, applications, and challenges: a comparative review," *IEEE Communication Surveys and Tutorials*, vol. 20, no. 3, pp. 2062–2100, 2018.

[3] H. A. Issad, R. Aoudjit, and J. J. Rodrigues, "A comprehensive review of data mining techniques in smart agriculture," *Engineering in Agriculture, Environment and Food*, vol. 12, no. 4, pp. 511–525, 2019.

[4] J. Flak, "Technologies for sustainable biomass supply-overview of market offering," *Agronomy*, vol. 10, no. 6, 2020.

[5] P. M. Kavita, "Satellite-based crop yield prediction using machine learning algorithm," in *2021 Asian Conference on Innovation in Technology (ASIANCON)*, pp. 1466–1470, PUNE, India, August 2021.

[6] W. Mupangwa, R. Makanza, L. Chipindu et al., "Temporal rainfall trend analysis in different agro-ecological regions of southern Africa," *Water SA*, vol. 47, no. 4, pp. 466–479, 2021.

[7] A. G. Djibo, H. Karambiri, O. Seidou et al., "Linear and nonlinear approaches for statistical seasonal rainfall forecast in the Sirba watershed region (SAHEL)," *Climate*, vol. 3, no. 3, pp. 727–752, 2015.

[8] N. Jain, A. Kumar, S. Garud, V. Pradhan, and P. Kulkarni, "Crop selection method based on various environmental factors using machine learning," *International Research Journal of Engineering and Technology (IRJET)*, vol. 4, no. 2, pp. 1530–1533, 2017.

[9] D. S. Wankhede, "Analysis and prediction of soil nutrients pH, N, P, K for crop using machine learning classifier: a review," *In International Conference on Mobile Computing and Sustainable Informatics*, pp. 111–121, Springer, Cham, 2020, January.

[10] Y. Bhojwani, R. Singh, R. Reddy, and B. Perumal, "Crop selection and IoT based monitoring system for precision agriculture," *International Research Journal of Engineering and Technology (IRJET)*, vol. 4, no. 2, 2017.

[11] J. S. Raj, *International Conference on Mobile Computing and Sustainable Informatics*, EAI/Springer Innovations in Communication and Computing, Springer Cham, 2020.

[12] P. Majumdar, S. Mitra, and D. Bhattacharya, "IoT for promoting agriculture 4.0: a review from the perspective of weather monitoring, yield prediction, security of WSN protocols, and hardware cost analysis," *Journal of Biosystems Engineering*, vol. 46, no. 4, pp. 440–461, 2021.

[13] S. Imran, "Effective crop selection and conservative irrigation using IoT," *International Journal of Science and Research (IJSR)*, 2016.

[14] P. Rekha, V. P. Rangan, M. V. Ramesh, and K. V. Nibi, "High yield groundnut agronomy: an IoT based precision farming framework," in *2017 IEEE Global Humanitarian Technology Conference (GHTC)*, vol. 2017, pp. 1–5, San Jose, CA, USA, Dec. 2017.

[15] M. Mulge, M. Sharnappa, A. Sultanpure, D. Sajjan, and M. Kamani, "An invitation to subscribe:the international journal of analytical and experimental modal analysis," vol. 10, no. 1, pp. 1112–1117, 2020.

[16] G. Nagasubramanian, R. K. Sakthivel, R. Patan, M. Sankayya, M. Daneshmand, and A. H. Gandomi, "Ensemble classification and IoT-based pattern recognition for crop disease monitoring system," *IEEE Internet of Things Journal*, vol. 8, no. 16, pp. 12847–12854, 2021.

[17] G. S. Pravallika, L. Kundana, K. S. Thanvi, G. Sirisha, and C. Rupa, "Proficient smart soil based IoT system for crop prediction," in *2020 Second International Conference on Inventive Research in Computing Applications (ICIRCA)*, pp. 752–757, July 2020.

[18] A. Ram and R. Kumar, *Prediction of the crop cultivating using resembling and IoT techniques in agricultural fields for increasing productivity 1*, European Journal of Molecular & Clinical Medicine, 2020.

[19] L. O. Colombo-Mendoza, M. A. Paredes-Valverde, M. D. P. Salas-Zárate, and R. Valencia-García, "Internet of Things-driven data mining for smart crop production prediction in the peasant farming domain," *Applied Sciences*, vol. 12, no. 4, 2022.

[20] K. Phasinam, T. Kassanuk, and M. Shabaz, "Applicability of Internet of Things in Smart Farming," *Journal of Food Quality*, Article ID 7692922, p. 7, 2022.

[21] K. Bakthavatchalam, B. Karthik, V. Thiruvengadam et al., "IoT framework for measurement and precision agriculture: predicting the crop using machine learning algorithms," *Technologies*, vol. 10, no. 1, p. 13, 2022.

[22] A. Gupta and P. Nahar, "Classification and yield prediction in smart agriculture system using IoT," *Journal of Ambient Intelligence and Humanized Computing*, 2022.

[23] A. Gupta, D. Nagda, P. Nikhare, and A. Sandbhor, "Smart crop prediction using IoT and machine learning," *International Journal of Engineering Research & Technology (IJERT)*, pp. 18–21, 2021.

[24] M. H. Kishan Das, D. Mishra, and D. Deepa, "Automation and integration of growth monitoring in plants (with disease prediction) and crop prediction," *Materials Today: Proceedings*, vol. 43, no. 1, pp. 3922–3927, 2021.

[25] W. U. Khan, X. Li, A. Ihsan, M. A. Khan, V. G. Menon, and M. Ahmed, "2021. NOMA-enabled optimization framework for next-generation small-cell IoV networks under imperfect SIC decoding," *IEEE Transactions on Intelligent Transportation Systems*, pp. 1–10, 2021.

[26] W. U. Khan, Z. Ali, M. Waqas, and G. A. S. Sidhu, "Efficient power allocation with individual QoS guarantees in future small-cell networks," *AEU-International Journal of Electronics and Communications*, vol. 105, pp. 36–41, 2019.

[27] W. U. Khan, J. Liu, F. Jameel, M. T. R. Khan, S. H. Ahmed, and R. Jantti, "Secure backscatter communications in multi-cell NOMA Networks: enabling link security for massive IoT networks," in *In IEEE INFOCOM 2020-IEEE Conference on Computer Communications Workshops (INFOCOM WKSHPS)*, vol. 2020, pp. 213–218, July 2020.

[28] M. Paul, S. K. Vishwakarma, and A. Verma, "Analysis of soil behaviour and prediction of crop yield using data mining approach," in *Proceedings -2015 International Conference on Computational Intelligence and Communication Networks, CICN*, vol. 2016, pp. 766–771, Jabalpur, India, 2015, August.

[29] N. Gnanasankaran and E. Ramaraj, "A multiple linear regression model to predict rainfall using Indian meteorological data," *International Journal of Advanced Science and Technology*, vol. 29, no. 8, pp. 746–758, 2020.

[30] M. Mulge, M. Sharnappa, A. Sultanpure, D. Sajjan, and M. Kamani, "Agricultural crop recommendation system using IoT and M.L," *The International Journal of Analytical and Experimental Modal Analysis*, vol. 12, no. 6, 2020.

[31] G. S. Pravallika and G. Sirisha, "Proficient smart soil based IoT system for crop prediction," *2020 Second International Conference on Inventive Research in Computing Applications (ICIRCA)*, pp. 752–757, 2020.

[32] V. C. Waikar, S. Y. Thorat, A. A. Ghute, P. P. Rajput, and M. S. Shinde, "Crop prediction based on soil classification using machine learning with classifier ensembling," *Int. Res. J. Eng. Technol.*, vol. 7, no. 5, 2020.

[33] S. Jain and D. Ramesh, "Machine learning convergence for weather based crop selection," in *2020 IEEE International Students' Conference on Electrical, Electronics and Computer Science*, vol. 2020, pp. 1–6, SCEECS, 2020, Feb.

[34] A. Chlingaryan, S. Sukkarieh, and B. Whelan, "Machine learning approaches for crop yield prediction and nitrogen status estimation in precision agriculture: a review," *Computers and Electronics in Agriculture*, vol. 151, pp. 61–69, 2018.

[35] J. Han, J. Pei, and M. Kamber, *Data mining: concepts and techniques*, Elsevier, 2011.

[36] K. Palanivel and C. Surianarayanan, "An approach for prediction of crop yield using machine learning and big data techniques," *International Journal of Computer Engineering and Technology*, vol. 10, no. 3, pp. 110–118, 2019.

[37] L. A. Yousif, A. A. Khatir, F. M. El-Hag et al., "Rainfall variability and its implications for agricultural production in Gedarif State, Eastern Sudan," *African Journal of Agricultural Research*, vol. 13, no. 31, pp. 1577–1590, 2018.

[38] W. M. Ridwan, M. Sapitang, A. Aziz, K. F. Kushiar, A. N. Ahmed, and A. El-Shafie, "Rainfall forecasting model using machine learning methods: case study Terengganu, Malaysia," *Ain Shams Engineering Journal*, vol. 12, no. 2, pp. 1651–1663, 2021.

[39] S. Parween, A. Pal, I. Snigdh, and V. Kumar, "An IoT and machine learning-based crop prediction system for precision agriculture," in *In Emerging Technologies for Smart Cities*, pp. 9–16, Springer, Singapore, 2021.

[40] R. Kumar and V. Singhal, "IoT enabled crop prediction and irrigation automation system using machine learning," *Recent Advances in Computer Science and Communications (Formerly: Recent Patents on Computer Science)*, vol. 15, no. 1, pp. 88–97, 2022.

Hindawi
Journal of Sensors
Volume 2023, Article ID 9839706, 1 page
https://doi.org/10.1155/2023/9839706

Retraction

Retracted: Research on Learner Modeling and Curriculum Recommendation Based on Emotional Factors

Journal of Sensors

Received 19 December 2023; Accepted 19 December 2023; Published 20 December 2023

This article has been retracted by Hindawi following an investigation undertaken by the publisher [1]. This investigation has uncovered evidence of one or more of the following indicators of systematic manipulation of the publication process:

(1) Discrepancies in scope
(2) Discrepancies in the description of the research reported
(3) Discrepancies between the availability of data and the research described
(4) Inappropriate citations
(5) Incoherent, meaningless and/or irrelevant content included in the article
(6) Manipulated or compromised peer review

The presence of these indicators undermines our confidence in the integrity of the article's content and we cannot, therefore, vouch for its reliability. Please note that this notice is intended solely to alert readers that the content of this article is unreliable. We have not investigated whether authors were aware of or involved in the systematic manipulation of the publication process.

Wiley and Hindawi regrets that the usual quality checks did not identify these issues before publication and have since put additional measures in place to safeguard research integrity.

We wish to credit our own Research Integrity and Research Publishing teams and anonymous and named external researchers and research integrity experts for contributing to this investigation.

The corresponding author, as the representative of all authors, has been given the opportunity to register their agreement or disagreement to this retraction. We have kept a record of any response received.

References

[1] X. Hua, H. Zhang, F. Xie, J. Wei, J. Wei, and H. Li, "Research on Learner Modeling and Curriculum Recommendation Based on Emotional Factors," *Journal of Sensors*, vol. 2022, Article ID 3296713, 9 pages, 2022.

Hindawi
Journal of Sensors
Volume 2022, Article ID 3296713, 9 pages
https://doi.org/10.1155/2022/3296713

Research Article

Research on Learner Modeling and Curriculum Recommendation Based on Emotional Factors

Xin Hua,[1] Hongchen Zhang,[2] Feihong Xie,[3] Juntian Wei,[4] Junjia Wei,[1] and Huimin Li[5]

[1]*Aviation University of Air Force, Changchun 130022, China*
[2]*Computer College of Changchun Guanghua University, Changchun 130022, China*
[3]*Hunan Qiangzhi Technology Development, Changsha 410205, China*
[4]*Jilin University Bionic Science and Engineering College, Changchun 130012, China*
[5]*School of Management, University of Science and Technology of China, Hefei 230026, China*

Correspondence should be addressed to Huimin Li; lhmin@mail.ustc.edu.cn

Received 14 March 2022; Revised 31 March 2022; Accepted 8 April 2022; Published 17 May 2022

Academic Editor: Han Wang

With the increasing with the number of courses, learners cannot find the courses they need quickly. Therefore, the primary problem to change the efficiency of online courses is to recommend corresponding courses for a certain group of people according to their needs. Learner characteristics are an important aspect of reflecting learner preferences, and learner models are abstract representations and descriptions of learner characteristics. It is necessary to enhance the use of online courses among students; we must build a relatively comprehensive curriculum model. At present, the construction of learner model is mostly based on cognitive level and learning style, ignoring the emotion expressed by learners to the curriculum, and emotion is a very important characteristic of learners. In order to establish a perfect learner model, it is necessary to incorporate learners' aspect emotion into the learner model to make the course recommendation process more accurate. Firstly, based on the attention mechanism long-term and short-term memory network, this paper extracts the learner's aspect emotion to the curriculum from the learner's curriculum review. At the same time, it studies various characteristics, such as demography, cognitive level, motor behavior, and learning style. By establishing a perfect model integrating researchers' emotional state, finally, the complex interaction between learner characteristics and curriculum characteristics is modeled by using deep factor natural decomposition, so as to achieve accurate curriculum recommendation. In this study, the learner's aspect emotion is included in the construction of learner model and enriched and perfected the learner model. It provides a reference for the theoretical research and applied research of learner model and has reference significance. At the same time, combining Deep learning can improve the accuracy of course recommendation, help learners' learning efficiency and personalized learning quality, and also contribute to the long-term development of online platform. The mathematical modeling in this paper uses learning analysis technology and general factor model based on matrix factorization to calculate and uses factorization machine to reduce the dimension of high-dimensional data, which is efficient and accurate.

1. Introduction

The influence of emotional factors on people lies in many aspects. For example, emotional factors play a role in attitude, which is a comprehensive evaluation of people's self, others, problems, abstract concepts, and other objects. For example, if a person likes ice cream, emotional factors affect a person's attitude. Similarly, influenced by personal emotional factors in modeling, learners will build their own favorite style [1]. A study of German students' learning process shows that emotional factors have a great influence on learning, positive emotions are more important in students' learning stage than in practice stage, and anxiety plays an ambiguous role in learning practice stage; in addition, the fun and interest of learning is particularly important in the learning process [2]. This paper compiles an emotional dictionary based on basic emotional words and phrases. With punctuation marks and emoticons, a set of emotional rules

is established, and a set of algorithms based on emotional rules and dictionaries is summarized. Experimental results show that the algorithm is effective [3]. Studies have shown that a dedicated pathway assesses the threat relevance of visual input, leading to priority acquisition of awareness of threat stimuli. Fearful faces are easier to get rid of depressed emotions; low-level faces and consciousness are not determined by emotional factors [4]. In this paper, Rorschach ink method and diagnostic interview form were used to explore the relationship between emotional factors and subjective quality of life of subjects with spinal cord injury. By comparison, the results show that the subjects with spinal cord injury are satisfied with the assessment of the overall subjective quality of life, but there are still some unsatisfactory places, which become the source of mental pain [5]. The observation results of this paper show that the total precipitation in many areas is amplified at the tail, which makes the social infrastructure more sensitive to extreme weather and climate, and extreme climate change will aggravate this situation. This extreme weather will affect the field modeling [6]. Homeostasis model evaluation is a method to evaluate beta cell function and drug resistance from baseline (fasting) and C concentration. The model was described by an approximate estimation formula in 1985 and has been verified by various physiological methods. When used, it can produce valuable data. Hybrid modeling is a data analysis technique used to identify unobserved heterogeneity in a population. Among the tests and indicators of potential class analysis, factor mixed model, and growth mixed model, Bayesian information criterion performs best in ICS, but bootsrap is still proved to be an indicator of very consistent test indicators in all models [7]. Agent modeling is a powerful simulation modeling technology, which has four application fields: flow simulation, organization simulation, market simulation, and diffusion simulation [8]. Polynomial is a discrete selection model, which is widely used in the modeling of ranking data. A scalable approach to approximate polynomials has been developed, which is suitable for selection-based network modeling [9]. Curriculum recommendation system has been proposed as a tool to help students make wise curriculum choices. A course recommendation system, which combines the data mining process with user rating in the recommendation process, provides users with the possibility of rating. RARE combines the experience of previous students with the scores of current students to recommend the most relevant courses to users [10]. Curriculum recommendation system plays an important role in managing curriculum and guiding students' studies, so as to promote students' academic progress. Previous systems were not perfect, and the hardware devices were not up to standard, so these systems were not based on industry standards. With the development of science and technology, mobile phones have become a typical terminal for learning, and many course recommendation systems have appeared. This paper introduces a mobile course recommendation system, which can help students choose and access the courses required by their professional fields. The system can assist the course coordinator in tutoring students [11]. Recommendation system is widely used in many Internet activities. This paper discusses the ability of recommendation system to support students' needs in learning management system or curriculum management system and designs a suggestion structure of learning management system, which can recommend courses for students [12]. This study uses ontology technology to realize course recommendation, provide students with adaptive learning recommendation, and let students reserve the knowledge they need to enter the workplace in the future [13]. Course selection is an important part of students' development, and a good learning strategy can be obtained from course recommendation methods. In this study, we propose a deep learning technology, multilayer perceptron, and preprocessing method of course recommendation system. The results show that these predictions have good results for students to provide suggestions for course selection and are expected to be applied in practical application [14].

2. Concepts Related to Learner Model

2.1. The Meaning of the Learner. The meaning of learner is a person who participates in social teaching activities. As its concept expands its scope, its characteristics begin to appear, such as consciousness, autonomy, and creativity. Under the condition of learning, learners can get more opportunities for plasticity and sustainable development. From other people's point of view, his goal is very clear, and then their attitude changes from passive to active. And then it has greater demand for its own development and richer connotation.

These changes also cause changes in characteristics. In traditional pedagogy, the characteristics of learners are very simple, including demographic characteristics. Nowadays, the characteristics of learners are very rich, including educational background, emotional attitude, goals, and family background. Learner characteristics play an important role in curriculum system design, instructional design, personalized learning resource recommendation, and other fields and are widely used. At present, people are keen to analyze the characteristics of learners to make accurate portraits of learners, so as to provide various learning services for personalized learning.

2.2. Learner Emotion. The various emotional states produced in the learning process are learners' emotion, which is a very important feature and can accurately express learners' learning hobbies. When the learner is in a positive mood, he likes this kind of course. Therefore, if we can find this positive emotion, we can describe the learners' hobbies more accurately, provide them with more perfect learning services, and improve learning efficiency. Usually, we can get the information of learners' hobbies through emotion mining in text comments, questions, and forum interactions.

2.3. Learner Model. With the rise of information technology, online courses have also increased, and the traditional education mode has changed. Learning is no longer limited to school classrooms. More and more people are learning on different learning platforms, leaving a large amount of learning data, which lays a foundation for providing personalized learning support services. Learner model appears with the

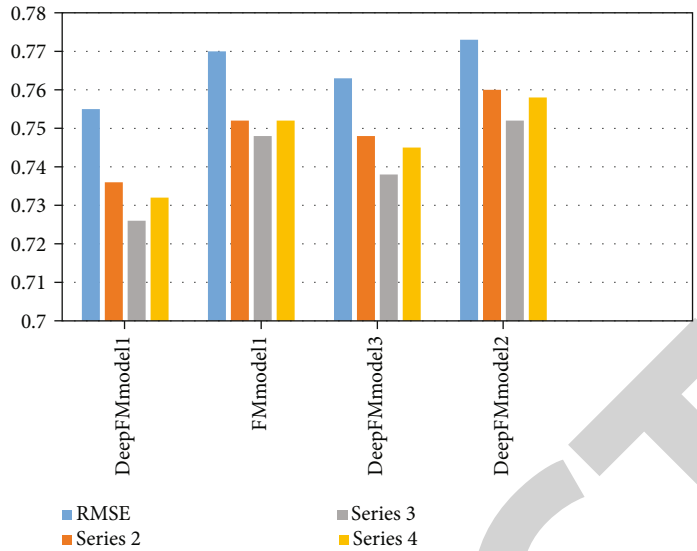

Figure 1: RMSE value of each model with the increase of iteration times.

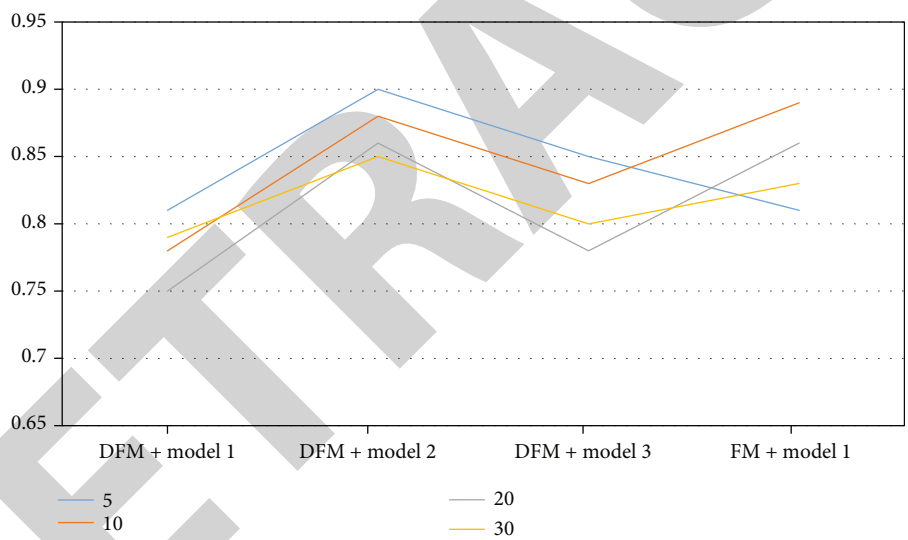

Figure 2: Comparison of MAE values of various models.

Table 1: MAE values of each model with the increase of iteration times.

Iteration times	DFM + Model 1	DFM + Model 2	DFM + Model 3	FM + Model 1
5	0.81	0.90	0.85	0.87
10	0.78	0.88	0.83	0.85
20	0.75	0.86	0.78	0.82
30	0.79	0.85	0.80	0.81

emergence of intelligent teaching system; it is an abstract representation and description of learners' characteristics. Its core elements are learner information and learner characteristics. It is a mathematical model mainly including learners' cognitive level, emotional attitude, learning style, and demographic information, and it is an important component of personalized learning support service system.

3. Related Learner Modeling Techniques

3.1. Learning Analysis Techniques. Facing the huge and complicated educational data, however, the previous statistical calculation methods cannot deal with data sets with different properties, and the computational complexity will increase with the increase of the number of features, the processing effect for high-dimensional sparse data is poor, and the data analysis cannot achieve the expected effect. Under the support of statistics, artificial intelligence, machine learning, and other fields, learning analysis technology came into being. Learning

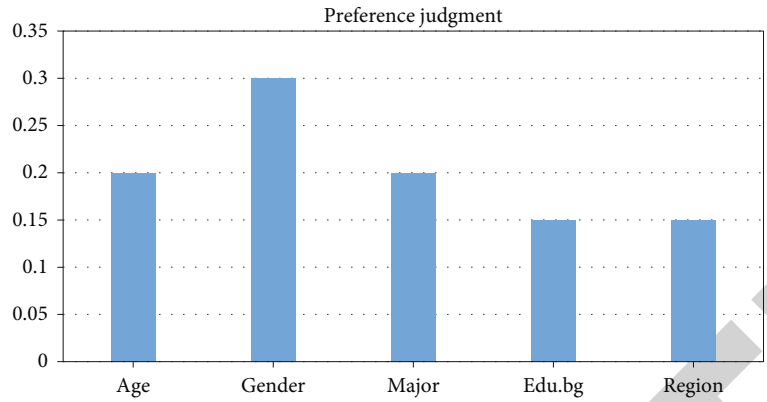

Figure 3: Influence degree of various factors on user preference.

analysis technology refers to the use of educational data mining implicit information that can reflect learning preferences to build a model, so as to predict learners' learning situation, so as to make benign intervention on learning or provide learning support services for learners. It is a decision-making aid tool. Learning analysis technology helps teachers to better understand learners, optimize teaching, and help learners learn independently and individually. In recent years, learning analysis technology is widely used in various fields of education, and it is becoming more and more common.

3.2. Factorize. Factorization machine is a commonly used decomposition model. Compared with the traditional factorization model, the factorization machine has unlimited number of features, strong expansibility, as well as the fickle characteristic change pattern; it can not only deal with complex data well, but also deal with high-dimensional data well.

For an n-dimensional eigenvector x, $X = (x_1, x_2 . \cdots x_n) \in R^n$, where $x_1, x_2 . \cdots x_n$ is not independent of each other and y_i is the predicted value of the corresponding target. When $n = 2$, the expression is

$$y(x) = w_0 + \sum_{i=1}^{n} w_i x_i + \sum_{i=1}^{n} \sum_{j=i+1}^{n} < v_i, v_j > x_i x_j, \quad (1)$$

where $w_0 \in R, w \in R^n, x_i x_j$ represents the interaction of eigenvectors x_i and x_j and the coefficient matrix, $V \in R^{n \times k}$, $<v_i, v_j>$, is the dot product of vectors v_i and v_j of size K, and the expression is

$$<v_i, v_j> = \sum_{f=1}^{k} v_{i,f} \cdot v_{j,f}, \quad (2)$$

where $k \in N^+$ is the hyperparameter that defines the decomposition dimension and $v_{i,j}, v_{j,f}$ is the hidden factor of the hidden vector corresponding to the feature vectors x_i and x_j, respectively.

The factorizer can decompose the transformation between a large value and a small function and then use the product of$v_i$and$v_j$for predictive modeling, which can effectively alleviate the problems caused by sparse data and improve the efficiency of recommendation.

Table 2: Statistical basic data of general characteristics of users.

Number of users	Number of courses	Number of features
2311	124	6

3.3. Deep Learning. RNN can hold internal information, so it can accurately predict the next information according to the previous input information, especially in the in-depth understanding of context, and plays a huge role. Hochreiter and Schmidhuber proposed a memory network at any time. In the LSTM structure, there are three gates: forget gate, input gate and output gate, and memory status. Red represents bitwise operation of elements, yellow represents neural network layer, and the arrow indicates the cell state, where the information is stable. There are two parts here: First, the input gate layer determines what value we will update; then, a tanh layer creates a new candidate value vector, which is added to the state. Next, the cell state is updated, and finally the output gate determines the information to be output based on the cell state. For example,

$$f_i = \sigma\left(w_f[x_i, h_{i-1}] + b_f\right). \quad (3)$$

Formula (3) is the formula of forgetting gate, and its content is x_i and h_{i-1} and outputs the value of each number in the cell C_{i-1}. 1 means "completely retained," and 0 means "completely discarded."

In Formulas (4) and (5), C represents the vector of new values, and I_i determines what value is updated:

$$I_i = \sigma(w_I[x_i, h_{i-1}] + b_I), \quad (4)$$

$$C = \tanh\left(W_c[x_i, h_{i-1}] + bc\right), \quad (5)$$

$$C_i = f_i^* C_{i-1} + I_i^* C_i. \quad (6)$$

Formula (6) indicates that an individual's emotional state changes fromC_{i-1}toC_i, $f_i^* C_{i-1}$, means to discard the information determined to be discarded in the previous step,

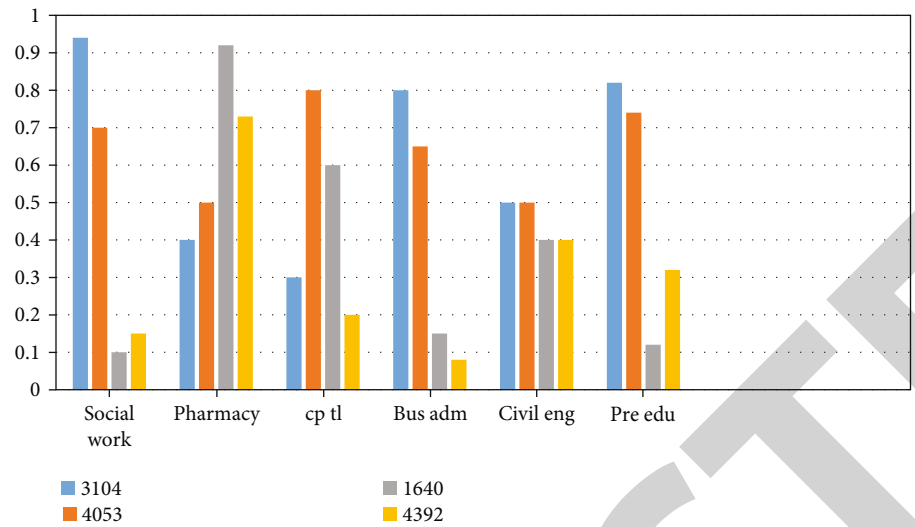

Figure 4: Distribution of elective courses for students of different majors.

which is the new candidate value vector

$$o_i = \sigma(W_0[x_i, h_{i-1}] + b_0), \tag{7}$$

$$h_i = o_i^* \tanh(C_i). \tag{8}$$

Equation (7) represents the state to be outputted and then is processed by Equation (8) to obtain a value between -1 and 1 and determine the part to be outputted.

3.4. Long-term and Short-term Memory Networks Based on Attention Mechanism. Standard memory neural networks cannot distinguish emotions in sentences. The attention mechanism in deep learning is similar to the selective attention mechanism of human beings. When different emotions appear, we can grasp the important parts of sentences. The ultimate goal is to select the information that is more critical to the current goal from the information and ignore the irrelevant information. Therefore, the attention mechanism can also reduce the computation of deep learning, which is the shortcoming of LSTM neural network. In order to solve this problem, Ren et al. proposed a variant of LSTM, that is, by introducing attention mechanism, a long-term and short-term memory network based on attention mechanism was proposed, which can capture key parts of sentences to respond to given aspects. The mathematical expressions are shown below:

$$M = \tanh\left(\begin{bmatrix} W_h H \\ W_v v_a \otimes e_N \end{bmatrix}\right), \tag{9}$$

$$\alpha = soft\max\left(w^T M\right), \tag{10}$$

$$r = H\alpha^T, \tag{11}$$

$$h^* = \tanh\left(W_{n^r} + W_x h_N\right). \tag{12}$$

where $M \in R^{(d+d_a)*N}$, N represents the sequence length of the sentence, H represents the hidden node of the input sentence, Formula (12) is the final prediction formula, W_{p^r} and W_x are the parameters to be learned in the model, h^* represents the sentence feature representation of the given input aspect, and h_N represents the hidden vector of the last layer of the hidden layer.

3.5. Deep Neurofactorization Machine. The factorization machine (FM) can reduce the dimension of high-dimensional data, but it can only model the low-order data linearly, while neural network can model the high-order data nonlinearly, but the parameter estimation will be very complicated when the data is sparse. In view of this, Guo and others put forward the Deep Neurofactorization Machine (DeepFM). DeepFM combines FM with DNN that can simulate both low-order feature interaction and high-order feature interaction, and DeepFM can carry out end-to-end training without any feature engineering. Its training mode is as follows:

$$y = \text{sign}\ moid(y_{FM} + y_{DNN}), \tag{13}$$

where y_{FM} is the output of FM component, y_{DNN} is the output of Deep component, and y∈ (0, 1) is the prediction result of DeepFM. The expression for Va is as follows:

$$y_{FM} = \langle w, x\rangle + \sum_{i=1}^{d}\sum_{j=i+1}^{d}\langle V_i, V_j\rangle x_i \cdot x_j, \tag{14}$$

where$\langle w, x\rangle$represents the first-order feature, the inner product represents the second-order cross feature, and the expression of$y_{DNN}$is shown below:

$$a^{(l+1)} = \sigma\left(w^{(l)} a^{(l)} + b^{(l)}\right), \tag{15}$$

$$y_{DNN} = W^{|H|+1} \cdot a^{|H|} + b^{|H|+1}, \tag{16}$$

where σ represents the activation function, l is the number of layers of DNN, $w^{(l)}$ represents the weight of DFM, $a^{(l)}$ represents the output of layer l, $b^{(l)}$ is the bias term, and $|H|$

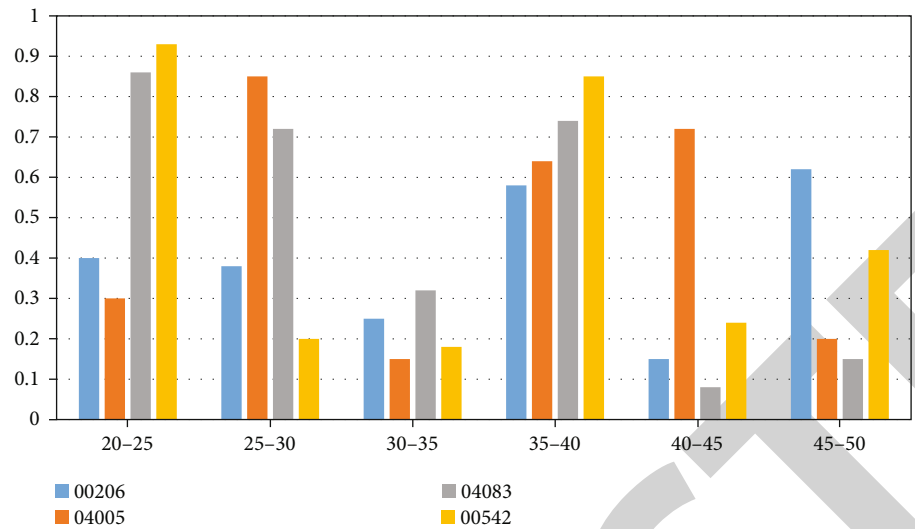

Figure 5: Distribution of elective courses of students of different ages.

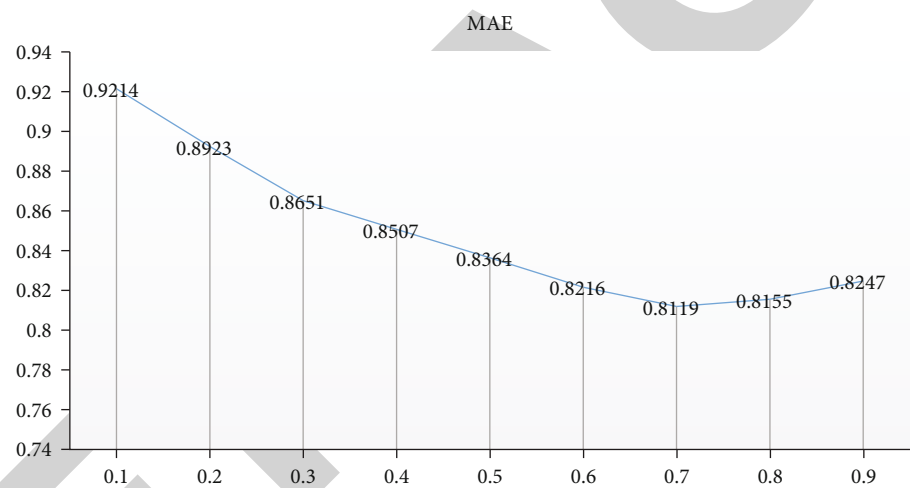

Figure 6: Effect of different μ values on MAE.

Table 3: Variation of MAE value with user's professional weight.

$\mu 1$	0.1	0.2	0.3	0.4	0.5	0.6	0.7	0.8	0.9
MAE	0.9214	0.8923	0.8651	0.8507	0.8364	0.8216	0.8119	0.8155	0.8247

represents the number of hidden layers. After Formula (15) is completed, a predicted value is generated. The so-called activation function is a function running on the neurons of artificial neural network, which is responsible for mapping the input of neurons to the output.

The data of depth neurofactors are input from deep to hidden places. If you report an error, the parameters will be adjusted to the allowable error range and then output through the output layer of the hidden layer. Different levels will be constantly adjusted, and the parameters will be trained in this mode, so as to complete the learning of the data by the model. Average loss function can improve the efficiency of the model:

$$L_{reg} = \sum_{x \in D} \left(r'_{u,i}(x) - r_{u,i}(x) \right)^2, \tag{17}$$

where D represents the training set and $r_{u,i}(x)$ is the user's satisfaction score with Series I.

3.6. Input Vector Representation of Decomposer. Feature recommendation has the greatest influence after use. On the basis of the established researcher function, the study describes this method from many aspects. Popular courses are determined by course scores, course participants, and score participants.

The formula is shown below:

$$Popularity(i) = AS_i * NP_i/CP_i, \tag{18}$$

where $Popularig\ (i)$ represents the popularity of the first course, AS_i represents the average score of the first course, NP_i represents the number of people who participated in the scoring, and CP_i represents the number of people who signed up for the course.

Prediction accuracy is the most commonly used evaluation index in recommendation field. RMSE represents the sum of squares of the deviations of two values and the square root of the data set m, calculated by

$$RMSE(x, h) = \sqrt{\frac{1}{m}\sum_{i=1}^{m}\left(h\left(x^{(i)}\right) - y^{(i)}\right)^2}. \tag{19}$$

MAE is calculated by

$$MAE(x, h) = \frac{1}{m}\sum_{i=1}^{m}\left|h\left(x^{(i)}\right) - y^{(i)}\right|. \tag{20}$$

The data obtained are more accurate when the root mean square error and absolute error values are small. In the field of information retrieval and statistics, accuracy and recall are measures and indicators to check experimental performance, which have been widely used. The calculation formulas of accuracy and recall rate are as follows:

$$Precision = \frac{TP}{TP + FP}, \tag{21}$$

$$Recall = \frac{TP}{TP + FN}. \tag{22}$$

Precision refers to the proportion of items that users are interested in recommended by the recommendation system in all recommendation lists. The higher the accuracy, the better the performance and better the effect of the algorithm. Recall refers to the proportion of the correct items recommended by the recommendation system in all the items that users are interested in. Similarly, the larger the ratio, the higher the coverage rate and the better the effect.

Prediction accuracy is the most widely used evaluation index in the recommended field as defined below:

$$MAE = \frac{\sum_{n=1}^{N}|pi - qi|}{N}, \tag{23}$$

$$RMSE = \sqrt{\frac{\sum_{n=1}^{N}(pi - qi)^2}{N}}, \tag{24}$$

where $\{pl, p2 \cdots pn\}$ is the user rating set predicted by the recommendation algorithm and $\{q1, q2 \cdots qn\}$ is the actual user rating set. The smaller the RMSE and MAE, the smaller the error between the predicted user score and the actual user score, and the higher the recommendation quality; on the contrary, it shows the lower the recommendation quality.

4. Comparative Experimental Selection

4.1. Selection of Curriculum Recommendation Indicators. In order to verify the feasibility of the proposed model, the learner model with emotion (Model 1), the learner model without emotion (Model 2), and the learner model with learner emotion (Model 3) are applied course recommendations to compare the advantages and disadvantages of the three methods. The experimental steps are divided into three steps:

(1) DeepFM is used to recommend courses based on courses: In the absence of an emotional state, this model can accurately reflect learners' learning hobbies

(2) Based on Model 3, DeepM is used for course recommendation: Being able to tell by integrating learners' aspect motion can reflect learner preference than simply integrating learners' whole emotion

(3) The course recommendation based on FM model 1 is based on the classical FM, and the traditional recommendation technology can also achieve good results in judging the learner model, while the recommendation accuracy of the deep learning technology is higher than that of the general FM

4.2. Experimental Data Analysis. Figure 1 is the root mean square error values recommended by Models 1, 2, and 3 that is calculated and counted using a factorizer, and the error Model 1-based data values use the traditional values' recommendation course. It is shown from the figure that with the increase of iteration times, the error value is constantly changing. When the number of times is 30, the error values when the accuracy is the highest, DFM and FM, are the lowest, so as to achieve the best state. The error value of DFM is the lowest in Model 1, followed by DFM recommendation based on Model 3, and finally DFM course recommendation based on Figure 2.

The comparison of MAE values of each model in Figure 2 shows that when the iteration times are 30, the sum of absolute values of the difference between the target value and the predicted value of Model 2 recommended by DeepFM is the largest; Model 3 recommended by DeepFM is the smallest.

The number of iterations in Table 1 refers to the gradual increase in the number of course recommendations for various models.

Table 1 shows the values calculated using a neural factorize, the RMS error values for the courses recommended by Model 1, Model 2, and Model 3, and the average of the absolute errors recommended by Model 1 using traditional FM recommendations. The data shows that when the number is 20, anyone of the course recommendation model is used, and which decomposition technology is based on, the average recommendation value of Model 1 is the smallest, and

DFM based on the same learning recommendation model has better performance and other aspects than FM.

4.3. Predictive Score Based on Statistical User Characteristics. At first, in the course recommendation system, the course recommendation algorithm often lacks considering the influence of user attributes on the results. Recommendation performance for new users is poor, but in practical application scenarios, the user feature attributes also affect recommendation accuracy. The users with the same attributes have similar preferences for courses. The distribution of users on different features is counted, and the factors that have great influence on the popularization of curriculum application are found. The weighted summation of the features is used to obtain the prediction score based on the statistical user characteristics.

Figure 3 shows that the common characteristics of users usually include the following: age, gender, major, occupation, region, educational background, and income. Usually these attributes will affect the judgment of users' preferences. Analyzing Figure 3, gender has the greatest influence on the judgment of user preference. Secondly, age and major, educational background and region, income, occupation, and so on have little influence on user preference judgment.

Through the statistical analysis of the data in Table 2 on the characteristics of users' age, gender, major, occupation, region, and educational background, the two characteristics with the largest gap in the number of students who choose the same course under different user characteristics are selected as the most important factors affecting the recommendation results. The statistical results are shown in Figures 4 and 5, and it is found that the major and age of users have the greatest influence on the course recommendation results.

However, a course may become a popular course because of its short class hours or kind attitude of teachers so that the F value calculated by any user will be very large and popular courses are largely recommended to target users. However, the courses that users choose less become unpopular courses, but these courses will also be helpful to different users. Therefore, the attenuation factor is introduced to give less weight to popular courses, thus reducing its influence on recommendation results.

The ordinate in Figure 6 represents the effect of different μ values on the sum of the absolute values of the difference between the target value and the predicted value.

In order to further determine the importance of user's specialty and age on course recommendation, the user's specialty weight μ is set between 0 and 1, and the value m which is beneficial to give the best recommendation result is found according to the average absolute error of users with different characteristics. According to the curve trend in Figure 6 and the average absolute error of user's professional characteristics in Table 3, it can be seen that the best recommendation result can be obtained when the weights of user's professional and age are 0.7 and 0.3, respectively.

According to the above analysis, we can draw a conclusion that whether using DFM or FM for personalized curriculum recommendation, Model 1 has the highest accuracy in the field of curriculum recommendation, and on the basis of Model 3, the accuracy of DFM curriculum recommendation is higher than other models. All this shows that the emotional state characteristics of learners play a key role in improving the accuracy of curriculum recommendation. In this study, the fusion of emotional factors is to build a model to improve and make up for the general model of emotional state deficiencies.

5. Conclusion

In this paper, emotional factors are integrated into the model and applied to online courses in colleges and universities and recommendation in universities after integrating emotional factors, and the personalized and accurate course recommendation for learners is realized by using matrix neural factorization. And then, after setting up the experimental group and comparing it, the experiment shows that the model of curriculum recommendation with affective factors has less error and better effect, while the learner model without emotional factors has higher recommendation accuracy, and the learner model with emotional factors has higher recommendation accuracy. Under the same model, DFM has higher accuracy than FM. This shows that the modeling calculated in this article is very useful and that whether learner's attitude is positive or not is the key to accurately describe the learning preference, as well as the advantages of learning recommendation technology applied to courses in various aspects. This study provides a reference for the study of learner model from the theoretical inquiry level to the practical application level.

Although this study has realized the application of learner model, it is not deep enough in the application field, only using deep learning technology to make recommendation, and lacks in-depth research on recommendation methods. In order to obtain higher recommendation accuracy, it is necessary to conduct in-depth research on recommendation methods based on learner model in the later stage.

Data Availability

The experimental data used to support the findings of this study are available from the corresponding author upon request.

Conflicts of Interest

The authors declared that they have no conflicts of interest regarding this work.

References

[1] R. E. Petty, L. R. Fabrigar, and D. T. Wegener, "Emotional factors in attitudes and persuasion," *Handbook of Affective Sciences*, vol. 12, no. 2, pp. 235–355, 2003.

[2] M. Laukenmann, M. Bleicher, S. Fuß, M. Gläser-Zikuda, P. Mayring, and C. von Rhöneck, "An investigation of the influence of emotional factors on learning in physics instruction," *International Journal of Science Education*, vol. 25, no. 4, pp. 489–507, 2003.

Hindawi
Journal of Sensors
Volume 2024, Article ID 9860895, 1 page
https://doi.org/10.1155/2024/9860895

Retraction

Retracted: Research on Interior Design and Space Layout Optimization Based on Multi-Intelligent Decision-Making

Journal of Sensors

Received 23 January 2024; Accepted 23 January 2024; Published 24 January 2024

This article has been retracted by Hindawi following an investigation undertaken by the publisher [1]. This investigation has uncovered evidence of one or more of the following indicators of systematic manipulation of the publication process:

(1) Discrepancies in scope
(2) Discrepancies in the description of the research reported
(3) Discrepancies between the availability of data and the research described
(4) Inappropriate citations
(5) Incoherent, meaningless and/or irrelevant content included in the article
(6) Manipulated or compromised peer review

The presence of these indicators undermines our confidence in the integrity of the article's content and we cannot, therefore, vouch for its reliability. Please note that this notice is intended solely to alert readers that the content of this article is unreliable. We have not investigated whether authors were aware of or involved in the systematic manipulation of the publication process.

Wiley and Hindawi regrets that the usual quality checks did not identify these issues before publication and have since put additional measures in place to safeguard research integrity.

We wish to credit our own Research Integrity and Research Publishing teams and anonymous and named external researchers and research integrity experts for contributing to this investigation.

The corresponding author, as the representative of all authors, has been given the opportunity to register their agreement or disagreement to this retraction. We have kept a record of any response received.

References

[1] J. Dong and M. Ran, "Research on Interior Design and Space Layout Optimization Based on Multi-Intelligent Decision-Making," *Journal of Sensors*, vol. 2022, Article ID 7158921, 10 pages, 2022.

Hindawi
Journal of Sensors
Volume 2022, Article ID 7158921, 10 pages
https://doi.org/10.1155/2022/7158921

Research Article

Research on Interior Design and Space Layout Optimization Based on Multi-Intelligent Decision-Making

Jian Dong and Meng Ran

HBU-UCLan School of Media Communication and Creative Industries, Hebei University, Baoding 071000, China

Correspondence should be addressed to Meng Ran; ranmeng@hbu.edu.cn

Received 14 March 2022; Revised 6 April 2022; Accepted 16 April 2022; Published 13 May 2022

Academic Editor: Han Wang

In order to meet people's diverse, complex, and changeable living requirements and aesthetic requirements, it is necessary to rationalize the design of indoor three-dimensional space. The optimization of the indoor environmental space layout is affected by the energy consumption and rationality of functional areas, resulting in indoor environmental space The performance of the layout optimization system deteriorates. In order to improve the performance of the indoor environment spatial layout and meet the living needs of more people, this paper proposes an optimal design of a spatial layout based on multi-intelligence decision-making. The research results of the article show that (1) the average confidence and the average recognition time of logo set *B* are both smaller than those of logo set *A*, indicating that logo set *B* is easier to be recognized by users in the same commercial building environment and can be more quickly recognized. In terms of discrimination, the time used to correct the misrecognition of identification set *B* is shorter than that of identification set *A*, which means that the different types of identifications in identification set *B* are easier to distinguish. (2) The spatial positioning algorithm proposed in this paper has good reliability and practicability, high positioning accuracy, and small error for indoor spatial coordinate positioning. Compared with the traditional method, the projection method of this paper has a significantly smaller error, and the maximum error is only 0.272, which makes the indoor space design more rational. (3) Comparing the energy consumption coefficients of the three spatial layout optimization systems, it can be seen that the indoor environmental spatial layout optimization system based on multi-intelligence decision-making has the lowest energy consumption when optimizing the indoor environmental spatial layout, because the system is in the design process. The indoor environment space layout model is designed, which effectively reduces the energy consumption of the indoor environment space layout optimization. When the indoor environment space layout optimization system based on multi-intelligence decision-making is used to optimize the indoor environment space layout, the average optimization accuracy is 98.32%, while the average indoor environment space layout optimization accuracy of the space layout optimization system with curved shading space layout optimization is 42.2% %, the layout optimization of binocular stereo vision space. When optimizing the indoor space layout, the average optimization accuracy is 70.87%.

1. Introduction

The optimal design of indoor environmental space layout refers to the corresponding arrangement of environmental space and home equipment in a given indoor environmental space, so that the indoor items can not only meet people's use functions but also meet people's aesthetic requirements and improve the efficiency of using the indoor environment space. In this paper, an improved point source perturbation method for the optimization of indoor environment spatial layout is designed, which realizes the collimation of the light emitted by the refractive power of a single free surface [1]. The article introduces an optimization tool and optimization algorithm for integrating CAD software in order to

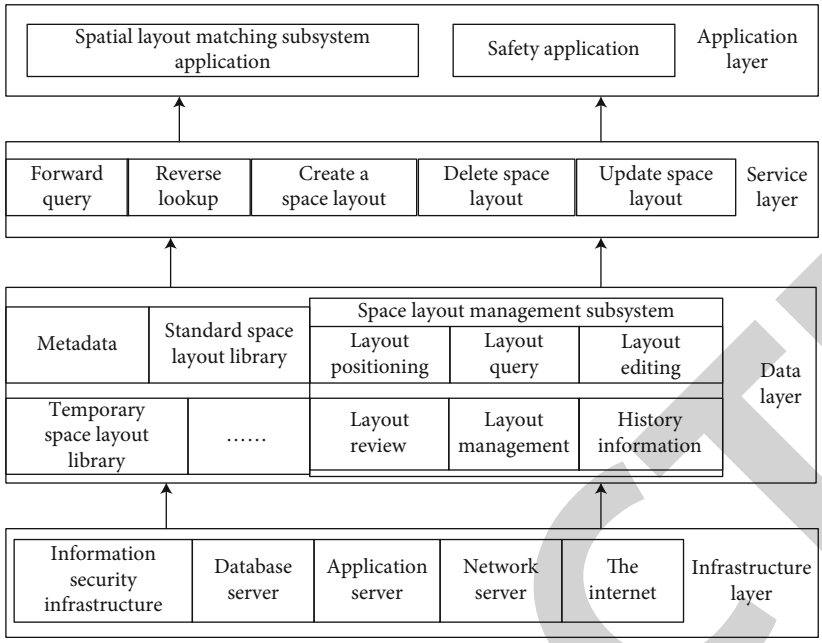

Figure 1: Spatial layout management and matching system.

automatically find the 3D layout of satellite equipment [2]. This article briefly introduces the RV and studies the layout optimization of the interior space of the RV from four aspects [3]. This article analyzes several typical small high-rise apartments in Shenzhen and discusses the optimization of small apartment space from the aspects of overall layout, model design, space utilization, etc. [4]. The article proposes an algorithm for optimal grip planning and fixture synthesis [5]. This paper proposes an optimization method to estimate the 3D indoor Manhattan scene layout from a single input image, and the algorithm can be applied to real images of multiple indoor scenes [6]. The article introduces a virtual environment for the vehicle interior layout design in order to design new defensive and security vehicles [7]. This paper introduces the development status, existing problems, and solutions of spatial layout technology in my country [8]. This paper focuses on the analysis and research on the optimal design of the interior space of the RV from the four aspects of the interior space layout, ergonomics, vehicle balance, and lightweight [9]. The article discusses the specific application of the furniture design in the interior space and the specific application of the furniture design in the interior space [10]. Based on the analysis of the limitations of traditional design methods, this paper designs an improved indoor environment spatial layout optimization method [11]. The article describes the gradual decline of the average area of residential commercial housing in my country, illustrating the importance of the layout optimization design [12]. This paper introduces the layout design principles of equipment with better application effect, which provides a friendly human-machine interface and a comfortable environment for radar operators [13]. This paper builds a virtual human body model of a passenger car driver; checks the layout for comfort, field of view, and interior space; and then optimizes design flaws [14]. This paper summarizes the principles of polite design and puts forward the key points of bus optimization design according to the needs of passengers [15].

2. Multi-Intelligent Decision-Making Interior Design and Space Layout

2.1. Basics of Indoor Space Layout. The indoor scene corresponds to the outdoor scene, and it is an important place for people to produce and live. In addition to realizing its basic production and life functions, indoor scenes also need to meet people's spiritual pursuits. Thus, the interior design was born as a professional discipline. The key to interior design is to use the principles of architectural design to endow the interior environment with specific functions according to the nature, environment, and standards of the interior space [16]. Indoor scenes are usually presented in the form of a certain layout. The layout is also the most distinctive feature of indoor scenes, and it is the attribute that best reflects the characteristics of indoor scenes. Therefore, indoor space layout has also become a key link in interior design. With the rapid development of 3D technology, 3D models of indoor scenes are gradually applied to more and more fields, such as CG animation movies, 3D game scenes, and virtual reality environments [17]. These applications often contain interactive indoor scenes that players can enter and explore. The urgent need for indoor scene modeling has directly spawned related research on indoor space layout. Although there are many research works on indoor space layout in academia, few mature research schemes are applied to practical applications.

Table 1: Typical shopping malls and floor plans.

Name	Flat	Interior photo
Shopping mall one		
Shopping mall two		
Shopping mall three	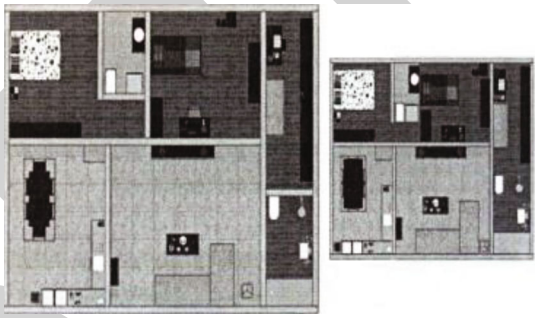	

2.2. Basic Data Module of Indoor Environment Layout. The basic data module of the indoor environment space layout includes the indoor environment space matching system, space layout information portal, space layout metadata service system, and space layout optimization management system. The basic data of the indoor environment space layout is extracted from the above subsystems. The spatial layout matching system is shown in Figure 1.

2.3. Research Significance of Spatial Layout. The automatic design and optimization of indoor space layout has important research significance [18]. On the one hand, due to the important application background of the indoor space layout in many fields, on the other hand, the traditional layout design relies heavily on labor and is inefficient. The existing layout design methods are simple and immature, with unsatisfactory effects and artificial A series of problems such as complex interaction. The automatic design and optimization of interior space layout can greatly reduce the workload of designers and even serve users directly. In the process of space design, simulation follows the designer's design thinking and realizes automatic design, which greatly

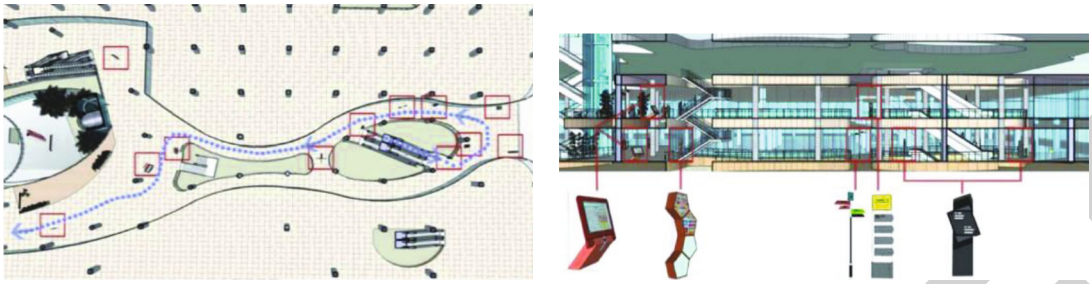

(a) Marking distribution plan (b) Sectional drawing of marking location

Figure 2: Schematic diagram of local space identification location.

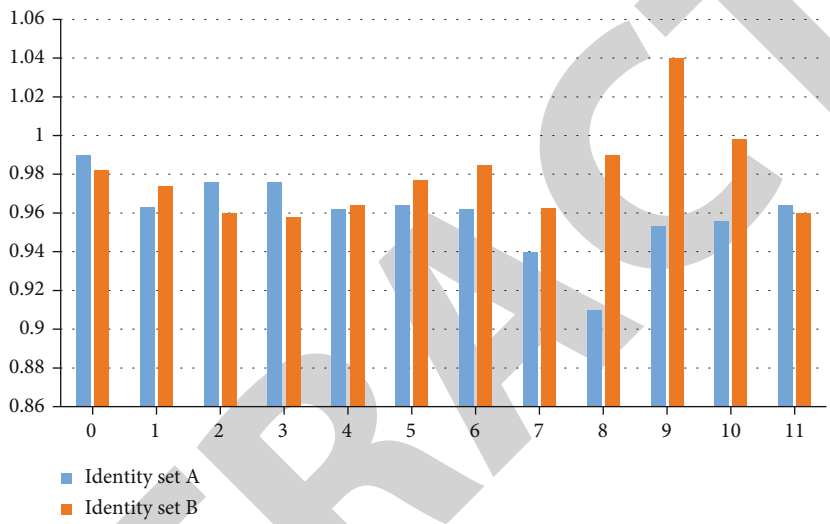

Figure 3: Mean confidence of the two sets of set identifiers.

reduces the designer's workload and improves the efficiency and workload of layout design. The biggest disadvantage of manual layout is that it will be limited by the professional ability and knowledge level of the designer, and the use of computer assistance will often achieve better results than manual design.

3. Interior Design and Space Layout Optimization Research

3.1. Establish the Indoor Environment Spatial Layout Model. The entrance position of the indoor environment space is normalized to obtain the normalized entrance door coordinate (E_x, E_y) of the indoor environment space, the indoor width is W, and the indoor length is L; then, the normalized entrance door coordinate is

$$E_x = \frac{E_{x_0}}{W}, \tag{1}$$

$$E_y = \frac{E_{y_0}}{L}. \tag{2}$$

Table 2: Matrix experimental data.

Spatial location	α_{00}	α_{01}	α_{10}	α_{11}
P1	0.55259	0.46108	-0.68205	0.33671
P2	0.52257	0.48667	-0.66375	0.33970
P3	0.53231	0.48636	-0.66795	0.34525
P4	0.52823	0.46011	-0.69036	0.36952
P	0.53656	0.46935	-0.68923	0.33600

Table 3: The projection error of the marked point picked by the space model.

Projection error	First picture	Second picture	The third
Maximum error	2.21	1.86	1.44
Average error	1.03	0.73	0.76
Standard deviation	0.25	0.52	0.21

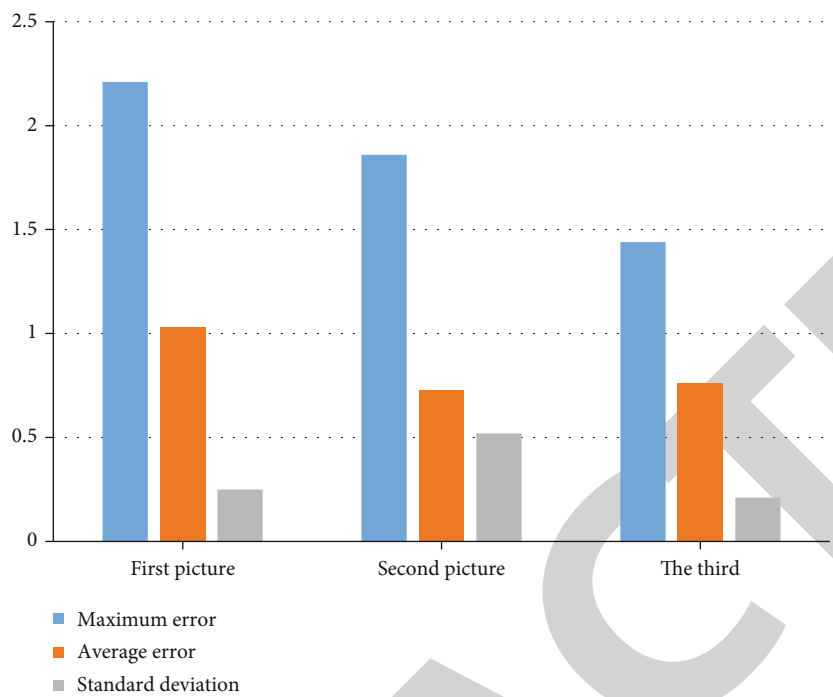

Figure 4: Projection error statistics.

The two-dimensional covariance matrix of the indoor environment [19]:

$$C_{2\times 2} = \begin{bmatrix} \operatorname{cov}(x,x) & \operatorname{cov}(x,y) \\ \operatorname{cov}(y,x) & \operatorname{cov}(y,y) \end{bmatrix}, \tag{3}$$

$$\operatorname{cov}(x,y) = \operatorname{cov}(y,x). \tag{4}$$

The geometric feature F of the indoor environment space is [20]

$$F = (E_x, E_y, S, R, C). \tag{5}$$

Among them, S is the area of the indoor environment space, the ratio of the length to the width of the indoor environment space is R, and the extension of the indoor environment space is C.

The location coordinates of the indoor environment space are

$$x_p = \frac{x}{W}, \tag{6}$$

$$y_p = \frac{y}{L}. \tag{7}$$

Among them, x represents the coordinate value of the position point of the indoor functional area on the x-axis of the indoor environment space layout coordinate system, and y represents the coordinate value of the indoor functional area location point on the y-axis of the indoor environment space layout coordinate system.

Table 4: Experimental results of spatial positioning.

Spatial location	Move1	Move2	Move3
P1	X: 21.1246 Y: 61.0321	X: 19.5467 Y: 60.5479	X: 20.8795 Y: 61.35668
P2	X: 80.9624 Y: 98.9722	X: 78.3256 Y: 012356	X: 81.2236 Y: 00.5625
P3	X: 198.9726 Y: 11.3709	X: 11.3546 Y: 209.2153	X: -112.0566 Y: 210.3705
P4	X: -152.0766 Y: 161.7352	X: -149.0324 Y: 158.7886	X: -151.4567 Y: 159.2356

Table 5: Automatic extraction of projection errors from spatial models.

Projection error	First picture	Second picture	The third
Maximum error	0.131	0.272	0.084
Average error	0.031	0.035	0.029
Standard deviation	0.026	0.028	0.012

Orientation attribute of indoor environment space:

$$\theta_p = \theta \cdot \frac{2}{\pi} + 1. \tag{8}$$

Indoor environment spatial scale [21]:

$$l_p = \frac{l_y}{L}, \tag{9}$$

$$w_p = \frac{l_x}{W}. \tag{10}$$

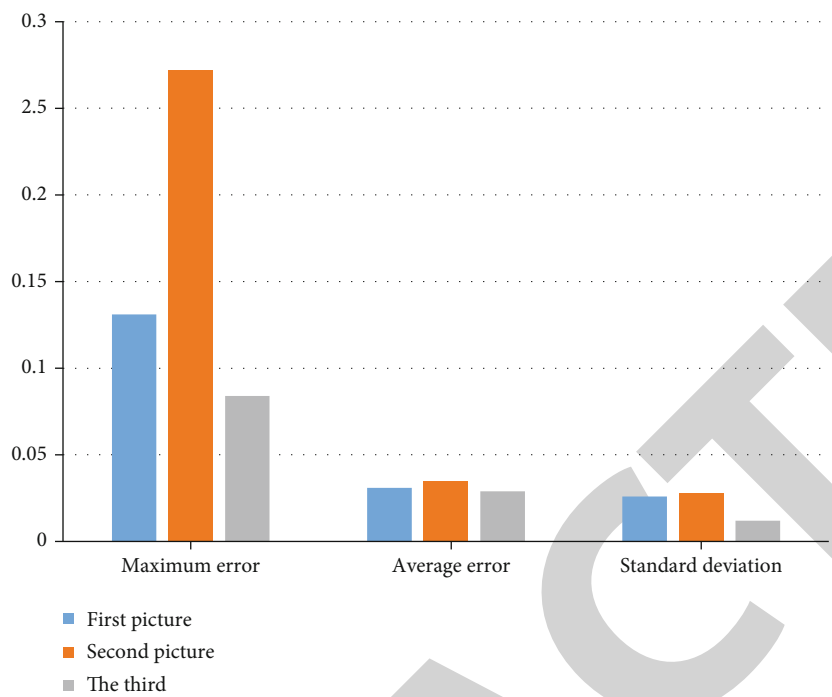

Figure 5: Projection error statistics.

Get the layout properties of the indoor functional area in the indoor environment space:

$$\pi(G) = \left(x_p, y_p, \theta_p, l_p, w_p\right). \tag{11}$$

Energy consumed in indoor environmental space:

$$E = a_1E_1 + a_2E_2 + a_3E_3 + a_4E_4. \tag{12}$$

Build an indoor environment space layout model:

$$M = \min E(\pi(G), F). \tag{13}$$

Calculate the fitness of a single indoor environment spatial layout:

$$\text{fitness}(i) = \frac{D}{f(R_i)}. \tag{14}$$

The probability that the spatial layout is selected is

$$p_i = \text{fitness}(i)\sum_{i=1}\text{fitness}(i). \tag{15}$$

The cumulative probability of indoor environment spatial layout is

$$Q_i = \sum_{j=1} p_i. \tag{16}$$

Table 6: Test results of energy consumption coefficient.

Time/min	Multi-intelligent decision-making optimization of indoor environment space layout	Surface shading space layout optimization	Binocular stereo vision spatial layout optimization
2	0.8	4.2	2.8
4	1.7	2.8	4
6	1.2	4.2	2.83
8	1.4	3.3	3.1
10	0.4	5.3	1.9
12	1.2	4	3.2
14	0.8	4.2	2.8

The crossover probability for the indoor environment layout is [22]

$$P_0 = \frac{g}{2d} + \frac{f_i\bar{f}}{2\left(f_{\max}\bar{f}\right)}. \tag{17}$$

3.2. Optimizing the Multilevel Layout of Spatial Features. The multilevel simulation model of spatial characteristics is used as the population, the population is initialized, and the fitness of different individuals in the entire population is calculated [23]:

$$f(i) = \frac{k}{f(U_i)}. \tag{18}$$

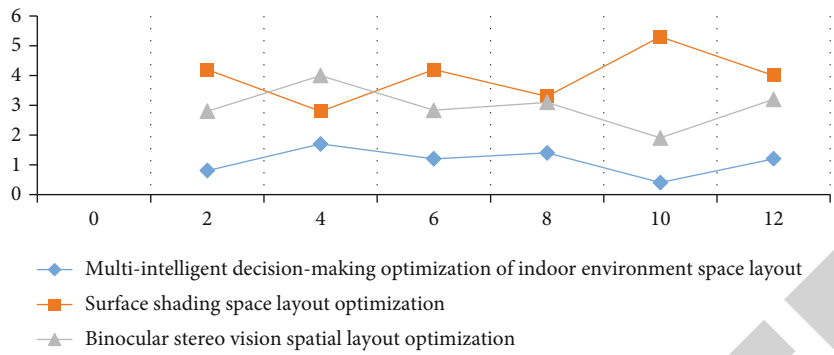

Figure 6: Test results of energy consumption coefficient.

The probability of an individual being selected in the population fitness [24]:

$$V_i = f(i)\sum_{i=1} f(i). \tag{19}$$

Cumulative probability of individuals in population fitness:

$$R_i = \sum_{j=1} V_i. \tag{20}$$

Crossover probability:

$$V_c = \frac{n}{2N} + \frac{f_i f}{2(f_{\max} f)}. \tag{21}$$

4. Simulation Experiments

4.1. Virtual Simulation. The experiment takes the optimization design of the indoor signage system of a commercial building in a shopping mall as an example and studies the design method of commercial building interaction. The purpose of the experiment is to find out the important factors that affect the user's choice of commercial space. The article conducts optimization research on commercial space signs, so as to improve the space awareness. The experiment summarizes and analyzes the indoor layout optimization of several well-known shopping malls in my country and draws on the logo design elements that are widely used and obtains the following plane models, as shown in Table 1.

After summarizing and analyzing the interior designs of the three shopping malls, two sets of different independent styles are obtained and models are established, denoted as set *A* and set *B*, and each set includes several signs of the same type. Logo set *A* is mainly gray in color, with 1 or 2 decorative colors, and the shape is dominated by a single rectangle; set *B* is mainly bright in color, with a variety of decorative colors and shapes. The above are mainly geometric or special shaped. In the experiment, two sets of sign sets were placed in the indoor space of the commercial street in the same distribution and arrangement, and the virtual space as shown in Figure 2 was obtained. Finally, the multi-intelligence decision-making technology is used, roaming in SA and SB with the same route and speed from the user's perspective, and the video data of the roaming field of view in different identification sets for subsequent analysis was obtained.

Table 7: Accuracy test results of indoor environment spatial layout optimization.

Testing frequency	Multi-intelligent decision-making optimization of indoor environment space layout	Surface shading space layout optimization	Binocular stereo vision spatial layout optimization
1	97.2	32.6	64.2
2	98.5	48.7	68.9
3	97.9	39.5	64.8
4	99.2	49.7	72.1
5	98.4	38.9	76.4
6	99.6	37.4	68.6
7	97.1	47.6	72.9
8	98.3	42.8	73.1
9	99.6	45.1	75.8
10	97.4	39.7	71.9

In terms of the significance of the logo, the confidence score is mainly used as the evaluation standard, which represents the confidence level of the detection model for the currently recognized logo, and corresponds to whether the user "sees clearly" the logo. When the marker is farther from the user, the confidence score is usually lower, and the opposite is true when the distance is closer. Therefore, the confidence score can express the distinctive feature of the logo, that is, whether the logo is easy to identify, easy to find, and so on. In terms of significance, the two sets of schemes have an average time of 0.68 s for all-category recognition of set *A* and an average of 0.46 s for all-category recognition of set B. It takes 0.11 s to correct the misidentification of all categories of set B. The average confidence level of different identification categories of each set of identification sets is shown in Figure 3.

According to the experimental results in Figure 3, we can conclude that the average of the confidence level and the

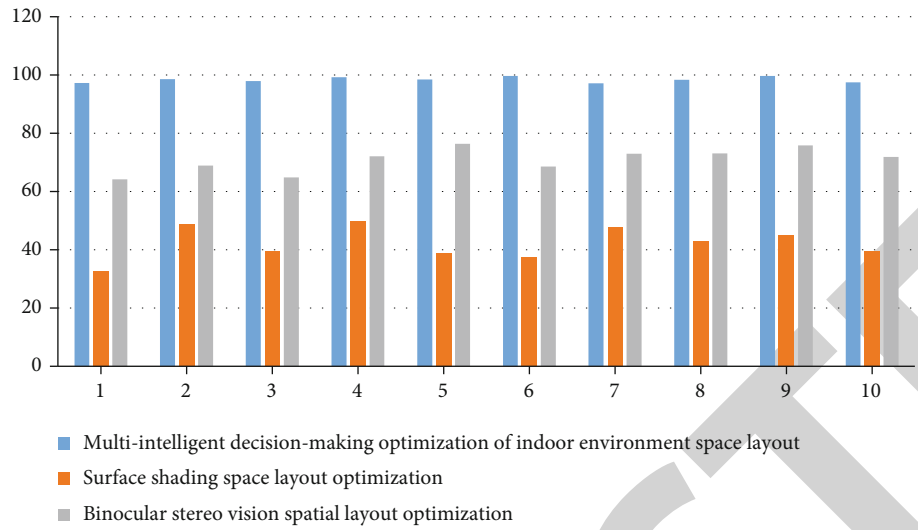

Figure 7: Indoor environment spatial layout optimization accuracy test.

average recognition time of logo set B are both smaller than those of logo set A, indicating that logo set B is easier to be recognized by users in the same commercial building environment. Relevant information can be transmitted more quickly; in terms of discrimination, the time used to correct the misrecognition of set B is shorter than that of set A, indicating that it is easier to distinguish between different types of identities in set B. The color, shape, and expression of the signboard have a great impact on the user's ease of identification and distinction. The B-type identification system in the commercial space is more likely to be noticed and accepted by users than the A-type identification system, indicating that the B-type identification system's morphological expression has higher visual perception. Therefore, the use of eye-catching colors and the use of various colors can effectively improve the ease of identification. The form design of the logo system should break the currently commonly used design methods of focusing on conventional shapes and a set of logos of a single form. The special-shaped combination can effectively improve the distinguishability, and the combination of pictures and text in the identification system is more effective than the simple text expression.

4.2. Analysis of Experimental Results. In the indoor space calibration experiment, the object is placed at any position in the space, the elements of the matrix are calculated, and the average value is obtained. The starting position data is shown in Table 2. According to the experimental data, we can conclude that the matrix elements have good stability.

The experiment selected three photos taken by a digital camera, in which the foreground of the small space was white and the background was black, and marked points were made on the space points. Manually picking the marked points in the space, because the positioning of the mouse picking space is not accurate enough, the solution of the photographic depth value is not accurate enough, and this method has a large error in the space design. The projection errors of the marked points are shown in Table 3 and Figure 4.

Using the article, the indoor space calibration method based on intelligent decision-making algorithm is proposed. Table 4 shows the X and Y coordinates of the actuator moving to different positions in space. The experimental results show that the spatial positioning algorithm proposed in this paper has good reliability and practicability and has high positioning accuracy. It is used for indoor spatial coordinate positioning error is small.

Using the projection error of the algorithm in the article as shown in Table 5 and Figure 5, according to the experimental results, we can conclude that the projection method of the method in this paper has a significantly lower error than the traditional method, and the maximum error is only 0.272, which makes the indoor space design more rational.

4.3. Test Analysis. In order to verify the performance of indoor environment spatial layout optimization based on multi-intelligence decision-making, the experiment introduces the energy consumption coefficient H of indoor environmental spatial layout optimization. The larger the value of energy consumption coefficient H, the higher the energy consumption of indoor environmental spatial layout optimization. The energy consumption coefficient H is used to test the indoor environment layout optimization system of the article and the optimization of the surface shading space layout and the optimization of the binocular stereo vision space layout. The test results are shown in Table 6.

It can be seen from the test results in Figure 6 that during the test process of the indoor environment spatial layout optimization system based on multi-intelligence decision-making, the energy consumption coefficient of indoor environmental spatial layout optimization is always less than 2 with the change of time, indicating that the system optimizes indoor environment The energy consumption of environmental space layout is low; while the space layout optimization system of curved shading shows that when the test time

reaches 10 minutes, the energy consumption coefficient of indoor environmental space layout optimization is as high as 5.5, indicating that the energy consumption of indoor environmental space layout optimization is the highest at this time. The spatial layout optimization system of stereo vision shows that with the change of test time, the energy consumption coefficient of indoor environment spatial layout optimization fluctuates between 2 and 4, indicating that the energy consumption coefficient of the system is high. Comparing the energy consumption coefficients of the three space layout optimization systems, it can be seen that the indoor environment space layout optimization system based on multi-intelligence decision-making has the lowest energy consumption when optimizing the indoor environment space layout, because the system designed the indoor environment in the design process. The environmental space layout model effectively reduces the energy consumption of indoor environmental space layout optimization.

On the basis of testing the energy consumption coefficient of indoor environment space layout optimization, the indoor environment space layout optimization system based on multi-intelligence decision-making, the curved shading space layout optimization system, and the binocular stereo vision space layout optimization system are used to test three systems. The optimal precision of the indoor environment spatial layout. The experimental results are shown in Table 7.

From the test results in Table 7 and Figure 7, it can be seen that when the indoor environment space layout optimization system based on multi-intelligence decision-making is used to optimize the indoor environment space layout, the average optimization accuracy is 98.32%. The average accuracy of environmental space layout optimization is 42.2%, and when optimizing the layout of binocular stereo vision space, the average optimization accuracy is 70.87%. By comparing the optimization accuracy of the three indoor environment space layout optimization systems, it can be seen that the optimization accuracy of the indoor environment space layout optimization system based on multi-intelligence decision-making is the highest. The steps of layout optimization are simpler, which effectively improves the optimization accuracy of the indoor environment space layout.

5. Conclusion

In order to meet people's diverse living needs and aesthetic needs, it is necessary to rationalize the design of interior space and to propose an intelligent and funny interior space design algorithm [25]. The rational design method of indoor space based on multi-intelligence decision-making proposed in this paper is to calibrate the indoor space, estimate the 3D visual space based on the calibration results, and reconstruct the visual space through the calibration results and estimation results, so as to realize the 3D reconstruction of the space. The indoor environment space layout optimization system design proposed in this paper on the basis of multi-intelligence decision-making technology realizes the optimization of the indoor environment space layout through the hardware design and software design of the indoor environment space layout optimization system. The test results show that the system has high performance in terms of energy consumption and optimization accuracy. In the future research, it is necessary to further analyze the hierarchical structure of the indoor environment space layout to improve the rationality of the optimization of the indoor environment space layout.

Data Availability

The experimental data used to support the findings of this study are available from the corresponding author upon request.

Conflicts of Interest

The authors declared that they have no conflicts of interest regarding this work.

References

[1] W. Guo, X. Guo, and Department E E, "Optimization design of spatial layout interior environment in point source small disturbance," *Bulletin of Science and Technology*, vol. 12, no. 3, pp. 11–17, 2016.

[2] Z. Qin, Y. G. Liang, and J. P. Zhou, "An optimization tool for satellite equipment layout," *Advances in Space Research*, vol. 61, no. 1, pp. 21–32, 2018.

[3] Y. H. Chen, "Research on the optimization design of interior space of China's RV," *Construction & Design for Engineering*, vol. 3, no. 12, pp. 112–121, 2018.

[4] Y. Wu, "Optimized interior space design of small high-rising flats," *From Engineering to Sustainability*, vol. 3, no. 10, pp. 52–63, 2008.

[5] Y. Zheng and C. M. Chew, "Efficient procedures for form-closure grasp planning and fixture layout design," *Journal of Manufacturing Science & Engineering*, vol. 131, no. 4, pp. 481–498, 2009.

[6] H. C. Chang, S. H. Huang, and S. H. Lai, "Using line consistency to estimate 3D indoor Manhattan scene layout from a single image," in *2015 IEEE International Conference on Image Processing (ICIP)*, vol. 10no. 3, pp. 11–17, Quebec City, QC, Canada, 2015.

[7] J. Kim, J. Yang, and K. Abdel-Malek, "Task-based vehicle interior layout design using optimization method to enhance safety," *Proceedings of SPIE - The International Society for Optical Engineering*, vol. 10, no. 3, pp. 58–65, 2005.

[8] D. Tomasi, E. C. Caparelli, H. Panepucci, and B. Foerster, "Fast optimization of a biplanar gradient coil set," *Journal of Magnetic Resonance*, vol. 140, no. 2, pp. 325–339, 1999.

[9] B. Liu, "Study on the optimal design of interior space of China's RV," *Applied Energy Technology*, vol. 3, no. 4, pp. 52–63, 2018.

[10] Y. Zheng and N. Zhi, "Application of furniture design in the interior space," *Packaging Engineering*, vol. 10, no. 3, pp. 12–16, 2018.

[11] G. Wenbin, G. Xiaoyong, and Department E E, "Optimization design of spatial layout interior environment in point source small disturbance," *Bulletin of Science and Technology*, vol. 3, no. 4, pp. 11–17, 2016.

Hindawi
Journal of Sensors
Volume 2024, Article ID 9858596, 1 page
https://doi.org/10.1155/2024/9858596

Retraction

Retracted: Intelligent Analysis and Application of Preschool Education Language Teaching Quality Based on Deep Neural Network

Journal of Sensors

Received 30 January 2024; Accepted 30 January 2024; Published 31 January 2024

This article has been retracted by Hindawi following an investigation undertaken by the publisher [1]. This investigation has uncovered evidence of one or more of the following indicators of systematic manipulation of the publication process:

(1) Discrepancies in scope
(2) Discrepancies in the description of the research reported
(3) Discrepancies between the availability of data and the research described
(4) Inappropriate citations
(5) Incoherent, meaningless and/or irrelevant content included in the article
(6) Manipulated or compromised peer review

The presence of these indicators undermines our confidence in the integrity of the article's content and we cannot, therefore, vouch for its reliability. Please note that this notice is intended solely to alert readers that the content of this article is unreliable. We have not investigated whether authors were aware of or involved in the systematic manipulation of the publication process.

In addition, our investigation has also shown that one or more of the following human-subject reporting requirements has not been met in this article: ethical approval by an Institutional Review Board (IRB) committee or equivalent, patient/participant consent to participate, and/or agreement to publish patient/participant details (where relevant).

Wiley and Hindawi regrets that the usual quality checks did not identify these issues before publication and have since put additional measures in place to safeguard research integrity.

We wish to credit our own Research Integrity and Research Publishing teams and anonymous and named external researchers and research integrity experts for contributing to this investigation.

The corresponding author, as the representative of all authors, has been given the opportunity to register their agreement or disagreement to this retraction. We have kept a record of any response received.

References

[1] H. Li and C. Niu, "Intelligent Analysis and Application of Preschool Education Language Teaching Quality Based on Deep Neural Network," *Journal of Sensors*, vol. 2022, Article ID 7548686, 11 pages, 2022.

Hindawi
Journal of Sensors
Volume 2022, Article ID 7548686, 11 pages
https://doi.org/10.1155/2022/7548686

Research Article

Intelligent Analysis and Application of Preschool Education Language Teaching Quality Based on Deep Neural Network

Hongping Li[1] and Chuanming Niu[2]

[1]*Xiangzhong Normal College for Preschool Education, Shaoyang, 422000, China*
[2]*Lu'an Vocational Technical College, Lu'an, 237158 Anhui Province, China*

Correspondence should be addressed to Chuanming Niu; 2001420017@lvtc.edu.cn

Received 14 March 2022; Revised 6 April 2022; Accepted 16 April 2022; Published 10 May 2022

Academic Editor: Han Wang

Language is the cornerstone of children's learning knowledge and exploring the world. Language teaching is an indispensable part of early childhood education, which can help children improve their communication ability and help children communicate with classmates and teachers in school. The teaching form of preschool language education is too single, which does not conform to children's own learning ability. Therefore, in teaching, teachers should actively optimize the language environment to make children willing to express themselves in language: introducing game activities to make children want to express themselves in language. With the help of situational display, children like to express themselves in language and carry out performance activities to give children the opportunity to express themselves in language. With the help of home force, children dare to express themselves in language. Children are in a dynamic stage of rapid growth. In order to enable children to learn language effectively, teachers should make clear the development center of children and their mastery of language. To guide language teaching in accordance with students' aptitude for a long time, at the same time, we should update our rigid views on children at any time, boldly innovate the content and thinking mode of children's language teaching activities, and mobilize children's initiative and enthusiasm to participate in language learning, so that they can achieve the language learning goals of being able to speak, loving to speak and bravely speaking. This paper selects the learning situation of preschool children as the object, establishes an evaluation model by using the hybrid GA-BP neural network method, and makes an empirical analysis on the development of preschool education in Liaoning Province. The GA-BP neural network model is trained by MATLAB 7.0, and the simulation results show that the model can evaluate the development of preschool education scientifically, and it is scientific and practical. According to the results of this paper, the corresponding evaluation model of preschool education language teaching quality is put forward, which makes a good prediction preparation for children to learn language better in advance.

1. Introduction

3-6 years old is the golden age of children's language learning and development. The relevant outline clearly points out: "The key to developing preschool education language is to create an environment in which they want to speak, dare to speak, like to speak, have the opportunity to speak and get positive responses." Literature [1] expounds the scientific evaluation of the development of preschool education based on the BP neural network algorithm. Literature [2] examines the two dimensions of family language policy—language ideology and language practice—and the relationship between family language policy and the development of children's narrative macrostructure and discusses the key factors to realize the sustainable development of early language education. Literature [3] is aimed at dealing with and discussing the dialogue between critical teaching method and language education in the context of English as a global lingua franca. Literature [4] explores literacy practices in adult intermediate second language teaching, involving two teachers and their different student groups who undertook a four-week literary work. Literature [5]

expounds the comparison of educational language policies in subjective language, minority language, and foreign language education between China and Australia. Literature [6] studied the language outcomes of 174 young children in the Bucharest Early Intervention Program, the first randomized trial of foster placement after institutional care. The purpose of literature [7] is to evaluate the content of vocabulary game application to children's language learning. Literature [8] shows a model of higher education quality evaluation and decision-making based on BP neural network and analytic hierarchy process. Literature [9] predicts the success or failure of education population based on the convolution neural network method. Reference [10] proposes a new penalty estimation method for sparse DNN, which solves the problems existing in sparse constraints. Literature [11] proposes a method based on the deep neural network for nonparametric regression of functional data. Reference [12] gives the numerical results of the sparse data problem of tomography. NETT has good performance even for different types of unknowns in training data. A new hybrid forecasting system CFML (complementary set empirical mode decomposition-(CEEMD-) fuzzy time series- (FTS-) multiobjective gray wolf optimizer- (MOGWO-) long-term and short-term memory (LSTM)) is proposed and tested in reference [13]. Literature [14] uses a new multivariate time series convolution network (M-TCN) model to analyze Beijing PM2.5 and ISO-NE data sets. Literature [15] expounds preschool teachers' understanding and needs for children's language education and focuses on the purpose, content, method, evaluation, and required facts of children's language education. Literature [16] studies the problems existing in the development of preschool education, the continuous reform aimed at solving these problems, and the importance of the "first step" of the national plan. Literature [17] is aimed at seeking the application direction of new media in preschool education, so as to promote the better development of preschool education under the background of new media era. Literature [18] expounds that the success of preschool education in Japan is closely related to Japan's economic development level and Japan's emphasis on education. Literature [19] expounds the practice and exploration of preschool education art curriculum reform under the new situation, hoping to provide reference for relevant personnel. Literature [20] designs an intelligent inventory forecasting system based on deep network technology. Based on stock financial indicators and stock changing trends, it studies the quantitative stock selection problem with multiple influencing factors and proposes a stock trend identification algorithm to build a stock selection model. Reference [21] uses a deep neural network to determine one-dimensional fast ion velocity distribution function from ion cyclotron emission data. Reference [22] uses neural networks to process phase-time measurement information. The novelty of the proposed method lies in the selection of classification attributes and the binary classification of perceptron algorithm. Reference [23] is aimed at applying ANN to predict the bulk density of composite aggregates, i.e. coarse, medium, and fine aggregates. In reference, the prediction model constructed by the BP neural network can provide a basis for corrosion control in refineries. Reference [24] describes the application of the neural network in nonlinear electronic equipment: building Volterra series model.

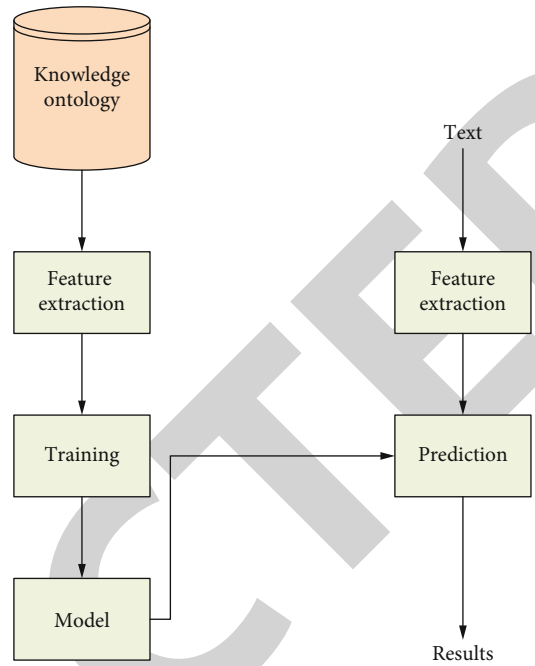

Figure 1: Language map construction.

2. Intelligent Language Teaching

An intelligent tutoring system (ITS) is a classroom teaching system widely used in the field of education. It interacts with children through intelligent teaching methods and means to help children learn language quickly and effectively. Since the last century, the intelligent tutoring system has not only achieved rapid development, resulting in the emergence of many intelligent tutoring websites and educational platforms, but also promote the development of the intelligent tutoring system. One of the core issues of the intelligent tutoring system is the acquisition and effective utilization of knowledge. In spite of the progress in this field, the acquisition and effective use of knowledge is still a prominent problem in the intelligent teaching system. Specifically, on the one hand, knowledge is still very limited and difficult to update. Most of the existing knowledge sets of the intelligent tutoring systems are still constructed at one time, and knowledge is obtained from limited data sets. Faced with the rapid growth of information, the limited knowledge set has been difficult to meet the needs of learners for knowledge acquisition. On the other hand, the traditional teaching mode is adopted, and today's children's thinking is very jumping, so it is necessary to analyze and integrate new thinking with existing thinking modes to reduce conflict rules. Its complex teaching process makes language learning a challenge.

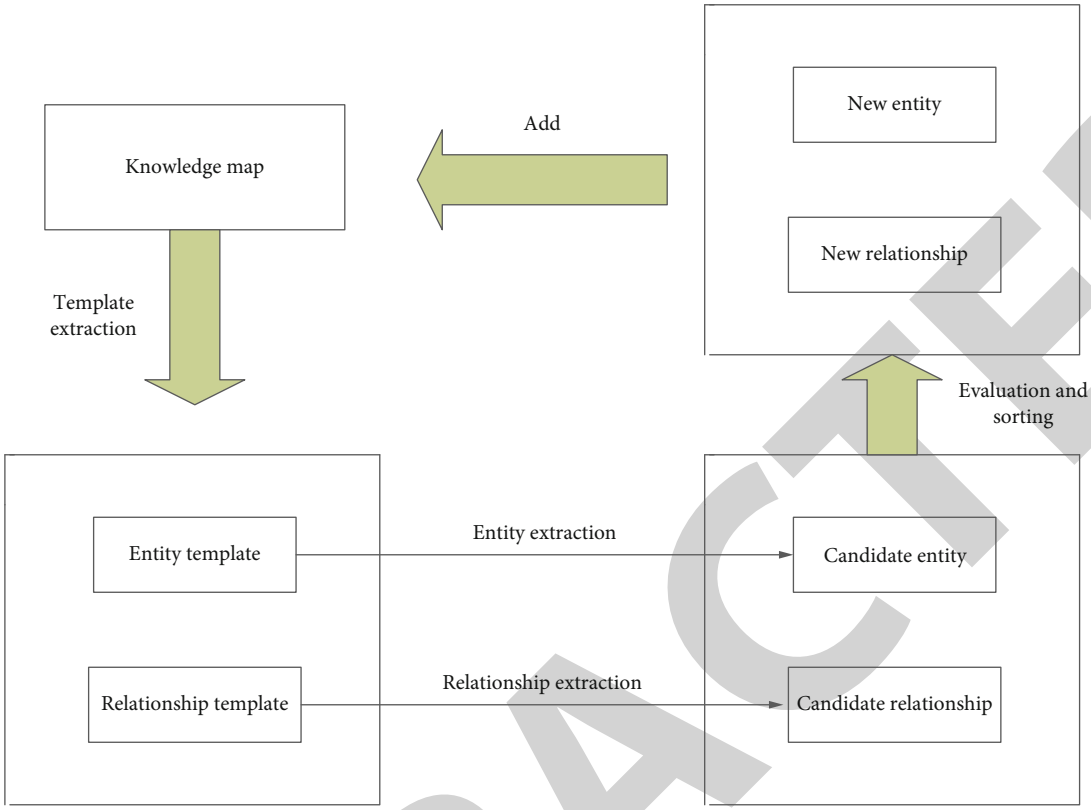

Figure 2: Extension of the knowledge map.

2.1. Meaning of Language Teaching Activities in Preschool Education. A kindergarten language teaching activity is a kind of collective growth activity, that is, to organize all children to learn language with others purposefully, organized, and planned, so that children can join in and improve their listening and expressing ability. In the effective accumulation and emotional development, we can get the development of cognitive things and correct behaviors and then help the improvement of language use ability. The development of language is inseparable from the development of children's thinking. Therefore, kindergarten language teaching activities can not only guide children to correctly master language as a social "tool" but also expand children's thinking through planned and purposeful language education, so that they can accumulate language experience and develop emotional behavior in the process of listening, expressing and reading. At the same time, language also plays an important role in children's cognitive development. It can help children intuitively understand things and learn knowledge and explore the world with curiosity. It is an indispensable cornerstone for children's growth and learning in all aspects. Children's language ability is an important prerequisite in his growth process, and the process of learning language is also a process of developing thinking. Children are taught how to learn language and how to use language correctly, and their intelligence is also developed accordingly. It can be seen that language education is a necessary way to help children grow up in an all-round way.

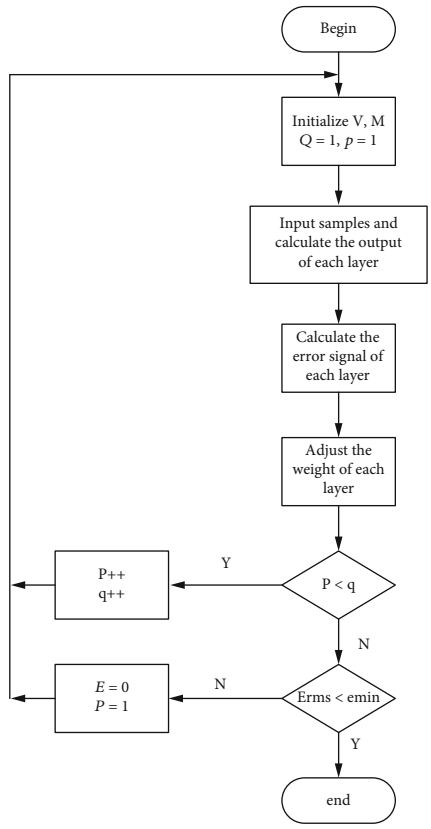

Figure 3: Step diagram.

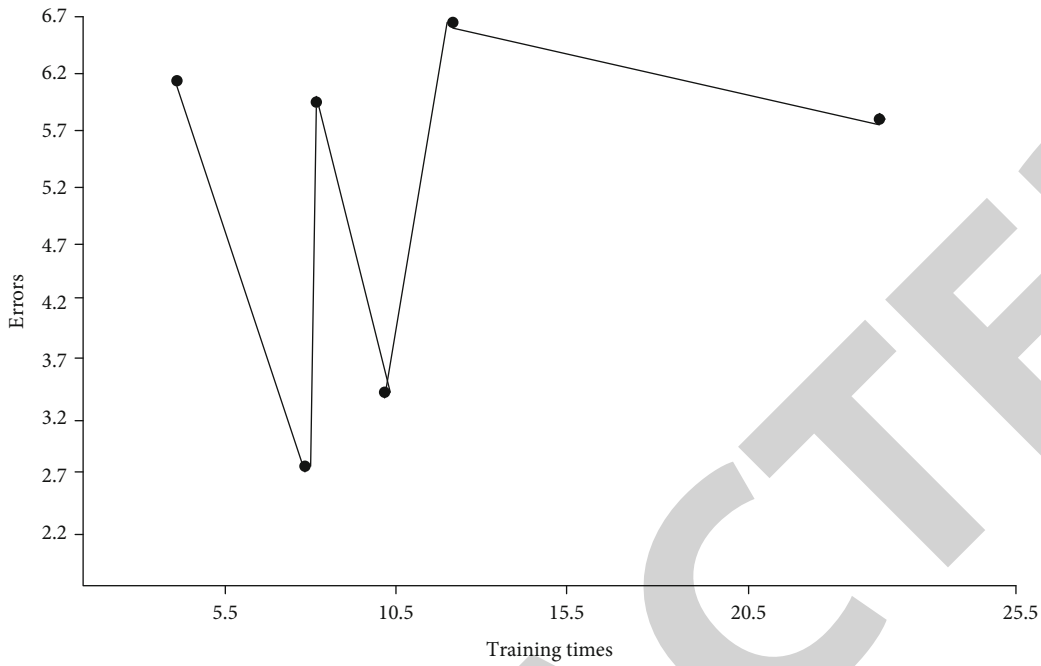

Figure 4: Simulation experiment.

2.2. Construction of Language Knowledge Map. The construction of the core knowledge map is an indispensable link in the construction of core map, and its purpose is to establish a relatively accurate knowledge set of entities and entity relations, so as to provide a good foundation for the expansion of knowledge map. We can use Chinese teaching ontology knowledge base to establish core knowledge map. An automatic identification method of entity association. This method can be regarded as a classification process, that is, judging that two entities belong to a certain relationship. Firstly, the domain experts give the basic set of entity relations and mark some entity relations. Then, the classification model is trained by using the above training data. In the prediction stage, after extracting the features from the text, the trained model predicts according to these features and confirms the relationship between entities through manual inspection. The process is shown in Figure 1.

2.3. Knowledge Map Expansion. The core knowledge map is the main body that provides accurate domain knowledge, but the number of entities is small and the capacity is limited, which does not have corresponding practical significance, so it is necessary to further expand the domain of the knowledge map. We can extract domain knowledge from the open network encyclopedia knowledge base. Encyclopedia knowledge corpus belongs to open knowledge text data on the Internet. It has the characteristics of large scale and continuous renewal and expansion. The main sources of Chinese encyclopedia knowledge corpus are Chinese Wikipedia and Baidu Encyclopedia. This kind of knowledge base is rich in entities and entity relationships, which can not only supplement a large number of entities and relationships but also examine the relationships between entities in the existing core knowledge map to supplement new relationships. On the other hand, entity and entity relationship extraction often needs enough training data. However, the number of entities in the core knowledge map is limited, so it is difficult to obtain ideal recognition performance by supervised learning method. To this end, this paper proposes a model of entities moving with each other, as shown in Figure 2.

Table 1: Comparison of results.

Sample number	Actual results	Simulation results	Errors	Relative errors
1	97.3	92.5	5.28	0.07
2	90.5	87.1	4.34	0.06
3	91.2	86.2	4.42	0.06
4	89.8	81.4	6.17	0.07
5	88.7	82.5	3.62	0.03
6	93.4	86.2	5.63	0.05
7	90.0	79.1	8.21	0.08
8	90.6	79.9	8.17	0.08
9	96.1	85.9	6.12	0.07
10	94.2	81.3	7.21	0.07
11	86.9	76.8	8.43	0.08
12	88.3	79.4	7.48	0.08
13	81.5	68.9	8.43	0.09
14	91.2	81.2	8.45	0.09
15	83.7	73.8	8.31	0.09

Table 2: Comparison of algorithms.

Algorithm	Training steps	Convergence accuracy
Gradient descent method	2000	0.000615
Adaptive learning rate gradient descent method	2000	0.00750
BL neural network algorithm for integrated wiring system	10	0.0851
RBF neural network algorithm	300	0.4532
Pacific application algorithm	30	0.2711
Proportional conjugate gradient algorithm	30	0.3421

Table 3: Experimental data of the gradient descent method.

	Accuracy	Recall	F1	AUC
Sample1	0.675	0.575	0.555	0.621
Sample2	0.643	0.591	0.679	0.592
Sample3	0.667	0.569	0.621	0.583
Sample4	0.698	0.588	0.541	0.557
Sample5	0.681	0.576	0.662	0.632

3. Teaching Evaluation Design of Preschool Education Neural Network

3.1. BP Neural Network Algorithm. The mathematical formulas involved in the training process of the BP neural network in preschool education language teaching are as follows:

$$x_i = \frac{x_{\max} - x_i}{x_{\max} - x_{\min}}. \tag{1}$$

Connection weights of nerve cells in hidden layer:

$$hi(k) = \sum_{i=1}^{n} w_{ih} x_i(k) - b_h. \tag{2}$$

The error E between the network output and the expected output is as follows:

$$E = \frac{1}{2}(d-0)^2 = \frac{1}{2}\sum_{k=1}^{1}(d_k - o_k)^2. \tag{3}$$

Output function is as follows:

$$f(x) = \frac{1}{1+e^{-x}} \tag{4}$$

Activation function is as follows:

$$f(x) = \frac{1}{a+be^{-Cx}}. \tag{5}$$

The formula of error E in hidden layer is as follows:

$$E = \frac{1}{2}\sum_{K=1}^{1}\left\{d_k - f\left[\sum_{j=0}^{m} f\left(\sum_{j=0}^{m} w_{jk} y_j\right)\right]\right\}^2. \tag{6}$$

Error E is expanded to the output layer by the following formula:

$$E = \frac{1}{2}\sum_{K=1}^{1}\left\{d_k - f\left[\sum_{j=0}^{m} w_{jk} f\left(\sum_{i=0}^{n} v_{ij} x_i\right)\right]\right\}^2. \tag{7}$$

Using the gradient descent method, the weights are continuously adjusted as follows. The formula is as follows:

$$\begin{aligned} \Delta w_{jk} &= -\eta \frac{\vartheta E}{\vartheta w_{jk}} \ (j = 0, 1, \cdots, m\,; k = 1, 2, \cdots, l), \\ \Delta v_{jk} &= -\eta \frac{\vartheta E}{\vartheta v_{jk}} \ (i = 0, 1, \cdots, n\,; k = 1, 2, \cdots, m). \end{aligned} \tag{8}$$

After continuous cycle, the value adjustment function of BP learning algorithm weight is

$$\begin{aligned} \Delta w_{jk} &= \eta \delta_k^0 y_j = \eta (d_k - o_k) o_k (1 - o_k) y_j, \\ \Delta v_{jk} &= \eta \delta_j^y x_i = \eta \left(\sum_{k=1}^{1} \sigma_k^0 w_{jk}\right) y_j \left(1 - y_j\right) x_i. \end{aligned} \tag{9}$$

Update BP parameters:

$$E_j^i = 0.5 * \left(T_j^i - yo_j^i\right),$$

$$\delta_j^{(2)}(k) = \left(T_j^k - yo_j^p\right) * yo_j^p * \left(1 - yo_j^p\right),$$

$$\delta_j^{(1)}(k) = \sum_{i=1}^{m}\left[w_{ij}^{(2)} * \delta_j^{(2)}(k)\right] * yi_j^k * \left(1 - yi_j^k\right),$$

$$E = \frac{\left(\sum_{i=1}^{k} E_i\right)}{k},$$

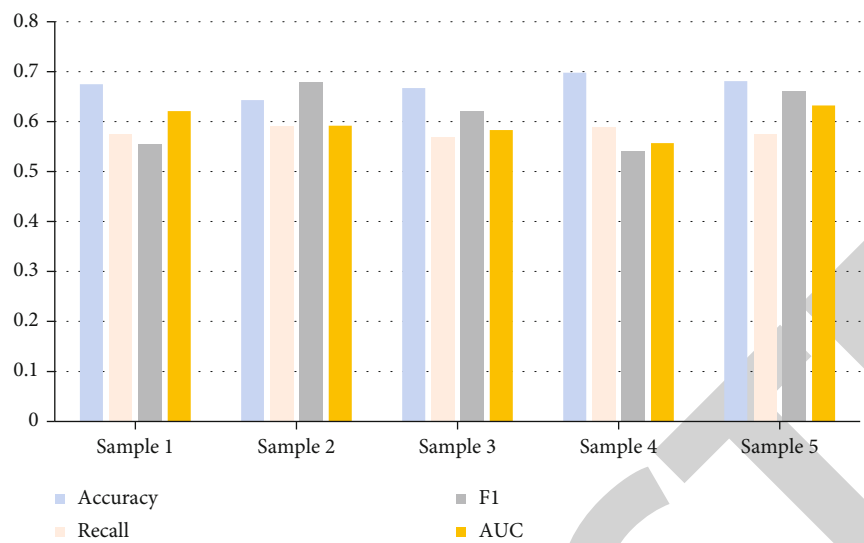

Figure 5: Index comparison chart of the gradient descent method.

Table 4: Experimental data of the adaptive learning rate gradient descent method.

	Accuracy	Recall	F1	AUC
Sample1	0.725	0.625	0.655	0.721
Sample2	0.713	0.631	0.699	0.692
Sample3	0.727	0.663	0.721	0.683
Sample4	0.718	0.668	0.741	0.757
Sample5	0.691	0.686	0.682	0.732

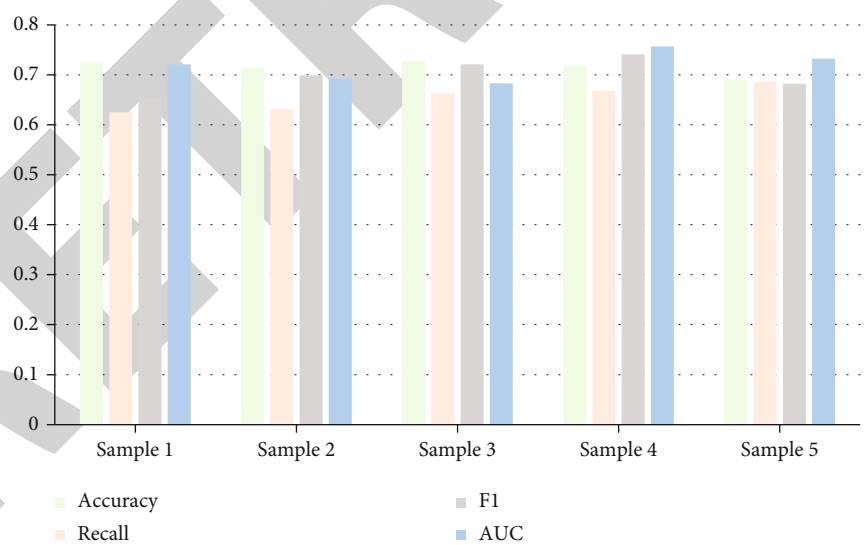

Figure 6: Index comparison chart of adaptive learning rate gradient descent method.

$$w_{ij}^{(2)} = w_{ij}^{(2)} + \eta * \sum_{i=1}^{k} \left[\delta_j^{(2)}(l) * yo_i^l \right],$$

$$w_{ij}^{(1)} = w_{ij}^{(1)} + \eta * \sum_{i=1}^{k} \left[\delta_j^{(1)}(l) * x_i^l \right]. \quad (10)$$

3.2. RBF Neural Network. The mathematical formulas involved in the training process of the RBF neural network are as follows:

Radial basis function:

$$y(x) = \sum_{i=1}^{N} w_i \varnothing(\|x - c_i\|). \quad (11)$$

Table 5: Experimental data.

	Accuracy	Recall	$F1$	AUC
Sample1	0.825	0.825	0.855	0.821
Sample2	0.813	0.831	0.899	0.892
Sample3	0.827	0.863	0.821	0.883
Sample4	0.818	0.868	0.841	0.857
Sample5	0.891	0.886	0.882	0.832

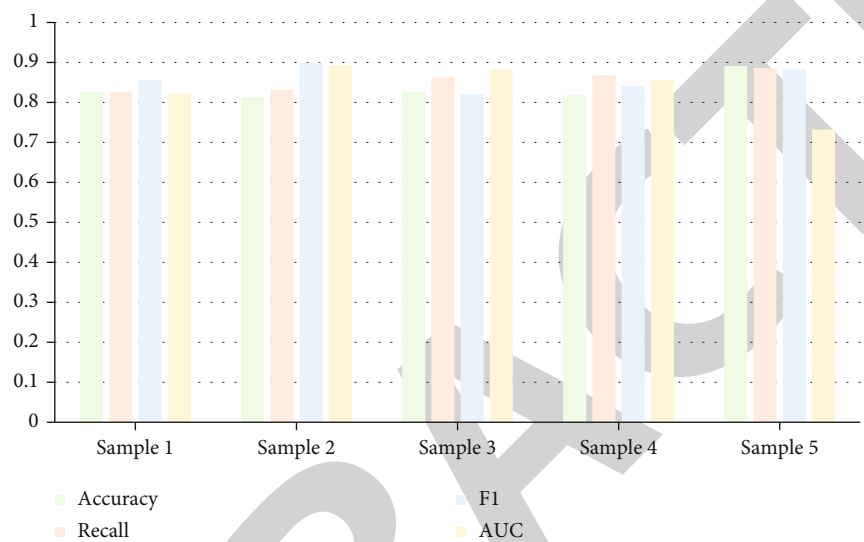

Figure 7: Comparison chart of the GA-BP neural network algorithm indexes.

Table 6: Experimental data.

	Accuracy	Recall	$F1$	AUC
Sample1	0.725	0.725	0.655	0.721
Sample2	0.713	0.731	0.699	0.692
Sample3	0.727	0.663	0.721	0.683
Sample4	0.718	0.668	0.741	0.657
Sample5	0.691	0.686	0.682	0.632

The result of this approximation function $y(x)$ can be regarded as the sum of many radial basis functions, each of which is associated with a different center $c_i$and weighted by an appropriate number w_i.

Calculate variance:

$$\sigma = \frac{d_{\max}}{K}. \tag{12}$$

Calculate $\widehat{y}_i(n)$ from $x(n)$:

$$\widehat{y}_i(n) = \sum_{k=1}^{M} W_K \varnothing[x(n), C_K, \sigma_K]. \tag{13}$$

Update RBF parameters:

$$W(n+1) = W(n) + \mu_w e(n) \varnothing(n),$$

$$C_K(n+1) = C_K(n) + \mu_c \frac{e(n) W_K(n)}{\sigma_k^2(n)},$$

$$\varnothing[x(n), C_K(n), \sigma_K][x(n) - C_K(n)],$$

$$\sigma_K(n+1) = \sigma_K(n) + \mu_\sigma \frac{e(n) W_K(n)}{\sigma_k^2(n)},$$

$$\varnothing[x(n), C_K(n), \sigma_K][x(n) - C_K(n)]^2,$$

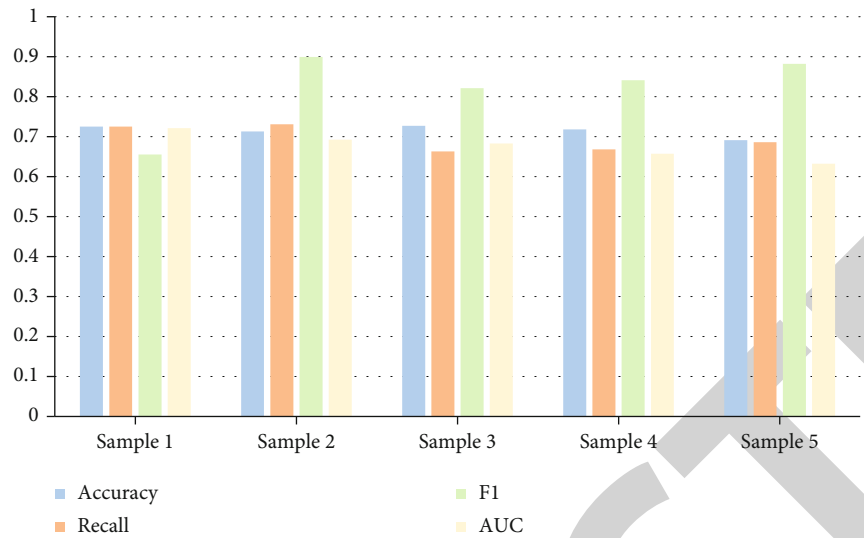

Figure 8: Comparison chart of the RBF neural network algorithm indexes.

Table 7: Experimental data.

	Accuracy	Recall	$F1$	AUC
Sample1	0.775	0.765	0.655	0.724
Sample2	0.773	0.761	0.659	0.694
Sample3	0.777	0.663	0.751	0.684
Sample4	0.778	0.668	0.751	0.654
Sample5	0.671	0.666	0.652	0.634

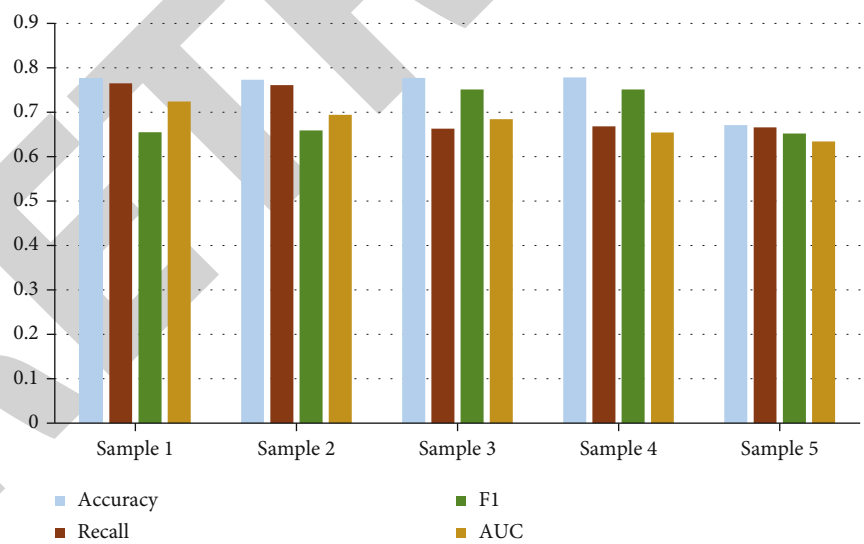

Figure 9: Comparison chart of PSO algorithm indexes.

$$\varnothing(n) = \begin{cases} \varnothing[x(n), c_1(n), \sigma_1], \varnothing[x(n), c_2(n), \sigma_2], \\ \cdots, \varnothing[x(n), c_N(n), \sigma_N], \end{cases}$$

$$e(n) = \widehat{y}_i(n) - y_d(n). \tag{14}$$

$y_d(n)$ is the failure output, and μ_c, μ_σ, $\sigma_N$are the mapping of three parameters.

4. Experiment

For the evaluation of teaching quality, the algorithm programming steps of the BP neural network of the student evaluation system are shown in Figure 3.

4.1. Simulation Experiment. We evaluate the teaching quality of preschool education language education, set the number of hidden layer neurons as 7, and determine 7 as the number of hidden layer neurons. The experimental data are shown in Figure 4.

Using the hybrid GA-BP neural network algorithm to the preschool education language teaching quality evaluation simulation experiment, it predicts the evaluation results of 15 groups of sample data and compares the simulation evaluation results with the actual evaluation results as shown in Table 1.

4.2. Model Comparison. Comparing different functions with different convergence accuracy and training steps, from the table and experimental data, GA-BP is the most suitable training function in this paper. Data are shown in Table 2.

Five samples are selected to test the performance index of language teaching quality for all the algorithm models in the above table, and the accuracy rate, recall rate, $F1$ value, and AUC value are compared, respectively. The experimental data are as follows.

Using the gradient descent method, the performance index of the teaching quality analysis model of preschool language education is tested. The experimental data are shown in Table 3.

According to the data in the above table, it is counted into a bar chart, as shown in Figure 5.

Test the performance index of the teaching quality analysis model of preschool language education by an adaptive learning rate gradient descent method. The experimental data are shown in Table 4.

According to the data in the above table, it is counted into a bar chart, as shown in Figure 6.

We test the GA-BP neural network algorithm for preschool language education teaching quality analysis model to achieve what level of performance indicators, and data are shown in Table 5.

According to the data in the above table, it is counted into a bar chart, as shown in Figure 7.

We test the performance index level of RBF algorithm on the teaching quality analysis model of preschool language education. The experimental data are shown in Table 6.

According to the data in the above table, it is counted into a bar chart, as shown in Figure 8.

We test the performance index of the PSO algorithm on the teaching quality analysis model of preschool language education. The data are shown in Table 7.

According to the data in the above table, it is counted into a bar chart, as shown in Figure 9.

4.3. Contrast Experiment. According to the abovementioned comparison chart of preschool education language teaching quality index test, through the model index data results of the chart, the hybrid neural network algorithm and RBF neural network algorithm are more practical for other models. We test and compare the language learning effects of these two models on children, as shown in Figures 10 and 11:

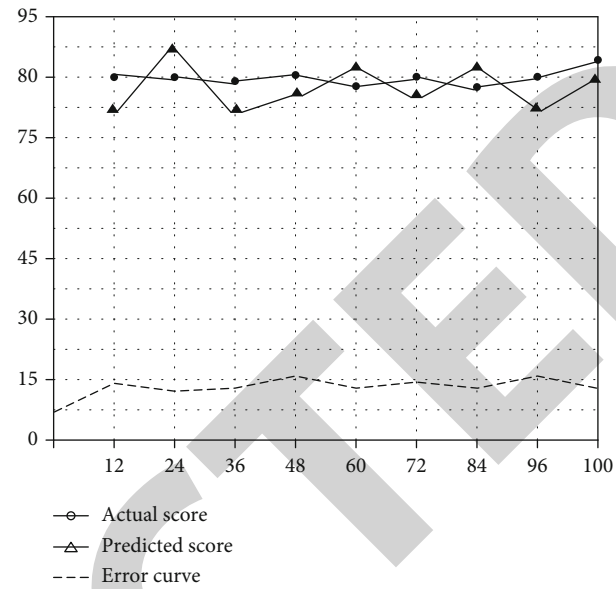

Figure 10: Learning renderings.

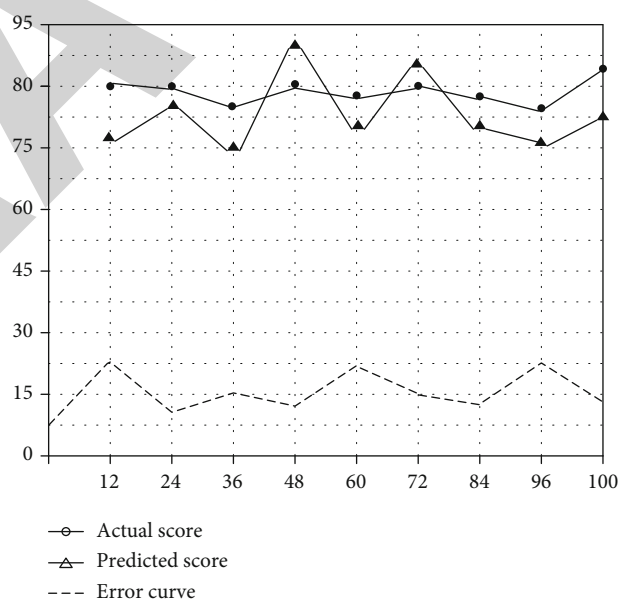

Figure 11: Learning renderings.

According to the comparison chart of the two algorithms, the error curve of the hybrid neural network algorithm is relatively flat, so it is more practical for the evaluation of teaching quality.

5. Conclusion

Teaching evaluation is regarded as an effective method to test teaching quality in colleges and universities. Through the observation and assessment of teachers' teaching in a working period, scientific and effective assessment results are formed, and the teaching process is constantly improved according to the assessment results. This paper is mainly

based on the intelligent analysis and application of language teaching quality in preschool education based on the deep neural network. The research results are as follows:

(1) Comparing the convergence accuracy and training steps of these algorithms in this paper, the hybrid GA-BP neural network algorithm has fast evaluation speed and high accuracy

(2) The results show that the hybrid GA-BP neural network algorithm and RBF algorithm are more suitable for preschool language teaching

(3) For the analysis of language teaching quality in preschool education, we can clearly see that the error of the hybrid GA-BP neural network algorithm is smaller and more stable in the children's learning effect diagram after comparative experiment

(4) For children in preschool education, we should provide new ideas and methods to guide children's teaching, which also plays a certain role in improving teaching quality

Data Availability

The experimental data used to support the findings of this study are available from the corresponding author upon request.

Conflicts of Interest

The authors declared that they have no conflicts of interest regarding this work.

References

[1] T. Jihong and Z. Xiuqi, "Evaluation of preschool education development in Liaoning Province based on BP neural network," *Computer and Digital Engineering*, vol. 41, no. 6, pp. 1015–1017, 2013.

[2] Y. Jing, D. Yan, and F. Lin, "Language ideologies, practices, and kindergarteners' narrative macrostructure development: crucial factors for sustainable development of early language education," *Sustainability*, vol. 13, no. 13, pp. 6985–6985, 2021.

[3] S. Sávio, "Critical pedagogy and language education: hearing the voices of Brazilian teachers of English," *Education Sciences*, vol. 11, no. 5, pp. 235–235, 2021.

[4] W. Robert, "Interconnected literacy practices: exploring classroom work with literature in adult second language education," *European Journal for Research on the Education and Learning of Adults*, vol. 11, no. 1, pp. 45–63, 2020.

[5] J. He and H. Liao, "The study of language policy in education in the context of belt and road—the contrast on language education policy between China and Australia," *Theory and Practice in Language Studies*, vol. 10, no. 11, pp. 1489–1493, 2020.

[6] W. Jennifer, "Effect of foster care on young children's language learning," *Child Development*, vol. 82, no. 4, pp. 1040–1046, 2011.

[7] E. Hyun, H. Yeon, J. Jang, and E. Lee, "Contents analysis of vocabulary learning game application on smart-phone and tablet PC for young children's language learning," *Journal Of The Korea Contents Association*, vol. 13, no. 11, pp. 551–561, 2013.

[8] Y. Mei and L. Chunyang, "Research on global higher education quality based on BP neural network and analytic hierarchy process," *Journal of Computer and Communications*, vol. 9, no. 6, pp. 158–173, 2021.

[9] L. Luo, J. Huang, and Y. Zhang, "Prediction of educational crowds' success or failure based on convolutional neural network," *Software Engineering and Applications*, vol. 8, no. 6, pp. 319–325, 2019.

[10] O. Ilsang and K. Yongdai, "Nonconvex sparse regularization for deep neural networks and its optimality," *Neural Computation*, vol. 34, no. 2, pp. 41-42, 2022.

[11] W. Shuoyang, C. Guanqun, and S. Zuofeng, "Estimation of the mean function of functional data via deep neural networks," *Stat*, vol. 10, no. 1, 2021.

[12] N. E. T. T. Li Housen, "NETT: Solving inverse problems with deep neural networks," *Inverse Problems*, vol. 36, no. 6, p. 065005, 2020.

[13] D. Wei, Wang, Ni, and Tang, "Research and application of a novel hybrid model based on a deep neural network combined with fuzzy time series for energy forecasting," *Energies*, vol. 12, no. 18, p. 3588, 2019.

[14] R. Wan, S. Mei, J. Wang, M. Liu, and F. Yang, "Multivariate temporal convolutional network: a deep neural networks approach for multivariate time series forecasting," *Electronics*, vol. 8, no. 8, p. 876, 2019.

[15] J. J. Youn, "The early childhood teacher's recognition and demand on children's language education - focused on purpose, contents, method, evaluation and the required facts of children's language education," *Korean Journal of Human Ecology*, vol. 16, no. 6, pp. 1083–1095, 2007.

[16] O. K. Tanzilovich and T. M. Jurakulovna, "Innovative approach and state training program "first step" in the implementation of the process of preschool education and training," *Academicia: An International Multidisciplinary Research Journal*, vol. 11, no. 4, pp. 817–821, 2021.

[17] X. Shan, "Research on content design of media facade and augmented reality for preschool education," *Region-Educational Research and Reviews*, vol. 3, no. 1, p. 41, 2021.

[18] G. Li, W. Cao, and W. Yi, "The enlightenment of Japan's preschool education to China's preschool children's social education," *Learning & Education*, vol. 9, no. 4, 2021.

[19] X. I. N. G. Yanya and L. I. Dongxi, "Stock forecasting system based on deep neural network," *Advances in Applied Mathematics*, vol. 10, no. 5, pp. 1721–1727, 2021.

[20] S. B. S. Determining, "Determining 1D fast-ion velocity distribution functions from ion cyclotron emission data using deep neural networks," *The Review of Scientific Instruments*, vol. 92, no. 5, p. 053528, 2021.

[21] D. D. Boldasov, J. V. Drozdova, A. S. Komshin, and A. B. Syritskii, "Neural network application for phasechronometric measurement information processing," *Measurement Techniques*, vol. 63, no. 9, pp. 708–712, 2020.

[22] S. K. Singh, B. M. Pranathi, and S. K. Kirthika, "Prediction of particle packing density of alternative fine aggregates by artificial neural network applications," *Journal of The Institution of Engineers (India: Series A)*, vol. 101, no. 1, pp. 127–140, 2020.

Hindawi
Journal of Sensors
Volume 2023, Article ID 9869108, 1 page
https://doi.org/10.1155/2023/9869108

Retraction

Retracted: Design of Virtual Machine Scheduling Algorithm in Cloud Computing Environment

Journal of Sensors

Received 19 December 2023; Accepted 19 December 2023; Published 20 December 2023

This article has been retracted by Hindawi following an investigation undertaken by the publisher [1]. This investigation has uncovered evidence of one or more of the following indicators of systematic manipulation of the publication process:

(1) Discrepancies in scope
(2) Discrepancies in the description of the research reported
(3) Discrepancies between the availability of data and the research described
(4) Inappropriate citations
(5) Incoherent, meaningless and/or irrelevant content included in the article
(6) Manipulated or compromised peer review

The presence of these indicators undermines our confidence in the integrity of the article's content and we cannot, therefore, vouch for its reliability. Please note that this notice is intended solely to alert readers that the content of this article is unreliable. We have not investigated whether authors were aware of or involved in the systematic manipulation of the publication process.

Wiley and Hindawi regrets that the usual quality checks did not identify these issues before publication and have since put additional measures in place to safeguard research integrity.

We wish to credit our own Research Integrity and Research Publishing teams and anonymous and named external researchers and research integrity experts for contributing to this investigation.

The corresponding author, as the representative of all authors, has been given the opportunity to register their agreement or disagreement to this retraction. We have kept a record of any response received.

References

[1] B. Liang, R. Liu, and D. Dai, "Design of Virtual Machine Scheduling Algorithm in Cloud Computing Environment," *Journal of Sensors*, vol. 2022, Article ID 3848165, 8 pages, 2022.

Hindawi
Journal of Sensors
Volume 2022, Article ID 3848165, 8 pages
https://doi.org/10.1155/2022/3848165

Research Article

Design of Virtual Machine Scheduling Algorithm in Cloud Computing Environment

Bin Liang,[1] **Ruifeng Liu**,[2] **and Dongfeng Dai**[1]

[1]*School of Electromechanical and Automotive Engineering, Jiuzhou Polytechnic, Xuzhou 221116, China*
[2]*School of Public Administration, Sichuan University, Chengdu, Sichuan 610000, China*

Correspondence should be addressed to Bin Liang; liangb@jzp.edu.cn

Received 14 March 2022; Revised 2 April 2022; Accepted 15 April 2022; Published 9 May 2022

Academic Editor: Han Wang

With the application of cloud computing services in more and more fields, it will undertake more computing tasks and storage tasks. The problem of high energy consumption in data centers will become more serious. Virtualization technology is very important in cloud computing, which can improve the utilization rate of resources. At the same time, it has flexibility in resource scheduling and can integrate multiple virtual machines to achieve power efficiency. Using online virtual machine migration technology for energy-saving planning in cloud environment is a hot research topic in academic circles. The scheduling strategy proposed in this paper can reduce the server downtime and the number of server hosts, so as to achieve the maximum use of resources. The main research work of this paper includes the following aspects: Firstly, the energy consumption in the process of virtual machine energy-saving design is modeled, and the relationship between energy consumption and resource usage under different load conditions is analyzed, and the problems are abstracted, e.g., packaging box problem. Secondly, this paper uses genetic algorithm to solve the problem of high energy consumption. Finally, based on the target allocation scheme of virtual machines obtained by the above method, the migration problem of virtual machines is abstracted as the problem of finding the maximum weighted independent set of graphs. And a greedy algorithm is designed to solve this problem. In this paper, CloudSim simulation platform is used to verify the effectiveness of the proposed algorithm. Experiments show that the proposed algorithm can reduce data energy consumption and avoid frequent migration of virtual machines.

1. Introduction

If the virtual machine scheduling problem is not considered carefully, the system load will be unbalanced. To solve this problem, this paper proposes a scheduling strategy based on genetic algorithm to reduce dynamic migration and achieve the best load balance [1]. Because cloud computing has many difficult problems to solve, so how to effectively solve these problems and improve efficiency, this paper proposes a dual fitness genetic algorithm. The research shows that this method can not only shorten the total task time but also shorten the average task time [2]. Big data technology cannot solve the problems in data mining efficiently. Therefore, this paper puts forward the model of cloud computing, which can provide more benefits. It has the characteristics of flexible cost and more flexibility in computing resources [3]. In cloud computing, providing appropriate and reliable application services is the basic requirement. The lightweight virtual machine scheduler of metascheduler proposed in this paper can improve resource utilization and can be further expanded to achieve adaptive load balancing [4]. Genetic algorithm can solve the load balancing problem well. Experiments show that this strategy solves the problems of unbalanced load and high migration cost to a great extent [5]. At present, the offline method cannot be used to solve the problems in uncertain environment, because this method can only solve the certain problems. Efficient cloud computing scheduling method can reduce the energy consumption of cloud computing platform and improve resource utilization [6]. Cloud computing has high requirements on basic equipment and resources. Efficient load balancing can improve the utilization of resources. In order to

solve different cloud environments, this paper proposes a variety of load balancing schemes [7]. Experimental results show that ant colony optimization resource allocation method be able to meet the needs of cloud computing environment [8]. In order to solve the problems in cloud security, this paper proposes keystroke dynamics method, which can provide a very effective solution [9]. Aiming at the problem of resource utilization in cloud computing, this paper proposes a virtual machine scheduling algorithm based on K-means clustering, which can make full use of resources and has strong stability [10]. In this paper, we propose a virtual machine scheduling algorithm to solve the mixed load scheduling problem, which uses processors to evaluate the recent energy consumption problem of virtual machines. Experiments show that this method is used in scheduling deviation and normalized energy efficiency [11]. Virtual machine has been widely used because it can improve the utilization rate of resources. With the change of cloud computing scale, the requirements for resource utilization are getting higher and higher, so a more efficient method is needed to improve the allocation of resources [12]. Sustainable green intelligent computer can solve the problem of high energy consumption in cloud computing. It only needs to pay attention to the scheduling of cloud virtual machines, consider the actual configuration of servers, and avoid overheating in the central local location [13]. Task scheduling is the focus of cloud data research. At present, the long execution time means that its cost is also very high, and reducing the execution time means reducing the cost, so this paper proposes a task scheduling algorithm with short average execution time to solve this problem [14]. There are many problems to be solved in resource scheduling of virtual machines. The algorithm proposed in this paper combines genetic algorithm to continuously adjust the host load, so as to achieve the optimal balance [15].

2. Features of Cloud Computing

2.1. Virtualization. The basic feature of cloud computing is virtualization technology. The resources retrieved by users in cloud services are virtualized, not real resources. Cloud services take advantage of virtualization technology to a certain extent, and eliminate the differences between different server architectures by protecting the details of specific hardware and virtualizing IT resources. In cloud services, virtualization of CPU resources is the purpose of virtualization. These resources are usually provided to users in the form of virtual machines, which is convenient for users to use. For cloud providers, resource virtualization helps build an easy-to-use management platform.

2.2. High Availability. Cloud computing platform provides reliable services according to users' needs. In the cloud server center, the stable operation of the whole system mainly depends on the centralized management of large-scale resources under the unified platform. Data redundancy technology and load balancing technology provide reliable guarantee for the high availability of services. Hadoop's heartbeat mechanism can monitor the survival of nodes at any time. Once a node goes down, it will be replaced immediately.

2.3. Low Cost. Cloud computing does not require high-performance computing components and professional storage devices. Users only need to pay a very low rent and a terminal that can connect to the Internet, and they can get high-performance computing power and large-scale storage capacity. Cloud application service providers are responsible for maintaining the software and hardware in the cloud, which greatly saves the purchase and maintenance costs of users' software and hardware.

2.4. On-Demand Service. Cloud service providers charge rent according to the actual usage of users, which can allocate resources in time to increase the actual service capacity of users when the number of resource requests suddenly increases and can also release the resources occupied by users when the number of resources required by users decreases to avoid wasting resources.

2.5. Scalability. Cloud computing architecture and scale have certain scalability, allowing computing nodes to join and exit computer clusters dynamically, which can not only build a usable high-performance computing platform in a short time but also facilitate data center maintenance personnel to maintain equipment.

2.6. Safe and Reliable. Data center uses virtual machines to schedule tasks and uses the isolation of virtual machines to provide users with good security. At the same time, the redundancy technology of the data center ensures the security of the data stored in the cloud. Even if a certain node or a certain area is paralyzed, the standby node in another area can replace the failed node at the first time.

3. Resource Model and Scheduling Algorithm Model

3.1. Basic Model. The basic model includes the virtual machine used in the algorithm and the host model, in which the virtual machine acquires the resources in the host and receives the tasks to execute. In this paper, the virtual machine set is expressed as Formula (1).

$$V = \{v_0, v_1, v_2, \cdots, v_{n-1}\}, \tag{1}$$

where V represents a virtual machine set, and each element in the set represents a virtual machine; N is the number of virtual machines, where each virtual machine can be expressed as Formula (2).

$$v_j = \left\{v_{j\_\mathrm{ID}}, v_{j\_\mathrm{storage}}, v_{j\_\mathrm{pes}}, v_{j\_\mathrm{RAM}}\right\}, \tag{2}$$

where v_j represents the J-th virtual machine; v_{j_ID} represents the ID of this virtual machine; v_{j_storage} represents the mirror size of this virtual machine; v_{j_pes} represents the number of CPU cores (Pe number) owned by the virtual machine; v_{j_RAM} represents the memory size of this virtual machine.

Each host has certain resources, and the host set is defined as Formula (3).

$$H = \{h_0, h_1, h_2, \cdots, h_{s-1}\}, \tag{3}$$

where H represents the host set and S represents the total number of hosts. Each host can be expressed as Formula (4).

$$h_k = \{h_{k\_\mathrm{ID}}, h_{k\_\mathrm{storage}}, h_{k\_\mathrm{mips}}, h_{k\_\mathrm{RAM}}, h_{k\_\mathrm{band}}, h_{k\_\mathrm{pes}}\}, \tag{4}$$

where h_{k_ID} represents the ID of this host; h_{k_storage} represents the storage size of this host, which determines how many virtual machines this host can accommodate; h_{k_RAM} represents the memory size of this host; h_{k_pes} represents the number of cores owned by this host.

3.2. Resource Request Model. In order to keep the load of the host stable and reduce the risk caused by excessive load of the host, the virtual machine scheduling algorithm in this paper limits the load to less than 80%, that is to say, it is necessary to limit the amount of virtual machine resource requests. If the virtual machine is placed on a host, so that the resource load of the host exceeds 80%, then the virtual machine will not be placed on the host, and other hosts need to be selected for placement, so the resource request amount of the virtual machine is limited here. The algorithm in this paper improves the host resource limitation of the original OpenStack algorithm. According to Equations (2) and (4), the three sources of host Pe number, memory size, and storage space are limited, as shown in Formula (5).

$$\begin{cases} \sum_{j=0}^{n-1} v_{j\_\mathrm{pes}} \cdot \mathrm{flag}_{jk} + v_{x\_\mathrm{pes}} \le h_{k\_\mathrm{pes}} \cdot 80\%, \\ \sum_{j=0}^{n-1} v_{j\_\mathrm{RAM}} \cdot \mathrm{flag}_{jk} + v_{x\_\mathrm{RAM}} \le h_{k\_\mathrm{RAM}} \cdot 80\%, \\ \sum_{j=0}^{n-1} v_{j\_\mathrm{storage}} \cdot \mathrm{flag}_{jk} + v_{x\_\mathrm{storage}} \le h_{k\_\mathrm{storage}} \cdot 80\%, \end{cases} \tag{5}$$

where v_{x_pes}, v_{x_RAM}, and v_{x_storage} denote various resource values of virtual machine v_x to be placed on host h_k, and $0 \le x \le n-1$, and flag_{jk} is defined as Formula (6).

$$\begin{cases} \mathrm{flag}_{jk} = 0, \text{virtual machine } v_j \text{not placed on host } h_k, \\ \mathrm{flag}_{jk} = 1, \text{virtual machine } v_j \text{not placed on host } h_k. \end{cases} \tag{6}$$

The above Formulas (5) and (6) indicate that when creating a virtual machine in host h_k, the corresponding sum of the various types of resources already allocated thereto plus the value of the corresponding resources to be allocated thereto cannot exceed 80% of the total value of the corresponding resources that this host can accommodate. This filtering can be called Filter filtering.

3.3. Host Resource Load Model. When a virtual machine is created, Pe resources, memory resources, and storage resources on the host need to be used. This will cause the host to produce the corresponding resource load. Therefore, this paper will consider the Pe load, memory load, and virtual machine storage load of the host here. The load model can be understood as follows: the corresponding resources that have been used are higher than the total corresponding resources, and the load model is established as shown in Formulas (7)–(10).

$$\mathrm{pe}_{jk\_\mathrm{load}} = \frac{\sum_{j=0}^{n-1} v_{j\_\mathrm{pes}} \cdot \mathrm{flag}_{jk}}{h_{k\_\mathrm{pes}}} \cdot 100\%, \tag{7}$$

$$\mathrm{RAM}_{jk\_\mathrm{load}} = \frac{\sum_{j=0}^{n-1} v_{j\_\mathrm{RAM}} \cdot \mathrm{flag}_{jk}}{h_{k\_\mathrm{RAM}}} \cdot 100\%, \tag{8}$$

$$\mathrm{Storage}_{jk\_\mathrm{load}} = \frac{\sum_{j=0}^{n-1} v_{j\_\mathrm{storage}} \cdot \mathrm{flag}_{jk}}{h_{k\_\mathrm{storage}}} \cdot 100\%, \tag{9}$$

$$h_{k\_\mathrm{average\_load}} = \frac{\mathrm{pe}_{jk\_\mathrm{load}} + \mathrm{RAM}_{jk\_\mathrm{load}} + \mathrm{Storage}_{jk\_\mathrm{load}}}{3} \cdot 100\%, \tag{10}$$

where $\mathrm{pe}_{jk\_\mathrm{load}}$, $\mathrm{RAM}_{jk\_\mathrm{load}}$, $\mathrm{Storage}_{jk\_\mathrm{load}}$, and $h_{k\_\mathrm{average\_load}}$ represent the Pe number load, memory load, virtual machine storage load, and the average load of host h_k, respectively. It can be seen that the more virtual machines placed on a host, the greater its load value. Therefore, it is necessary to choose the placement of virtual machines reasonably to keep the load of various resources of the host in a stable range.

3.4. Scheduling Target Model. After building the above model, we also need to build a scheduling target model. The scheduling target model is the ultimate goal of the algorithm developed in this paper. And it is also an important index to evaluate the performance gap between the two algorithms. The goal of this resource-sensitive virtual machine scheduling algorithm is to balance the resource load of each host as much as possible, That is to say, you cannot overload or underload resources on individual hosts. To minimize the difference between the resource loads of all hosts and keep the resource loads of all hosts at a balanced level, in order to achieve this goal, we first need to know the average load of all hosts, which can be obtained according to Equation (10), and then, we can calculate the load variance and load standard deviation of all hosts. In addition, because we have limited Formula (5) for resource requests of virtual machines, therefore, it is necessary to analyze the success rate of creating virtual machines in all kinds of hosts, which can show the satisfaction of scheduling algorithm to the request of creating virtual machines (the higher the success rate, the better the satisfaction). Therefore, this paper establishes Formulas (11)–(14).

$$h_{\mathrm{all\_average\_load}} = \frac{\sum_{k=0}^{s-1} h_{k\_\mathrm{average\_load}}}{s} \cdot 100\%, \tag{11}$$

$$\text{Variance}_{\text{host}} = \frac{\sum_{k=0}^{s-1}\left(h_{k\_\text{average\_load}} - h_{\text{all\_average\_load}}\right)^2}{s}, \quad (12)$$

$$\text{Std}_{\text{host}}\sqrt{\text{Variance}_{\text{host}}}, \quad (13)$$

$$\text{Ratio}_{\text{vm\_success}} = \frac{\text{Num}_{\text{vm\_success}}}{n} \cdot 100\%. \quad (14)$$

In the above formula, $h_{\text{all\_average\_load}}$ represents the average load of all hosts, $\text{Variance}_{\text{host}}$ represents the load variance of all hosts, Std_{host} represents the load standard deviation of all hosts, and $\text{Ratio}_{\text{vm\_success}}$ represents the success rate of creating virtual machines. The load dispersion of each host can be clearly expressed by variance and standard deviation.

3.5. Host Estimates Remaining Resources. According to Formula (2), the resource requests of virtual machines are generally PE, RAM, and storage, which will not be introduced here. As for the estimated remaining resources of the host, it represents the resource remaining situation of the host calculated by the algorithm when the virtual machine is scheduled, which is the estimated remaining resources of the host. This paper improves the definition of remaining resources in the original algorithm of OpenStack (the original algorithm only considers the virtual machine resources created by the host species). An estimation mechanism is added, which considers not only the created virtual machine in the host, but also the resource request of the virtual machine to be created. According to the Formulas (2), (4), and (6), the following Formula (15) is constructed.

$$\begin{cases} h_{k\_\text{free\_pes}} = h_{k\_\text{pes}} - \sum_{j=0}^{n-1} v_{j\_\text{pes}} \cdot \text{flag}_{jk} - v_{x\_\text{pes}}, \\ h_{k\_\text{free\_RAM}} = h_{k\_\text{RAM}} - \sum_{j=0}^{n-1} v_{j\_\text{RAM}} \cdot \text{flag}_{jk} - v_{x\_\text{RAM}}, \\ h_{k\_\text{free\_storage}} = h_{k\_\text{storage}} - \sum_{j=0}^{n-1} v_{j\_\text{storage}} \cdot \text{flag}_{jk} - v_{x\_\text{storage}}, \end{cases} \quad (15)$$

where $h_{k\_\text{free\_pes}}$, $h_{k\_\text{free\_RAM}}$ and $h_{k\_\text{free\_storage}}$, respectively, represent the estimated remaining Pe, estimated remaining memory and estimated remaining storage of host h_k, and their values are equal to the total corresponding resources owned by this host minus the corresponding resources of all virtual machines created on it and then minus the corresponding resources of virtual machines to be placed on it. Combined with Equation (5), it can be seen that the more remaining resources the host estimates, the more likely the scheduling algorithm is to put virtual machines on it.

3.6. Predicted Average Weight of Host Computer. In this paper, the estimated residual resources are used to calculate the corresponding estimated weights. Firstly, the maximum estimated residual resources and the minimum estimated residual resources of each resource need to be calculated. Then, the maximum estimated residual resource value and the minimum estimated residual resource value are used to calculate the estimated residual resource difference of each resource. Finally, using the estimated residual resource difference, the host residual resource value and the minimum estimated residual resource value, the estimated weight value corresponding to each resource is calculated, and the estimated weight value is added to take the average as the final estimated average weight value of the host.

(1) Calculate the estimated maximum residual resource value and the estimated minimum residual resource value of each resource. The purpose of calculating this value is to obtain the available residual resources on the host, so as to judge which host is more suitable for creating a new virtual machine. According to Formula (15), the following Formula (16) is defined as

$$\begin{cases} \begin{cases} \max_{\text{free\_pes}} = \text{Max}\left\{h_{0\_\text{free\_pes}}, \cdots, h_{s-1\_\text{free\_pes}}\right\}, \\ \min_{\text{free\_pes}} = \text{Min}\left\{h_{0\_\text{free\_pes}}, \cdots, h_{s-1\_\text{free\_pes}}\right\}, \end{cases} \\ \begin{cases} \max_{\text{free\_RAM}} = \text{Max}\left\{h_{0\_\text{free\_pes}}, \cdots, h_{s-1\_\text{free\_pes}}\right\}, \\ \min_{\text{free\_RAM}} = \text{Min}\left\{h_{0\_\text{free\_RAM}}, \cdots, h_{s-1\_\text{free\_RAM}}\right\}, \end{cases} \\ \begin{cases} \max_{\text{free\_storage}} = \text{Max}\left\{h_{0\_\text{free\_storage}}, \cdots, h_{s-1\_\text{free\_storage}}\right\}, \\ \min_{\text{free\_storage}} = \text{Min}\left\{h_{0\_\text{free\_storage}}, \cdots, h_{s-1\_\text{free\_storage}}\right\}, \end{cases} \end{cases} \quad (16)$$

where $\max_{\text{free\_pes}}$ denotes an estimated maximum value of the remaining Pe resource, $\min_{\text{free\_pes}}$ denotes an estimated minimum value of the remaining Pe resource, $\max_{\text{free\_RAM}}$ denotes an estimated maximum value of the remaining memory resource, $\min_{\text{free\_RAM}}$ denotes an estimated minimum value of the remaining memory resource, $\max_{\text{free\_storage}}$ denotes an estimated maximum value of the remaining memory resource, and $\min_{\text{free\_storage}}$ denotes an estimated minimum value of the remaining memory resource.

(2) Calculating the estimated residual resource difference of each resource (which is equal to the estimated maximum resource value minus the estimated minimum resource value), the purpose of calculating the value is to obtain the difference between the estimated residual resources of all hosts and calculate the estimated weight value of each host accordingly. According to Formula (16), Formula (17) is defined as

$$\begin{cases} \text{range}_{\text{pes}} = \max_{\text{free\_pes}} - \min_{\text{free\_pes}}, \\ \text{range}_{\text{RAM}} = \max_{\text{free\_RAM}} - \min_{\text{free\_RAM}}, \\ \text{range}_{\text{storage}} = \max_{\text{free\_storage}} - \min_{\text{free\_storage}}, \end{cases} \quad (17)$$

where $\text{range}_{\text{pes}}$ represents the estimated remaining Pe resource difference of all hosts, $\text{range}_{\text{RAM}}$ represents the estimated remaining memory resource difference of all hosts, and $\text{range}_{\text{storage}}$ represents the estimated remaining storage resource difference of all hosts, which can be used to calculate the estimated average weight of each host.

(3) This paper improves the calculation method of host weights in OpenStack's original algorithm (the original algorithm only considers the weights of a single resource), calculates the estimated average weights of the whole host by using the weights of multiple resources, and defines Formula (18) according to Formulas (15)–(17).

$$h_{jk\_\text{average}\_\text{weight}} = \frac{1}{3} \cdot \left(\frac{h_{k\_\text{free}\_\text{pes}} - \min_{k\_\text{free}\_\text{pes}}}{\text{range}_{jk\_\text{pes}\_\text{weight}}} + \frac{h_{k\_\text{free}\_\text{RAM}} - \min_{k\_\text{free}\_\text{RAM}}}{\text{range}_{jk\_\text{RAM}\_\text{weight}}} + \frac{h_{k\_\text{free}\_\text{storage}} - \min_{k\_\text{free}\_\text{storage}}}{\text{range}_{jk\_\text{storage}\_\text{weight}}} \right), \tag{18}$$

where $h_{jk\_\text{average}\_\text{weight}}$ represents the estimated average weight generated by host h_k when creating virtual machine v_j. The estimated weight value of each host is equal to the difference between the estimated remaining resources and the estimated minimum remaining resources and the estimated remaining resources, and then, the estimated weights of the three resources are added and averaged to obtain the estimated average weight, and the one with the highest estimated average weight is more likely to create virtual machines. The purpose of this is to reduce the impact of excessive resources on the weight of the end host and make the weight consideration more diversified.

4. Experiment of Virtual Machine Placement Algorithm

4.1. Experimental Simulation Environment. In order to test the performance of the algorithm, 10000 MIPs CPU, 50 GB memory, 1 TB storage, and 10 G bandwidth are set up. Specific settings of virtual machine and algorithm parameters are shown in Tables 1 and 2.

In order to analyze the performance of the algorithm, the virtual machines with loads of 100, 200, 300, 400, and 500 are run 10 times, respectively, and the average value of 10 times is taken as the final data of experimental evaluation.

4.2. Experimental Analysis. In order to verify the performance and efficiency of IGGA proposed in this paper, the virtual machine placement algorithm based on FFD is compared with the traditional virtual machine placement algorithm based on GA. FFD algorithm is a commonly used heuristic algorithm, which is generally used to solve the problem of virtual machine placement, while GA algorithm is the basis of improved genetic algorithm, and is often used to evaluate the performance of improved algorithm.

Table 1: Virtual machine parameter information.

Virtual machine type	CPU (MIPs)	Memory (GB)	Storage (GB)	Bandwidth (G)
1	1000	4	20	1
2	2000	8	50	2
3	3000	16	100	2
4	5000	24	200	4

Table 2: Setting algorithm parameters.

Algorithm parameters	Value
Population sizeS	50
Number of iterationsG	100
Crossing rateRc	0.8
Variation rateRm	0.02

As shown in Figures 1and 2, under the same virtual machine request scale, IGGA algorithm is obviously superior to FFD algorithm and GA algorithm in terms of the number of physical machines activated and the comprehensive utilization rate of resources. Compared with the other two algorithms, the number of physical machines activated is reduced by about 13% and 7%, respectively, and the resource utilization rate is increased by about 30% and 14%. Moreover, the number of activated physical machines is closely related to the request scale of virtual machines. At the same time, the request scale of virtual machine also affects the comprehensive utilization of resources, which fluctuates in a certain range.

As shown in Figure 3, IGGA algorithm is superior to FFD algorithm and GA algorithm in system energy consumption, and the energy consumption is reduced by about 12% and 6%, respectively. It has the least number of physical machines, the highest comprehensive utilization rate of resources, and the minimum energy consumption required by the system. Therefore, the less the number of physical machines started by the system, the higher the resource utilization rate, and then, the energy consumption of the system can be reduced.

As shown in Figure 4, it reflects the fluctuation of load imbalance of the three algorithms under different virtual machine sizes. Under the same virtual machine request size, IGGA algorithm is less unbalanced than FFD algorithm and GA algorithm, which shows that the improved algorithm is better than them in load balancing performance. The performance of FFD algorithm is the worst in load balancing and energy consumption. The algorithm reduces the number of active physical machines to a great extent, which makes the load of individual hosts too high, and the unbalanced load leads to waste of resources and energy consumption. Traditional GA algorithm has the disadvantages of high redundancy and repeated coding, resulting in poor performance of the algorithm. The algorithm proposed in this paper is optimized in energy consumption and load

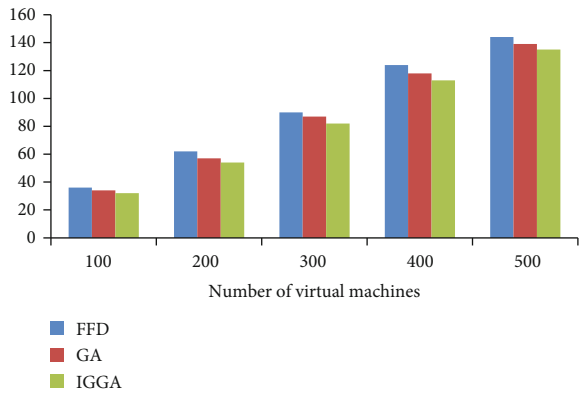

Figure 1: Comparison of the number of activated physical machines.

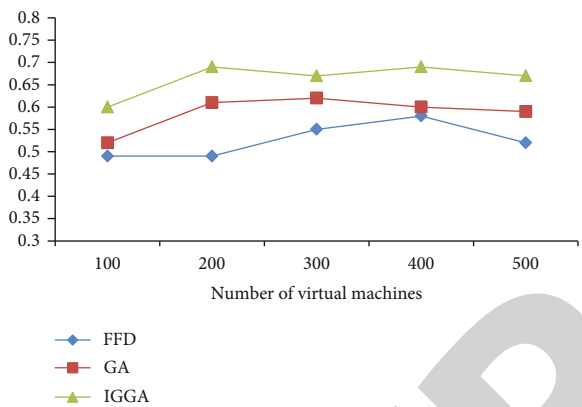

Figure 2: Comparison of comprehensive utilization rate of resources.

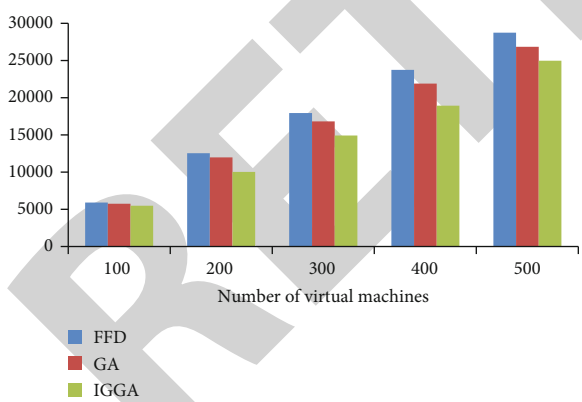

Figure 3: Comparison of system energy consumption.

balancing and improves the energy efficiency of the data center as a whole.

How to improve the overall energy efficiency of data center is a problem worthy of people's attention. By establishing the equilibrium index and combining with the traditional algorithm, the genetic algorithm proposed in this paper can be better optimized. Experiments show that the optimized algorithm can minimize data energy consumption.

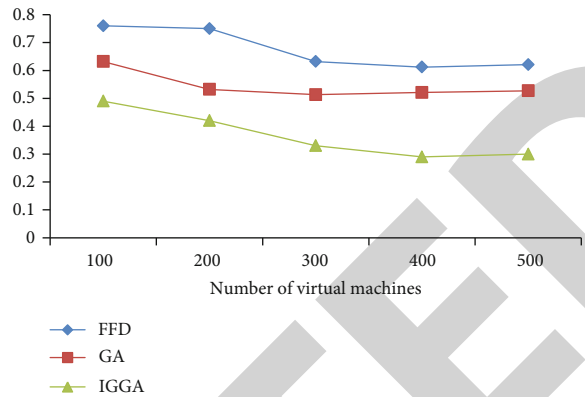

Figure 4: Comparison of load unbalance degree.

4.3. Experimental Simulation Environment. The experiment extends the cloud simulation platform and compares it with set-top box.

In the experiment, 500 physical machines are selected to form a data center. Each physical machine contains four resources with the same performance to verify the algorithm. The experiment also sets virtual machine parameters, specific data center, and algorithm, as shown in Tables 3 and 4.

The data processing method is the same as that in Tables 1 and 2.

4.4. Experimental Results and Analysis. In order to build a green data center, we should try to avoid the adverse effects of virtual machine migration, and this algorithm also considers minimizing unnecessary migration of virtual machines. In the algorithm, the statistics of migration times of virtual machines are mainly based on the situation that virtual machines are not in the source physical machines after integration.

As shown in Figure 5, the migration number of virtual machines in different virtual machine sizes is compared between DTMA algorithm and STMA algorithm, and both algorithms set resource load threshold intervals of 0.4 and 0.8. Compared with DTMA algorithm, the number of virtual machines migrated in STMA algorithm fluctuates greatly, which is due to the frequent migration of virtual machines caused by the changing load of physical machines reaching instantaneous peak and valley values. However, DTMA algorithm is lower than STMA algorithm in the number of virtual machine migration under all sizes of virtual machines, which is reduced by about 19%. This is because DTMA algorithm considers the overall load of the data center, dynamically changes the threshold interval of resource load, and deals with unnecessary migration caused by instantaneous peak and valley according to the load of the data center.

The system energy consumption is the sum of the energy consumption of all physical machines in the data center during the system operation, as shown in Figure 6, which reflects the energy consumption of DTMA algorithm and STMA algorithm under different virtual machine scales, and the system energy consumption increases with the increase of the number of virtual machines. Under the same

Table 3: Data center resource parameter.

Resource type	Physical machinery	Virtual machine
CPU	1000/2000/3000 MIPs	250/500/850/1000 MIPs
Memory	100 GB	256 MB
Storage	1 TB	2.5 GB
Bandwidth	20 Gbps	20 Mbps

Table 4: Setting algorithm parameters.

Algorithm parameters	Value
Threshold interval[Tlow,Thigh]	[0.4,0.8]
Load saturation interval[Lmin,Lmax]	[0.85,0.9]
Threshold backlashCoffset	0.05
RdcUpper bound constantR0	0.1

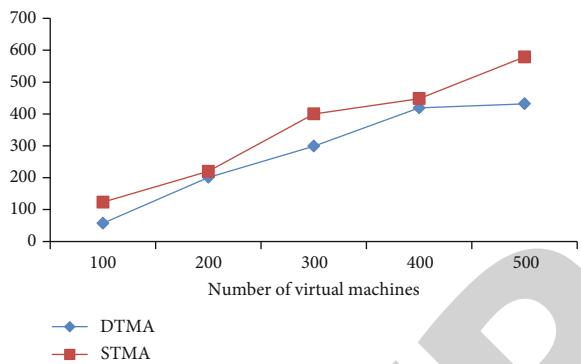

Figure 5: Comparison of the number of virtual machine migrations.

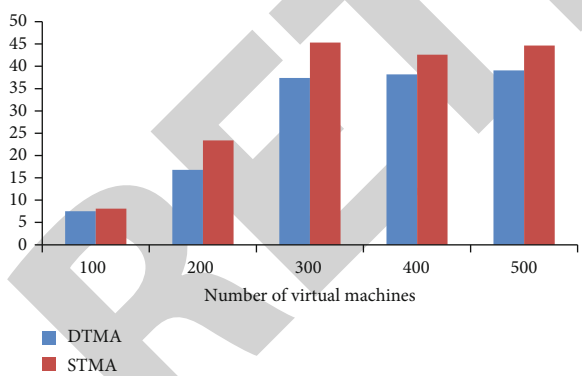

Figure 6: Comparison of system energy consumption.

virtual machine request size, the system energy consumption of DTMA algorithm is less than that of STMA algorithm, which is about 12% lower than that of STMA algorithm, indicating that DTMA algorithm is better than STMA algorithm in system energy consumption. Compared with STMA algorithm, DTMA algorithm reduces the energy consumption of cloud data center.

In this paper, a virtual threshold migration algorithm is proposed to solve the problem of unreasonable use of resources. This method can predict load, select migration opportunity, object, and destination physical machine, dynamically changes the threshold value, and migrate in combination with policies, thus reducing the number of servers, thus reducing the power consumption of the data center to the lowest. Through simulation experiments, this method can consider the load change of the whole data center and the dynamic adjustment of threshold interval, avoid unnecessary migration times of virtual machines, and play an important role in reducing energy consumption of data center.

This chapter mainly compares and analyzes the simulation results. Firstly, the simulation results of server number, energy consumption, and load imbalance between the proposed virtual machine placement algorithm and other algorithms are compared and analyzed, and then, the simulation results of virtual machine migration times and energy consumption between the proposed virtual machine migration algorithm and other algorithms are compared and analyzed, respectively.

5. Conclusion

In recent years, virtual machine scheduling based on virtual machines has become an important supporting technology for power management and dynamic expansion of cloud servers. Virtual machine resource scheduling problems can be divided into two categories: deployment and migration. Virtual machine deployment is the process of checking and selecting the appropriate physical target machine from the empty cloud service center according to the virtual machine type and resource request, which has been proved to be a NP-hard problem, similar to the compression problem. In the virtual machine placement stage, the virtual machine placement mainly adopts the corresponding greedy or heuristic virtual machine placement strategy, which is difficult to ensure the balanced utilization of resources and lacks consideration of the data center load type. The purpose of migration is to study the process of data change. The whole process must be handled according to the load of the computer room. In the phase of virtual machine migration, we need to consider the following aspects, choose the migration timing, object, and target physical machine, and adjust the source physical machine according to the load.

Data Availability

The experimental data used to support the findings of this study are available from the corresponding author upon request.

Conflicts of Interest

The authors declared that they have no conflicts of interest regarding this work.

Acknowledgments

This work was sponsored in part by the 2020 Teaching Research and Scientific Research Project of Jiuzhou Polytechnic (Yjx202003).

Hindawi
Journal of Sensors
Volume 2022, Article ID 1817781, 11 pages
https://doi.org/10.1155/2022/1817781

Research Article

The Key Technology of Wireless Sensor Network and Its Application in the Internet of Things

Yao Zhang[1] and Wanxiong Cai[2]

[1]*Xinjiang Changji Military Subarea, Changji 831100, Xinjiang, China*
[2]*College of Electrical Engineering, Guangxi Technological College of Machinery and Electricity, Nanning, 530007 Guangxi, China*

Correspondence should be addressed to Wanxiong Cai; wanxch83@gxcme.edu.cn

Received 14 January 2022; Revised 22 March 2022; Accepted 31 March 2022; Published 9 May 2022

Academic Editor: Han Wang

At present, sensor networks and the Internet of Things have made rapid development and received more and more attention. Wireless sensor network technology is widely applied in many industries. As an important part of IoT sensor layer, it is an important infrastructure for IoT development. The purpose of this paper is to enhance the existing wireless sensor networks on the basis of existing technologies for better application in IoT. In this article, we introduce the structural features, key techniques, and some specific applications of wireless sensor networks in the IoT. Secondly, this paper studies and analyzes the principle of the cell membrane algorithm and its own characteristics. Aiming at the problem of energy constraint in wireless sensor network, an energy equilibrium clustering algorithm based on the cell membrane optimization algorithm is proposed in order to realize energy balance of nodes and distribution of network cluster heads. This algorithm divides the nodes by concentration and energy factors and divides them into globally balanced clusters by combining distance factors, which can well solve the problems of uneven distribution of cluster heads and unbalanced global power usage in sensor networks. On the basis of a lot of previous researches, this paper presents a QoS model, which is based on the routing protocol, clustering protocol, and data fusion scheme discussed in this paper. Through analysis and experiments, it is proved that this scheme improves energy consumption and flexibility by 78% compared with the previous one and achieves better network performance.

1. Introduction

The so-called IoT, which is something connected to the Internet, founded in 2009 in China "experience China" center, and also, developing the IoT of the national IoT "twelfth five-year" development plan is also in the process of development; this move is to determine that IoT has an irreplaceable role in the new era, which is a significant position in the emerging technology sector. Wireless sensor network technology, as the backbone of the Internet of Things, needs continuous development to promote the whole IoT and even Huliang network and becomes a catalyst for global economic development.

A wireless sensor network is a distributed sensor network with sensors at the tip that can sense and inspect the outside world. Sensors in WSN communicate wirelessly, so network settings are flexible, device locations can be changed at any time, and wired or wireless connections to the Internet are possible. A multihop self-organizing network formed by wireless communication.

The Internet of Things is an emerging technology that connects various forms of wired and wireless networks with the Internet, thus connecting objects to each other and forming a huge network for monitoring, analysis, and control. Wireless sensor technology is used in many applications like battlefield surveillance, ambient and traffic detection, and industrial and agricultural production. Wireless sensor network is an essential component of the sensor layer of IoT, which is a deep extension of the original network and an important material basis for the growth of IoT. Applying

the key technologies of wireless sensor networks in the Internet of Things will greatly improve the performance of related applications of the Internet of Things.

An appropriate sensor node clustering algorithm can improve the efficiency of sensor networks in terms of power. Nevertheless, clusters require extra expenses, like the selection and assignment of cluster heads and the building of clusters. Leu et al. proposed a wireless sensor network area energy perception clustering method based on isolated nodes, which is called isolated node area energy perception clustering. To extend the lifespan of the network, the mean energy of the area and the proximity of the sensors to the confluence are employed to decide if individual nodes send data to the CH node or the confluence in the preceding round [1, 2]. Wang and Jiang presented a detailed comparison of the design and protocol architecture [3, 4]. To facilitate the monitoring of dissolved oxygen in large-scale aquaculture ponds, Ma et al. have realized distributed measurement, intelligent control, and centralized management [5]. IoT is ubiquitous in our daily life. It is used in our homes, hospitals, and deployed outdoors to control and report changes in the environment. It prevents fires, and it has many other beneficial functions. Yang et al.'s investigation consists of four parts. The first part will explore the most relevant limitations of IoT devices and their solutions. The second will introduce the classification of IoT attacks. The next section will focus on the mechanisms and architecture of authentication and access control. The final part will analyze security issues at different levels [6]. To sum up, most of the literature cited in this paper is about sensors, which is insufficient in the Internet of Things. Next, this paper will focus on the application of wireless sensor networks in the Internet of Things.

Firstly, the thesis gives an overview of wireless sensor network. Then, the constraint relationship between the key technologies of wireless sensor network is analyzed. Then, the route management scheme based on clustering is described, and the detailed process of SCBRP algorithm and JAQ algorithm is given. Second is mainly based on the clustering of head inherit the protocol (ICBPWSN) which is described in detail, and the results of simulation experiment are given: first, it discusses the related data fusion technology and routing and topological structure, describes the data fusion (ALBDA) scheme based on the application layer, and finally gives the simulation and analysis results, and the fifth chapter is summary and outlook [7].

2. Proposed Method

2.1. Wireless Sensor Network

2.1.1. Wireless Sensor Network. The wireless sensor network originated in the cold war period and was initially used in the military field to monitor the activities of the enemy. Wireless sensor network (WSN) technology is highly valued and widely used in many countries. It can be expected to play a greater part in industrial and farming production, urban planning as well as management, environmental monitoring, and battlefield monitoring in the future [8, 9]. As wireless sensor network has a very broad range of uses, especially in the military and smart home applications, it has become an international concern, involving a high degree of interdisciplinary and knowledge integration of the forefront of the hot research field; there are many technical issues to be further studied. Many developed countries have invested heavily in research on wireless sensor networks and are eager to apply them to a broad range of uses [10].

2.1.2. Architecture of Wireless Sensor Network. Wireless sensor network is a kind of wireless ad hoc networks: it has several dozens to hundreds of even more a sensor node, through wireless communication links into a dynamic, more mobile peer-to-peer networks, usually including sensor node, the node, and the management node. The sensor node transmits the sensed data to the sink node in some way through wireless communication in the monitoring area and then finally reaches the user through other communication links. Through dynamic routing and mobile management technology, the network protocol stack of the whole network transmits information flow up to a certain level on unreliable and unstable channels. Figure 1 shows the architecture of the wireless sensor [11, 12].

2.1.3. Wireless Sensor Network Nodes. Sensor node is a kind of miniature embedded device, which requires low price and low power consumption. These constraints will inevitably lead to the relatively weak processor capability and small memory capacity carried by it. Generally, the sensor node supplies energy through the battery pack. The architecture of the node is presented in Figure 1. However, the energy of nodes, the constraints of various computing resources, the dynamic change of network topology, and the unstable connection status of links all make sensor networks more challenging, as shown in Figure 2.

2.1.4. Characteristics of Wireless Sensor Network

(1) Limited Resources. Extreme finite availability of resources for sensor nodes is shown in Table 1.

(2) Large-Scale Networks. Large scale is reflected in two aspects: the sensor network covers a larger area, and the sensor nodes are deployed in a larger density. In this way, the sensor network can obtain more real and comprehensive information. Collecting information from a large number of nodes can increase the information precision and decrease the accuracy requirements for individual node sensing data [13]. The existence of redundant nodes in large-scale multi-node distributed deployment can make wireless sensor networks more fault tolerant.

(3) Self-Organizing Dynamic Adaptive Network. Because of the wireless sensor network (WSN) is in most cases were randomly deployed (such as by aircraft or from animals carry) to the object to be observed environment, this requires that the sensor network nodes have the capability of self-organization as well as the ability to collaborate on network information transmission [14].

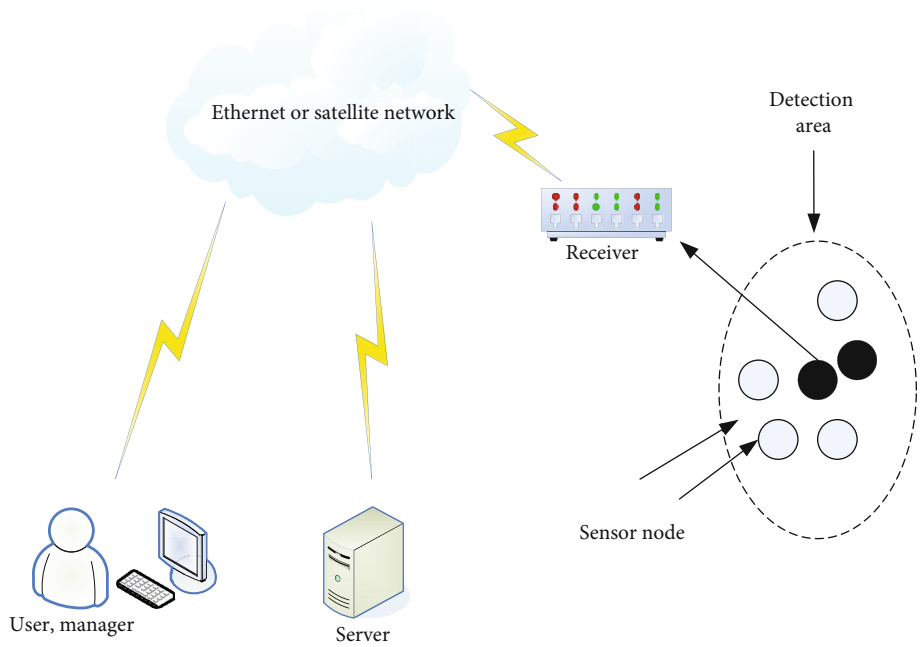

Figure 1: The architecture of a wireless sensor.

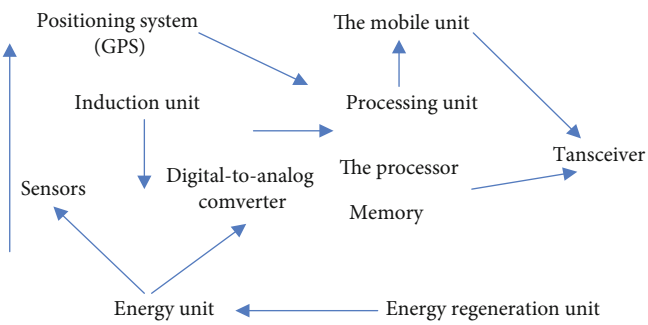

Figure 2: The components of sensor node.

Table 1: Limited representation of sensor node resources.

Limited aspects	The specific performance
Energy Co., Ltd.	Nonrecyclable, button battery powered and nonreplaceable, energy must be used efficient
Induction ability	A single node has only partial inductive capability, such as acceleration, electromagnetic field, sound, light intensity, and some other characteristics, and must make full use of inductive data
Ability to calculate	The memory is generally less than 100 KB, and the main frequency is less than 1000 MHZ, but there are also 128 K, such as Atmega128
The ability to communicate	The coverage range of node radio waves is less than 100 meters, and the communication bandwidth of dozens of kbps will also have uncertain changes

In addition, existing roofing structures of wireless sensor systems may fail as a result of external interference (environmental elements and vandalism) or power depletion. The capacity of a wireless connection can change depending on the environment or its own conditions. Sensor nodes, observed objects, and observers may change their positions. Sensor nodes, observed objects, and observers may change their positions; and dynamic human intervention to the control center (e.g., militarily preventing certain sensor nodes from falling into enemy forces). In order to effectively use energy to prolong the life of nodes, the nodes can be added or withdrawn dynamically. All these require wireless sensor networks to have dynamic adaptive capability [15].

(4) Bad Environment. Wireless sensor networks typically work in the wild or at least unattended and often work

without interruption but can also be subject to malicious human interference, information leakage, or the transmission of bug messages (similar to Byzantine errors, the implication is that trying to achieve consistency by means of message passing on an unreliable channel with message loss is impossible).

(5) Data-Centric Networks. General networks, network devices, and other resources are located by the unique port address in the network in different ways. Sensor networks are event and mission networks, and it is meaningless to talk about a single node without sensor networks. The uniqueness of the node number in a wireless sensor network is determined by the designing of the specific network traffic agreement. The upper application of wireless sensor network only tells the network whether there is an event happening in the area it is concerned about monitoring, or the network actively notifies the upper application of an event, and the user will not give a query task to a node. In this way, the wireless sensor network is a data-centric network because of the way to query or communicate with data [16].

The wireless sensor network is in a harsh environment, and its storage and energy are strictly limited. Therefore, when designing a WSN security solution, storage overhead must be considered. In Yeh, the gateway node needs to save the public keys of all users. In this solution, the smart card only needs to save the GWN identification data [17]. GWN only needs to save its own private key and public key, and each sensor node only needs to save the public key, which greatly reduces the storage space. The LED light block cipher was proposed at the CHES 2011 conference. The LED algorithm has a block length of 64 bits, supports a key length of 64/128 bits, and has 32 encryption rounds. At the same time, the encryption algorithm used in this scheme is an LED lightweight encryption algorithm, which does not require the use of a private key, and is simple and efficient. Sorting out and summarizing the memory space required by several lightweight block encryption algorithms under different plaintext lengths, the outcomes are presented in Table 2. The Advanced Encryption Standard in Cryptography, also known as Rijndael encryption, is a block encryption standard adopted by the US federal government.

Table 2: Comparison of memory space required by each algorithm.

Encryption algorithm	63	126	252	504	1008
AES	10009.25	10234.3	10120.34	10254.31	10234.63
TWINE	2661.38	2354.01	2415.65	2365.21	3651.13
LED	2569.34	2145.21	2136.36	2145.35	3425.12

2.2. Application of Wireless Sensor Network Technology in the Internet of Things

2.2.1. Application in the Military Field. Wireless sensor networks have many features that are useful in the military, such as rapid deployment, free organization, high concealability, and high fault tolerance, which make them popular in the battlefield and can work great in extremely harsh environments. Aimed at this one big advantage, there will be a huge amount of sensor nodes, through the mode of transportation, including aircraft artillery, around the goal of all kinds of parameters, such as temperature humidity, terrain, voice, and coordinates, such as information acquisition, and then through the secret transmission channel, the information back to the processing, in this way, the real-time monitoring of the enemy's movements and battlefield assessment, and implementation of simulation way work out a plan for the best, make the combat forces and its effectiveness, and reduce the unnecessary loss [18].

2.2.2. Application in Industrial Field. Wireless sensor network is very popular in the industrial field; it eliminates the artificial instability, making it possible to work every day, in the field of industrial safety, traffic control, security systems, logistics management, and so on. The application in the field of industrial safety is the most. In after dealing with the explosion of sensor node and the optimized technology, it can be put on people have hurt environment, real-time monitoring of the safety of staff, and process line for dangerous working environment environmental parameters in time and can let a person even remote control instead of people to work; therefore, wireless sensor network technology can optimize industrial process, reduce the probability of safety accidents in industrial production, and can ensure the quality of industrial production under the premise of improving the quality of the products.

2.2.3. Application in the Field of Medical Care. China has begun the aging of the population; in the medical care, problems are increasingly prominent, and real-time attention to the disease of patients has become a major problem to be solved. However, wireless sensor network monitoring system plays a significant role in this respect. Doctors can install tiny and precise sensors on patients to detect and collect real-time physiological information of patients, so as to understand the development of patients' conditions at any time. On the other hand, real-time monitoring also provides more reference materials for medical institutions. Through the analysis and processing of various parameters, the root causes of diseases can be found, so as to develop effective drugs and save more people [19].

2.2.4. Application in the Field of Smart Home. In the last few years, the Internet of Things is developing into a smart home. Intelligent home means highly intelligent home automation system, the application of a lot of high-tech system products and equipment, and artificial intelligence, improves the safety and comfort of the home environment, and in this premise achieves energy conservation and environmental protection. The principle is to use a large number of wireless sensor network nodes to make it self-organizing interconnection, so as to achieve the interconnection and control of home devices; this is the smart home [20].

2.3. Ant Colony Algorithm and Its Application in Wireless Sensor Network Routing. Ant colony algorithm has the

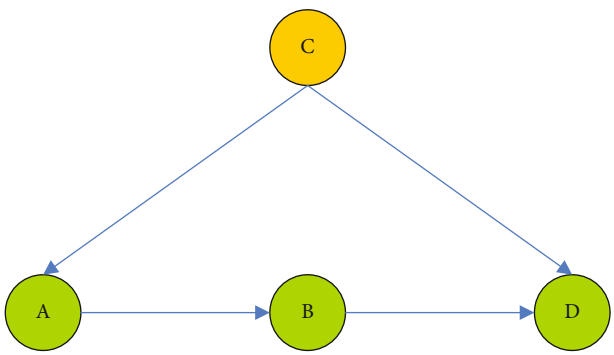

Figure 3: Ant colony algorithm path diagram.

characteristics of distributed computing, positive feedback of information, and heuristic search and is essentially a heuristic global optimization algorithm in evolutionary algorithms. To illustrate the ant colony method better, we use the figure below to illustrate it in detail. As shown in Figure 3, assuming that the ant starts from point A of the ant nest and the food source is at point D, the ant walks at the same speed. The length of ACD path is 20 units of distance, while the length of ABD path is 10 units of distance. As the ant departs from site A, it does not have prior knowledge of which route is optimal (no pheromone), so the probabilities of ABD and ACD are the same. After a distance of 10 units, the ants on the ABD route have managed to find food, and the ants on the ACD route have arrived at point C just now. After 20 units of distance, the ants of ABD path have successfully returned to point A of the ant nest, and the ants of ACD path have reached point D and found food. After 40-unit distance, the ants of ACD return from food source D to ant nest A, and they have a concentration of 2 units of pheromone, while the concentration of the pheromones in the ABD pathway changes to 4 units, that is, the pheromone concentration of ABD path: the pheromone concentration of ACD path = 2 : 1. Then, when the subsequent ant colony selects the ABD and ACD paths, two ants will be sent to the ABD path, and one ant will be sent to the ACD path. After 40-unit distance, the concentration of the ABD path pheromone is equal to 3 : 1. If this is repeated, the ratio will increase from 4 : l.5 : 1.6: l, that is, positive feedback will be formed, and finally, the route ABD will be chosen by every ant in the colony [21, 22].

2.3.1. Implementation of Ant Colony Algorithm. The connecting route pheromone among city i and city j at time t was set as $t_{ij}(t)$, and the pheromone concentration on each city path was the same at the initial moment, set as $t_{ij}(0) = t_0$.

When the ant k determines the next city to arrive based on the pheromone intensity of intercity connectivity routes,

$$P_{ij}^{k}(t) = \begin{cases} \dfrac{\left[t_{ij}(t)\right]^{\alpha} \cdot \left[\eta_{ij}(t)\right]^{\beta}}{\sum\left[t_{iu}(t)\right]^{\alpha} \cdot \left[\eta_{iu}(t)\right]^{\beta}}, & u \in N_k(i), \\ 0, & \text{otherwise}. \end{cases} \tag{1}$$

Table 3: Values of each parameter of the algorithm.

Parameter	Parameter
Ant colony population size	49
a	2
b	3
Pheromone initial volatilization coefficient	0.4
Pheromone enhancement factor	99
Maximum iteration coefficient	98

After all ants finish a period, the information of pheromones on each city route is updated according to Equation (2):

$$t_{ij}(t+1) = (1-p)t_{ij}(t) + \Delta t_{ij}, 0 < p < 1. \tag{2}$$

Among them,

$$\Delta t_{ij} = \sum_{k=1}^{n} \Delta t_{ij}{}^{k}. \tag{3}$$

According to different pheromone update strategies, the basic ant colony algorithm has different models:

$$\Delta t_{ij}^{k} = \begin{cases} \dfrac{Q}{L_k}, & ij \in l_k, \\ 0, & \text{otherwise}, \end{cases} \tag{4}$$

$$\Delta t_{ij}^{k} = \begin{cases} \dfrac{Q}{d_{ij}}, & ij \in l_k, \\ 0, & \text{otherwise}, \end{cases} \tag{5}$$

$$\Delta t_{ij}^{k} = \begin{cases} Q, & ij \in l_k, \\ 0, & \text{otherwise}. \end{cases} \tag{6}$$

In the above three models, Q is a constant, representing the total amount of pheromone released by the ant once in a cycle, L_k is the path length of ant k between city i and city j, L_k is the path taken by the ant, and d_{ij} is the side length.

The simulation experiment is programmed and tested using MATLAB2010b; the algorithm uses various parameters to be derived from experience and trial calculations, and the initial value settings are shown in Table 3.

2.4. Relationship between Key Technologies of Wireless Sensor Networks. The critical wireless sensor network technologies include network topology control, network protocols, data fusion, data management, QoS assurance, embedded operating system, time synchronization, and location information. Key technical issues, such as low-power short-range wireless telecommunication technique 1171 and security, have some challenging relationships.

2.4.1. Topology Control and Other Key Technologies. Topology management in wireless cell networks is used to

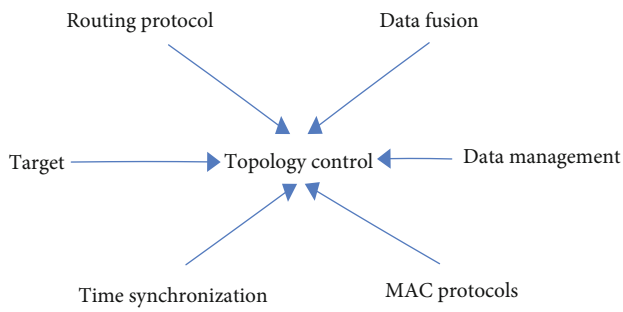

Figure 4: Their location between topology and other key technologies.

eliminate unnecessary communication links between nodes by power management and selection of backbone web nodes and finally form a network topology structure of efficient data forwarding under the premise of satisfying the coverage and connectivity of the network. Its relationship to other key technologies is shown in Figure 4.

Due to the relatively large size of wireless sensor network (WSN), the node number is numerous, and adopting the method of plane management will become very difficult with the increase of network scale and at the same time make data in order from the sensor nodes for data management and integration. MAC protocol and time synchronization protocol are needed in the formation of hierarchical topology control. The MAC protocol determines when a node is allowed to send packets and generally controls all access to the physical layer. Conversely, when topology control is formed, a good topology will also improve the efficiency of MAC protocol and time synchronization protocol. In other words, they have a two-way relationship [23, 24].

The same is true for target location. With hierarchical structure, when a node detects the occurrence of an event, it will immediately obtain the bit yellow of the event or the location of the node, so that cluster cooperation can obtain the location information to locate the event. Topology structure also has a great impact on routing protocol. After the formation of hierarchical structure, the node only needs to know the routing information of the neighbor node, that is, it needs to know that the neighbor node can relay to the cluster-head node, and the cluster-head node needs to maintain the routing information of the base station and all its member nodes. Hierarchical structure refers to a structure of automated test code. The feature of this structure is that the complex test code is divided into three levels of one-way dependencies, and the test logic in the test code built with the hierarchical structure becomes clear and easy to understand and maintain [25].

After the formation of the hierarchical topology structure, in order to save energy, the induction data in each cluster can wait for the induction data of the downstream node and then forward to the upstream node after fusion, while the cluster head periodically waits for the induction data of all members in the cluster to arrive and send back to the base station through fusion. For the data management requests required by the application layer, the corresponding logic layer semantics can be mapped to the corresponding physical entity semantics, and then, the requested cluster makes the final response to the request through the cluster head.

3. Experiments

3.1. Experimental Environment. In the experimental scenario, more than 100 sensor nodes are randomly deployed in a grid of 100″100. The energy of each node is set to the same initial value, and the communication radius of the nodes is 50. In other words, only two nodes with a distance of less than 50 are considered as adjacent nodes. The formula for calculating energy consumption was tested with the previous data. Channel of the data transfer rate of 2.5 Kbps, the length of each packet is 40 bytes, and every node looms induction data at a time.

In order to demonstrate the performance of ALBDA data fusion scheme through experimental comparison using the above experimental environment settings, we chose two other data fusion schemes. No fusion scheme (NoAgg): each node does not know the existence of other nodes, and the data is not sent back to the base station through fusion; PerfectAgg: the node knows the optimal fusion node without additional communication and sends it to the base station after fusion. We recorded the event response latency, energy consumption, packet latency, packet loss rate, and the number of packets received by running each experimental scheme separately.

3.2. Experimental Parameters. Each node in the wireless sensor network is abstracted into nodes in the algorithm. If there are n nodes, the total number of nodes is n. The maximum iteration times of each selected cluster head is Gmax. The radius coefficient used to calculate the node concentration is r. The critical value is pa for the current optimal node to stop searching. The shrinkage of the search radius is pb.

n nodes were randomly deployed in the wireless sensor network, and the concentration con of the surviving nodes within the radius of each node was calculated according to the radius coefficient r. For example, the concentration con of node I is defined as the sum of the distance from all valid nodes contained in the radius to node I and the percentage of the total number of nodes n times the radius, namely, formula (7):

$$\text{con} = \frac{r * Y}{n * \sum \left| \sqrt{(X - X_1)^2 + (Y - Y_1)^2} \right|}, \tag{7}$$

where Y is the total number of nodes within the radius coefficient r. It can be seen from this that the higher the concentration of the node, the greater the number of nodes around the node radius, or the smaller the sum of the distances from all nodes to this node if the number is the same. E is the ratio of the energy of each node to the mean power of the web. The factor value (p) of each node is determined by the concentration con of the node and the energy ratio of the node, e, that is, $p = a * \text{con} + b * e$, where $a + b = 1$ and both a and b are greater than 0. Carrier factors are introduced to regulate the trajectory of node motion. The carrier factor of each

Table 4: Experimental parameter setting.

Parameter	Value
Network coverage area	140*90 m^2
Number of sensor nodes	100
Initial energy of node	8 J
Packet size	465 bytes
Metadata size	18 bytes
Energy consumption per unit of data	1 nJ/bit
Maximum distance of communication between nodes	30 m

node is defined as the ratio of the inverse of the distance between all effective nodes and this node and the total number of nodes n within the 2-search radius ($2r$), as shown in formula (8):

$$g = \frac{1}{n}\sum \frac{1}{\left|\sqrt{(X - X_1)^2 + (Y - Y_1)^2}\right|}. \quad (8)$$

Among them, g is the average distance parameter, which means that the distance between nodes within 2 search radius and this node is small and vice versa. The routing algorithm was simulated in the simulation environment of MATLAB7.0, and the convergence of the algorithm was analyzed. The relevant test data are displayed in Table 4.

3.3. Initialization of Experimental Nodes. In n nodes, the nodes are sorted according to the size of factor value (p), and the nodes are divided according to the following proportion, as shown in Table 5.

According to the above table, three node groups are divided, where X represents the distribution ratio. The optimal solution can only emerge through multiple iterations, so the different allocation ratio will not have a great impact on the number of cluster heads and the optimal solution in each round. However, if X is too low or too high, it will lead to a large proportion gap between the three kinds of node groups and frequent jitter between the three kinds of node groups, which will extend the iteration times of the optimal solution and the iteration times of the three kinds of node groups and increase the calculation amount. In combination, the proportion of X is 15-20% in the experiment.

We use the standard variance formula to evaluate the resource load. According to the resource load, calculate the total time for task scheduling and execution, as shown in Table 6 below.

4. Discussion

4.1. Performance Analysis

4.1.1. Routing Overhead. The calculation is displayed in Figure 5. Improved ACO algorithm is given to ants before and after the ant packets are small, so the routing control information to increase the network load is small, meanwhile with the increase of transmission speed, while the

Table 5: The partition way of nodes.

The node type	Allocation proportion
Low concentration node group (L)	Sort the first X times n nodes
High concentration nonfat-soluble node group (HF)	Sort the first X times n to $2X$ times n nodes
High fat-soluble node group (H)	All the remaining nodes

Table 6: Task allocation time comparison.

Algorithm name	Task allocation execution time
ACA algorithm	79.8
Min–Min arithmetic	89.4
FOA_ACA algorithm	75.3

routing control data increases but essentially unchanged routing control information, so the improved ACO algorithm of routing control information costs will be reduced.

4.1.2. Total Energy Analysis. The lower the overall energy usage of the network, the lower the cabling expense of the network, and therefore, the longer the life-cycle of the system. The overall power consumed by the sensor is used as a measure, and the calculation is evaluated against the flood and basic ACO methods. The outcome is presented in Figure 5.

As can be seen from Figure 6, the energy consumption of this algorithm is higher than that of the flood model and the ACO algorithm. However, due to the flooding, all nodes in the model are involved in the benefit and the detection data of the flooding, and with the extension of time, energy consumption presents sharp steep increase: MAC OS used the network time delay information update paths, and optimizing the path requires more ants work together. The improvement of ACO algorithm can prolong the life cycle of the path by taking into account the energy balance characteristics of ant dynamic optimization, avoid cyclic ant proliferation, and save the power consumed by the network.

4.2. Multicore Wavelet Vector Machine Algorithm Analysis. Statistical learning theory is a small-sample learning theory proposed by Vapnik et al., focusing on the study of statistical laws and learning method properties in the case of small samples. Based on the characteristics of known samples, it finds the interdependent relationship between data through learning methods, so as to predict the future data or judge its properties.

Suppose the practice model set of size n is $\{x_i, y_i\}_{i=1}^{n}$, $\{x_i\} \subset R^n$, where x_i represents the sample input data, and if it belongs to the first category, then $y_i = 1$. If you are in the second category, then y_i is equal to minus 1.

If there is a classification hyperplane,

$$wx + b = 0. \quad (9)$$

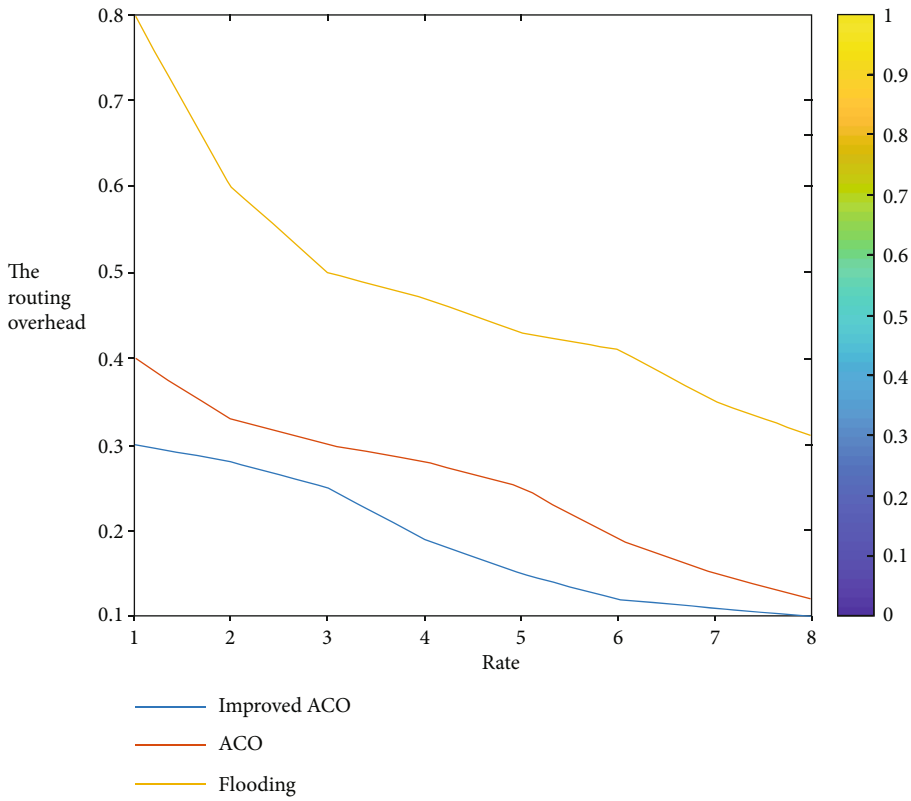

Figure 5: Routing information overhead.

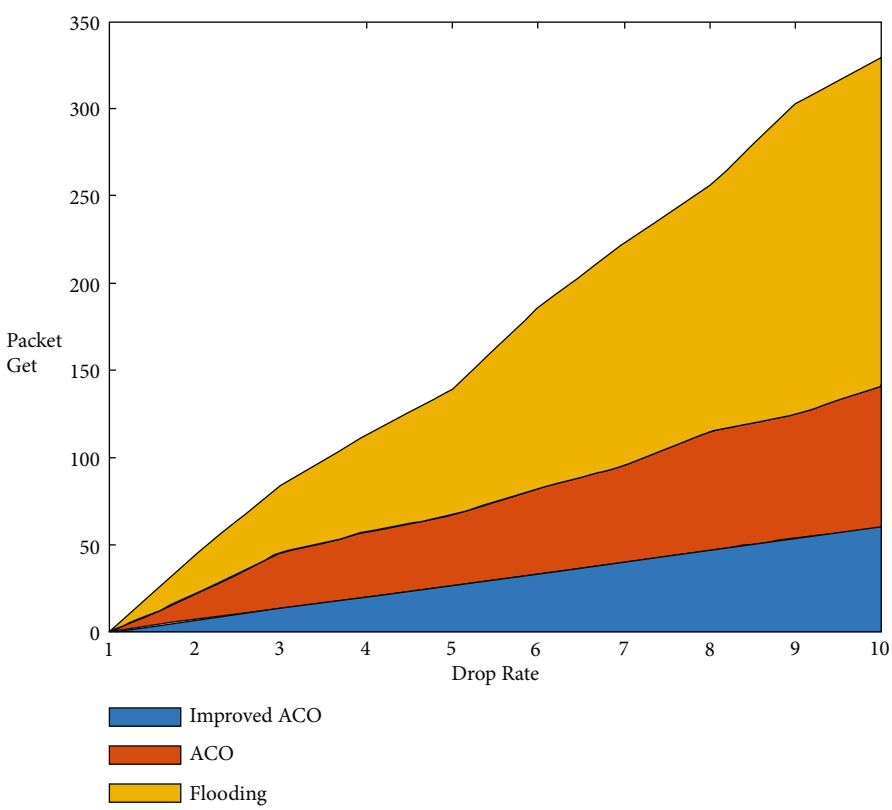

Figure 6: Comparison of energy consumption.

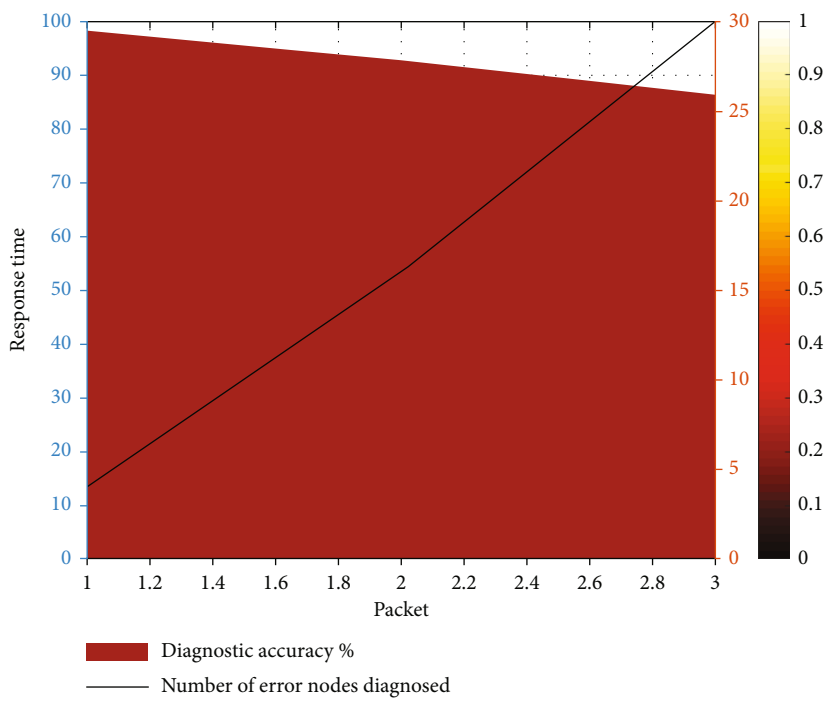

Figure 7: Comparison of results of MKWRVM, RVM, and SVM of three diagnostic models of wireless sensor.

If samples can be separated without error, that is, samples of the same category are on the same side of the classification hyperplane, the sample set is said to be linearly separable, namely, to meet

$$\begin{cases} wx_i + b \geq 1, & y_i = 1, \\ wx_i + b \leq -1, & y_i = -1, \end{cases} \tag{10}$$

where W is the weight vector and b is the bias.

The distance from the point x_i of the sample to the categorical hyperplane is defined as follows:

$$\Delta_i = y_i(wx_i + b) = |wx_i + b|, \tag{11}$$

$$\delta = \min \delta_i, \quad i = 1, 2, \cdots, n. \tag{12}$$

4.2.1. Comparison of the Results of Three Diagnostic Models. Figure 7 shows a comparison of the diagnostic results for MKWRVM, RVM, and SVM. It can be seen that the number of error nodes diagnosed by the three diagnostic models is 4, 16, and 30, respectively, and the accuracy rate is 98.18%, 92.73%, and 86.36%, respectively. The results show that wavelet multicore correlation vector is better than RVM and SVM in diagnosis of wireless sensor nodes.

4.2.2. Comparison of Node Consumption Capacity. In the nonfusion scheme, the sensor data of the nodes are not fused and sent directly to the base station, so the transmission of a large amount of redundant data will consume too much energy. More importantly, due to the different distance between the nodes and the base station, some nodes will consume too much energy, so the energy consumption of the nodes is uneven. We can also see from the energy consumption of the node in Figure 8 that in addition to the energy consumed by selecting the cluster head, the energy consumption of ALBDA is close to the ideal fusion scheme, far less than that of the nonfusion scheme. In moreover, the power consumption of each node in ALBDA is relatively uniform.

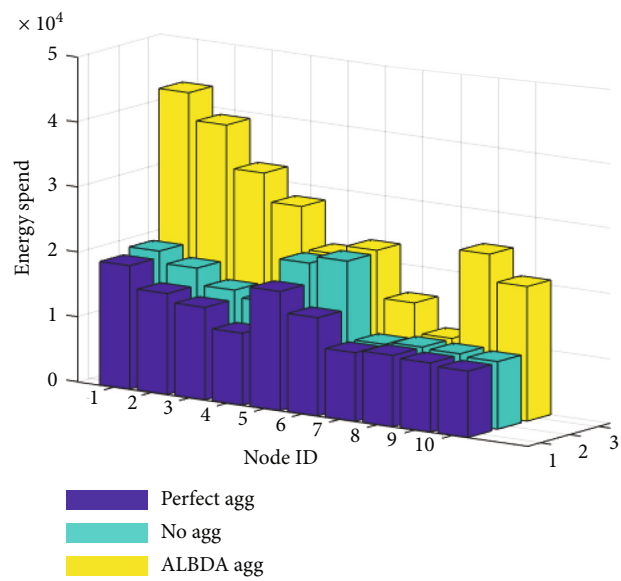

Figure 8: The comparison for node energy spent.

5. Conclusions

Wireless sensor network as a new special distributed system can be obtained from its environment, several characteristics, so as to realize the remote sensing, fundamentally

changed the process of human to obtain information, process information, and in this sense, the wireless sensor network (WSN) is extended to its tentacles in the natural environment. Wireless sensor networks tend to focus more on the data itself and less on other information, somewhat like grids. From its birth, it is destined to have huge application prospects, not only in the current fields of military, industrial, environmental, and scientific research, but also in our lives. This puts forward more challenges to our research. As a key technology for wireless sensor nets, the research will face more formidable challenges.

This article first detailed analysis of the key technology of wireless sensor network's (WSN's) several aspects of the relationship between interdependence and mutual influence between them; thus, we are thinking about the key technology of any time; on the one hand, it cannot be isolated; we must consider other relevant aspects at the same time and provide the theoretical basis for our discussion later. The proposed SCBRP routing protocol provides the routing basis for the following clustering protocols, data fusion schemes and QoS schemes. Based on the features of wireless sensor networks, hierarchical network organization can be adopted for specific applications, and a clustering protocol ICBPWSN based on cluster head inheritance is proposed, which can quickly and energy-saving make the network form a hierarchical structure and avoid the random cluster head selection conflict in LEACH. Due to data fusion to the induction of network data processing, remove redundant, save energy, and increase the accuracy of the data, but due to limited resource extreme in the wireless sensor network (WSN), abnormal operating conditions may, with the time sensitivity of the handling of data cannot be too complicated, so in view of the existing research results, we suggest a fusion scheme based on a simple fusion function ALBDA; experiments show that it has obvious energy saving and the advantages of low bandwidth consumption and fast response data. With the progress of various related technologies of wireless sensor network, it is far from enough to only provide the classical wireless sensor network with the best possible service. This is the same with QoS in effect as in traditional networks, but it is a very difficult challenge to achieve this goal under the harsh conditions of wireless sensor networks. After the previous research in this paper, according to the previous research results, we proposed an energy-saving service scheme to provide QoS assurance, and we analyzed its advantages of energy saving and better adaptability.

Wireless sensor has attracted great attention from the whole academic circle. However, due to the extremely restricted working environment of wireless sensor network, the research progress largely depends on the progress of electronic technology, communication technology, microelectromechanical technology, and computing technology. Under the current technical conditions, resource constraints make the research of key technologies very difficult, and the research of one aspect must also consider other relevant aspects. This paper only considers four aspects. If we can combine all aspects of key technologies, then we can more reasonably meet the demand, which is also the next step of research. For the clustering protocol, it is necessary to consider the optimization of the number of clusters. The flexibility of data acquisition and processing in data fusion needs further study. At present, QoS guarantees have the largest research space and the most formidable challenges, but it is also most affected by resource constraints. In addition, another important research topic for wireless sensor networks is network security, and more research is needed in the next step, especially the consideration of security policies and security mechanisms when considering other key technologies.

Data Availability

No data were used to support this study.

Conflicts of Interest

There is no potential conflict of interest in this study.

References

[1] J.-S. Leu, T.-H. Chiang, and Y. Min-Chieh, "Energy efficient clustering scheme for prolonging the lifetime of wireless sensor network with isolated nodes," *IEEE Communications Letters*, vol. 19, no. 2, pp. 259–262, 2015.

[2] L. Ma, B. Wang, S. Yan, and X. Gu, "Temperature error correction based on BP neural network in meteorological wireless sensor network," *International Journal of Sensor Networks*, vol. 23, no. 4, p. 265, 2017.

[3] Q. Wang and J. Jiang, "Comparative examination on architecture and protocol of industrial wireless sensor network standards," *IEEE Communications Surveys & Tutorials*, vol. 18, no. 3, pp. 2197–2219, 2016.

[4] Y. Zhang, D. Upton, A. Jaber et al., "Radiometric wireless sensor network monitoring of partial discharge sources in electrical substations," *International Journal of Distributed Sensor Networks*, vol. 11, no. 9, Article ID 438302, 2015.

[5] C. Ma, D. Zhao, and J. Wang, "Intelligent monitoring system for aquaculture dissolved oxygen in pond based on wireless sensor network," *Transactions of the Chinese Society of Agricultural Engineering*, vol. 31, no. 7, pp. 193–200, 2015.

[6] Y. Yang, L. Wu, G. Yin, L. Li, and H. Zhao, "A survey on security and privacy issues in internet-of-things," *Internet of Things Journal, IEEE*, vol. 4, no. 5, pp. 1250–1258, 2017.

[7] S. Galmés, "Markovian characterization of node lifetime in a time-driven wireless sensor network," *Numerical Algebra Control & Optimization*, vol. 1, no. 4, pp. 763–780, 2011.

[8] C. Xu, M. Zheng, and W. Liang, "Cooperative spectrum sensing of the cognitive wireless sensor network," *Information and Control*, vol. 44, no. 4, pp. 430–435, 2015.

[9] S. Zahurul, N. Mariun, I. V. Grozescu et al., "Future strategic plan analysis for integrating distributed renewable generation to smart grid through wireless sensor network: Malaysia prospect," *Renewable & Sustainable Energy Reviews*, vol. 53, no. 1, pp. 978–992, 2016.

[10] Y. Li, Y. Zuo, H. Song, and Z. Lv, "Deep learning in security of Internet of Things," *IEEE Internet of Things Journal*, vol. 99, p. 1, 2021.

[11] V. Henriques and R. Malekian, "Mine safety system using wireless sensor network," *IEEE Access*, vol. 4, no. 4, pp. 3511–3521, 2016.

[12] H. Li and J. Liu, "Double cluster based energy efficient routing protocol for wireless sensor network," *International Journal of Wireless Information Networks*, vol. 23, no. 1, pp. 40–48, 2016.

[13] B. Dou, J. Wen, X. Li et al., "Wireless sensor network of typical land surface parameters and its preliminary applications for coarse-resolution remote sensing pixel," *International Journal of Distributed Sensor Networks*, vol. 12, no. 4, Article ID 9639021, 2016.

[14] M. Singh and P. M. Khilar, "An analytical geometric range free localization scheme based on mobile beacon points in wireless sensor network," *Wireless Networks*, vol. 22, no. 8, pp. 1–14, 2015.

[15] G. Rajeshkumar and K. R. Valluvan, "An energy aware trust based intrusion detection system with adaptive acknowledgement for wireless sensor network," *Wireless Personal Communications*, vol. 94, no. 4, pp. 189–192, 2016.

[16] J. Chen, G. Wang, and J. Sun, "Power scheduling for Kalman filtering over lossy wireless sensor networks," *IET Control Theory & Applications*, vol. 11, no. 4, pp. 531–540, 2017.

[17] T. Hong, W. Zhao, R. Liu, and M. Kadoch, "Space-air-ground IoT network and related key technologies," *IEEE Wireless Communications*, vol. 27, no. 2, pp. 96–104, 2020.

[18] X. Li, H. Liu, W. Wang, Y. Zheng, H. Lv, and Z. Lv, "Big data analysis of the internet of things in the digital twins of smart city based on deep learning," *Future Generation Computer Systems*, vol. 128, pp. 167–177, 2022.

[19] Z. Lv, Y. Han, A. K. Singh, G. Manogaran, and H. Lv, "Trustworthiness in industrial IoT systems based on artificial intelligence," *IEEE Transactions on Industrial Informatics*, vol. 17, pp. 1496–1504, 2020.

[20] T. Olofsson, A. Ahlen, and M. Gidlund, "Modeling of the fading statistics of wireless sensor network channels in industrial environments," *IEEE Transactions on Signal Processing*, vol. 64, no. 12, pp. 3021–3034, 2016.

[21] I. Cvitić, D. Peraković, M. Periša, and M. D. Stojanović, "Novel classification of IoT devices based on traffic flow features," *Journal of Organizational and End User Computing (JOEUC)*, vol. 33, no. 6, pp. 1–20, 2021.

[22] B. Zhang, K. Wen, J. Lu, and M. Zhong, "A top-K QoS-optimal service composition approach based on service dependency graph," *Journal of Organizational and End User Computing (JOEUC)*, vol. 33, no. 3, pp. 50–68, 2021.

[23] M. Shuai, N. Yu, H. Wang, L. Xiong, and Y. Li, "A lightweight three-factor anonymous authentication scheme with privacy protection for personalized healthcare applications," *Journal of Organizational and End User Computing (JOEUC)*, vol. 33, no. 3, pp. 1–18, 2021.

[24] R. S. Bhadoria and N. S. Chaudhari, "Pragmatic sensory data semantics with service-oriented computing," *Journal of Organizational and End User Computing (JOEUC)*, vol. 31, no. 2, pp. 22–36, 2019.

[25] L. Li and J. Zhang, "Research and analysis of an enterprise E-commerce marketing system under the big data environment," *Journal of Organizational and End User Computing (JOEUC)*, vol. 33, no. 6, pp. 1–19, 2021.

Hindawi
Journal of Sensors
Volume 2024, Article ID 9891450, 1 page
https://doi.org/10.1155/2024/9891450

Retraction

Retracted: A Weighted Cluster Head Selection Algorithm for Energy Efficient Wireless Sensor Networks

Journal of Sensors

Received 23 January 2024; Accepted 23 January 2024; Published 24 January 2024

This article has been retracted by Hindawi following an investigation undertaken by the publisher [1]. This investigation has uncovered evidence of one or more of the following indicators of systematic manipulation of the publication process:

(1) Discrepancies in scope
(2) Discrepancies in the description of the research reported
(3) Discrepancies between the availability of data and the research described
(4) Inappropriate citations
(5) Incoherent, meaningless and/or irrelevant content included in the article
(6) Manipulated or compromised peer review

The presence of these indicators undermines our confidence in the integrity of the article's content and we cannot, therefore, vouch for its reliability. Please note that this notice is intended solely to alert readers that the content of this article is unreliable. We have not investigated whether authors were aware of or involved in the systematic manipulation of the publication process.

Wiley and Hindawi regrets that the usual quality checks did not identify these issues before publication and have since put additional measures in place to safeguard research integrity.

We wish to credit our own Research Integrity and Research Publishing teams and anonymous and named external researchers and research integrity experts for contributing to this investigation.

The corresponding author, as the representative of all authors, has been given the opportunity to register their agreement or disagreement to this retraction. We have kept a record of any response received.

References

[1] S. A. Ali, M. Sarfraz, S. A. Ghauri et al., "A Weighted Cluster Head Selection Algorithm for Energy Efficient Wireless Sensor Networks," *Journal of Sensors*, vol. 2022, Article ID 3055178, 13 pages, 2022.

Hindawi
Journal of Sensors
Volume 2022, Article ID 3055178, 13 pages
https://doi.org/10.1155/2022/3055178

Research Article

A Weighted Cluster Head Selection Algorithm for Energy Efficient Wireless Sensor Networks

Syed Asif Ali,[1] Mubashar Sarfraz,[2] Sajjad A. Ghauri,[1] Asad Mahmood,[3] Shahid Basir,[1] Teweldebrhan Mezgebo Kebedew,[4] and Sheraz Alam[2]

[1]*School of Engineering & Applied Sciences, ISRA University, Islamabad, Pakistan*
[2]*Faculty of Engineering and Computer Science, National University of Modern Languages, Islamabad, Pakistan*
[3]*Department of Electrical and Computer Engineering, Comsats University, Islamabad, Wah Campus, Wah Cantt, Pakistan*
[4]*Ethio Telecom, Addis Ababa, Ethiopia*

Correspondence should be addressed to Teweldebrhan Mezgebo Kebedew; tewelde2000@gmail.com

Received 6 February 2022; Revised 24 March 2022; Accepted 29 March 2022; Published 6 May 2022

Academic Editor: Han Wang

The wireless sensor network's (WSNs) lifetime is mainly dependent on the RE of the sensor nodes (SeN). In recent years, energy minimization in a WSN has been a prominent research topic, and numerous solutions have been proposed. This research focuses on the energy minimization of the SeNs where firstly, K-medoid clustering algorithm is applied to create clusters. Second, a weighted cluster head selection technique is used to choose a cluster head (CH) by integrating three independent weights associated with an SeN: energy, distance from the centroid, and distance from the sink node (SN). According to the energy level and distance from the SN and cluster's centre, each node is assigned a constant weight. The simulation results are compared to existing methodologies, and the results show that the suggested network's lifetime enhances.

1. Introduction

1.1. Background and Related Work. With recent advancements in sensor devices, microelectronics, and wireless communication systems, WSNs are gaining more and more interest. A WSN is a network of dispersed sensors with low power, low storage capacity, and limited processing capabilities that sense and relay data to a SN [1–5]. In the concept of a 5G communication system, WSNs can be used to monitor the health system, agriculture, oil and gas exploration, smart homes and security, military applications, environmental monitoring, and industrial machine status [6–8]. In contrast, sensors constitute of finite battery life that bottleneck the efficiency of the network [9–12]. Figure 1 depicts a high-level overview of WSN applications in which sensor nodes are mostly placed in harsh environments where it is challenging to replace the battery resources at short intervals. Thus, the constraint of finite battery life or network lifespan can be alleviated by making efficient use of available energy resources and devising an optimal method of delivering packets [13].

Similarly, numerous strategies for extending network lifetime by improving CH selection for load balancing have been described in the literature; however, updating the CH selection to prolong the network's lifetime is a significant challenge. A clustered network (based on LEACH) is chosen, the monitoring area is divided into smaller clusters, and each cluster has a CH responsible for collecting and forwarding sensed data from cluster members to the sink. Clustering the network not only helps to optimize energy consumption and load balancing, but it also increases network scalability [13]. In [14], the authors proposed LEACH, the first hierarchical clustering approach for balancing the network's load across all nodes. There are no defined criteria for adequately sharing the workload among everyone, and the CH is picked probabilistically. It is possible that a node will be picked numerous times, depleting its energy rapidly, because the CH selection procedure is decentralized. Later in [15], LEACH-C is a

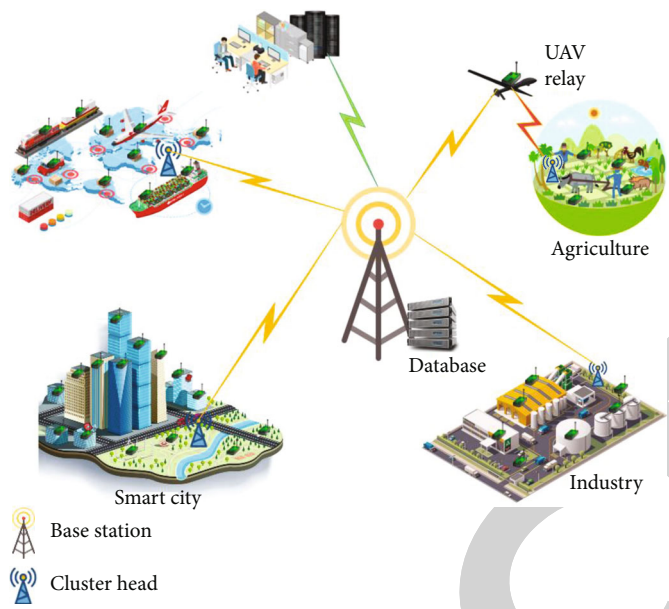

Figure 1: System model.

suggested solution to the existing problem by permitting the sink node to choose the CH and properly share the load over all nodes. When compared to the traditional LEACH, LEACH-C has been demonstrated to optimize the system energy consumption.

The threshold-sensitive energy-efficient sensor network (TEEN) protocol [16], threshold-sensitive stable election protocol (TSEP) [17], a highly efficient adaptive periodic threshold-sensitive energy network (APTEEN) [18], power-efficient gathering in sensor information system (PEGASIS) [19] whereas hybrid energy-efficient distributing (HEED) clustering techniques are all used to improve the network's efficiency [20]. Additionally, a substantial amount of work has been done to modify the clustering algorithms in order to increase their efficiency while decreasing their energy consumption. S-SEECH (secured-scalable energy-efficient clustering hierarchy) is a revolutionary protocol that considers the network's better scalability [21].

Researchers recently proposed a new solution to extend the network's life cycle. The authors in [22] consider an energy-efficient cluster-based routing protocol rotates the CH based on the node's current energy, distance from the SN, and density. The proposed protocol outperforms LEACH by 56% in terms of energy consumption. Similarly, according to the authors of [23], the proposed event detection tree reduces the amount of data to be transmitted by 20% compared to TED, MSFT, and centralized approaches. According to the authors in [24], by establishing an appropriate fixed packet size, analyzing the standard weight of the nodes, and selecting the next CH, the energy consumed is further minimized. Additionally, authors in [25] evaluated a trust-aware routing protocol to improve the energy efficiency in the presence of malicious SeNs. In [26], a load balancing technique is proposed based on the energy collection, energy transfer, and energy conservation. A modified LEACH (LEACH-M) is proposed in [27] to improve the threshold for CH selection by considering the residual energy (RE) and SeN location.

In [28], a sampling-based spider monkey optimization (SMO) approach is proposed for selecting an optimal set of CH. The CH is chosen using krill head optimization [29], in which the proposed scheme's effectiveness is demonstrated by comparison to LEACH and genetic algorithm-(GA-) based optimization. In the same way, three attribute indices for network nodes are formed in [30]: Data traffic, RE of nearby nodes, and closeness of the node's path to the shortest path. The weights of these indexes are then computed using the entropy weight approach. Finally, using the dempster shafer (DS) probability theory fusion rule, the back propagation algorithm (BPA) function of each index value is fused to determine the next hop. The RE of nodes is determined more accurately than with the multi-criterion-based centrality protocol (MCRP) or the fuzzy logic-based energy-optimized routing protocol (FLEOR). In [31], clustering using zone-based clustering and a hybrid PSO method, duty cycle scheduling with the deep reinforcement learning and routing with ant colony optimization, and the firefly algorithm are all done with the energy efficient scheduling-deep reinforcement learning (EES-DRL).

After making changes to the LA and GWO, the CH selection process is called updated lion-GWO [32]. SEP, IHCR, and the evolutionary routing protocol were found to be inferior in terms of network lifetime and RE. In [33], a hybrid approach based on fuzzy C-means and moth flame optimization (MFO) is proposed for cluster formation and CH selection optimization. It is used to form clusters by using fuzzy-based unequal clustering, while the CH optimization is done using PSO-WZ to determine the best CH [34]. The Gini coefficient is employed to keep the energy gap between nodes equal and the network's load balanced. For network coverage and convergence rate, lion optimization performs better than the nature-inspired algorithm reviewed in [35]. The WSN is

```
input: SN ⟵ Number of devices, BS ⟵ Base Station,
    SA ⟵ Simulation Area {SA ∈ (U_b, L_b)}, U_b ⟵ Upper
    Bound of SA, L_b ⟵ Lower Bound of SA, CH ⟵ Cluster
    Head {CH ∈ max (SN)}, C_HG ⟵ Cluster Head Group
    {C_HG ∈ CH(SN)}, l_e ⟵ Nodes Residual
    Energy{le(n) ∈ le}
output: Dead Nodes, Node's latency, Energy consumption, Time complexity,
    Packets delivery
Initialization: ∀ parameters, ∀ variables
Execution:;
while termination criterion metdo
  for i=1:SN do
    ∀ nodes
    get (x_cord, y_cord)
    Deploy (i-th node) in SA (U_b, L_b)
      if nodes deployment = = true then
        break;
      else
        continue;
      end
  end
  Distance-WSN (Nodes, Rounds)⟵get distance(n)
  K-medoids-Clustering (x_cord(i), y_cord(i)), Deploy clusters, get CH
  IDs (x_cord(i), y_cord(i), CHG)⟵calculate IDs(n)
    opt-route (Distance(i), (x_cord(i), y_cord(i), CHG)
  get next hop ∀ CHs//Communication phase
  while rounds max round ∀ nodes ≠ dead do
    rounds++22      Energy Consumption Model ⟵get residual energy
    for ∀nodes do
      get next hop
      if next hop (CH) == BS then
        receive M × data length
        //CH receives data from M SeNs
        transmit N × data length;
        // CH transmits data of N SeNs
      else
        if next hop (CH) == CH(k) then
          receive M × data length
          transmit N × data length
        end
        Node(n) transmit⟵ CH(k)
      end
      if energy i -th node < threshold then
        declare ith node as a dead node
      end
    end
  end
end
```

Algorithm 1: Weighted CH selection scheme (WCHSS).

modelled using an overall point factor in [36]. After that, the authors extracted near-optimal solutions and their efficiency factors to demonstrate that it is possible to quickly route uniformly load-balanced networks by randomly searching a narrow margin of the solution space.

A distributed GA is presented in [37] for the purpose of optimizing the lifetime of WSNs. This is accomplished by dividing the network into subnetworks and distributing CH selection and sensor activity scheduling-based GA optimization to each CH. The proposed work is divided into rounds, with each round consisting of three phases, namely, discovery, CH selection using GA-based decision making, and sensing. The proposed algorithm contributes to the network's longevity. In order to improve the LEACH protocol's initial setup phase, a genetic algorithm (GA) was used to consider compactness, separation, and several CHs as the perimeters of the objective function [1]. Later, the objective is iteratively optimized through GA to achieve the objectives.

Table 1: Simulation parameters.

Parameters	Values
K (SeNs)	100
Area	$(100 * 100)\ \mathrm{m}^2$
Normal nodes E_{int}	0.5 J
ANs E_{int}	1 J
κ	10
Percentage of AN's	10%, 20%
υ_{fs}	0.1 pJ
υ_{mp}	$13 * 10^{-16}$ J
λ	4 kb
ξ_r, ξ_s	50 nJ
E_{da}	5 nJ

However, a simple CH selection method that converts energy and distance into unit-less quantities and selects the CH based on their weight-age has yet to be investigated.

1.2. Motivation and Contribution. The optimal CH selection helps to optimize the energy consumption, and there are various approaches available in the literature for CH selection. The RE of the network, distance from sink node, number of CHs, and optimal path selection are the various methods used in the literature to increase the lifetime of the network. For the optimal CH selection, the selected node must have higher RE and minimum distance from the SN, and it must be closer to the centre point within a cluster. The proposed work is compared with [1] by considering three different parameters and introducing a new objective function.

The major contributions of the proposed weighted CH selection algorithm (WCHSA) are summarized as follows:

(1) To the best of author's knowledge, this is the first work that proposes a new WCHSA based on the RE of the node, distance from the sink node, and distance from the center of the cluster

(2) The three different factors are mapped to a unit less quantity in such a way that higher energy node acquires maximum weight and a node with the higher distance assigns the minimum weight. Finally, the weighted combination of these three approaches is combined to select the optimal CH for minimum energy consumption

(3) The WCHSA selects a CH that have maximum energy in a cluster, nearest to its centroid, as well as nearest to the SN. The CH selects the shortest path in a multihop scenario to transfer the sensed information to the SN

(4) SeNs are divided into clusters using K-medoid clustering algorithm

(5) The proposed WCHSA is compared with the existing techniques for 10% and 20% ANs

The rest of the paper consists of four sections. Section 1 discusses the literature review and existing methods of CH selection. The detailed system model is presented and discussed in Section 2. The simulation results are presented and discussed in Section 3. Finally, in Section 4, the proposed work is summarized, and the future directions are presented.

2. System Model

This section represents mathematical model of proposed algorithm named: weighted CH selection algorithm (WCHSA) used to determine the optimal path for packet transmission while minimizing energy consumption and maximizing the network's lifecycle through iteratively updating the CH within each cluster. The network architecture of the WSN is presented in Figure 1, where a CH collects information from sensors placed in the sensing field. Afterwards, CH relays the sensed information to the SN, and finally, SN forwards all the information to control centre.

2.1. Selection of CH. For increased energy efficiency, the whole WSN has been divided into clusters. Each cluster has a CH, who is in charge of ensuring that information flows smoothly from one cluster to the next. The K-medoid clustering approach has been successfully utilised to produce clusters and CH's. In the K-medoid algorithm, it is necessary to locate a medoid in a cluster that is located in the middle of the cluster. The K-medoid performs better and is more robust than the K-mean. It is denoted as k representative object because it minimizes the summation of differences of information, whereas K-medoid minimizes the sum of squared Euclidean distances and is denoted as k representative object because it minimizes the sum of differences of information.

2.2. Optimal Weights Selection. The rotation of CH's weighted fitness function is dependent on three parameters: number of CHs, compactness, and spacing [1]. The node's current energy, its distance from the SN, and its distance from the cluster's midpoint are all adjusted, resulting a new weighted equation. The modified function for CH rotation is given in (1). The function in (1) is transformed into a cost function (2), and it is solved iteratively to find the optimal set of weights under certain constraints.

$$F = \omega_1 \eta_k + \omega_2 \Upsilon_k + \omega_3 \nu_k \tag{1}$$

$$\begin{aligned} \mathbf{P}_1 &= \max_{\{\mathbf{W},\eta,Y,\nu\}} \sum_{k=1}^{K} F_k \\ C_1 &: \eta_k \geq \varepsilon_{\mathrm{th}} \\ C_2 &: \aleph_k \in \Lambda \\ C_3 &: \Upsilon_k \leq \hbar_{\mathrm{th}} \end{aligned} \quad , \tag{2}$$

where $\mathbf{W}$ is the vector with (w_1, w_2, w_3) the set of optimal weights that are obtained iteratively. $R_{1,4}$, η is the constant value that is evaluated from the contribution of

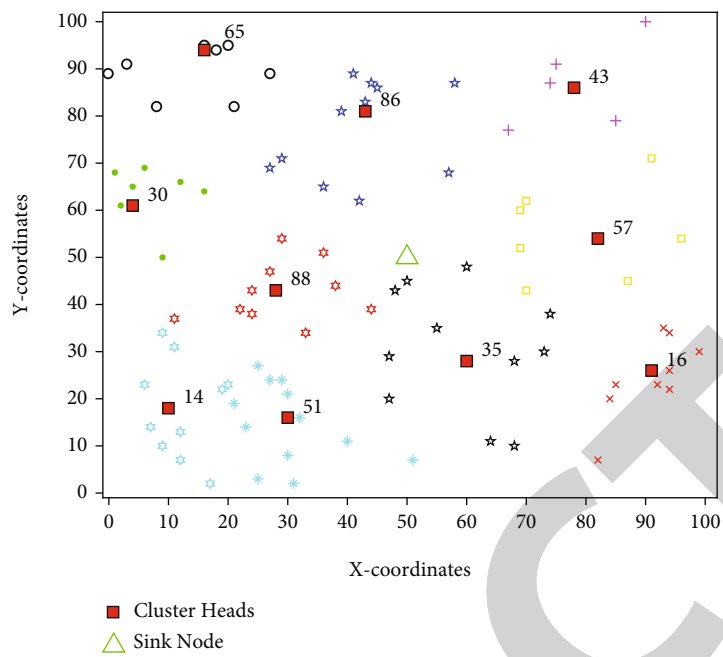

Figure 2: Network deployment.

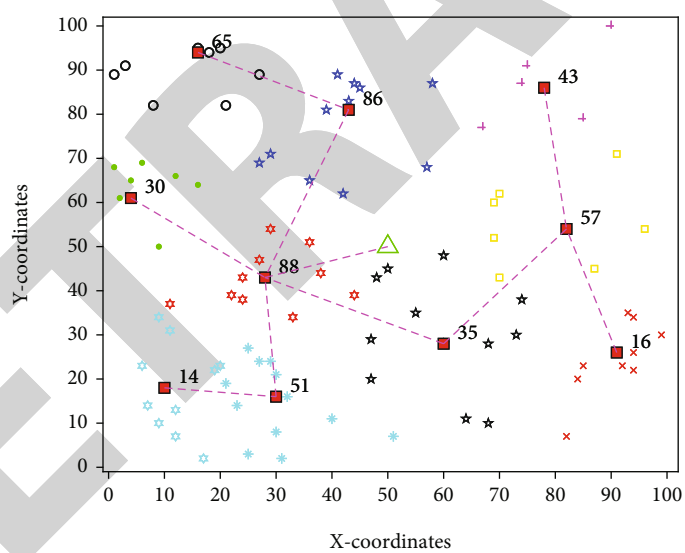

Figure 3: Distance-based routing.

current energy of each node, Y is the constant obtained by mapping the contribution of distance of each node, and ν is the constant calculated after mapping the contribution of its distance to the center point. ε_{th} is the threshold RE of a node, $\aleph_k$ is the kth node, Λ are the clusters created by the clustering algorithm, and $\hbar_{\text{th}}$ is the threshold distance. Finally, the node's maximum weigh is evaluated through P_1 and designated that node as the CH. To select the next CH, the proposed scheme takes into account the RE, the distance to the SN, and the distance of the node to the cluster's center point. Due to the fact that energy and distance have distinct units that cannot be added directly, their contributions are mapped onto some units of lower extent.

As a result, the total energy is divided into η points that are distributed evenly between the minimum and maximum energies. Additionally, these points are assigned a constant value (higher for more energy, lower for less energy) to convert the energy contribution to a unit-less quantity. Similarly, the distance between nodes and SN is divided into Y points equal to the difference between their minimum and maximum distances. Following that, these points are assigned a constant value (high for short distances, low for long distances) in order to convert the effect of distance to a unit-less quantity. Finally, the distance between each cluster node and the cluster's center point is divided into ν equal points. Later, a constant value is assigned to this distance in order

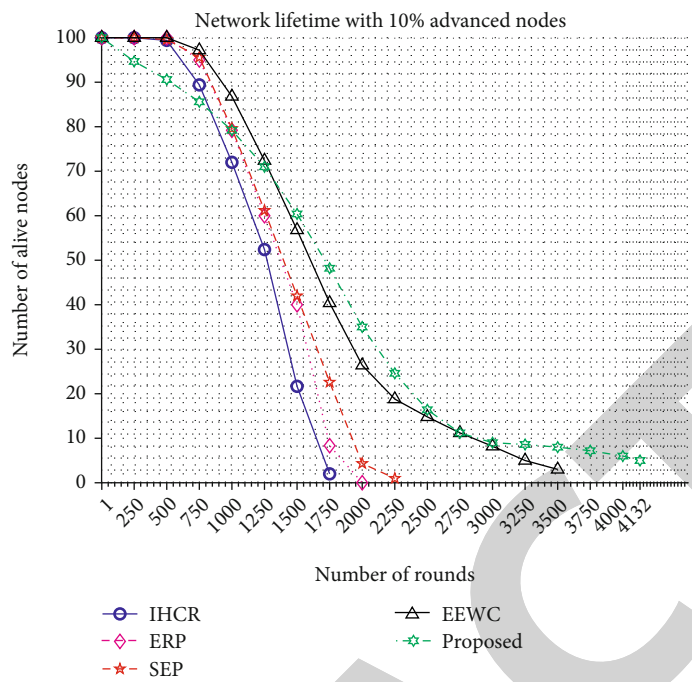

Figure 4: Network lifetime for 10% ANs.

to convert it to a unit-less quantity (high value for low distance and lower value for higher distance).

2.3. Optimal Path Selection. Sensors require a reliable path to relay sensed data to the SN for further analysis or decision-making. The choice of a reliable path is critical, as the information may be lost or the path may result in increased energy consumption if the path is unreliable. For multihop links, the optimal path is chosen from the set of CHs, as a CH may consume more energy if the longer path is chosen.

As a result, in order to determine the most optimal path for packet transmission, the proposed scheme evaluates the Euclidean distance between a CH and all of the other CHs and SNs and then selects the shortest path possible. The Euclidean distance between two points in a coordinate system can be calculated as follows:

$$D = \sqrt{\left(p_1 - q_1^i\right)^2 + \left(p_2 - q_2^i\right)^2}, \tag{3}$$

where D is the shortest distance between a CH and the next hop in the direction of SN, p_1 and p_2 are the coordinates of a CH, and q_1 and q_2 are the coordinates of the next hop.

2.4. Energy Model (LEACH). SeNs are deployed in a specific environment to sense the amount of data and relay it to the next hop. In contrast, these devices constitute of finite battery life, whereas the magnitude of energy consumption is environment-dependent, depending on whether data is transmitted from the common node to the CH or from the CH to the SN. Each level consumes a different amount of energy, which varies according to the distance traveled and the amount of data transferred. The predefined energy model of [14] is used in this study for energy transmission and reception, as shown as follows:

$$E_T(\lambda, d) = \begin{cases} \lambda \times \left(\xi_t + \upsilon_{fs} \times \hbar^2\right), & \text{if } \hbar \le \hbar_o \\ \lambda \times \left(\xi_t + \upsilon_{\text{amp}} \times \hbar^4\right), & \text{if } \hbar > \hbar_o \end{cases}, \tag{4}$$

$$E_R = \lambda \xi_r, \tag{5}$$

where λ is the size of data, $\hbar$ is distance between the nodes, ξ_t and ξ_r signifies transmit and receive energy, υ_{fs} is free space energy, υ_{amp} is the transmit amplifier energy, and $\hbar_{\text{th}}$ is the threshold distance. Additionally, the threshold distance $\hbar_{\text{th}}$ is calculated using the formula given as follows:

$$\hbar_{\text{th}} = \sqrt{\frac{\upsilon_{fs}}{\upsilon_{\text{amp}}}}. \tag{6}$$

Setup and communication phase are the two phases of the WSN. Each node communicates its position to the SN and receives input from the SN during the initial setup phase. Equations (4) and (5) show how much energy nodes require for message transmit and receive. The communication phase begins after the setup phase, when nodes begin sensing and transmitting their observed data to the sink. The data is detected by the common nodes and transmitted to the CH, then broadcasts it to the SN. The quantity of energy needed to send and receive data to (or from) the

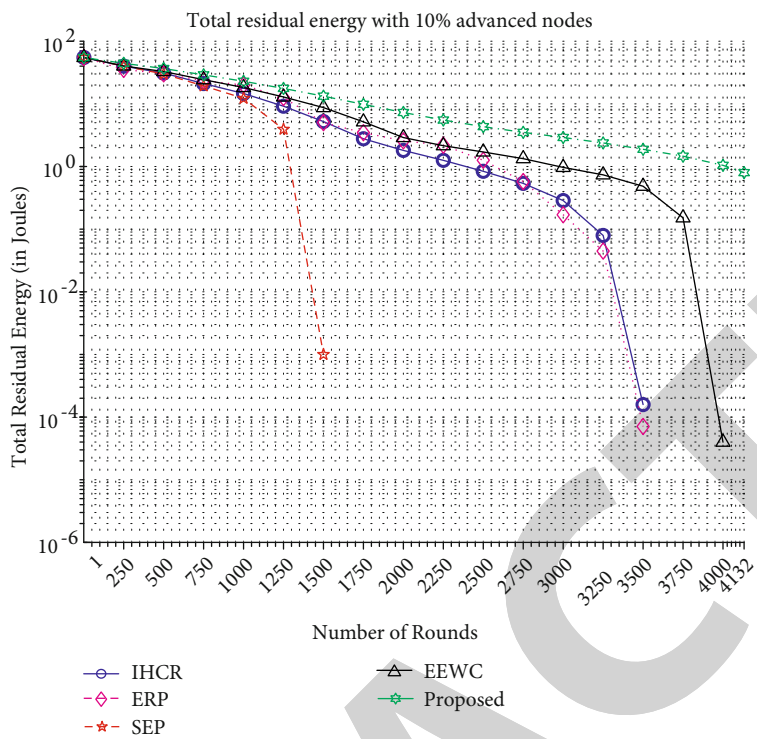

Figure 5: Total energy consumption for 10% ANs.

Table 2: Energy consumption for 10% ANs.

Rounds	RE (joules) ERP	EEWC	WCHSS
360	28.564	34.347	43.1543
720	6.918	13.525	36.0548
1080	3.092	3.746	28.9744
1140	0.996	1.852	27.8007
1800	0.232	0.647	15.2424
2160	0	0.12	8.6

Table 3: Dead nodes vs. rounds for 10% ANs.

Dead nodes	Rounds ERP	EEWC	WCHSS
10	1326	1348	1130
20	1382	1411	2169
30	1425	1476	2236
40	1500	1525	2336
50	1529	1574	2470
60	1575	1668	2785
70	1689	1784	3500
80	1851	1892	3771
90	1754	3250	4017
100	2008	3512	4872

CH is stated as follows:

$$E_{Tx} = \varpi \times \lambda \times \left(\xi_t + \upsilon_{fs} \times \hbar^2\right), \tag{7}$$

$$E_{Rx} = \varpi \times \lambda \times \xi_r, \tag{8}$$

where ϖ is the number of nodes in a cluster apart from CH. The CH collects data from the cluster's members and aggregates it with its own sensed data before forwarding it to the next hop. The energy required for this process is deduced from (9) and (10), respectively, for transmission and reception.

$$E_{\mathrm{CH}_{Tx}} = \zeta \times \lambda \times \left(\xi_t + \upsilon_{fs} \times \hbar^2\right), \tag{9}$$

$$E_{\mathrm{CH}_{Rx}} = \zeta \times \lambda \times \left(\xi_r + E_{\mathrm{agg}}\right), \tag{10}$$

where ζ is the total number of nodes in the cluster. Data packets supplied by other CHs are received, aggregated, and relayed to the SN by the primary CH nearest to the SN. The amount of energy required for the process is expressed as follows:

$$E_{\mathrm{CH}_{Tx}} = \kappa \times \lambda \times \left(\xi_t + \upsilon_{fs} \times \hbar^2\right), \tag{11}$$

$$E_{\mathrm{CH}_{Rx}} = \kappa \times \lambda \times \left(\xi_r + E_{\mathrm{agg}}\right), \tag{12}$$

where κ is the total number of CHs. The main CH is responsible for transmitting data from all of the CHs and their cluster members to the sink node, and the energy required is as

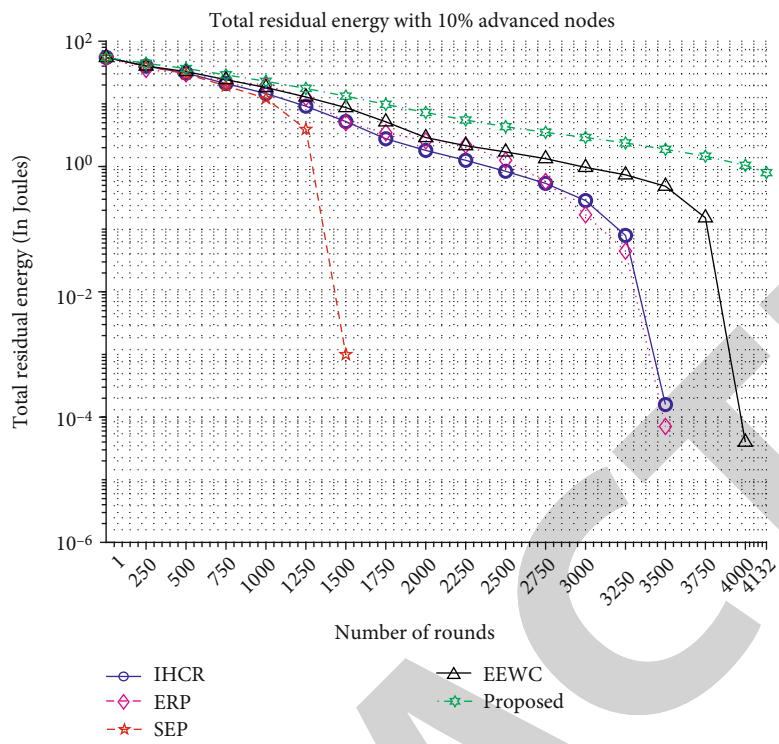

Figure 6: Network lifetime using 20% ANs.

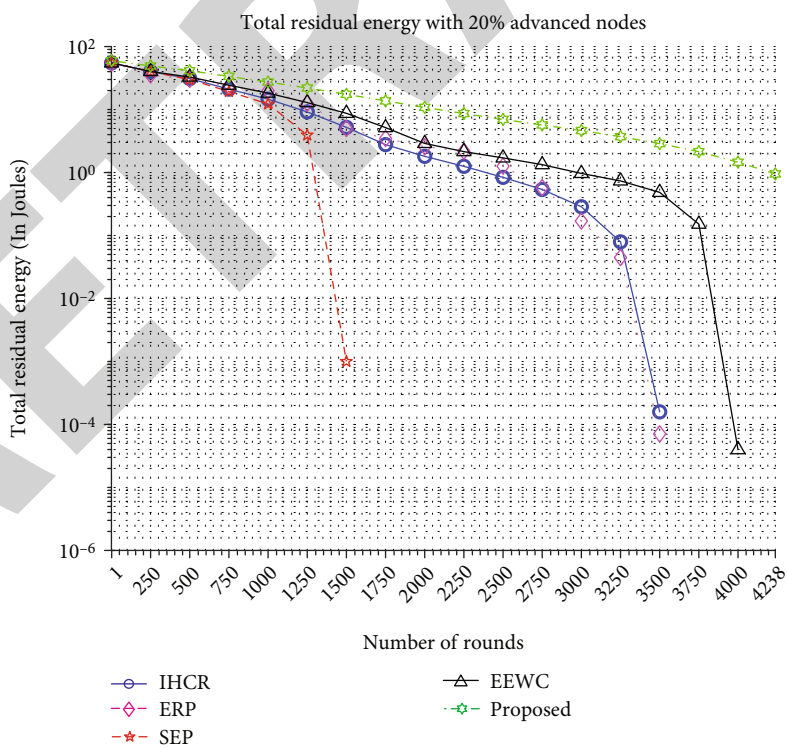

Figure 7: Total RE for 20% ANs.

follows:

$$E_{\mathrm{SN}_{Tx}} = K \times \lambda \times \left(\xi_t + \upsilon_{fs} \times \hbar^2\right). \quad (13)$$

3. Simulation Results

This section summarizes the numerical results of our proposed scheme. Following that, a weighted algorithm is used to select the CH that provides the optimal path for packet transmission. Additionally, the proposed scheme's performance is validated through extensive simulations carried out in MATLAB using Algorithm 2.4 named: weighted CH selection scheme (WCHSS) and numerical results compared to baseline schemes. Additionally, Table 1 represents the simulation parameters.

3.1. K-Medoid Clustering. The network is deployed with random distributed nodes over an area of 100×100 square meters. From Figure 2, the SN is in the center of the network. From K-medoid clustering technique, $\kappa = 10$ clusters are selected, and using WHCSS algorithm, the CH is obtained as shown in Figure 2. K-Medoid is a robust segregating method that forms κ clusters for the K nodes deployed in the network using data points as centers as shown with different color scheme in Figure 2.

3.2. Selection of Path. After clustering the K users into κ clusters, the next step is to determine the optimal path for packet transmission while minimizing energy consumption by iterative updating the location of CHs within each cluster. Figure 3 illustrates the transfer of data from SeNs in a cluster to the network's SN, which is located in the network's center, via respective CHs in a multihop mode of communication. Each CH calculates its distance from the SN and from all other CHs in the network. The data is then transmitted from a CH to its neighboring CH in the shortest possible route to the SN. The CH is updated with the optimal energy consumption, taking the following constraints into consideration: (1) the shortest possible distance between the SeN and SN and (2) the SeN's maximum energy is closer to the cluster's centroid.

After clustering and determining the optimal path by iteratively updating the location of the CH within each cluster, the proposed scheme's performance is validated for 10% and 20% AN scenarios. Similarly, numerical results are compared with the benchmark schemes to further validate the proposed scheme.

3.3. WCHSS for 10% ANs

3.3.1. Number of Alive Nodes. This section represents the comparative analysis of the proposed scheme, and the results are compared with some benchmark scheme names: ERP (evolutionary routing protocol) and EEWC (energy-efficient weighted clustering), by considering network lifetime as a performance matrix as shown in Figure 4. Initially, the algorithm tries to balance the network, and therefore, the SeN consumes slightly higher energy. Afterwards, the proposed algorithm performs better and improves the overall lifetime of the network. The results show that the proposed scheme outperforms all other schemes and improves by 28.13% over the EEWC technique and 58.93% over the ERP.

Table 4: Energy consumption for 20% ANs.

Rounds	RE (joules)		
	ERP	EEWC	WCHSS
360	33.825	39.401	47.7131
720	12.334	18.515	40.4952
1080	3.859	7.483	33.4403
1140	1.671	3.658	32.2987
1800	0.160	1.507	19.7403
2160	0	0.461	13.098

Table 5: Dead nodes vs. rounds for 20% ANs.

Dead nodes	Rounds		
	ERP	EEWC	WCHSS
10	1309	1324	1040
20	1384	1439	1856
30	1443	1499	2304
40	1500	1575	2379
50	1549	1643	2525
60	1628	1730	2811
70	1707	1861	3538
80	1889	1917	3811
90	1801	3262	4100
100	2024	3527	4885

3.3.2. Total Residue Energy. The total RE with 10% ANs is shown in Figure 5 and is also compared to the RE produced by existing techniques. As illustrated in Figure 5, the proposed algorithm consumes less energy in the WSN than other techniques. The proposed algorithm has an RE of 0.63 J, whereas other techniques have an RE of 4×10^{-5} J for EEWC and 7×10^{-5} J for ERP.

The RE of the proposed protocol is compared quantitatively to that of existing protocols in Table 2. As shown in Table 2, the proposed WSN has a significantly lower RE than the EEWC and ERP. The proposed algorithm has an RE of 8.6 J, compared to 0.12 J for EEWC and zero for other protocols.

3.3.3. Number of Dead Nodes. Similarly, the total number of dead nodes in the WSN is compared to the total number of dead nodes in other protocols and is shown quantitatively in Table 3. Results demonstrate that proposed algorithm outperforms existing protocols. For the 50% of dead nodes, there are 1529, 1574, and 2470 rounds for ERP, EEWC, and WCHSS, respectively.

3.4. WCHSS for 20% ANs

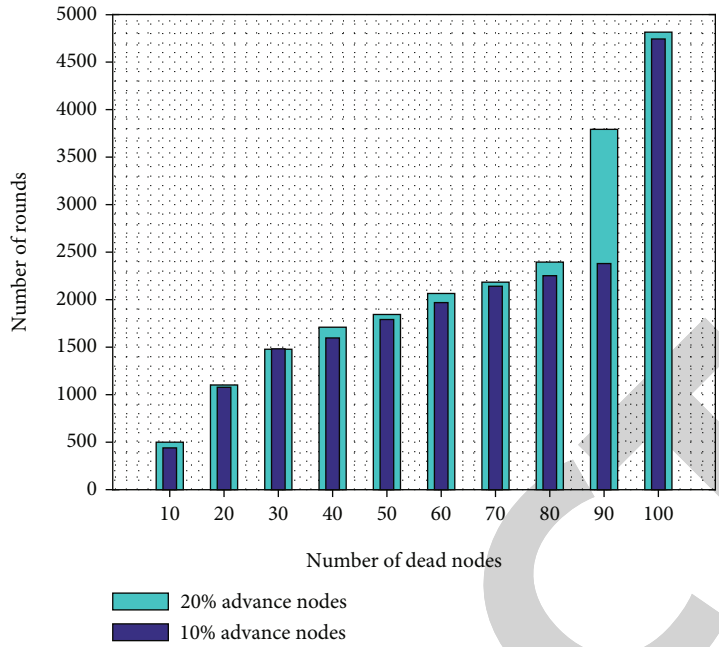

Figure 8: Network life for 10% and 20% ANs.

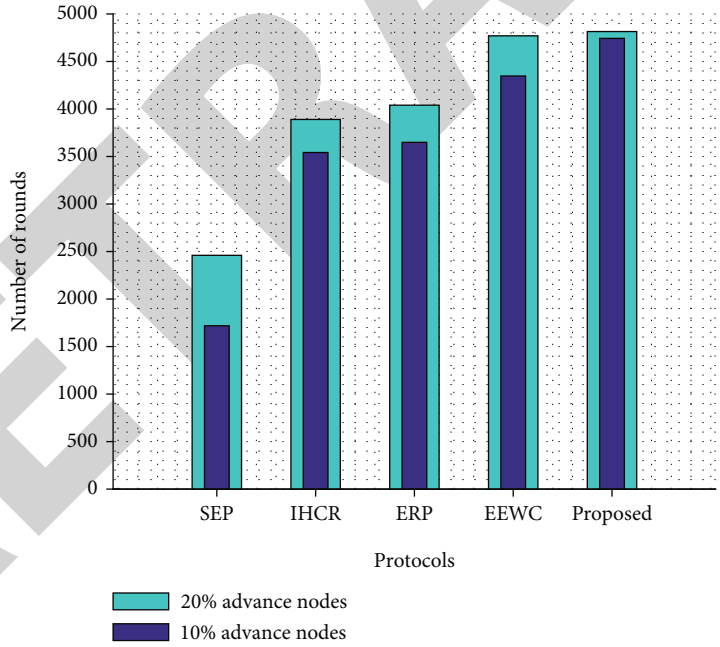

Figure 9: Network life with existing protocols.

3.4.1. Number of Alive Nodes. The simulations for 20% ANs for the number of alive nodes are presented in Figure 6. The proposed WCHSS gives better performance and increases the network lifetime by 28.6% and 59.6% as compared to EEWC and ERP, respectively. The network life of the proposed algorithm is 4881 cycles, and 99% of all nodes are taken into account during this period. The previous WSN protocols died at 2008 and 3500 rounds for the ERP and EEWC, respectively.

3.4.2. Total Residue Energy. The total RE for the proposed 20% ANs is evaluated in Figure 7. The simulation results demonstrate that the proposed algorithm outperforms established protocols such as ERP and EEWC.

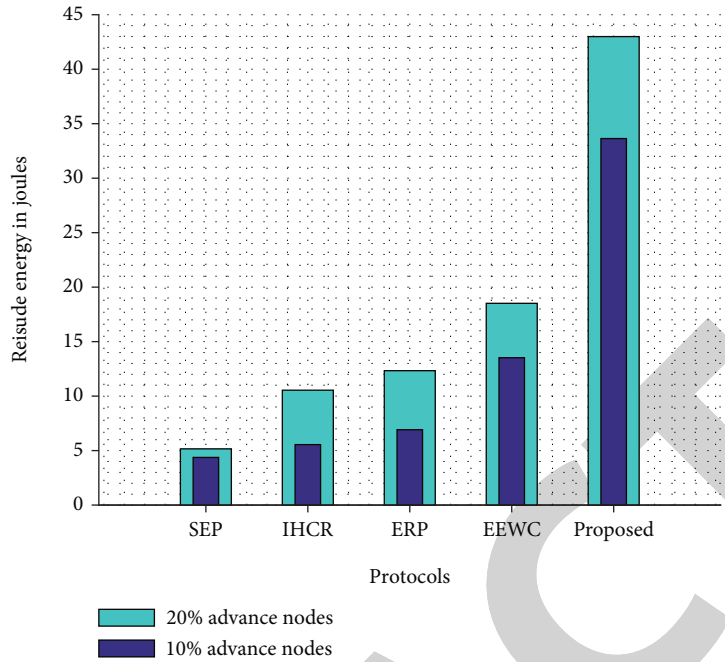

Figure 10: RE comparison (after 720 rounds).

Table 4 shows the quantitative analysis where the proposed WCHSS has an RE of approximately 19.74 joules after 1800 cycles, whereas the EEWC has only 1.507 joules and ERP has consumed all the energy. Similarly, results demonstrating that the proposed algorithm outperforms existing protocols in terms of RE.

3.4.3. Number of Dead Nodes. The dead nodes of the proposed algorithm with 20% ANs are shown in Table 5 and Figure 8. The total number of nodes considered is 100, and simulations are performed till all nodes of the WSN have died. From the table, it is clear that the network lifetime of the proposed network is 4885 rounds, whereas other protocols such as ERP have 2024 rounds and EEWC has 3527 number rounds.

3.5. Comparison of Results with 10% and 20% ANs. The proposed WCHSS is also compared to 10% and 20% ANs, and the comparative analysis is shown in Figure 9. The proposed WCHSS increases the overall lifetime of the proposed network whereas 20% ANs give better performance compared to the 10% ANs. Figure 10 shows that the proposed WCHSS outperforms as compared to the existing ERP and EEWC algorithms in terms of energy consumption.

4. Conclusion

This research work examined the difficult problem of energy minimization and optimistic path selection in WSNs. This research focuses on refining the process for selecting CHs in WSNs based on three separate weights: the CH's distance from the cluster center, the CH's distance from the SN, and the CH's RE. The proposed WCHSS algorithm outperforms existing algorithms such as ERP and EEWC in terms of energy consumption. The network lifetime is increased by 28.5% and 59.62%, respectively, for the existing technologies, namely, ERP and EEWC. In future, the higher energy consumption at the start of the network will be improved by further stabilizing the network.

Data Availability

This paper does not require any dataset whereas the required data is generated uniformly using MATLAB tool.

Conflicts of Interest

The authors declare that they have no conflicts of interest.

References

[1] R. Pal, S. Yadav, and R. Karnwal, "EEWC: energy-efficient weighted clustering method based on genetic algorithm for hwsns," *Complex & Intelligent Systems*, vol. 6, no. 2, pp. 391–400, 2020.

[2] A. Mahmood, A. Ahmed, M. Naeem, and Y. Hong, "Partial offloading in energy harvested mobile edge computing: a direct search approach," *IEEE Access*, vol. 8, pp. 36757–36763, 2020.

[3] W. U. Khan, F. Jameel, X. Li, M. Bilal, and T. A. Tsiftsis, "Joint spectrum and energy optimization of NOMA-enabled small-cell networks with QoS guarantee," *IEEE Transactions on Vehicular Technology*, vol. 70, no. 8, pp. 8337–8342, 2021.

[4] W. U. Khan, E. Lagunas, A. Mahmood, S. Chatzinotas, and B. Ottersten, "Integration of backscatter communication with multi-cell noma: a spectral efficiency optimization under imperfect sic," 2021, arXiv preprint arXiv:2109.11509.

[5] M. Ashraf, S. Hassan, S. Rubab, M. A. Khan, U. Tariq, and S. Kadry, "Energy-Efficient Dynamic Channel Allocation

Algorithm in Wireless Body Area Network," *Environment, Development and Sustainability*, 2022.

[6] B. Prabhu and S. Sophia, "A survey of adaptive distributed clustering algorithms for wireless sensor networks," *International Journal of Computer Science & Engineering Survey*, vol. 2, no. 4, pp. 165–176, 2011.

[7] A. Mahmood, M. Q. Usman, K. Shahzad, and N. Saddique, "Evolution of optimal 3D placement of UAV with minimum transmit power," *International Journal of Wireless Communications and Mobile Computing*, vol. 7, no. 1, pp. 13–18, 2019.

[8] C.-L. Chen and I.-H. Lin, "Location-aware dynamic session-key management for grid-based wireless sensor networks," *Sensors*, vol. 10, no. 8, pp. 7347–7370, 2010.

[9] A. Mahmood, Y. Hong, M. K. Ehsan, and S. Mumtaz, "Optimal resource allocation and task segmentation in iot enabled mobile edge cloud," *IEEE Transactions on Vehicular Technology*, vol. 70, no. 12, pp. 13294–13303, 2021.

[10] W. U. Khan, T. N. Nguyen, F. Jameel et al., "Learning-based resource allocation for backscatter-aided vehicular networks," *IEEE Transactions on Intelligent Transportation Systems*, pp. 1–15, 2021.

[11] A. Mahmood, S. S. Khan, M. Q. Usman et al., "Optimal placement of UAV for coverage maximization with minimum path loss," *International Journal of Wireless Communications and Mobile Computing*, vol. 7, no. 1, pp. 27–31, 2019.

[12] O. I. Khalaf, C. A. T. Romero, S. Hassan, and M. T. Iqbal, "Mitigating hotspot issues in heterogeneous wireless sensor networks," *Journal of Sensors*, vol. 2022, Article ID 7909472, 14 pages, 2022.

[13] J.-L. Liu and C. V. Ravishankar, "LEACH-GA: genetic algorithm-based energy-efficient adaptive clustering protocol for wireless sensor networks," *International Journal of Machine Learning and Computing*, vol. 1, no. 1, pp. 79–85, 2011.

[14] W. R. Heinzelman, A. Chandrakasan, and H. Balakrishnan, "Energy-efficient communication protocol for wireless microsensor networks," in *Proceedings of the 33rd annual Hawaii international conference on system sciences*no. 2, p. 10, Maui, HI, USA, 2000.

[15] W. B. Heinzelman, A. P. Chandrakasan, and H. Balakrishnan, "An application-specific protocol architecture for wireless microsensor networks," *IEEE Transactions on Wireless Communications*, vol. 1, no. 4, pp. 660–670, 2002.

[16] A. Manjeshwar and D. P. Agrawal, "TEEN: a routing protocol for enhanced efficiency in wireless sensor networks," in *Proceedings 15th International Parallel and Distributed Processing Symposium. IPDPS 2001*, vol. 1, pp. 2009–2015, San Francisco, CA, USA, 2001.

[17] A. Kashaf, N. Javaid, Z. A. Khan, and I. A. Khan, "TSEP: threshold-sensitive stable election protocol for WSNs," in *2012 10th International Conference on Frontiers of Information Technology*, pp. 164–168, Islamabad, Pakistan, 2012.

[18] R. Vadlamudi and S. Umar, "A review of APTEEN in wireless sensor networks," *International Journal of Science, Engineering and Computer Technology*, vol. 3, no. 9, p. 306, 2013.

[19] S. Lindsey and C. S. Raghavendra, "PEGASIS: power-efficient gathering in sensor information systems," in *Proceedings, IEEE aerospace conference*, vol. 3, Big Sky, MT, USA, 2002.

[20] O. Younis and S. Fahmy, "HEED: a hybrid, energy-efficient, distributed clustering approach for ad hoc sensor networks," *IEEE Transactions on Mobile Computing*, vol. 3, no. 4, pp. 366–379, 2004.

[21] M. Tarhani, Y. S. Kavian, and S. Siavoshi, "SEECH: scalable energy efficient clustering hierarchy protocol in wireless sensor networks," *IEEE Sensors Journal*, vol. 14, no. 11, pp. 3944–3954, 2014.

[22] K. M. Awan, A. Ali, F. Aadil, and K. N. Qureshi, "Energy efficient cluster based routing algorithm for wireless sensors networks," in *2018 International Conference on Advancements in Computational Sciences (ICACS)*, pp. 1–7, Lahore, Pakistan, 2018.

[23] W. Zhu, J. Cao, and M. Raynal, "Energy-efficient composite event detection in wireless sensor networks," *IEEE Communications Letters*, vol. 22, no. 1, pp. 177–180, 2018.

[24] M. Razzaq, D. D. Ningombam, and S. Shin, "Energy efficient K-means clustering-based routing protocol for WSN using optimal packet size," in *2018 International Conference on Information Networking (ICOIN)*, pp. 632–635, Chiang Mai, Thailand, 2018.

[25] B. Sun and D. Li, "A comprehensive trust-aware routing protocol with multi-attributes for WSNs," *IEEE Access*, vol. 6, pp. 4725–4741, 2017.

[26] F. Engmann, F. A. Katsriku, J.-D. Abdulai, K. S. Adu-Manu, and F. K. Banaseka, "Prolonging the lifetime of wireless sensor networks: a review of current techniques," *Wireless Communications and Mobile Computing*, vol. 2018, Article ID 8035065, 23 pages, 2018.

[27] L. Zhao, S. Qu, and Y. Yi, "A modified cluster-head selection algorithm in wireless sensor networks based on LEACH," *EURASIP Journal on Wireless Communications and Networking*, vol. 2018, Article ID 287, 8 pages, 2018.

[28] J.-G. Lee, S. Chim, and H.-H. Park, "Energy-efficient cluster-head selection for wireless sensor networks using sampling-based spider monkey optimization," *Sensors*, vol. 19, no. 23, p. 5281, 2019.

[29] P. Karthick and C. Palanisamy, "Optimized cluster head selection using krill herd algorithm for wireless sensor network," *Automatika*, vol. 60, no. 3, pp. 340–348, 2019.

[30] L. Tang, Z. Lu, and B. Fan, "Energy efficient and reliable routing algorithm for wireless sensors networks," *Applied Sciences*, vol. 10, no. 5, p. 1885, 2020.

[31] R. Sinde, F. Begum, K. Njau, and S. Kaijage, "Refining network lifetime of wireless sensor network using energy-efficient clustering and DRL-based sleep scheduling," *Sensors*, vol. 20, no. 5, p. 1540, 2020.

[32] R. K. Yadav and R. P. Mahapatra, "Energy aware optimal cluster head selection using hybrid algorithm for clustering routing in wireless sensor networks," *International Journal of Intelligent Engineering and Systems*, vol. 13, no. 3, pp. 222–231, 2020.

[33] W. Fei, B. Hexiang, L. Deyu, and W. Jianjun, "Energy-efficient clustering algorithm in underwater sensor networks based on fuzzy c means and moth-flame optimization method," *IEEE Access*, vol. 8, pp. 97474–97484, 2020.

[34] Y. Zhang and Y. Wang, "A novel energy-aware bio-inspired clustering scheme for IoT communication," *Journal of Ambient Intelligence and Humanized Computing*, vol. 11, no. 10, pp. 4239–4248, 2020.

[35] A. Singh, S. Sharma, and J. Singh, "Nature-inspired algorithms for wireless sensor networks: a comprehensive survey," *Computer Science Review*, vol. 39, article 100342, 2021.

Hindawi
Journal of Sensors
Volume 2022, Article ID 1901058, 10 pages
https://doi.org/10.1155/2022/1901058

Research Article

FSR-Based Smart System for Detection of Wheelchair Sitting Postures Using Machine Learning Algorithms and Techniques

Mujtaba Hussain Jaffery,[1] Muhammad Adil Ashraf,[1] Ahmad Almogren,[2] Hafiza Mahnoor Asim,[1] Jehangir Arshad,[1] Javed Khan,[3] Ateeq Ur Rehman,[4,5] and Seada Hussen[6]

[1]*Department of Electrical and Computer Engineering, COMSATS University Islamabad, Lahore 54000, Pakistan*
[2]*Department of Computer Science, College of Computer and Information Sciences, King Saud University, Riyadh 11633, Saudi Arabia*
[3]*Department of Electrical Engineering, University of Science and Technology Bannu, Pakistan*
[4]*Department of Electrical Engineering, Government College University, Lahore 54000, Pakistan*
[5]*Faculty of Engineering, Uni de Moncton, Moncton, NB E1A3E9, Canada*
[6]*School of Electrical and Computer Engineering, Haramaya Institute of Technology, 138 Diredawa, Ethiopia*

Correspondence should be addressed to Ateeq Ur Rehman; ur.rehman.hamam@umoncton.ca and Seada Hussen; seada.hussen@aastu.edu.et

Received 16 February 2022; Revised 24 March 2022; Accepted 9 April 2022; Published 5 May 2022

Academic Editor: Han Wang

This paper presents an intelligent system containing FSR-based posture detection using machine learning algorithms. This paper is aimed at detecting the sitting posture of a wheelchair user. Individuals using wheelchairs are at increased risk of pressure ulcers when they hold an incorrect position for too long because the blood supply desists at some points of their skin due to increased pressure. The main objective of this research is to find a better configuration combined with the best machine learning algorithm for the detection of posture to prevent pressure ulcers. In the proposed monitoring system, two configurations consisting of a 3×3 matrix configuration (9 sensors) and a crossconfiguration (5 sensors) of FSR sensors are embedded on a wheelchair seat to get pressure data generated and collected in a real-time processing unit and then compared. The posture recognition is performed for five sitting positions: ideal, backward-leaning, forward-leaning, right-leaning, and left-leaning based on five machine learning algorithms: K-nearest neighbors (K-NN), logistic regression (LR), decision tree (DT), support vector machines (SVM), and LightGBM. The research study provides a system to detect a real-time pressure sitting posture on a processing unit (laptop) wirelessly using the ESP32 module. Consequently, a posture classification accuracy of up to 95.41% is accomplished using a 3×3 matrix configuration. The proposed system helps prevent pressure ulcers and is valuable in risk assessment related to pressure ulcers. This system describes the relationship between accuracy, different sensor configurations, and performance of the multiple machine learning algorithms.

1. Introduction and Literature Review

A sedentary lifestyle affects a person's health mentally and welcomes many physical health problems. According to WHO-World Health Organization, 60 to 85% of people live a sedentary lifestyle [1] which may cause many unwanted health problems and diseases, including pressure ulcers. Pressure ulcers or bedsores are diseases that can cause damage to the skin and underlying tissues due to the exertion of prolonged pressure on a specific point in the body. Persons with pressure ulcers have a 4.5-times more significant risk of dying than those with the same risk factors without pressure ulcers [2]. Individuals who use a wheelchair may face many difficulties other than immobility, which counts pressure

ulcers. According to an estimation, 1% of the world's population uses a wheelchair which covers around 65 million of the population [3], and approximately 60,000 people face death because of pressure ulcers annually [2].

Much research has been done to reduce the risk of getting pressure ulcers, and the most appropriate way to avoid getting pressure ulcers is to reduce the exertion of pressure on the body. People with a sedentary lifestyle can improve their lives by increasing their physical activity rate, but a wheelchair user has to sit every time on a chair due to immobility. The high-probability sites for a wheelchair user to get pressure ulcers are where most of their body weight lies and the points of their skin that frequently get rubbed by wheelchair seats such as hips, back, and heels [4]. If the sitting patterns are wrong, there are increased risks of getting pressure ulcers sooner than expected. 30%-85% of people with spinal cord injuries get pressure ulcers in their first month of injury [5]. Sites having increased risk of development of pressure ulcers are over the sacrum due to prolonged sitting in a wrong posture, such as if the patient sits slumped down the seat without using backrest support, the angle of backrest increases, and this arrangement exerts shear forces over the sacrum causing pressure ulcers [6].

Incorrect posture can disturb the natural distribution of the human body weight resulting in higher pressure on the buttocks; the increased pressure decreases the blood flow and malnourished the area from oxygen and nutrients, and if this goes unhealed, it begins to break down of the skin resulting in the development of a pressure ulcer. Similarly, incorrect posture can increase pressure on the spine and other joints, making them more prone to pressure ulcers. An ideal sitting posture maintains four natural bends of the spine: the concaved cervical spine bend, the forthcoming thoracic spine bend, the lower concaved lumbar spine bend, and the lower outward sacral bend. The back is straight or slightly forward, and the legs 5°-8° apart. The back and the legs should make an angle of 90° with feet and heels touching the floor to preserve ideal sitting posture [7]. An angle between legs and spine of 90° is considered optimal for daily life [8]. Sitting in a correct posture distributes body weight primarily to the buttocks; nevertheless, it can be reduced 12.4% by chair armrests, 4.4% by the backrest, and 18.4% by supporting feet properly [7]. In conclusion, a balanced sitting posture can reduce the risk of getting a pressure ulcer or cause a delay in that. The best way to adopt an ideal sitting posture is to eliminate an incorrect posture by analyzing daily sitting patterns and rectifying them. Numerous other research has been done to examine the sitting habits of a wheelchair user using different methods and techniques [8–10, 27].

This paper presents a system developed to analyze and monitor the posture of a wheelchair user to prevent pressure ulcers and indicate to the patient or caretaker if the patient holds an incorrect posture for too long. The five sitting patterns are included: one is an ideal posture, and the other four are incorrect postures subsumed backward-leaning, forward-leaning, left-leaning, and right-leaning. The description of these postures and the impairment caused by these are given in Table 1. Many previous studies are centered on sitting posture detection with the purpose of the reduction of risks of getting pressure ulcers. J. Ahmad proposed a system of a Life Chair for posture detection, using a pressure sensing technique, a cellphone API, and machine learning (ML). Accuracy of 98.93% is achieved by the life chair system in recognition of 13 different postures using a supervised learning algorithm [11]. Analogously, a chair with six flexible force sensors and Nod red application for the whole process solution from QNAP stored in the Mongo dB database is developed [12]. A different approach to detecting sitting posture is the WiSAT sensor mat placed on a wheelchair seat. Posture detection is carried out by predicting weight shifts and in-seat movements in the mat [13].

In another previous work, five supervised classification techniques, including decision tree (J48), support vector machines, multilayer perceptron, Naive Bayes, and k-nearest neighbor, are compared in accuracy, precision, recall, and F-measure [14]. Nevertheless, only a support vector machine (SVM) is used in some studies, including a polynomial kernel to categorize four different sitting postures, with a classification precision of 89.6% [15]. The accuracy achieved in some studies is up to 99.03%, in which five different classifiers have been used, and their accuracy and computational time are computed using the embedded device and GPU [10]. Focusing on the sitting poses of travelers in airplanes is also considered, a study has been done with 24 subjects tested, and 489 sitting positions are obtained, and the pressure data among subjects and seats have been collected, while eight different sitting postures are classified in this work. By using a support vector machine (SVM), a classification rate of 89.26% is obtained in the aircraft study [16]. Artificial neural networks could also achieve the highest accuracy of 97.07% [17, 18]. Research on gait detection with various techniques has also been done in [19]. A concise comparison of existing works has been presented in Table 2.

2. Materials and Methods

This paper includes a system to detect the posture of wheelchair users and other sitting environments using an FSR-force sensitive resistor [20]. It covers comparison of two configurations with five different machine learning algorithms, including logistic regression (LR), LightGBM, K-nearest neighbor (KNN), support vector machine (SVM), and decision tree (DT), to find out which configuration combination with which algorithm is better to detect the posture of the user with higher efficiency. This paper contains the following contributions for the detection of posture.

(a) Designing the embedded system

(b) Dataset generation and compilation

(c) Processing machine learning algorithms

2.1. Designing the Embedded System. This study uses FSR (force-sensitive resistor) sensors that exhibit varying resistance to the force applied to it to design an embedded system. Arranging the FSR sensors on a wheelchair seat, such as when a person sits on it, the FSR sensors give variation in output value according to the force exerting on it. The

Table 1: Sitting postures and their effects.

Posture arrangement	Description	Pressure points	Possible health problems
Ideal posture	Back and legs make an angle of 90′	Balanced pressure on buttocks, arms, legs, and back	No harm
Forward leaning	The slope of 40′, no back support	Knee, abdomen, shoulder, upper spinal cord	Knee issue, back pain, back stiffness
Backward leaning	Upper back against chair backrest	Lumbar spine and neck	Spinal dysfunction, the strain on soft tissues
Right-leaning	Leaning to the right exerts more pressure on the right side of the body	Liver, stomach and right kidney, lower spinal cord	Respiratory issues, muscle imbalance, tightness of right muscles, spine curve to the right
Left-leaning	Leaning to the left exerts more pressure on the left side of the body	Spleen, left kidney, lower spinal cord	Respiratory issues, muscle imbalance

Table 2: Previous work comparison.

Sr #	Reference #	Type of sensors	No. of postures	Classifiers/software	Accuracy	Limitations
1	[23]	Pressure sensor	13	(DT-CART), (RF), (KNN), (LR), (LDA), and (NB)	98.93%	Subjects for the dataset are minimal
2	[13]	Wisat mat	5	Wisat algorithms in MATLAB	81%	Only 17 datasets are available
3	[8]	3 pressure sensors, 1 sonar	4	KNN	76.05%	Less accuracy and classifier comparison is significantly less
4	[14]	12 pressure sensors	5	Decision tree (J48), (SVM), (MLP), Naive Bayes, and (k-NN)	99.47%	Can record up to only 12 pressure points simultaneously
5	[15, 26]	A 32×32 pressure sensor	4	Support vector machine (SVM)	89.6%	Multiple data collected by only using 10 subjects
6	[10]	16 sensors with 16 matrix	4	k-nearest neighbors (k-NN), random forest (RF), decision tree (DT) support vector machines (SVM), and LightGBM	99.03%	Not proposed a system through which it can correct wrong user posture

force exerted on FSR sensors equals the pressure times area (1). Output voltage varies according to the variation in the force exerting on this sensor [21].

$$\text{Force} = \text{Pressure} * \text{Area}. \tag{1}$$

Two configurations are compared in this study to determine which configuration of sensors is better to detect the posture with higher accuracy. The standard and usual sitting patterns and the pressure distribution at different postures are observed, which vary depending on height, weight, and body mass.

2.1.1. Configuration 01. In this configuration, five sensors are placed in the cross (X) position, given the body mass and pressure distribution of sitting patterns [22]. This configuration is designed to detect posture detection using fewer sensors. The sensor arrangement of crossconfiguration is shown in Figure 1. The total cost of this configuration is approximately $18.

2.1.2. Configuration 02. The other configuration is the 3×3 matrix sensor configuration which covers an almost complete chair area. This configuration attracts most researchers, and research has already been done on this configuration [10], but in our study, we compared this configuration to another configuration by applying five different machine learning algorithms to gain higher accuracy. The 3×3 matrix arrangement of sensors is shown in Figure 2. The total cost of this system is $15. Thus, this configuration costs less than configuration 01.

The wheelchair seat consists of nine sensors embedded in a 3×3 matrix arrangement named configuration 01 and six sensors in a cross arrangement named configuration 02. The samples are collected of all subjects on both configurations, and an ESP 32 module is used for communication between wheelchair seat sensors and operating system—windows. The sensor data is sent to Arduino IDE serial communication and converted to CSV dataset format. A laptop used for data collection has the following specifications: Intel core i5, 6th generation, G3 2.40 Ghz processor, and 8 Gb RAM. The hardware system overview diagram is given in Figure 3.

Figure 1: Crossconfiguration of sensors on wheelchair.

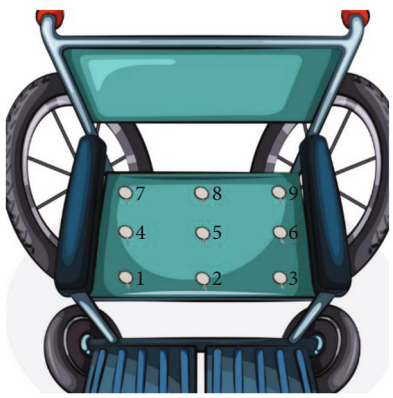

Figure 2: 3 × 3 matrix sensor configuration.

2.2. Dataset Generation and Compilation. In this study, people of both genders contributed, having different heights and weights. Thirty males and ten females participated in the generation of the dataset, 600 male and 200 female samples of five different postures are recorded as given in Table 3, and a graphical representation of the dataset is given in Figure 4. The subject's weight, height, and BMI range is 156 cm-190 cm, 45 kg-110 kg, and 16 kg/m^2-36 kg/m^2, respectively.

The samples are recorded in five different postures: ideal position, forward-leaning, backward leaning, left-leaning, and right-leaning. This research is made keeping in view the average height and weight and optimal range of BMI, So, four types of people are included in this research according to their height and weight: underweight (BMI ≤ 20), healthy weight (20 ≤ BMI ≤ 25), overweight (25 ≤ BMI ≤ 30), and obese (30 ≤ BMI). The height, weight, and BMI ranges are given in Table 4 and shown in Figure 4.

The sensor's data is sent to Arduino IDE serial monitor using the ESP32 module, and simultaneously, the data is recorded into Excel through Arduino IDE to Excel data streaming technique as shown in Figure 5. Figure 5 shows the dataset of a male subject with 20 samples, four samples per posture of configuration 02. The position column represents the sitting patterns including ideal posture, forward-leaning, backward leaning, left-leaning, and right-leaning as 0, 1, 2, 3, and 4, respectively, and the G, H, W columns present gender, height, and weight, respectively. Gender is represented by 0 and 1 as male and female.

2.3. Machine Learning Algorithms. This paper compares five different algorithms after generating the dataset, including KNN, SVM, LightGBM, logistic regression, and decision tree. The KNN algorithm calculates the nearest things or objects to it and predicts values [23]. The straight-line distance is the Euclidean distance, a famous method for calculating the distance between two points in the dataset—selecting the K, which is suitable for data. Running the KNN algorithm again and again for different values of K helps in choosing the proper value of K, which is very necessary to reduce the number of errors. For achieving higher accuracy in the KNN algorithm, the preprocessing technique is used in this study which is essential to maintain the algorithm's ability to make predictions accurately. As the value of k becomes less than one, predictions become less stable; by increasing the value of k, predictions become more stable due to majority voting/averaging and start making more accurate predictions. Distance functions used to calculate the distance from the nearest neighbor are Euclidean calculated as in (2), Manhattan given in (3), and Minkowski given in (4).

$$\text{Euclidean} = \sqrt{\sum_{i=1}^{k} (x_i - y_i)^2}, \tag{2}$$

$$\text{Manhattan} = \sum_{i=1}^{k} |x_i - y_i|, \tag{3}$$

$$\text{Minkoswski} = \left(\sum_{i=1}^{k} (|x_i - y_i|)^q \right)^{1/q}. \tag{4}$$

The SVM algorithm finds a hyperplane in N-dimensional space. N shows total features distinctly to classify the data points [24]. The margin between the data points is maximized by using SVM. The hyperplane and the loss function helps in maximizing the margin, which is called hinge loss.

$$l(y) = \max\left(0, 1 + \max_{y \neq t} w_y x - w_t x\right), \tag{5}$$

Hinge Loss Function : $t \longrightarrow$ target variable, $w \longrightarrow$ model parameters, $x \longrightarrow$ Input variable.

The decision tree algorithm is the most straightforward and efficient supervised learning algorithm. In the decision tree, algorithm data points are split continuously according to some parameters, and the algorithm tries to solve the problem [25]. Other names of decision trees are classification and regression trees. Decision trees follow a top-down approach. The tree leaves represent the outcomes of the decision tree. Decision trees are called Divide, and Conquer means recursive partitioning. The function of Entropy is an information theory metric that measures the impurity or uncertainty using a group of observations built using a heuristic given in (6). In the meantime, when selected randomly,

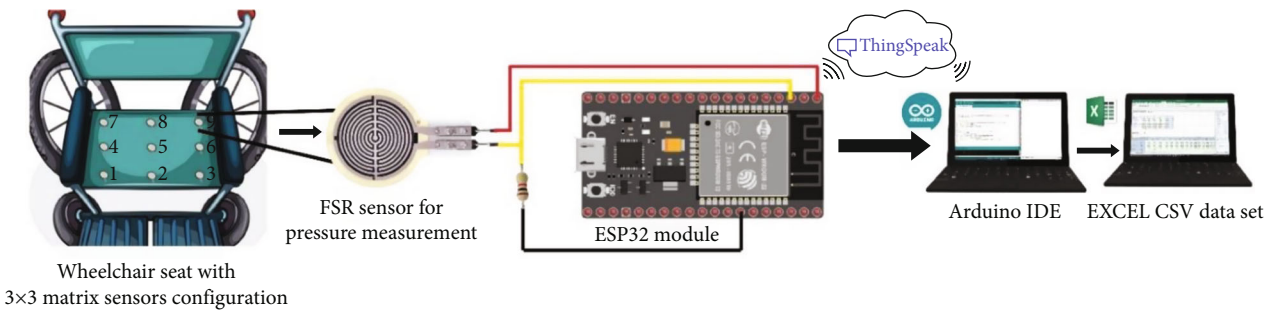

Figure 3: An overview of system hardware schematic.

Table 3: Subjects details.

Genders	No. of subjects	No. of samples	Age range
Male	30	600	19-35
Female	10	200	18-25

Gini calculates the probability of a specified feature classified incorrectly as in (7).

$$\text{Entropy} = \sum_{i=1}^{C} -p_i * \log_2(pi), \tag{6}$$

$$\text{Gini} = 1 - \sum_{i=1}^{C} (p_i)^2. \tag{7}$$

The statistical analysis method that predicts a binary outcome in the form of 0 and 1 is called logistic regression, based on the prior observations of a given dataset. After analyzing the relationship between existing independent variables, a logistic regression model predicts a dependent data variable [19] and the cost function of logistic regression modeled as in (8). The probability of a record belonging to the positive class given features is predicted by the logistic regression given in (9).

$$\text{Cost}(h_\theta(x), y) = \begin{cases} -\log\left(h_\theta(x)\right), \text{ if } y = 1, \\ -\log\left(1 - h_\theta(x)\right), \text{ if } y = 0, \end{cases} \tag{8}$$

$$P = \frac{1}{1 + e^{-(\beta_0 + \beta_1 X_1 + \beta_2 X_2 + \beta_3 X_3 \cdots\cdots\cdots\cdots + \beta_n X_n)}}. \tag{9}$$

LightGBM is used to extend the gradient boosting of an algorithm, focusing on boosting examples with more significant gradients [25]. Predictive performance can be improved by speeding up the training process, which is accomplished through automatic feature selection. The LightGBM algorithm uses two novel techniques called Gradient-Based One-Side Sampling (GOSS) and Exclusive Feature Bundling (EFB); these techniques make the algorithm run faster while maintaining a high level of accuracy.

If $\mathbf{Y}$ is the prediction and $\mathbf{X}$ is the feature vector:

$$\mathbf{Y} = \text{Base\_tree}(\mathbf{X}) - \text{lr} * \text{Tree1}(\mathbf{X}) - \text{lr} * \text{Tree2}(\mathbf{X}) - \text{lr} * \text{Tree3}(\mathbf{X}). \tag{10}$$

In this study, five algorithms are applied to the dataset of two configurations and compared based on their accuracy, precision, and execution time—these all algorithms combined structure the backend process of the posture detection system. The dataset is trained using the machine learning algorithms, and then, different predictions are made to detect the posture. Predictions are tested by comparing them with test values. The overall system diagram of a real-world environment consisting of FSR sensors and the backend posture detection process is given in Figure 6.

3. Results and Discussion

For the performance evaluation, the classification algorithms' results (including logistic regression, SVM, KNN, decision tree, and LightGBM) are determined on the basics of precision, accuracy, and execution time. The classifiers are trained using the training data consisting of five different sitting postures: ideal, forward-leaning, backward-leaning, left-leaning, and right-leaning.

3.1. 3 × 3 Matrix. The accuracy, precision, and execution time comparison charts are shown in Figures 7 and 8. In 3 × 3 matric configuration, KNN (K-nearest neighbor) algorithm prediction precision is 89.8%, accuracy 90.3%, and execution time is about 0.92 s. KNN is better than SVM, logistic regression, and decision tree in this configuration. However, it takes more execution time as compared to other classification algorithms. For this reason, KNN is also known as a slow learner because of its slow learning rate. The decision tree algorithm generates precision of 88.6% and accuracy of 88.26% with an execution time of 0.163 s. For this configuration, the highest accuracy is achieved by LightGBM (95.41%) but with a higher execution time (1.27 sec).

LightGBM generates the highest accuracy and precision compared to other classifiers with a high-performance gradient boosting framework based on decision tree algorithms. This study concluded that LightGBM gives the highest accuracy and detects the posture with higher accuracy and precision rate but with maximum execution time. The

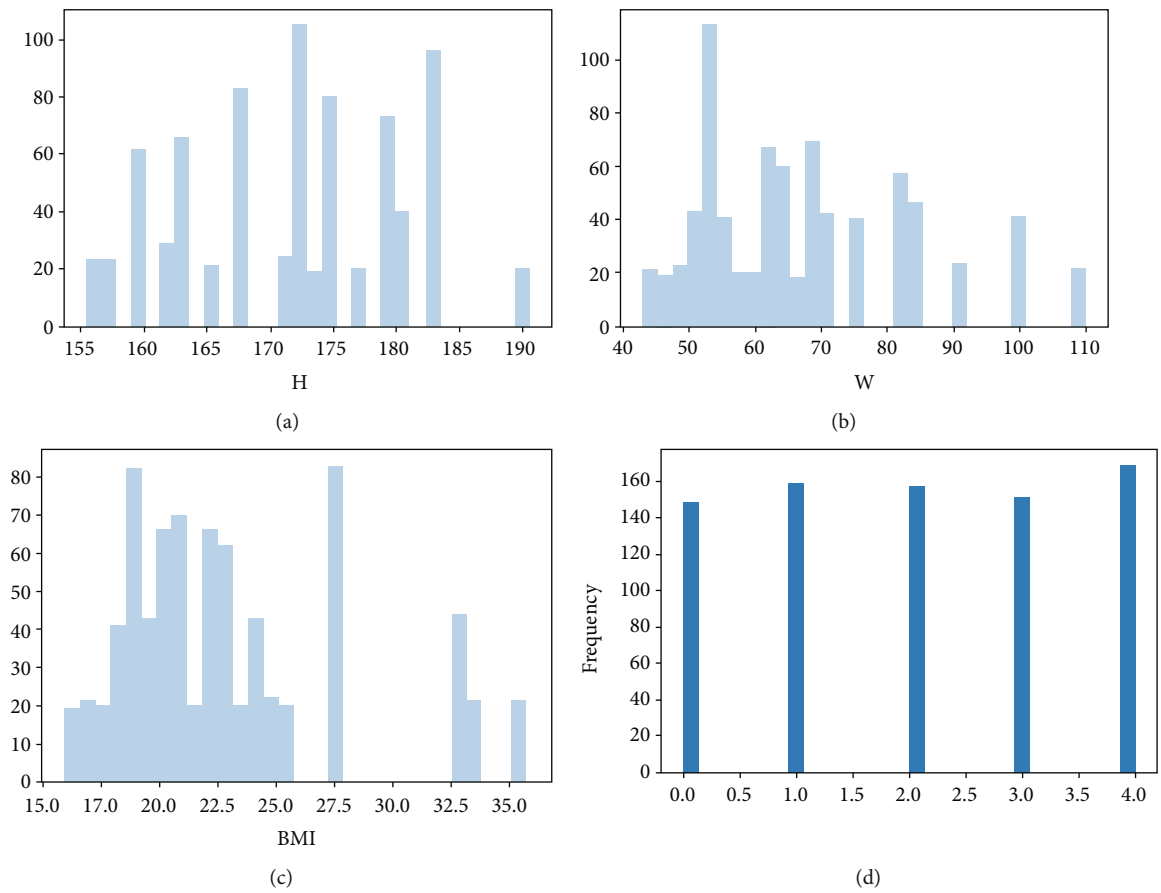

Figure 4: This figure shows the graphical representation of dataset parameters as follows: (a) height; (b) weight; (c) BMI; (d) samples per posture.

Table 4: Samples details of dataset.

Total no of samples	Total no. of postures	Samples per posture	Height range (cm)	Weight range (kg)	BMI range (kg/m^2)
800	5	4	156-190	45-110	16-36

performance parameters are shown in Figure 9. Figure 9(a) shows that LightGBM is achieving 95.41% accuracy with 600 training examples, and for the generation of 600 training examples to achieve this accuracy, it consumed 1.27 seconds with better scalability.

The classification algorithm of logistic regression gave precision of 80.3% and accuracy of 79.61%, achieved with the execution time of 0.114 s. Logistic regression used for binary classification did not produce such good results in the posture detection classification task, a multiclass classification. SVM (support vector machine) algorithm is used to predict posture, and the precision recorded is 85.5%; the accuracy of 85.35% is achieved with the execution time of 0.112 s. SVM works better where there is a definite distinction between two classifications, so in this scenario, the accuracy of SVM is higher than logistic regression. The precision, accuracy, and execution time of logistic regression, SVM, KNN, decision tree, and LightGBM are given in Table 5.

3.2. Crossconfiguration. Logistic regression is applied, and a precision of 80.7% is achieved with an accuracy of 80.8% and execution time of 0.078 s. SVM (support vector machine) algorithm is used to predict posture 87.2% precision, and accuracy is about 83.4% with the execution time of 0.083 s. KNN algorithm gave precision of about 87.2%, accuracy 86.6%, and execution time is about 0.73 s. The decision tree algorithm generates a precision of 88.6% and an accuracy of 88.26% with an execution time of 0.052 s. LightGBM accuracy is about 89.8%, and precision is 90.5%, and its execution time is 0.84 s. The crossconfiguration classification results consisting of accuracy, precision, and execution time are given in Table 6.

3.3. Comparative Analysis and System Limitations. The comparison of these configurations is based on accuracy, precision, and execution time. The 3×3 matrix configuration gave better results for posture detection with the highest accuracy of 95.41% when processed in the LightGBM

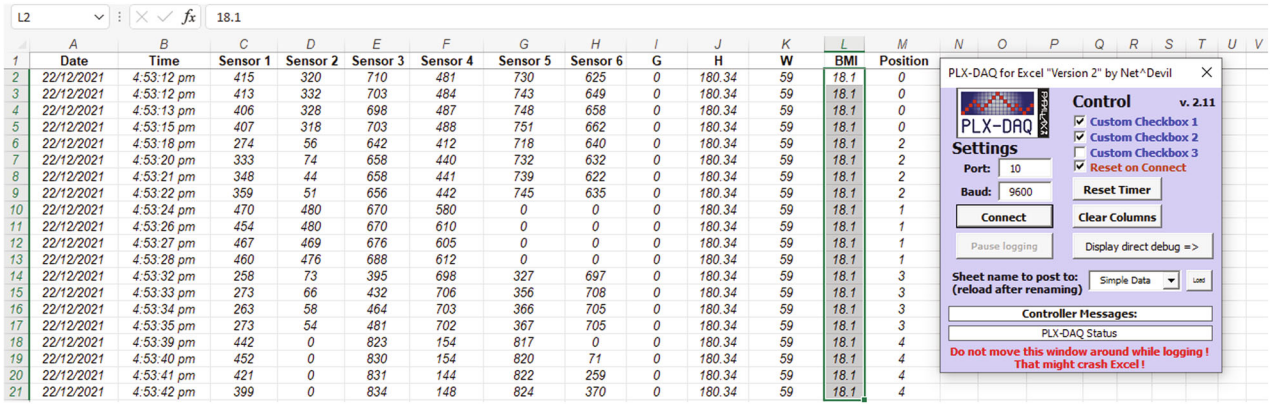

	Date	Time	Sensor 1	Sensor 2	Sensor 3	Sensor 4	Sensor 5	Sensor 6	G	H	W	BMI	Position
2	22/12/2021	4:53:12 pm	415	320	710	481	730	625	0	180.34	59	18.1	0
3	22/12/2021	4:53:12 pm	413	332	703	484	743	649	0	180.34	59	18.1	0
4	22/12/2021	4:53:13 pm	406	328	698	487	748	658	0	180.34	59	18.1	0
5	22/12/2021	4:53:15 pm	407	318	703	488	751	662	0	180.34	59	18.1	0
6	22/12/2021	4:53:18 pm	274	56	642	412	718	640	0	180.34	59	18.1	2
7	22/12/2021	4:53:20 pm	333	74	658	440	732	632	0	180.34	59	18.1	2
8	22/12/2021	4:53:21 pm	348	44	658	441	739	622	0	180.34	59	18.1	2
9	22/12/2021	4:53:22 pm	359	51	656	442	745	635	0	180.34	59	18.1	2
10	22/12/2021	4:53:24 pm	470	480	670	580	0	0	0	180.34	59	18.1	1
11	22/12/2021	4:53:26 pm	454	480	670	610	0	0	0	180.34	59	18.1	1
12	22/12/2021	4:53:27 pm	467	469	676	605	0	0	0	180.34	59	18.1	1
13	22/12/2021	4:53:28 pm	460	476	688	612	0	0	0	180.34	59	18.1	1
14	22/12/2021	4:53:32 pm	258	73	395	698	327	697	0	180.34	59	18.1	3
15	22/12/2021	4:53:33 pm	273	66	432	706	356	708	0	180.34	59	18.1	3
16	22/12/2021	4:53:34 pm	263	58	464	703	366	705	0	180.34	59	18.1	3
17	22/12/2021	4:53:35 pm	273	54	481	702	367	705	0	180.34	59	18.1	3
18	22/12/2021	4:53:39 pm	442	0	823	154	817	0	0	180.34	59	18.1	4
19	22/12/2021	4:53:40 pm	452	0	830	154	820	71	0	180.34	59	18.1	4
20	22/12/2021	4:53:41 pm	421	0	831	144	822	259	0	180.34	59	18.1	4
21	22/12/2021	4:53:42 pm	399	0	834	148	824	370	0	180.34	59	18.1	4

Figure 5: Streaming data from Arduino IDE to Excel.

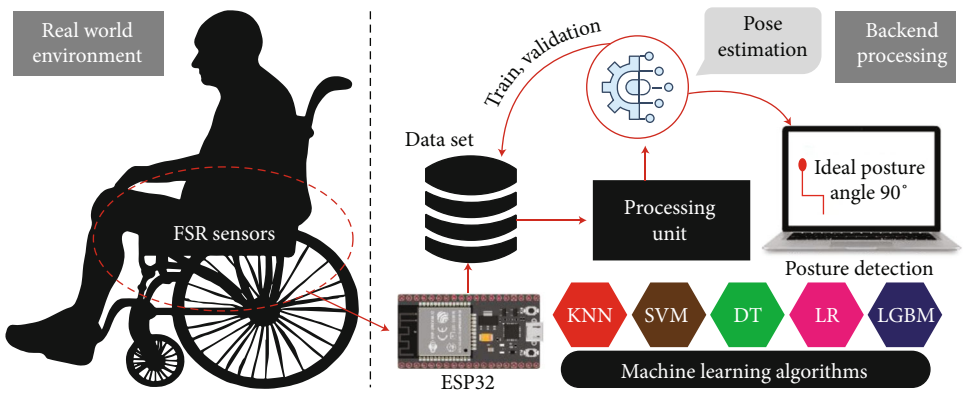

Figure 6: Real-world environment and backend processing diagram.

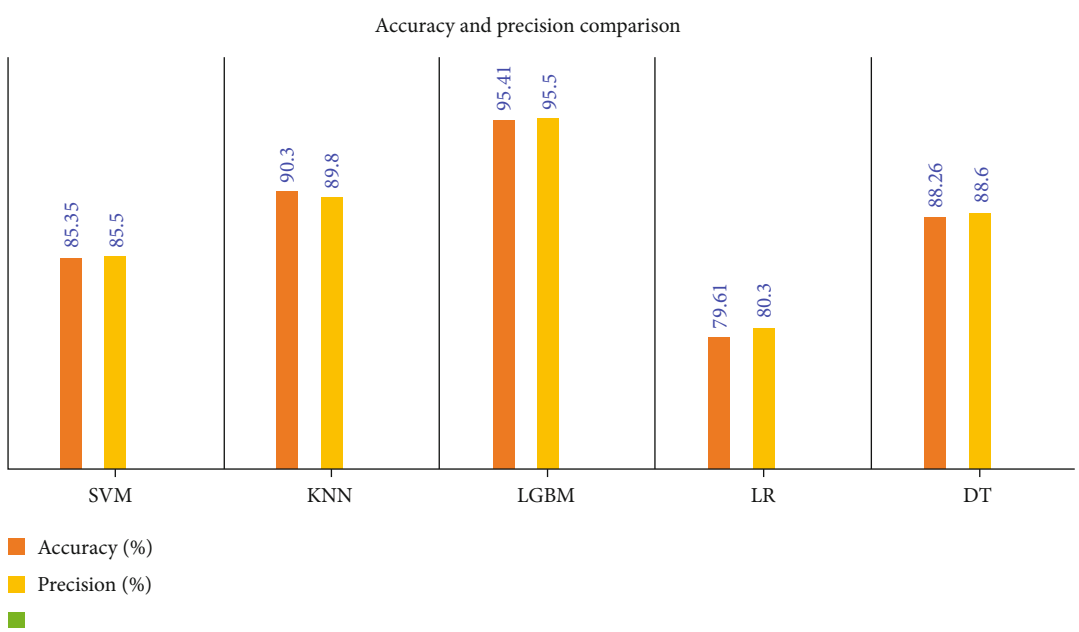

Figure 7: Accuracy and precision comparison.

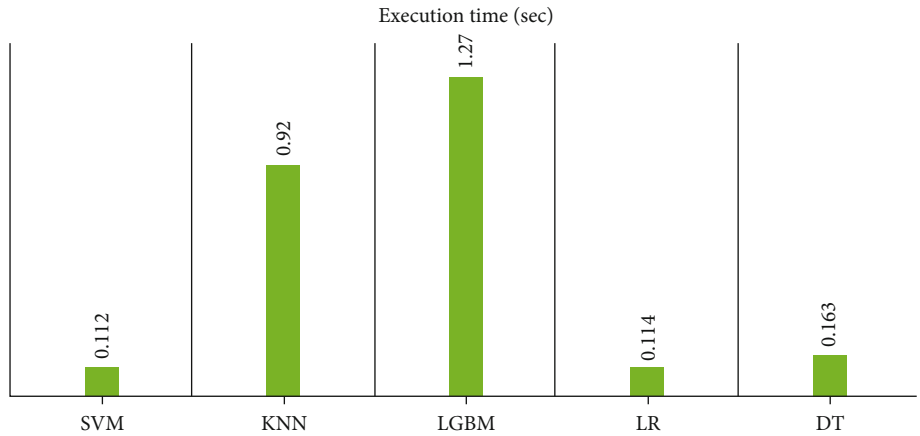

Figure 8: Execution time comparison.

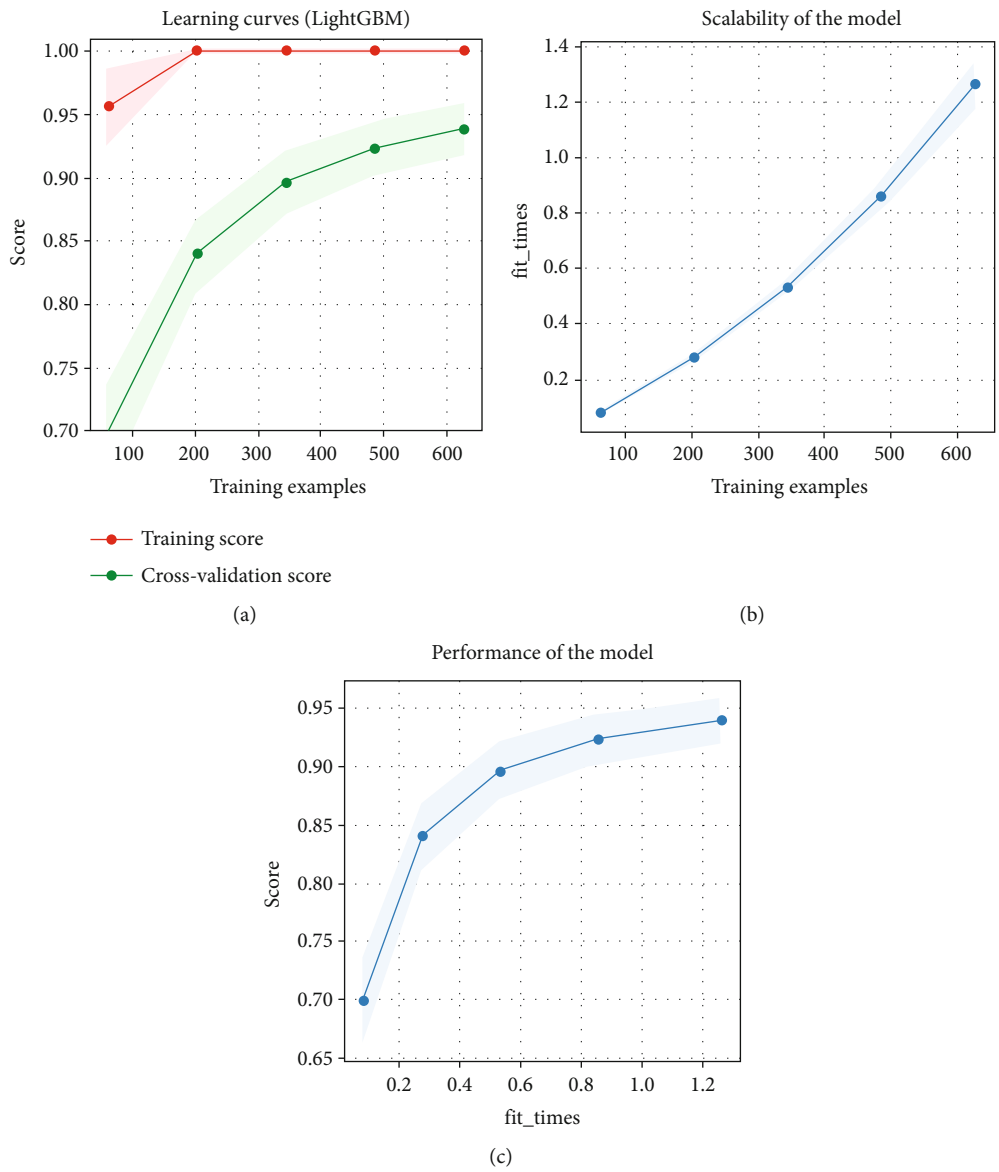

Figure 9: Performance parameters of LightGBM.

Table 5: 3×3 matrix classification parameters.

Algorithms	Precision	Accuracy	Execution time
Logistic regression	80.3%	79.61%	0.114 s
SVM	85.5%	85.35%	0.112 s
KNN	89.8%	90.3%	0.92 s
Decision tree	88.6%	88.26%	0.163 s
LightGBM	95.5%	95.41%	1.27 s

Table 6: Crossconfiguration classification results.

Algorithms	Precision	Accuracy	Execution time
Logistic regression	80.7%	80.8%	0.078 s
SVM	87.2%	83.4%	0.083 s
KNN	87.2%	86.6%	0.73 s
Decision tree	88.6%	88.26%	0.052 s
LightGBM	90.5%	89.8%	0.84 s

Table 7: Crossconfiguration classification results.

Configuration	Highest accuracy	Average execution time	Highest precision	Better ML algorithm
3×3 matrix	95.41	0.5158 sec	95.5%	LightGBM
Cross	89.8%	0.3566 sec	90.5%	LightGBM

algorithm. The comparison of both configurations with machine learning algorithms is given in Table 7. The 3×3 matrix configuration achieved higher accuracy and precision, so this configuration provides give better and more accurate results of posture detection.

The number of subjects who participated in the generation of the dataset for this study is limited. Thus, the number of subjects can be increased to have an extensive dataset as the number of predictions increases with the increase in the dataset. Moreover, more configurations can be designed to compare and find the best sensor distribution arrangement according to body mass and weight distribution. More machine learning algorithms can be applied to find the highest accuracy and precision with the lowest execution time. The deep learning algorithms can also be helpful in the better prediction of posture detection.

4. Conclusions

This research presents an intelligent system for detecting sitting postures of wheelchair users using FSR sensors and machine learning algorithms. The designed system will help to prevent the development of pressure ulcers. Wheelchair users are often troubled with pressure ulcers caused by cutting blood supply to a particular skin area due to prolonged increased pressure. The proposed system is designed into three sections, including (i) two types of sensor distribution arrangement, (ii)gathering of dataset of five sitting positions including ideal, forward-leaning, backward-leaning, right-leaning, and left-leaning, and (iii) applying five different machine learning algorithms consisting of KNN, SVM, LightGBM, decision tree, and logistic regression and compared algorithms with sensor configuration based on accuracy, precision, and execution time.

The 3×3 matrix sensor array configuration combined with the LightGBM algorithm gave the highest accuracy of 95.41%. It is visible that using a 3×3 matrix configuration gives more accurate results than crossconfiguration. Hence, this configuration is better for the detection of sitting patterns. The proposed system is helpful for the prevention of pressure ulcers in wheelchair users and can be used for the users without mobility issues for analyzing their sitting patterns for the long-term prevention of pressure ulcers. This system describes the relationship between accuracy, different sensor configurations, and performance of the multiple machine learning algorithms.

Data Availability

No data were used to support this study.

Disclosure

Mujtaba Hussain Jaffery and Jehangir Arshad are co-first authors.

Conflicts of Interest

The authors declare no conflict of interest.

Authors' Contributions

Mujtaba Hussain Jaffery, Muhammad Adil Ashraf, Ahmad Almogren, Hafiza Mahnoor Asim, and Jehangir Arshad contributed to actualization, validation, methodology, formal analysis, investigation, software, and initial draft. Mujtaba Hussain Jaffery, Javed Khan, Ateeq Ur Rehman, and Seada Hussen contributed to actualization, validation, methodology, formal analysis, investigation, and initial draft. All authors read and approved the final version.

Acknowledgments

This work was supported by the King Saud University, Riyadh, Saudi Arabia, through Researchers Supporting Project number RSP-2022/184.

References

[1] World Health Organization, "Physical inactivity a leading cause of disease and disability, warns who. World Health Organization," 2022, https://www.who.int/news/item/04-04-2002-physical-inactivity-a-leading-cause-of-disease-and-disability-warns-who#:~:text=According%20to%20WHO%2C%2060%20to,health%20problems%20of%20our%20time/.

[2] W. Armstrong, J. Borg, M. Krizack et al., *Guidelines on the Provision of Manual Wheelchairs in Less-Resourced Settings*,

World Health Organization, 2008, 2022, https://www.who.int/publications/i/item/9789241547482.

[3] C. N. Kirman, "What is the mortality rate for pressure injuries (pressure ulcers)? Latest medical news, clinical trials," *Guidelines - Today on Medscape*, 2021, 2022, https://www.medscape.com/answers/190115-82434/what-is-the-mortality-rate-for-pressure-injuries-pressure-ulcers.

[4] G. N. Awuku Follow, "Designing a system to prevent pressure ulcers in wheelchair users in ... slideshare," 2018, 2022, https://www.slideshare.net/GodfredAwuku/designing-a-system-to-prevent-pressure-ulcers-in-wheelchair-users-in-ghana.

[5] B. Leblebici, N. Turhan, M. Adam, and M. N. Akman, "Clinical and epidemiologic evaluation of pressure ulcers in patients at a university hospital in Turkey," *Journal of Wound, Ostomy, and Continence Nursing*, vol. 34, no. 4, pp. 407–411, 2007.

[6] W. U. Khan, F. Jameel, X. Li, M. Bilal, and T. A. Tsiftsis, "Joint spectrum and energy optimization of NOMA-enabled small-cell networks with QoS guarantee," *IEEE Transactions on Vehicular Technology*, vol. 70, no. 8, pp. 8337–8342, 2021.

[7] L. Stockton and M. Flynn, "Sitting and pressure ulcers 2: ensuring good posture and other preventive techniques. Nursing times," 2021, 2022, https://www.nursingtimes.net/roles/older-people-nurses-roles/sitting-and-pressure-ulcers-2-ensuring-good-posture-and-other-preventive-techniques-25-06-2009/#:~:text=The%20pelvis%20is%20upright%20and,usually%20at%20a%2090%C2%BA%20angle/.

[8] P. D. Rosero-Montalvo, D. H. Peluffo-Ordóñez, V. F. López Batista, J. Serrano, and E. A. Rosero, "Intelligent system for identification of wheelchair user's posture using machine learning techniques," *In IEEE Sensors Journal*, vol. 19, no. 5, pp. 1936–1942, 2019.

[9] D. Bibbo, M. Carli, S. Conforto, and F. Battisti, "A sitting posture monitoring instrument to assess different levels of cognitive engagement," *Sensors*, vol. 19, no. 3, p. 455, 2019.

[10] J. Ahmad, J. Sidén, and H. Andersson, "A proposal of implementation of sitting posture monitoring system for wheelchair utilizing machine learning methods," *Sensors*, vol. 21, no. 19, p. 6349, 2021.

[11] K. Taunk, S. De, S. Verma, and A. Swetapadma, "A brief review of nearest neighbor algorithm for learning and classification," in *International Conference on Intelligent Computing and Control Systems (ICCS)*, pp. 1255–1260, Madurai, India, 2019.

[12] S. Matuska, M. Paralic, and R. Hudec, "A smart system for sitting posture detection based on force sensors and mobile application," *Mobile Information Systems*, vol. 2020, 13 pages, 2020.

[13] Q. Wan, H. Zhao, J. Li, and P. Xu, "Hip positioning and sitting posture recognition based on human sitting pressure image," *Sensors*, vol. 21, no. 2, p. 426, 2021.

[14] C. Ma, W. Li, R. Gravina, and G. Fortino, "Posture detection based on smart cushion for wheelchair users," *Sensors*, vol. 17, no. 4, p. 719, 2017.

[15] N. Ahad, S. E. Sonenblum, M. A. Davenport, and S. Sprigle, "Validating a wheelchair in-seat activity tracker," *Assistive Technology*, pp. 1–11, 2021.

[16] W. Cun, R. Mo, J. Chu et al., "Sitting posture detection and recognition of aircraft passengers using machine learning," *Artificial Intelligence for Engineering Design, Analysis and Manufacturing*, vol. 35, no. 3, pp. 284–294, 2021.

[17] X. Ran, C. Wang, Y. Xiao, X. Gao, Z. Zhu, and A. Bin Chen, "Portable sitting posture monitoring system based on a pressure sensor array and machine learning," *Sensors and Actuators A: Physical*, vol. 924, article 112900, p. 4247, 2021.

[18] J. Roh, H. J. Park, K. J. Lee, J. Hyeong, S. Kim, and B. Lee, "Sitting posture monitoring system based on a low-cost load cell using machine learning," *Sensors*, vol. 18, no. 2, p. 208, 2018.

[19] P. Patil, K. S. Kumar, N. Gaud, and V. B. Semwal, "Clinical human gait classification: extreme learning machine approach," in *2019 1st international conference on advances in science, engineering and robotics technology (ICASERT). IEEE*, Dhaka, Bangladesh, 2019.

[20] A. Sadun, J. Jalani, and J. A. Sukor, "Force sensing resistor (FSR): a brief overview and the low-cost sensor for active compliance control," *In First International Workshop on Pattern Recognition*, vol. 10011, pp. 222–226, 2016.

[21] W. U. Khan, M. A. Javed, T. N. Nguyen, S. Khan, and B. M. Elhalawany, "Energy-efficient resource allocation for 6G backscatter-enabled NOMA IoV networks," *In IEEE Transactions on Intelligent Transportation Systems*, 2021.

[22] H. Miller, "The art and science of pressure distribution," *Research - Herman Miller*, 2013, 2022, https://www.hermanmiller.com/research/categories/white-papers/the-art-and-science-of-pressure-distribution.

[23] J. Cervantes, F. Garcia-Lamont, L. Rodríguez-Mazahua, and A. Lopez, "A comprehensive survey on support vector machine classification: applications, challenges and trends," *Neurocomputing, Volume*, vol. 408, pp. 189–215, 2020.

[24] W. U. Khan, T. N. Nguyen, F. Jameel et al., "Learning-based resource allocation for backscatter-aided vehicular networks," *IEEE Transactions on Intelligent Transportation Systems*, pp. 1–15, 2021.

[25] D. Weisburd, D. B. Wilson, A. Wooditch, and C. Britt, "Logistic regression," in *In Advanced Statistics in Criminology and Criminal Justice*, pp. 127–185, Springer, Cham, 2022.

[26] S. Liaqat, K. Dashtipour, K. Arshad, K. Assaleh, and N. Ramzan, "A hybrid posture detection framework: integrating machine learning and deep neural networks," *In IEEE Sensors Journal*, vol. 21, no. 7, pp. 9515–9522, 2021.

[27] A. U. Rehman, R. A. Naqvi, A. Rehman, A. Paul, M. T. Sadiq, and D. Hussain, "A Trustworthy SIoT Aware Mechanism as an Enabler for Citizen Services in Smart Cities," *Electronics*, vol. 9, no. 6, p. 918, 2020.

Hindawi
Journal of Sensors
Volume 2022, Article ID 1049535, 11 pages
https://doi.org/10.1155/2022/1049535

Research Article

Design and Optimization of University Management Information System Based on Internet of Things and Intelligent Computing Model

Qin Lei,[1] Yuxi Li,[2] and Shi Yan[3]

[1]*Department of Force Management, Officers College of People's Armed Police, Chengdu 610213, China*
[2]*Business School, Sichuan University, Chengdu 610064, China*
[3]*Modern Educational Technology Center, Mudanjiang Medical University, Mudanjiang 157011, China*

Correspondence should be addressed to Shi Yan; yanshi@mdjmu.edu.cn

Received 14 March 2022; Revised 31 March 2022; Accepted 11 April 2022; Published 30 April 2022

Academic Editor: Han Wang

After the preliminary design of university management information system is completed, the related systems are optimized through IOT and intelligent computing. The data of the system is monitored and trained through IOT. Through the training data, it can be seen that the maximum difference between the actual output and the predicted output data of the Internet of Things is about 4. By calculating the error percentage of the predicted and actual output values, it is found that the maximum error percentage is about 0.0632, and less than 0.1 is a normal error. The IIA model is compared with MQT model, HAMT model, and SAR model in four different function states. Through the analysis of iteration times, it is found that the best value of IIA model is 12 and the average value is 14. Compared with the other three models, the convergence degree is higher, the calculation time is shorter, and the calculation results are more accurate. In order to explore whether the IIA optimization model proposed in this paper can run normally, the performance of the optimization system is tested by dividing the number of users into three groups: 100, 400, and 1000, and testing and analyzing the average response time, peak traffic response time, and test conclusion. According to the data, the average response time of IIA optimization model system is 2.031, 3.211, and 4.421. The average response time of related systems in traditional universities is 3.075, 4.563, and 5.097, respectively, and the test conclusions are all passed. According to the data analysis, it is known that the average response time of IIA optimization system is greatly reduced compared with the traditional system, which shows that this model has a good optimization effect for management information system. Finally, the success rate of IIA optimization model and traditional system is analyzed, which shows that performance is greatly improved after IIA optimization model is optimized. At present, the management information system is of great help to the entry of college students' information. The management information system is used to enter, classify, and manage student information. The design and optimization of the system through IOT technology and intelligent computing-related models are helpful in improving the average response time of the system and improving the data processing capability of the system, which is convenient for register student information.

1. Introduction

Through IOT technology with intelligent computing to design and optimize the university management information system, the design process includes admission, educational administration system, and related units. Through the data monitoring and training to improve the operation speed, through the system test to judge the optimization performance, this paper optimizes the system by proposing the IIA optimization model. After optimizing the IIA model, it analyzes and compares the performance-related data. Compared with other models, the IIA model has the advantage of improving the data computing ability and the success rate. To facilitate and the life of urban residents, IOT and other technologies are combined [1]. Through relevant research to achieve the Internet of Things for the later more convenient to meet people's needs to prepare [2], create and analyze the physical world and the real-time state of

applications. Involve intelligent devices in the work of related enterprises to blur the boundaries between virtual world and real world [3]. In order to explore the connection between the Internet of Things and many fields, we analyze the basic state, application, and characteristics of the Internet of Things and also study and analyze the sensor network structure which is related to the Internet of Things. Through a series of analysis, this paper makes analysis and planning suggestions for the related applications of the Internet of Things in order to maximize the use value of the Internet of Things [4]. The concept that the Internet of Things is a belated communication world view is obtained [5]. Through the research and analysis of intelligent computing, we can see that it plays an important role in medical planning, diagnosis, and treatment. Combining ICM algorithm with GA, ANN, FL, and other algorithms, a study illustrates the role of intelligent computing in the medical field. Through the combination of KBS and ICM methods, RBR-ANN and other algorithms are obtained. Therefore, it is concluded that this method is helpful to the development of medical field and novice researchers in most medical diagnosis [6]. The uncertainty of receiver position plays an important role in passive source location. In this paper, the joint location estimation model is introduced to analyze the location accuracy reduction caused by the uncertainty of receiver position. The calculation results show that this method is more accurate than other methods when the TDOA calculation error is large [7]. In this paper, the potential physical meaning and domain of tanh function and sigmoid function are studied and analyzed. Through correlation analysis, we know that ANN such as tanh function and sigmoid function cannot be deduced accurately in the range of data used for model calibration. Attribute recording and statistical verification for different data subsets [8]. Through the research of cable induction and LWD tools, the concept of inductive resistivity equipment is studied. This paper explores the potential benefits of electromagnetic dipoles by analyzing related models and finds that the research results are similar to those of previous studies by analyzing mandrel, borehole, and intrusion effects [9]. Combining GA model with initial model and optimizing parameters, the following conclusions can be obtained, which can be carried out without knowing any prior knowledge. Through the research, it is found that this method greatly optimizes the random and subjective problems of traditional methods. This experiment also lays a theoretical foundation for the next large-scale application [10]. An interaction model between rational and selfish agents for coding is called DAG model. Two models are used to deal with the problems encountered in modeling calculation in real life to design and show interesting modeling cases. At the same time, the two methods proposed in this paper are verified, and the results show that the results obtained by this model are novel [11]. The research goal is to improve enterprise information system and realize the new management mode to break through the development direction of enterprises to e-commerce. The updated enterprise information system can improve the accuracy of information, thus improving the cooperation satisfaction between customers and employees [12]. In this paper, IT technology is very useful in the knowledge, information, and other aspects of promotion. The improvement of university system under IT technology the improvement of multimedia technology is carried out in the fields of library service, teacher activities, and administration. In order to maximize the potential and utility of IT technology under the goal of system reform [13], this paper explains the information system through a series of studies. According to the research results, the successful operation of information system is supported by many fields such as data accessibility, reliability, consistency, and relevance. In order to understand the defects of the information system, 863 interviewees were investigated to improve the defects faced by the information system and related management problems [14]. In order to model the system design and optimization, and to minimize the variance of reliability estimation in the modeling process, four different models are used to demonstrate. The design problem is solved by four model designs, and the correlation is also considered [15].

2. Design of University Management Information System

2.1. IoT Structure. The structure of the Internet of Things includes three aspects: platform layer, transport layer, and physical layer [16]. The security problems faced by the platform layer are system failures and virus attacks, and the technical solution is to verify relevant identity information [17]. Transport layer security issues include network theft and data theft, and the related solution to its technology is to encrypt and protect the transmitted information through related keys to prevent information leakage. The security problems faced by the physical layer include the security problems of devices and terminals, and the technical solutions include physical protection and access control [18] as shown in Figure 1.

2.2. Process of University Management Information System. The design of university management information is as follows. The design of university management information includes the admission of university students, and the admission information includes basic information, admission management, and accommodation management to report student-related information [19]. Information management for students in school includes student status management, related files, semester registration, student status change, and graduation processing. Financial assistance for poor students' enrollment includes student aid processing, poverty subsidies, and student loans [20]. The educational administration system needs to manage the relevant student status information. For the employment management of graduates, it can efficiently manage the graduates' leaving school by analyzing and summarizing the employment intentions of relevant units [21] as shown in Figure 2.

For admission, you need to enter student information, colleges, departments, accommodation management, and other information.

The educational administration system includes registering the student's file status information.

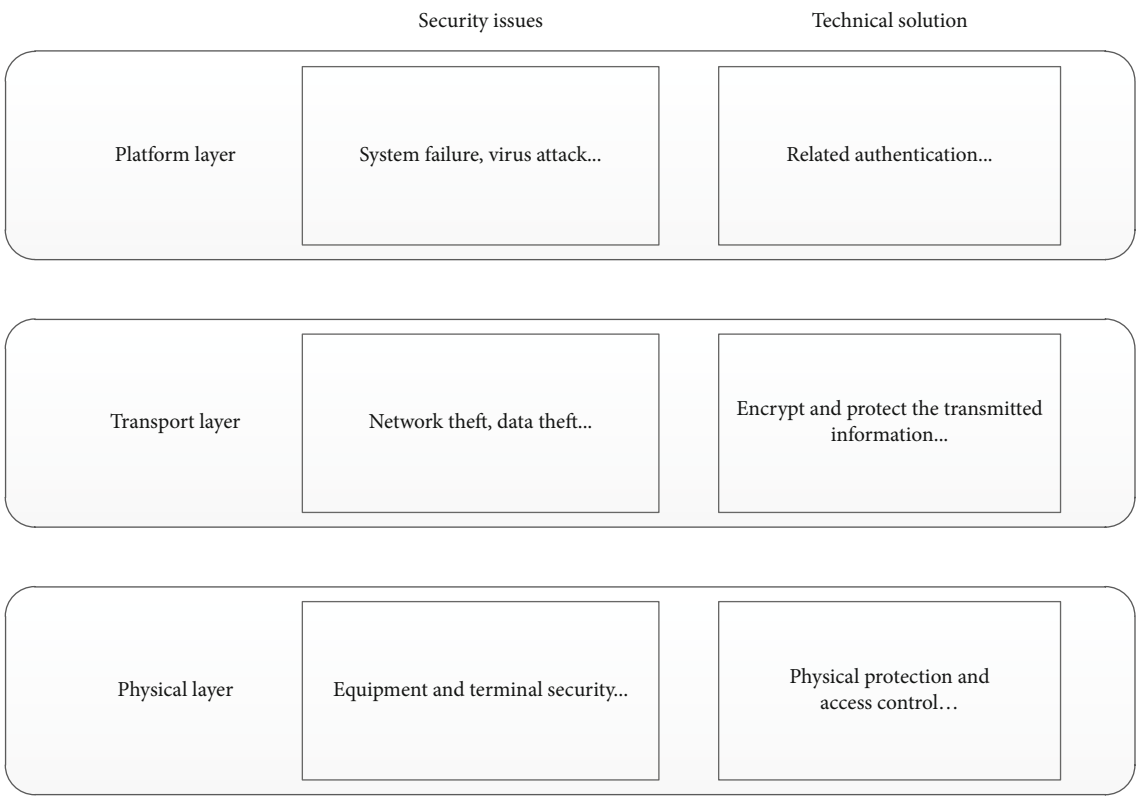

Figure 1: Internet of Things structure.

Relevant units mainly provide consultation on graduate employment issues.

3. Correlation Formula

3.1. IoT Algorithm Definition

3.1.1. Establish. The range of D is $[1, n-1]$.

Admin stands for administrator; Fog stands for Fog Computing; Device stands for a sensing device.d is a random number key.

$$\mathrm{PK}_{\mathrm{Admin}} = \{d_{\mathrm{Admin}}G, E, G, n\}, \mathrm{PS}_{\mathrm{Admin}} = \{d_{\mathrm{Admin}}\}, \tag{1}$$

$$\mathrm{PK}_{\mathrm{Fog}} = \{d_{\mathrm{Fog}}G, E, G, n\}, \mathrm{PS}_{\mathrm{Fog}} = \{d_{\mathrm{Fog}}\}, \tag{2}$$

$$\mathrm{PK}_{\mathrm{Device}} = \{d_{\mathrm{Device}}G, E, G, n\}, \mathrm{PS}_{\mathrm{Device}} = \{d_{\mathrm{Device}}\}, \tag{3}$$

$$M(x, y) = \begin{cases} x = Q * K_{ID_p} + j, \text{Q is a large integer}, 0 \le j \le Q \\ y^2 \equiv (x^3 + ax + b) \bmod p, \text{Take } y \text{ with smaller } K_{\mathrm{ID}_p} \text{ offset} \end{cases}, \tag{4}$$

$$\mathrm{EK}_{\mathrm{ID}_p} = \mathrm{Enc}_{\mathrm{PK}_{\mathrm{Fog}}}(M) = (\mathrm{rG}, \mathrm{M} + \mathrm{rPK}_{\mathrm{Fog}}) = (rG, M + rd_{\mathrm{Fog}}G). \tag{5}$$

3.1.2. Certification Stage.

$$\begin{aligned} M(x, y) &= Dec_{\mathrm{PS}_{\mathrm{Fog}}}\left(\mathrm{EK}_{\mathrm{ID}_p}\right) = \mathrm{Dec}_{\mathrm{PS}_{\mathrm{Fog}}}(\mathrm{rG}, M + \mathrm{rPK}_{\mathrm{Fog}}) \\ &= (M + \mathrm{rd}_{\mathrm{Fog}}G) - d_{\mathrm{Fog}}(\mathrm{rG}) = M(x, y), \end{aligned} \tag{6}$$

$$K_{ID_p} = |x/Q|, |x/Q| \text{ is the largest integer less than or equal to } x/Q, \tag{7}$$

$$r_1 = x_1 P \bmod n, \tag{8}$$

$$\begin{aligned} s_1 &= k_1^{-1}(H(\mathrm{Token}_{\mathrm{Device1}}) + r_1 \mathrm{PS}_{\mathrm{Device1}}) \bmod n \\ &= k_1^{-1}(H(\mathrm{Token}_{\mathrm{Device1}}) + r_1 d_{\mathrm{Device1}}) \bmod n, \end{aligned} \tag{9}$$

$$\begin{aligned} P' &= U_1 G + U_2 \mathrm{PK}_{\mathrm{Device1}} = U_1 G + U_2 d_{\mathrm{Device1}} G \\ &= \left(s_1^{-1} H(\mathrm{Token}_{\mathrm{Device1}}) + s_1^{-1} r_1 d_{\mathrm{Device1}}\right) G \\ &= s_1^{-1}(H(\mathrm{Token}_{\mathrm{Device1}}) + r_1 d_{\mathrm{Device1}}) G. \end{aligned} \tag{10}$$

If $P = P'$, the verification is successful:

$$P = k_1 G = s_1^{-1}(H(\mathrm{Token}_{\mathrm{Device1}}) + r_1 d_{\mathrm{Device1}}) G \bmod n = P'. \tag{11}$$

3.2. Intelligent Computing

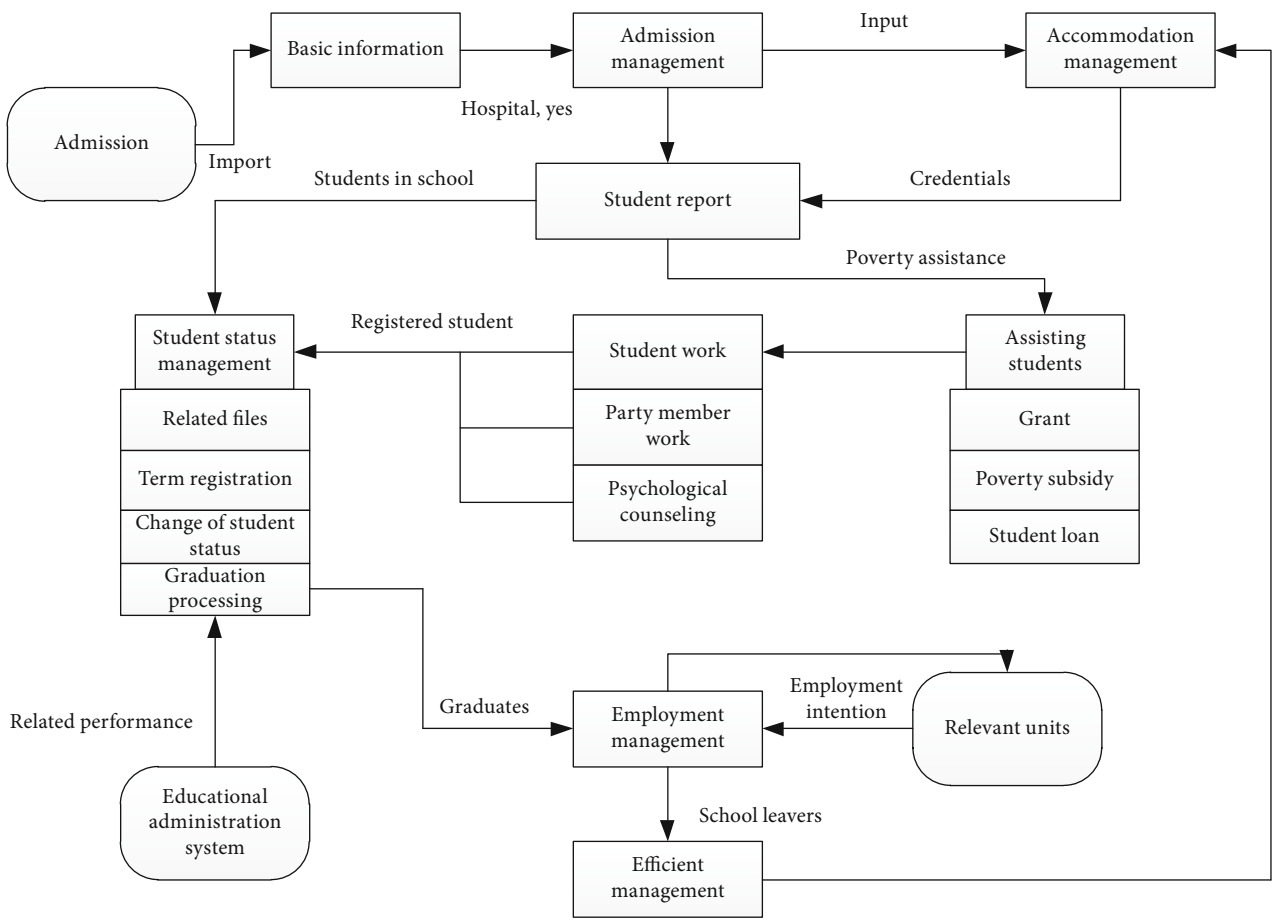

Figure 2: Design of efficient management information system.

3.2.1. Bayesian Optimization.

$$X^* = \arg\ \max_{x \subseteq X \subseteq R^d} f(x), \tag{12}$$

where x is the decision variable of d dimension [22].

$$p(f \mid D_{1:t}) = \frac{p(D_{1:t} \mid f)p(f)}{p(D_{1:t})} \tag{13}$$

Bayesian optimization theorem [23] is a method to search for the global extremum of function in random process and probability space.

3.2.2. Probability Formula.

$$\begin{aligned} f(X) &\sim N\left(m(X), K\left(X, X^T\right)\right), \\ m(X) &= E(f(X)), \\ K\left(X, X^T\right) &= E\left(\left(f(X) - m(X)\right)\left(f(X) - m(X)\right)^T\right). \end{aligned} \tag{14}$$

Covariance matrix K.

$$p(f \mid X, \theta) = N(0, \Sigma), \tag{15}$$

$$p(y \mid f) = N\left(f, \sigma^2 I\right), \tag{16}$$

$$p(y \mid X, \theta) = \int p(y \mid f) p(f \mid X, \theta) df = N\left(0, \sum + \sigma^2 I\right). \tag{17}$$

The Gaussian process is shown in

$$\begin{bmatrix} y \\ f^* \end{bmatrix} \sim N\left(0, \begin{bmatrix} \sum + \sigma^2 I & K_* \\ K_*^T & K_{**} \end{bmatrix}\right). \tag{18}$$

3.3. System Design and Optimization

3.3.1. Regression Analysis.

$$y = a + bx, \tag{19}$$

$$y_i = a + bx_i + \varepsilon_i\ \varepsilon_i \sim N\left(0, \delta^2\right), \tag{20}$$

$$y_k = a + \sum_{i=1}^{m} b_i x_{ik} + \varepsilon_k k = 1, 2, \cdots, n, \tag{21}$$

where M is m independent variables.

3.3.2. System Test.

$$C = \frac{nL}{T}. \tag{22}$$

The time of performance test [24] is expressed by Formula (23) and Formula (24).

$$F = \frac{N_{vu} \times R}{T}, \tag{23}$$

$$R = \frac{T}{T_s}. \tag{24}$$

User thinking time is expressed by Formula (24).

$$Z = \sqrt{p + t} + k. \tag{25}$$

4. Design and Optimization of Management Information

4.1. Data Monitoring in Internet of Things

4.1.1. Data Training. Through the data training in the data monitoring under the related IOT, train the data multiple times, and the training results as shown in the figure are obtained. When the training times range from 0 to 16 times, the training variance results is 104 at first, and when the training times reach 4 times, the mean square error drops to about 3.4364, and when the training times reach 16 times, the mean square error is about 3.4364. Through the relevant data training test, it can be seen that the best training result is about 3.4364 mean square error, and when the training times exceed four times, the training result reaches the best training result. Through data investigation and test, we can see that the mean square error of the target is about 10-2, and there is a big difference between the training results. We should constantly train the data, so as to select the appropriate test times according to the training results to improve the data monitoring under IOT technology and realize the high efficiency of the university management information system. Improve the accuracy and applicability of the system through continuous training [25] as shown in Figure 3.

4.1.2. Sample Data Comparison. By comparing and analyzing the training results of 30 groups of data tested by the management information system under IOT, the training effect under IOT can be obtained by comparing the predicted value with the actual value. Through chart analysis, it can be seen that in 30 groups of sample groups, the trend of actual output data and predicted output data is not much different. When the number of samples is 5 groups, the predicted output value is 69.833, and the actual output value is 71.229, and the comparison results are not much different. When the sample number is 10, the actual output value is 71.566, the predicted output value is 74.995, and the maximum difference value in 30 sample groups is controlled within 5. When the number of groups is 20, the actual output value is closest to the predicted output value. Through images and data, we can see that the training advantages of university management information system data under IOT are more prominent, which is basically consistent with reality, as shown in Figure 4.

Through the analysis of the error percentage between the actual output and the predicted output value, we can see that the error percentage value is small in 30 groups of data through the trend of line chart image, which shows that the detection value is more accurate. In 0-5 groups, the highest error percentage is -0. 0231, the lowest is -0. 0227, and the numerical error percentage is relatively small. In 5-10 groups, the maximum error percentage is 0.0372 in 10 groups, and the error less than 0.1 is small. The highest error percentage in 10-15 groups is 0.0172. Among 15-20 groups of data, the maximum error value of 18 groups of data is 0.0632, which is the largest group in the whole group but still less than 0.1. The average error percentage of 20-25 groups is about 0.0031, which can be ignored. The highest error percentage in 25-30 groups is 0.0279. Through the analysis of the chart, it can be seen that the error percentage values are small; it shows that the difference between the actual value and the predicted value is small; and the value is more accurate. Therefore, the Internet of Things technology is feasible for data monitoring of university management information. Through this test, the numerical difference between the actual value and the predicted value can be reduced to provide a better performance university management information system as shown in Figure 5.

The relevant system data is monitored and trained through the Internet of Things, and relevant conclusions are drawn through the analysis of the sample data and the error percentage. The Internet of Things can improve the calculation speed of the system data and improve the calculation accuracy. Therefore, IOT can improve the optimization of system data.

4.2. Intelligent Computing Information Management System Model of Colleges and Universities

4.2.1. Comparison of Optimization Structures of Different Models. Through the four different models in four different function states for the best value and average value of comparative analysis, under the condition of F1 function, the best value and average value of IIA model are the lowest, which shows that the global ability of IIA model is better. The optimum value of IIA model is 6.1503, and the average value is 20.0537 in F2 function state. The optimum value and average value of IIA model in F3 function state are 0 and -4.0532, respectively; the optimum value of IIA model in F4 function state is 0, and the average value is 0.573. Compared with MQT model, HAMT model, and SAR model, the optimal value and average value of IIA model are analyzed by relevant numerical analysis, and the optimization ability of IIA model is higher, so it should be preferred for university management system under intelligent computing as shown in Table 1.

By comparing the average optimal values of IIA model, MQT model, HAMT model, and SAR model in F1-F4 states, we can see that the average value of IIA model is lower, the

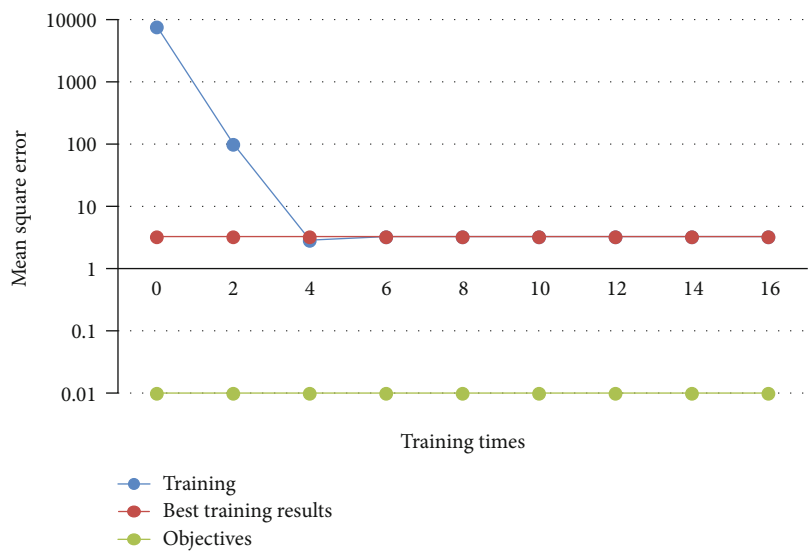

Figure 3: Data training.

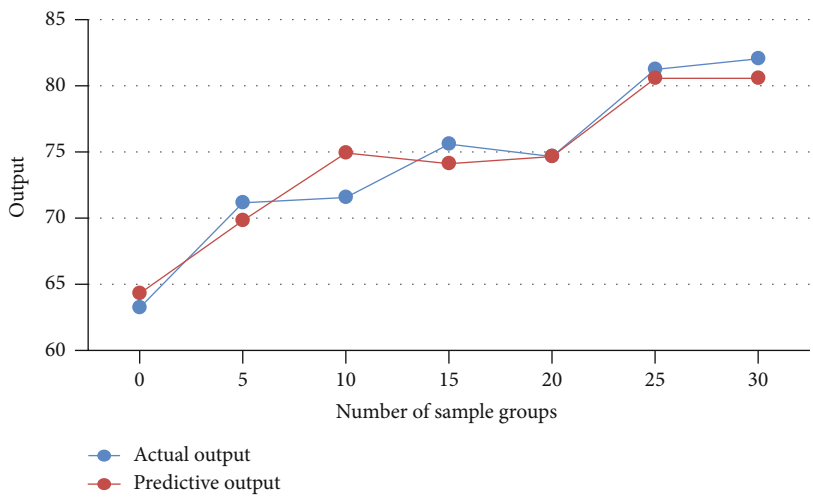

Figure 4: Comparison of sample data.

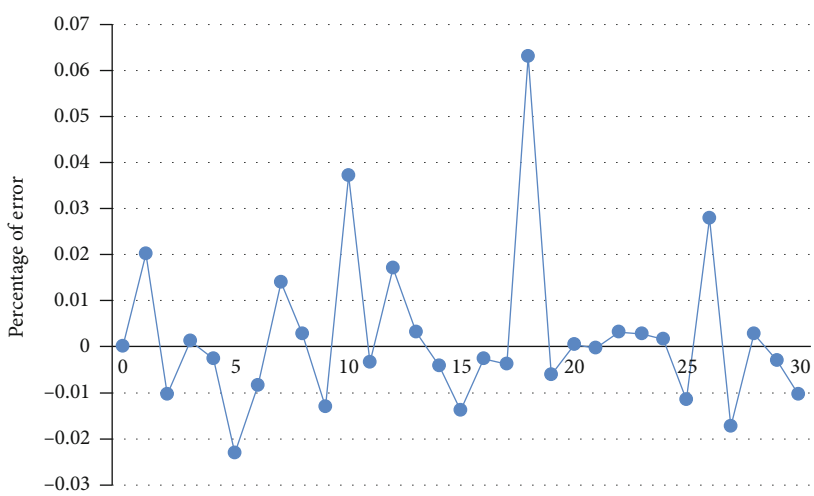

Figure 5: Error percentage analysis.

Table 1: Comparison of optimized structures.

Function	IIA		MQT		HAMT		SAR	
	Optimum value	Average	Optimum value	Average	Optimum value	Average	Optimum value	Average
F1	0	0	0	-2.8731	0	1.0187	17.1148	7.625
F2	6.1503	20.0537	-1.92	17.631	-0.0093	5.842	-0.9003	13.532
F3	0	-4.0532	0	4.875	-0.2738	1.4327	4.2816	10.007
F4	0	0.573	1.257	0.793	2.574	0.535	0.552	0.983

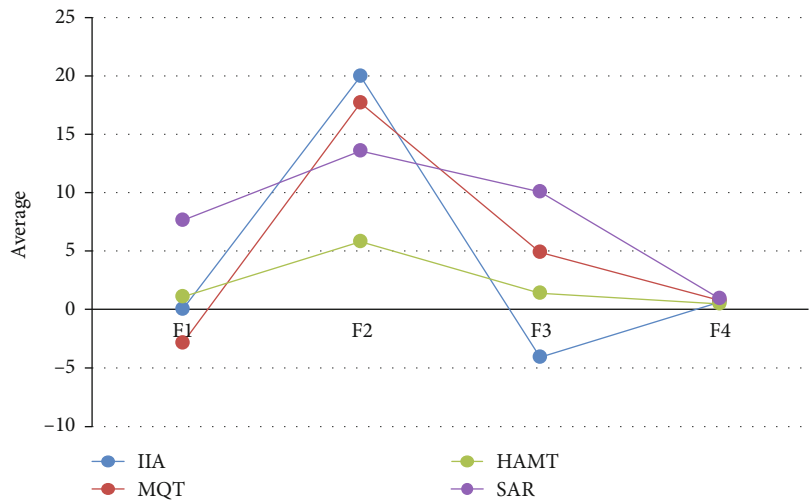

Figure 6: Comparison of model optimization average value.

Table 2: Comparison of iteration times.

Function	IIA		MQT		HAMT		SAR	
	Optimum value	Average	Optimum value	Average	Optimum value	Average	Optimum value	Average
F1	12	14	24	57	40	93	60	95
F2	14	47	19	93	80	96	33	56
F3	51	60	28	81	100	100	100	100
F4	46	51	100	100	100	100	100	100

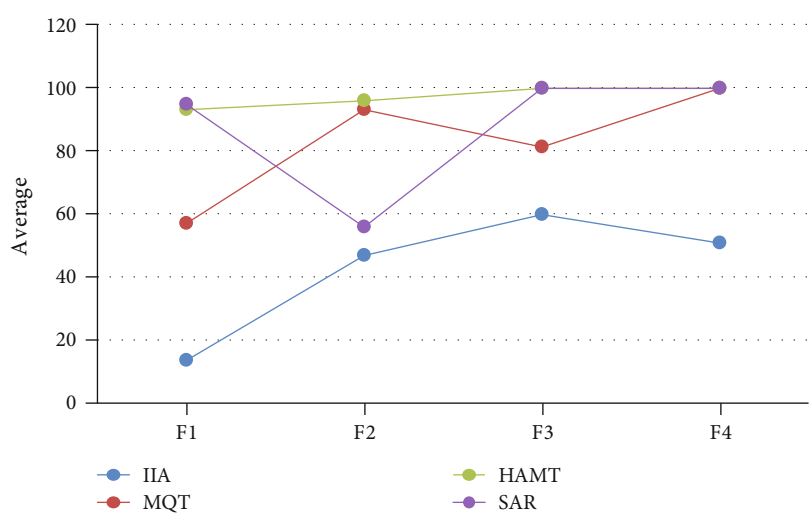

Figure 7: Comparison of average iteration times.

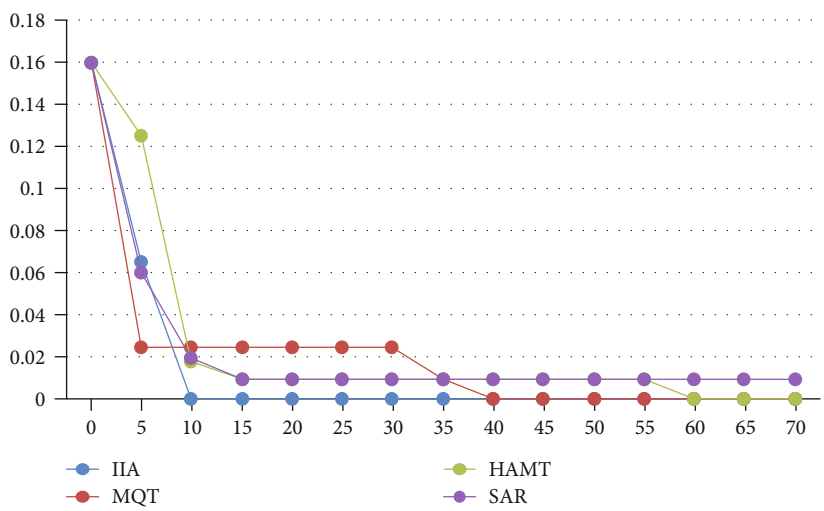

Figure 8: Convergence curve analysis.

Table 3: Blockchain test.

Number of users	Average response time	Corresponding time of peak flow	Test conclusion
100	0.965	1.098	Pass
400	1.374	1.895	Pass
1000	2.209	2.873	Pass

Table 4: IIA model testing.

Number of users	Average response time	Corresponding time of peak flow	Test conclusion
100	2.031	2.213	Pass
400	3.211	3.401	Pass
1000	4.421	4.765	Pass

Table 5: Traditional system testing.

Number of users	Average response time	Corresponding time of peak flow	Test conclusion
100	3.075	3.231	Pass
400	4.563	4.771	Pass
1000	5.097	5.192	Pass

accuracy is more accurate, the independence is better, the calculation time is shorter, and the accuracy is higher in F1, F3, and F4 states, so IIA optimization model should be preferred as shown in Figure 6.

4.2.2. Comparison of Iteration Times of Different Methods. By analyzing the iteration times of IIA model, MQT model, HAMT model, and SAR model in four different function states, the best value of IIA model is 12, and the average value is 14 in F1 function state, which is the lowest in comparison, while the best value of SAR model is 60, and the average value is 95, which is the highest among the four models. The optimum value and average value of IIA model are the lowest in the state of function F2-F4, which shows that the number of iterations is less, the operation time is lower, and the operation stability is better as shown in Table 2.

The average value of IIA model is lower, the lowest is 14, and the highest is 60. The highest average value of MQT model is 100, and the lowest is 57. The highest average value of SAR model is 100, and the lowest is 56. Through the numerical analysis of the mean value, we can see that the IIA model has the lowest mean value, the least iteration times, the shorter operation time, and the higher accuracy and is superior to the other three models in convergence degree as shown in Figure 7.

Comparing the models through the number of iterations, the data related to the IIA model is better in comparison, indicating that the convergence of the IIA model is better in comparison, so the IIA model has excellent optimization for the management information system of colleges and universities.

4.2.3. Convergence Curve Analysis. The convergence curve shows that the convergence of IIA model is very fast, about 10 generations of convergence, MQT model about 40 generations of convergence, and HAMT model about 60 generations of convergence, and SAR model convergence is poor. The convergence of the four models from high to low is IIA model, MQT model, HAMT model, and finally SAR model. The convergence of IIA model is the fastest compared with other models, so IIA model should be preferentially selected to optimize the system under intelligent computing and improve the system performance and computing ability as shown in Figure 8.

4.3. Performance Test of System Optimization Model. The university management information system under IIA model is compared with the system under blockchain and traditional management information system to test optimized system model.

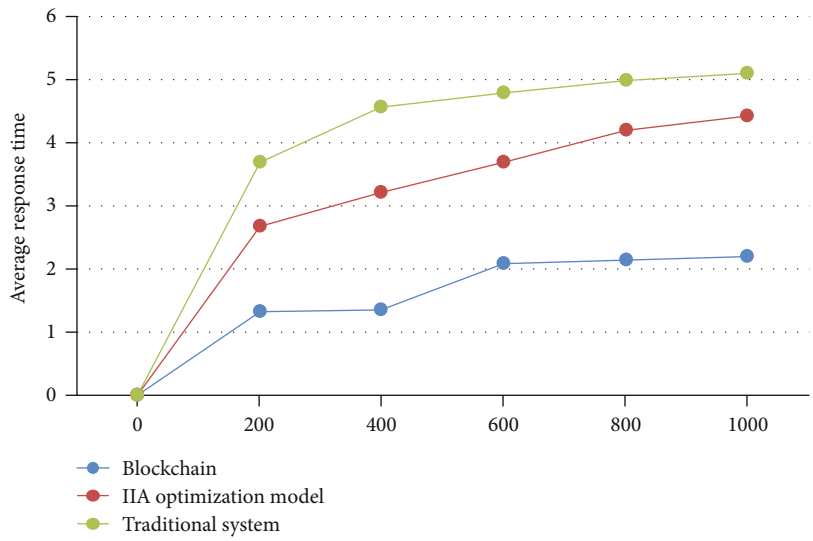

Figure 9: Average response time analysis.

Table 6: Performance comparison.

System	Number of query requests	1000	1500	2000	2500	3000	3500	4000
Blockchain	Mean response time (MS)	20	32	53	87	120	198	255
	Success rate (%)	100	100	100	100	100	100	100
IIA optimization model	Mean response time (MS)	27	42	63	105	144	208	298
	Success rate (%)	100	99.7	99.62	99.5	99.44	98.79	99.25
Traditional system	Mean response time (MS)	35	62	87	176	263	321	397
	Success rate (%)	100	99.43	99.25	99.1	98.7	99.1	99

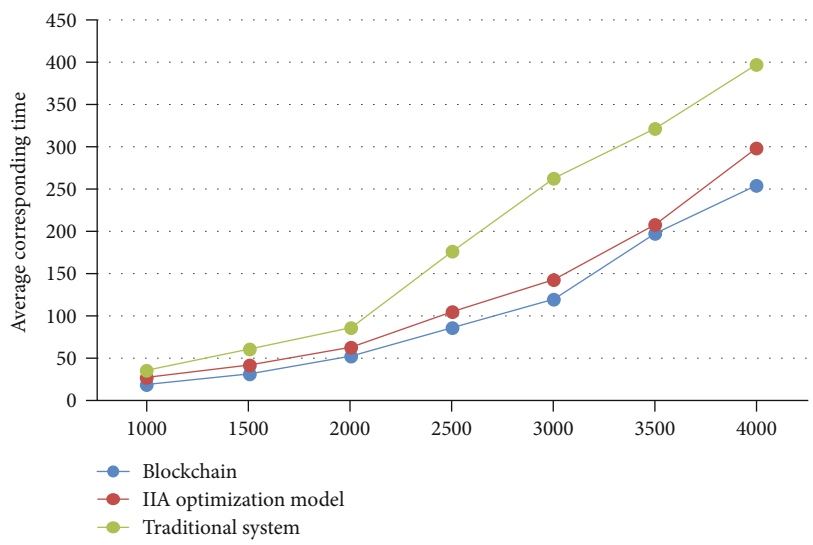

Figure 10: Average response time comparison.

4.3.1. Test of University Management Information Blockchain. Through the research and test, the test conclusions are all passed, and the response time of peak traffic is slightly higher than the average response time. When the number of users is 100, 400, and 1000, the average response time is 0.965, 1.374, and 2.209, respectively, which is faster as shown in Table 3.

4.3.2. IIA Optimization Model System Test under IOT and Intelligent Computing. IIA optimizes the system model

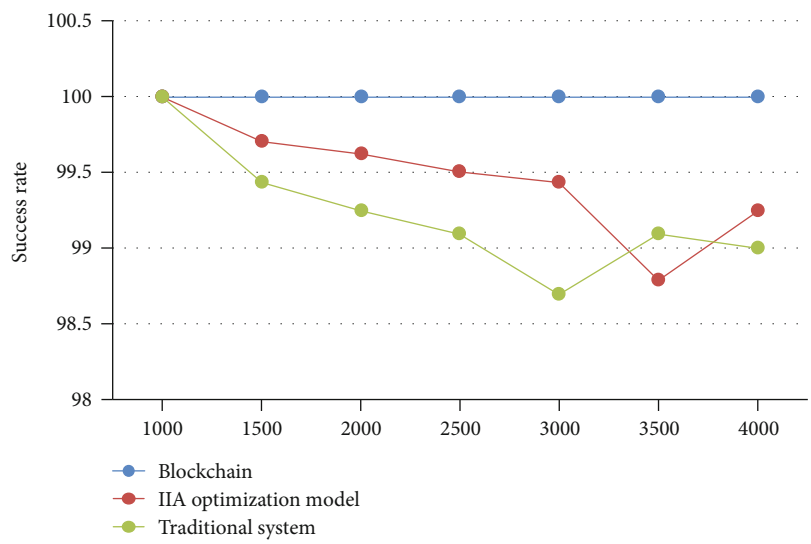

Figure 11: Success ratio comparison.

under IOT and intelligent computing to detect three groups of experiments with 100, 400, and 1000 users, respectively, and the detection conclusions are all passed, with average response times of 2.031, 3.211, and 4.421, respectively, which are higher than those in blockchain scenarios as shown in Table 4.

4.3.3. Testing of Traditional Information Management System. Three groups of data with 100, 400, and 1000 users are tested under the traditional university management information system, and the test conclusions are all passed. The average response time is 3.231 when the number of users is 100, 4.563 when the number of users is 400, and 5.097 when the number of users is 1000 as shown in Table 5.

By comparing and analyzing the average response time of university management information systems under blockchain environment, IIA optimization model, and traditional system, it can be seen from the image that the average response time of the system under IIA optimization model is slightly higher than that under blockchain environment, but it is greatly improved compared with the traditional system, which shows that IIA model under IOT and intelligent computing has obvious advantages for system optimization, which improves the average response time of the system and optimizes the system performance as shown in Figure 9.

According to the analysis of relevant data, the average response time under IIA optimization model is slightly higher than that under blockchain. The success rate is relatively low, but compared with the traditional university management information system, IIA model has greatly shortened the average response time and greatly improved the success rate. Compared with the traditional system, IIA model has better optimization ability, so IIA model has higher optimization ability for university management information system as shown in Table 6.

By comparing and analyzing the average response time and success rate of blockchain, IIA optimization model, and traditional systems, the average response time and success rate of IIA optimization model are slightly lower than those of blockchain, but the overall performance is better than that of traditional systems. Therefore, through relevant system testing, the IIA model has an optimization effect on system analysis.

The average response time of IIA model is obviously lower than that of traditional system through the query times of 1000, 1500, 2000, 2500, 3000, 3500, and 4000, so IIA model has strong optimization ability for this system and has passed the system optimization test as shown in Figure 10.

Through the analysis of the success rate in three states, we know that the success rate of IIA model is higher than that of traditional system, so IIA model also plays an optimization ability in the success rate, and improves the optimization ability and efficiency of management information system as shown in Figure 11.

5. Conclusion

In order to design and optimize the management information system, the combination of IOT technology and intelligent computing model is adopted. Through IOT technology data training and sample data research and comparison, as well as error percentage analysis, IOT technology for university management information system data detection has a significant, obvious positive effect. Through the analysis of relevant data, we can see that the data error percentage under the Internet of Things technology is small, which shows that the technology has high accuracy and high efficiency. Through the comparison of IIA optimization model with MQT model, HAMT model, and SAR model in four different states, IIA model has the best advantage in operation time and efficiency. Finally, the IIA optimization model is tested to judge whether the optimization system can run normally. Through the test conclusion, we can see that the test of the system is through, but through the average response time and success rate of data analysis, we can see

that IIA model has more advantages than the traditional system, which shows that IIA model has a good optimization ability for university management information system. Through the relevant performance tests, it is known that the IIA model proposed in this paper passes the performance tests and has good optimization ability. Therefore, for the management information system, the Internet of Things, intelligent computing, and IIA model should be combined to design and optimize the system to improve the computing and processing capabilities of the management information system.

Data Availability

The experimental data used to support the findings of this study are available from the corresponding author upon request.

Conflicts of Interest

The authors declared that they have no conflicts of interest regarding this work.

References

[1] A. Zanella, N. Bui, A. Castellani, L. Vangelista, and M. Zorzi, "Internet of things for smart cities [J]," *IEEE Internet of Things Journal*, vol. 1, no. 1, pp. 22–32, 2014.

[2] A. Al-Fuqaha, M. Guizani, M. Mohammadi, M. Aledhari, and M. Ayyash, "Internet of things: a survey on enabling technologies, protocols, and Applications," *IEEE Communication Surveys and Tutorials*, vol. 17, no. 4, pp. 2347–2376, 2015.

[3] D. Guinard, V. Trifa, S. Karnouskos, P. Spiess, and D. Savio, "Interacting with the SOA-based internet of things: discovery, query, selection, and on-demand provisioning of web services[J]," *IEEE Transactions on Services Computing*, vol. 3, no. 3, pp. 223–235, 2010.

[4] Q. B. Sun, J. Liu, S. Li, C. X. Fan, and J. J. Sun, "Internet of things: summarize on concepts, architecture and key technology problem[J]," *Journal of Beijing University of Posts and Telecommunications*, vol. 33, no. 3, pp. 1–9, 2010.

[5] S. Li, L. D. Xu, and S. Zhao, "The internet of things: a survey," *Information Systems Frontiers*, vol. 17, no. 2, pp. 243–259, 2015.

[6] B. Pandey and R. B. Mishra, "Knowledge and intelligent computing system in medicine," *Computers in Biology and Medicine*, vol. 39, no. 3, pp. 215–230, 2009.

[7] D. S. Huang, K. H. Jo, H. H. Lee, H. J. Kang, and V. Bevilacqua, "Emerging intelligent computing technology and applications. With aspects of artificial intelligence[J]," *Lecture Notes in Computer Science*, vol. 7390, no. 4, pp. 953-954, 2009.

[8] M. A. Shahin, "Intelligent computing for modeling axial capacity of pile foundations[J]," *Canadian Geotechnical Journal*, vol. 47, no. 2, pp. 230–243, 2010.

[9] L. Sheremetov, M. Alvarado, R. Bañares-Alcántara, F. Aminzadeh, and G. A. Mansoori, "Intelligent computing in petroleum engineering," *Journal of Petroleum Science & Engineering*, vol. 47, no. 1-2, pp. 1–3, 2005.

[10] Y. Yuan, M. Li, and L. Li, "Algorithm of fertilization model based on intelligent computing[J]," *Transactions of the Chinese Society of Agricultural Engineering*, vol. 24, no. 12, pp. 116–119, 2008.

[11] E. M. Tadjouddine, "Computational complexity of some intelligent computing systems[J]," *International Journal of Intelligent Computing & Cybernetics*, vol. 4, no. 2, pp. 144–159, 2011.

[12] W. U. Min, X. Q. Liu, and J. X. Chen, "Web services based university management information system integrated architecture[J]," *Journal of Donghua University,Natural Science*, vol. 30, no. 1, pp. 28–32, 2004.

[13] S. G. George, "Multimedia computer utility framework intervention for Moi University management information system[J]," *Campus-Wide Information Systems*, vol. 19, no. 2, pp. 59–66, 2002.

[14] R. Marcella and K. Knox, "Systems for the management of information in a university context: an investigation of user need," *Information systems, Universities, Information strategy[J]. Information Research An International Electronic Journal*, vol. 9, no. 2, 2004.

[15] N. Wattanapongskorn and D. W. Coit, "Fault-tolerant embedded system design and optimization considering reliability estimation uncertainty[J]," *Reliability Engineering & System Safety*, vol. 92, no. 4, pp. 395–407, 2007.

[16] K. M. Huseynova, "Development of university management information systems[J]," *International Journal of Sports Medicine*, vol. 29, no. 12, pp. 987–993, 2002.

[17] N. Gershenfeld, R. Krikorian, and D. Cohen, "The internet of things[J]," *Scientific American*, vol. 291, no. 4, pp. 76–81, 2004.

[18] F. Chen, P. Deng, J. Wan, D. Zhang, A. V. Vasilakos, and X. Rong, "Data mining for the Internet of things: literature review and Challenges," *International Journal of Distributed Sensor Networks*, vol. 11, 431014 pages, 2015.

[19] C. Perera, A. Zaslavsky, P. Christen, and D. Georgakopoulos, "Context aware computing for the internet of things: a survey[J]," *IEEE Communication Surveys and Tutorials*, vol. 16, no. 1, pp. 414–454, 2014.

[20] G. Kortuem, F. Kawsar, and D. Fitton, "Smart objects as building blocks for the Internet of things," *IEEE Internet Computing*, vol. 14, no. 1, pp. 44–51, 2010.

[21] R. H. Weber, "Internet of things – new security and privacy challenges[J]," *Computer Law & Security Review the International Journal of Technology & Practice*, vol. 26, no. 1, pp. 23–30, 2010.

[22] H. Zhao, K. Min, and B. Luo, "Intelligent computing in signal processing and pattern recognition. International conference on intelligent computing, ICIC 2006, Kunming, China, August 16–19, 2006[J]," *Lecture Notes in Control and Information Sciences*, vol. 5855, no. 2, pp. 95–99, 2006.

[23] M. Alvarado, L. Sheremetov, R. Bañares-Alcántara, and F. Cantú-Ortiz, "Current challenges and trends in intelligent computing and knowledge management in industry," *Knowledge and Information Systems*, vol. 12, no. 2, pp. 117–127, 2007.

[24] N. N. El-Emam and R. H. Al-Rabeh, "An intelligent computing technique for fluid flow problems using hybrid adaptive neural network and genetic algorithm[J]," *Applied Soft Computing Journal*, vol. 11, no. 4, pp. 3283–3296, 2011.

[25] P. Zhang and L. Na, "An assessment of human–computer interaction research in management information systems: topics and methods[J]," *Computers in Human Behavior*, vol. 20, no. 2, pp. 125–147, 2004.

Hindawi
Journal of Sensors
Volume 2022, Article ID 6283481, 12 pages
https://doi.org/10.1155/2022/6283481

Research Article

Influence and Effectiveness Analysis of Urban Community Planning on Children's Play Environment Based on Artificial Intelligence

Tianzhu Zheng[1] **and Haifang Qin**[2]

[1]*School of Preschool Education, Qiongtai Normal University, Haikou 571100, China*
[2]*School of Electronics Engineering and Computer Science, Peking University, Beijing 100871, China*

Correspondence should be addressed to Tianzhu Zheng; tianzhuzheng@mail.qtnu.edu.cn

Received 25 February 2022; Revised 24 March 2022; Accepted 4 April 2022; Published 30 April 2022

Academic Editor: Han Wang

With the development of the times, the progress of science and technology, and the growing needs of people, more and more urban community planning chooses artificial intelligence to replace the traditional urban community planning, at the same time, it also brings new influences and changes to children's play environment. Firstly, GA, BP, and GA-BP algorithms are explained, and IGA-BP algorithm is proposed. Secondly, the planning and allocation schemes of different communities in children's environment are planned, and genetic algorithm and BP neural network are used to plan and apply children's play environment in urban communities. Finally, the experiment compares and predicts the optimal path of the above three algorithms, and the results show that IGA-BP algorithm can wait for the optimal path. Then, GA-BP and IGA-BP algorithms were used to compare the heat of children's community and other related indicators. IGA-BP algorithm has obvious advantages in heat prediction, absolute error, and relative error.

1. Introduction

Artificial intelligence will promote the development of various technologies and create new impetus for economic transformation. By promoting the development of artificial intelligence, it can promote technological breakthroughs in many fields. Of course, it brings us not only the macrolevel but also has slowly entered our lives. Concern and thinking about urban problems have promoted modern urban planning, and the combination of the two is an inevitable trend. The combination of the two makes our urban planning more modern and scientific. Artificial intelligence is becoming more and more popular and is used to solve various problems in different fields as an alternative to traditional technologies or as a component of integrated systems. This technology has fault tolerance and flexibility in solving problems and has the possibility of continuous progress [1]. At present, this technology has been applied to many technical fields to solve many complex problems. Decision-making made by artificial intelligence is related to reasoning, so it is inevitable to understand the relationship between artificial intelligence and decision-making. This paper distinguishes two aspects of decision-making [2]. On the one hand, artificial intelligence has many relationships with diagnosis. On the other hand, artificial intelligence pays insufficient attention to prospective reasoning due to uncertainty and preference. With the continuous development of artificial intelligence technology, it is more widely used in cities, such as transportation. Technology not only brings new choices and experiences but also makes people aware of the problem of information security. Nevertheless, with the support of artificial intelligence technology, urban planning will be upgraded more widely in the future. This paper reviews the development process of urban model under the application of artificial intelligence and also introduces the artificial life computer model [3]. Some features and functions of the simple form of CA (cellular automata) model are understood through a case, which can be self-taught based on its

ability and has wide universality. Its ability will have a far-reaching impact on urban planning. Artificial intelligence technology provides a better way to analyze urban development and is the best technology to deal with complex and dynamic problems in urban research [4]. This paper reviews the latest development of urban planning artificial field and explores how to apply artificial technology to urban dynamic planning. Therefore, this paper discusses various uncertain problems in the process of urban evolution and thinks that it is possible to solve the dynamic problems of cities based on artificial intelligence. People are increasingly using knowledge-based or artificial intelligence technology to replace the classical environmental system modeling technology [5]. The technologies covered include case-based reasoning, rule-based systems, artificial neural networks, fuzzy models, genetic algorithms, cellular automata, multiagent systems, swarm intelligence, reinforcement learning, and hybrid systems. The modeling and implementation of various urban planning processes symbolizes an intensive research field [6]. This paper presents a hybrid artificial intelligence system, which uses knowledge-based methods, neural networks, and fuzzy logic and can automatically execute the decision-making process of urban planning. This system integrates a variety of systems and improves on it, which increases the functional breadth of the application program. Through this method, the best technologies are combined to solve complex urban problems. The key aspects of the relationship between artificial intelligence and urban planning development, the breakthrough point of mutual promotion, and the value orientation of future development are discussed [7]. Artificial intelligence will bring about great changes and revolutions in urban research and urban planning. Through the practical application cases of the working group, the author expounds the frontier development of artificial intelligence-assisted urban planning methods, especially in intelligent data collection, intelligent allocation of urban functions, and intelligent urban design. Due to the limitations of artificial intelligence planning tools, urban planning practice faces various open problems and insufficient ability, which limits our ability to perceive the environment and deal with temperament [8]. Therefore, we propose two simple philosophical and systematic causal models to help software engineers understand from the perspective of urban planning. The first model proposes only limited aspects of general intelligence to solve some problems in urban planning. The second model lays a philosophical foundation for responsive artificial super intelligence (ASI). Literature [9] focuses on the influence of games on children's lifestyles, which is also an essential element of childhood, because it involves cognition, imagination, creativity, emotion, body, and society. The vast majority of students today spend most of their time at school, so the outdoor playgrounds at these centers should be well equipped and designed to ensure their full development. This is especially important for children's physical development, because most children are active and in a rapid growth stage. When studying the game environment of ECD in Kisumu, Kenya, we found that the amount of game materials provided by most ECD centers is small and unchanged, which indicates that children have limited opportunities for physical development outdoors. The research suggests that teachers and class teachers should prepare sufficient materials and design outdoor environment, so that children can fully participate in games and promote physical development. Children's participation in development activities, including planning, is still a new method [10]. Urban planning for child participation in development activities has many advantages, such as promoting children's civic skills, developing children's perceived problems and needs, and developing children's self-esteem and self-confidence. At that time, for various reasons, children's participation in community or national decision-making or activities was not supported. This study studies the feasibility of involving children in community planning in Asunafo South District. In addition, the study revealed interesting information from children. The Great East Japan Earthquake on March 11, 2011, and the subsequent disasters still make the children who have experienced it suffer mentally, physically, and socially [11]. Games are a way to play naturally and help them recover. This paper discusses the role of some games in the health triangle. The triangle solved the psychological, physical, and social problems of children after the disaster, and the children released their stress in the game, and the situation improved. As the nature of children's games has been continuously improved in the past decade, many outdoor games have been rapidly reduced [12]. This phenomenon is attributed to social changes, parents' expectations, and children's own needs. Parents are trying to cope with the positive or negative influences related to it. Specific types of outdoor environment can give children opportunities to develop and grow in many aspects. This paper analyzes and understands the research design structure and steps of seven research precedents in the past ten years and obtains the following research results [13]. Firstly, the relationship between children's play environment and behavior is tested by qualitative and quantitative methods. Secondly, children's play environment shows the characteristics of children's amusement behavior, which is different from the existing residential areas. In addition, the study emphasizes the commonness of common problems and methodologies existing among different disciplines. The results of this study lay a foundation for the future research of children's play environment. This paper puts forward the concept of environmental autobiography, which is a method to understand children's views on their living environment more directly [14]. This kind of autobiography may have a deep understanding of children's environmental behavior, support children's needs for exploration, imagination, etc., and avoid being ignored. Therefore, children's play environment will also be affected by urban community planning. In the above research work, the layout of public facilities in smart city communities from the perspective of artificial intelligence, especially in the optimization of children's environment, many design schemes do not consider the layout and optimization of community children's environment. It also fails to take into account the sharing of public facilities among different communities, especially the sharing of public facilities for children. Therefore, in the above-mentioned problems, this paper puts

forward the scheme of sharing children's environment in the community and provides a solution to the conflict of community resources.

2. Artificial Intelligence Algorithm Analysis

2.1. Environmental Impact of Children's Games. With the rapid development of cities, children's play environment has also changed. Different planning communities have different children's play facilities. However, there are differences in children's play environment, and the facilities provided by different communities cannot meet the needs of children in different communities. Generally, this kind of resource utilization effect is not ideal. Through the planning of different communities, the sharing and application of children's play facilities between different communities can be realized. The planning of children's play facilities in different communities is shown in Figure 1.

In Figure 1, there is a shared children's play environment among different communities, and there is a distance between different children's play areas and corresponding communities. Therefore, different communities share the game environment in a common area and uniformly arrange the game environment to realize the optimal allocation and management of public resources in smart cities.

2.2. Genetic Algorithm Model. The concept of genetic algorithm is as follows: this is a viewpoint put forward by a scholar according to the theory of biological evolution. Generally speaking, genetic algorithm is to digitally crack the process of biological inheritance in the biological world, so that the algorithm corresponds to it one by one. We regard the living environment of the individual population as the search range of the algorithm. The genetic material (that is, chromosome) possessed by an individual is regarded as the decoding and coding needed in the algorithm. And calculate the fitness value of genetic material of each individual. Genetic material is copied synchronously by copying. The genetic material existing in chromosomes will cross with the cross of chromosomes. Finally, in the process of decoding, the arrangement order of genetic material will be wrong, resulting in variation. In these processes, the best data can be selected according to the adaptation degree of genetic material. The genetic algorithm flow is shown in Figure 2.

Generally speaking, genetic algorithm has six steps, which correspond to the biological point of view one by one, namely, coding, decoding, solving fitness, copying, crossover, and mutation. Let us explain the above nouns one by one.

Step 1. Coding. Many coding methods can be adopted in genetic algorithm. In this paper, we mainly use binary coding.

Here is an example on the Internet:

$$f(x) = x * \sin(10 * \pi * x) + 2x \in [-1, 2]. \tag{1}$$

Suppose that the accuracy of our solution is $e = 0.01$.

Then, we need to divide the interval of x into 300 parts.

In this example, we use binary encoding, so the number of encoded bits is greater than 300, and we can get at least 9 bits.

From this, we get that the actual solution accuracy is $e = 3/512 \approx 0.00586$.

Step 2. Decoding. Decoding refers to the data transmitted by translating and encoding the original numbers.

We still use the above example, and we can get $000000000 = -1$ and $11111111 = 2$.

The conversion formula used in the above example is as follows:

$$(b_0 b_1 \cdots b_{20} b_{21})_2 = \left(\sum_{i=0}^{21} b_i \bullet 2^i\right)_{10} = x^t. \tag{2}$$

So we get the following decoding formula:

$$\begin{cases} (111111111)_{\text{into } 10} * e - 1 = 2, \\ (000000000)_{\text{into } 10} * e - 1 = -1. \end{cases} \tag{3}$$

Step 3. Replication. In the process of replication, each individual has different adaptability to the environment. Those who adapt well to the living environment can be left and inherited all the time, while those who adapt poorly will be eliminated and randomly generated by the old population of replication operations. In order to ensure the continuity of replication, it will not be interrupted on an individual, so each individual has an independent random possibility of replication. The stronger the adaptability of individuals, the greater the possibility of being copied and inherited.

This paper introduces two common methods of individual replication probability.

Probability setting method based on fitness

$$p_i = \frac{f(x_i)}{\sum_{j=1}^{n} f(x_j)}, \tag{4}$$

where n represents the total number of individuals in the population and $f(x_i)$ is the fitness value of individual i.

Therefore, the stronger the fitness of an individual, the greater the p_i value and vice versa.

Probability setting method based on ranking

Let the population have a total of k individuals, and when the fitness of each individual is known, it is arranged from large to small according to the fitness. The better the individual, the higher the arrangement.

$$P_i = e(1 - e)^{i-1}. \tag{5}$$

In this formula, the greater $i - 1$, the smaller the probability, and vice versa, the greater the probability.

In biological evolution, crossover refers to the interchange of genes of the same part by paired chromosomes for some reason, thus forming two new individuals. The same is true of crossover in genetic algorithm.

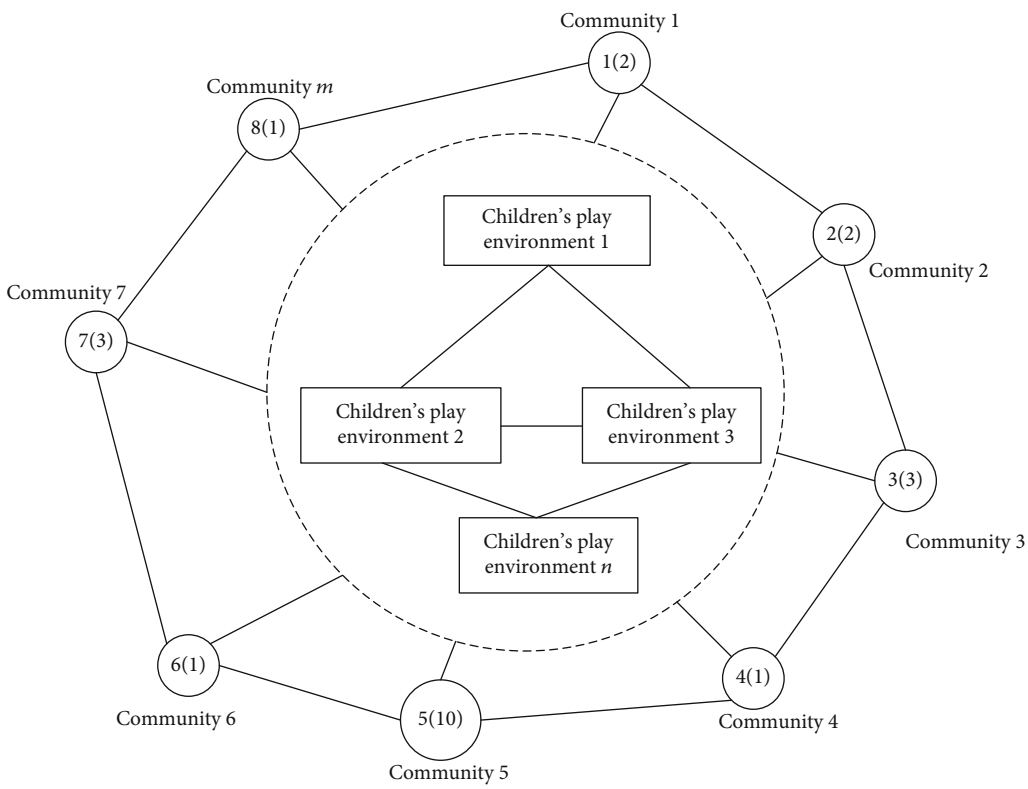

Figure 1: Children's play environment planning under multicommunity planning.

$$a_{ij} = \begin{cases} a_{ij} + \left(a_{ij} - a_{\max}\right) * f(g) r > 0.5, \\ a_{ij} + \left(a_{\min} - a_{ij}\right) * f(g) r \leq 0.5, \end{cases} \tag{6}$$

where $a_{\max}$ is the upper bound and $a_{\min}$ is the lower bound [15].

$$f(g) = r_2 \left(1 - \frac{g}{G_{\max}}\right)^2, \tag{7}$$

where r_2 is a random number, g is the current iteration number, $G_{\max}$ is the maximum evolution number, and r is a random number between [0, 1].

Step 4. Variation. Generally speaking, the function of mutation in this algorithm is to prevent missing important information, because through mutation operation, the population can ensure the biodiversity of the environment and optimize to the maximum extent.

This is based on the concept of survival of the fittest in the theory of evolution. Individuals with high adaptability to the environment are more competitive in participating in reproduction. Once the competitiveness is improved, more and more offspring will be bred. However, if the fitness is low, it will have the opposite outcome.

This paper still refers to the expression in the example mentioned above, where the fitness corresponds to the result, which is x, and correspondingly, $f(x)$ is the calculation formula of fitness.

In AG-BP algorithm, it is inevitable to optimize the function $f(x)$, so this function is set up one-to-one correspondence in $f(x)$, that is, fitness, which is equivalent to a coordinate point of plane coordinate axis. The following two regulations apply to solving fitness:

(i) The value of fitness function is not less than zero

(ii) The change direction of objective function is the same as that of fitness function in the process of population evolution

For this reason, genetic algorithms usually use the following formula to transform $f(x)$ into $f(x)$. $C_{\min}$ is an appropriate smaller number that meets the requirements.

The optimization of $f(x)_{\max}$ can be transformed by the following formula:

$$f(x) = \begin{cases} f(x) - C_{\max}, f(x) > C_{\max}, \\ 0, f(x) < C_{\max}. \end{cases} \tag{8}$$

The optimization of $f(x)_{\min}$ can be transformed by the following formula:

$$f(x) = \begin{cases} -f(x) - C_{\min}, f(x) < C_{\min}, \\ 0, f(x) > C_{\min}. \end{cases} \tag{9}$$

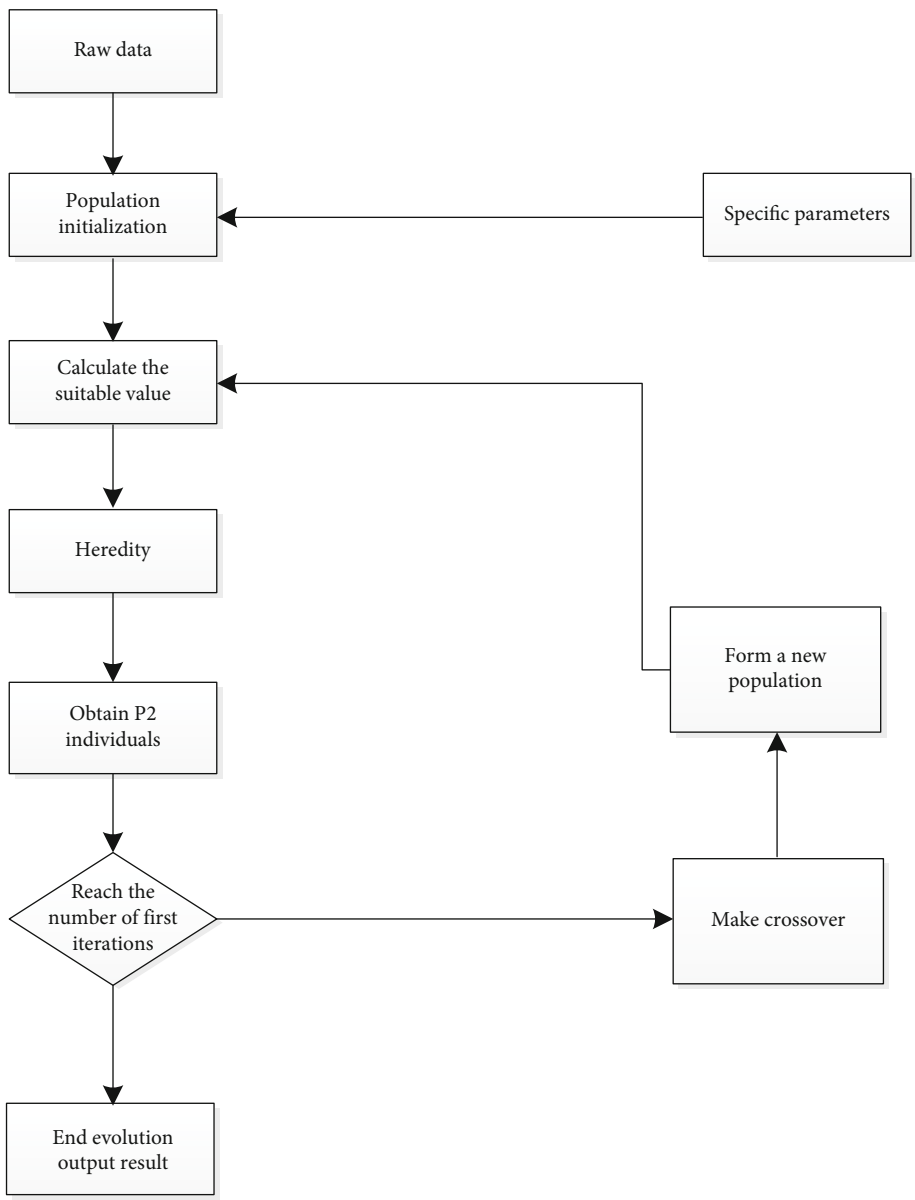

Figure 2: Genetic algorithm flow.

For exponential function problems, the general method is

$$F(x) = c^y\,;\, y = f(x). \tag{10}$$

2.3. BP Neural Network. BP neural network is a multilayer feedforward neural network trained according to error back propagation algorithm, and it is the most widely used neural network. It can solve the learning problem of hidden layer connection weight of multilayer neural network systematically and give a complete derivation in mathematics. In addition, it also has excellent pattern classification ability and excellent multidimensional function mapping ability. Structurally speaking, BP network has input layer, hidden layer, and output layer. In essence, BP algorithm takes the square of network error as the objective function and uses gradient descent method to calculate the minimum value of the objective function.

The BP neural network model is shown in Figure 3.

2.3.1. Activation Function. Generally, it can be expressed by the following formula:

$$f(x) = \begin{cases} \dfrac{1}{1+e^{-x}}, \\ \dfrac{1-e^{-x}}{1+e^{-x}}. \end{cases} \tag{11}$$

Under normal circumstances:

$$f(x) = \frac{A}{1+e^{-x/B}}. \tag{12}$$

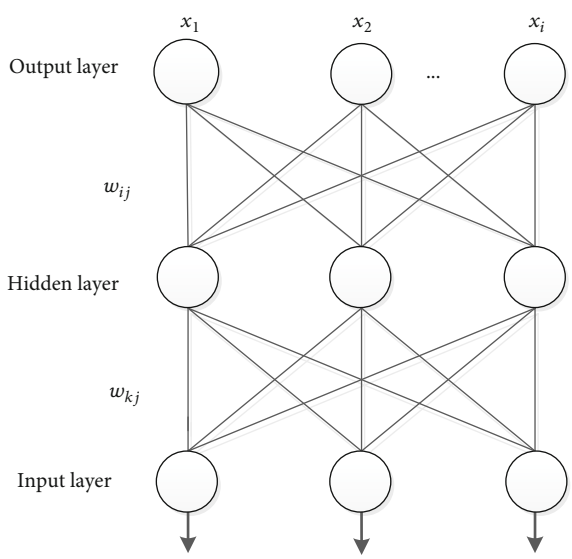

Figure 3: BP neural network model.

Its derivative is defined:

$$y_k = \sum_{i=0}^{I} W_{ik} * X_i + B_k. \tag{13}$$

2.3.2. Forward Propagation. In BP neural network, according to the above model diagram, we can see that the output value of any node is not determined by only one condition but considers many factors: the activation function used by the algorithm, all the output values and weights of the upper node, and the weights and thresholds of the current node. Therefore, we can use the following formula as a reference.

$$\begin{aligned} Y_k &= f(y_k), \\ y_k &= \sum_{k=0}^{H} W_{kj} * Y_i + B_j, \\ Y_j &= f\left(y_j\right). \end{aligned} \tag{14}$$

2.3.3. Back Propagation. At the output layer of the network, we can judge the error between the standard result and the output result according to the following formula:

$$E = \frac{1}{2}\sum_{j=0}^{O}\left(S_j - Y_j\right)^2. \tag{15}$$

The so-called back propagation refers to the reverse propagation of the error signal obtained from the experiment, so that the value of the error signal function can be reduced and better optimized. With the decrease of the function value, the advantages of back propagation can also be reflected. In order to minimize the error function, gradient descent is one of the methods used to correct weights and thresholds, and the following formula is obtained by this method:

$$\Delta W_{kj} = -a\frac{\partial E}{\partial W_{kj}}. \tag{16}$$

Then, the above formula is derived to make

$$\begin{aligned} \delta_{kj} &= \sum_{j=0}^{O}\left(S_j - Y_j\right)Y_j\left(1 - Y_j\right). \\ \Delta W_{kj} &= \delta_{kj} * \left(\sum_{k=0}^{H}\left(Y_k\right)\right) \end{aligned} \tag{17}$$

Also for B_j are

$$\Delta B_{kj} = -a\frac{\partial E}{\partial B_{kj}}. \tag{18}$$

By derivation
Order: $\delta_{kj} = \sum_{j=0}^{O}(S_j - Y_j)Y_j(1 - Y_j)$.
Then: $\Delta B_{kj} = \delta_{kj}$.

3. Optimizing BP Network Model Based on Genetic Algorithm

3.1. Model Description. This section can be divided into three parts: BP neural network structure determination, genetic algorithm optimization, and BP neural network prediction.

The BP neural structure is determined by two important parameters in the fitting function, and the length of individual genetic algorithm is also obtained. The optimization of genetic algorithm refers to the AG-BP algorithm, through which all thresholds and ownership values in the network can be optimized. As long as there is an entity in the population, it is used for the ownership value and threshold of the network. Genetic algorithm finds out the optimal individual through three important operations (selection, crossover, and mutation) and then uses BP neural network to predict. Genetic algorithm is used to get the optimal individual to assign the initial weight and threshold value of the network and predict the output of the function [16]. The specific model is shown in Figure 4.

3.2. Implementation of Genetic Algorithm

3.2.1. Population Initialization. A group of individuals constitutes a population, and each individual is a single subset of the population that will not be repeated. In the process of initialization, we should pay attention to expand the scope of the search problem space to avoid the occurrence of local minima.

3.2.2. Fitness Function. First of all, there is an initial data, that is, the weights and thresholds of individuals in BP neural network. In order to calculate the fitness of individuals, this paper chooses BP algorithm to get data first and then takes the expectation obtained by prediction and the absolute error of output as the application data in the formula, as shown in the following formula:

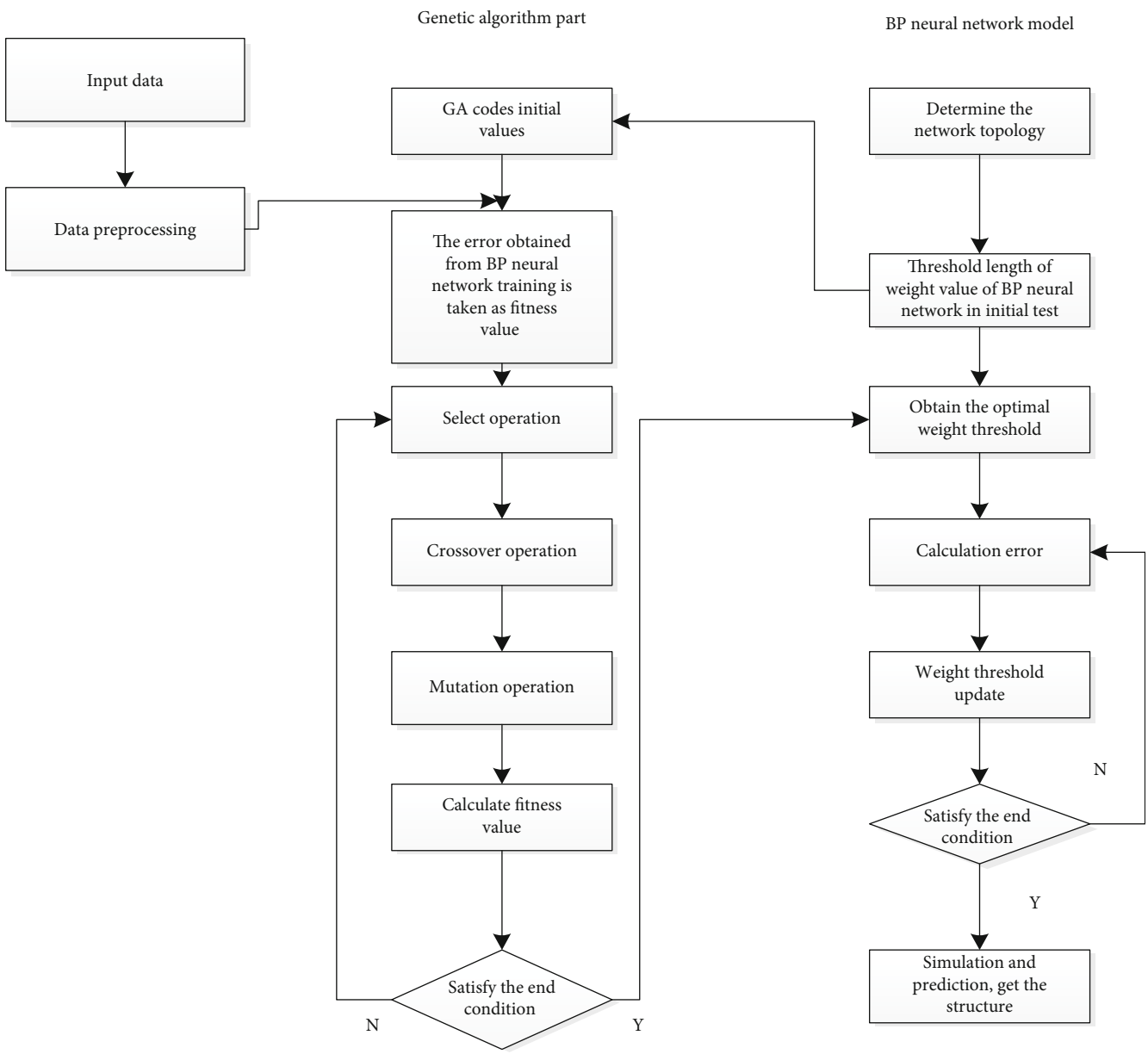

Figure 4: AG-BP algorithm flow.

$$F = k\left(\sum_{i=1}^{n} abs(y_i - o_i)\right), \tag{19}$$

where n is the number of network output nodes, o_i is the actual output of the i-th node, K is the coefficient, and y_i is the expected output of the i-th node of BP neural network.

3.2.3. Select the Action. There are many methods for genetic algorithm selection operation, such as roulette. When choosing roulette, that is, the selection strategy based on fitness ratio, the selection probability p_i of each individual i is

$$f_i = \frac{k}{F_i}\,; p_i = \frac{f(i)}{\sum_{j=1}^{n} f(j)}, \tag{20}$$

where K is the coefficient and N is the number of individuals in the population. F_i is the fitness value of individual i, and the smaller the better.

3.2.4. Crossover Operation. The crossover operation formula is as follows:

$$\begin{cases} a_{kj} = a_{kj}(1-b) + ba_{lj}, \\ a_{lj} = a_{lj}(1-b) + ba_{kj}. \end{cases} \tag{21}$$

Formula (21) means that chromosome K and chromosome 1 are interchanged at the same site J, and B is a random number between [0, 1].

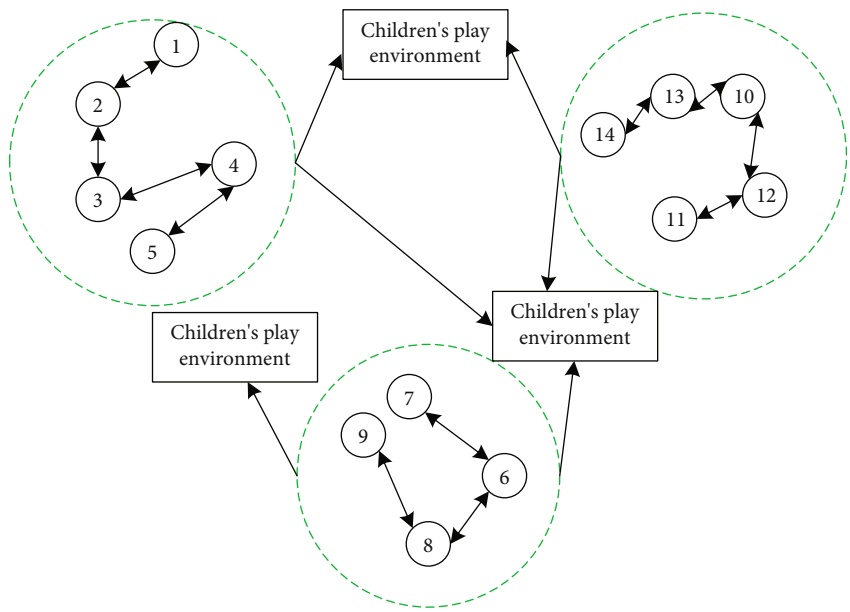

Figure 5: Optimal path optimization model.

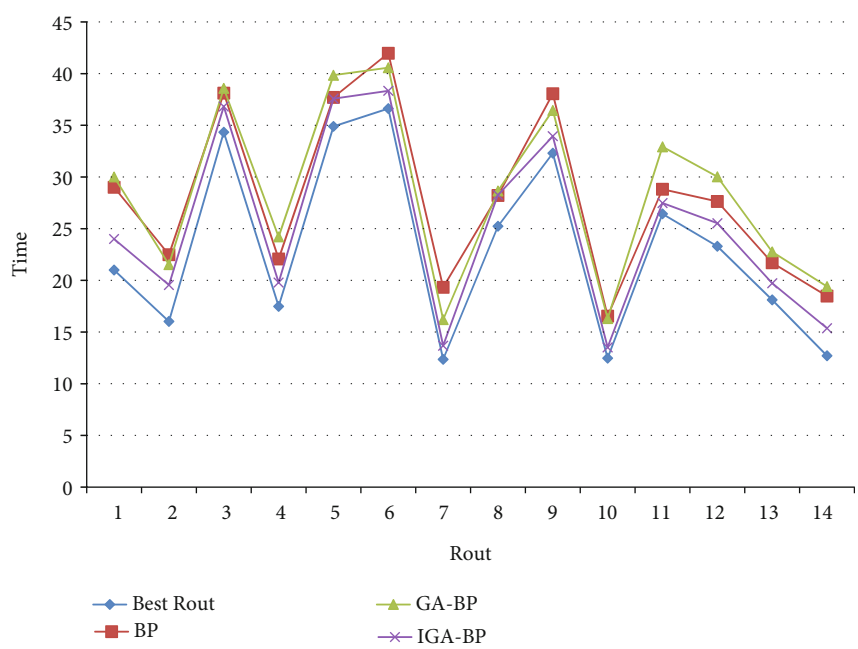

Figure 6: Path comparison under different algorithms.

Table 1: Comparison of distance under different communities.

Algorithm	Best (m)	Worst (m)	Avg (km)	Time (ms)
BP	2015	2354	2104	1354
GA-BP	1824	2041	1857	1028
IGA-BP	1574	1931	1698	895

4. Experimental Simulation Based on IGA-BP

In order to better verify the superiority of this algorithm and the help of the optimized algorithm to urban community planning, this study selects three examples of optimization effect compared with other algorithms.

4.1. Performance Comparison between IGA-BP and Other Models. First of all, I found the following optimization schemes from the community and compared them with different routes under each algorithm, as shown in Figure 5.

In order to better show the performance of IGA-BP global algorithm, the experimental part gives three global optimal algorithms for children's game path selection in different communities in Figure 5. The comparison of path

Table 2: Child environmental index in community area.

Data	Average wind speed (m/s)	Average temperature (°C)	Sunshine time (h)	Environmental heat in the first three days (MJ/h)	Environmental heat in the first two days (MJ/h)	The environmental heat of the previous day (MJ/h)	Ambient heat (MJ/h)
1	5.5	-7	5.7	7503.6	7461.2	7375.1	7283.5
2	1.9	-9	6.3	7461.2	7375.2	7283.5	7046.4
3	2.4	-8.5	6.4	7435.2	7283.6	7046.5	6837.1
4	1.5	-7	6.1	72883.5	7046.5	6837.1	6720.4
5	2.2	-6	6.4	7046.6	6837.1	6723.4	6657.7
6	2.5	-5.5	6	6837.2	6720.5	6657.7	6578.1
7	1.8	-5	5.4	6720.3	6657.6	6578.1	6687.2
8	0.9	-2	4.3	6657.8	6578.1	6687.2	6234.7
9	2.2	-7	4.8	6687.3	6234.8	6438.4	6782.1

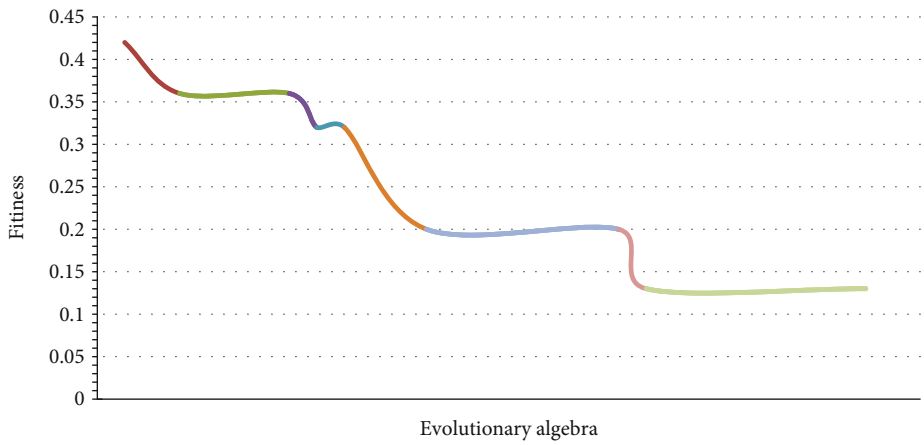

Figure 7: Fitness of GA-BP network.

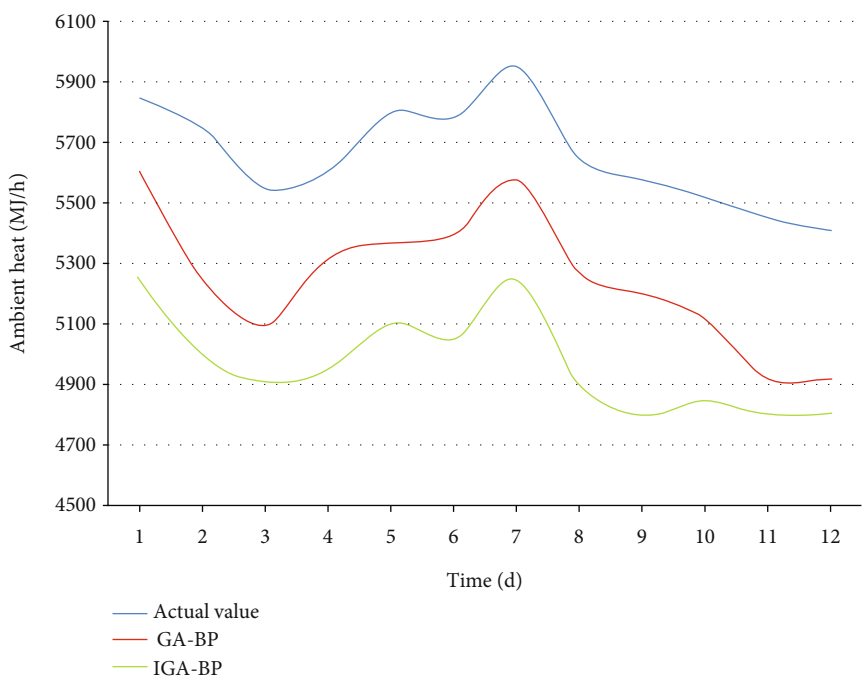

Figure 8: Actual and predicted values of environmental heat of different algorithms.

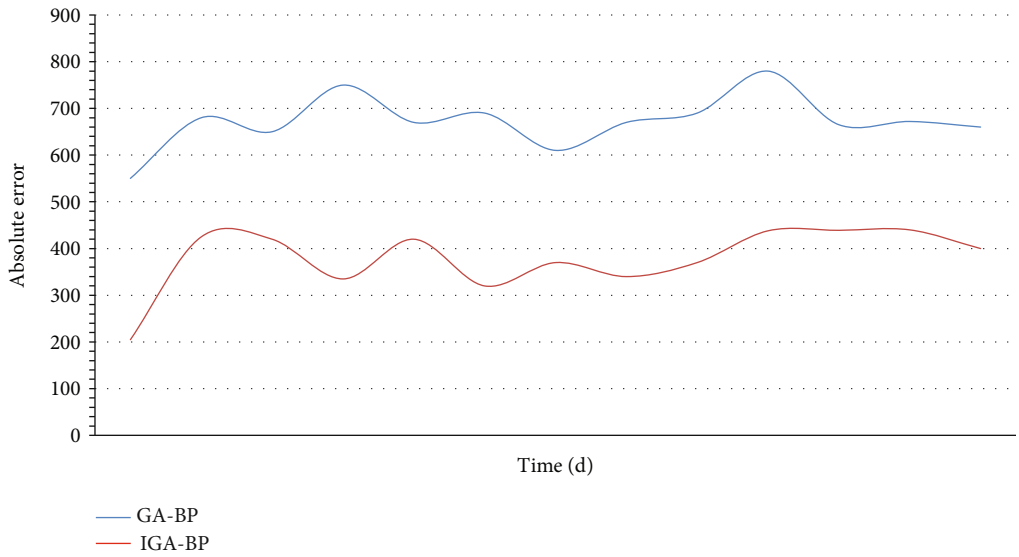

Figure 9: Comparison of absolute errors of different algorithms.

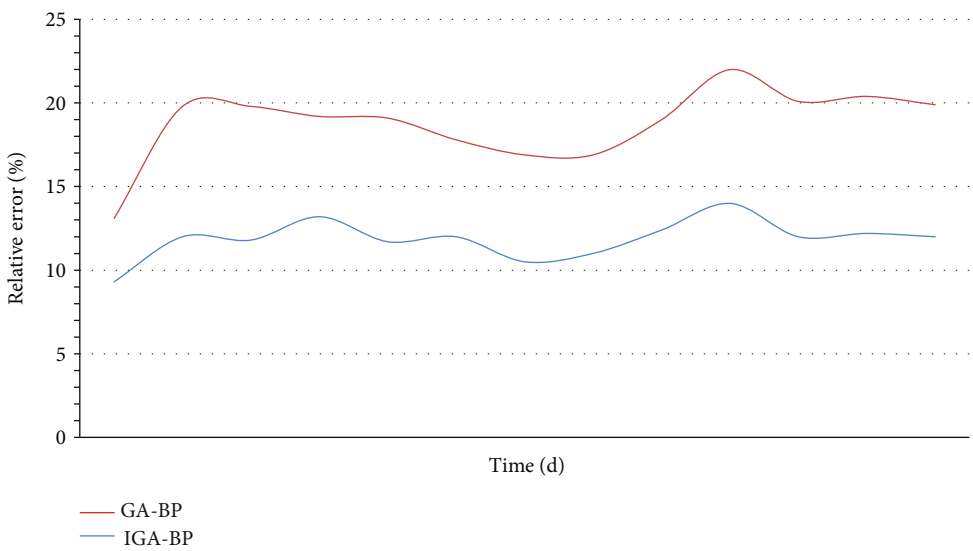

Figure 10: Comparison of relative errors of different algorithms.

selection performance of these three algorithms is intuitively shown, as shown in Figure 6.

As can be seen from Table 1, compared with BP algorithm and GA-BP algorithm, IGA-BP algorithm has obvious advantages in the whole position distance. Especially in time, the advantage is more obvious.

4.2. Application of IGA-BP Network to Prediction of Children's Play Environment. In this study, the data of the district central heating system in a community in China in the past few years were collected as training and prediction samples. Taking days as a unit, dozens of data were collected, and the middle segment function of Sigmoid activation function was selected and adopted, and these data were normalized, as shown in Table 2.

Because this paper adopts the intelligent optimization algorithm combined with BP neural network, the advantage is that it does not need historical data, and it needs the data of the first three days to predict the recent value. Therefore, in Table 2, the environmental data of the first three days are listed.

Next, the sample data is trained, and the BP algorithm and GA-BP algorithm are compared, and the following comparison charts are obtained, as shown in Figures 7–10, respectively.

It can be intuitively seen that the BP network algorithm optimized by improved genetic algorithm is smaller than the average relative error and average absolute error of a single BP network neural algorithm, so we can get that BP-AG algorithm has higher prediction accuracy than BP neural algorithm.

4.3. Analysis of Positional Relationship in Children's Environment with IGA-BP Application. In this comparative

Table 3: Overview of datasets.

Community	Ambient heat (kW)	Wind speed ($m \bullet s^{-1}$)	Theoretical heat (kW • h)	Wind direction (°)
1	380.0478	5.3113	416.3289	259.9949
2	453.7692	5.6272	519.9171	268.6411
3	306.3765	5.216	390.9	272.5647

Table 4: Prediction results of GA-BP neural network.

Serial number	Training mean square error	Prediction average error	Minimum prediction error	Maximum error of prediction
1	0.0713	0.1562	0.00368	0.3174
2	0.0824	0.2237	0.00028	1.0607
3	0.064	0.1576	0.00298	0.7585

Table 5: Prediction results of IGA-BP algorithm.

Serial number	Training mean square error	Prediction average error	Minimum prediction error	Maximum error of prediction
1	0.00224	0.0646	0.00124	0.1306
2	0.00225	0.0676	0.00467	0.1361
3	0.00228	0.0549	0.00105	0.1151

Table 6: Comparison of algorithm prediction results.

Algorithm type	Average time spent (s)	Mean square error	Average error	Minimum error	Maximum error
GA-BP	4.37	0.06267	0.1762	0.00631	0.8296
IGA-BP	27.14	0.00226	0.0624	0.00231	0.1225

experiment, different children's game environments are set in different communities, so as to achieve the optimal value of environmental heat in different areas. Below, choose different community children's play facilities environment as shown in Table 3.

The parameters are described in Table 3 such as wind speed and energy, which mainly evaluate the children's environment effectively, so as to put forward relevant requirements for the setting and layout of children's environment more effectively.

On the basis of the data, we make a comparison between the two algorithms. First of all, we use BP algorithm to train and predict children's environmental heat for many times, and the prediction effect is shown in Table 4. Next, we use IAG-BP algorithm to predict, and the prediction results are shown in Table 5. Finally, we compare the prediction errors obtained by these two algorithms and get the prediction data in Table 6.

According to the data in the above four different tables, compared with GA-BP algorithm, IGA-BP neural network prediction algorithm based on genetic algorithm has a significant improvement in prediction accuracy, and the maximum error is close to 0, which obviously proves that the optimized GA-BP model has absolute advantages in children's environmental heat prediction. At the same time, the algorithm effectively improves the stability of the algorithm and reduces the fluctuation of prediction.

5. Conclusion

After understanding the functions of these algorithms, the improved BP neural network based on genetic algorithm proposed in this paper is more superior to other algorithms and can make urban construction planning more reasonable in many aspects, such as climate prediction and power grid planning. According to the above three experimental simulation results, the AG-BP algorithm is more powerful and has achieved good results in practical application. Nevertheless, artificial intelligence is still not very flexible, so there are still many problems that need further improvement, so we will not repeat them in this study, but I believe that in the near future, the algorithm will get better development.

Data Availability

The experimental data used to support the findings of this study are available from the corresponding author upon request.

Conflicts of Interest

The authors declared that they have no conflicts of interest regarding this work.

Acknowledgments

This work was sponsored in part by the Hainan Province Education Science "13th Five-Year Plan" Project (Project No. QJY20201013): "Research on the strategy of constructing supportive environment for free plays at kindergarten" and Hainan Higher Education and Teaching Reform Research Project (Hnjg2018-80): "Research on the reform of talent training mode of primary education specialty in normal colleges and Universities Based on 'collaborative innovation'."

References

[1] A. Mellir and S. A. Kalogirou, "Artificial intelligence techniques for photovoltaic applications: a review," *Progress in Energy and Combustion Science*, vol. 34, no. 5, pp. 574–632, 2008.

[2] J. C. Pomerol, "Artificial intelligence and human decision making," *European Journal of Operational Research*, vol. 99, no. 1, pp. 3–25, 1997.

[3] E. A. Silva, "The DNA of our regions: artificial intelligence in regional planning," *Futures*, vol. 36, no. 10, pp. 1077–1094, 2004.

[4] P. Kamal Jain, "A review study on urban planning & artificial intelligence," *International journal of soft computing & engineering*, vol. 1, no. 5, pp. 101–104, 2011.

[5] S. H. Chen, A. J. Jakeman, and J. P. Norton, "Artificial intelligence techniques: an introduction to their use for modelling environmental systems," *Mathematics and Computers in Simulation*, vol. 78, no. 2-3, pp. 379–400, 2008.

[6] F. Shan and D. X. Li, "Hybrid artificial intelligence approach to urban planning," *Expert Systems*, vol. 16, no. 4, pp. 248–261, 2010.

[7] W. U. Zhiqiang, "Artificial intelligence assisted urban planning," *Time Architecture*, vol. 1, pp. 6–11, 2018.

[8] M. A. Hawas, "Are we intentionally limiting urban planning and intelligence? a causal evaluative review and methodical redirection for intelligence systems," *IEEE Access*, vol. 5, pp. 13253–13259, 2017.

[9] I. Journals, M. E. Kerich, and L. Momanyiokioma, "Suitability of children's outdoor play environment in city ECD centers for their physical development," *International Journal of Innovative Research and Development*, vol. 4, no. 8, 2015.

[10] E. A. Agyapong, J. A. Lugushie, and B. Fei-Baffoe, "Effect of organochlorine pesticides usage on water quality of Tano River in the Asunafo South district of Brong Ahafo region of Ghana," *Pollution Research*, vol. 32, no. 4, pp. 699–706, 2013.

[11] K. Isami and W. Helen, "Children's play environment after a disaster: the great East Japan earthquake," *Children*, vol. 2, no. 1, pp. 39–62, 2015.

[12] M. B. Staempfli, "Reintroducing adventure into children's outdoor play environments," *Environment and Behavior*, vol. 41, no. 2, pp. 268–280, 2009.

[13] S. H. Park, D. U. Yoo, Y. M. Choi, H. M. Kang, and H. J. Kim, "Characteristics of research designs for inquiring children's play environment and play behavior in residential neighborhoods - based on analysis of recent causality studies," *Journal Of The Architectural Institute Of Korea Planning & Design*, vol. 31, no. 12, pp. 29–40, 2015.

[14] M. A. Boschetti, "Memories of childhood homes: some contributions of environmental autobiography to interior design education and research," *Journal of Interior Design*, vol. 13, no. 2, pp. 27–36, 1987.

[15] S. Ren, J. Niu, Z. Luo et al., "Cough expired volume and cough peak flow rate estimation based on GA-BP method," *Complexity*, vol. 2020, Article ID 9036369, 9 pages, 2020.

[16] G. Chen, L. Wang, and M. M. Kamruzzaman, "Spectral classification of ecological spatial polarization SAR image based on target decomposition algorithm and machine learning," *Neural Computing and Applications*, vol. 32, no. 10, pp. 5449–5460, 2020.

Hindawi
Journal of Sensors
Volume 2022, Article ID 7554560, 11 pages
https://doi.org/10.1155/2022/7554560

Research Article

Research on GPS User Trajectory Analysis and Behavior Prediction Based on Swarm Intelligence Algorithm

Guangyong Zhou

School of Civil Engineering, Guangdong Construction Polytechnic, Guangzhou 510440, China

Correspondence should be addressed to Guangyong Zhou; zhougygz@zcmu.edu.cn

Received 14 March 2022; Revised 31 March 2022; Accepted 12 April 2022; Published 29 April 2022

Academic Editor: Han Wang

Under the social background of the rapid development of big data, human beings have gradually moved towards a comprehensive digital era, and people have begun to apply digital technology in various fields. Therefore, it is necessary to study methods that can efficiently process big data and solve problems such as data intelligence. Intelligent products and applications that we use everywhere in our lives are changing people's lives. Among them, location service is one of the important technical supports. No matter which software is opened on the mobile phone, it will prompt us to open location service. Location prediction is an important part of location-based services and plays an indispensable role in the recommendation system and urban resource planning. At present, GPS-based trajectory data is widely concerned in position prediction task. GPS trajectory data belongs to spatiotemporal series data, which not only contains time and position information but also contains abundant context information in trajectory sequence. Most of the traditional position prediction methods focus on the position sequence in GPS trajectory but do not fully mine the context information in the trajectory, which leads to poor prediction results. The intelligent optimization algorithm greatly enriches the optimization technology and provides a feasible solution for those combinatorial optimization problems which are difficult to deal with by traditional optimization technology. GPS trajectory data has the advantages of wide coverage, quick update, easy collection, and low cost, and it also implies abundant road network information. As a result, GPS trajectory data of users has gradually become a new data source for automatic construction of urban road network and has also become a research hotspot of many scholars. In this paper, the idea of swarm intelligence algorithm and swarm intelligence algorithm are used to design and implement a data analysis and behavior prediction system for calculating GPS user trajectory, aiming at solving the shortcomings of existing GPS tracking and positioning.

1. Introduction

Invisible information resources are closely related to our lives. How to mine useful value from these important information resources has become a hot topic discussed by many scholars. Big data contains all kinds of important information of people, such as users' travel habits, consumption habits, and behavior characteristics. We can collect important information for big data analysis and further tap the diversified value of users, so as to provide more targeted services. With the continuous development of positioning technology, vehicles, mobile phones, smart and convenient products, and other devices with GPS, services are collecting user trajectory data every minute. Reference [1] proposes an intelligent swarm algorithm, which can accurately estimate the posterior state in nonlinear systems and show higher tracking accuracy. Literature [2] describes that the improved SFLA algorithm has faster convergence in cloud computing. Reference [3] analyzes the techniques of well trajectory prediction and collision risk assessment, which can improve drilling efficiency and ensure the safety and reliability of drilling process. Literature [4] expounds the analysis of the unbalanced entrance space and, on this basis, puts forward relevant suggestions and measures to optimize it. Reference [5] based on the GRNN algorithm for ship trajectory analysis and [6] ocean transport ship trajectory analysis. In reference [7], the flight trajectory of stratospheric airship was analyzed and studied in view of the influence of traditional propeller on environmental changes such as atmospheric density. Literature [8] analyzes and studies the

multidimensional and sparse trajectory data of downhole workers, and improves the accuracy of abnormal trajectory discrimination. The analysis of trajectory characteristics and the relationship between trajectory and the position of car body parts in reference [9] provides reference for cab design. Reference [10] analyzes three applications of ship trajectory clustering, extracts three ship motion patterns, and enriches the characteristics of ship behavior patterns. Reference [11] studies the establishment of dynamic equations to analyze the flight trajectory of rotating oblique projectile under wind speed. Reference [12] studies the analysis of urban vehicle trajectory to predict whether the road condition information is congested and studies the intelligent vehicle trajectory of SD card in [13], which realizes the offline debugging function and improves the debugging efficiency. Literature [14] describes multivariable trajectory analysis for fault detection. In reference [15], the trajectory equation of projectile under the influence of air resistance and the equation of projectile angle when the range is maximum are derived. With the help of MATLAB numerical calculation function, the trajectory curves under different resistance coefficients, projectile mass, initial velocity, and projectile angle are simulated. Literature [16] describes the detection of heart disease by swarm intelligence optimization algorithm. Literature [17] analyzes and summarizes the research and development direction of train operation control technology based on swarm intelligence. In reference [18], a multi-UAV autonomous control algorithm is proposed to improve the success rate of UAV cluster in air combat. Literature [19] discusses the multidisciplinary viewpoints and methods of swarm intelligence computing, the parallel implementation of multiswarm cooperation and bionic network hardware, and swarm intelligence has important applications in aerospace TT&C, UAV intelligent TT&C, and other fields. Reference [20] proposes a new multiobjective virtual machine merging algorithm based on ant swarm intelligence. Literature [21] expounds the advantages of swarm intelligence algorithm, and literature [22] expounds the core ideas and basic principles of swarm intelligence optimization algorithm. Literature [23] expounds the intelligent bee colony firefly algorithm to predict the national electricity consumption in China. The swarm intelligence algorithm optimized in reference [24] has remarkable effect on engineering structure optimization, which can effectively improve the functionality and safety of engineering structure, improve the benefit and value of engineering projects, and is worth popularizing and practicing. Literature [25] studies innovative policies from the perspective of the ant colony swarm intelligence theory.

2. Overview and Superiority of Swarm Intelligence Algorithm

2.1. Introduction to Intelligent Swarm Algorithms. The swarm intelligence algorithm is a kind of intelligent algorithm evolved from nature, which establishes a mathematical model by observing the living habits of biological groups in nature and then solves practical problems in reality. Cluster is a common phenomenon in nature, such as birds foraging, ants looking for food, bees collecting honey, fish rear-end collision, and clustering. In the long process of evolution, individuals constantly adapt and develop through mutual cooperation and competition with groups, accept various tests of nature, and finally win the common victory of the whole group. Different scholars have carried out in-depth research on cluster phenomenon, and the development of swarm intelligence algorithm has a broader prospect and will be widely used. Applied in various fields, calculation and modeling are relatively simple and easy to implement. The requirements of computer CPU and memory in data processing are not high. In addition, it is not limited to a specific problem, so we can solve various problems through heuristic search. The development process of swarm intelligence algorithm is shown in Figure 1:

2.2. Advantages of Intelligent Swarm Algorithm. A swarm intelligence optimization algorithm includes many algorithms, such as random forest algorithm and particle swarm optimization. In recent years, many new algorithms have emerged, such as forest algorithm, bird swarm algorithm, and pigeon swarm algorithm. The new swarm intelligence algorithm provides new ideas and methods for solving many problems that need to be optimized in reality. The characteristic of these algorithms is to combine group optimization method with big data mining to choose the optimal solution. By analyzing all the solutions of practical problems, the distribution of solutions is obtained according to the problem characteristics and algorithm optimization process, and the solution structure of the problem to be solved is established. On the basis of the association between the problem to be solved and the algorithm, the problem can be solved better. The practical problem is modeled as a search problem that searches the optimal value in the space formed by all solutions, and the swarm intelligence optimization algorithm guides the search process through heuristic information. In the search process, multiple individuals search for the optimal solution together through competition and cooperation. Because there are many individuals working together to search at the same time, the swarm optimization algorithm has a kind of potential parallelism. Different from the conventional numerical solution, the swarm optimization algorithm has almost no restrictions on the properties (monotonicity, differentiability, and modality) of the objective function. It does not even need to know the expression of the objective function, so the swarm intelligence optimization algorithm greatly expands the range of solvable optimization problems, and can be widely used in various optimization problems, such as dynamic optimization problems, constrained optimization problems, uncertain environment optimization problems, and multiobjective optimization problems.

3. Algorithm Set

3.1. Decision Tree Algorithm. Decision tree is a common supervised machine learning algorithm. The algorithm structure of self-decision tree is presented as a tree, which

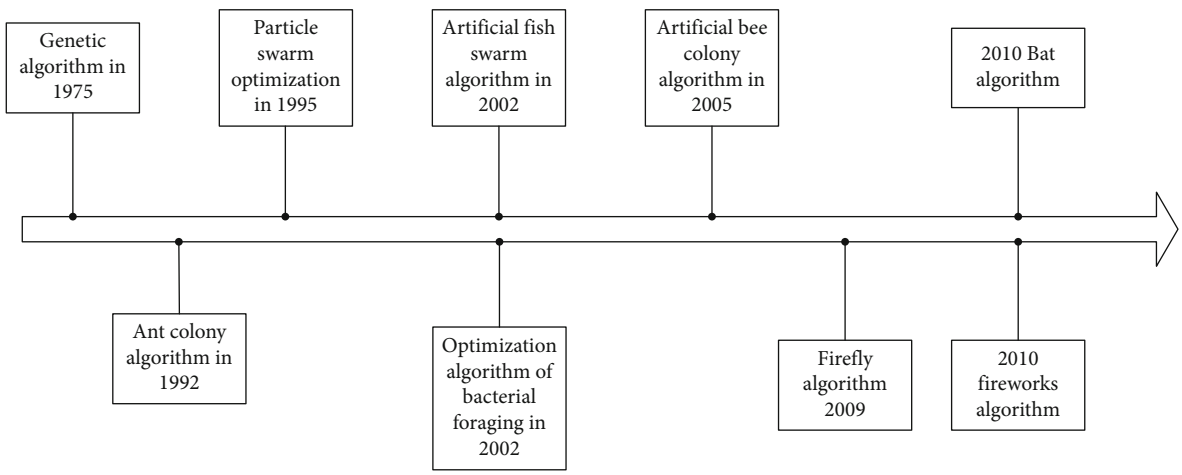

Figure 1: Development chart.

is similar to the way of thinking when human beings make choices in life.

(1) Information gain: information entropy is an index used to measure information uncertainty and is the basis for calculating information gain. Calculation formula:

$$\mathrm{Ent}(D) = -\sum_{k=1}^{n} p_k \log_2 p_k \tag{1}$$

The smaller the Ent (D), the higher the purity of D.

For the information gain of GPS trajectory feature α to sample set D, the expression is

$$\mathrm{Gain}(D, \alpha) = \mathrm{Ent}(D) - \sum_{v=1}^{v} \frac{|D^v|}{|D|} \mathrm{Ent}(D) \tag{2}$$

(2) Information gain rate: the decision tree can use the information gain rate to select the optimal partition attribute, and the calculation formula is as follows:

$$\mathrm{Gain\_ratio}(D, \alpha) = \frac{\mathrm{Gain}(D, \alpha)}{IV(a)}, \tag{3}$$

where the expression for $IV(a)$ is

$$IV(a) = -\sum_{V}^{v=1} \frac{|D^v|}{|D|} \log_2 \frac{|D^v|}{|D|} \tag{4}$$

(3) Gini index: the probability that any two samples in the GPS trajectory feature sample set are inconsistent in their categories. The formula is as follows:

$$\mathrm{Gain\_index}(D, \alpha) = \sum_{V}^{v=1} \frac{|D^v|}{|D|} \mathrm{Gini}(D^v) \tag{5}$$

3.2. Ensemble Learning Method. By constructing multiple classifiers to achieve the learning purpose, the generalization performance can generally be better than that of a single classifier. The structure of ensemble learning is shown in Figure 2.

3.3. Random Forest Algorithm. Random forest algorithm is an extended variant of ensemble learning. Random forest is an ensemble learning algorithm based on decision tree. The random forest algorithm flow is shown in Figure 3.

3.4. XGBoost Algorithm and GBDT Algorithm. XGBoost algorithm is optimized on the basis of traditional algorithm, which is an efficient implementation of traditional algorithm, and can be applied to classification and regression problems. The algorithm flow is as follows:

(1) Initialize $f_0(x) = 0$

(2) When $m = 1, 2, \cdots, M$

Calculate residual value:

$$r_{mi} = y_i - f_{m-1}(x_i), i = 1, 2, \cdots. \tag{6}$$

Fitting residual r_{mi} learns a regression tree to update $f_m(x)$, and the formula is as follows:

$$f_m(x) = f_{m-1}(x) + T(x; \varnothing m). \tag{7}$$

Get the ascending tree:

$$f_M(x) = \sum_{m=1}^{M} T(x; \varnothing m). \tag{8}$$

GBDT algorithm flow:

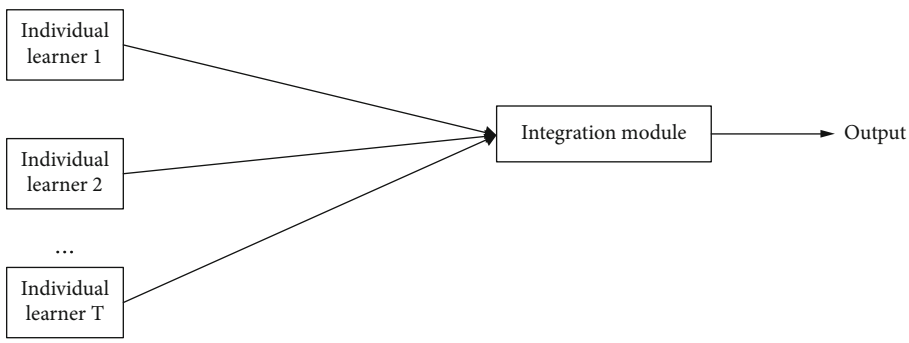

Figure 2: Ensemble learning structure diagram.

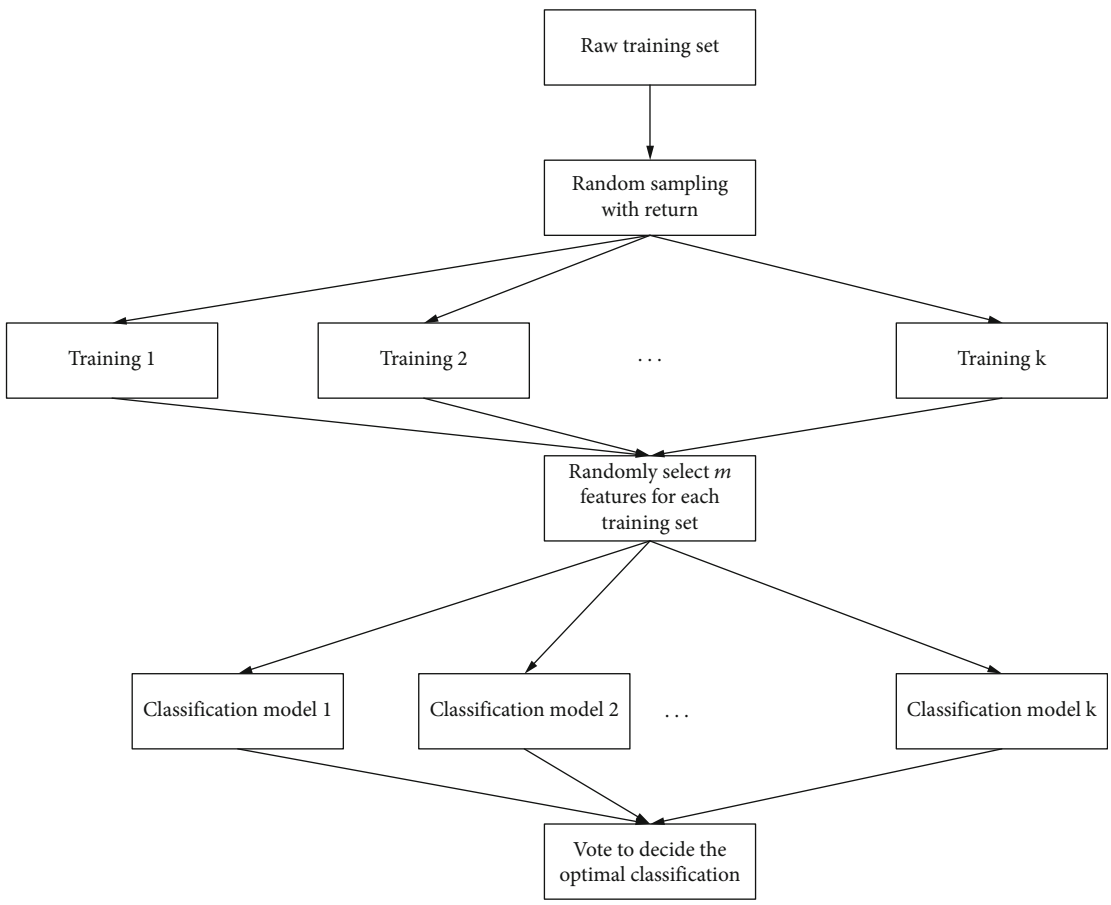

Figure 3: Random forest algorithm flow.

Input: training set sample

$$T = \{(x_1, y_1), (x_2, y_2), \cdots, (x_m, y_m)\}. \tag{9}$$

Output: suppose sample $i = 1, 2, 3, \cdots, m$, number of iterations $t = 1, 2, 3, \cdots t$.

Calculate the negative gradient:

$$r_{ti} = -\left[\frac{\partial L(y_i, f(x_i))}{\partial f(x_i)}\right]_{f(x)=f_{t-1}(x)}. \tag{10}$$

Suppose the leaf region $J = 1, 2, \cdots, J$.

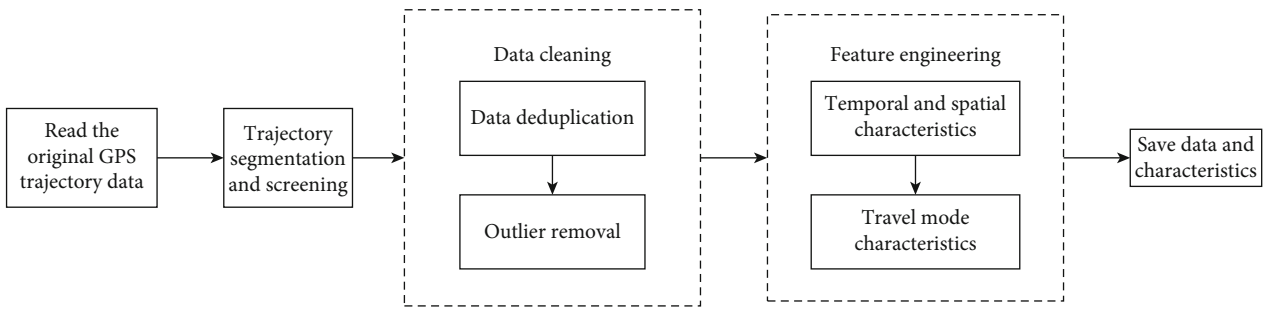

Figure 4: Trajectory data preprocessing.

Calculate the best fit value:

$$c_{tj} = \operatorname{argmin} \sum_{x_i \in R_{tj}} L(y_i, f_{t-1}(x) + c). \tag{11}$$

Update learner:

$$f_t(x) = f_{t-1}(x) + \sum_{j=1}^{J} c_{tj} I\left(x \in R_{tj}\right), \tag{12}$$

get

$$f(x) = f_t(x) = f_0(x) + \sum_{t=1}^{T} \sum_{j=1}^{J} c_{tj} I\left(x \in R_{tj}\right). \tag{13}$$

3.5. GPS Trajectory Feature Calculation. Trajectory feature is the motion parameter that describes the whole trajectory. This paper uses statistical method to extract trajectory feature based on GPS point feature.

Coefficient of variation: $\mathrm{CV} = \sigma/\mu$,including σ is standard deviation and μ is mean value.

Skewness:

$$\mathrm{skew} = E\left[\left(\frac{X-\mu}{\sigma}\right)^3\right]. \tag{14}$$

Kurtosis:

$$\mathrm{kurt} = E\left[\left(\frac{X-\mu}{\sigma}\right)^4\right] - 3. \tag{15}$$

Autocorrelation coefficient:

$$\sum_{n-h}^{i=1} \frac{(x_i-\mu)(x_{i+h}-\mu)}{\sum_n^{i=1}(x_i-\mu)^2}. \tag{16}$$

The calculation formula of the above characteristic parameters is as follows:

$$\begin{cases} \mathrm{HCR} = \dfrac{|P_c|}{\eta} \\ P_c = \{p_i | p_i \in P, p_i H > H_t\} \end{cases}, \quad \begin{cases} \mathrm{SR} = \dfrac{|P_s|}{n} \\ P_s = \{p_s | p_s \in P, p_i V > V_s\} \end{cases}, \quad \begin{cases} p_i \mathrm{VCRate} = \dfrac{|v_{i+1} - v_i|}{v_i} \\ \mathrm{VCR} = \dfrac{|P_v|}{\eta} \\ P_v = \{p_i | p_i \in P, p_i \mathrm{VCRate} > V_c\} \end{cases}. \tag{17}$$

Table 1: GPS data.

Latitude	Longitude	Altitude	Date	Time
38.968014	113.5152364	381	2018-2-23	06 : 23 : 01
38.584079	113.6122363	381	2018-2-23	06 : 23 : 11
38.884063	113.2152367	381	2018-2-23	06 : 23 : 22
38.314064	113.7152364	381	2018-2-23	06 : 23 : 33
38.184051	113.1242356	381	2018-2-23	06 : 23 : 39
39.740946	114.2132236	393	2018-2-23	06 : 23 : 49

Table 2: Distribution of track samples.

Travel mode	Number of trajectory segments	Location prediction accuracy
Walking	1580	87.6%
Bicycle	239	86.4%
Bus	1834	89.9%
Car	2108	76.8%
Subway	3290	96.7%
Train	766	97.9%

3.6. Evaluation Index of Forecast Model

(1) Precision and recall:

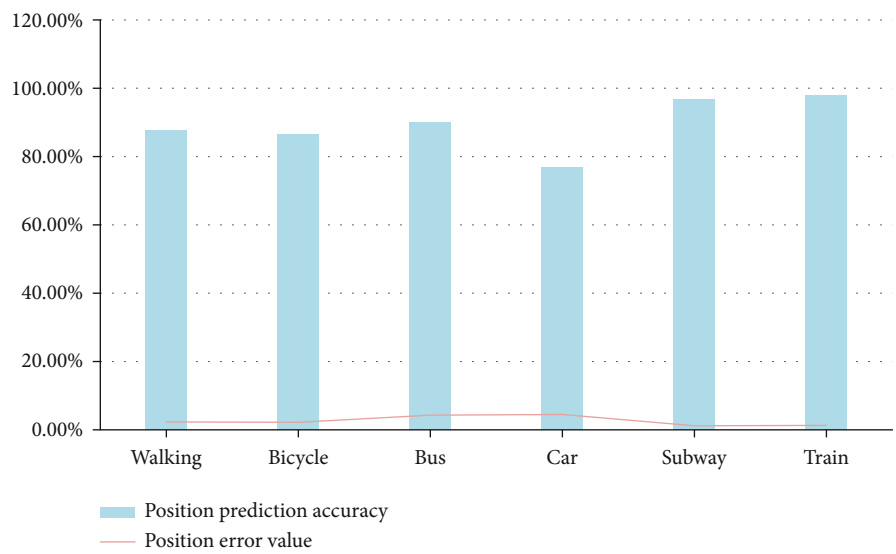

Figure 5: Statistical chart of position prediction accuracy and error.

$$\text{Precision} = \frac{\text{TP}}{\text{TP} + \text{FP}}, \quad \text{Recall} = \frac{\text{TP}}{\text{TP} + \text{FN}} \tag{18}$$

(2) Accuracy:

$$\text{Accuracy} = \frac{\text{TP} + \text{TN}}{\text{TP} + \text{FP} + \text{FN} + \text{TN}} \tag{19}$$

(3) $F1$-score:

$$F\text{-Score} = \frac{(\beta^2 + 1) \times \text{Precision} \times \text{Recall}}{(\beta^2 \times \text{Precision}) + \text{Recall}} \tag{20}$$

(4) The ROC curve takes the rate of false positive cases and the rate of true cases as x-axis and y-axis and selects all the partition thresholds to draw the curve, which plays a great role in dealing with the unbalanced period of model input samples. The calculation formula is as follows:

$$\text{FPR} = \frac{\text{FP}}{\text{FP} + \text{TN}}, \quad \text{TPR} = \frac{\text{TP}}{\text{TP} + \text{FN}} \tag{21}$$

Positive examples of prediction results are expressed by TP and FP, while negative examples are expressed by FN and TN.

Table 3: Data table of different accelerations and velocities.

Travel mode	Velocity (m/s)	Acceleration (m/s^2)
Walking	5	2
Bicycle	12	4
Bus	42	3
Car	55	10
Subway	78	5
Train	82	4.5

4. Experiment

4.1. Data Preprocessing. The original GPS trajectory data will inevitably have abnormal data due to the instability of acquisition equipment and interference during acquisition, so it is necessary to preprocess the original GPS trajectory data. The trajectory preprocessing flow is shown in Figure 4:

The preprocessing of original GPS trajectory data includes trajectory segmentation and screening and data cleaning. The purpose is to remove the interference of abnormal data to feature engineering.

Examples of GPS data: each set of data contains latitude, longitude, and time data, as shown in Table 1:

4.2. Experimental Analysis of the Trajectory of Different Travel Modes. When GPS data is segmented, too few trajectory points mean that the trajectory duration is short, which cannot reflect the user's motion pattern. Different travel modes will affect the accuracy of travel feature calculation and location prediction. Under such trajectory segmentation rules, the sample distribution of trajectory segments is as shown in Table 2:

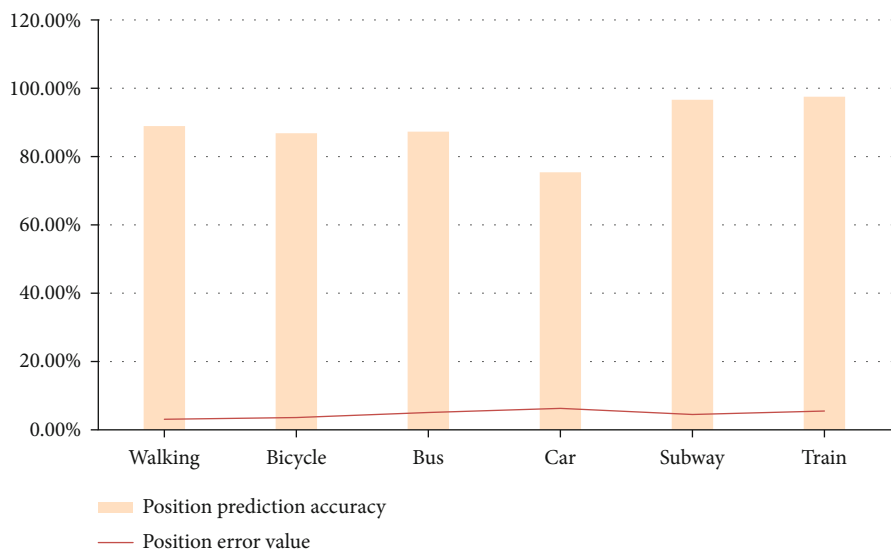

Figure 6: Statistical chart of position prediction accuracy and error.

Table 4: Confusion matrix of random forest classification.

Random forest	Prediction category						Recall
	Walking	Bicycle	Bus	Car	Subway	Train	
Walking	58	0	10	0	0	0	66.8%
Bicycle	6	30	5	0	0	0	
Bus	0	1	16	55	0	2	
Car	12	2	200	10	0	3	
Subway	0	0	0	1	4	1	
Train	1	0	1	1	0	33	
Precision	72.3%						
Accuracy	81.76%						

Table 5: XGBoost classification confusion matrix.

XGBoost	Prediction category						Recall
	Walking	Bicycle	Bus	Car	Subway	Train	
Walking	48	3	5	0	0	0	80.8%
Bicycle	5	33	3	0	0	0	
Bus	1	0	25	55	0	1	
Car	12	1	205	10	0	3	
Subway	1	0	1	1	2	1	
Train	0	0	1	1	4	29	
Precision	80.13%						
Accuracy	82.66%						

Table 6: CatBoost classification confusion matrix.

CatBoost	Prediction category						Recall
	Walking	Bicycle	Bus	Car	Subway	Train	
Walking	60	1	9	1	0	0	79.89%
Bicycle	5	34	6	1	0	0	
Bus	0	0	19	55	0	1	
Car	13	5	180	12	2	0	
Subway	0	0	1	1	2	1	
Train	1	1	2	1	0	28	
Precision	79.13%						
Accuracy	81.96%						

Table 7: Classification confusion matrix of improved deep forest algorithm.

CatBoost	Prediction category						Recall
	Walking	Bicycle	Bus	Car	Subway	Train	
Walking	60	1	9	1	1	1	83.87%
Bicycle	8	32	6	1	1	0	
Bus	0	1	19	55	1	1	
Car	11	3	205	12	2	2	
Subway	0	0	0	0	2	1	
Train	1	1	1	1	1	26	
Precision	85.13%						
Accuracy	86.96%						

The statistics of positioning prediction accuracy and position error based on the above table data are shown in Figure 5.

The influence of different speed and acceleration values of vehicles on positioning prediction values is shown in Table 3:

According to the different speeds and accelerations of different vehicles, the prediction accuracy and prediction error of the prediction model are shown in Figure 6:

4.3. Experimental Results. Based on the classification result confusion matrix of random forest intelligence algorithm,

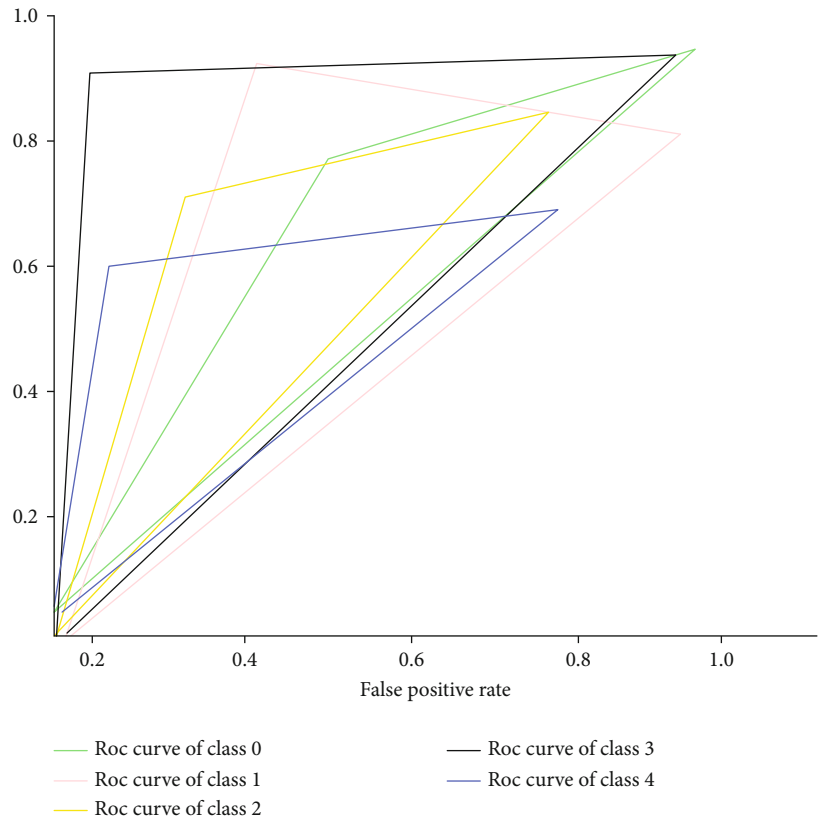

Figure 7: Random forest ROC curve.

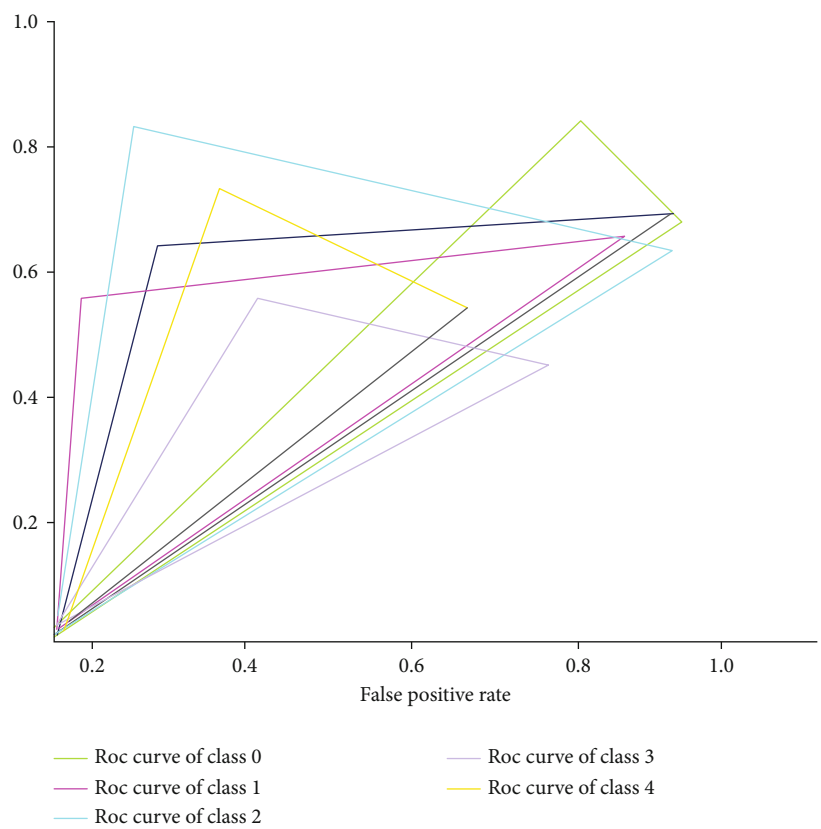

Figure 8: XGBoost ROC curve.

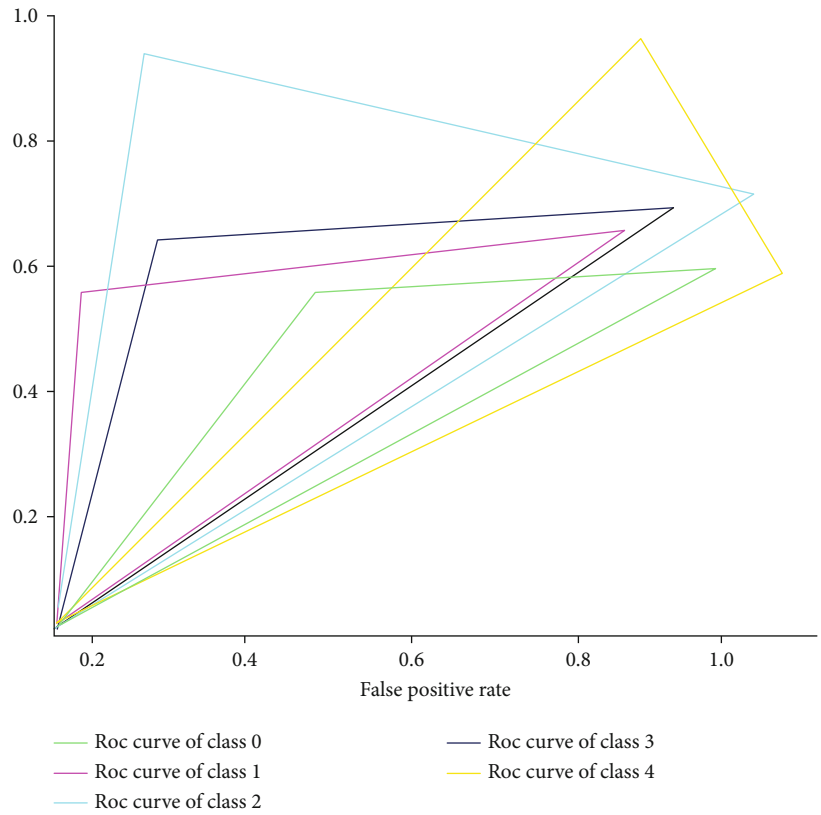

Figure 9: CatBoost ROC curve.

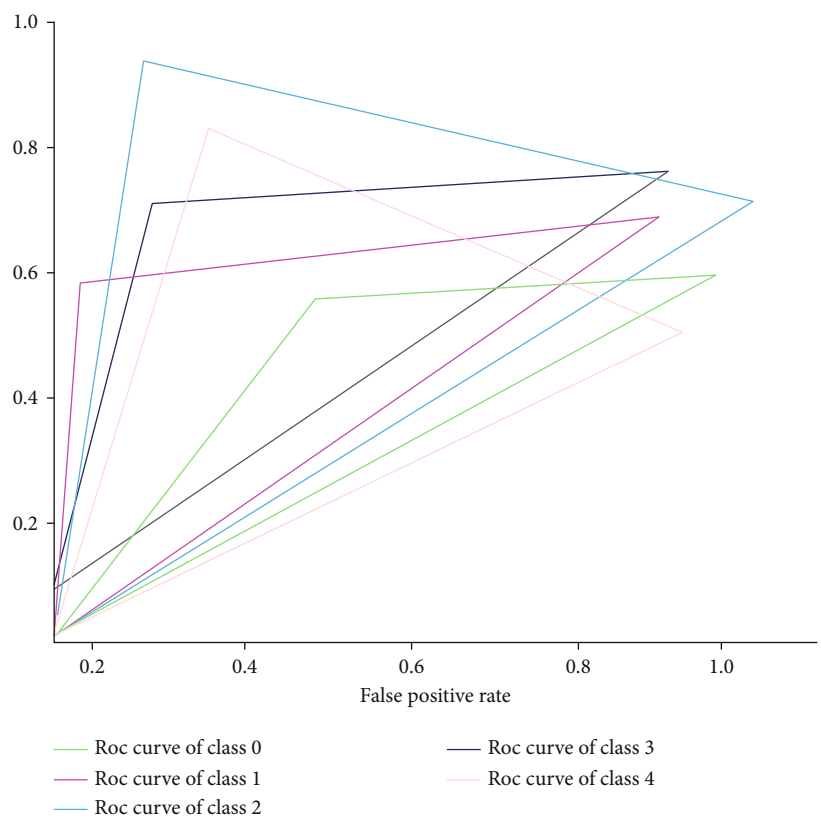

Figure 10: Improved deep forest ROC curve.

Table 8: Index comparison table.

	Accuracy	Precision	Recall	$F1$	AUC
Random forest	0.79	0.84	0.87	0.85	0.75
CatBoost	0.84	0.85	0.921	0.802	0.793
XGBoost	0.84	0.85	0.924	0.808	0.799
Improved deep forest	0.87	0.88	0.95	0.91	0.82

XGBoost algorithm, CatBoost, and improved deep forest algorithm, the positioning prediction results are as follows: Tables 4–7:

From the data in the above table, it can be seen that the comprehensive recognition performance of the improved deep forest is better than the three basic classifiers in the improved forest, because the deep forest structure combines Bagging and Boosting ideas to process feature vectors and optimize the training process.

4.4. Model Comparison. Comparison of ROC values of each class of four models: random forest intelligent algorithm, XGBoost algorithm, CatBoost, and improved deep forest algorithm, as shown in Figures 7–10:

The area of the lower area corresponding to each classification category in the above figure, that is, area, represents the AUC value of the model. The larger the area, the better the comprehensive recognition effect of the model; otherwise, the effect is the worst.

4.5. Contrast Experiment. Compare the four algorithms comprehensively, as shown in Table 8:

From the F1 value in the table, we can find that the improved deep forest model has the best performance; the algorithm and model proposed in this paper are effective and can provide high-accuracy recognition results as the trajectory classification basis of the position prediction model.

5. Conclusion

The rapid development and popularization of mobile Internet and positioning algorithm, artificial intelligence-led technologies, and applications are changing people's lives. Among them, location prediction is an important part of location-based service, and the research results of this paper are effective for GPS trajectory prediction, as follows:

(1) A series of preprocessing methods are used to solve the problem of abnormal data sum of the original GPS trajectory data due to the instability of acquisition equipment and interference during acquisition

(2) The travel mode is one of the final factors that affect the location prediction results. The improved travel mode of deep forest recognition users is used as an assistant to the location prediction task to improve the accuracy of the location prediction model

(3) By comparing the ROC curves of random forest intelligence algorithm, XGBoost algorithm, CatBoost, and improved deep forest, it is found that the improved deep forest intelligence algorithm has the largest area under ROC curve, that is, the largest AUC value, and the better the model effect

(4) In the contrast experiment, the comprehensive comparison of five indexes of four intelligent algorithms is carried out, and it is further known that the improved intelligent algorithm for deep forest has the highest prediction efficiency

Data Availability

The experimental data used to support the findings of this study are available from the corresponding author upon request.

Conflicts of Interest

The author declared that he/she has no conflicts of interest regarding this work.

References

[1] X. Qi, W. Huabin, Z. Jian, and T. Liang, "Intelligent swarm optimization filtering algorithm for target tracking," *Journal of Intelligent Systems*, vol. 14, no. 4, pp. 697–707, 2019.

[2] S. R. Pratap, A. Haleem, M. Javaid, R. Kataria, and S. Singhal, "Cloud computing in solving problems of COVID-19 pPandemic," *Journal of Industrial Integration and Management*, vol. 6, no. 2, pp. 209–219, 2021.

[3] L. Haichuan, "Research on real-time borehole trajectory analysis and collision risk assessment technology," *China Petroleum and Chemical Standards and Quality*, vol. 41, no. 24, pp. 1–3, 2021.

[4] Z. Xia and H. Yu, "Analysis of entrance space of Wuhan University based on behavior track," *Huazhong Architecture*, vol. 39, no. 11, pp. 92–98, 2021.

[5] N. Ho and K. JooSung, "Vessel trajectory analysis in designated harbor route considering the influence of external forces," *Journal of Marine Science and Engineering*, vol. 8, no. 11, pp. 860–860, 2020.

[6] X. Xianwei, "Research progress of ocean transport ship trajectory analysis," *Ship Materials and Market*, vol. 29, no. 6, pp. 5-6, 2021.

[7] M. Jiaxing, Q. Ronghui, T. Haishan, and Y. Hang, "Flight trajectory analysis of stratospheric airship based on ion wind power propulsion system," *Acta Astronautica Sinica*, vol. 42, no. 5, pp. 642–649, 2021.

[8] Z. Fulong, "Research on abnormal trajectory analysis method based on underground personnel," *Computer Knowledge and Technology*, vol. 17, no. 9, 2021.

[9] G. Hui, L. Dezhi, Y. Yin, and Y. Gending, "Trajectory analysis of drivers entering and leaving tractors based on RAMSIS," *Tractors and Agricultural Transport Vehicles*, vol. 47, no. 6, pp. 37–41, 2020.

[10] Z. Hai, C. Yaojie, and C. Li, "Cluster analysis and application of ship trajectory," *Simulation*, vol. 37, no. 10, 2020.

[11] Z. Bingyan, L. Weijun, and C. Zonghua, "Flight path analysis of rotating oblique throwing ball under wind speed," *Journal of Yulin Normal University*, vol. 41, no. 3, pp. 36–42, 2020.

[12] L. Changsheng, "Discussion on data mining algorithm for vehicle trajectory analysis," *Journal of Changsha Aviation Vocational and Technical College*, vol. 18, no. 4, pp. 60–63, 2018.

[13] Y. Kai, Q. Hang, C. Donghong, Z. Wei, and C. Xiai, "Track analysis of smart car based on SD card," *Science and Technology Information*, vol. 16, no. 16, pp. 13–15, 2018.

[14] S. Feifan, S. Zhihuan, and G. Zhiqiang, "Process fault detection method based on multivariate trajectory analysis," *Journal of Xi'an Jiaotong University*, vol. 51, no. 3, pp. 122–128, 2017.

[15] G. Caiyun, "Analysis of projectile trajectory based on Matlab," *Journal of Datong University*, vol. 31, no. 5, pp. 28–30, 2015.

[16] "Detection of heart disorders using an advanced intelligent swarm algorithm," *Intelligent Automation & Soft Computing*, vol. 23, no. 3, pp. 419–424, 2017.

[17] L. Ling, "Research and prospect of train swarm intelligent control technology based on virtual coupling," *Railway Communication Signal Engineering Technology*, vol. 17, no. 2, pp. 1–9, 2020.

[18] Z. Wenqing, Z. Jihong, and K. Minchi, "An unmanned air combat system based on swarm intelligence," *Science of China: Information Science*, vol. 50, no. 3, pp. 363–374, 2020.

[19] S. Y. Jiang Zhaochang and D. Kaimeng, "Research progress of multidisciplinary methods of swarm intelligent computing," *Computer and Digital Engineering*, vol. 47, no. 12, pp. 3053–3058, 2019.

[20] B. Anari, J. A. Torkestani, and A. M. Rahmani, "A learning automata-based clustering algorithm using ant swarm intelligence," *Expert Systems*, vol. 35, no. 6, 2018.

[21] W. Zongzhuo, "Research on the superiority of swarm intelligence algorithm in the era of big data," *Wireless Internet Technology*, vol. 16, no. 2, pp. 110-111, 2019.

[22] C. Shi, W. Rui Wang, G. Y. Guohua, M. Lianbo, and S. Yuhui, "Swarm intelligence optimization algorithm," *Journal of Zhengzhou University (Engineering Edition)*, vol. 39, no. 6, pp. 1-2, 2018.

[23] G. Zhang, Y. Chen, Y. Li, H. Yu, o. Hu, and S. Wu, "Intelligent swarm firefly algorithm for the prediction of China's national electricity consumption," *International Journal of Bio-Inspired Computation*, vol. 13, no. 2, pp. 111–118, 2019.

[24] F. Juanyan, W. Yanting, and W. Changcheng, "Analysis of swarm intelligence algorithm for engineering structure optimization," *Journal of Huzhou Normal University*, vol. 38, no. 10, pp. 54–57, 2016.

[25] Y. Li, "Optimization of multi-objective virtual machine based on ant colony intelligent algorithm," *International Journal of Performability Engineering*, vol. 15, no. 9, pp. 2494–2503, 2019.

Hindawi
Journal of Sensors
Volume 2022, Article ID 4437446, 10 pages
https://doi.org/10.1155/2022/4437446

Research Article

A Deep Neural Network Based on Circular Representation for Target Detection

Cong Lin,[1] Zhoujian Chen,[1] Yiquan Huang,[1] Haoyu Jiang,[1] Wencai Du,[2] and Qiong Chen[3]

[1]*College of Electronics and Information Engineering, Guangdong Ocean University, Zhanjiang 524025, China*
[2]*Institute of Data Engineering and Sciences, University of Saint Joseph, Macao, China*
[3]*Department of Earth System Science, Ministry of Education Key Laboratory for Earth System Modeling, Institute for Global Change Studies, Tsinghua University, Beijing 100084, China*

Correspondence should be addressed to Wencai Du; george.du@usj.edu.mo and Qiong Chen; qiongchen@mail.tsinghua.edu.cn

Received 26 January 2022; Revised 28 February 2022; Accepted 30 March 2022; Published 25 April 2022

Academic Editor: Waliullah Khan

Convolutional neural network (CNN) model based on deep learning has excellent performance for target detection. However, the detection effect is poor when the object is circular or tubular because most of the existing object detection methods are based on the traditional rectangular box to detect and recognize objects. To solve the problem, we propose the circular representation structure and RepVGG module on the basis of CenterNet and expand the network prediction structure, thus proposing a high-precision and high-efficiency lightweight circular object detection method RebarDet. Specifically, circular tubular type objects will be optimized by replacing the traditional rectangular box with a circular box. Second, we improve the resolution of the network feature map and the upper limit of the number of objects detected in a single detect to achieve the expansion of the network prediction structure, optimized for the dense phenomenon that often occurs in circular tubular objects. Finally, the multibranch topology of RepVGG is introduced to sum the feature information extracted by different convolution modules, which improves the ability of the convolution module to extract information. We conducted extensive experiments on rebar datasets and used AB-Score as a new evaluation method to evaluate RebarDet. The experimental results show that RebarDet can achieve a detection accuracy of up to 0.8114 and a model inference speed of 6.9 fps while maintaining a moderate amount of parameters, which is superior to other mainstream object detection models and verifies the effectiveness of our proposed method. At the same time, RebarDet's high precision detection of round tubular objects facilitates enterprise intelligent manufacturing processes.

1. Introduction

The detection and recognition of circular tubular objects are always a basic problem and difficult problem in image processing. Circular tubular objects are common in the production practice of traditional manufacturing, so the intelligent detection of circular tubular objects is also an important part of the process of enterprise intelligence. Many traditional feature-based images processing methods had been proposed for detection of circular tubular objects, such as Genetic algorithms [1, 2], Gradient pair vectors [3], and Hough transform filters [4–6]. Such methods have low detection accuracy and strongly rely on "hand-crafted" features from feature engineering, which have great limitations.

In recent years, data-driven deep learning technology has shown superior performance in the field of artificial intelligence, and convolutional neural network is one of the most popular deep learning structures [7, 8]. In the field of computer vision, detection methods based on convolutional neural networks have made great breakthroughs in many fields, such as image classification [9], target detection [10, 11], semantic segmentation [12], instance segmentation [13], and gesture recognition [14]. In 2012, Krizhevsky et al. constructed an 8-layer convolutional neural network

AlexNet [15]. AlexNet used ReLU as the activation function of CNN for the first time, successfully solving the problem of gradient diffusion of Sigmoid when the network was deep and applied Dropout in the network to randomly ignore some neurons to avoid model overfitting. Since then, more and more neural network models have been proposed. The VGG (Visual Geometry Group) [16] network designed by Simonyan and Zisserman mainly improved network performance by increasing the depth of the network. The convolutional layer of the network uses a 3×3 small-size convolution kernel. Compared with a large-size convolutional layer, a small-size convolutional layer has fewer parameters and can increase the nonlinearity of the mapping function. With the deepening of network layer, the VGG network reaches a performance bottleneck at the 16th layer and then tends to be saturated. Increasing the depth of the neural network like VGG can improve the performance of the network to a certain extent, but this approach has two bottlenecks. On the one hand, the deeper the network structure needs to learn more parameters, making the network easy to overfit. On the other hand, the network with more layers requires more computing resources. The GoogLeNet [17] network model developed and designed by Szegedy et al. used a novel inception structure as the basic module for cascading, and the network reaches a depth of 22 layers. Inception uses 3 convolution kernels of different sizes to extract feature information of different scales from the previous input layer. The 1×1 convolution kernel is used to reduce the data dimension of the previous layer and the amount of convolution calculations for the subsequent 3×3 and 5×5 convolutional layers to greatly reduce network parameters while increasing the depth of the network and make full use of computing resources to improve the computational efficiency of the algorithm. Although methods such as ReLU and batch normalization can solve the gradient disappearance or explosion of deep neural networks to a certain extent, the problem of gradient disappearance or explosion is still very serious when training a very deep network. In 2015, He et al. proposed a 152-layer residual networks (ResNet) [18], which added shortcut connections when constructing the network, so that the output of subsequent layers was not the input mapping in the traditional neural network, but the input mapping and the superposition of the input, which solves the problem of the disappearance or explosion of the gradient of the deep neural network training. This type of detection method based on deep learning technology has high accuracy, strong model robustness, and strong transferability, but it also has the disadvantage of slow inference speed due to the large model. At the same time, most of these detection methods are based on the traditional rectangular box to detect and recognize objects, so they are not optimized for circular or tubular objects, resulting in poor recognition and detection of such objects.

The detection and recognition of circular tubular objects are a basic problem in the field of image processing. Zelniker et al. [19] used a maximum likelihood estimation method based on convolutional neural network to better estimate the circular parameters of the center and radius of the circle in digital images as a method of circular object detection. Ayala-Ramirez et al. [20] propose a circle detection method based on genetic algorithm (GA), which can detect subpixel circles in composite images, but this method has poor performance in dealing with small circle targets. Yang et al. propose a circular object detection algorithm based on convolutional neural network in CircleNet [21], which is used to identify and detect the glomeruli of spherical biomedical objects. CircleNet improves the network's detection accuracy of circular tubular objects to a certain extent by adding a circular detection head to the network, but this model also has the problems of high model complexity and low detection efficiency. Because circular tubular objects often appear in a large number of clusters, another difficulty in detecting and identifying circular tubular objects is dense scene detection. Recognition and detection of objects in dense scenes are a difficult problem in the field of object detection. There are roughly two reasons. One is that highly overlapping instances are likely to have very similar features, making it difficult for the detector to generate distinguishable prediction results for each instance; the other is that there is a serious overlap between instances, and the prediction results may be incorrectly suppressed by NMS. For these reasons, mainstream algorithms in the object detection field, such as R-CNN [22–24], YOLO [25–27], and SSD [28], have poor detection effects in dense scenes.

In order to solve the above problems, based on the network architecture of object detection algorithm CenterNet [29], combining with the characteristics of circular tubular type image and the particularity of circular tubular object detection, we design a high-precision and high-efficiency lightweight circular object detection method RebarDet. First, a circular representation structure is introduced on the basis of the CenterNet network architecture, and a circular box representation is used to replace the traditional rectangular box representation. The circular box representation is optimized for the spherical shape of the circular tubular target and has better rotation consistency than the rectangular box representation. At the same time, the parameter amount of detection representation is reduced from 4 to 3 to improve the detection effect of the network while reducing the model parameters. Then, we expand the prediction structure of the CenterNet network. The specific method is to increase the resolution of the network feature map and the upper limit of the number of single detection objects in the network and optimize for the dense phenomenon of circular tubular object detection. In addition, by combining the advantages of RepVGG [30] block in information fusion and information extraction, we introduce RepVGG block into the CenterNet network structure, which reduces the amount of model calculation and improves the feature extraction capability of the network. Combining the above improvements, we obtain our work RebarDet, a high-precision and high-efficiency lightweight circular object detection method. Based on the rebar dataset provided by Glodon, extensive experiments have been done to verify the performance of RebarDet in the rebar detection environment. The experimental results show that our work has brought about a significant improvement in detection performance. We also compare with the current mainstream target detection network on the three

performance indicators of AB-Score, inference speed, and parameter quantity. The experimental results show that the accuracy and inference speed of our proposed RebarDet exceed the existing mainstream object detectors when the parameters are moderate.

In general, the main contributions of this work are as follows:

(1) The circular representation structure is introduced on the basis of the CenterNet network structure, and the spherical shape of the circular tubular object is optimized to improve the detection effect of the network while reducing the model parameters

(2) Improve the resolution of the network feature map and the upper limit of the number of single detection objects in the network, expand the prediction structure of the CenterNet network, and optimize the dense phenomenon of circular tubular object detection

(3) By combining the advantages of RepVGG block in information fusion and information extraction, the RepVGG block is introduced into the CenterNet network structure, which reduces the amount of model calculation and improves the feature extraction ability of the network

(4) The proposed work RebarDet under the condition of moderate parameter quantity, the accuracy and inference speed are both higher than the existing mainstream object detectors, and it reaches 0.8114 AB-Score and 6.9 fps on the rebar dataset provided by Glodon, significantly better than mainstream object detection models

2. Methods

This work follows the general process of key point detection. Suppose the input image is $I \in R^{W\times H\times 3}$, where W and H are the width and height of the image, respectively. In the prediction phase, the network generates a heat map of key points as $\hat{Y} \in [0,1]^{W/R\times H/R\times C}$, where R is the step size corresponding to the original image, and C corresponds to the number of detection points in the object detection. For example, in the COCO [31] object detection task, the value of C is 80, representing 80 categories. In this way, $\hat{Y}_{x,y,c} = 1$ represents a predicted value of a detected object, indicating that for category c, an object of this category is detected at the current coordinate (x, y), and $\hat{Y}_{x,y,c} = 0$ indicates that there is no object of category c at the current (x, y) coordinate. For a certain C category in each label map, calculate the real key point $p \in R^2$ in it for training, the calculation method of the center point is

$$p = \left(\frac{x_1 + x_2}{2}, \frac{y_1 + y_2}{2}\right), \tag{1}$$

and the coordinate after downsampling is set to $\tilde{p} = [p/R]$, where R is the downsampling factor 4, so the final calculated center point is the center point corresponding to the low resolution. Next, use $Y \in [0,1]^{W/R\times H/R\times C}$ to mark the image, and use a Gaussian kernel:

$$Y_{xyc} = \exp\left(-\frac{(x-\tilde{p}_x)^2 + \left(y-\tilde{p}_y\right)^2}{2\sigma_p^2}\right), \tag{2}$$

to distribute the key points on the feature map in the form of markers in the downsampled image, where σ_p is a standard deviation related to the object size w and h. In the whole process, if two Gaussian distributions of a certain class overlap, the one with the larger element is directly selected.

2.1. Overview. Figure 1 shows the overall network structure of RebarDet. We introduce the circular representation structure and RepVGG module into the network and expand the network prediction structure. Compared with the usual object detection backbone networks such as VGG and ResNet, the Hourglass [32] is better used as the feature extraction network of the model. Because compared to other backbone networks, Hourglass is more conducive to key point detection. The Hourglass network structure includes convolutional layers, deconvolutional layers, fully connected layers, etc., repeatedly using top-down and bottom-up methods, and continuously encoding and decoding to infer the location of detection points. The overall network structure is stacked with submodules and subnetworks. It is constructed in such a way that Hourglass has a high degree of flexibility while having a complex structure and has an excellent performance in describing complex features. The repeated encoding and decoding operations of the network make the network has stronger presentation ability and can better mix global and local information. Compared with other object detection networks, the advantage of using the Hourglass network is that the feature points of the object may appear in different layers of the network, and the final feature map of Hourglass can better detect all the key points of the object. We introduced the RepVGG module at the beginning of the network. After the input image enters the network, it first passes through two RepVGG modules for feature extraction. The multibranch topology of RepVGG will sum up the information extracted by different convolution modules, improve the ability of the shallow network to extract image features, reduce the loss of image details, and be more conducive to the subsequent deep network to extract high-level semantic information of the image. Then, the image passes through the residual module of the network and is downsampled, where RebarDet reduces the original two residual modules to one residual module, and the number of downsampling is also reduced from 2 to 1, which increases the resolution of subsequent feature maps and is more conducive to the detection of dense objects by the network. Then, the image enters the Hourglass backbone network for feature extraction, and the extracted key point feature information is input to the final circular detection head. As can be seen from Figure 1, the network has three detection heads: heat map head, local offset head, and circle

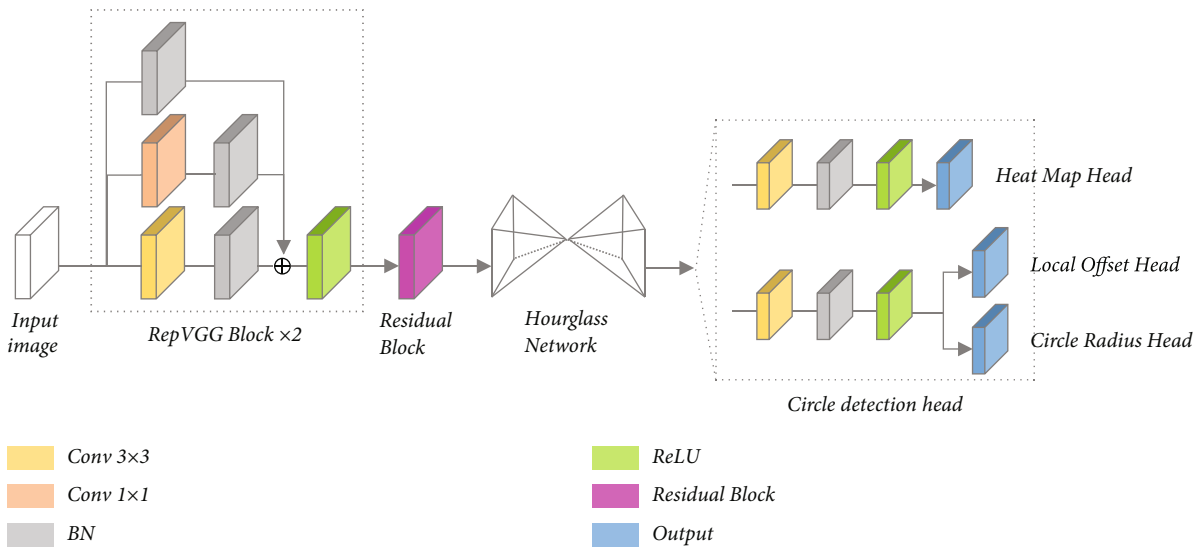

Figure 1: The overall network structure of RebarDet. We introduce the RepVGG module and circular detection head on the basis of CenterNet and expanded the network prediction structure.

radius head, which, respectively, detect the object category, center point coordinates, and radius to complete the recognition and detection of circular objects.

2.2. Circle Representation. Existing detectors in the field of object detection, such as Faster R-CNN, YOLO, SSD, etc., generally use rectangular boxes parallel to the horizontal axis to represent the object of network prediction and recognition. Comprehensive considerations are given to the best fitting effect of rectangular boxes for most objects. However, the fitting effect of rectangular boxes is poor in some specific scenes, such as the recognition task of circular tubular objects. As shown in Figure 2(a), the detection effect of using a rectangular box to fit the rebar object is not very good, and the number of missed detections is 5. The reason for the poor performance of rectangular box in circular tubular object recognition task may be that the cross-section of circular tubular object is round, and the distribution of circular tubular object is mostly dense, so it is difficult to fit rectangular box. RebarDet introduces a circular representation structure, using a circular box instead of a traditional rectangular box, to optimize for the spherical shape of a circular tubular object. Specifically, we build a circular detection head to enable the convolutional neural network to predict the regression of the center point (px, py) and the radius r of the circular box and finally obtain the circular representation of the recognition object. As shown in Figure 1, the network uses heat map head ($H \times W \times C$), local offset head ($H \times W \times 2$), and circle radius head ($H \times W \times 1$) to complete the identification and detection of circular objects. Figure 2 (b) is the detection effect of the rebar object after applying the circular box. It can be seen that the detection effect of the circular box on the rebar object is better than that of the rectangular box, which can achieve the industrial accuracy of zero missed detection. Figure 3 is the experimental comparison of the rotation consistency of the rectangular box and the circular box. After the original image is rotated by 90 degrees for the rectangular box, the number of missed objects increases significantly, while the circular box only has 2 missed objects after the original image is rotated. The above experimental results show that the circular box has better rotation consistency than the rectangular box.

2.3. Expansion of Prediction Structure. The CenterNet proposed by Zhou et al. have a shortcoming in actual training, that is, if the center points of multiple objects of the same category in the image overlap when the network is sampled, CenterNet is also powerless for this situation, because there is only one center point, so these two objects can only be trained as one object. For the detection of circular tubular objects, the distribution of circular tubular objects is dense and compact in most cases, so the overlapping phenomenon of object centers is more serious. To alleviate this phenomenon, we expand the prediction structure of the network in RebarDet. Specifically, we increase the resolution of the feature map before the Hourglass subnetwork, so that the network can detect the center point of the object at a larger feature map level, which can reduce the overlap of the object center point. As shown in Figure 4(a), the size of the feature map has been increased from the original 128×128 to 256×256. Figure 4(b) is a simplified schematic diagram of the object detection effect after the feature map is enlarged. It can be seen that compared to the small feature map, the large feature map can divide the object to be detected more dispersed, improve the detection ability of the network in dense scenes, and reduce the risk of missed detection. In addition, we expand the upper limit of the number of objects that the network can detect at a time from 128 to 256, which makes the network perform better in dense multitarget recognition scenarios.

2.4. RepVGG Block. The architecture of RepVGG is very simple and effective, which is equivalent to adding identity and residual branches to the block of the VGG network.

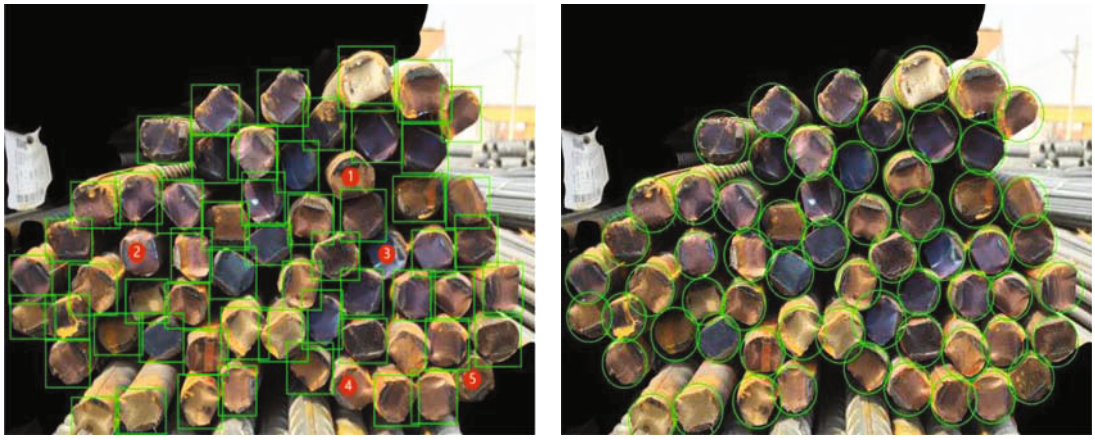

(a) (b)

Figure 2: The actual effect of RebarDet under the background of rebar detection, (a) is the detection effect of the rectangular box with the number of missed detection being 5, and (b) is the detection effect of the circular box, achieving zero missed detection.

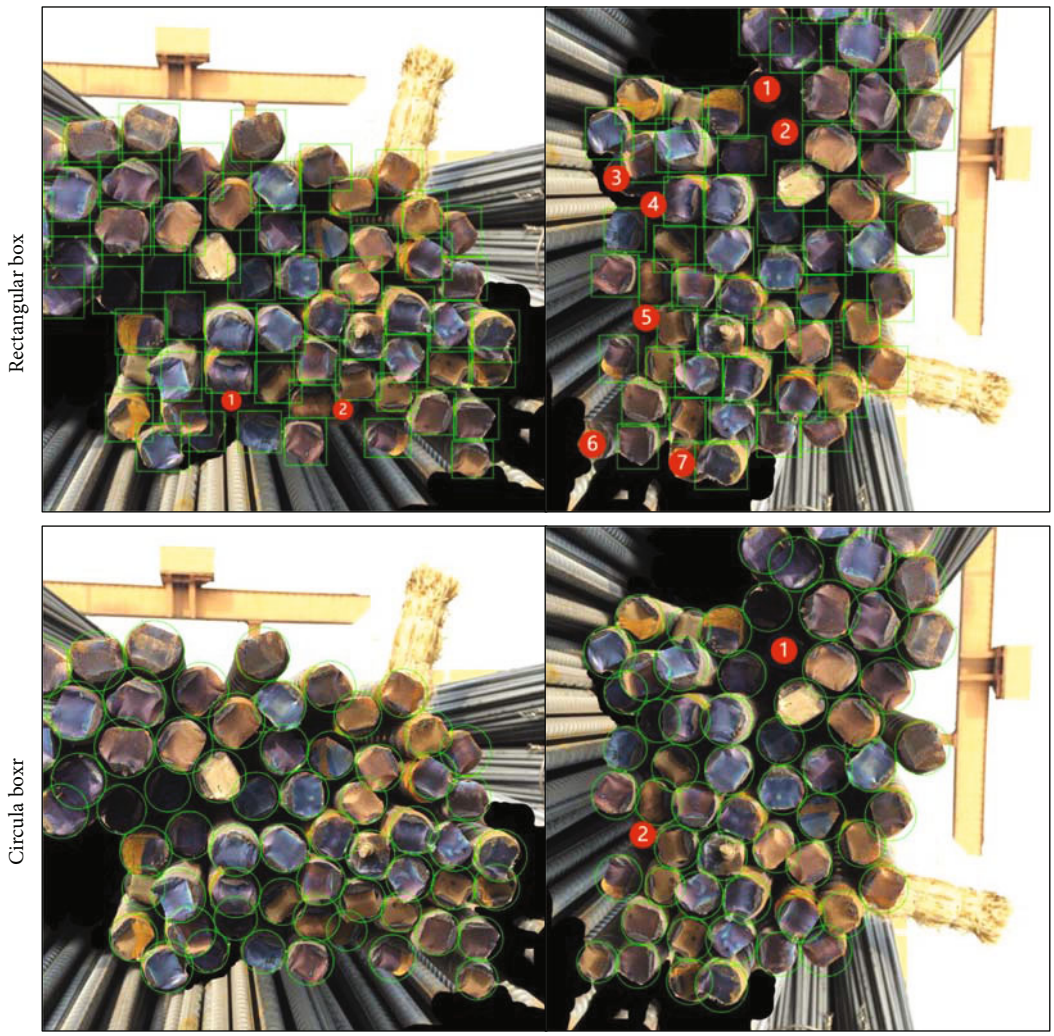

Original Rotate 90°

Figure 3: Experimental comparison of the rotation consistency between the rectangular box and the circular box.

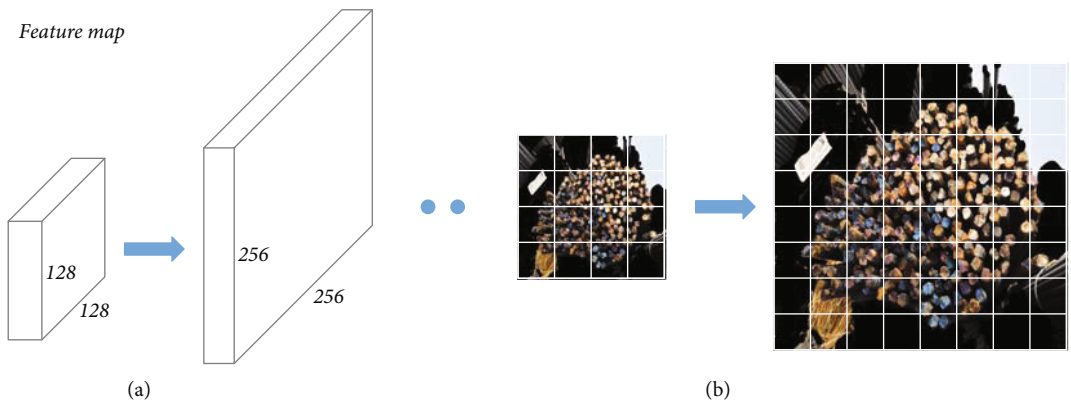

Figure 4: (a) is a schematic diagram of the enlarged network feature map, and (b) is a schematic diagram of the effect. For the purpose of simplification and easy observation, in (b) the schematic diagram of the effect is simplified from 128- >256 to 4- >8.

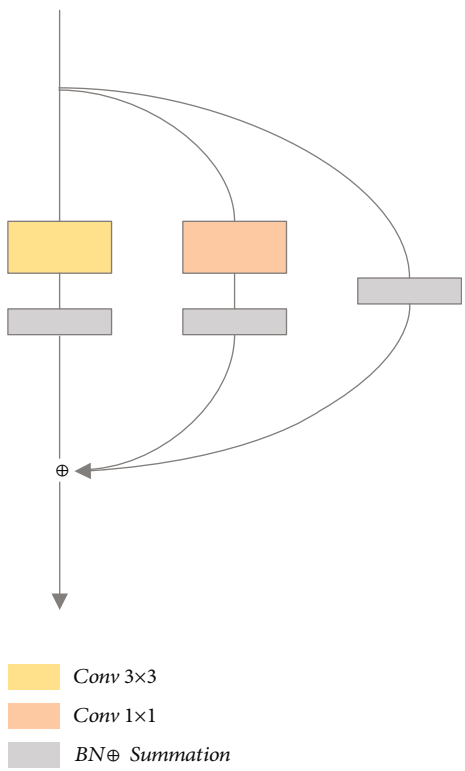

Figure 5: Schematic diagram of the RepVGG block structure, a 1 × 1 convolution (additional BN layer) and a BN layer are connected in parallel on both sides of the 3 × 3 convolution (additional BN layer), then, the sum operation is performed.

Table 1: The score table of part B of AB-score. If the predicted number is completely correct, the score is 1. If the predicted number differs by 1, the score is 0.5. If the predicted number differs by 2, the score is 0.1. In other cases, the score is 0.

Number deviation range	Score (task B)
0	1
±1	0.5
±2	0.1
Other	0

The entire network is only composed of 3 × 3 convolution, BN layer, and ReLU modules. Figure 5 is a schematic diagram of the structure of RepVGG block. In the training phase, RepVGG has a multibranch topology in which 1 × 1 convolution (additional BN layer) and BN layer are connected in parallel on both sides of 3 × 3 convolution (additional BN layer). This structure sums up the feature information extracted by different convolution modules, which can improve the information extraction ability of a single convolution module. Considering that the shallow convolution of the network is responsible for extracting low-level semantic features, and the information richness of this part of the low-level semantic features directly determines the effectiveness of the high-level semantic features of the subsequent convolutional layer, so we set the first two layers of the backbone network as RepVGG block. The feature of multiple modules in parallel is utilized to improve the information extraction ability of the network's shallow convolution and improve the feature extraction ability of the whole network while reducing the amount of model calculation [33]. Regarding the number of RepVGG blocks and the number of channels, we discuss in Section 3.3.3 and obtain experimental results.

3. Experiments

3.1. Rebar Dataset. To verify the effectiveness of RebarDet on circular tubular object detection, we evaluate RebarDet in the context of rebar detection. All experiments in this paper are based on the rebar dataset released by Glodon on the DataFountain platform in 2019, which is also the only open-source rebar dataset so far. The dataset contains a total of 250 cross-sectional images of rebars and provides rectangular box annotations for object detection task training. Among them, 24,442 rebar samples in 200 rebar images are used as training data, and 6,499 rebar samples in 50 rebar images are used as test data. Eventually, we formed a cohort with 200 training and 50 testing images.

3.2. Score Metrics. In the rebar quantity counting competition published by Glodon on the DataFountain platform, the competition uses $F1$-score as the scoring algorithm.

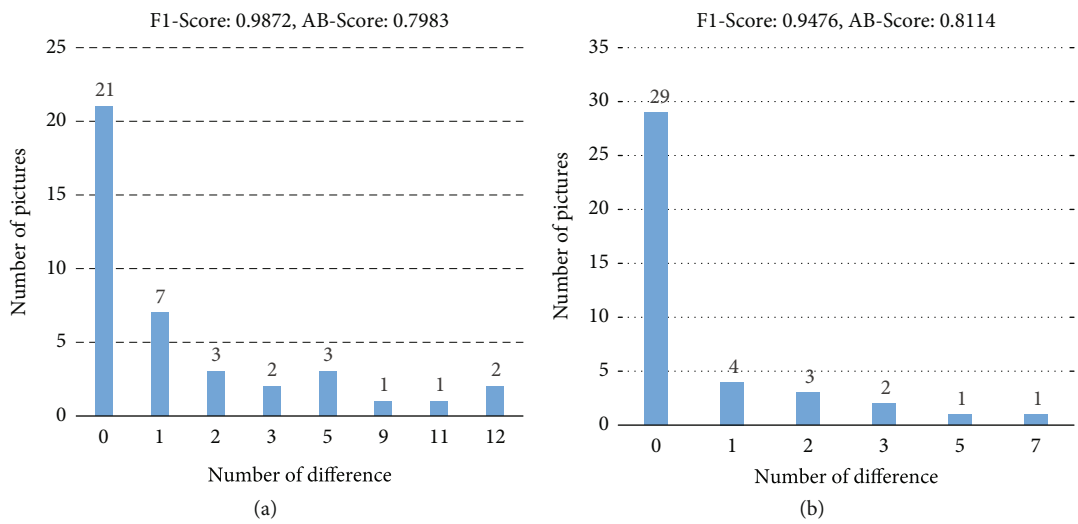

Figure 6: Statistics of the test results of the trained RebarDet model in 40 rebar pictures, the abscissa is the difference between the predicted results and the real results, and the ordinate is the number of predicted pictures. (a) is the statistical chart of the test results of the RebarDet model with $F1$-score of 0.9872 and AB-score of 0.7983, (b) is the statistical chart of the test results of the RebarDet model with $F1$-score of 0.9476 and AB-score of 0.8114.

Table 2: RebarDet ablation experiment results table.

Component	RebarDet				
Circle representation	√	√	√	√	
Expansion of prediction structure					
Max objects	√	√	√		
Feature map resolution	√	√			
RepVGG block	√				
AB-score	0.8114	0.7751	0.7568	0.6984	0.4631

However, $F1$-score is actually a measure of classification problems, and it is not necessarily suitable for counting problems such as rebar counting. In our research, it is found that the model with high $F1$-score is not effective in the actual rebar counting detection on the construction site. So in this paper, we use the scoring algorithm AB-score of a counting competition on iFLYTEK OPEN PLATFORM to evaluate RebarDet. AB-score consists of two parts, A and B. Part A is the mAP value with IoU equal to 0.5. For part B, as shown in Table 1, different scores are assigned to different counting results obtained from a single picture. If the predicted number is completely correct, the score is 1. If the predicted number differs by 1, the score is 0.5. If the difference is 2, the score is 0.1. Otherwise, the score is 0. The final score in part B is the mean of all the image scores. The final score of AB-score is as follows:

$$\text{AB-Score} = A * 0.4 + B * 0.6. \tag{3}$$

Figure 6 is a comparison chart of the detection effect of the trained circular tubular object detection model on the test set. The abscissa is the difference between the predicted result and the real result, and the ordinate is the number of predicted pictures. The $F1$-score and AB-score of the model in Figure 6(a) are 0.9872 and 0.7983, and the $F1$-score and AB-score of the model in Figure 6(b) are 0.9476 and 0.8114. It can be seen from the figure that the number of pictures that are completely predicted correctly by the latter is more than that of the former, and the error in a smaller range is also better than that of the former. This shows that the model with high $F1$-score is not as effective as the model with high AB-score in the actual test, indicating that AB-score is more suitable for the detection task of circular tubular objects.

3.3. Loss Function. The loss function of network training follows CenterNet and consists of three parts: L_k, L_{radius}, and L_{off}. The predicted heat map is optimized by pixel regression loss L_k with focal loss:

$$L_k = \frac{-1}{N}\sum_{xyc}\begin{cases}\left(1-\hat{Y}_{xyc}\right)^{\alpha}\log\left(\hat{Y}_{xyc}\right) & \text{if } Y_{xyc}=1,\\ \left(1-\hat{Y}_{xyc}\right)^{\beta}\left(\hat{Y}_{xyc}\right)^{\alpha}\log\left(1-\hat{Y}_{xyc}\right) & \text{otherwise,}\end{cases} \tag{4}$$

where α and β are the hyperparameters of the focal loss, and N is the number of keypoints in the image I. The radius of the circular box is optimized with L_{radius}:

$$L_{\text{radius}} = \frac{1}{N}\sum_{k=1}^{N}\left|\hat{R}_{pk} - r_k\right|, \tag{5}$$

where r_k is the true radius of each circular object k. CenterNet performs an $R = 4$ downsampling operation on the image in the network. When the feature map is remapped to the original image, it will cause an accuracy error. Therefore, an additional local offset: $\hat{O} \in R^{W/R\times H/R\times 2}$ is used for

Table 3: The experimental result table of the number of RepVGG Blocks and the number of channels. Using two RepVGG blocks and the number of channels of 128, the experimental accuracy is the highest.

Number of blocks Number of channels	128	256
RepVGG block × 1	0.7525	0.7437
RepVGG block × 2	0.8114	0.7758
RepVGG block × 3	0.7825	0.7638

Table 4: Comparison table between RebarDet and other mainstream object detection models in AB-score, inference speed, and parameter quantity.

Method	Backbone	Input size	AB-score	Inference speed (fps)	Params (M)
SSD	VGG-16	512 × 512	0.7233	3.5	33.51
RetinaNet [34]	ResNet-101	512 × 512	0.7536	3.7	55.37
Faster-RCNN	ResNet-101	512 × 512	0.7745	3.5	60.18
ATSS [35]	ResNet-101	512 × 512	0.7812	3.5	50.91
YOLOv5	yolov5x	512 × 512	0.7983	7.1	40.97
RebarDet (ours)	Hourglass-104	512 × 512	0.8114	6.9	35.24

each center point to compensate. All center points of class c share the same offset prediction, and this offset value is trained by $L1$ loss:

$$L_{\text{off}} = \frac{1}{N}\sum_{p}\left|\widehat{O}_{\tilde{p}} - \left(\frac{p}{R} - \tilde{p}\right)\right|. \tag{6}$$

Finally, the overall objective is

$$L_{\text{det}} = L_k + \lambda_{\text{radius}} L_{\text{radius}} + \lambda_{\text{off}} L_{\text{off}}, \tag{7}$$

we set $\lambda_{\text{radius}} = 0.1$ and $\lambda_{\text{off}} = 1$ referring from CenterNet.

3.4. Ablation Study. To verify the effectiveness of our proposed RebarDet model on detection of circular tubular objects, we conduct ablation experiments on the rebar dataset provided by Glodon. In addition, we conduct comparative experiments on mainstream object detection models and compare the performance of various parameters of the models to prove the superiority of the RebarDet model. Specifically, we resize all training set images to 512 × 512 resolution and keep the relevant hyperparameters of model training consistent to ensure a fair comparison. All models are evaluated using AB-score, see Section 3.2 for details of AB-score.

3.5. Circle Representation. In order to verify the effectiveness of the circular representation structure, we use the original CenterNet model and our improved CenterNet model with the circular representation structure for comparative experiments. The experimental results are shown in the fifth and sixth columns of Table 2. We obtained an AB-score of 0.6984 after adding the improved circular representation structure to the basic CenterNet model. Compared with the basic CenterNet model, adding the circular representation structure can bring an improvement of 0.2353 AB-score to the detector, which proves that by adding a circular representation structure to the network can improve the performance of the detector. We think there are several reasons why the circular representation structure can bring such a big improvement. First, in the detection of circular tubular objects, the fitting effect of the circular box is better than that of the traditional rectangular box. Second, the circular detection head is used to detect and represent the object, which reduces the amount of parameters for detection and representation. Third, the circular box has better rotation consistency than the traditional rectangular box.

3.6. Expansion of Prediction Structure. Max objects represent the upper limit of the number of objects detected by the network at a time. As shown in the third and fourth columns of Table 2, max objects and feature map resolution obtain AB-scores of 0.7568 and 0.7751, respectively. The entire expansion of prediction structure brings an improvement of 0.0767 AB-score to the model, which proves the effectiveness of our designed expansion of prediction structure. We believe that increasing the size of the feature map can divide the objects to be detected more scattered, which greatly improves the detection ability of the network in dense scenes. The increase of max objects improves the loadability of network detection of dense objects to a certain extent.

3.7. RepVGG Block. In order to verify the effectiveness of RepVGG Block, we discuss how many RepVGG blocks are applied in the network and how many channels are adopted and conduct corresponding comparative experiments and obtain the optimal number and number of channels for applying RepVGG block. The experimental results are as

shown in Table 3. Applying a number of RepVGG blocks of 2 and a number of channels of 128, the model achieves the best accuracy. As shown in the second and third columns of Table 2, applying RepVGG block brings an improvement of 0.0363 AB-score to the model, which proves the effectiveness of the multibranch topology of RepVGG on the model. We think that the multibranch topology of RepVGG can improve the extraction ability of shallow convolutions at the beginning of the network, which parallels 1×1 convolution (additional BN layer) and BN layer on both sides of 3×3 convolution (additional BN layer) and BN layer to sum up the feature information extracted by different convolution modules, thus improving the information extraction ability of a single convolution module. The richness of low-level semantic information extracted by this part of the convolutional module has a great influence on the high-level semantic features of the subsequent convolutional layers. Therefore, improving the extraction ability of this part of the convolutional module can improve the performance of the entire network.

3.8. Network Performance. In order to prove the superiority of the model, we use three performance indicators of AB-score, inference speed, and parameter quantity to conduct comparative experiments on mainstream object detection models. The experimental results are shown in Table 4. In terms of detection accuracy, RebarDet obtains the highest AB-score, 0.8114. While obtaining the highest detection accuracy, RebarDet also maintains a high model inference speed of 6.9 fps, which is only slightly lower than the model inference speed of YOLOv5 of 7.1 fps. On the model parameters, the SSD model using VGG-16 as the backbone network has the least amount of parameters, but the AB-score and inference speed of the SSD model are not satisfactory. While the RebarDet model based on Hourglass-104 maintains a moderate amount of parameters, its detection accuracy is the highest and the model inference speed is also better than other mainstream object detection models.

4. Conclusion

In this paper, we introduce RebarDet, a high-accuracy and high-efficiency lightweight circular tubular object detection method. By introducing the circle representation structure and RepVGG module on the basis of CenterNet and expanding the network prediction structure, the circle detection performance of the network has been greatly improved. RebarDet is tested on rebar dataset for object detection. The experimental results show that RebarDet's detection accuracy and model inference speed are better than existing mainstream object detectors with moderate parameters.

Data Availability

The datasets used and analysed during the current study are available from the corresponding author upon reasonable request.

Conflicts of Interest

The authors declare that there are no conflicts of interest associated with the manuscript.

Acknowledgments

Cong Lin and Zhoujian Chen are the co-first authors and contributed equally to this work. Qiong Chen and Wencai Du are the cocorrespondence authors. This work was supported by the National Natural Science Foundation of China under Grant 62072121 and Natural Science Foundation of Guangdong Province 2021A1515011847.

References

[1] L. M. Schmitt, C. H. Garcia-Capulin, A. Perez-Garcia, and R. E. Sanchez-Yanez, "Theory of genetic algorithms," *Theoretical Computer Science*, vol. 259, no. 1-2, pp. 1–61, 2001.

[2] M. Srinivas and L. M. Patnaik, "Genetic algorithms: a survey," *Computer*, vol. 27, no. 6, pp. 17–26, 1994.

[3] A. A. Rad, K. Faez, and N. Qaragozlou, *Fast circle detection using gradient pair vectors*, Dicta, 2003.

[4] D. J. Kerbyson and T. J. Atherton, *Circle Detection Using Hough Transform Filters*, IET, 1995.

[5] T. D'Orazio, C. Guaragnella, M. Leo, and A. Distante, "A new algorithm for ball recognition using circle Hough transform and neural classifier," *Pattern Recognition*, vol. 37, no. 3, pp. 393–408, 2004.

[6] M. Smereka and I. Duleba, "Circular object detection using a modified Hough transform," *International Journal of Applied Mathematics and Computer Science*, vol. 18, no. 1, pp. 85–91, 2008.

[7] J. Garland, M. Hu, K. Kesha et al., "An overview of artificial intelligence/deep learning," *Pathology*, vol. 53, p. S6, 2021.

[8] A. Khan, A. Sohail, U. Zahoora, and A. S. Qureshi, "A survey of the recent architectures of deep convolutional neural networks," *Artificial Intelligence Review*, vol. 53, no. 8, pp. 5455–5516, 2020.

[9] W. Rawat and Z. Wang, "Deep convolutional neural networks for image classification: a comprehensive review," *Neural Computation*, vol. 29, no. 9, pp. 2352–2449, 2017.

[10] L. Jiao, F. Zhang, F. Liu et al., "A survey of deep learning-based object detection," *IEEE Access*, vol. 7, pp. 128837–128868, 2019.

[11] X. Wu, D. Sahoo, and S. C. H. Hoi, "Recent advances in deep learning for object detection," *Neurocomputing*, vol. 396, pp. 39–64, 2020.

[12] S. Minaee, Y. Y. Boykov, F. Porikli, A. J. Plaza, N. Kehtarnavaz, and D. Terzopoulos, "Image segmentation using deep learning: a survey," *IEEE transactions on pattern analysis and machine intelligence*, 2021.

[13] A. M. Hafiz and G. M. Bhat, "A survey on instance segmentation: state of the art," *International Journal of Multimedia Information Retrieval*, vol. 9, no. 3, pp. 171–189, 2020.

[14] Y. Chen, Y. Tian, and M. He, "Monocular human pose estimation: a survey of deep learning-based methods," *Computer Vision and Image Understanding*, vol. 192, article 102897, 2020.

[15] A. Krizhevsky, I. Sutskever, and G. E. Hinton, "Imagenet classification with deep convolutional neural networks," *Advances*

in Neural Information Processing Systems, vol. 25, pp. 1097–1105, 2012.

[16] K. Simonyan and A. Zisserman, "Very deep convolutional networks for large-scale image recognition," 2014, https://arxiv.org/abs/1409.1556.

[17] C. Szegedy, W. Liu, Y. Jia et al., "Going deeper with convolutions," in *Proceedings of the IEEE conference on computer vision and pattern recognition*, Boston, MA, USA, 2015.

[18] K. He, X. Zhang, S. Ren, and J. Sun, "Deep residual learning for image recognition," in *Proceedings of the IEEE conference on computer vision and pattern recognition*, Las Vegas, NV, USA, 2016.

[19] E. E. Zelniker, I. Vaughan, and L. Clarkson, "Maximum-likelihood estimation of circle parameters via convolution," *IEEE Transactions on Image Processing*, vol. 15, no. 4, pp. 865–876, 2006.

[20] V. Ayala-Ramirez, C. H. Garcia-Capulin, A. Perez-Garcia, and R. E. Sanchez-Yanez, "Circle detection on images using genetic algorithms," *Pattern Recognition Letters*, vol. 27, no. 6, pp. 652–657, 2006.

[21] H. Yang, R. Deng, Y. Lu et al., "CircleNet: anchor-free detection with circle representation," 2020, https://arxiv.org/abs/2006.02474.

[22] R. Girshick, J. Donahue, T. Darrell, and J. Malik, "Rich feature hierarchies for accurate object detection and semantic segmentation," in *Proceedings of the IEEE conference on computer vision and pattern recognition*, pp. 580–587, Columbus, OH, USA, 2014.

[23] R. Girshick, "Fast r-cnn," in *Proceedings of the IEEE international conference on computer vision*, Santiago, Chile, 2015.

[24] S. Ren, K. He, R. Girshick, and J. Sun, "Faster r-cnn: towards real-time object detection with region proposal networks," *Advances in Neural Information Processing Systems*, vol. 28, pp. 91–99, 2015.

[25] J. Redmon, S. Divvala, R. Girshick, and A. Farhadi, "You only look once: unified, real-time object detection," in *Proceedings of the IEEE conference on computer vision and pattern recognition*, Las Vegas, NV, USA, 2016.

[26] J. Redmon and A. Farhadi, "YOLO9000: better, faster, stronger," in *Proceedings of the IEEE conference on computer vision and pattern recognition.*, Honolulu, HI, USA, 2017.

[27] J. Redmon and A. Farhadi, "Yolov3: an incremental improvement," 2018, https://arxiv.org/abs/1804.02767.

[28] W. Liu, D. Anguelov, D. Erhan et al., *Ssd: Single Shot Multibox Detector*, European Conference on Computer Vision, Springer, Cham, 2016.

[29] X. Zhou, D. Wang, and P. Krähenbühl, "Objects as points," 2019, https://arxiv.org/abs/1904.07850.

[30] X. Ding, X. Zhang, N. Ma, J. Han, G. Ding, and J. Sun, "Repvgg: making vgg-style convnets great again," in *Proceedings of the IEEE/CVF Conference on Computer Vision and Pattern Recognition*, pp. 13733–13742, 2021.

[31] T.-Y. Lin, M. Maire, S. Belongie et al., "Microsoft coco: common objects in context," in *European conference on computer vision*, Springer, Cham, 2014.

[32] A. Newell, K. Yang, and J. Deng, *Stacked Hourglass Networks for Human Pose Estimation*, European conference on computer vision, Springer, Cham, 2016.

[33] C. Lin, Y. Zheng, X. Xiao, and J. Lin, "CXR-RefineDet: single-shot refinement neural network for chest X-ray radiograph based on multiple lesions detection," *Journal of Healthcare Engineering*, vol. 2022, Article ID 4182191, 11 pages, 2022.

[34] T.-Y. Lin, P. Goyal, R. Girshick, K. He, and P. Dollár, "Focal loss for dense object detection," in *Proceedings of the IEEE international conference on computer vision*, pp. 2980–2988, Venice, Italy, 2017.

[35] S. Zhang, C. Chi, Y. Yao, Z. Lei, and S. Z. Li, "Bridging the gap between anchor-based and anchor-free detection via adaptive training sample selection," in *Proceedings of the IEEE/CVF conference on computer vision and pattern recognition*, pp. 9759–9768, Seattle, WA, USA, 2020.

Hindawi
Journal of Sensors
Volume 2022, Article ID 2690164, 11 pages
https://doi.org/10.1155/2022/2690164

Review Article

Intelligence of Autonomous Vehicles: A Concise Revisit

Neelma Naz,[1] Muhammad Khurram Ehsan,[2] Muhammad Rizwan Amirzada,[3] Md Yeakub Ali,[4] and Muhammad Aasim Qureshi[5]

[1]*National University of Sciences and Technology (NUST), Islamabad 44000, Pakistan*
[2]*Faculty of Engineering Sciences, Bahria University, Lahore Campus, Lahore 54000, Pakistan*
[3]*Faculty of Engineering and Computer Science, National University of Modern Languages, Islamabad 44000, Pakistan*
[4]*Department of Electronics and Telecommunication Engineering, Rajshahi University of Engineering & Technology (RUET), Rajshahi 6204, Bangladesh*
[5]*Department of Computer Sciences, Bahria University, Lahore Campus, Lahore 54000, Pakistan*

Correspondence should be addressed to Md Yeakub Ali; yeakub@ete.ruet.ac.bd

Received 25 February 2022; Revised 16 March 2022; Accepted 21 March 2022; Published 23 April 2022

Academic Editor: Waliullah Khan

Artificial intelligence- (AI-) empowered machines are devised to mimic human actions. In the automotive industry, AI plays a significant role in the development of vehicular technology. AI joins hands with the field of mechatronics to assist in the accurate execution of the vehicle functionalities. Autonomous vehicles get the scene information by using onboard sensors such as laser, radar, lidar, Global Positioning System (GPS), and vehicular communication networks. The data obtained is then used for various path planning and control techniques to make the vehicles capable of autonomously driving in complex environments. Autonomous vehicles use very up-to-date AI algorithms to localize themselves in known and unknown environments. AI algorithms are also exploited for perception, path planning, and motion control. A concise review of the state-of-the-art techniques to improve the performance of autonomous vehicles is presented.

1. Introduction

The world is progressing in technology and automation impressively with every passing day. It results in the establishment of smart cities by interconnecting the intelligent Home Area Networks (IHAN), Intelligent Industrial Area Networks (IIAN), Intelligent Vehicular Communication Networks (IVCN), and Smart Grids (SG). The key enabler of IVCN is included in an autonomous vehicle as an intelligent node of the Internet of Vehicles (IoV), Vehicle to Everything (V2X), Vehicle to Vehicle (V2V), and Vehicle to Infrastructure (V2I). People started working on autonomous driving in 1920, and since then, many advancements have been introduced in that domain. But technology still needs human support even with a certain level of intelligence. Current research is focused on introducing vehicles as completely driverlesswhich means no human intervention is required anymore. Intelligent vehicles can move around independently withtheir decision-making capabilities [1–3].

According to the Society of Automobile Engineers (SAE) [4], automated vehicles are categorized into six different levels. The initial level is level 0; in this level, the driver is responsible for all decisions which means no autonomy. The highest level is level 5, where the vehicle alone is responsible for all driving tasks and decisions (fully autonomous). These levels are presented in Figure 1.

Although many companies such as Uber, Google, and Tesla have invested a lot in the advancement of this technology, the autonomous system is still an active research area due to its very large challenges. A good autonomous system is one that is able to make correct decisions intelligently in real-time scenarios [5–8]. Active researchers are still focusing on devising better algorithms for localization, perception, and detection.

The most important questions the autonomous vehicle technology is built upon are as follows:

(1) Where am I at the time?

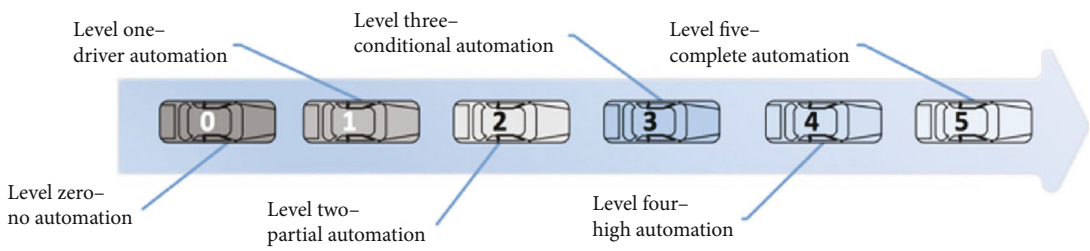

Figure 1: Six levels of autonomous vehicles as described by the Society of Automobile Engineers (SAE) [4].

(2) What is around me?

(3) What is going to happen next?

(4) What should be done?

The first question, "Where am I at the time," is the localization problem. The vehicle must be able to locate/localize itself in the current environment. The next question is getting information about surroundings, and it deals with perception.. Based upon the information perceived/detected, the prediction about the environment falls under the territory of the third question, that is, "What is going to happen next?" Finally, the course of action to be taken by the vehicle is discussed by, "What should be done?" All these fundamental questions are addressed by the use of different sensors and algorithms that make these cars reliable and safe to drive.

Autonomous vehicles sense the world by using various sensors mounted on the vehicle's assembly as shown in Figure 2. Information received from these sensors is then used to make decision like the safest path to reach the destination considering the optimality with respect to time and distance required to reach the place. To complete the task, more cutting-edge solutions, like localization, object detection and identification path planning, and data fusion received from different sensors, are needed.

With the availability of very powerful computational tools like graphics processing units (GPUs) and a very large amount of data, a subset of artificial intelligence known as deep learning(DL) has gained enormous popularity to solve these problems and to achieve the optimal performance [10]. (DL) algorithms have improved the performance of AVs by ensuring accuracy and fast processing speed. In this paper, different AI technologies being used in autonomous vehicles are reviewed. In Section 2, the generic structure of Auntonomous Vehicles (AVs) is discussed. Section 3 discusses the state-of-the-art techniques used for localization. In Section 4, techniques used for path planning are discussed, and in Section 5, a brief discussion on motion controllers is made.

2. Autonomous Vehicle Decision-Making Architecture

Autonomous decision-making is required in AVs to process the observation data received from the sensors mounted on the vehicle. The car's computer uses these observations to make optimal decisions. These decisions can be computed in two possible ways: either by using the integrated perceive-plan-act method or by end-to-end learning methods. In the end-to-end method, the information obtained from sensors is mapped to control outputs directly without any intermediate steps. An AI-based AV is shown in Figure 3. As can be seen in Figure 3, each step in AVs' perceive-plan-act method can be implemented either by classical methods with no learning or the latest AI or DL techniques. The end-to-end method of implementation always uses DL techniques. Learning and nonlearning methods can be used together in various arrangements; for example, an object detector based upon deep learning techniques provides input to the A∗ algorithm that is used for path planning.

Figure 2: Sensor set-up of MadeInGermany. Externally visible part of sensors [9].

An integrated perceive-plan-act method has four components of perception and localization, path planning, behavioral mediation, and motion control, and these components are discussed one by one in this paper.

3. Perception and Localization in AVs

Autonomous vehicles must be able to perceive the environment and be able to locate themselves in the environment correctly. This section reviews various techniques for perception and localization implemented in the literature.

3.1. Hardware for Sensing: Cameras or LiDAR. For better understanding of surroundings, 3D perception is usually preferred. Images taken through cameras can only capture a 2D environment. LiDAR sensors are generally used for

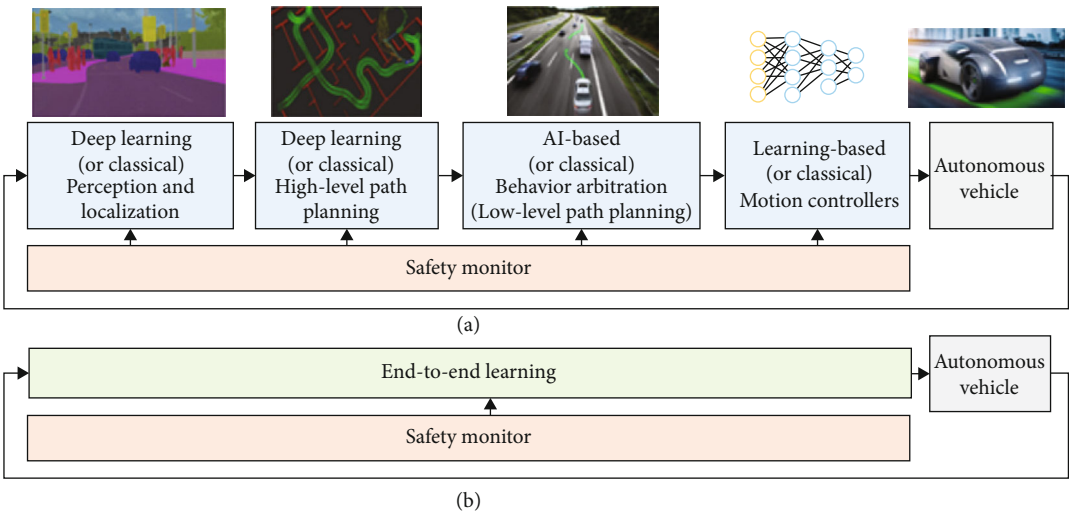

Figure 3: Architecture of AVs implanted in (a) the integrated perceive-plan-act method and (b) the end-to-end method [11].

3D perception. LiDAR's performance is measured by its range, rotation/frame rate, field of view, and resolution. Velodyne is also a 3D sensor that has a 360° field view. Autonomous vehicles cannot afford any delays in information communication, so to ensure processing at very high speeds, a range with a minimum of 200 m is required.

The debate of camera usage or LiDAR technology is still a hot topic. For example, Tesla is using its camera system for environment perception while Waymo's vehicle technology is based on LiDAR. Every sensing approach has its own positives and negatives. LiDARs ensure very high resolution and accurate environment perception but show poor performance in the case of bad weather. Moreover, LiDAR technology right now is very expensive. On the other hand, cameras are cheap, but they have very low depth perception and also show poor performance under bad weather conditions. In addition to LiDAR/cameras, ultrasonic sensors and RADAR are also used to enhance the system's perception capability. Waymo makes use of three LiDAR sensors.

3.2. Understanding the Driving Scene. The environments that autonomous vehicles work in are as follows:

(1) Multiagent environment

(2) Dynamic

(3) Unknown

(4) Stochastic

(5) Sequential

(6) Partially observable

All these features of the environment make the task of autonomous driving extremely challenging. Cars should be able to detect every possible scenario like all other agents in the environment, drivable areas, and pedestrians. The task becomes more and more challenging while driving in an urban area where a variety of objects appear and blockings are very high.

For environment perception, deep neural networks (DNNs) are playing a very important role. Various deep neural network (DNN) algorithms have been proposed for the detection of objects where objects are taken as 2D regions of interest [12–14]. In some other studies, DNNs are used for environment perception based upon pixel-wise segmentation in images [15], 3D bounding boxes in LiDAR [16], and, in some cases, 3D representation of objects in LiDAR + camera-combined data [17]. On a lighter note, for object identification, image data can be useful. However, while estimating 3D positions of the objects as 2D images, depth information of the scene is lost. The two most popular methods of driving scene detection are as follows:

(1) Semantic and instance segmentation

(2) Bounding boxes like object detectors

For safe navigation and to understand surrounding environments, semantic and instance segmentation are of utmost importance. For this purpose, several studies using efficient deep learning-based frameworks have been reported recently in the literature. FSNeT, a failure detection framework, is proposed for pixel-level misclassifications in the images [18]. In [19], the transformer-based knowledge distillation framework is proposed for efficient semantic segmentation of road driving scenes. A convolutional neural network method using multiscale attentions is proposed for instance segmentation [20].

3.3. Localization. Localization is the task of finding the vehicle's pose (orientation + position) when it moves in the environment. Localization is an elemental requirement for navigation. It is important to mention here that some of the latest research trends in AVs [21, 22] propose DL-based algorithms that do not need localization and mapping and instead produce end-to-end driving decisions based

upon the sensor information. This is termed as the behavior reflex approach [22].

GPS is most commonly used for localization in autonomous vehicles. GPS data is integrated with other sensor data to compensate for the signal loss in case of any possible outage. Various techniques for sensor fusions exist in the literature. The most commonly used traditional methods for sensor fusion are the Kalman filter, extended Kalman filter, unscented Kalman filter, particle filters, and multimodal Kalman filters [23–26]. A robust cooperative positioning (RCP) [27] scheme to acquire accurate position has been proposed that augments GPS with ultra wide band (UWB). However, the latest trends deal with visual-based localization that uses DL techniques. This method of localization is also called visual odometry (VO). Visual localization is achieved by key point landmarks matching in adjacent video frames. Based upon the vehicle's current frame information, key points are fed as input to the n-point mapping algorithm for the vehicle's pose detection with respect to the previous frame. Accuracy of visual odometry can be enhanced by using deep learning algorithms. These algorithms can affect the key point detector's precision. A DNN is trained for key point distractors learning in monocular VO [28]. The incremental mapping of the environment's structure can also be done by computing the camera pose. This method belongs to SLAM (simultaneous localization and mapping) [29].

SLAM is the act of online map making and localizing the vehicle in it at the same time. A priori information about the environment is not required in SLAM. Because of the enormous improvements of deep learning approaches in image classification and detection, these algorithms are being recommended to enhance traditional SLAM algorithms. Although the deep learning applications in this field are still not mature enough, some studies have proposed to replace classical SLAM blocks with deep learning modules to attain better accuracy and robustness.

To ensure safe navigation, AVs should be able to predict the surrounding environment's motions as well. This is known as scene flow. LiDAR-based estimation of the scene flow is a common approach in literature. Current research proposes to replace the method with DL techniques for automatic learning of the scene flow.

Despite that the research reports much progress in DL-based localization, classical key point matching techniques still dominate VO (visual odometry) mainly because of computational efficiency and easy deployment on embedded devices.

3.4. Perception. For the task of perception, occupancy maps are used frequently. These can also be termed as the Occupancy Grid (OG). It is environment representation in cells. In this method, driving space is divided into a set of cells and the probability of occupancy is calculated for each cell. The technique is very famous in robotics and is now a viable solution in AVs as well.

DL techniques are being used to detect and track the dynamic objects, to probabilistically estimate the occupancy map around vehicle, and to derive the driving scene context. In the case of driving scene derivation, deep learning is used to label the environment into highway drive, intercity drive, or parking area. Deep learning plays a vital role in OG estimation. It helps in extracting the information from LiDAR data and image processing that is required to populate grid cells. A multitask recurrent neural network is proposed to predict grid maps [30]. Grid maps provide sematic information, occupancies, velocity estimates, and drivable area.

4. Path Planning

Once an AV is able to localizes itself in the environment, next comes path planning. Path planning is defined as the ability of autonomous vehicles to find the optimal path between the start position and its destination (desired location) considering the kinematics and dynamic model of vehicles. The path planning process should make the autonomous vehicle capable of calculating the optimal trajectory to ensure the collision-free route while considering all possible obstacles it might come across in the surrounding environment. As mentioned earlier in the paper, autonomous driving is a multiagent problem, so according to the author in [31], the host vehicle must be capable of and apply good negotiation skills with all other users of the road while performing any action like taking a turn or changing lanes. Mission planning is defined as the full pursuit of the generated path by path planning.

Path planning also includes mission planning, motion planning, and behavior planning. Every time the vehicle undergoes a driving experience, a huge amount of data also termed as big data is stored on the server. AVs can use the information contained in the previously stored data to make correct decisions in the future. Route finding algorithms are very complicated because of all the obstacles that cross the vehicle's path. The AV should be capable of identification as well as avoiding these obstacles that make the planning algorithm's task more complicated. The AV must know exactly what to do in a specific driving environment and/or driving situation. For example, for a vehicle driving on the road, it should obey the sequence of waypoints designed by the planning algorithm as shown in Figure 4.

The problem of path planning has been the subject of study for many years and is often divided into two categories, global and local path planning. The techniques used for path planning were divided into four groups: graph search methods, interpolation, numerical optimization, and sampling. Most common motion planning techniques in autonomous vehicles are described below. Figures 5, 6, and 7 show the various techniques as presented in the literature.

4.1. Graph Search-Based Planning Techniques. The autonomous driving path planning techniques work on the basic idea of traversing a complete state space from source point A to goal point B. The state space tells where the objects in the dynamic environment are and is usually represented as a lattice or as an occupancy grid. The graph search algorithms visit the state space in the occupancy grid and return an optimal/nonoptimal solution if it exists or return no solution at all in case it does not exist. The most common search

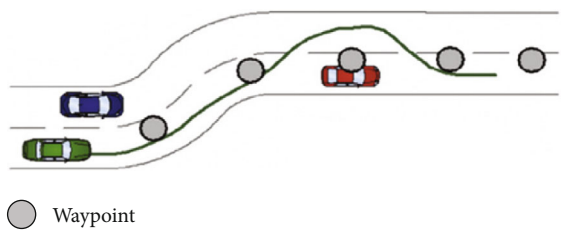

Figure 4: Path planning [32].

algorithms implemented for autonomous vehicle path planning are described below.

4.1.1. Dijkstra Algorithm. It is a graph search algorithm that finds the shortest path in a grid or series of nodes. It works well for global path planning in both structured and unstructured environments. In [33], the authors detailed the basic description of the algorithm and how to implement it. However, the algorithm has been implemented in [34] in multivehicle simulations. Despite its advantages, a large number of nodes are needed to be traversed in the vast areas making the algorithm slow. Moreover, the algorithm does not use any heuristics function to optimize the search cost. The path obtained is not continuous, so it is not suitable for real-time scenarios. Figure 6 shows different planning algorithms as they are presented in the literature.

4.1.2. A-Star Algorithm. It is an extended version of the Dijkstra algorithm as it implements heuristics to ensure optimality and a faster node search, reducing the computation time [35–37]. The advantage of the A-star algorithm comes from the fact that to define the node weights, it calculates the cost. It is costly in terms of speed and memory for searching large areas but is very suitable for searching spaces that are mostly known by the vehicle theoretically beforehand. Various modified versions of A-star are being utilized in mobile applications such as the dynamic A ∗ (D ∗) and anytime repairing A ∗ (ARA ∗) [38]. For path planning in unstructured spaces and parking spaces, A ∗ using Voronoi cost functions has been implemented in [39]. The winner of the DARPA Urban Challenge, the Boss used the AD ∗ algorithm [40]. Despite its advantages, the path found by the A-star algorithm is not continuous. Moreover, sometimes finding the heuristic rule becomes very complex.

4.1.3. State Lattice Algorithm. The algorithm uses spatiotemporal lattices (including velocity and time dimensions) [41, 42]. Depending upon the maneuver's complexity, the environment is decomposed in a local grid, making it suitable for dynamic environments and local planning. Despite its advantages, the algorithm has to evaluate every feasible solution in the database that makes it computationally expensive.

4.2. Sampling-Based Planning Techniques. This approach works by sampling the state space or configuration space randomly and tries to look for the connectivity inside the space [46]. These techniques try to solve timing restrictions by planning in higher dimensional spaces. However, the techniques result in suboptimal solutions. Most commonly used sampling-based techniques are the Rapidly-Exploring Random Tree (RRT) and Probabilistic Roadmap Method (PRM). Both are probabilistically complete while RRT is much faster than PRM. RRT is used for online path planning. It executes a random search in the navigation space allowing itself to plan quickly in semistructured spaces. In autonomous vehicles, the algorithm has been used by the MIT team in the DARPA Urban challenge [47]. However, the path resulted is jerky, noncontinuous, and suboptimal. A modified version of this algorithm named RRT ∗ is discussed in [48]. The solution generated is optimal, although at the cost of computational efficiency.

4.3. Interpolating Curve Planning Techniques. Interpolation is defined as the generation of a new set of data points that are in the range of known data points (reference points). These algorithms take previously known waypoints that describe a global roadmap and generate new data points. The points generated ensure a smooth and continuous trajectory and are also beneficial for the dynamic environment in which the AV moves as well as for AV constraints [51]. During path execution, if an obstacle occurs, it generates a set of new data points to avoid it and then continues on the previously planned path. Different techniques are used for curve generation and path smoothing, some of which are reviewed below.

4.3.1. Lines and Circles. Through the interpolation of known waypoints with circular and linear/straight shapes, segments of different road networks can be represented. It is computationally inexpensive and is easy to implement. It guarantees the shortest path for car-type vehicles [52]. However, on the downside, the path generated is jerky, thus making uncomfortable changes between path segments. It also needs global waypoints.

4.3.2. Clothoid. In this technique, the linear change in curvature is used to make the transitions from and to the curves [53]. These types of curves are implemented in road designs and highways. It is suitable for local path planning. On the downside, although the path generated is continuous, it is not smooth because of the linear behavior. It also has time complexity because of the integrals defining the curve. It also needs global waypoints for path planning.

4.3.3. Polynomial. To meet the limitations in the points being interpolated, polynomial curves are commonly implemented [54]. The limitations in the points include angle, curvature, and position. The coefficients of the curve are determined by limitations in the beginning and ending segments or desired values. This method of interpolation is computationally less expensive and is suitable for comfort. However, on the downside, a 4th or higher degree implementation of curves makes the coefficient computation very difficult and challenging.

4.3.4. Bézier. Bézier curves are the parametric curves that are defined by the set of control points. The Bézier curves are related to the Bernstein polynomial. The advantages of using

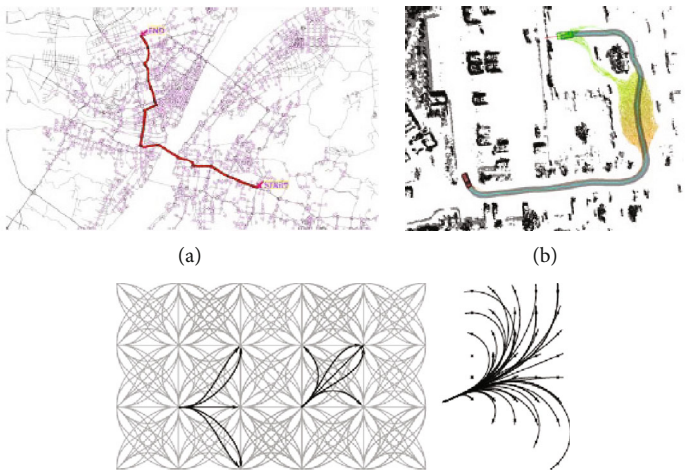

Figure 5: Graph search-based planning algorithms as presented in the literature. (a) A global path representation by the Dijkstra algorithm in [43]. (b) Hybrid implementation in the DARPA Challenge by Junior [44]. (c) Motion primitives and lattices as presented in [45].

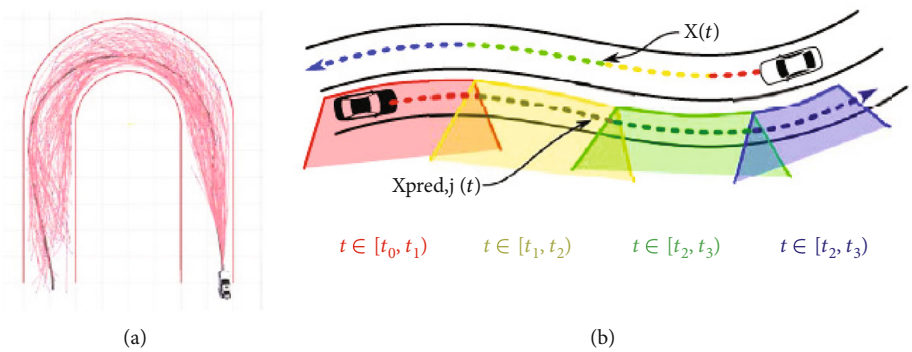

Figure 6: Sampling-based and numerical optimization-based planning algorithms as presented in the literature. (a) RRT as presented in [49]. (b) Trajectory optimization by considering the vehicle in the other lane [50].

these curves are their reduced computational cost and intuitive manipulation of the curve because of the control points defining it [55]. It is also possible to continuously concatenate the curves which makes it suitable for comfort. However, with the increase in the curve's degree and computational time, more and more control points need to be evaluated and placed. It also depends upon global waypoints.

4.3.5. Spline. A spline is a piecewise curve that is defined by the polynomials, clothoid or B-splines. A knot is a junction between each subsegment of the curve, and it possesses a higher degree of smoothness constraint between the spline pieces at the joint [56].

4.4. Numerical Optimization Techniques. In path planning, numerical methods are most often used to smooth already computed paths/trajectories as in [57]. The most commonly used technique is the function optimization. To minimize the outcome of variables, this technique finds real valued roots of a function. Using this technique, a plan can be generated by taking ego-vehicle limitations, road constraints, and other users on the road into account. On the downside, at each motion state, the optimization of the function needs to take place, because of which, the optimization needs to be stopped at a given time. This planning technique also depends on global waypoints.

4.5. Deep Learning-Based Techniques. Latest research shows increased interest in the application of DL techniques in path planning. The two most discussed DL techniques in the path planning scenario are imitation learning and planning based upon reinforcement learning. The fundamental task of imitation learning (IL) [58] is to imitate the human driver's behavior. The human driver's behavior is recorded in the form of big data, and then, a convolutional neural network (CNN) is used to make the vehicle learn, how to plan from imitation. Imitation learning is also termed as the inverse of reinforcement learning [59, 60]. This method uses the human driver's behavior to learn how to maximize reward functions and then to generate driving trajectories just like humans. The DRL method is also used to plan the path. In this method, the agent learns driving trajectories in a simulator environment [61]. On the basis of a transfer

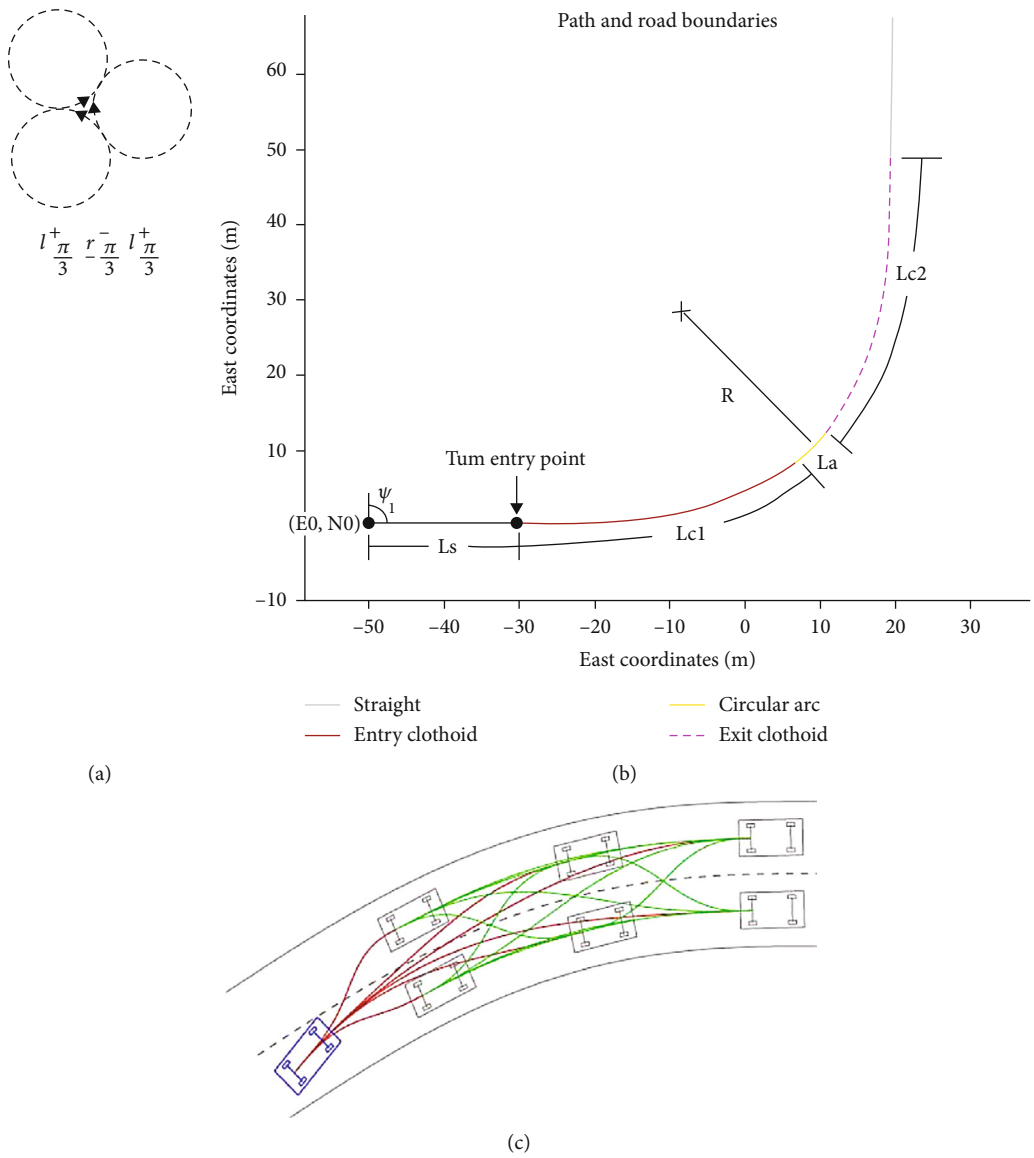

Figure 7: Continued.

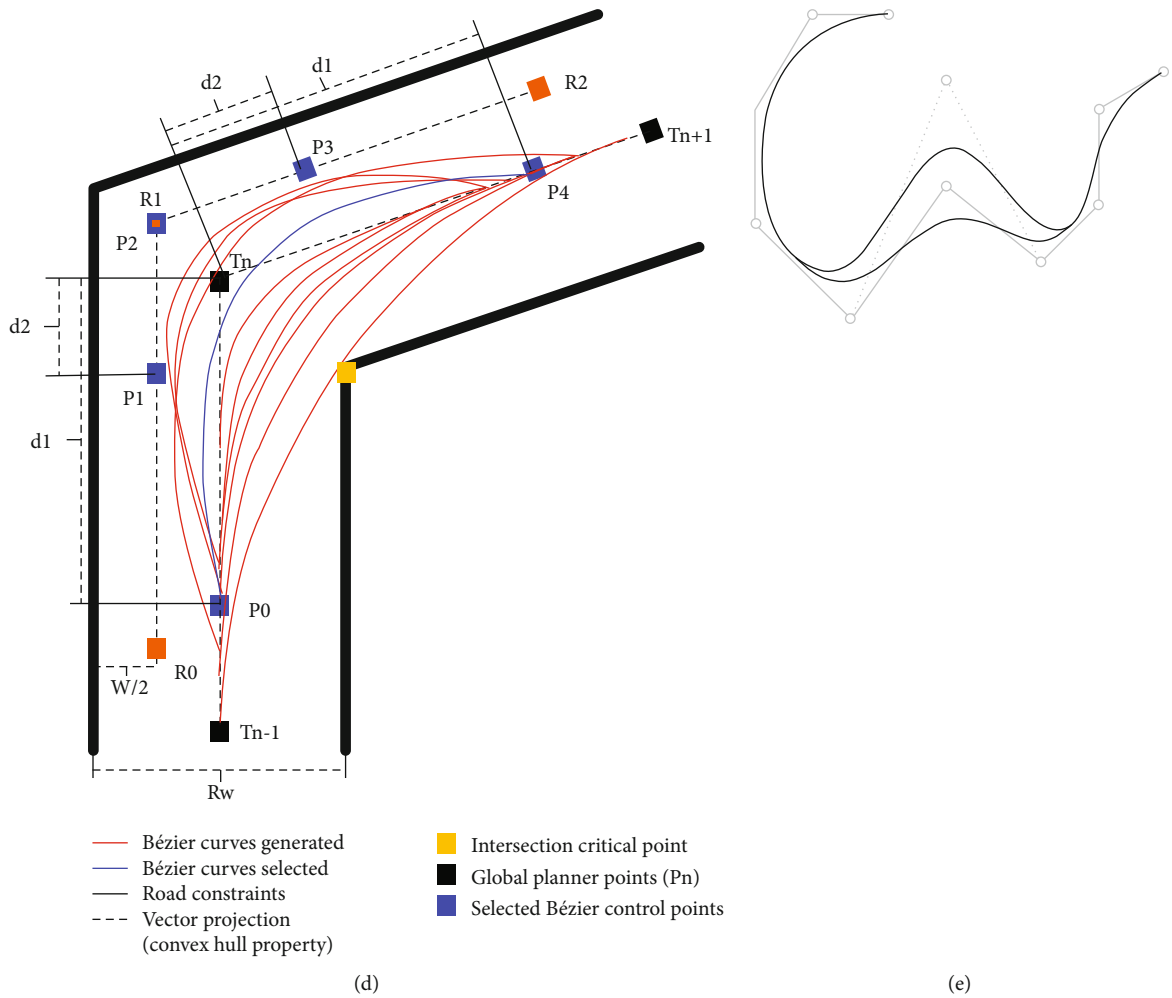

Figure 7: Interpolating curve-based planning algorithms as presented in the literature. (a) Optimal path to turn the vehicle around as proven in [52]. (b) Planning a turn for the Audi TTS from Stanford [53]. (c) Different motion states planned with polynomial curves as presented in [54]. (d) Evaluation of several Bézier curves in a turn, as shown in [55]. (e) Spline behavior when a knot changes place as presented in [56].

model, the real environment model is transformed into a virtual one. Both of these methods have their own advantages and disadvantages. IL has the advantage of being trained on real-world data, but as data is rare on corner cases (e.g., driving off the lanes), the trained network might give errors when it handles unseen scenarios. On the other side, DRL shows good performance in simulations, but the performance is not that good under real-world scenarios. Although the use of deep learning-based techniques to perform perception, localization, path planning, and control is getting much attention, it has also increased concerns of transparency and accountability in autonomous vehicles because of the black box nature of deep neural networks. So to build the trust on these deep frameworks, explainable AI (xAI) is the field that has gained researchers' interest in recent years. Explanations generated either in numerical form or textual forms or in the form of heat/saliency maps (visual form) provide insights into the decision-making process of autonomous vehicles. Various approaches are being used to produce these explanations. An imitation learning-(IL-) based agent equipped with an attention model is proposed [62]. The attention model helps to understand regions of images considered important in the decision-making process.

5. Motion Controllers/Act

The task of calculating steering commands (longitudinal and lateral) comes under the territory of the motion controller. The motion controller makes use of learning algorithms as part of an incomplete entity, or they work as a complete entity as an end-to-end controller to generate the steering commands from sensory data. Traditional controllers work on a model composed of fixed parameters. Learning controllers use the training information and data to make themselves capable of learning their models over time. The more information gathered, the more accurate the system model is. Commonly used learning controllers are the iterative learning control (ILC) [63] and model predictive control (MPC) [64]. ILC works efficiently for controlling systems

that work in repetitive mode, e.g., tracking a defined trajectory in autonomous vehicles. MPC finds the appropriate control actions by solving the optimization problem. MPC also helps us in the prediction of disturbances and uncertainties in the system leading to optimal solutions. The data for training is mostly available in the form of the vehicle's past states and observations. A use of CNN can then be made by training it to find the dense occupancy grid map. This map is then passed to the cost function of MPC to find the optimal trajectory to be followed by the vehicle over a finite horizon. The maximum advantage of these learning controllers can be achieved as they make use of a model-based control as well as learning algorithms. Deep learning-based techniques have gained much importance in the motion control of autonomous vehicles [30, 65]. A visual attention model is used to train an end-to-end (from images to control commands) convolutional neural network model [66]. These attentions learned by the attention model identify the image regions influencing the network's output. To generate textual explanations, an attention-based video-to-text model is used. Finally, the controller's attention map and explanations are aligned to ground the explanations in the image regions that mattered to the controller. In most existing works on autonomous driving, three main modules of autonomous vehicles, i.e., sensing, decision making, and motion controlling, have been studied separately. However, the power of DNN can also be exploited for joint optimization of sensing, decision making, and motion control [67].

6. Conclusion

The development of intelligent and efficient algorithms for the safe operation of AVs is one of the key issues in vehicle design. This work presents a complete layout of an autonomous vehicle. A survey of various state-of- the-art AI algorithms used by the AVs to achieve the best possible and optimal solutions to the problems of perception, localization, path planning, and motion control has been presented. Although the field of AVs is vast and involves a wide variety of challenges to address, this very challenging nature of the problem makes endless research opportunities in this field.

Conflicts of Interest

The authors declare that they have no conflicts of interest.

References

[1] P. J. Jin, D. Fagnant, A. Hall, and C. M. Walton, *Emerging Transportation Technologies White Papers*, University of Texas, TRB, 2015.

[2] W. U. Khan, E. Lagunas, A. Mahmood, S. Chatzinotas, and B. Ottersten, "When RIS meets GEO satellite communications: a new optimization framework in 6G," 2022, https://arxiv.org/abs/2202.00497.

[3] M. K. Ehsan, A. A. Shah, M. R. Amirzada et al., "Characterization of sparse WLAN data traffic in opportunistic indoor environments as a prior for coexistence scenarios of modern wireless technologies," *Alexandria Engineering Journal*, vol. 60, no. 1, pp. 347–355, 2021.

[4] Mobilus, *Taxonomy and Definitions for Terms Related to Driving Automation Systems for On-Road Motor Vehicles*, SAE International, 2018.

[5] H. Khayyam, B. Javadi, M. Jalili, and R. N. Jazar, *Artificial Intelligence and Internet of Things for Autonomous Vehicles*, Springer International Publishing, Cham, Switzerland, 2020.

[6] M. K. Ehsan, "Performance analysis of the probabilistic models of ISM data traffic in cognitive radio enabled radio environments," *IEEE Access*, vol. 8, pp. 140–150, 2020.

[7] A. Mahmood, Y. Hong, M. K. Ehsan, and S. Mumtaz, "Optimal resource allocation and task segmentation in IoT enabled mobile edge cloud," *IEEE Transactions on Vehicular Technology*, vol. 70, no. 12, pp. 13294–13303, 2021.

[8] M. K. Ehsan and D. Dahlhaus, "Statistical modeling of ism data traffic in indoor environments for cognitive radio systems," in *in 2015 Third International Conference on Digital Information, Networking, and Wireless Communications (DINWC)*, pp. 88–93, Moscow, Russia, 2015.

[9] D. Göhring, D. Latotzky, M. Wang, and R. Rojas, "Semiautonomous car control using brain computer interfaces," in *Intelligent Autonomous Systems 12*, S. Lee, H. Cho, K.-J. Yoon, and J. Lee, Eds., pp. 393–408, Springer, Berlin, Heidelberg, 2013.

[10] X. Chen, Y. Chen, and H. Najjaran, "3D object classification with point convolution network," in *2017 IEEE/RSJ International Conference on Intelligent Robots and Systems (IROS)*, pp. 783–788, Vancouver, BC, Canada, 2017.

[11] S. Grigorescu, B. Trasnea, T. Cocias, and G. Macesanu, "A survey of deep learning techniques for autonomous driving," *Journal of Field Robotics*, vol. 37, no. 3, pp. 362–386, 2020.

[12] J. Redmon, S. Divvala, R. Girshick, and A. Farhadi, "You only look once: unified, real-time object detection," in *in 2016 IEEE Conference on Computer Vision and Pattern Recognition (CVPR)*, pp. 779–788, Las Vegas, NV, USA, 2016.

[13] S. Zhang, L. Wen, X. Bian, Z. Lei, and S. Z. Li, "Single-shot refinement neural network for object detection," in *in 2018 IEEE/CVF Conference on Computer Vision and Pattern Recognition*, pp. 4203–4212, Salt Lake City, UT, USA, 2018.

[14] R. Girshick, "Fast R-CNN," in *in 2015 IEEE International Conference on Computer Vision (ICCV)*, pp. 1440–1448, Santiago, Chile, 2015.

[15] V. Badrinarayanan, A. Kendall, and R. Cipolla, "SegNet: a deep convolutional encoder-decoder architecture for image segmentation," *IEEE Transactions on Pattern Analysis and Machine Intelligence*, vol. 39, no. 12, pp. 2481–2495, 2017.

[16] W. Luo, B. Yang, and R. Urtasun, "Fast and furious: real time end-to-end 3D detection, tracking and motion forecasting with a single convolutional net," in *in 2018 IEEE/CVF Conference on Computer Vision and Pattern Recognition*, pp. 3569–3577, Salt Lake City, UT, USA, 2018.

[17] C. Qi, W. Liu, C. Wu, H. Su, and L. Guibas, "Frustum PointNets for 3D object detection from RGB-D data," in *in 2018 IEEE Conference on Computer Vision and Pattern Recognition*, pp. 918–927, Salt Lake City, UT, USA, 2018.

[18] Q. Rahman, N. Sunderhauf, P. Corke, and F. Dayoub, "Fsnet: A failure detection framework for semantic segmentation," *IEEE Robotics and Automation Letters*, vol. 7, no. 2, pp. 3030–3037, 2022.

[19] R. Liu, K. Yang, H. Liu, J. Zhang, K. Peng, and R. Stiefelhagen, "Transformer based knowledge distillation for efficient semantic segmentation of road-driving scenes," 2022, https://arxiv.org/abs/2202.13393.

[20] W. Gaihua, L. Jinheng, C. Lei, D. Yingying, and Z. Tianlun, "Instance segmentation convolutional neural network based on multi-scale attention mechanism," *PLoS One*, vol. 17, no. 1, article e0263134, 2022.

[21] C. Chen, A. Seff, A. Kornhauser, and J. Xiao, "Deepdriving: Learning affordance for direct perception in autonomous driving," in *2015 IEEE International Conference on Computer Vision (ICCV)*, pp. 2722–2730, Santiago, Chile, 2015.

[22] X. Chen, H. Ma, J. Wan, B. Li, and T. Xia, "Multi-view 3D object detection network for autonomous driving," in *in 2017 IEEE Conference on Computer Vision and Pattern Recognition (CVPR)*, pp. 6526–6534, Honolulu, HI, USA, 2017.

[23] F. Caron, E. Duflos, D. Pomorski, and P. Vanheeghe, "GPS/IMU data fusion using multisensor Kalman filtering: introduction of contextual aspects," *Information Fusion*, vol. 7, no. 2, pp. 221–230, 2006.

[24] H. Qi and J. Moore, "Direct kalman filtering approach for gps/ins integration," *IEEE Transactions on Aerospace and Electronic Systems*, vol. 38, no. 2, pp. 687–693, 2002.

[25] G. Wang, Y. Han, J. Chen et al., "A GNSS/INS integrated navigation algorithm based on Kalman filter," *IFACPapersOnLine*, vol. 51, no. 17, pp. 232–237, 2018.

[26] E. Wan and R. Van Der Merwe, "The unscented Kalman filter for nonlinear estimation," in *in Proceedings of the IEEE 2000 Adaptive Systems for Signal Processing, Communications, and Control Symposium*, pp. 153–158, Lake Louise, AB, Canada, 2000.

[27] Y. Gao, H. Jing, M. Dianati, C. M. Hancock, and X. Meng, "Performance analysis of robust cooperative positioning based on gps/uwb integration for connected autonomous vehicles," *IEEE Transactions on Intelligent Vehicles*, 2022.

[28] D. Barnes, W. Maddern, G. Pascoe, and I. Posner, "Driven to distraction: self-supervised distractor learning for robust monocular visual odometry in urban environments," in *2018 IEEE International Conference on Robotics and Automation (ICRA)*, pp. 1894–1900, Brisbane, QLD, Australia, 2018.

[29] G. Bresson, Z. Alsayed, L. Yu, and S. Glaser, "Simultaneous localization and mapping: a survey of current trends in autonomous driving," *IEEE Transactions on Intelligent Vehicles*, vol. 2, no. 3, pp. 194–220, 2017.

[30] M. Schreiber, V. Belagiannis, C. Glaser, and K. Dietmayer, "A multi-task recurrent neural network for end-to-end dynamic occupancy grid mapping," 2022, https://arxiv.org/abs/2202.04461.

[31] S. S. Shwartz, S. Shammah, and A. Shashua, "Safe, multiagent, reinforcement learning for autonomous driving," *CoRR*, 2016.

[32] C. Katrakazas, M. Quddus, W.-H. Chen, and L. Deka, "Real-time motion planning methods for autonomous on-road driving: State-of- the-art and future research directions," *Transportation Research Part C: Emerging Technologies*, vol. 60, pp. 416–442, 2015.

[33] J. Y. Hwang, J. S. Kim, S. S. Lim, and K. H. Park, "A fast path planning by path graph optimization," *IEEE Transactions on Systems, Man, and Cybernetics-Part A: Systems and Humans*, vol. 33, no. 1, pp. 121–128, 2003.

[34] R. Kala and K. Warwick, "Multi-level planning for semi-autonomous vehicles in traffic scenarios based on separation maximization," *Journal of Intelligent and Robotic Systems*, vol. 72, no. 3-4, pp. 559–590, 2013.

[35] M. Likhachev and D. Ferguson, "Planning long dynamically feasible maneuvers for autonomous vehicles," *The International Journal of Robotics Research*, vol. 28, no. 8, pp. 933–945, 2009.

[36] W. U. Khan, E. Lagunas, A. Mahmood, S. Chatzinotas, and B. Ottersten, "Integration of backscatter communication with multi-cell NOMA: a spectral efficiency optimization under imperfect SIC," 2021, https://arxiv.org/abs/2109.11509.

[37] M. K. Ehsan and D. Dahlhaus, "A framework for statistical characterization of indoor data traffic for efficient dynamic spectrum access in the 2.4 ghz ism band," *International Journal of Digital Information and Wireless Communications (IJDIWC)*, vol. 5, no. 4, pp. 210–220, 2015.

[38] M. Likhachev, D. Ferguson, G. Gordon, A. Stentz, and S. Thrun, "Anytime search in dynamic graphs," *Artificial Intelligence*, vol. 172, no. 14, pp. 1613–1643, 2008.

[39] J. Ziegler, M. Werling, and J. Schroder, "Navigating car-like robots in unstructured environments using an obstacle sensitive cost function," in *2008 IEEE Intelligent Vehicles Symposium*, pp. 787–791, Eindhoven, Netherlands, 2008.

[40] D. Ferguson, T. M. Howard, and M. Likhachev, "Motion planning in urban environments: part i," in *2008 IEEE/RSJ International Conference on Intelligent Robots and Systems*, pp. 1063–1069, Nice, France, 2008.

[41] M. Pivtoraiko and A. Kelly, "Efficient constrained path planning via search in state lattices," in *Proceedings of 8th International Symposium on Artificial Intelligence, Robotics and Automation in Space*, Munich, Germnay, 2005.

[42] W. U. Khan, M. A. Jamshed, A. Mahmood, E. Lagunas, S. Chatzinotas, and B. Ottersten, "Backscatter-aided noma v2x communication under channel estimation errors," 2022, https://arxiv.org/abs/2202.01586.

[43] Q. Li, Z. Zeng, B. Yang, and T. Zhang, "Hierarchical route planning based on taxi GPS-trajectories," in *2009 17th International Conference on Geoinformatics*, pp. 1–5, Fairfax, VA, USA, 2009.

[44] M. Montemerlo, J. Becker, S. Bhat et al., *Junior: the Stanford entry in the Urban Challenge*, Springer Berlin Heidelberg, Berlin, Heidelberg, 2009.

[45] J. Ziegler and C. Stiller, "Spatiotemporal state lattices for fast trajectory planning in dynamic on-road driving scenarios," in *2009 IEEE/RSJ International Conference on Intelligent Robots and Systems*, pp. 1879–1884, St. Louis, MO, USA, 2009.

[46] M. Elbanhawi and M. Simic, "Sampling-based robot motion planning: a review," *IEEE Access*, vol. 2, pp. 56–77, 2014.

[47] Y. Kuwata, J. Teo, G. Fiore, S. Karaman, E. Frazzoli, and J. P. How, "Real-time motion planning with applications to autonomous urban driving," *IEEE Transactions on Control Systems Technology*, vol. 17, no. 5, pp. 1105–1118, 2009.

[48] S. Karaman and E. Frazzoli, "Optimal kinodynamic motion planning using incremental sampling-based methods," in *49th IEEE Conference on Decision and Control (CDC)*, pp. 7681–7687, Atlanta, GA, USA, 2010.

[49] J. H. Jeon, R. V. Cowlagi, S. C. Peters et al., "Optimal motion planning with the half-car dynamical model for autonomous high-speed driving," in *2013 American Control Conference*, pp. 188–193, Washington, DC, USA, 2013.

[50] J. Ziegler, P. Bender, T. Dang, and C. Stiller, "Trajectory planning for bertha - a local, continuous method," in *2014 IEEE*

Intelligent Vehicles Symposium Proceedings, pp. 450–457, Dearborn, MI, USA, 2014.

[51] L. Labakhua, U. Nunes, R. Rodrigues, and F. S. Leite, *Smooth trajectory planning for fully automated passengers vehicles: spline and clothoid based methods and its simulation*, Springer Berlin Heidelberg, Berlin, Heidelberg, 2008.

[52] J. A. Reeds and L. A. Shepp, "Optimal paths for a car that goes both forwards and backwards," *Pacific Journal of Mathematics*, vol. 145, no. 2, pp. 367–393, 1990.

[53] J. Funke, P. Theodosis, R. Hindiyeh et al., "Up to the limits: autonomous Audi TTS," in *2012 IEEE Intelligent Vehicles Symposium*, pp. 541–547, Madrid, Spain, 2012.

[54] W. Xu, J. Wei, J. M. Dolan, H. Zhao, and H. Zha, "A real-time motion planner with trajectory optimization for autonomous vehicles," in *2012 IEEE International Conference on Robotics and Automation*, pp. 2061–2067, Saint Paul, MN, USA, 2012.

[55] A. Valera, F. Valero, M. Vallés, A. Besa, V. Mata, and C. Llopis-Albert, "Navigation of autonomous light vehicles using an optimal trajectory planning algorithm," *Sustainability*, vol. 13, no. 3, p. 1233, 2021.

[56] R. T. Farouki, *Pythagorean-hodograph curves: algebra and geometry inseparable, geometry and computing*, Springer, 2008.

[57] D. Dolgov, S. Thrun, M. Montemerlo, and J. Diebel, "Path planning for autonomous vehicles in unknown semi-structured environments," *The International Journal of Robotics Research*, vol. 29, no. 5, pp. 485–501, 2010.

[58] L. Sun, C. Peng, W. Zhan, and M. Tomizuka, "A fast integrated planning and control framework for autonomous driving via imitation learning," *Dynamic Systems and Control Conference*, vol. 9, 2018.

[59] W. U. Khan, T. N. Nguyen, F. Jameel et al., "Learning-based resource allocation for backscatter-aided vehicular networks," *IEEE Transactions on Intelligent Transportation Systems*, 2021.

[60] W. U. Khan, X. Li, A. Ihsan, M. A. Khan, V. G. Menon, and M. Ahmed, "Noma-enabled optimization framework for next-generation small-cell iov networks under imperfect sic decoding," *IEEE Transactions on Intelligent Transportation Systems*, 2021.

[61] A. I. Panov, K. S. Yakovlev, and R. Suvorov, "Grid path planning with deep reinforcement learning: preliminary results," *Procedia Computer Science*, vol. 123, pp. 347–353, 2018.

[62] L. Cultrera, L. Seidenari, F. Becattini, P. Pala, and A. Del Bimbo, "Explaining autonomous driving by learning end-to-end visual attention," in *2020 IEEE/CVF Conference on Computer Vision and Pattern Recognition Workshops (CVPRW)*, pp. 1389–1398, Seattle, WA, USA, 2020.

[63] Y. Zhao, F. Zhou, Y. Li, and Y. Wang, "A novel iterative learning pathtracking control for nonholonomic mobile robots against initial shifts," *International Journal of Advanced Robotic Systems*, vol. 14, no. 3, 2017.

[64] M. Brunner, U. Rosolia, J. Gonzales, and F. Borrelli, "Repetitive learning model predictive control: an autonomous racing example," in *in 2017 IEEE 56th Annual Conference on Decision and Control (CDC)*, pp. 2545–2550, Melbourne, VIC, Australia, 2017.

[65] Y. Du, J. Chen, C. Zhao, C. Liu, F. Liao, and C.-Y. Chan, "Comfortable and energy-efficient speed control of autonomous vehicles on rough pavements using deep reinforcement learning," *Transportation Research Part C: Emerging Technologies*, vol. 134, article 103489, 2022.

[66] J. Kim, A. Rohrbach, T. Darrell, J. Canny, and Z. Akata, "Textual explanations for self-driving vehicles," in *Proceedings of the European Conference on Computer Vision (ECCV)*, pp. 563–578, Munich, Germany, 2018.

[67] L. Chen, Y. He, Q. Wang, W. Pan, and Z. Ming, "Joint optimization of sensing, decision-making and motion-controlling for autonomous vehicles: A deep reinforcement learning approach," *IEEE Transactions on Vehicular Technology*, 2022.